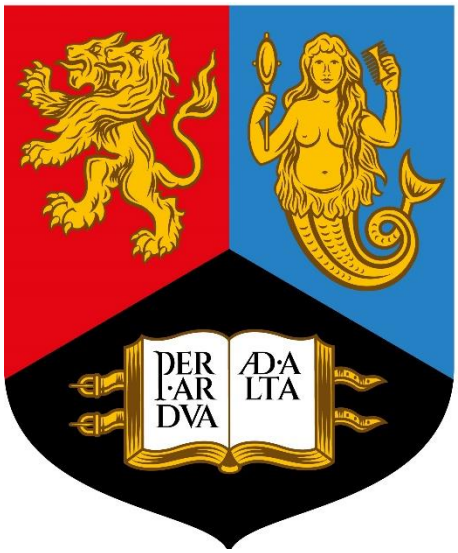
Synthesis and crystallisation-driven self-assembly of ε-substituted poly(ε-caprolactones).

by

Ana Cubillo Álvarez



A thesis submitted to the University of Birmingham for the degree of

DOCTOR OF PHILOSOPHY

School of Chemistry

College of Engineering and Physical Sciences

University of Birmingham

May 2024

UNIVERSITY OF
BIRMINGHAM

University of Birmingham Research Archive

e-theses repository

This unpublished thesis/dissertation is copyright of the author and/or third parties. The intellectual property rights of the author or third parties in respect of this work are as defined by The Copyright Designs and Patents Act 1988 or as modified by any successor legislation.

Any use made of information contained in this thesis/dissertation must be in accordance with that legislation and must be properly acknowledged. Further distribution or reproduction in any format is prohibited without the permission of the copyright holder.

Abstract

The ability to control the morphology and dimensions of nanostructures is critical to enhance their bioavailability and biological interactions. However, the preparation of non-spherical nanoparticles that can covalently incorporate small molecules in the inner core remains challenging and has not been extensively explored. In this regard, crystallisation-driven self-assembly is a powerful strategy that uses amphiphilic block copolymers containing at least one semi-crystalline block to access a great variety of well-defined 1D and 2D nanostructures. Among these semi-crystalline polymers, poly(ε-caprolactone) (PCL) is of high interest owing to its biocompatibility and biodegradability. However, the lack of side group functionality prevents the modification or addition of small molecules, restricting the application of the resultant nanostructures as delivery systems. To overcome this limitation, this thesis focused on the synthesis and self-assembly of substituted PCL-containing amphiphilic block copolymers. The synthesis of semicrystalline substituted PCL was investigated *via* ring-opening polymerisation following three approaches: i) polymerisation of enantioenriched ε-allyl-ε-caprolactone, ii) stereoselective polymerisation using a chiral catalyst and iii) copolymerisation of ε-caprolactone and ε-allyl-ε-caprolactone, in which the allyl functional handle enables the attachment of small molecules post-polymerisation. Following this, crystallisation-driven self-assembly of substituted block copolymers with various degrees of functionalisation was explored on different solvent conditions and at different temperatures to give a range of anisotropic structures. Moreover, biological studies demonstrated well-defined 1D and 2D nanoparticles bearing functionalities in the core-forming block exhibited high biocompatibility and considerable internalisation within the cellular cytoplasm, highlighting the great potential of the system for drug delivery applications.

Acknowledgements

Firstly, I would like to thank my supervisors Prof. Andrew Dove and Maria Chiara Arno for giving me the opportunity to join their groups and for their guidance and support over the past three and a half years. I have enjoyed, learned, and grown a lot during this time, and you have been part of the reason. In special, thank you Andrew for sharing your knowledge and life experiences with me (some of your advice will always be a part of me!). Moreover, I would like to thank Dr Dan Smith for being the best lab technician of all time and Ms Tessa Kintail for your help and for making my life so much easier during these past years.

Next, a massive thanks to all Dove and O'Reilly group members past and present who helped, trained, and supported me during my whole PhD. These years have been an emotional roller-coaster with a lot of ups and downs, and you have always been there to celebrate my small victories or listen to my infinite complaints. I don't know what the future has prepared for me or even if we will see each other again (because I am honestly terrible at keeping in touch) but believe me when I say it was an absolute pleasure to meet you all, I wouldn't be the person I have become without you. Of course, I couldn't leave behind the Arno group members, thank you for your kindness and support, I will always think Chiara's group socials were the best! Special thanks to Amaziah Alipio for training me in the biolab and giving me so much help.

The warmest thanks go to Dr Viviane Chiaradia (Bibi) for going above and beyond with me. You can't imagine how grateful I feel Andrew assigned you as my "super buddy" during my first year, you shaped me as a scientist, taught me how to properly prepare a presentation and write a report, and included me in your group of friends as if we had known each other for years. You are one of the most wonderful and inspiring persons I have ever met, and the mark you have left in me I will carry it forever. Equally, I want to thank Dr Cinzia Clamor for being

the kindest of all. Thank you for letting me hug you during COVID, for all coffee breaks, trips, talks about life and science, and of course for those old happy days in 706 with Vivi and Maher. Even though, it broke my heart seeing you leave the group, it made me realise how lucky I am for having something that is so hard to say goodbye to.

Special thanks to Maher, Natalia, Thiago, Alexis, Sam, Connor, Anissa, Marjo and Jenni for being the best friends ever and making me feel comfortable and loved. I would never forget our trips to the pub (regardless of the place, time, or day of the week), the eternal brunches at Jenni's place or our daily breaks (specially with you Alexis). You have made my time in Birmingham so much happier and fun. Also, I couldn't forget to thank David, Gabi, Bige, Daniele, Flore, and Claire (or as I secretly call them: "the travellers" as they are always in the move) for "forcing" me to take breaks from time to time and for supporting me with everything I have gone through.

Thank you, Arianna and Julia, for being always so helpful and understanding. Also, for being part of the crew that corrected my thesis chapters, you are stars! It was a great experience working next to you (in a very literal way), you both deserve the best and I can't wait to see how far you will go.

It would be impossible not to mention our "most recent" group incorporations: Megan and Susanna, who I feel they have always been in the group, and my favourite dynamic duo Emma and Louisa. Getting to know you and spend time with you was amazing. Thank you for all the good moments in the office and lab, you are the sweetest, I will miss you a lot.

Lastly but not least, I would like to thank my housemate Inesa that has put up with me and cheered me up every day for the past three and a half years. During this time, you have become the closest thing to family I have (I guess is what happens after going through so many

traumatic housing experiences). And my dearest friend (and former housemate) Pete for all the unforgettable memories we built in Gillott Road and your crazy scientific ideas.

Table of Contents

1 Introduction 2

1.1 Nanoparticles for drug delivery 3

1.1.1 Impact of shape for overcoming biological barriers 4

1.2 Polymer crystallisation, stereochemistry, and phase structure. 7

1.2.1 Nucleation and growth of crystals 8

1.2.2 Factors determining crystal structure 11

1.3 Chain-growth polymerisation and “living” polymerisations 13

1.3.1 Ring-opening polymerisation 15

1.3.2 Reversible addition-fragmentation chain-transfer polymerisation 20

1.4 Solution self-assembly of block copolymers 22

1.4.1 Crystallisation-driven self-assembly 24

1.5 Summary 30

1.6 Project aims 32

1.7 References 33

2 Towards enantiopurity: Synthesis of enantioenriched poly(allyl-ε-caprolactones) 42

2.1 Manuscript and overview 42

2.2 Supporting information 61

2.2.1 Experimental details 61

Materials 61

Instrumentation 61

Experimental procedures 63

2.3 Supplementary figures 72

2.4 References 87

3 Synthesis of semicrystalline allyl-functionalised poly(ε-caprolactone) copolymers *via* ring-opening polymerisation 89

3.1 Introduction 89
3.2 Results and discussion 91
3.2.1 Ring-opening polymerisation of ε-caprolactone and ε-allyl-ε-caprolactone 91
3.2.2 Ring-opening copolymerisation (ROCOP) of ε-caprolactone and ε-allyl-ε-caprolactone 93
3.2.3 Thermal properties of PCL-*co*-PACL copolymers 99
3.2.4 Scale-up ring-opening copolymerisation 101
3.3 Conclusions 105
3.4 Experimental 106
3.4.1 Materials 106
3.4.2 Characterisation techniques 106
3.4.3 Experimental procedures 108
3.5 References 112
3.6 Appendix (supporting figures) 115
4 Crystallisation-driven self-assembly of semicrystalline functional PCL amphiphilic block copolymers 126
4.1 Introduction 126
4.2 Results and discussion 129
4.2.1 Synthesis of PDMA-*b*-PCL block copolymers as "control" 129
4.2.2 Synthesis of PDMA-*b*-PCL-*co*-PACL copolymers and functionalisation 130
4.2.3 Crystallisation-driven self-assembly of PCL-based block copolymers. 140
4.2.4 Exploring the optimal conditions for CDSA of PCL-based copolymers. 158
4.3 Conclusions 172
4.4 Experimental section 173
4.4.1 Materials 173
4.4.2 Characterisation techniques 173

4.4.3 Experimental procedures....175
4.5 References....180
4.6 Supporting figures....183
4.6.1 $PDMA_w$-*b*-PCL_x copolymers....183
4.6.2 Amphiphilic functional block copolymers....185
4.6.3 Crystallisation-driven self-assembly....198
5 Understanding the living CDSA and biological performance of $PDMA_w$-*b*-($PMMA_{20}$)-*b*-PCL_x-*co*-$PACL_y$ copolymers. 205
5.1 Introduction....205
5.2 Results and discussion....207
5.2.1 Synthesis of amphiphilic, semicrystalline, functional BCPs....207
5.2.2 Crystallisation-driven self-assembly....216
5.2.3 Living CDSA of functional PCL-containing copolymers....220
5.2.4 Biological essays....232
5.3 Conclusions....241
5.4 Experimental section....242
5.4.1 Materials....242
5.4.2 Characterisation techniques....242
5.4.3 Experimental procedures....245
5.5 References....251
5.6 Supporting figures....255
6 Conclusions and future perspectives....277

List of symbols and abbreviations

δ	Chemical shift
λ	Wavelength
χ_c	Crystallisation degree
ΔG	Free Gibbs energy
ΔH_m	Enthalpy of melting
ΔS_m	Entropy of melting
$[\ ]_0$	Initial concentration
1D	One-dimensional
2D	Two-dimensional
Å	Amstrong
A_n	Number area average
ACH	2-Allyl-cyclohexanone
εACL	ε-Allyl- ε-caprolactone
AIBN	2,2'-Azobis(2-methylpropionitrile)
AFM	Atomic Force Microscopy
AKRP	Asymmetric kinetic resolution polymerisation
BCP	Block copolymer
BINOL	1,1'-binaphthyl-2,2'-diyl hydrogenphosphate
BODIPY	4,4-difluoro-1,3,5,7-tetramethyl-8-[(10-mercapto)]-4-bora-3a,4a-diaza-*s*-indacene
°C	Celsius degree
CHPET	2-cyano-5-hydroxypentan-2-yl ethyl carbonotrithioate
C_6D_6	Deuterated benzene
$CDCl_3$	Deuterated chloroform
CDSA	Crystallization-driven self-assembly
$CHCl_3$	Chloroform
CHPET	2-cyano-5-hydroxypentan-2-yl ethyl carbonotrithioate
εCL	ε-Caprolactone
CLSM	Confocal laser scanning microscopy
C_p	Heat capacity

CO_2	Carbon dioxide
Conc.	Concentration
Conv.	Conversion
CTA	Chain transfer agent
DCM	Dichloromethane
DLS	Dynamic light scattering
$Đ_M$	Molecular weight dispersity
DMA	*N*,*N*-dimethylacrylamide
DMEM	Dulbecco's modified eagle medium
DMF	*N*,*N*-Dimethyl formaldehyde
DMPA	2,2-dimethoxy-2-phenylacetophenone
DP	Degree of polymerisation
DPP	Diphenyl phosphate
DOSY	Diffusion-Oriented Spectroscopy
DSC	Differential scanning calorimetry
ee	Enantiomeric excess
equiv.	Equivalents
er	Enantiomeric ratio
Et_3N	Triethyl amine
EtOAc	Ethyl acetate
EtOH	Ethanol
Et_2O	Diethyl ether
FBS	Fetal bovine serum
GCMS	Gas chromatography – Mass spectrometry
h	Hours
HRMS	High-resolution mass spectroscopy
Hz	Hertz
IPA	2-Isopropanol
K	Kelvin
KCO_3	Potassium carbonate
kDa	Kilodaltons

LA	Lactic acid
L_n	Number average length
L_w	Weigh average length
mg	Milligram
mL	Millilitre
µJ	Microjoule
µL	Microlitre
µm	Micrometre
MMA	Methyl methacrylate
MeOH	Methanol
$MgSO_4$	Magnesium sulphate
min	Minutes
mmol	Millimole
M_n	Number average molar mass
Mol	Mole
M_w	Mass average molar mass
mW	Milliwatts
N_2	Nitrogen
$NaHCO_3$	Sodium bicarbonate
NaOH	Sodium hydroxide
NH_4Cl	Ammonium chloride
nm	nanometres
NMR	Nuclear Magnetic Resonance
NPs	Nanoparticles
PACL	Poly(ε-allyl-ε-caprolactone)
PBS	Phosphate-buffered saline solution
PCL	Poly(ε-caprolactone)
PCR	Polymerase chain reaction
PDMA	Poly(dimethylacrylamide)
PFS	Polyferrocenylsilane
PLA	Poly(lactic acid)

PMMA	Poly(methyl methacrylate)
ppm	Part per million
rac	racemic
RAFT	Reversible addition-fragmentation chain transfer
ROCOP	Rin-opening copolymerisation
ROP	Ring-opening polymerisation
RT	Room temperature
s	Second
***s*-factor**	Selectivity factor
SεCLs	Substituted ε-caprolactones
SEC	Size-exclusion chromatography
SLS	Static light scattering
T	Temperature
t	Time
TADDOL	α,α,α',α'-tetraaryl-1,3-dioxolane-4,5-dimethanols
T_c	Crystallisation temperature
TCEP	Tris(2-carboxyethyl)phosphine
TEM	Transmission electron microscopy
T_g	Glass transition temperature
THF	Tetrahydrofuran
TLC	Thin-layer chromatography
T_m	Melting temperature
TRIP	2,4,6-triisopropylphenyl
UA	Uranyl acetate
UV	Ultraviolet
***vs*.**	versus
v/v	Volume per volume
W_n	Number width average
wk	weeks
wt. %	Weight percent

List of Figures

Figure 1.1. Overview highlighting some of the applications of polymeric nanoparticles. 2

Figure 1.2. Nanoparticle rational design implementation for overcoming delivery barriers. Nanoparticle size, shape, and surface charge (a, b, and c, respectively) dictate biodistribution among the different organs including the lungs, liver, spleen, and kidneys. Figure reproduced from Ferrari and coworkers.[18] 4

Figure 1.3. Types of cellular internalisation and nanoparticle size limitations. Large solid particles (> 1 μm) are internalised by (a) phagocytosis, while extracellular solutes and fluids (up to 10 μm) can undergo non-specific internalisation through (b) macropinocytosis. Submicron particles can be uptaken through several pathways: c) caveolar-mediated endocytosis, d) clathrin-mediated endocytosis and d) chlatrin-independent and caveolin-independent endocytosis. Figure reproduced from DeSimone and coworkers.[31] 6

Figure 1.4. Schematic representation of semicrystalline chain arrangement models. a) Fringed-Micelle model proposed by Staudinger. b) Chain-Folding model proposed by Keller. 8

Figure 1.5. Schematic diagrams showing (a) power compensation and (b) heat-flux DSC and expected thermograms of a semicrystalline polymer. Figure adapted from references [53, 58]. 10

Figure 1.6. Stereochemistry of polypropylene (PP) and thermo-mechanical properties. 12

Figure 1.7. Growth of polymers with time. a) Linear relationship between $\ln([M]_0/[M]_t)$ and time indicates first order kinetics, characteristic of living polymerisations. b) increase in active species because of slow initiation c) decrease in propagating species as a result of termination reactions ("dead" chains formation). Figure adapted from Matyjaszewski and coworkers.[92] 14

Figure 1.8. Example of macromolecular architectures achieved through living polymerisation. 15

Figure 1.9. Routes to control polymer tacticity. a) Polymerisation of a stereopure monomer. b) asymmetric kinetic resolution polymerisation of a racemic monomer using a stereoselective catalyst. 20

Figure 1.10. a) Types of chain-transfer agents (CTA). b) Mechanism of reversible addition-fragmentation chain-transfer (RAFT) polymerisation. * Correspond to active radical species, M and P correspond to monomer and polymer respectively. 22

Figure 1.11. a) Changes on self-assembly interfacial curvatures with increasing packing parameter (ρ). b) Equilibrium morphology of AB copolymers while varying the block's mole fraction (*f*). Figure reproduced from ref.[156] 23
Figure 1.12. Thermally induced crystallisation-driven self-assembly (CDSA) of amphiphilic semicrystalline block copolymers. 25
Figure 1.13. Schematic illustration of living CDSA of PFS-containing block copolymers by epitaxial growth. a-d) TEM images of monodisperse cylindrical micelles of PFS-*b*-PI with various lengths obtained by addition of PFS-*b*-PI solutions at increasing concentrations. e) Length distribution and linear dependence of cylindrical micelles. Figure reproduced from Manners and coworkers.[178] 28
Figure 1.14. Platelets micelles with rectangular and hexagonal geometry obtained from the 2D epitaxial growth *via* living CDSA using different PFS-based crystalline seeds. Figure reproduced from Manners and corworkers.[182] 29
Figure 2.1. (A) Asymmetric syntheses of enantiopure substituted ε-caprolactones (ε-SCL). **(B)** Classical stereoselective ring-opening polymerizations (ROP) of ε-SCL. **(C)** This work: preparation of stereoregular allyl-substituted poly(caprolactones) combining a highly enantioenriched monomer with a stereoselective catalysts. 48
Figure 2.2. (A) Kinetic plots for the polymerisation of rac-εACL catalysed by (R)- and (S)-TRIP BINOL at 40 °C. **(B)** GC-MS chromatograms of rac-εACL (left), residual ACL after polymerisation with (R)-TRIP BINOL (middle) and residual εACL after polymerisation with (S)-TRIP BINOL (right)..... 52
Figure 2.3. (A) Synthesis of enantioenriched (S)-allylcaprolactone ((S)-εACL) through deracemization of racemic 2-allylcyclohexanone (rac-ACH) via host-guest chemistry using a TADDOL as the chiral host molecule, followed by Bayer-Villiger oxidation. **(B)** Stacked ^{1}H NMR spectra ($CDCl_3$, 300 MHz) of (S)-εACH (top) and (S)-εACL (bottom). **(C)** GC-MS chromatogram of enantioenriched (S)-εACL. 53
Figure 2.4. (A) Kinetic plots for the polymerisation of rac-ACL catalysed by DPP and enantioenriched εACL catalysed by (R)- and (S)-TRIP BINOL. Polymerisations were quenched before 50% conversion. **(B)** Model of AKRP of enantioenriched εACL with TRIP BINOL catalyst. **(C)** GC-MS chromatogram of unreacted monomer from (R)-TRIP BINOL-catalysed polymerization with enantioenriched (R)-ACL. **(D)** GC-MS chromatograms of unreacted

monomer from (R)-TRIP BINOL-catalysed ROP with enantioenriched (S)-ACL (left) and (S)-TRIP BINOL-catalysed ROP with enantioenriched (R)-ACL (right). 55
Figure 2.5. (A) SEC chromatograms of enantioenriched (R)- and (S)- polymers (**10** and **11**) and "stereoblock" PACL (**7**) ($CHCl_3$, with 0.5% Et_3N, PMMA standard). **(B)** DSC thermograms of rac-PACL, enantioenriched (R)-PACL catalysed by DPP (**8**), enantioenriched (R)-PACL catalysed by (S)-TRIP BINOL (**10**), enantioenriched (R)-PACL catalysed by (S)-TRIP BINOL (**11**) and of rac-PACL catalysed by (R)- and (S)-TRIP BINOL (**7**) (−100 to 100 °C, 10 °C min^{-1}) showing the second heating cycle. 57
Figure 3.1. First order kinetic plot for the ROP of εCL and rac-εACL at 40 °C using DPP (10 mmol%), $[monomer]_0$:$[CTA]_0$ = 50 in C_6D_6. 93
Figure 3.2. ^1H NMR spectrum (300 MHz, 298 K, $CDCl_3$) of PCL_{46}-co-$PACL_{20}$ copolymer (**CP6** in Table 3.1) with an initial PCL:PACL target = 50:35. 95
Figure 3.3. Kinetic plot of monomer conversion against time for the copolymerisation of εCL and εACL (**CP8** in Table 3.1). Conditions: overall monomer concentration ([M]) = 2 M in C_6D_6, [CL]:[ACL]:[CTA] = 50:50:1 using 2-cyano-5-hydroxypentan-2-yl ethyl carbonotrithioate (CHPET) as initiator, 10 mol% of DPP. 97
Figure *3.4*. DOSY ^1H NMR spectra (400 MHz, 298 K, $CDCl_3$) of PCL-*co*-PACL copolymer targeted at 50:50 (**CP8** in Table 3.1). 97
Figure 3.5. Quantitative ^{13}C NMR spectrum (500 MHz, 298 K, $CDCl_3$) corresponding to the carbonyl region of PCL-co-PACL copolymers targeted at 50:10 (left, **CP2** in Table 3.1) and 50:50 (right, **CP8** in Table 3.1). 98
Figure 3.6. DSC thermograms of the PCL_x-co-$PACL_y$ copolymers (−100 to 100 °C, 10 °C min^{-1}) showing the second heating-cooling cycle. **(a)** and **(b)** correspond to the heating cycles (endothermic process). **(c)** and **(d)** correspond to the cooling cycles (exothermic process). 101
Figure 3.7. Stacked ^1H NMR spectra ($CDCl_3$, 300 MHz) of copolymers with 6 wt.%, 15 wt.% and 18 wt.% of εACL incorporation (entry **CP9, CP10** and **CP11** in Table 3.3). 103
Figure 3.8. (A) SEC chromatograms of the PCL-co-PACL copolymers ($CHCl_3$, with 0.5% Et_3N, PMMA standard); **(B)** DSC thermograms of the respective copolymers (−100 to 100 °C, 10 °C min^{-1}) showing the second heating-cooling cycle (endo-down and exo-up). 103
Figure 4.1. ^1H NMR spectrum ($CDCl_3$, 300 MHz) of $PDMA_{208}$-b-PCL_{44}-co-$PACL_7$ block copolymer. 132

Figure 4.2. SEC chromatogram of $PDMA_{208}$-b-PCL_{44}-co-$PACL_7$ block copolymer ($CHCl_3$, with 0.5% Et_3N, PMMA standard). 132
Figure 4.3. (A) Scheme for the RAFT polymerisation scheme of DMA with poly(ε-allyl-ε-caprolactone) macroinitiator (CTA-PACL). **(B)** Schematic illustration of hypothesised crosslinking side reaction. **(C)** PDMA-b-$PACL_{55}$ gel. 133
Figure 4.4. SEC chromatograms of $PDMA_w$-b-PCL_x-co-$PACL_y$ copolymers T1, T5 and T11 in Table 4.2 ($CHCl_3$, with 0.5% Et_3N, PMMA standard). 135
Figure 4.5. Stacked ^1H NMR spectra ($CDCl_3$, 300 MHz) of PCL_{54}-co-$PACL_3$ copolymer (bottom) and $PMMA_{20}$-b-PCL_{54}-co-$PACL_3$ block copolymers (top). 137
Figure 4.6. SEC chromatograms of PCL_{54}-co-$PACL_3$, $PMMA_{20}$-b-PCL_{44}-co-$PACL_3$ and $PDMA_{156}$-b-$PMMA_{20}$-b-PCL_{44}-co-$PACL_3$ block copolymers ($CHCl_3$, with 0.5% Et_3N, PMMA standard). 137
Figure 4.7. Stacked ^1H NMR spectra ($CDCl_3$, 300 MHz) of $PDMA_{130}$-b-PCL_{43}-co-$PACL_7$ copolymer (**T2** in Table 4.2, top) and benzyl functionalised $PDMA_{130}$-b-PCL_{43}-co-$PACL_7$ block copolymers (**Thiol-T2** in Table S4.2, bottom). Zoom showing the allyl protons. *Correspond to diethyl ether peaks. 139
Figure 4.8. SEC chromatograms of $PDMA_{130}$-b-PCL_{43}-co-$PACL_7$ (**T2**, black line) and benzyl functionalised $PDMA_{130}$-b-PCL_{43}-co-$PACL_7$ block copolymers (**Thiol-T2**, purple line) ($CHCl_3$, with 0.5% Et_3N, PMMA standard). 140
Figure 4.9. Self-assembly of $PDMA_x$-b-PCL_{49} block copolymers with different corona lengths. TEM micrographs of $PDMA_{96}$-b-PCL_{49} (ratio 2:1), $PDMA_{163}$-b-PCL_{49} (ratio 3:1), $PDMA_{204}$-b-PCL_{49} (ratio 4.2:1), $PDMA_{309}$-b-PCL_{49} (ratio 6.3:1), $PDMA_{474}$-b-PCL_{49} (ratio 9.6:1) after one week of aging. Samples were negatively stained using uranyl acetate (0.5 wt.%)..... 142
Figure 4.10. Self-assembly of $PDMA_w$-b-PCL_x-co-$PACL_y$ block copolymers with different corona lengths (Table 4.2). Samples were negatively stained using uranyl acetate (0.5 wt.%)..... 144
Figure 4.11. TEM images for the self-assembly of $PDMA_{474}$-b-PCL_{49} (left) and $PDMA_{456}$-b-PCL_{43}-co-$PACL_7$ (T10, right). Samples were imaged after 1 and 18 weeks respectively. Samples were negatively stained using uranyl acetate (0.5 wt.%), and white marks in TEM images correspond to grid artefacts. 146
Figure 4.12. Changes in the morphology of $PDMA_w$-b-PCL_x-co-$PACL_y$ assemblies with increased allyl content (wt.%) maintaining similar corona block length. **A)** Self-assembly of $PDMA_{94}$-b-PCL_{44}-co-$PACL_3$ (**T1**) and $PDMA_{130}$-b-PCL_{43}-co-$PACL_7$ (**T2**) block copolymers (red boxes). **B)** Self-assembly of $PDMA_{237}$-b-PCL_{36}-co-$PACL_3$ (**T6**) and $PDMA_{362}$-b-PCL_{46}-co-$PACL_8$ (**T7**) block

copolymers (green boxes). Samples were negatively stained using uranyl acetate (0.5 wt.%). 147

Figure 4.13. Changes in the morphology of $PDMA_w$-b-PCL_x-co-$PACL_y$ assemblies with increased corona block length maintaining the same allyl content (wt. %). Self-assembly of $PDMA_{130}$-b-PCL_{43}-co-$PACL_7$ block copolymers (**T2**, left) and $PDMA_{456}$-b-PCL_{43}-co-$PACL_7$ (**T10**, right). Samples were aged for 11 weeks and 18 weeks respectively. Samples were negatively stained using uranyl acetate (0.5 wt.%). 148

Figure 4.14. Self-assembly of $PDMA_w$-b-$PMMA_n$-b-PCL_x-co-$PACL_y$ block copolymers with different corona lengths (Table 4.4). Samples were negatively stained using uranyl acetate (0.5 wt.%). 150

Figure 4.15. Growth over time of cylindrical micelles from $PDMA_{57}$-b-$PMMA_{20}$-b-PCL_{38}-co-$PACL_4$ (**M1**). Samples were negatively stained using uranyl acetate (0.5 wt.%). 151

Figure 4.16. Self-assembly of benzyl functionalised $PDMA_w$-b-PCL_x-co-$PACL_y$ block copolymers with different corona lengths (Table S4.3). Samples were negatively stained using uranyl acetate (0.5 wt.%). White spots correspond to grid artefacts. 153

Figure 4.17. A) Self-assembly of T1 (left) and Thiol-T1 (right). **B)** Self-assembly of T5 (left) and Thiol-T5 (right). **C)** Self-assembly of T2 (left) and Thiol-T2 (right). **D)** Self-assembly of T10 (left) and Thiol-T10 (right). All samples were 100% functionalized. Samples were negatively stained using uranyl acetate (0.5 wt.%). White spots correspond to grid artefacts. 154

Figure 4.18. Nano DSC thermograms of $PDMA_{130}$-*b*-PCL_{43}-*co*-$PACL_7$ and benzyl conjugated $PDMA_{130}$-*b*-PCL_{43}-*co*-$PACL_7$ assemblies (**T2** and **Thiol-T2**, respectively) (100 to 0 °C, 1 °C min^{-1}) at a conc. = 5 mg mL^{-1}, showing the first heating-cooling cycle. 155

Figure 4.19. Changes in nanostructure morphology with the increase of benzyl conjugation (%). **A)** Schematic illustration of hypothesised benzyl groups effect during self-assembly. **B)** Self-assembly of benzyl functionalised $PDMA_{362}$-b-PCL_{46}-co-$PACL_8$ (**Thiol-T7**) with 50% conjugation (left) and 100% conjugation (right). **C)** Self-assembly of benzyl functionalised $PDMA_{412}$-b-PCL_{36}-co-$PACL_4$ (**Thiol-T11**) with 50% conjugation (left) and 100% conjugation (right). All samples were aged for 18 weeks before imaging. Samples were negatively stained using uranyl acetate (0.5 wt.%). 156

Figure 4.20. Self-assembly of benzyl functionalised $PDMA_{156}$-b-$PMMA_{20}$-b-PCL_{54}-co-$PACL_3$ (**Thiol-M2**), benzyl functionalised $PDMA_{57}$-b-$PMMA_{20}$-b-PCL_{38}-co-$PACL_4$ (**Thiol-M1**) and benzyl functionalised $PDMA_{330}$-b-$PMMA_{18}$-b-PCL_{46}-co-$PACL_8$ (**Thiol-M4**). Samples were aged for 2, 3

and 6 weeks before imaging respectively. Samples were negatively stained using uranyl acetate (0.5 wt.%). White spots correspond to grid artefacts. 157
Figure 4.21. Self-assembly of $PDMA_x$-b-PCL_{49} block copolymers with corona:core ratios of 4.2:1, 6.3:1 and 9.6:1 after one week of aging at room temperature (20 °C) (up) and in the fridge (4 °C) (down). Samples were negatively stained using uranyl acetate (0.5 wt.%)..... 160
Figure 4.22. TEM micrographs of $PDMA_{456}$-b-PCL_{43}-co-$PACL_7$ (**T10**, left) and $PDMA_{412}$-b-PCL_{36}-co-$PACL_4$ (**T11**, right) at room temperature (20 °C) (up) and in the fridge (4 °C) (down). Samples were negatively stained using uranyl acetate (0.5 wt.%)..... 161
Figure 4.23. A-B) TEM micrographs of **Thiol-T1** aged at 20 °C and 4 °C respectively (light blue box). **C-D)** TEM micrographs of **Thiol-T6** aged at 20 °C and 4 °C respectively (pink box). **E-F)** TEM micrographs of **Thiol-T11** aged at 20 °C and 4 °C respectively (purple box). Samples were negatively stained using uranyl acetate (0.5 wt.%) and analysed at a conc. = 5 mg mL^{-1}..... 162
Figure 4.24. Effect of aging temperature on the quantitative appearance. TEM micrographs of $PDMA_{122}$-b-PCL_{53}-co-$PACL_3$ (**T1**, up) and $PDMA_{330}$-b-$PMMA_{18}$-b-PCL_{46}-co-$PACL_8$ (**M4**, down) at room temperature (20 °C) (left) and in the fridge (4 °C) (right). Samples were negatively stained using uranyl acetate (0.5 wt.%) and analysed at a conc. = 5 mg mL^{-1}..... 163
Figure 4.25. TEM micrographs of $PDMA_{89}$-b-PCL_{39}-co-$PACL_3$ cylindrical micelles. **A)** slow cool down to $T < T_c$ and aged at room temperature (20 °C). **B)** fast cool down to $T < T_c$ and aged at room temperature (20 °C). **C)** slow cool down to $T < T_c$ and aged in the fridge (4 °C). **D)** fast cool down to $T < T_c$ and aged in the fridge (4 °C) (right). Samples were aged for 2 weeks and negatively stained using uranyl acetate (0.5 wt.%)..... 165
Figure 4.26. TEM micrographs of self-assembly in **MeOH** of T5 (blue box), T6 (pink box) T7 (red box), T10 (green box) and T11 (purple box) aged for 1, 3 and 2 weeks respectively, at 20 °C and 4 °C. Samples were negatively stained using uranyl acetate (0.5 wt.%) and analysed at conc. = 5 mg mL^{-1}..... 168
Figure 4.27. TEM micrographs of self-assembly in **IPA** of T5 (blue box), T6 (pink box) T7 (red box), T10 (green box) and T11 (purple box) aged for 1, 3 and 2 weeks respectively, at 20 °C and 4 °C. Samples were negatively stained with uranyl acetate (0.5 wt.%) and analysed at conc. = 5 mg mL^{-1}. White spots correspond to grid artefacts. 169
Figure 4.28. TEM micrographs of **Thiol-T6** and **Thiol-T11** in MeOH and IPA after 3 weeks aging at 20 °C and 4 °C respectively. Samples were negatively stained using uranyl acetate (0.5 wt.%) and analysed at conc. = 5 mg mL^{-1}. White spots correspond to grid artefacts. 171

Figure 5.1. Stacked ^{1}H NMR spectra ($CDCl_3$, 300 MHz, 298 K) of PCL_{54}-*co*-$PACL_3$, $PMMA_{20}$-*b*-PCL_{54}-*co*-$PACL_3$, and $PDMA_{156}$-*b*-$PMMA_{20}$-*b*-PCL_{54}-*co*-$PACL_3$ block copolymers (P3, P4, and P7 in Table 5.1 respectively)..... 210

Figure 5.2. Photo-initiated thiol-ene addition of BODIPYC_{10}SH to εACL using irgacure 819 (20 mmol%) as photo-intiator. [Monomer]:[thiol] ratio 1:1, 56 wt. %, UV source of 405 nm**. (A)** Stacked ^{1}H NMR spectra ($CDCl_3$, 300 MHz, 298 K) of allyl monomer (bottom), bodipyC_{10}SH (middle) and reaction mixture after 4.5 h of UV radiation (top). * Correspond to BODIPY-C_{10}-SH degradation peaks. **(B)** Image of reaction mixture before (left) and after UV radiation (right) indicating photo-bleaching of BODIPY dye. 213

Figure 5.3. (A) Stacked ^{1}H NMR spectra (d_8-toluene (*), 300 MHz, 298 K) of the reaction crude for the thermo-initiated thiol-ene addition of BODIPYC_{10}SH to allyl(ε-caprolactone) after 1.5 days and 2.5 days. **(B)** Thin layer chromatography of monomer (left spot), BODIPYC_{10}SH (middle spot) and reaction crude after 2.5 days (right spot) under UV-light..... 214

Figure 5.4. Stacked ^{1}H NMR spectra ($CDCl_3$, 300 MHz) of $PDMA_{89}$-*b*-PCL_{39}-*co*-$PACL_3$ (P5, top) and BODIPY-conjugated $PDMA_{89}$-*b*-PCL_{43}-*co*-$PACL_3$ block copolymer (bottom). 215

Figure 5.5. SEC chromatograms of $PDMA_{89}$-*b*-PCL_{39}-*co*-$PACL_3$ (**P5**) before and after functionalisation with BODIPYC_{10}SH *via* thermo-initiated thiol-ene addition ($CHCl_3$, with 0.5% Et_3N, PMMA standard, UV sensors λ = 309 nm and 500 nm). 216

Figure 5.6. General procedure for the crystallization-driven self-assembly (CDSA) of amphiphilic block copolymers with a semicrystalline core block. **A)** TEM micrograph of $PDMA_{89}$-*b*-PCL_{39}-*co*-$PACL_3$ (P5) assemblies. **B)** TEM micrograph of $PDMA_{94}$-*b*-PCL_{44}-*co*-$PACL_3$ (P6) assemblies. **C)** TEM micrograph of $PDMA_{156}$-*b*-$PMMA_{20}$-*b*-PCL_{54}-*co*-$PACL_3$ (P7) assemblies. Samples were negatively stained using uranyl acetate (0.5 wt %). 217

Figure 5.7. TEM micrographs of the self-assembly of BODIPY conjugated $PDMA_{89}$-*b*-PCL_{39}-*co*-$PACL_3$ (**P5**) and $PDMA_{156}$-*b*-$PMMA_{20}$-*b*-PCL_{54}-*co*-$PACL_3$ (**P7**) assemblies. Samples were negatively stained using uranyl acetate (0.5 wt %). 218

Figure 5.8. Nano DSC thermograms (100 to 0 °C, 1 °C min^{-1}) showing first cooling-heating cycle of $PDMA_{156}$-*b*-$PMMA_{20}$-*b*-PCL_{54}-*co*-$PACL_3$ (P7) and BODIPY conjugated $PDMA_{156}$-*b*-$PMMA_{20}$-*b*-PCL_{54}-*co*-$PACL_3$ (Bodipy-P7). 218

Figure 5.9. (A-B) TEM micrographs of $PDMA_{89}$-*b*-PCL_{39}-*co*-$PACL_3$ in ethanol and water, respectively**. (C-D)** TEM micrographs of BODIPY conjugated $PDMA_{156}$-*b*-$PMMA_{20}$-*b*-PCL_{54}-*co*-$PACL_3$. 219

Figure 5.10. TEM micrographs of polymer seeds after sonication for 4 h. **A)** $PDMA_{117}$-*b*-PCL_{48} seed solution. **B)** $PDMA_{154}$-*b*-PCL_{48} seed solution. **C)** of $PDMA_{94}$-*b*-PCL_{44}-*co*-$PACL_3$ seed solution. **D)** of $PDMA_{112}$-*b*-PCL_{53}-*co*-$PACL_3$ seed solution. Samples were negatively stained using uranyl acetate (0.5 wt %). 221

Figure 5.11. 1D living CDSA of $PDMA_{117}$-*b*-PCL_{48} and $PDMA_{122}$-*b*-PCL_{53}-*co*-$PACL_3$ block copolymers using both BCPs seed solutions with targeted unimer/seed ratios 2 and 4. Samples were negatively stained using uranyl acetate (0.5 wt %). 222

Figure 5.12. TEM micrographs for the 1D epitaxial growth of $PDMA_{94}$-*b*-PCL_{44}-*co*-$PACL_3$ (P6) self-assembled in ethanol using $PDMA_{154}$-*b*-PCL_{48} seeds with m_{unimer}/m_{seeds} ratios 2, 4, 6, and 8. Samples were negatively stained using uranyl acetate (0.5 wt %). 224

Figure 5.13. A) Size distribution averaged by intensity over the same time. Measured by dynamic light scattering (DLS). Each sample was repeated three times. **B)** Number length average (L_n) *vs*. unimer/seed ratio for the 1D epitaxial growth of $PDMA_{94}$-*b*-PCL_{44}-*co*-$PACL_3$ (P6), calculated from particle analysis-based TEM images. 224

Figure 5.14. TEM micrographs for the 1D epitaxial growth of BODIPY-conjugated $PDMA_{156}$-*b*-$PMMA_{20}$-*b*-PCL_{54}-*co*-$PACL_3$ (BODIPY-P7) using $PDMA_{154}$-*b*-PCL_{48} seeds with m_{unimer}/m_{seed} ratios varying from 2, 4, and 6. Samples were negatively stained using uranyl acetate (0.5 wt %). Table with micelle length summary. 225

Figure 5.15. 2D epitaxial growth of BODIPY conjugated $PDMA_{156}$-*b*-$PMMA_{20}$-*b*-PCL_{54}-*co*-$PACL_3$ (BODIPY-P7) self-assembled in ethanol at 0.01 mg ml^{-1} with m_{PCL48}/m_{unimer} = 1. **A)-E)** TEM micrographs showing platelet growth with m_{unimer}/m_{seeds} ratios of 5, 10, 20, 30 and 45 respectively. Samples were negatively stained using uranyl acetate (0.5 wt %). **F)-J)** Confocal images of corresponding BODIPY-conjugated platelets, showing the fluorescence field. (confocal images collected by Mr. Tianlai Xia). 227

Figure 5.16. Number area average (A_n) *vs*. unimer/seed ratio, calculated from particle analysis-based TEM images, for the 2D epitaxial growth of BODIPY-P7 using $PDMA_{154}$-*b*-PCL_{48} seeds. 228

Figure 5.17. TEM micrographs of 2D platelets of $PDMA_{94}$-*b*-PCL_{44}-*co*-$PACL_3$ (**P6**) and $PDMA_{156}$-*b*-$PMMA_{20}$-*b*-PCL_{54}-*co*-$PACL_3$ (**P7**) with m_{PCL48}/m_{unimer} = 1 and m_{unimer}/m_{seeds} ratios corresponding to 30 and 10 respectively, before dialysis to water and after aging for 1 month in water. Samples were negatively stained using uranyl acetate (0.5 wt.%). 229

Figure 5.18. TEM micrographs of 2D platelets of BODIPY functionalized $PDMA_{156}$-*b*-$PMMA_{20}$-*b*-PCL_{54}-*co*-$PACL_3$ with m_{PCL48}/m_{unimer} = 1 and m_{unimer}/m_{seeds} ratios corresponding to 10, 20 and 30 before dialysis to water and after 1 month into water. Samples were negatively stained using uranyl acetate (0.5 wt %). 230

Figure 5.19. 2D epitaxial growth of multilayered platelets of bodipy-conjugated $PDMA_{156}$-*b*-$PMMA_{20}$-*b*-PCL_{54}-*co*-$PACL_3$ (BODIPY-P7) self-assembled in ethanol at 0.1 mg ml^{-1}. **A)** Schematic illustration for the 2D epitaxial growth of multilayered platelets **B)** TEM micrographs of bilayered platelets. Samples were negatively stained using uranyl acetate (0.5 wt %). **C)** Confocal images of correspondent multilayered platelets, showing the fluorescence field (confocal images collected by Mr. Tianlai Xia). 232

Figure 5.20. TEM micrographs of 2D living growth solutions of $PDMA_{94}$-*b*-PCL_{44}-*co*-$PACL_3$ unimer co-crystallized with PCL_{48} homopolymer onto seeds of $PDMA_{154}$-*b*-PCL_{48} where m_{PCL48}/m_{unimer} = 1, with m_{unimer}/m_{seeds} ratios 5 and 10. 233

Figure 5.21. Cell viability at 24 and 72 h of NIH 3T3 cell using concentrations of $PDMA_{94}$-*b*-PCL_{44}-*co*-$PACL_3$ from 0 to 2 mg mL^{-1} 235

Figure 5.22. Cell viability percentages at 24 and 72 h of NIH 3T3 using platelet particles with **(A)** m_{unimer}/m_{seeds} ratio 5 and **(B)** ratio 10 at concentrations ranging from 0 to 2 mg mL^{-1} after 24 h drying. 236

Figure 5.23. (A-B) Cell viability percentages at 24 and 72 h using platelet with m_{unimer}/m_{seeds} ratios 5 and 10 at concentrations ranging from 0 to 2 mg mL^{-1} after 5 days drying. **(C)** Cell viability percentages at 24 and 72 h using platelet with ratio 5 at concentrations ranging from 0 to 0.4 mg mL^{-1} after 5 days drying. **(D)** Cell viability percentages over 24 and 72 h after placing cells on top of platelet solutions from 0.5 to 2 mg mL^{-1}. 238

Figure 5.24. Confocal imaging of NIH 3T3 after 24 h of incubation with BODIPY-Platelets (1 mg mL^{-1}). Cells were washed with PBS and cell tracker (NucRed) was added before imaging. Showing fluorescent fields at λ = 647-665 nm (NucRed) and λ = 503-512 nm (BODIPY), and merged fields. Scale bar = 20 μm. 240

List of Supporting Figures

Figure S2.1. ^{1}H NMR spectrum of CEPA 300 MHz, 298 K, $CDCl_3$..... 72

Figure S2.2. ^{1}H NMR spectrum of CHPET 300 MHz, 298 K, $CDCl_3$. 72

Figure S2.3. ^{13}C NMR spectrum of CHPET, 101 MHz, 298 K, $CDCl_3$..... 73

Figure S2.4. ^{1}H NMR spectrum of 2,3-O-benzylidene L-tartrate, $CDCl_3$, 298 K, 300 Hz. 73

Figure S2.5. ^{1}H NMR spectrum of (4R ,5R)-Pentaphenyl-1,3-dioxolane-4,5-dimethanol (TADDOL), 101 MHz, 298 K, $CDCl_3$..... 74

Figure S2.6. ^{13}C NMR spectrum of (4R ,5R)-Pentaphenyl-1,3-dioxolane-4,5-dimethanol (TADDOL), 101 MHz, 298 K, $CDCl_3$..... 74

Figure S2.7. ^{1}H NMR spectrum of ε-allyl-ε-caprolactone (εACL), 400 MHz, 298 K, $CDCl_3$..... 75

Figure S2.8. ^{13}C NMR spectrum of ε-allyl-ε-caprolactone (εACL), 101 MHz, 298 K, $CDCl_3$..... 75

Figure S2.9. Example of kinetic studies for the ROP of εACL. Stacked ^{1}H NMR spectra at different times of polymerisation, C_6D_6, 298 K, 300Hz. 76

Figure S2.10. SEC chromatograms ($CHCl_3$, with 0.5% Et_3N, PMMA standard) for the polymerisation of rac-εACL catalysed by (R)-TRIP BINOL at 25 °C quenched at 50% monomer conversion and 100% monomer conversion (**entries 1 and 2, table 1**). 77

Figure S2.11. SEC chromatograms ($CHCl_3$, with 0.5% Et_3N, PMMA standard) for the polymerisation of rac-εACL catalysed by (R)-TRIP BINOL at 40 °C, quenched at 50% monomer conversion and 100% monomer conversion (**entries 3 and 4, table 1**). 77

Figure S2.12. Kinetic plots for the polymerisation of rac-εACL catalysed by (R)-TRIP BINOL at 25 °C (**entry 2 table 1**)..... 78

Figure S2.13. GC-MS chromatograms and s-factor of residual εACL resulting from the polymerisation of rac-εACL catalysed by (R)-TRIP BINOL at 25 °C (**entry 1, table 1**)..... 78

Figure S2.14. SEC chromatograms ($CHCl_3$, with 0.5% Et_3N, PMMA standard) for the polymerisation of rac-εACL catalysed by (S)-TRIP BINOL at 40 °C, quenched at 50% monomer conversion and 100% monomer conversion (**entries 5 and 6, table 1**). 79

Figure S2.15. DSC thermograms for the polymerisations of rac-εACL (**Table 1**), showing the second heating cycle (−100 to 100 °C, 10 °C min^{-1}). 79

Figure S2.16. ^{1}H NMR spectrum of racemic poly(allyl-ε-caprolactone) (rac-PACL), $CDCl_3$, 298 K, 300Hz. 80

Figure S2.17. ^{1}H NMR spectrum of (S)-enantioenriched poly(allyl-ε-caprolactone) (PACL) obtained from the polymerisation of rac-εACL with (R)-TRIP BINOL (**entry 4 in Table 1**), $CDCl_3$, 298 K, 300Hz..... 80
Figure S2.18. ^{1}H NMR spectrum of (R)-enantioenriched poly(allyl-ε-caprolactone) (PACL) obtained from the polymerisation of rac-εACL with (S)-TRIP BINOL (**entry 6 in Table 1**), $CDCl_3$, 298 K, 300Hz..... 81
Figure S2.19. ^{1}H NMR spectrum of theoretical (R/S) poly(allyl-ε-caprolactone) stereoblock obtained from the polymerisation of rac-εACL with (R)+(S)-TRIP BINOL (1:1) (**entry 7 in Table 1**), $CDCl_3$, 298 K, 300 Hz. 81
Figure S2.20. ^{13}C NMR spectrum of poly(allyl-ε-caprolactone) (PACL), 101 MHz, 298 K, $CDCl_3$. 82
Figure S2.21. GC-MS chromatogram of racemic 2-allylcyclohexanone (rac-ACH) (left), enantioenriched (R)-ACH (middle) and enantioenriched (S)-ACH (right). 82
Figure S2.22. GC-MS chromatograms of rac-εACL (left), enantioenriched (R)-εACL (middle) and enantioenriched (S)-εACL (right). 83
Figure S2.23. ^{1}H NMR spectrum of (R)-enantioenriched poly(allyl-ε-caprolactone) (PACL) obtained from the polymerisation of (R)-εACL (79.0% ee) with DPP (**entry 8 in Table 2**), $CDCl_3$, 298 K, 300 Hz..... 83
Figure S2.24. SEC chromatogram ($CHCl_3$, with 0.5% Et_3N, PMMA standard) for the polymerisation of (R)-εACL catalysed by DPP at 40 °C, polymerization quenched at 90% monomer conversion (**entry 8 in Table 2**). 84
Figure S2.25. ^{1}H NMR spectrum of (R)-enantioenriched poly(allyl-ε-caprolactone) (PACL) obtained from the polymerisation of (R)-εACL (80.3% ee) with (S)-TRIP BINOL (**entry 10 in Table 2**), $CDCl_3$, 298 K, 300 Hz. 84
Figure S2.26. ^{1}H NMR spectrum of (S)-enantioenriched poly(allyl-ε-caprolactone) (PACL) obtained from the polymerisation of (S)-εACL (87.3% ee) with (R)-TRIP BINOL (**entry 11 in Table 2**), $CDCl_3$, 298 K, 300 Hz. 85
Figure S2.27. SEC chromatogram ($CHCl_3$, with 0.5% Et_3N, PMMA standard) for the polymerisation of (R)-εACL catalysed by (R)-TRIP BINOL at 40 °C, polymerization quenched at 50% monomer conversion (**entry 9, table 2**). 86

Figure S2.28. SEC chromatograms ($CHCl_3$, with 0.5% Et_3N, PMMA standard) for the polymerisation of (S)-εACL catalysed by (R)-TRIP BINOL at 40 °C, polymerization quenched at 35% and 23% monomer conversion (**entry 12 and 13, table 2**). 86
Figure S2.29. DSC thermograms for the polymerisations of (*S*)-εACL (*ee* = 87.3%) with (*R*)-TRIP BINOL after quenching the polymerization at 35% and 23% monomer conversion (**entries 12 and 13, Table 2**) showing the second heating cycle (−100 to 100 °C, 10 °C min^{-1})..... 87
Figure S3.1. Kinetic studies for the polymerisation of ε-caprolactone (εCL) catalysed by DPP at 40 °C. Stacked ^1H NMR spectra (300 MHz, 298 K, C_6D_6) of εCL homopolymerisation at different reaction times with pink and green circle representing monomer and polymer peaks, respectively. 115
Figure S3.2. Kinetic plots for the homopolymerisation of εCL. Polymer conversion over time (left) and monomer consumption (right). 116
Figure S3.3. ^1H NMR spectrum (300 MHz, 298 K, $CDCl_3$) of poly(ε-caprolactone) (PCL)..... 116
Figure S 3.4. ^{13}C NMR (101 MHz, 298 K, $CDCl_3$) spectrum of poly(ε-caprolactone) (PCL)..... 117
Figure S3.5. Kinetic studies for the polymerisation of εACL catalysed by DPP at 40 °C. Stacked ^1H NMR spectra (300 MHz, 298 K, C_6D_6) of εACL homo-polymerisation at different reaction times with pink and green circle representing monomer and polymer peaks, respectively. 118
Figure S3.6. Kinetic plots for the homo-polymerisation of εACL. Polymer conversion over time (left) and monomer consumption (right). 118
Figure S3.7. SEC chromatograms of PCL and PACL resulting from the ROP of εCL and εACL ($CHCl_3$, with 0.5% Et_3N, PMMA standard). 119
Figure S3.8. Stacked ^1H NMR spectra (300 MHz, 298 K, C_6D_6) of the ring-opening copolymerisation of εCL and εACL at 1:1 ratio (**CP8** in Table 3.1) at different reaction times. % conversion correspond to the conversion of εCL. Blue box: $CH_2OC{=}O$ monomer resonance. Red box: CH_2OH polymer resonance. 119
Figure S3.9. Stacked ^1H NMR spectra (300 MHz, 298 K, $CDCl_3$) of copolymers PCL_{56}-co-$PACL_4$, PCL_{54}-co-$PACL_7$ and, PCL_{54}-co-$PACL_9$ (targeted at 50:5, 50:10 and 50:15 respectively). * Peak corresponding to residual DCM. ** Peak corresponding to residual n-hexane. 120
Figure S3.10. Stacked ^1H NMR spectra (300 MHz, 298 K, $CDCl_3$) of copolymers PCL_{60}-co-$PACL_{15}$, PCL_{55}-co-$PACL_{20}$ and, PCL_{46}-co-$PACL_{20}$ (targeted at 50:20, 50:25 and 50:35 respectively). * Peak corresponding to residual DCM. ** Peak corresponding to residual n-hexane. 120

Figure S3.11. Stacked ^{1}H NMR spectra (300 MHz, 298 K, $CDCl_3$) of copolymers PCL_{48}-co-$PACL_{24}$, PCL_{62}-co-$PACL_{36}$ and, PCL_{65}-co-$PACL_{42}$ (targeted at 50:40, 50:45 and 50:50 respectively). * Peak corresponding to residual DCM. ** Peak corresponding to residual n-hexane. 121

Figure S3.12. Quantitative ^{13}C NMR spectrum (500 MHz, 298 K, $CDCl_3$) of PCL_{54}-co-$PACL_7$. Zoom showing the carbonyl region. 121

Figure S3.13. Quantitative ^{13}C NMR spectrum (500 MHz, 298 K, $CDCl_3$) of PCL_{108}-co-$PACL_{79}$. Zoom showing the carbonyl region..... 122

Figure S3.14. SEC chromatograms of the respective PCL_x-co-$PACL_y$ copolymers in Table 3.1 ($CHCl_3$, with 0.5% Et_3N, PMMA standard). 123

Figure S3.15. SEC chromatograms of PCL_x-co-$PACL_y$ copolymers synthesised in larger scales presented in Table 3.3 ($CHCl_3$, with 0.5% Et_3N, PMMA standard). 124

Figure S3.16. SEC thermograms (−100 to 100 °C, 10 °C min^{-1}) of PCL_x-co-$PACL_y$ copolymers synthesised in larger scales presented in Table 3.3 showing the second heating-cooling cycle (endo-down and exo-up)..... 124

Figure S4.1. ^{1}H NMR spectrum ($CDCl_3$, 300 MHz, 298 K) of $PDMA_{96}$-b-PCL_{49} (entry 1 in Table 4.2). * Correspond to diethyl ether peaks and **correspond to dioxane peak. 183

Figure S4.2. ^{1}H NMR spectrum ($CDCl_3$, 300 MHz, 298 K) of $PDMA_{163}$-b-PCL_{49} (entry 2 in table 4.2). * Correspond to diethyl ether peaks. 183

Figure S4.3. ^{1}H NMR spectrum ($CDCl_3$, 300 MHz, 298 K) of $PDMA_{204}$-b-PCL_{49} (entry 3 in table 4.2). * Correspond to diethyl ether peaks and **correspond to dioxane peak. 184

Figure S4.4. ^{1}H NMR spectrum ($CDCl_3$, 300 MHz, 298 K) of $PDMA_{309}$-b-PCL_{49} (entry 4 in table 4.2). * Correspond to dioxane peak. 184

Figure S4.5. ^{1}H NMR spectrum ($CDCl_3$, 300 MHz, 298 K) of $PDMA_{474}$-b-PCL_{49} (entry 5 in table 4.2). * Correspond to dioxane peaks. 185

Figure S4.6. Stacked ^{1}H-NMR spectra ($CDCl_3$, 300 MHz, 298 K) of CHPET-CTA (down), PCL_{44}-co-$PACL_3$ copolymer (middle) and $PDMA_{94}$-b-PCL_{44}-co-$PACL_3$ (T1 in table 4.2) block copolymers (top)..... 186

Figure S4.7. ^{1}H NMR spectrum ($CDCl_3$, 300 MHz, 298 K) of $PDMA_{130}$-b-PCL_{43}-co-$PACL_7$ (T2 in Table 4.2). *Correspond to diethyl ether peaks. 187

Figure S4.8. ^{1}H NMR spectrum ($CDCl_3$, 300 MHz, 298 K) of $PDMA_{165}$-b-PCL_{48}-co-$PACL_3$ (T3 in Table 4.2). 187

Figure S4.9. ^{1}H NMR spectrum ($CDCl_3$, 300 MHz, 298 K) of $PDMA_{175}$-b-PCL_{47}-co-$PACL_3$ (T4 in Table 4.2). 188
Figure S4.10. ^{1}H NMR spectrum ($CDCl_3$, 300 MHz, 298 K) of $PDMA_{295}$-b-PCL_{58}-co-$PACL_4$ (T5 in Table 4.2). *Correspond to diethyl ether peaks. 188
Figure S4.11. ^{1}H NMR spectrum ($CDCl_3$, 300 MHz, 298 K) of $PDMA_{237}$-b-PCL_{37}-co-$PACL_3$ (T6 in Table 4.2). 189
Figure S4.12. ^{1}H NMR spectrum ($CDCl_3$, 300 MHz, 298 K) of $PDMA_{362}$-b-PCL_{48}-co-$PACL_8$ (T7 in Table 4.2). 189
Figure S4.13. ^{1}H NMR spectrum ($CDCl_3$, 300 MHz, 298 K) of $PDMA_{350}$-b-PCL_{41}-co-$PACL_6$ (T8 in Table 4.2). *Correspond to diethyl ether peaks. 190
Figure S4.14. ^{1}H NMR spectrum ($CDCl_3$, 300 MHz, 298 K) of $PDMA_{328}$-b-PCL_{31}-co-$PACL_7$ (T9 in Table 4.2). *Correspond to dioxane peak. **Correspond to acetone peak. 190
Figure S4.15. ^{1}H NMR spectrum ($CDCl_3$, 300 MHz, 298 K) of $PDMA_{456}$-b-PCL_{43}-co-$PACL_7$ (T10 in Table 4.2). *Correspond to acetone peak. 191
Figure S4.16. ^{1}H NMR spectrum ($CDCl_3$, 300 MHz, 298 K) of $PDMA_{412}$-b-PCL_{36}-co-$PACL_4$ (T11 in Table 4.2). 191
Figure S4.17. ^{1}H NMR spectrum ($CDCl_3$, 300 MHz, 298 K) of $PDMA_{57}$-b-$PMMA_{20}$-b-PCL_{37}-co-$PACL_4$ (**M1** in Table S4.1). 193
Figure S4.18. ^{1}H NMR spectrum ($CDCl_3$, 300 MHz, 298 K) of $PDMA_{156}$-b-$PMMA_{20}$-b-CL_{54}-co-$PACL_3$ copolymer (**M2** in table S4.1). *Corresponds to acetone peak. 193
Figure S4.19. ^{1}H NMR spectrum ($CDCl_3$, 300 MHz, 298 K) of $PDMA_{233}$-b-$PMMA_{19}$-b-PCL_{43}-co-$PACL_7$ (**M3** in Table S4.1). *Correspond to diethyl ether peak and ** correspond to dichloromethane peak. 194
Figure S4.20. ^{1}H NMR spectrum ($CDCl_3$, 300 MHz, 298 K) of $PDMA_{330}$-b-$PMMA_{18}$-b-PCL_{46}-co-$PACL_8$ (**M4** in Table S4.1). *Correspond to diethyl ether peak. 194
Figure S4.21. ^{1}H NMR spectrum ($CDCl_3$, 300 MHz, 298 K) of $PDMA_{348}$-b-$PMMA_{20}$-b-PCL_{36}-co-$PACL_4$ (**M5** in Table S4.1). *Correspond to diethyl ether peak. 195
Figure S4.22. ^{1}H NMR spectrum ($CDCl_3$, 300 MHz, 298 K) of benzyl functionalised $PDMA_{57}$-b-$PMMA_{20}$-b-PCL_{37}-co-$PACL_4$ (Thiol-M1 in Table S4.2). 197
Figure S4.23. Nano DSC thermograms of $PDMA_w$-b-PCL_x-co-$PACL_y$ assemblies (100 to 0 °C, 1 °C min^{-1}) showing the first cooling-heating cycle (exo-down, endo-up). 198

Figure S4.24. Nano DSC thermograms of benzyl functionalised $PDMA_w$-b-PCL_x-co-$PACL_y$ assemblies (100 to 0 °C, 1 °C min^{-1}) showing the first cooling-heating cycle (exo-down, endo-up). 200

Figure S4.25. ^1H NMR spectrum ($CDCl_3$, 300 MHz, 298 K) of 50% benzyl functionalised $PDMA_{362}$-b-PCL_{46}-co-$PACL_8$ (Thiol-T7). *Corresponds to diethyl ether peak and red dots correspond to non-conjugated allyl pendant group protons..... 201

Figure S4.26. ^1H NMR spectrum ($CDCl_3$, 300 MHz, 298 K) of 50% benzyl functionalised $PDMA_{412}$-b-PCL_{36}-co-$PACL_4$ (Thiol-T11). *Corresponds to diethyl ether peak and red dots correspond to non-conjugated allyl pendant group protons..... 201

Figure S4.27. Effect of aging temperature on the self-assembly morphology. TEM micrographs of $PDMA_{295}$-b-PCL_{56}-co-$PACL_4$ (T5 in table 4.3) (left), $PDMA_{237}$-b-PCL_{36}-co-$PACL_3$ (T6 in table 4.3) (middle) and $PDMA_{233}$-b-$PMMA_{19}$-b-PCL_{43}-co-$PACL_7$ (M3 in table 4) (left) at room temperature (20 °C) (up) and in the fridge (4 °C) (down). Samples were negatively stained using uranyl acetate (0.5 wt. %). 202

Figure S4.28. Effect of aging temperature on the self-assembly morphology. A) and C) TEM micrographs of benzyl functionalised $PDMA_{57}$-b-$PMMA_{20}$-b-PCL_{38}-co-$PACL_4$ (**Thiol-M1**) aged at 20 °C and 4 °C respectively. B) and D) TEM micrographs of benzyl functionalised $PDMA_{330}$-b-$PMMA_{18}$-b-PCL_{46}-co-$PACL_8$ (**Thiol-M4**) aged at 20 °C and 4 °C respectively. Samples were negatively stained using uranyl acetate (0.5 wt. %). White spots correspond to grid artifacts. 202

Figure S4.29. Nano DSC thermograms (100 to 0 °C, 1 °C min^{-1}) showing first cooling-heating cycle of $PDMA_{89}$-b-PCL_{39}-co-$PACL_3$ self-assemblies in ethanol (conc. = 5 mg mL^{-1}) after slow cooling and aging at 20 °C (left) and fast cooling and aging at 4 °C (right). Showing the melting enthalpy ($\Delta H_{melting}$) and entropy ($\Delta S_{melting}$) of the processes in the mentioned conditions... 203

Figure S5.1. ^1H NMR spectrum of PCL_{39}-*co*-$PACL_3$ (P1), 300 MHz, 298 K, $CDCl_3$..... 255

Figure S5.2. ^1H NMR spectrum of $PDMA_{89}$-*b*-PCL_{39}-*co*-$PACL_3$ (P5), 300 MHz, 298 K, $CDCl_3$.. 255

Figure S5.3. ^1H NMR spectrum PCL_{44}-*co*-$PACL_3$ (P2), 300 MHz, 298 K, $CDCl_3$. 256

Figure S5.4. ^1H NMR spectrum of $PDMA_{94}$-*b*-PCL_{44}-*co*-$PACL_3$ (P6), 300 MHz, 298 K, $CDCl_3$. * Correspond to diethyl ether peaks..... 257

Figure S5.5. ^1H NMR spectrum PCL_{54}-*co*-$PACL_3$ (P3), 300 MHz, 298 K, $CDCl_3$. 257

Figure S5.6. ^{1}H NMR spectrum of $PMMA_{20}$-*b*-PCL_{54}-*co*-$PACL_3$ (P4), 300 MHz, 298 K, $CDCl_3$. * Correspond to water peak. 258
Figure S5.7. ^{1}H NMR spectrum of $PDMA_{156}$-*b*-$PMMA_{20}$-*b*-PCL_{54}-*co*-$PACL_3$ (P7), 300 MHz, 298 K, $CDCl_3$. * Correspond to acetone peak. 258
Figure S5.8. SEC chromatograms of block copolymers P4 to P7 in Table 5.2 ($CHCl_3$, with 0.5% Et_3N, PMMA standard). 259
Figure S5.9. ^{1}H NMR spectrum (300 MHz, 298 K, $CDCl_3$) of $PDMA_{89}$-*b*-PCL_{39}-*co*-$PACL_3$ (P5) after photo-initiated thiol-ene addition in chloroform (DMPA, 320-500 nm, 20 min). * Correspond to diethyl ether peaks. ** Correspond to acetone peak. 260
Figure S5.10. ^{1}H NMR spectrum (300 MHz, 298 K, $CDCl_3$) of $PDMA_{89}$-*b*-PCL_{39}-*co*-$PACL_3$ (P5) after photo-initiated thiol-ene addition in THF (DMPA, 320-500 nm, 30 min). * Correspond to diethyl ether peaks. ** Correspond to acetone peak. 260
Figure S5.11. ^{1}H NMR spectrum (300 MHz, 298 K, $CDCl_3$) of $PDMA_{87}$-*b*-PCL_{47}-*co*-$PACL_7$ after photo-initiated thiol-ene addition in chloroform (Irgacure 918, 405 nm, 180 min)..... 261
Figure S5.12. Stacked ^{1}H NMR spectra (300 MHz, 298 K, $CDCl_3$) of photo-initiated thiol-ene addition in chloroform (Irgacure 918, 405 nm) of $PDMA_{143}$-*b*-PCL_{47}-*co*-$PACL_7$ in the presence of TCEP. 262
Figure S5.13. TEM images of cylindrical micelles obtained from the CDSA in ethanol of $PDMA_{89}$-*b*-PCL_{39}-*co*-$PACL_3$ block copolymer (P5) after 3 weeks of aging at room temperature. Samples were negatively stained using uranyl acetate (0.5 wt %). 263
Figure S5.14. TEM images of cylindrical micelles obtained from the CDSA in ethanol of BODIPY-conjugated $PDMA_{89}$-*b*-PCL_{39}-*co*-$PACL_3$ block copolymer (BODIPY-P5) after 3 weeks of aging at room temperature. Samples were negatively stained using uranyl acetate (0.5 wt.%). 263
Figure S5.15. TEM micrographs of cylindrical micelles obtained from the CDSA in ethanol of $PDMA_{156}$-*b*-$PMMA_{20}$-*b*-PCL_{54}-*co*-$PACL_3$ block copolymer (P7) after 1 week of aging at room temperature. Samples were negatively stained using uranyl acetate (0.5 wt %). 264
Figure S5.16. TEM micrographs of cylindrical micelles obtained from the CDSA of $PDMA_{156}$-*b*-$PMMA_{20}$-*b*-PCL_{54}-*co*-$PACL_3$ block copolymer (P7) after dialysis to water. Samples were negatively stained using uranyl acetate (0.5 wt %). 264
Figure S5.17. Number length average (L_n) plots, calculated from particle analysis-based TEM images, for the polymer seeds after sonication for 4 h (20 s – ON; 100 s – OFF). **A)** $PDMA_{117}$-*b*-

PCL_{48} seed solution. **B)** $PDMA_{154}$-*b*-PCL_{48} seed solution. **C)** of $PDMA_{94}$-*b*-PCL_{44}-*co*-$PACL_3$ seed solution. **D)** of $PDMA_{112}$-*b*-PCL_{53}-*co*-$PACL_3$ seed solution. 265
Figure S5.18. Number length average (L_n) plots, calculated from particle analysis-based TEM images, for the 1D epitaxial growth of $PDMA_{94}$-*b*-PCL_{44}-*co*-$PACL_3$ (P6) block copolymer **(A)** m_{unimer}/m_{seed} = 2; **(B)** m_{unimer}/m_{seed} = 4; **(C)** m_{unimer}/m_{seed} = 6; **(D)** m_{unimer}/m_{seed} = 8; using $PDMA_{154}$-b-PCL_{48} seeds. 266
Figure S5.19. A) Number length average (L_n) vs unimer/seed ratio, calculated from particle analysis-based TEM images, for the 1D epitaxial growth of bodipy conjugated $PDMA_{156}$-*b*-$PMMA_{20}$-*b*-PCL_{54}-*co*-$PACL_3$ (Bodipy-P7) block copolymers using $PDMA_{154}$-*b*-PCL_{48} seeds. **B)** Size distribution averaged by intensity over the same time. Measured by dynamic light scattering (DLS). Each sample was repeated three times. 266
Figure S5.20. Number length average (L_n) plots, calculated from particle analysis-based TEM images, for the 1D epitaxial growth of BODIPY-P7 block copolymers **(A)** m_{unimer}/m_{seed} = 2; **(B)** m_{unimer}/m_{seed} = 4; **(C)** m_{unimer}/m_{seed} = 6; using $PDMA_{154}$-*b*-PCL_{48} seeds. 267
Figure S5.21. TEM micrographs for the 1D epitaxial growth $PDMA_{94}$-*b*-PCL_{44}-*co*-$PACL_3$ (P6) block copolymers using P6 crystalline seeds with unimer/seed ratios of 2, 4, and 6. Samples were negatively stained using uranyl acetate (0.5 wt %). 268
Figure S5.22. Number length average (L_n) plots, calculated from particle analysis-based TEM images, for the 1D epitaxial growth $PDMA_{94}$-*b*-PCL_{44}-*co*-$PACL_3$ (P6) block copolymers using P6 crystalline seeds with unimer/seed ratios of 2, 4, and 6. Table summary with lengths. 269
Figure S5.23. A) Number length average (L_n) *vs.* unimer/seed ratio, calculated from particle analysis-based TEM images, for the 1D epitaxial growth of $PDMA_{94}$-*b*-PCL_{44}-*co*-$PACL_3$ (P6) block copolymers using P6 crystalline seeds with unimer/seed ratios of 2, 4, and 6. **B)** Size distribution averaged by intensity over the same time. Measured by dynamic light scattering (DLS). Each sample was repeated three times. 269
Figure S5.24. TEM micrographs for the 2D epitaxial growth of $PDMA_{94}$-*b*-PCL_{44}-*co*-$PACL_3$ (P6) block copolymers using $PDMA_{154}$-*b*-PCL_{48} seeds with different unimer/seed ratios. Samples were negatively stained using uranyl acetate (0.5 wt %). 270
Figure S5.25. Number area average (A_n) *vs*. unimer/seed ratio, for the 2D epitaxial growth of $PDMA_{94}$-*b*-PCL_{44}-*co*-$PACL_3$ (P6) block copolymers using $PDMA_{154}$-*b*-PCL_{48} seeds, calculated from particle analysis-based TEM images. Table summary with particle dimensions. 270

Figure S5.26. TEM micrographs of 2D multilayered platelets described in Table S5.1. Samples were negatively stained using uranyl acetate (0.5 wt %). 271
Figure S5.27. Confocal images of $PDMA_{127}$-*b*-PCL_{48} + BODIPY-conjugated conjugated $PDMA_{156}$-*b*-$PMMA_{20}$-*b*-PCL_{54}-*co*-$PACL_3$ multilayered platelets, sowing the fluorescence field. Image taken by Mr. Tianlai Xia. 271
Figure S5.28. Number length average (L_n) and number witdh average (W_n) of 2D platelets used in biological studies of $PDMA_{94}$-*b*-PCL_{44}-*co*-$PACL_3$ unimer co-crystallized with PCL_{48} homopolymer onto seeds of $PDMA_{154}$-*b*-PCL_{48} with m_{unimer}/m_{seeds} ratios 5 and 10. 272
Figure S5.29. 2D platelets used in biological studies **A)** TEM micrographs of 2D living growth solutions of BODIPY-conjugated $PDMA_{156}$-*b*-$PMMA_{20}$-*b*-PCL_{54}-*co*-$PACL_3$ (BODIPY-P7) unimer co-crystallized with PCL_{48} homopolymer onto seeds of $PDMA_{154}$-*b*-PCL_{48} where m_{PCL48}/m_{unimer} = 1, with m_{unimer}/m_{seeds} ratio 10. **(B)** Number length average (L_n) and **(C)** Number witdh average (W_n) of respective particles. 273
Figure S5.30. Confocal imaging NIH 3T3 + BODIPY-Platelets (1 mg mL^{-1}) before washing the excess of nanoparticle aggregates with PBS (*Z*-scan slides). Showing bright, fluorescent (λ = 503 -512 nm), and merged fields. Scale bar = 20 µm. 274
Figure S5.31. Confocal imaging of NIH 3T3 control group during internalisation studies after addition of NucRed Live 647, showing the bight, fluorescent (λ = 647 – 665 nm), and merged fields. Scale bar = 20 µm. 274
Figure S5.32. Confocal imaging NIH 3T3 + BODIPY-Platelets (1 mg mL^{-1}) after washing the with PBS and adding cell tracker (NucRed Live 647). Showing fluorescent fields at λ = 647 – 665 nm (NucRed) and λ = 503 – 512 nm (BODIPY), and merged fields. Scale bar = 20 µm. 275

List of Schemes

Scheme 1.1. Kinetic factors during living ring-opening polymerisation, where I, M and P correspond to initiator, cyclic monomer, and polymer respectively; m*denotes the active species leading the polymerisation; and k_i, k_p and k_d represent the rate constants of initiation, propagation and depropagation, respectively. 15
Scheme 1.2. Activated monomer mechanism for the ROP of ε-caprolactone (εCL) using an alcohol and DPP as initiator and catalyst respectively. 19
Scheme 2.1. Stereo-selectivity studies of (R)- and (S)-TRIP BINOL catalysts. 49

Scheme 3.1. ROP of ε-caprolactone (εCL) or ε-allyl-ε-caprolactone (εACL). Reaction conditions: [monomer] = 1 M and $[monomer]_0:[CTA]_0 = 50$. 92
Scheme 3.2. Ring-opening copolymerisation (ROCOP) of ε-caprolactone (εCL) and ε-allyl-ε-caprolactone (εACL). Deuterated benzene (C_6D_6) or toluene were used as solvents. 94
Scheme 4.1. General procedure for the synthesis of functional amphiphilic BCPs with x and y corresponding to εCL and εACL units. (a) DMA monomer, AIBN (10 mmol%), 1,4-dioxane, 70 °C; (b) benzyl mercaptan (thiol:ene ratio = 10:1), Irgacure 819 (10 mmol% based on thiol), chloroform, 25 °C, 3 h. 131
Scheme 4.2. Synthesis of PDMA-b-PMMA-b-PCL-co-PACL amphiphilic block copolymers via RAFT polymerisation of methyl methacrylate (MMA) and dimethyl acrylamide (DMA). (a) MMA (100 equiv.), AINB (20 mmol %), dioxane (30 wt.%), 70 °C, N_2 atmosphere. (b) DMA (600 equiv.), AINB (10 mmol %), dioxane (30 wt.%), 70 °C, N_2 atmosphere. 136
Scheme 5.1. Synthesis of amphiphilic PCL-based block copolymers by ring-opening copolymerisation of ε-caprolactone (1) and ε-allyl-ε-caprolactone (2) using a chain-transfer agent as initiator, followed by RAFT polymerisation of PMMA or/and PDMA. (a) DPP (10 mol%), toluene with $[monomers]_0:[initiator]_0 = 50$ and [monomers] = 2 M, 40 °C, N_2 filled glovebox, 7 h. (b) MMA (100 equiv.), AIBN (20 mmol %), dioxane (30 wt. %), 70 °C, N_2 atmosphere, 2.5 h. (c) DMA (600 equiv.), AINB (10 mmol %), dioxane (30 wt. %), 70 °C, N_2 atmosphere, 50 min. 208
Scheme 5.2. General scheme for the thiol-ene addition of $BODIPYC_{10}SH$ (2 equiv./allyl unit) to amphiphilic PCL-based block copolymers. (a) DMPA or Irgacure 819 (10 mmol % of thiol), chloroform (b) AINB (10 mmol % of thiol), toluene (10-15 wt. %), 80 °C, N_2 atmosphere, 24 h. 210
Scheme 5.3. General procedure for the seeded growth living CDSA. **a)** 1D epitaxial growth – seed solution at 2.5 mg mL^{-1}, addition of triblock copolymer solubilised in THF, aging at room temperature. **b)** 2D epitaxial growth – seed solution at 0.01-0.1 mg mL^{-1}, addition solution of homopolymer (PCL) + triblock copolymer (1:1) solubilised in $CHCl_3$, 30 °C, aging at room temperature. 220

List of Tables

Table 2.1. Screening of ε-ACL polymerisations conditions catalysed by TRIP-BINOL.[(a)] 51

Table 2.2. Studies of the polymerization of enantioenriched (S)- or (R)-εACL with stereoselective catalysts.[(a)] 56
Table 3.1. ROCOP of εACL and εCL.[a] 95
Table 3.2. Thermal properties of PCL-co-PACL copolymers. 100
Table 3.3. Scaling-up of the copolymerisation of εACL and εCL.[a] 102
Table 4.1. Synthesis of $PDMA_x$-b-PCL_{49} block copolymer with different core and corona lengths. 130
Table 4.2. Triblock copolymers of $PDMA_w$-b-PCL_x-co-$PACL_y$ with different core and corona lengths.[a] 134
Table 4.3. Crystallisation-driven self-assembly of triblock copolymers of $PDMA_w$-b-PCL_x-co-$PACL_y$ with different core and corona lengths. 143
Table 4.4. CDSA of block copolymers of $PDMA_w$-b-$PMMA_n$-b-PCL_x-co-$PACL_y$ with different core and corona lengths. 150
Table 5.1. Synthesis of amphiphilic PCL-based copolymers. 209
Table 5.2. Summary of thiol-ene click additions of BODIPY-C_{10}-SH (screening reactions). ... 212
Table 5.3. Length dispersity of $PDMA_{94}$-*b*-PCL_{44}-*co*-$PACL_3$ cylindrical micelles. 223
Table 5.4. Dimensions of BODIPY-conjugated $PDMA_{156}$-*b*-$PMMA_{20}$-*b*-PCL_{54}-*co*-$PACL_3$ platelets. 226

List of Supporting Tables

Table S4.1. Synthesis of $PDMA_w$-*b*-PMMA-*b*-PCL_x-*co*-$PACL_y$ block copolymers with different core and corona lengths. 193
Table S4.2. Summary of thiol-ene addition reactions with 2-mercapto benzyl. 197
Table S4.3. Summary of CDSA of benzyl-functionalised block copolymers. 200
Table S5.1. Summary for 2D uniform multilayered platelets. 270

List of Equations

Equation 2.1. % Polymer conversion. 71
Equation 2.2. Kinetic resolution or selectivity factor (*s*). 72
Equation 3.1. % Polymer conversion. 122

Declaration of authorship

This thesis is submitted to the University of Birmingham in support of my application for the degree of Doctor of Philosophy. This work has not been previously submitted for any degree or any other institution. Experiments, materials characterisation, data collection and analysis, writing and figure design was performed by myself between October 2020 and March 2024, except for:

Chapter 5 – where clearly stated, confocal laser scanning microscopy (CLSM) imaging was performed by Mr. Tianlai Xia at the University of Birmingham.

Some parts of this thesis are displayed in a pre-publication format suitable for publication as outlined in the University of Birmingham alternative thesis format guidelines.

Chapter 2 – Manuscript prepared: Ana Cubillo Álvarez, Maria C. Arno, Andrew P. Dove, Towards enantiopurity: Synthesis of enantioenriched poly(allyl-ε-caprolactones), *Manuscript prepared*.

Chapter 1.

Introduction

1 Introduction

The study of micro- and nano-engineered materials in the biomedical field to overcome the limitations of free therapeutics and navigate biological barriers has increased exponentially over the past decades. Nanoparticles (NPs) have proven to enhance the stability and solubility of therapeutic cargos, prolong the circulation lifetimes, and promote their accumulation in damaged tissues, which translates in higher efficiency and bioavailability, reducing undesirable side effects.[1-3] In particular, polymeric nanoparticles have attracted special attention because of their diverse chemical composition, which enables surface modification for additional targeting, and their versatile drug delivery capabilities.[4] These NPs have shown great potential for a broad range of applications such as biosensors,[5, 6] immunomodulators,[7, 8] imaging agents,[9, 10] phototherapeutic agents,[11, 12] and drug delivery systems (**Figure 1.1**).[13-16]

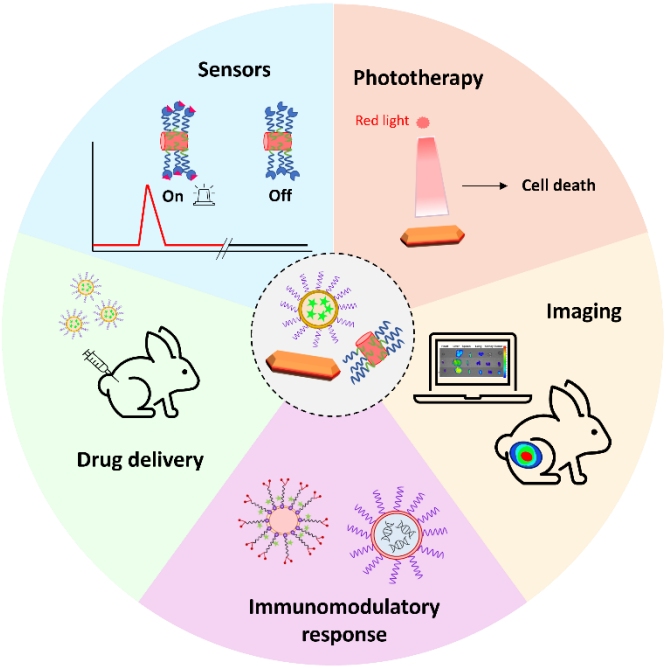


Figure 1.1. Overview highlighting some of the applications of polymeric nanoparticles.

1.1 Nanoparticles for drug delivery

Nanoparticle-based drug delivery platforms have shown a powerful ability for overcoming pharmacokinetic limitations associated with conventional drug formulations, exhibiting improved outcomes and morbidity levels. However, the major limitation of conventional nanoparticle delivery systems is their inability to reach therapeutic levels of drug at disease sites because of premature degradation, inefficient transport through biological barriers or non-specific biodistribution in healthy organs.[17] To enhance *in vivo* biodistribution and cell targeting, there are several nanoparticle design parameters that can be optimised such as size, shape, and surface chemistry (**Figure 1.2**).[18] For example, Cabral *et al*. demonstrated the critical role of nanoparticle size to penetrate poorly permeable tumours.[19] Whilst all polymeric micelles with diameters varying from 30 to 100 nm showed comparable accumulation and antitumour activity in hyperpermeable carcinomas, only smaller micelles (30 and 50 nm) were able to penetrate low vascularised tumours, allowing homogenous drug distribution. In another study,[20] Kataoka and coworkers reported the advantage of negatively charged polymeric micelles for long circulation times and lower unspecific uptake rates in liver and spleen, suggesting anionic particles are repelled in higher extent than their cationic or neutral counterparts by cellular membranes which are naturally negatively charged. Wang and coworkers[21] further explored the effect of nanoparticle surface charge on the biodistribution by designing zwitterionic nanoparticles with tuneable charge based on environmental acidity. Prolonged circulation times were observed at physiological pH, whereas increased cellular uptake and therapeutic effect resulted from the change on the surface charge, from anionic to cationic, at the tumour site (pH = 6.8). In recent years the design of non-spherical particles with low surface curvature, such as filaments, rods, or nanodiscs, have received increased attention because of their higher surface area and unique hemodynamic flow.[22]

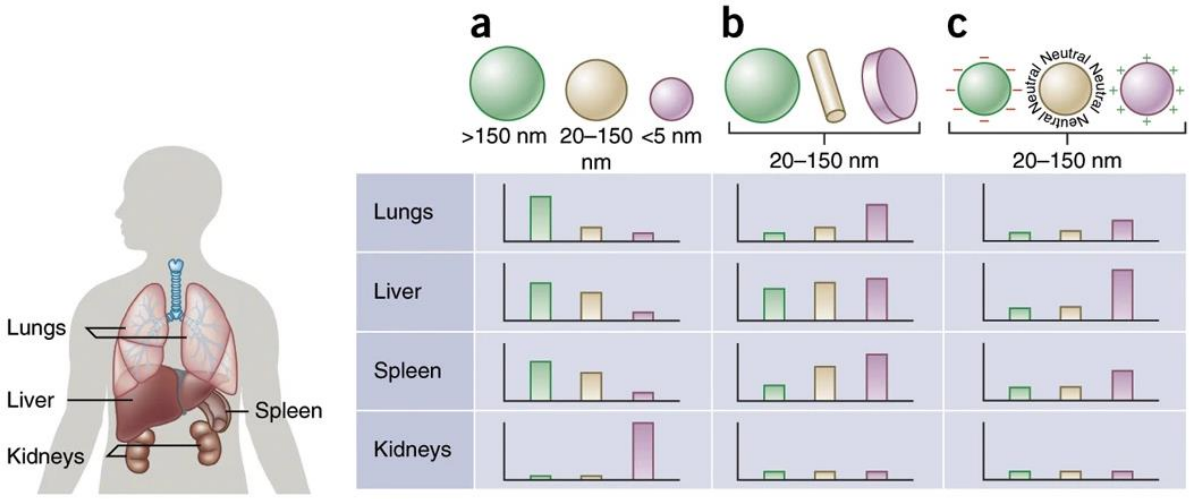


Figure 1.2. Nanoparticle rational design implementation for overcoming delivery barriers. Nanoparticle size, shape, and surface charge (a, b, and c, respectively) dictate biodistribution among the different organs including the lungs, liver, spleen, and kidneys. Figure reproduced from Ferrari and coworkers.[18]

1.1.1 Impact of shape for overcoming biological barriers

Nanoparticle fluid dynamics within blood vessels is a key parameter to consider during the design of drug delivery platforms and it is highly influenced by the size and geometry of the carrier.[23, 24] Non-spherical nanoparticles with high aspect ratios have proven to be more advantageous at prolonging the circulation lifetime and extravasating into surrounding tissue than their spherical counterparts. In 2007, Discher and coworkers[25] reported the preparation of degradable filomicelles of poly(ethylene glycol)-*block*-poly(caprolactone) (PEG-*b*-PCL) with lengths ranging from 2 to 18 µm and demonstrated that longer filomicelles (> 8 µm) were able to persist significantly longer in the circulation, and consequently, exhibited higher apoptosis rate and tumour suppression activity than spherical micelles and shorter fibre-like micelles (< 4 µm). Similarly, Qi *et al.* studied the role of particle geometry for oral drug delivery and revealed that polystyrene nanorods persisted for longer times in the gastrointestinal system and were more efficiently taken up by intestinal cells than nanospheres and nanodiscs.[26, 27]

Additional studies on particle margination have shown that NPs with spherical shape are less prone to interact with the endothelial cells of blood vessels as they move linearly in the centre of the vessel, exhibiting minimal lateral drift compared to cylindrical or platelet-like structures that exhibit shearing flow.[22, 28, 29]

1.1.1.1 Cell internalisation and endosomal compartmentalisation

After making contact with the targeted cells, NPs still need to be taken up by cells and overcome internal cellular trafficking in order to determine their functional delivery. This process is called endocytosis, and it can occur by numerous mechanisms depending on numerous parameters such as nanoparticle size, shape, surface moieties and cell type (**Figure 1.3**). While larger micron-sized particles are usually engulfed and internalised into a membrane-bounded vesicular compartment by phagocytosis and micropinocytosis, smaller particles can be internalised by other mechanisms usually involving receptor-mediated responses.[30, 31] It is well established in literature that particle geometry plays a dominant role in endocytosis.[32, 33] Extensive research on the impact of particle shape in phagocytosis has been carried out by the Mitragotri group. These studies demonstrated that the phagocytosis process is governed by the particle's orientation at the point of initial contact, therefore anisotropic polymeric particles with high curvature such as ellipsoids were internalised faster than nanospheres when the initial approach was from the major axis, whereas no internalisation was observed in cells that attached to the flat surface.[34-36] Moreover, negligible phagocytosis was observed for worm-like particles with very high aspect ratios and low surface curvature.[37] Subsequent studies by Agarwal *et al*.[38] revealed that cell mechanisms for NP uptake are geometry-dependent and cell type-specific. Larger nanodiscs were more efficiently internalised through different pathways by endothelial and epithelial cells than nanorods and smaller particles or nanospheres because of their higher surface contact with the cell

membrane. In another study, Hinde *et al.*[39] examined how the intracellular transport is affected by the shape of polymeric nanoparticles. Here, high aspect-ratio nanorods and worm-shape particles loaded with doxorubicin were able to travel and accumulate in the nuclear envelope more efficiently than spheres or vesicles, whose presence in the nucleus was barely detectable, promoting higher cytotoxicity and drug delivery efficiency.

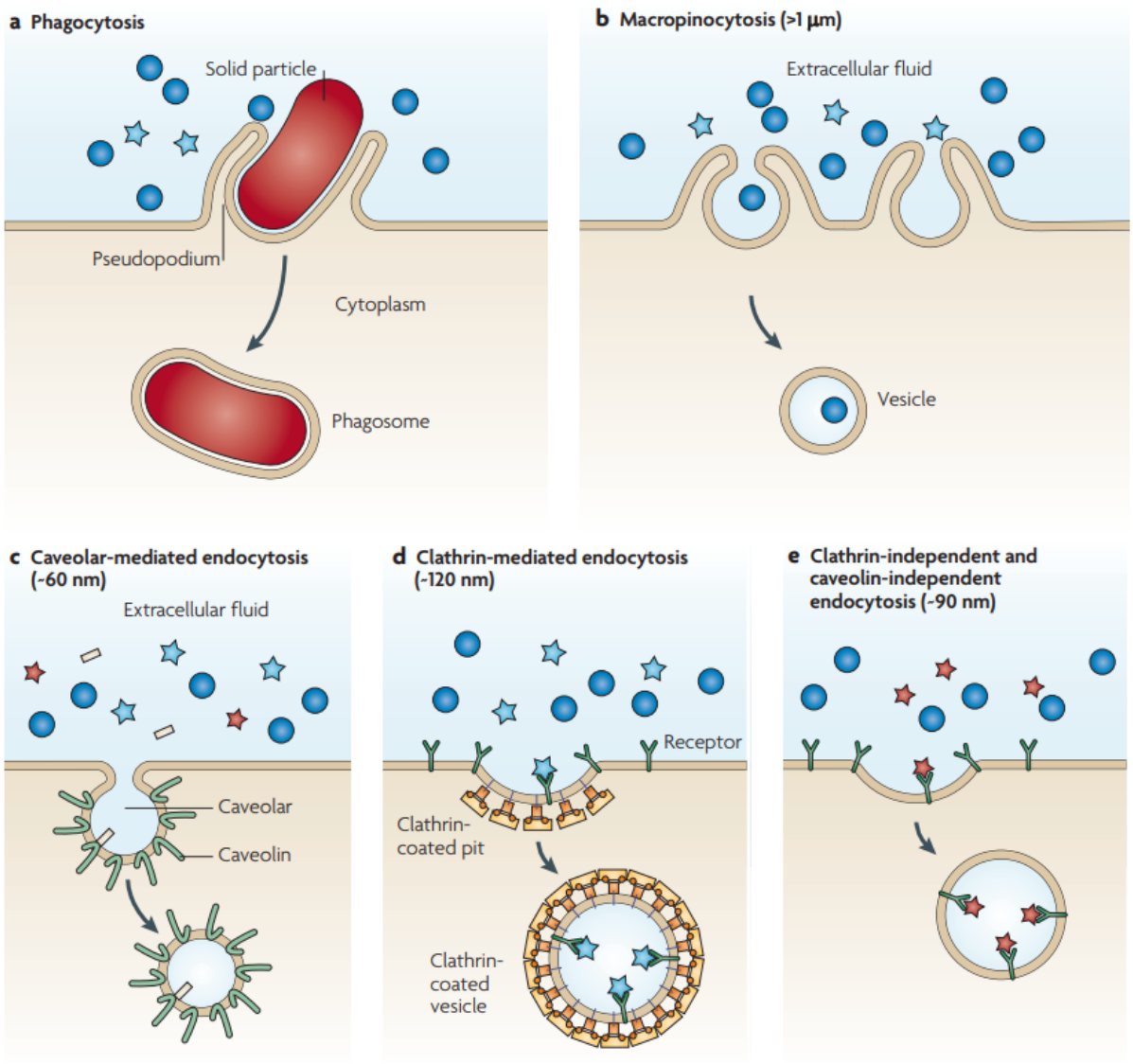


Figure 1.3. Types of cellular internalisation and nanoparticle size limitations. Large solid particles (> 1 µm) are internalised by (a) phagocytosis, while extracellular solutes and fluids (up to 10 µm) can undergo non-specific internalisation through (b) macropinocytosis. Submicron particles can be uptaken through several pathways: c) caveolar-mediated endocytosis, d) clathrin-mediated endocytosis and d) chlatrin-independent and caveolin-independent endocytosis. Figure reproduced from DeSimone and coworkers.[31]

Taking everything into consideration, control over the size, surface charge and the shape of the nanocarrier has been found to be crucial for successful drug-delivery. One strategy that enables concomitant tuneability of these three parameters is crystallisation-driven self-assembly (CDSA), which is a versatile methodology that uses amphiphilic block copolymers with a semicrystalline block to create anisotropic nanostructures with controlled shape and dimensions.[40] Among semicrystalline polymers used in CDSA, poly(ε-caprolactone) (PCL) has proven to be an ideal candidate for the design of novel biomaterials because of its remarkable biocompatibility, gradual degradability, and robust mechanical properties.[41, 42] PCL is a semicrystalline hydrophobic polymer, first synthesised by Carothers and coworkers in 1934.[43] Owing to its inherent low glass transition temperature (T_g ≈ −60 °C) and high melting temperature (T_m ≈ 60 °C), PCL-based materials remain semicrystalline at room and body temperatures. These characteristics have facilitated the production of a range of advanced polymer architectures with great potential for applications in tissue engineering,[44] wound healing,[45] and drug delivery.[46] However, the lack of side-chain functionality in PCL prevents the introduction of small molecules or therapeutic agents, which highly limits its use as drug delivery systems.

1.2 Polymer crystallisation, stereochemistry, and phase structure.

Since the concept of “polymer” was introduced by Hermann Staudinger in 1920 as long chains formed by the repetition of covalently linked monomeric units, it has been recognised that polymer molecules have the ability to crystallise.[47] In early studies, Staudinger demonstrated that only some segments of polyoxymethylene occupied the crystallographic unit cell, revealing the semicrystalline nature of polymers that contain both crystalline and amorphous components. In addition, the fringed-micelle model (**Figure 1.4a**), in which crystalline parallel stacked regions are embedded within amorphous entangled regions, was proposed to support

the material elastic properties observed.[48] Later, Keller studied the morphology and orientation of polyethylene single crystals grown from dilute solutions by electron microscopy and electron diffraction and observed the formation of uniform thin lamellae lattices.[49] This led to the concept of chain-folding in semicrystalline polymers, where the chains folded back and forth on itself in an orderly manner (**Figure 1.4b**). Flory and Zachman further confirmed this theory through theorical calculations and thermodynamic studies suggesting the chain-folding arrangement was more favourable than the fringe-micelle model first proposed.[50, 51]

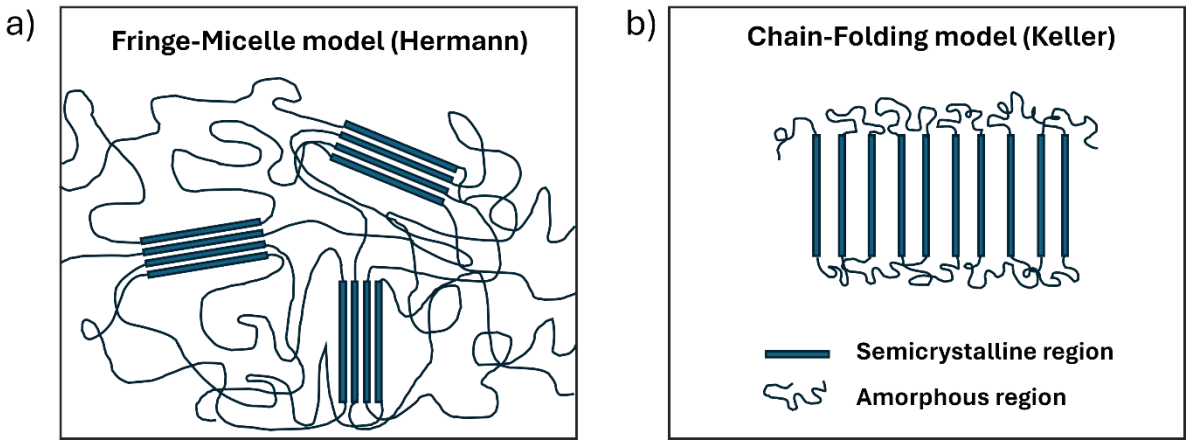


Figure 1.4. Schematic representation of semicrystalline chain arrangement models. a) Fringed-Micelle model proposed by Staudinger. b) Chain-Folding model proposed by Keller.

1.2.1 Nucleation and growth of crystals

The crystallisation process is composed by a primary nucleation, where new crystals (nuclei) are formed from a clear oversaturated solution, followed by a secondary slower nucleation and crystal growth, in which more polymeric units from the oversaturated solution will attach to their parent crystal to form larger crystalline structures.[52] Both of these processes are controlled by the crystallisation kinetics, therefore, the rate of cooling down, which allows the melt crystals to nucleate and grow, becomes important. Slow crystallisation kinetics (high ΔT) allows the chains to fold adjacently in an ordered manner, promoting instantaneous nucleation

as consequence of lower surface free energy barrier. This process leads to the formation of smaller spherulites with fewer defects, resulting in semicrystalline materials with enhanced optical and thermo-mechanical properties. On the other hand, fast crystallisation processes (low ΔT) render materials with inferior mechanical properties in which the crystallinity can be completely absent as there is not sufficient thermal energy available to allow the necessary molecular motion to take place, leading to sporadic nucleation and therefore, smaller imperfect crystals.[53] The overall crystallisation kinetics is usually described using the Avrami equation:

$$1 - \chi_c(t) = e^{(-kt^n)}$$

where χ_c represents the weight fraction of crystallised polymer after a length of time (t), k corresponds to the overall crystallisation rate constant, and n is the Avrami index, respectively, related to the nucleation rate and dimensionality of the crystal growth.[54, 55]

1.2.1.1 Differential Scanning Calorimetry techniques

The different phase structures of semicrystalline polymers (melt, crystalline and amorphous) and degree of crystallinity (χ_c) can be determined through differential scanning calorimetry (DSC). This method allows the analysis of solid samples as well as samples in solution, and measures changes in heat capacity (C_p) and enthalpy (H) of a compound in comparison to a reference material. During DSC analysis, a sample is heated or cooled at a constant rate while the energy uptake and heat flow of both sample and reference are evaluated. As the sample goes through a phase transition, structural and thermodynamic changes occur, and the difference in heat flow required to equalise the temperature in the sample and reference cells is measured.[56] There are two classes of DSC instruments: power compensation and heat-flux.[57] In the first one, the sample and reference are independently heated, therefore when the

sample undergoes an endothermic event, such as melting, a higher input of energy (Δ*E*) will be required to maintain the sample cell at the same temperature causing an upward displacement from the baseline, and the opposite occurs during exothermic events (crystallisation). The amorphous component in semicrystalline polymers is characterised by the glass transition, as the chains are not able to pack and crystallise when decreasing the temperature, the polymer chains become hard and glassy and as the temperature increases the amorphous component undergoes a transformation from a glassy to a rubbery state. This glass transition temperature (T_g) is represented as an abrupt positive change in the Δ*E* baseline because the heat capacity in the rubbery state is higher than in the glassy state (**Figure 1.5a**). On the other hand, in heat-flux DSC both sample and reference are heated in the same cell and the temperature difference (ΔT) between the sample and reference is recorded. During endothermic events a reduction in temperature occurs as the sample absorbs part of the heat produced, whereas in exothermic events, which are thermodynamically favourable, the opposite effect will be observed. This causes the thermogram traces to appear inverted compared to the power compensation DSC (**Figure 1.5b**).

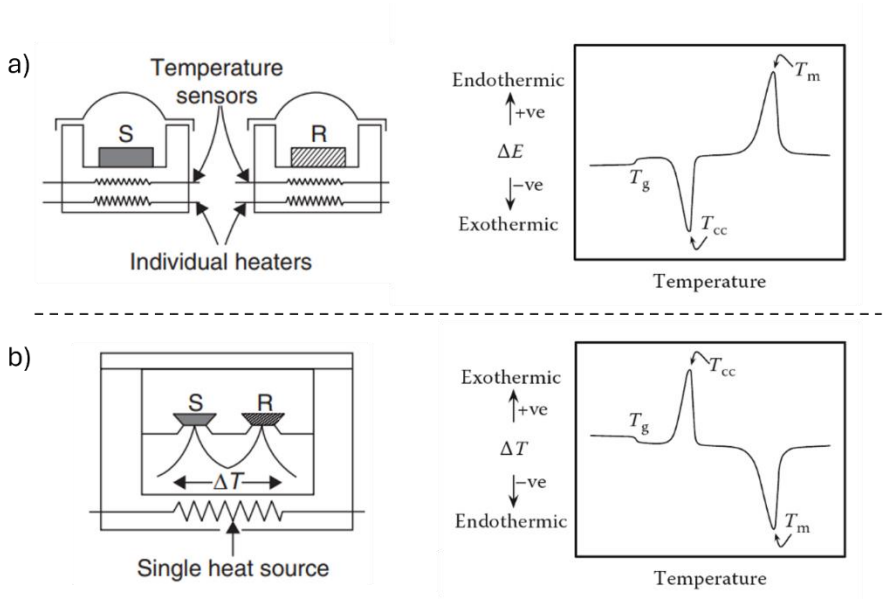


Figure 1.5. Schematic diagrams showing (a) power compensation and (b) heat-flux DSC and expected thermograms of a semicrystalline polymer. Figure adapted from references [53, 58].

1.2.2 Factors determining crystal structure

Crystal growth is a complex process that requires the organisation of polymer chains and can be influenced by numerous parameters. Semicrystalline polymers are characterized by their ability to melt at a certain temperature (T_m) and to crystallise at a temperature between the T_m and T_g. In the melt stage, the polymer chains are highly entangled and upon the cooling process molecular rearrangements take place to yield thermodynamically stable ordered structures. Moreover, the crystallisation process proceeds differently if the polymer is in solution, in dilute solutions polymer chains are separated from each other, which favours the folding process and consequently the crystals formed are usually more regular than those obtained from solid-state melt polymer.[59, 60] Additionally, factors such as composition and molecular weight of the polymer, amount of branching or substituents, and presence of additives play a crucial role during the crystallisation process. Koch *et al*. studied the microstructure development of poly(3-hexylthiophene) (P3HT) with molecular weights (M_n) ranging from 4.0 to 130 kg mol^{-1} and observed a linear increase in T_m for samples up to 35 kg mol^{-1}. For P3HT of higher molecular weights, as the polymer chain are more entangled, thinner crystals were produced resulting in lower crystallisation and melting points.[61] This behaviour has also been observed in other semicrystalline polymers such as poly(L-lactide) (PLA)[62] and poly(ε-caprolactone) (PCL),[63] in which the level of crystallinity generally increased with the molecular weight of the polymer until it reached a critical M_n. Above this threshold, lower T_m values are observed as consequence of high chain entanglement and a decrease in chain mobility. In another study, Meyer and coworkers[64] reported the impact of branching in monodisperse polyethylene systems showing how the lamellae thickness as well as crystalline properties of the material decrease with increasing the branching length and content. Similarly, it is well established in the literature that the presence of short or medium-length

side chains and bulky substituents disrupt the crystallinity of polymers.[65-68] Overall, these reports suggest that certain structural requirements are necessary for a polymer to crystallise. The linearity of the chains has proven to be a critical factor to achieve highly crystalline materials, although the presence of a limited number of branches or small substituents have proven to affect the crystallisation but not disrupt it.

1.2.2.1 Tacticity and stereochemistry of polymers

In addition to the composition and structural effects of the repeating units defining the polymer backbone, the thermal and mechanical properties of a polymer are strongly influenced by its molecular microstructure and tacticity. These concepts depict the different spatial and configurational arrangements for the monomeric units and their substituents along the polymer chain, including geometric (cis/trans–*E*/*Z*) and optical (*R*/*S*) stereoisomerisms. There are several ways that stereochemistry can be incorporated into polymers (**Figure 1.6**), when all repeating units have the same configuration, the polymer is isotactic, whereas in syndiotactic polymers the stereocentres are regularly alternated. Polymers with defined stereochemistry usually result in semicrystalline materials with enhanced mechanical properties, as the polymeric chains can pack in an ordered manner, compared to their atactic counterparts where the substituents are randomly distributed, preventing chain folding.[69]

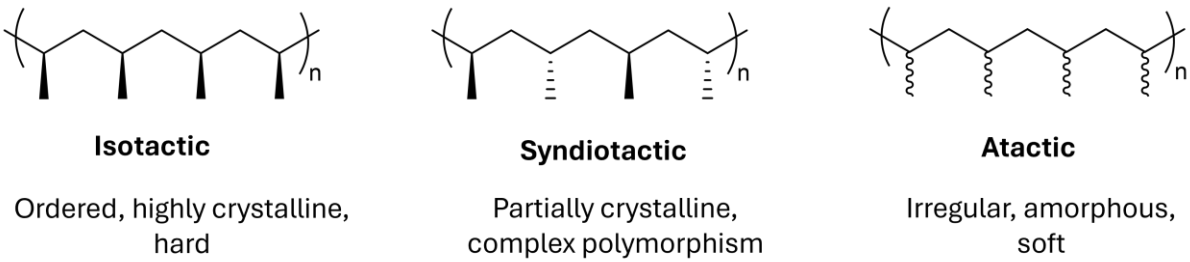


Figure 1.6. Stereochemistry of polypropylene (PP) and thermo-mechanical properties.

Extensive research has been conducted to disclose the impact of cis/trans stereochemistry on the thermo-mechanical properties of polymers *via* step-growth polymerisation using several organocatalytic nucleophilic click chemistry techniques[70-75] and ring-opening metathesis polymerisation (ROMP).[76-78] However, the study of large macromolecules with controlled optical steroisomerism has been limited to vinyl polymers such as polypropylene (PP), polystyrene (PS) and poly(methyl methacrylate) (PMMA) obtained from metal-coordination polymerisations,[79-82] and tactic polymers prepared from monomers with an already stablished stereochemistry such as PLA or sugar-based polymers, where precise control over the polymerisation is required to achieve highly ordered structures.[83-88] To overcome this limitation, many recent studies have focused on the development of novel catalytic systems for stereoselective polymerisations.[89] Nevertheless, many stereo-controlled polymers remain unexplored as consequence of the lack of stereoselective synthetic methods.

1.3 Chain-growth polymerisation and "living" polymerisations

In contrast to other conventional synthetic methods such as step-growth polymerisation, where the growing chains can react with other growing chains rendering polymers with low control over the molecular weight (M_n), chain-growth polymerisation has proven advantageous at preparing polymers with narrow dispersities ($Đ_M$) and predictable degree of polymerisation (DP) and M_n, since the growth of the polymer proceed exclusively from the addition of monomer to polymeric active sites.[90] Living polymerisation is a type of chain-growth polymerisation in which the rate of initiation (k_i) is greater than the rate of propagation (k_p) causing a constant and irreversible addition of monomers to the polymer chain. As a result, all polymer chains grow at the same rate without irreversible transfer or termination side reactions that would generate a high amount of "dead" chains with various lengths (**Figure 1.7**).[91]

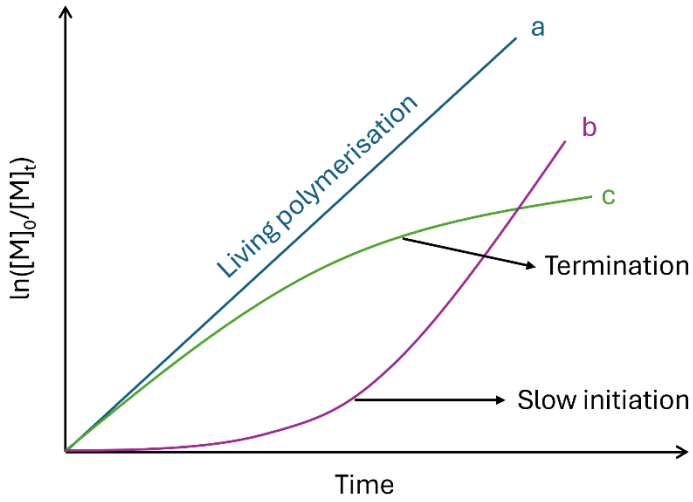


Figure 1.7. Growth of polymers with time. a) Linear relationship between $\ln([M]_0/[M]_t)$ and time indicates first order kinetics, characteristic of living polymerisations. b) increase in active species because of slow initiation c) decrease in propagating species as a result of termination reactions ("dead" chains formation). Figure adapted from Matyjaszewski and coworkers.[92]

Since the introduction of living anionic polymerisation by Szwarc in 1956,[93] the general concept of "living" has expanded to other polymerisation methods including, among others, cationic polymerisation,[94, 95] coordination/organometallic polymerisation,[96, 97] and to some extent reversible deactivation radical polymerisations.[98, 99] This development has led to the design of defined macromolecules with tuneable functional groups and complex architectures such as multiblock copolymers, graft and brush copolymers, or star polymers (**Figure 1.8**).[100]

Some examples of living chain-growth polymerisation that allow the preparation of functional polymers with diverse architectures are ring-opening polymerisation (ROP) and reversible addition-fragmentation chain-transfer (RAFT) polymerisation.

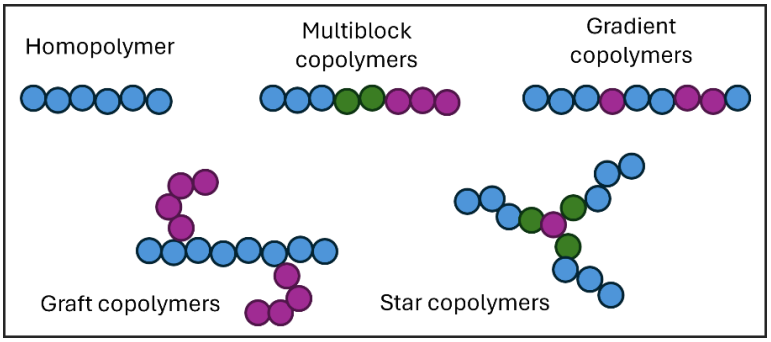
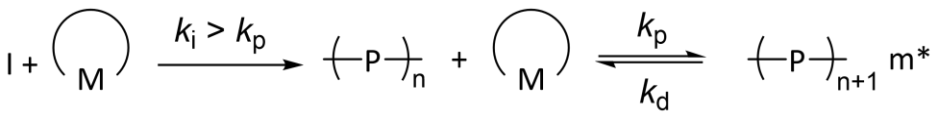


Figure 1.8. Example of macromolecular architectures achieved through living polymerisation.

1.3.1 Ring-opening polymerisation

Ring-opening polymerisation (ROP) uses cyclic monomers such as lactones,[101-103] lactides,[104, 105] carbonates[106] or epoxides[107] to yield linear polymers with narrow dispersities and high molecular weights. Depending on the nature of the monomer, catalyst, or initiator used, the ROP can undergo several mechanisms including ionic, radical, coordination-insertion, and enzymatic. However, the ability of these functional monomers to polymerise will be dictated by thermodynamic and kinetic factors of the ring-opening. The polymerisability of a cyclic monomer is depicted by the monomer-polymer equilibrium (**Scheme 1.1**). At high concentrations of monomer, the propagation rate (k_p) increases, which shifts the equilibrium to the macromolecule formation. As the monomer concentration decreases during the polymerisation, the k_p decreases and the depropagation rate (k_d) increases until an equilibrium between the monomer and polymer ($k_p = k_d$) is reached, at which point further polymerisation ceases.[108]



Scheme 1.1. Kinetic factors during living ring-opening polymerisation, where I, M and P correspond to initiator, cyclic monomer, and polymer respectively; m*denotes the active species leading the polymerisation; and k_i, k_p and k_d represent the rate constants of initiation, propagation and depropagation, respectively.

The driving force behind most ROP is the monomer's conformational ring strain, which is closely related to the sign of the free enthalpy of polymerisation, also called Gibbs free energy of polymerisation (ΔG_p), which is defined as:

$$\Delta G_p = \Delta H_p^\circ - T(\Delta S_p^\circ + Rln[M])$$

where ΔH_p° and ΔS_p°correspond to the standard enthalpy and entropy of polymerisation respectively, *T* is the absolute temperature, *R* is the gas constant and [*M*] is the concentration of the cyclic monomer. Following the general thermodynamic rules, the ring-opening polymerisation of a given cyclic monomer will occur only when the Gibbs free energy is negative ($\Delta G_p < 0$). Cyclic monomers with a small number of carbons (3- and 4-membered rings) will easily polymerise, as the higher angular strain increases the ΔH_p°, promoting the ring-opening. Medium-sized rings (n = 5-6) are enthalpically and entropically disfavoured because of their size and lower strain.[109] Consequently, they are more resistant to undergo ring-opening polymerisation. In contrast, macrolactones (n ≥ 16) exhibit very low ring strains ($\Delta H_p^\circ << 0$) owing to the relatively high cycle flexibility. However, their large ring size results in extremely high entropic effects ($\Delta S_p^\circ >> 0$), which enables their polymerisation at low temperatures.[110]

Moreover, it has been previously demonstrated that the presence of substituents and their position within the ring strongly affect the polymerisation rate and physical properties of the resultant polymer.[68, 108] Hillmyer and coworkers reported the impact of alkyl substituent length and location on the ROP of δ-valerolactone (δVL, 6-membered ring) over the thermodynamic parameters and physical characteristics.[111] While the entropy and enthalpy of polymerisation were highly influenced by the substituent position, monomers with alkyl chains close to the

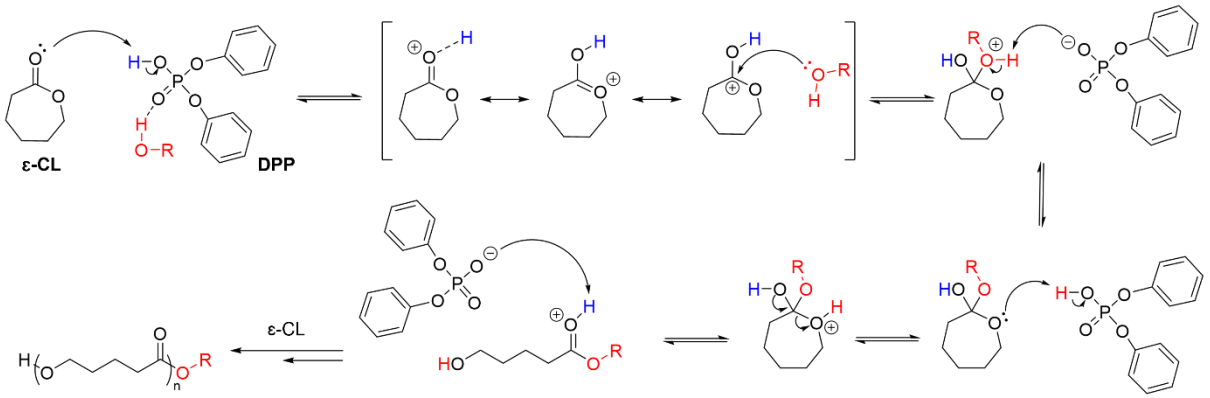
secondary alcohol (δ-position) exhibited significantly lower reactivity than α- and β-substituted δVL, insignificant thermodynamic changes were observed when varying the chain length. In a recent study,[112] Clamor *et al*. observed similar thermodynamic and kinetic effects during the ROP of C_{18}-substituted ε-caprolactones (εCL, 7-membered ring) with different regiochemistries. These studies are fundamental to understand the polymer structure-property relationships and synthetic limitations for the design of new functional monomers.

1.3.1.1 Catalysts for ring-opening polymerisation

While the monomer structure and chemical composition have proven crucial to thermodynamically drive the ROP, the kinetic factors are intrinsically linked to the catalysts used. Therefore, a careful choice of catalysts is essential for achieving optimal polymerisation effectiveness while retaining control over the polymer composition, tacticity, and physical-chemical properties. Extensive research on polymerisation catalysis has led to the design of abundant catalytic systems that can be divided into three categories: metallo-based,[113-115] organic,[116] and enzymatic.[117, 118] Moreover, some catalysts inside these groups have proven not only high activity but also certain stereoselectivity allowing the synthesis of stereoregular polymers (isotactic or syndiotactic) with enhanced thermo-mechanical properties.[119, 120]

Metal-based complexes including aluminium,[121, 122] magnesium,[123, 124] zinc,[125] and tin,[126] have been widely studied for ROP of lactones owing to their high activity and selectivity, which can be easily tuned through the variation of the steric bulkiness and donating capabilities of the metal-ligands. Metal-catalysed ROP typically proceeds through a coordination-insertion mechanism to yield well-defined polymers. However, the resultant polymers are often contaminated with trace amounts of metal impurities, which are challenging to remove, limiting their use in the biomedical field.[127]

Alternatively, acidic or basic organic catalysts have demonstrated notable efficiency and control of the polymerisation, while reducing toxic effects as they can be simply removed *via* precipitation or washing, making them more attractive for biomedical applications.[128] Since Hedrick and coworkers first reported the use of 4-dimethylaminopyridine (DMAP) as catalyst for the ROP of lactide,[129] the field of organocatalysis has rapidly expanded to provide a wide range of organocatalysts including guanidines,[130] thiourea/amines,[131] *N*-heterocyclic carbenes,[132] and phosphazene bases.[133] In addition, Brønsted acid organocatalysts such as phosphoric acid derivates have garnered considerable attention owing to their commercial availability, higher stability, and bifunctional initiation.[134, 135] Phosphoric acid catalysed polymerisations proceed according to the activated monomer mechanism, in which the phosphoric Brønsted-acidic group (P−OH) activates the monomer through carbonyl protonation, making it more electrophilic and susceptible of external nucleophilic attacks, and the phosphoric Lewis basic group (P=O) coordinates with the initiating alcohol increasing its nucleophilicity. The initiating alcohol can then attack the activated monomer leading to ring-opening and subsequent chain extension (**Scheme 1.2**). For example, Kakuchi and coworkers reported the use of diphenyl phosphate (DPP) for the controlled ROP of δVL and εCL to provide polymers with narrow dispersities ($Đ_M$ < 1.1) even at high monomer conversions (≥ 95% conversion).[136]



Scheme 1.2. Activated monomer mechanism for the ROP of ε-caprolactone (εCL) using an alcohol and DPP as initiator and catalyst respectively.

1.3.1.2 Asymmetric kinetic resolution polymerisation

As previously discussed, controlling the tacticity of the polymer is fundamental to achieve polymers with robust thermo-mechanical properties. Stereoregular polymers can be obtained through two main routes: 1) the polymerisation of a stereopure monomer, where the polymerisation proceeds with retention of the pre-stablished stereochemistry (**Figure 1.9a**), or 2) *via* asymmetric kinetic resolution polymerisation (AKRP) of a racemic monomer, in which the catalyst, often containing a chiral scaffold, polymerises preferentially one enantiomer of the monomer, yielding polymers with a patterned structure (**Figure 1.9b**).

The stereoselective ROP of cyclic esters such as lactides,[137-139] lactones,[122] epoxides,[140] and carbonates[141] has been widely explored. In this field, chiral organometallic catalysts have demonstrated to be the most active and stereoselective group, enabling the preparation of polymers with defined stereochemistry. However, the use of metal-based catalysts can be unfavourable depending on the final application of the material. Despite the abundance of known chiral organic catalysts for asymmetric synthesis,[142, 143] the majority of stereoselective organocatalysts for ROP generally exhibits significant lower selectivity values than their metal-based counterparts.

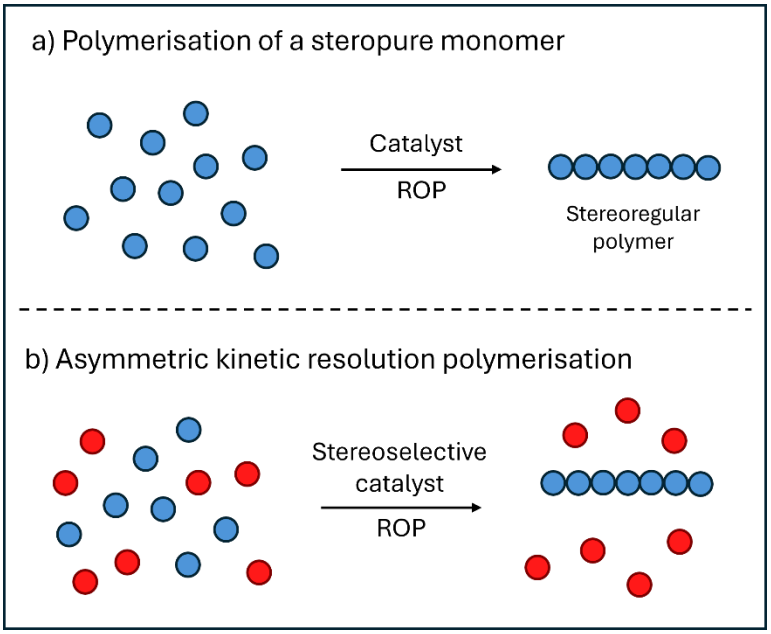


Figure 1.9. Routes to control polymer tacticity. a) Polymerisation of a stereopure monomer. b) asymmetric kinetic resolution polymerisation of a racemic monomer using a stereoselective catalyst.

Extensive research has been conducted on the organocatalysed stereocontrolled ROP of lactide (LA) in different diastereomeric forms using either chiral or achiral catalysts.[104, 144-147] For example, Mecerreyes and Cossio reported the synthesis of isotactic poly(*L*-lactide) (PLLA) with excellent isotactic selectivity, with P_m = 0.96 (where P_m is the probability of *meso* linkage between monomer units), from racemic LA using a diastereomeric densely *exo*-N-substituted proline and 1,8-diazabicyclo[5.4.0]undec-7-ene (DBU) as a co-catalyst.[148] Unfortunately, the extension of these catalytic systems to other cyclic esters besides LA remains underexplored.[120]

1.3.2 Reversible addition-fragmentation chain-transfer polymerisation

RAFT polymerisation is a type of reversible deactivation radical polymerisation, in which termination and chain-transfer reactions are suppressed by use of an equilibrium between dormant and propagating chains. Consequently, the controlled radical polymerisation will

continue upon subsequent addition of monomer leading to well-defined polymers and block copolymers with various architectures.[149] This polymerisation requires a chain-transfer agent (CTA) to regulate the radical exchange between active and dormant polymer chains. These CTAs are thiocarbonylthio compounds bearing a free radical leaving group (R group) and an electron-withdrawing or donating group (Z group), which governs the reactivity of the propagating radicals and stability of the intermediate (**Figure 1.10a**). Therefore, a careful selection of the Z and R groups is crucial to achieve control over the polymerisation. During RAFT, the generated free radicals will react with the monomer to produce a propagating polymer chain (P_1^*) that is rapidly capped by the CTA, generating a dormant radical intermediate. The radical then transfers to the R group (R^*), which fragments from the CTA and reacts with a monomer to start a new propagating chain (P_2^*). This new polymer chain will be quickly capped by the CTA, and the active radical will be transferred to the dormant chain (P_1^*), creating an equilibrium between dormant and propagating chains (**Figure 1.10b**).[150] The propagation step is highly influenced by the concentration of radicals, higher concentrations lead to uncontrolled polymerisation and increasing amount of dead polymer chains. However, in normal conditions, termination reactions are highly minimised as consequence of the low concentrations of active radical species.[151]

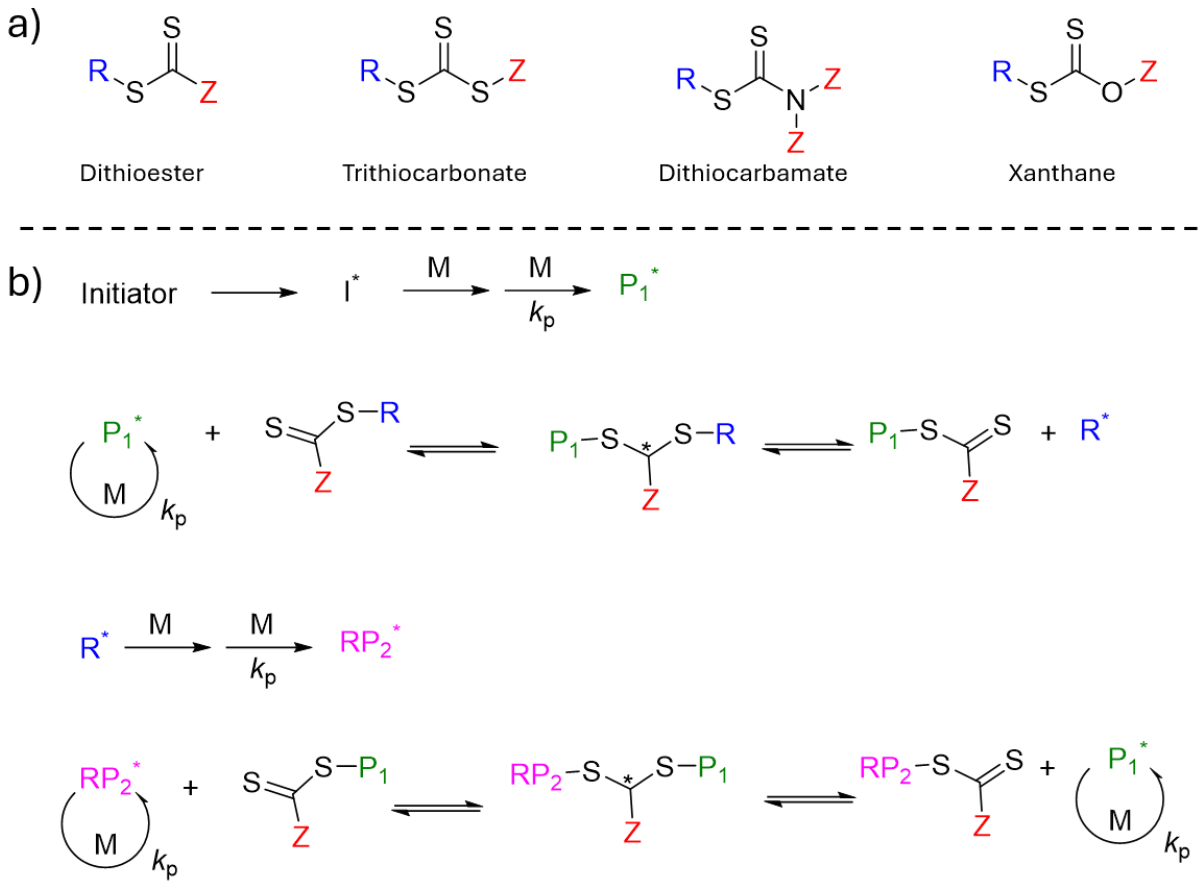


Figure 1.10. a) Types of chain-transfer agents (CTA). b) Mechanism of reversible addition-fragmentation chain-transfer (RAFT) polymerisation. * Correspond to active radical species, M and P correspond to monomer and polymer respectively.

1.4 Solution self-assembly of block copolymers

Living/controlled polymerisation techniques have allowed the preparation of well-defined block copolymers (BCPs). Amphiphilic BCPs, where one segment is soluble (solvophilic block) and the other one is insoluble (solvophobic block), can spontaneously self-assemble in solution to reduce the free energy and minimise unfavourable interactions between the solvophobic block and the solvent.[152] While the dimensions of the self-assembled particles are largely defined by the molecular weight of the BCP, the morphology is controlled by the packing parameter (ρ) that determines the interfacial curvature of the resultant micelles, and it is defined as:

$$\rho = \frac{v}{a_0 l_c}$$

where *v* is the relative volume of the hydrophobic segment, a_0 corresponds to the area of the head-group (hydrophilic block) and l_c is the volume of the hydrophobic segment. Manipulation of these parameters leads to changes in the interfacial curvature resulting in particles with different morphologies (**Figure 1.11**).[153] Generally, higher order morphologies with lower interfacial curvature such as cylinders or lamellar structures are obtained with increasing ρ, whereas spherical micelles are obtained with low ρ values.[154] Nevertheless the packing parameter is closely related to the mole fraction of the hydrophilic and hydrophobic building blocks (*f*), there are other factors that influence the self-assembly structure such as the arrangement of particles, the number of constituent particles and the presence of branching or ring structures.[155]

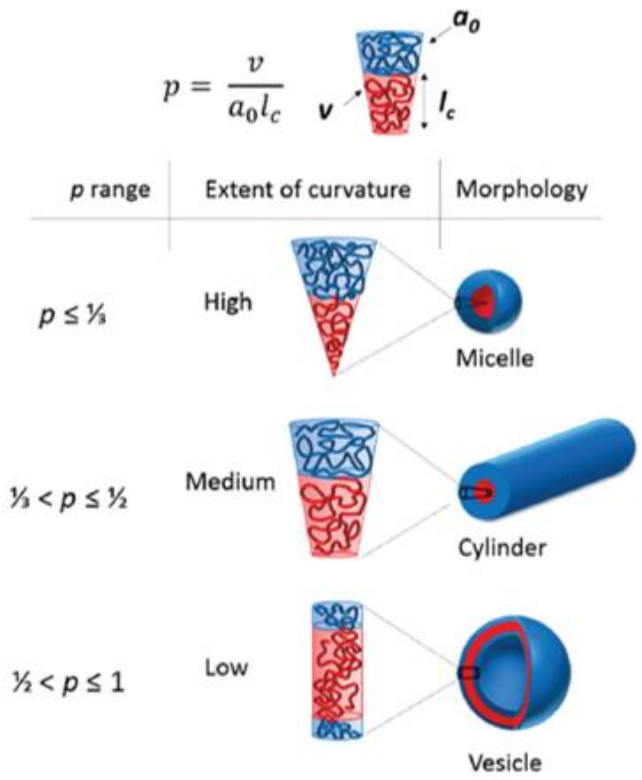


Figure 1.11. Changes on self-assembly interfacial curvatures with increasing packing parameter (ρ). Figure reproduced from ref.[153]

Spherical micelles are the most accessible and studied nanostructures since they exhibit the smallest packing parameter. Typically, block copolymers bearing larger solvophilic than solvophobic segments will self-assemble at a concentration above the critical micelle concentration, leading to spherical micelles or vesicles polydisperse in size.[156] In contrast, well-defined 1D and 2D anisotropic nanoparticles such as cylinders, worms and platelets, are inaccessible *via* conventional self-assembly methods.

More recent work has focused on the preparation of non-spherical hierarchical structures with remarkable complexity. In this thesis, 1D and 2D morphologies with controlled dimensions have been achieved by using BCPs with a semicrystalline core-forming block *via* crystallisation-driven self-assembly (CDSA).[157]

1.4.1 Crystallisation-driven self-assembly

The first example of self-assembly of BCPs bearing a semicrystalline core-forming block traces back to 1965. Keller and coworkers documented the synthesis of single 2D lamellar micelles through the self-assembly of poly(ethylene oxide)-*b*-polystyrene block copolymers (PEO-*b*-PS) in ethyl benzene.[158] However, the concept of crystallisation-driven self-assembly (CDSA) was not introduced until the late 1990s – early 2000s when Winnik and Manners reported the formation of poly(ferrocenyldimethylsilane)-*b*-poly(dimethylsiloxane) (PFDMS)-*b*-(PDMS) rod-like micelles in hexane and underscored the crucial role of the semicrystalline polyferrocene block during self-assembly process.[159, 160] Since then, the use of CDSA has expanded to a wide range of semicrystalline core-forming blocks including poly(ferrocenylsilane) (PFS),[161] PLLA,[162] PCL,[163] poly(2-isopropyl-2-oxazoline) (P*i*PrOx),[164] oligo(p-phenylenevinylene) (OPV),[165] poly(3-hexylthiophene) (P3HT),[166] and poly(peptoids).[167]

Similar to the growth of a polymer single crystal, a typical CDSA process comprises two key mechanistic steps: nucleation and crystallisation. The self-nucleation of the crystalline block is usually induced by heating the BCP to promote its dissolution in a selective solvent.[168] Nevertheless, some reports have proven that it can also be induced through solvent switch, where the injection of a concentrate solution of BCP in a common good solvent into a solvent selective for the corona block promotes nucleation.[161, 169] During CDSA, a BCP containing at least one crystalline block is suspended in a solvent that is selective for the non-crystalline block (corona block) and poor for the crystalline core-forming block, and heated above its melting temperature (T_m). Upon heating, the BCP is fully dissolved to afford polymer unimers in solution. The solution is then slowly cooled below the crystallisation temperature (T_c) of the crystalline polymer block. This change in temperature coupled with the nature of the solvent triggers the aggregation of the semicrystalline blocks to form small irregular nuclei. This makes crystallisation thermodynamically favourable, promoting slow and random crystal growth and the obtention of cylindrical micelles with broad length and distributions (**Figure 1.12**).

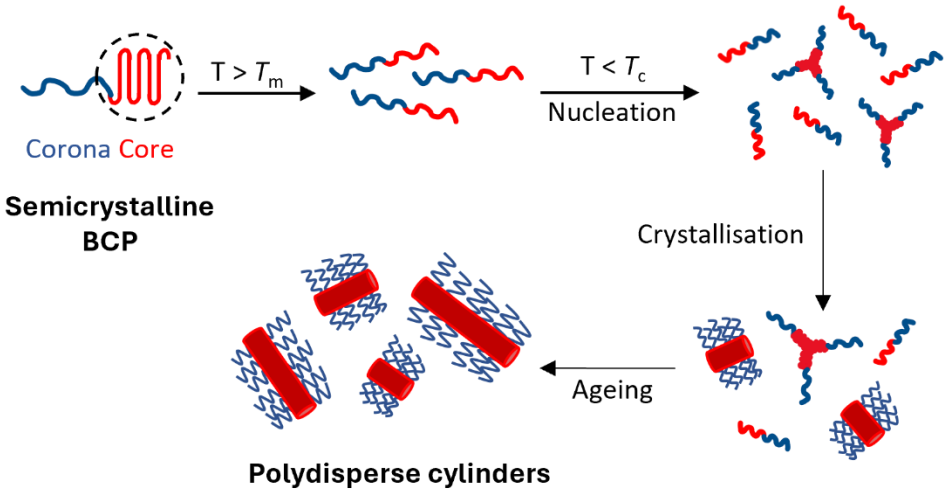


Figure 1.12. Thermally induced crystallisation-driven self-assembly (CDSA) of amphiphilic semicrystalline block copolymers.

In conventional self-assembly methods, the formation of nanostructures is mainly driven by solvophobic interactions. Conversely, CDSA is a more complex process, in which the resultant morphologies are defined by the crystallisation of core block, area of crystal in contact with the solvent and solvent-corona block interactions.[170] Consequently, the self-assembly process can be influenced by multiple parameters such as block copolymer composition, hydrophilic/hydrophobic molar fractions, solvent properties, temperature, time of aging, or presence of additives.[171] For example, Cao *et al*. found that large corona blocks in PFDMS-based BCPs favoured the formation of thin fibre-like micelles, whereas the self-assembly of copolymers with low corona-to-core ratios led to long 2D nano-sheets.[172] It was theorised that when the corona and core block exhibit similar lengths, few chain folds are made in order to minimised the area of crystalline core in contact with the solvent, leading to lamellar structures. However, in copolymers with larger solvophilic blocks, more chain folds are made to reduce the stretching of the corona block, leading to cylindrical morphologies. By contrast, Inam *et al*.[173] observed the opposite transition in the morphology of $PDMA_m$-*b*-$PLLA_{48}$ assemblies with different corona-to-core ratios (PDMA = poly(dimethyl acrylamide)). Well-defined 2D platelets resulted from the self-assembly of copolymers with long corona blocks as a result of an increase in polymer solubility, which favours slow crystallisation process and formation of thermodynamically preferred lamellar morphology. However, copolymers with shorter corona blocks are less soluble in solution triggering the formation of kinetically preferred 1D cylindrical micelles. In this study, changes in morphology were also observed with different solvent conditions and heating periods, showing the complexity of CDSA, where rules cannot be generalised and translated to different polymer systems. Recently, Song *et al*. reported the obtention of monodisperse 1D patchy and block comicelles formed by the addition of a trace of crystalline PFS homopolymer to a solution of PFS-*b*-PI

(PI = poly(isoprene)) in decane.[174] However, controlling the dimensions of nanostructures via one-step CDSA is very challenging and the particle morphology is usually limited to 1D cylindrical micelles.

1.4.1.1 Living CDSA: controlling the morphology and size.

As previously mentioned, the nucleation events during CDSA are not synchronized or controlled, leading to the formation of non-uniform core-shell particles. To overcome this limitation, Manners and Winnik groups developed a strategy that enables the separation of the nucleation and growth stages by using small uniform crystallites as seed initiators, termed living CDSA.[175] Initial work showed that small rod-like micelles with uniform lengths could be accessed by sonicating a solution of polydisperse cylinders. These crystalline seeds can act as efficient initiation sites for micelle growth upon addition of dissolved BCP, resulting in uniform addition of unimers to seeds, i.e. epitaxial growth, which led to monodisperse PFS-containing cylindrical micelles of variable length ($L_w/L_n \leq 1.03$). As a result of the uniform epitaxial growth, the length of the resultant cylinders is linearly dependent on the amount of unimer added to the pre-formed seeds (**Figure 1.13**). Later studies have proven that the epitaxial growth can be also promoted through a self-seeding approach, in which the seed solution is heated to a temperature dissolving most of the BCP, and then cooled down to promote uniform structure growth from the surviving crystalline seeds.[176]

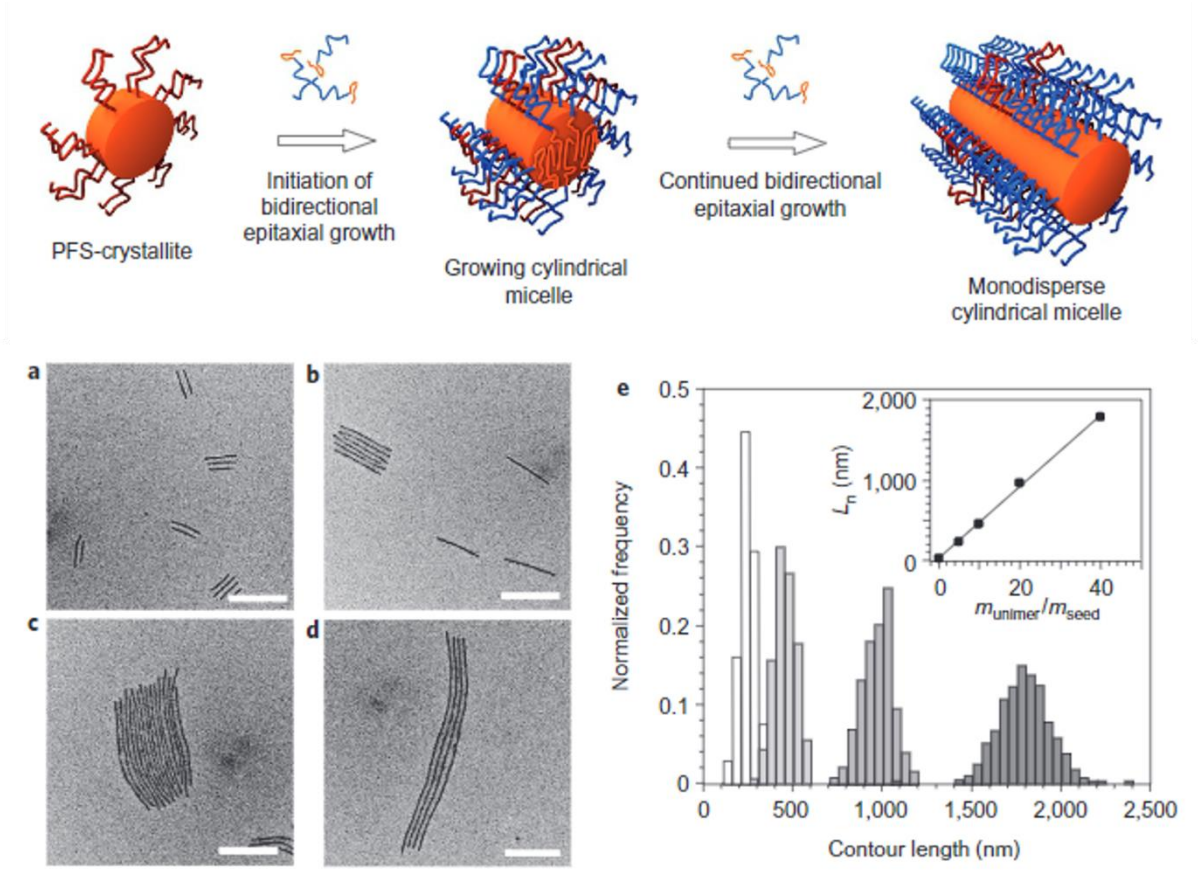


Figure 1.13. Schematic illustration of living CDSA of PFS-containing block copolymers by epitaxial growth. a-d) TEM images of monodisperse cylindrical micelles of PFS-*b*-PI with various lengths obtained by addition of PFS-*b*-PI solutions at increasing concentrations. e) Length distribution and linear dependence of cylindrical micelles. Figure reproduced from Manners and coworkers.[177]

- 2D epitaxial growth

Two-dimensional nanostructures are of great interest owing to many of their unique characteristics such as large surface area, defined shape, and adjustable aspect ratio. However, the preparation of customizable 2D structures from BCPs in solution remains challenging.[178] In 2014, Hudson *et al*. demonstrated that uniform lenticular structures could also be obtained *via* living CDSA through addition of semicrystalline BCPs with similar corona-core block lengths to seeds.[179] The formation of lenticular platelets over cylindrical micelles was based on the packing parameter attributed to BCPs with quasi-equal mole fraction. Later studies proved that

structures with 2D morphologies could be accessed from the living CDSA of block copolymers with variable corona-to-core ratios that in normal conditions would lead to uniform 1D structures.[180] Manners and coworkers employed a co-crystallisation approach by combining the dissolved unimer with semicrystalline PFS homopolymer to achieve 2D nano-sheets with various geometries (**Figure 1.14**).[181] It is believed that the PFS homopolymer, as it presents faster crystallisation rates than the amphiphilic BCP, crystallises first onto the seed. As a result, the seed micelles covered by the semicrystalline polymers provide a two-dimensional initiation site, leading to bidirectional unimer addition and crystal growth.

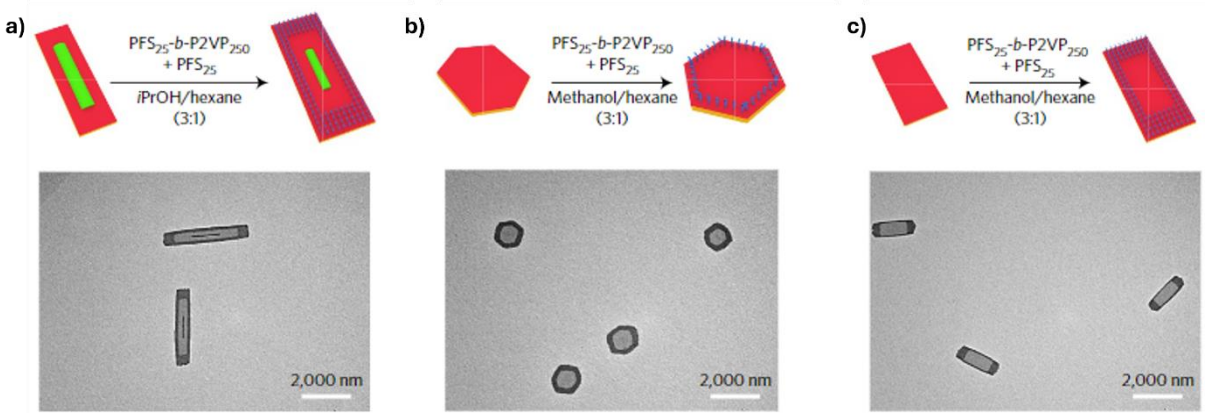


Figure 1.14. Platelets micelles with rectangular and hexagonal geometry obtained from the 2D epitaxial growth *via* living CDSA using different PFS-based crystalline seeds. Figure reproduced from Manners and corworkers.[181]

Following these pioneering reports with PFS-containing copolymers, living CDSA methodologies have been extended to a range of semicrystalline systems including polythiophenes, PLLA, PCL, and P*i*PrOX to access a wide range of 1D and 2D structures with controlled dimensions.[182, 183] Moreover, the size and special defined assemblies achieved through living CDSA have proven great potential for an extensive variety of applications from sensing systems, electronic devices, emulsion stabilisers and drug delivery systems.[184]

1.5 Summary

The morphology of nanoparticles has emerged as a critical factor in overcoming biological barriers. Particles with low surface curvature have proven more advantageous at reaching and delivering small molecules into damaged tissues than their spherical counterparts. This has been attributed to their unique thermodynamic flow characteristics and higher surface area, which provides enhanced cell-nanoparticle interactions and longer life-times circulation. Therefore, the design of functional non-spherical nanoparticles is crucial to develop novel and efficient drug delivery systems. However, the preparation of non-spherical structures containing functionality in their core requires precise synthetic control and alternative self-assembly methodologies. In this regard, crystallisation-driven self-assembly (CDSA) emerged as an ideal candidate to access complex high order morphologies from block copolymers that contain a semicrystalline core-forming block. This introductory chapter outlines key concepts for the synthesis of well-defined semicrystalline block copolymers and the design of core-functionalised anisotropic nanoparticles with potential applications as drug delivery systems. Initially, the use and current limitations of polymeric nanoparticles for drug delivery were underscored with a focus on the impact of nanoparticle shape on the biodistribution. CDSA is then presented as a potential strategy to achieve well-defined 1D and 2D non-spherical structures from semicrystalline polymers. Following this, the conception of semicrystalline polymers was presented, highlighting the effects of polymer constitution and the presence of substituents and their spatial distribution over the tacticity and crystallisation process. Subsequent to this, ring-opening polymerisation (ROP) and RAFT polymerisation techniques were introduced as types of living polymerisations to access well-defined functional block copolymers with potential regiocontrol of substituents and retained crystallinity. This leads us to the last section of the chapter focused on self-assembly of amphiphilic block copolymers in

solution and the challenges encountered when targeting non-spherical nanoparticles. Finally, the concepts of CDSA and "living" CDSA were further developed as a potential alternative to access nanoparticles with defined dimensions and morphology. A wide range of biocompatible and biodegradable semicrystalline polymers have demonstrated to undergo CDSA resulting in anisotropic nanoparticles with potential applications in the biomedical field. Overall, the concepts and strategies outlined in this chapter provide a solid foundation for designing biocompatible non-spherical nanostructures using semicrystalline substituted polymers.

1.6 Project aims

The main aim of this thesis was to develop non-spherical biocompatible nanoparticles containing functionalities attached to the core-forming block, which can be potentially used as drug delivery systems. For this, amphiphilic block copolymers containing a semicrystalline block of ε-substituted poly(ε-caprolactones) were prepared and self-assembled *via* CDSA.

Therefore, the first objective of the thesis was to synthesise functional poly(ε-caprolactones) while retaining the semicrystalline nature of PCL. It was hypothesised that semicrystalline materials could be assessed either by controlling the stereochemistry and tacticity of the polymer, or through the copolymerisation of aliphatic and substituted monomers. To accomplish this, ε-allyl-ε-caprolactone (εACL) was selected as the substituted monomer owing to its straightforward synthesis and the ability to attach functionalities post-polymerisation. In this thesis, four different strategies towards the preparation of semicrystalline allyl-containing PCLs were explored: i) asymmetric kinetic resolution polymerisation of *rac*-εACL with chiral TRIP BINOL catalyst, ii) ring-opening polymerisation of highly enantioenriched (*R*)- and (*S*)-monomers, iii) stereoselective polymerisation of steroenriched monomers with chiral TRIP BINOL catalysts, and iv) ring-opening copolymerisation of ε-caprolactone and εACL. Next, the aim was to achieve amphiphilic block copolymers with small molecules attached in the semicrystalline core-block. For this, RAFT polymerisation and thiol-ene click addition were investigated to chain-extend and functionalise the PCL-based polymers respectively, since they have demonstrated high control and chemical yields.

In the third stage, the crystallisation-driven self-assembly of these copolymers was explored. It was envisioned that this strategy would enable access to well-defined 1D and 2D structures bearing small molecules in the core-forming block in polar solvents. Herein, the intention was

to understand how the polymer composition, temperature, and solvent of choice affected the resultant morphology. It was anticipated that this tool could be used to design novel delivery systems with anisotropic morphologies that can result in enhanced drug biodistribution. For this reason, the last objective of the thesis was to explore the effect of the morphology and size of these particles on biological activity.

1.7 References

1. L. Kou, Y. D. Bhutia, Q. Yao, Z. He, J. Sun and V. Ganapathy, *Front. pharmacol.*, 2018, **9**.
2. M. J. Mitchell, M. M. Billingsley, R. M. Haley, M. E. Wechsler, N. A. Peppas and R. Langer, *Nat. Rev. Drug Discov.*, 2021, **20**, 101-124.
3. N. Nishiyama, *Nat Nanotechnol*, 2007, **2**, 203-204.
4. S. Yadav, A. K. Sharma and P. Kumar, *Front. bioeng. biotechnol.*, 2020, **8**.
5. Y. Li, J. Wu, H. Oku and G. Ma, *Adv Nanobiomed Res*, 2022, **2**, 2200074.
6. J. Lee, H.-S. Min, D. G. You, K. Kim, I. C. Kwon, T. Rhim and K. Y. Lee, *J. Contr. Release*, 2016, **223**, 197-206.
7. A. Nag, K. Banerjee, R. Barman, J. Kar, D. P. Sarkar, S. S. Jana and S. Ghosh, *J. Am. Chem. Soc*, 2023, **145**, 579-584.
8. S. He, X. Fu, L. Wang, Y. Xue, L. Zhou, S. Qiao, J. An and T. Xia, *Small*, 2023, **19**.
9. A. E. Masucci, M. Ghasemi, C. W. Pester and E. D. Gomez, *Mater. Adv.*, 2023, **4**, 2586-2594.
10. A.-L. Buckinx, A. M. Rozario, T. D. M. Bell, J. J. Michels and T. Junkers, *Polym. Chem.*, 2022, **13**, 2057-2064.
11. M. Zhang, X. Xiao, L. Liu, S. Liu, H. Liu, T. Fan, B. Zhang, S. Wageh, A. Al-Ghamdi, M. Wang, J. Wang, C. Du, N. Jiang, H. Zhang and Q. Peng, *Adv Nanobiomed Res*, 2022, **2**, 2200014.
12. M. Kim, J.-H. Lee and J.-M. Nam, *Adv. Sci.*, 2019, **6**, 1900471.
13. T. K. Dash and V. B. Konkimalla, *Mol. Pharm.*, 2012, **9**, 2365-2379.
14. S. De Luca, J. Treny, F. Chen, P. Seal, M. H. Stenzel and S. C. Smith, *Adv. Theory Simul.*, 2021, **4**, 2000247.
15. A. Travanut, P. F. Monteiro, S. Smith, S. M. Howdle, A. M. Grabowska, B. Kellam, M. A. R. Meier and C. Alexander, *J. Mater. Chem. B*, 2022, **10**, 3895-3905.
16. J. Weng, H. H. Y. Tong and S. F. Chow, *Pharmaceutics*, 2020, **12**, 732.
17. W. Poon, B. R. Kingston, B. Ouyang, W. Ngo and W. C. W. Chan, *Nat. Nanotechnol*, 2020, **15**, 819-829.
18. E. Blanco, H. Shen and M. Ferrari, *Nat. Biotechnol.*, 2015, **33**, 941-951.

19. H. Cabral, Y. Matsumoto, K. Mizuno, Q. Chen, M. Murakami, M. Kimura, Y. Terada, M. R. Kano, K. Miyazono, M. Uesaka, N. Nishiyama and K. Kataoka, *Nat. Nanotechnol*, 2011, **6**, 815-823.
20. Y. Yamamoto, Y. Nagasaki, Y. Kato, Y. Sugiyama and K. Kataoka, *J. Contr. Release*, 2001, **77**, 27-38.
21. Y. Y. Yuan, C. Q. Mao, X. J. Du, J. Z. Du, F. Wang and J. Wang, *Adv. Mater.*, 2012, **24**, 5476-5480.
22. J. Tan, S. Shah, A. Thomas, H. D. Ou-Yang and Y. Liu, *Microfluid. Nanofluidics*, 2013, **14**, 77-87.
23. P. Decuzzi, R. Pasqualini, W. Arap and M. Ferrari, *Pharm. Res.*, 2009, **26**, 235-243.
24. S. Shah, Y. Liu, W. Hu and J. Gao, *J. Nanosci. Nanotechnol.*, 2011, **11**, 919-928.
25. Y. Geng, P. Dalhaimer, S. Cai, R. Tsai, M. Tewari, T. Minko and D. E. Discher, *Nat. Nanotechnol*, 2007, **2**, 249-255.
26. A. Banerjee, J. Qi, R. Gogoi, J. Wong and S. Mitragotri, *J. Contr. Release*, 2016, **238**, 176-185.
27. D. Li, J. Zhuang, H. He, S. Jiang, A. Banerjee, Y. Lu, W. Wu, S. Mitragotri, L. Gan and J. Qi, *ACS Appl Mater Interfaces*, 2017, **9**, 42492-42502.
28. P. Decuzzi, S. Lee, B. Bhushan and M. Ferrari, *Ann. Biomed. Eng.*, 2005, **33**, 179-190.
29. J. T. Lovegrove, R. Raveendran, P. Spicer, S. Förster, C. J. Garvey and M. H. Stenzel, *ACS Macro Lett.*, 2023, **12**, 344-349.
30. R. Duncan and S. C. W. Richardson, *Mol. Pharm.*, 2012, **9**, 2380-2402.
31. R. A. Petros and J. M. DeSimone, *Nat. Rev. Drug Discov.*, 2010, **9**, 615-627.
32. Q. Yu, S. Othman, S. Dasgupta, T. Auth and G. Gompper, *Nanoscale*, 2018, **10**, 6445-6458.
33. S. Niaz, B. Forbes and B. T. Raimi-Abraham, *Nanomanufacturing*, 2022, **2**, 1-16.
34. J.-W. Yoo, N. Doshi and S. Mitragotri, *Macromol. Rapid Commun.*, 2010, **31**, 142-148.
35. J. A. Champion and S. Mitragotri, *PNAS*, 2006, **103**, 4930-4934.
36. P. Decuzzi and M. Ferrari, *Biophys. J.*, 2008, **94**, 3790-3797.
37. J. A. Champion and S. Mitragotri, *Pharm. Res.*, 2009, **26**, 244-249.
38. R. Agarwal, V. Singh, P. Jurney, L. Shi, S. V. Sreenivasan and K. Roy, *PNAS*, 2013, **110**, 17247-17252.
39. E. Hinde, K. Thammasiraphop, H. T. T. Duong, J. Yeow, B. Karagoz, C. Boyer, J. J. Gooding and K. Gaus, *Nat. Nanotechnol*, 2017, **12**, 81-89.
40. S. Mahapatra, P. Dey and G. Ghosh, *Polym. J.*, 2024, DOI: 10.1038/s41428-024-00931-8.
41. M. C. Arno, M. Inam, Z. Coe, G. Cambridge, L. J. Macdougall, R. Keogh, A. P. Dove and R. K. O'Reilly, *J. Am. Chem. Soc*, 2017, **139**, 16980-16985.
42. J. H. Park, H. J. Park, S. J. Tucker, S. K. Rutledge, L. Wang, M. E. Davis and S. J. Hollister, *Adv. Funct. Mater.*, 2023, **33**, 2215220.
43. F. J. v. Natta, J. W. Hill and W. H. Carothers, *J. Am. Chem. Soc*, 1934, **56**, 455-457.

44. O. Gil-Castell, I. Ontoria-Oviedo, J. D. Badia, E. Amaro-Prellezo, P. Sepúlveda and A. Ribes-Greus, *React Funct Polym*, 2022, **170**, 105064.
45. N. Raina, R. Pahwa, J. K. Khosla, P. N. Gupta and M. Gupta, *Polym. Bull.*, 2022, **79**, 7041-7063.
46. A. Bhadran, T. Shah, G. K. Babanyinah, H. Polara, S. Taslimy, M. C. Biewer and M. C. Stefan, *Pharmaceutics*, 2023, **15**, 1977.
47. R. Mülhaupt, *Angew. Chem. Int. Ed.*, 2004, **43**, 1054-1063.
48. H. Staudinger, H. Johner, R. Signer, G. Mie and J. Hengstenberg, *Zeitschrift für physikalische Chemie*, 1927, **126**, 425-448.
49. A. Keller, *Phil. Mag.*, 1957, **2**, 1171-1175.
50. H. G. Zachmann, *Kolloid-Zeitschrift & Zeitschrift für Polymere*, 1967, **216-217**, 180-191.
51. P. J. Flory, *J. Am. Chem. Soc*, 1962, **84**, 2857-2867.
52. J. Hoffmann, J. Flannigan, A. Cashmore, M. L. Briuglia, R. R. Steendam, C. J. Gerard, M. D. Haw, J. Sefcik and J. H. Ter Horst, *Faraday Discuss.*, 2022, **235**, 109-131.
53. R. J. Young and P. A. Lovell, *Introduction to polymers*, CRC press, 3rd edn., 2011.
54. M. R. Caputo, A. Olmos, B. Li, J. L. Olmedo-Martínez, A. Malafronte, C. De Rosa, H. Sardon, R. K. O'Reilly, A. P. Dove and A. J. Müller, *Biomacromolecules*, 2023, **24**, 3256-3267.
55. J. Yang, B. J. McCoy and G. Madras, *Chem. Phys.*, 2005, **122**, 064901.
56. P. Gill, T. T. Moghadam and B. Ranjbar, *J Biomol Tech*, 2010, **21**, 167-193.
57. C. Schick, *Anal. Bioanal. Chem.*, 2009, **395**, 1589-1611.
58. Y. Z. Zhan, Y. Du and Y. H. Zhuang, in *Methods for Phase Diagram Determination*, ed. J. C. Zhao, Elsevier Science Ltd, Oxford, 2007, DOI: https://doi.org/10.1016/B978-008044629-5/50004-5, pp. 108-150.
59. Y.-Q. Zheng, Z.-F. Yao, J.-H. Dou, Y. Wang, W. Ma, L. Zou, S. Nikzad, Q.-Y. Li, Z.-H. Sun, Z.-A. Yu, W.-B. Zhang, J.-Y. Wang and J. Pei, *Giant*, 2021, **7**, 100064.
60. M. Zhang, B.-H. Guo and J. Xu, *Crystals*, 2016, **7**, 4.
61. F. P. V. Koch, J. Rivnay, S. Foster, C. Müller, J. M. Downing, E. Buchaca-Domingo, P. Westacott, L. Yu, M. Yuan, M. Baklar, Z. Fei, C. Luscombe, M. A. McLachlan, M. Heeney, G. Rumbles, C. Silva, A. Salleo, J. Nelson, P. Smith and N. Stingelin, *Prog. Polym. Sci*, 2013, **38**, 1978-1989.
62. S. Xiang, S. Jun, G. Li, X.-C. Bian, L.-D. Feng, X.-S. Chen, F.-Q. Liu and S.-Y. Huang, *Chin. J. Polym. Sci.*, 2016, **34**, 69-76.
63. A. Fernández-Tena, R. A. Pérez-Camargo, O. Coulembier, L. Sangroniz, N. Aranburu, G. Guerrica-Echevarria, G. Liu, D. Wang, D. Cavallo and A. J. Müller, *Macromol.*, 2023, **56**, 4602-4620.
64. W. S. Fall, J. Baschnagel, O. Lhost and H. Meyer, *Macromol.*, 2022, **55**, 8438-8450.
65. Z. He, F. J. Davis and G. R. Mitchell, *Eur. Polym. J.*, 1996, **32**, 735-746.
66. Z. Ates, P. D. Thornton and A. Heise, *Polym. Chem.*, 2011, **2**, 309-312.

67. H. Marubayashi, R. Mizukami, Y. Hamada and S. Nojima, *Polym. Degrad. Stab.*, 2018, **153**, 318-324.
68. C. Clamor, B. N. Cattoz, P. M. Wright, R. K. O'Reilly and A. P. Dove, *Polym. Chem.*, 2021, **12**, 1983-1990.
69. J. C. Worch, H. Prydderch, S. Jimaja, P. Bexis, M. L. Becker and A. P. Dove, *Nat. Rev. Chem.*, 2019, **3**, 514-535.
70. L. J. Macdougall, M. M. Pérez-Madrigal, J. E. Shaw, J. C. Worch, C. Sammon, S. M. Richardson and A. P. Dove, *Angew. Chem. Int. Ed.*, 2021, **60**, 25856-25864.
71. J. C. Worch and A. P. Dove, *Acc. Chem. Res.*, 2022, **55**, 2355-2369.
72. C. A. Bell, J. Yu, I. A. Barker, V. X. Truong, Z. Cao, A. V. Dobrinyin, M. L. Becker and A. P. Dove, *Angew. Chem. Int. Ed.*, 2016, **55**, 13076-13080.
73. Y. Shi, T. Bai, W. Bai, Z. Wang, M. Chen, B. Yao, J. Z. Sun, A. Qin, J. Ling and B. Z. Tang, *Chem. Eur. J.*, 2017, **23**, 10725-10731.
74. J. Liu, J. W. Y. Lam, C. K. W. Jim, J. C. Y. Ng, J. Shi, H. Su, K. F. Yeung, Y. Hong, M. Faisal, Y. Yu, K. S. Wong and B. Z. Tang, *Macromol.*, 2011, **44**, 68-79.
75. A. L. Khalfa, M. L. Becker and A. P. Dove, *J. Am. Chem. Soc*, 2021, **143**, 17510-17516.
76. B. Autenrieth and R. R. Schrock, *Macromol.*, 2015, **48**, 2493-2503.
77. S. Ahmed, S. A. Bidstrup, P. Kohl and P. Ludovice, *Macromol. Symp.*, 1998, **133**, 1-10.
78. R. R. Schrock, *Dalton Trans.*, 2011, **40**, 7484.
79. G. W. Coates and R. M. Waymouth, *Science*, 1995, **267**, 217-219.
80. G. W. Coates, *Chem. Rev.*, 2000, **100**, 1223-1252.
81. G. Natta, *J. Polym. Sci.*, 1959, **34**, 531-549.
82. T. Fox, B. Garrett, W. Goode, S. Gratch, J. Kincaid, A. Spell and J. Stroupe, *J. Am. Chem. Soc*, 1958, **80**, 1768-1769.
83. T. M. McGuire, J. Bowles, E. Deane, E. H. E. Farrar, M. N. Grayson and A. Buchard, *Angew. Chem. Int. Ed.*, 2021, **60**, 4524-4528.
84. E. F. Clark, G. Kociok-Köhn, M. G. Davidson and A. Buchard, *Polym. Chem.*, 2023, **14**, 2838-2847.
85. S. R. Petersen, H. Prydderch, J. C. Worch, C. J. Stubbs, Z. Wang, J. Yu, M. C. Arno, A. V. Dobrynin, M. L. Becker and A. P. Dove, *Angew. Chem. Int. Ed.*, 2022, **61**, e202115904.
86. C. J. Stubbs, J. C. Worch, H. Prydderch, Z. Wang, R. T. Mathers, A. V. Dobrynin, M. L. Becker and A. P. Dove, *J. Am. Chem. Soc*, 2022, **144**, 1243-1250.
87. L. Mezzasalma, A. P. Dove and O. Coulembier, *Eur. Polym. J.*, 2017, **95**, 628-634.
88. P. Bexis, J. De Winter, O. Coulembier and A. P. Dove, *Eur. Polym. J.*, 2017, **95**, 660-670.
89. C. M. Thomas, *Chem. Soc. Rev.*, 2010, **39**, 165-173.
90. C. H. Chan, J.-T. Chen, W. S. Farrell, C. M. Fellows, D. J. Keddie, C. K. Luscombe, J. B. Matson, J. Merna, G. Moad, G. T. Russell, P. Théato, P. D. Topham and L. Sosa Vargas, *Polym. Chem.*, 2022, **13**, 2262-2270.
91. R. B. Grubbs and R. H. Grubbs, *Macromol.*, 2017, **50**, 6979-6997.
92. J. Qiu, B. Charleux and K. Matyjaszewski, *Polimery*, 2001, **46**, 453-460.
93. M. Szwarc, *Nature*, 1956, **178**, 1168-1169.

94. J. Kennedy, S. Feinberg and S. Huang, *J. Polym. Sci., Polym. Chem. Ed.*, 1978, **16**, 243-259.
95. T. Higashimura, M. Mitsuhashi and M. Sawamoto, *Macromol.*, 1979, **12**, 178-182.
96. Y. Doi, S. Suzuki and K. Soga, *Macromol.*, 1986, **19**, 2896-2900.
97. T. Ouhadi, C. Stevens and P. Teyssié, *Die Makromolekulare Chemie*, 1975, **1**, 191-201.
98. J. Chiefari, Y. Chong, F. Ercole, J. Krstina, J. Jeffery, T. P. Le, R. T. Mayadunne, G. F. Meijs, C. L. Moad and G. Moad, *Macromol.*, 1998, **31**, 5559.
99. J.-S. Wang and K. Matyjaszewski, *J. Am. Chem. Soc*, 1995, **117**, 5614-5615.
100. H. Sun, C. P. Kabb, Y. Dai, M. R. Hill, I. Ghiviriga, A. P. Bapat and B. S. Sumerlin, *Nat Chem*, 2017, **9**, 817-823.
101. D. Mecerreyes, R. D. Miller, J. L. Hedrick, C. Detrembleur and R. Jerome, *J. Polym. Sci., Part A: Polym. Chem.*, 2000, **38**, 870-875.
102. L. Liao, L. Liu, C. Zhang and S. Gong, *Macromol. Rapid Commun.*, 2006, **27**, 2060-2064.
103. Y. Xia, P. Yuan, Y. Zhang, Y. Sun and M. Hong, *Angew. Chem. Int. Ed.*, 2023, DOI: 10.1002/anie.202217812.
104. S. Moins, S. Hoyas, V. Lemaur, B. Orhan, K. Delle Chiaie, R. Lazzaroni, D. Taton, A. P. Dove and O. Coulembier, *Catalysts*, 2020, **10**, 620.
105. K. Makiguchi, S. Kikuchi, K. Yanai, Y. Ogasawara, S.-I. Sato, T. Satoh and T. Kakuchi, *J. Polym. Sci., Part A: Polym. Chem.*, 2014, **52**, 1047-1054.
106. W. Yu, E. Maynard, V. Chiaradia, M. C. Arno and A. P. Dove, *Chem. Rev.*, 2021, **121**, 10865-10907.
107. J. M. Longo, M. J. Sanford and G. W. Coates, *Chem. Rev.*, 2016, **116**, 15167-15197.
108. A. Duda and A. Kowalski, *Handbook of Ring-Opening Polymerization*, 2009, 1-51.
109. C. Alemán, O. Betran, J. Casanovas, K. N. Houk and H. K. Hall, Jr., *J. Org. Chem.*, 2009, **74**, 6237-6244.
110. E. V. Anslyn and D. A. Dougherty, in *Modern physical organic chemistry*, University science books, 2006, ch. 2, pp. 65-137.
111. D. K. Schneiderman and M. A. Hillmyer, *Macromol.*, 2016, **49**, 2419-2428.
112. C. Clamor, J. Beament, P. M. Wright, B. N. Cattoz, R. K. O'Reilly and A. P. Dove, *Polym. Chem.*, 2024, **15**, 1227-1233.
113. N. Ajellal, J.-F. Carpentier, C. Guillaume, S. M. Guillaume, M. Helou, V. Poirier, Y. Sarazin and A. Trifonov, *Dalton Trans.*, 2010, **39**, 8363.
114. Z. Grobelny, S. Golba and J. Jurek-Suliga, *Polym. Bull.*, 2019, **76**, 3501-3515.
115. Lin and Jheng, *Polym.*, 2019, **11**, 1530.
116. N. E. Kamber, W. Jeong, R. M. Waymouth, R. C. Pratt, B. G. G. Lohmeijer and J. L. Hedrick, *Chem. Rev.*, 2007, **107**, 5813-5840.
117. J. W. Peeters, O. van Leeuwen, A. R. A. Palmans and E. W. Meijer, *Macromol.*, 2005, **38**, 5587-5592.
118. Y. Hu, Y. Zhang, W. Xu, J. Xu, X. Lin and Q. Wu, *ACS Macro Lett.*, 2019, **8**, 1432-1436.
119. N. G. Turrini, R. C. Cioc, D. J. H. Van Der Niet, E. Ruijter, R. V. A. Orru, M. Hall and K. Faber, *Green Chem.*, 2017, **19**, 511-518.

120. X. Xie, Z. Huo, E. Jang and R. Tong, *Commun. Chem.*, 2023, **6**.
121. S. R. Kosuru, T.-H. Sun, L.-F. Wang, J. K. Vandavasi, W.-Y. Lu, Y.-C. Lai, S. C. N. Hsu, M. Y. Chiang and H.-Y. Chen, *Inorg. Chem.*, 2017, **56**, 7998-8006.
122. M. R. T. Breteler, Z. Zhong, P. J. Dijkstra, A. R. A. Palmans, J. Peeters and J. Feijen, *J. Polym. Sci., Part A: Polym. Chem.*, 2007, **45**, 429-436.
123. J. A. Wilson, S. A. Hopkins, P. M. Wright and A. P. Dove, *Polym. Chem.*, 2014, **5**, 2691-2694.
124. H. J. Fang, P. S. Lai, J. Y. Chen, S. C. N. Hsu, W. D. Peng, S. W. Ou, Y. C. Lai, Y. J. Chen, H. Chung, Y. Chen, T. C. Huang, B. S. Wu and H. Y. Chen, *J. Polym. Sci., Part A: Polym. Chem.*, 2012, **50**, 2697-2704.
125. Martyn P. Coles and Peter B. Hitchcock, *Eur. J. Inorg. Chem.*, 2004, **2004**, 2662-2672.
126. H. R. Kricheldorf and S. M. Weidner, *Polym. Chem.*, 2022, **13**, 1618-1647.
127. A.-C. Albertsson and I. K. Varma, *Biomacromolecules*, 2003, **4**, 1466-1486.
128. A. P. Dove, *ACS Macro Lett.*, 2012, **1**, 1409-1412.
129. F. Nederberg, E. F. Connor, M. Möller, T. Glauser and J. L. Hedrick, *Angew. Chem. Int. Ed.*, 2001, **40**, 2712-2715.
130. B. G. G. Lohmeijer, R. C. Pratt, F. Leibfarth, J. W. Logan, D. A. Long, A. P. Dove, F. Nederberg, J. Choi, C. Wade, R. M. Waymouth and J. L. Hedrick, *Macromol.*, 2006, **39**, 8574-8583.
131. A. P. Dove, R. C. Pratt, B. G. G. Lohmeijer, R. M. Waymouth and J. L. Hedrick, *J. Am. Chem. Soc*, 2005, **127**, 13798-13799.
132. S. Naumann and A. P. Dove, *Polym. Int.*, 2016, **65**, 16-27.
133. L. Zhang, F. Nederberg, R. C. Pratt, R. M. Waymouth, J. L. Hedrick and C. G. Wade, *Macromol.*, 2007, **40**, 4154-4158.
134. D. Delcroix, A. Couffin, N. Susperregui, C. Navarro, L. Maron, B. Martin-Vaca and D. Bourissou, *Polym. Chem.*, 2011, **2**, 2249.
135. T. Akiyama, J. Itoh and K. Fuchibe, *Adv. Synth. Catal.*, 2006, **348**, 999-1010.
136. K. Makiguchi, T. Satoh and T. Kakuchi, *Macromol.*, 2011, **44**, 1999-2005.
137. B. M. Chamberlain, M. Cheng, D. R. Moore, T. M. Ovitt, E. B. Lobkovsky and G. W. Coates, *J. Am. Chem. Soc*, 2001, **123**, 3229-3238.
138. C.-X. Cai, A. Amgoune, C. W. Lehmann and J.-F. O. Carpentier, *Chem. Commun.*, 2004, DOI: 10.1039/b314030j, 330.
139. M. Cheng, A. B. Attygalle, E. B. Lobkovsky and G. W. Coates, *J. Am. Chem. Soc*, 1999, **121**, 11583-11584.
140. J. Li, B.-H. Ren, Z.-Q. Wan, S.-Y. Chen, Y. Liu, W.-M. Ren and X.-B. Lu, *J. Am. Chem. Soc*, 2019, **141**, 8937-8942.
141. W. M. Ren, Y. Liu, G. P. Wu, J. Liu and X. B. Lu, *J. Polym. Sci., Part A: Polym. Chem.*, 2011, **49**, 4894-4901.
142. T. James, M. van Gemmeren and B. List, *Chem. Rev.*, 2015, **115**, 9388-9409.
143. Z. D. Susam and C. Tanyeli, *Asian J. Org. Chem.*, 2021, **10**, 1251-1266.
144. J.-B. Zhu and E. Y. X. Chen, *J. Am. Chem. Soc*, 2015, **137**, 12506-12509.

145. C. Lv, L. Zhou, R. Yuan, Q. Mahmood, G. Xu and Q. Wang, *New J Chem*, 2020, **44**, 1648-1655.
146. S. Liu, H. Li, N. Zhao and Z. Li, *ACS Macro Lett.*, 2018, **7**, 624-628.
147. K. Makiguchi, T. Yamanaka, T. Kakuchi, M. Terada and T. Satoh, *Chem. Commun.*, 2014, **50**, 2883-2885.
148. A. Sanchez-Sanchez, I. Rivilla, M. Agirre, A. Basterretxea, A. Etxeberria, A. Veloso, H. Sardon, D. Mecerreyes and F. P. Cossío, *J. Am. Chem. Soc*, 2017, **139**, 4805-4814.
149. N. Corrigan, K. Jung, G. Moad, C. J. Hawker, K. Matyjaszewski and C. Boyer, *Prog. Polym. Sci*, 2020, **111**, 101311.
150. G. Moad, J. Chiefari, Y. K. Chong, J. Krstina, R. T. A. Mayadunne, A. Postma, E. Rizzardo and S. H. Thang, *Polym. Int.*, 2000, **49**, 993-1001.
151. G. Moad, E. Rizzardo and S. H. Thang, *Aust. J. Chem.*, 2005, **58**, 379.
152. F. Ahmed, P. J. Photos and D. E. Discher, *Drug Dev. Res.*, 2006, **67**, 4-14.
153. Y. Mai and A. Eisenberg, *Chem Soc Rev*, 2012, **41**, 5969.
154. K. E. B. Doncom, L. D. Blackman, D. B. Wright, M. I. Gibson and R. K. O'Reilly, *Chem Soc Rev*, 2017, **46**, 4119-4134.
155. Y. Ishiwatari, T. Yokoyama, T. Kojima, T. Banno and N. Arai, *Mol. Syst. Des.*, 2024, **9**, 20-28.
156. A. Aliabadi, M. Hasannia, M. Vakili-Azghandi, F. Araste, K. Abnous, S. M. Taghdisi, M. Ramezani and M. Alibolandi, *J. Mater. Chem. B*, 2023, **11**, 9325-9368.
157. U. Tritschler, S. Pearce, J. Gwyther, G. R. Whittell and I. Manners, *Macromol.*, 2017, **50**, 3439-3463.
158. B. Lotz, A. Kovacs, G. Bassett and A. Keller, *J. Appl. Phys.* , 1965, **36**, 2618-&.
159. J. Massey, K. N. Power, I. Manners and M. A. Winnik, *J. Am. Chem. Soc*, 1998, **120**, 9533-9540.
160. J. A. Massey, K. Temple, L. Cao, Y. Rharbi, J. Raez, M. A. Winnik and I. Manners, *J. Am. Chem. Soc*, 2000, **122**, 11577-11584.
161. M.-S. Hsiao, S. F. M. Yusoff, M. A. Winnik and I. Manners, *Macromol.*, 2014, **47**, 2361-2372.
162. W. Yu, M. Inam, J. R. Jones, A. P. Dove and R. K. O'Reilly, *Polym. Chem.*, 2017, **8**, 5504-5512.
163. J. Wang, W. Zhu, B. Peng and Y. Chen, *Polymer*, 2013, **54**, 6760-6767.
164. J. R. Finnegan, E. H. Pilkington, K. Alt, M. A. Rahim, S. J. Kent, T. P. Davis and K. Kempe, *Chem. Sci.*, 2021, **12**, 7350-7360.
165. C. Wang, F. Huang, X. Huang, G. Lu and C. Feng, *Macromol. Rapid Commun.*, **n/a**, 2300482.
166. S.-J. Park, S.-G. Kang, M. Fryd, J. G. Saven and S.-J. Park, *J. Am. Chem. Soc*, 2010, **132**, 9931-9933.
167. Z. Wang, M. Lin, C. Bonduelle, R. Li, Z. Shi, C. Zhu, S. Lecommandoux, Z. Li and J. Sun, *Biomacromolecules*, 2020, **21**, 3411-3419.
168. J. Raez, I. Manners and M. A. Winnik, *J. Am. Chem. Soc*, 2002, **124**, 10381-10395.

169. W. Yu, J. C. Foster, A. P. Dove and R. K. O'Reilly, *Macromol.*, 2020, **53**, 1514-1521.
170. J. Schmelz, F. H. Schacher and H. Schmalz, *Soft Matter*, 2013, **9**, 2101-2107.
171. W. Xu, Y. Zheng and P. Pan, *J. Polym. Sci.*, 2022, **60**, 2136-2152.
172. L. Cao, I. Manners and M. A. Winnik, *Macromol.*, 2002, **35**, 8258-8260.
173. M. Inam, G. Cambridge, A. Pitto-Barry, Z. P. L. Laker, N. R. Wilson, R. T. Mathers, A. P. Dove and R. K. O'Reilly, *Chem. Sci.*, 2017, **8**, 4223-4230.
174. S. Song, X. Liu, E. Nikbin, J. Y. Howe, Q. Yu, I. Manners and M. A. Winnik, *J. Am. Chem. Soc*, 2021.
175. X. Wang, G. Guerin, H. Wang, Y. Wang, I. Manners and M. A. Winnik, *Science*, 2007, **317**, 644-647.
176. D. Tao, C. Feng, Y. Lu, Y. Cui, X. Yang, I. Manners, M. A. Winnik and X. Huang, *Macromol.*, 2018, **51**, 2065-2075.
177. J. B. Gilroy, T. Gadt, G. R. Whittell, L. Chabanne, J. M. Mitchels, R. M. Richardson, M. A. Winnik and I. Manners, *Nat Chem*, 2010, **2**, 566-570.
178. J. Zhu, S. Zhang, K. Zhang, X. Wang, J. W. Mays, K. L. Wooley and D. J. Pochan, *Nat. Commun.*, 2013, **4**.
179. Z. M. Hudson, C. E. Boott, M. E. Robinson, P. A. Rupar, M. A. Winnik and I. Manners, *Nat Chem*, 2014, **6**, 893-898.
180. G. Cambridge, M. J. Gonzalez-Alvarez, G. Guerin, I. Manners and M. A. Winnik, *Macromol.*, 2015, **48**, 707-716.
181. X. He, M.-S. Hsiao, Charlotte, Robert, A. Nazemi, X. Li, Mitchell and I. Manners, *Nat. Mater.*, 2017, **16**, 481-488.
182. Z. Coe, A. Weems, A. P. Dove and R. K. O'Reilly, *J. Vis. Exp.*, 2019, DOI: doi:10.3791/59772, e59772.
183. T. Gädt, N. S. Ieong, G. Cambridge, M. A. Winnik and I. Manners, *Nat. Mater.*, 2009, **8**, 144-150.
184. L. Macfarlane, C. Zhao, J. Cai, H. Qiu and I. Manners, *Chem. Sci.*, 2021, **12**, 4661-4682.

Chapter 2.

Towards enantiopurity: Synthesis of enantioenriched poly(allyl-ε-caprolactones)

2 Towards enantiopurity: Synthesis of enantioenriched poly(allyl-ε-caprolactones)

2.1 Manuscript and overview

Title: Towards enantiopurity: Synthesis of enantioenriched poly(allyl-ε-caprolactones).

Authors: **Ana Cubillo Álvarez**[1], Maria C. Arno[1]*, Andrew P. Dove[1]*

Affiliations: [1]School of Chemistry, University of Birmingham, Edgbaston, Birmingham, B15 2TT, UK.

Manuscript Prepared

Overview:

The objective of this chapter was to investigate how stereochemistry influences the thermal properties of ε-substituted poly(ε-caprolactones), to produce semicrystalline polymers bearing functional pendant groups by controlling their stereochemistry. Previous reports have demonstrated that stereoregular polymers possess enhanced thermo-mechanical properties compared to their atactic counterparts. However, their synthesis has been restricted to the use of monomers with fixed or highly controlled stereochemistry, which are limited and challenging to prepare. Whilst asymmetric kinetic resolution polymerisations (AKRP) of racemic monomers have shown promising results, the lack of catalytic enantioselective protocols hinders the preparation of highly stereoregular polymers.

In this work, the concept of AKRP was exploited through the polymerisation of racemic ε-allyl-ε-caprolactone using stereopure 3,3'-Bis(2,4,6-triisopropylphenyl)-1,1'-binapthyl-2,2'-diyl hydrogen phosphate (TRIP BINOL). Gas chromatography-mass spectrometry analyses of the recovered monomers revealed moderate enantioselectivity. Subsequently, to obtain highly

enantioenriched poly(ε-allyl-ε-caprolactones), the stereoselective polymerisation of enantioenriched allyl-functional ε-caprolactones (up to 87.3% *ee*), using a stereoselective TRIP BINOL catalyst was explored. Enantio-defined monomers were obtained on a large scale *via* ring-expansion of their enantioenriched cyclic ketone precursors, which were prepared employing host-guest chemistry techniques, where an optically active host molecule selectively binds one of the enantiomers of a racemic mixture.

The thermal properties of the resultant polymers obtained from both racemic and enantioenriched monomers were assessed through a differential scanning calorimeter. Unfortunately, despite the use of enantioenriched monomers and stereoselective catalysts, crystallinity was not retained for any of the polymers obtained.

Towards enantiopurity: Synthesis of enantioenriched poly(allyl-ε-caprolactones)

Ana Cubillo Álvarez[1], Maria C. Arno[1]*, Andrew P. Dove[1]*

[1]School of Chemistry, University of Birmingham, Edgbaston, Birmingham, B15 2TT, UK

Abstract

The synthesis of stereoregular polymers has garnered significant attention over the past decades, thanks to their ability to enhance the thermo-mechanical properties of materials in contrast to their atactic counterparts. Asymmetric kinetic resolution polymerisation of substituted ε-caprolactones, as example of biodegradable and biocompatible monomers, has been explored to generate stereo-controlled polymers. However, this process is hindered by low catalyst enantioselectivity and limited scope of monomer substituents. Thus, the influence of the stereochemistry on the polymer's thermal properties remains poorly understood. In this work, we present a novel strategy to obtain enantioenriched poly(allyl-ε-caprolactones) through ring-opening polymerisation of enantioenriched allyl-ε-caprolactones (εACL) using a chiral phosphoric acid (TRIP BINOL) as a stereoselective catalyst. Kinetic and enantioselectivity studies of TRIP BINOL were conducted with the racemic allyl monomer achieving selectivity factors up to 15 at 40 °C. Enantioenriched εACLs were further prepared through deracemization of 2-allylcyclohexanone using an environmentally friendly host-guest protocol, followed by their ring expansion to yield monomers with enantiomeric excess values up to 87.3%. Subsequent polymerisation of enantioenriched (*R*)- and (*S*)-monomer with the chiral catalyst was explored and the thermal properties of the resultant polymers were investigated.

Introduction

Chirality is an innate characteristic found in nature where molecules with different spatial arrangements can have different physicochemical, mechanical, and biological properties. In the same way, stereoregular polymers have shown improved thermal,[1, 2] mechanical,[3, 4] and conductive[5] properties compared to their atactic counterparts. Stereoregular polymers can be obtained either through the polymerization of enantiopure monomers,[6, 7] or *via* asymmetric kinetic resolution polymerisation (AKRP) where the catalyst preferentially interacts with one of the monomer enantiomers.[8] In recent years, the stereoselective polymerization of different types of monomers, such as lactones,[9-13] epoxides,[14, 15] thiiranes,[16] α-olefins,[17, 18] and methacrylates,[19, 20] has been widely investigated. For example, Coates and Ovitt[21-23] reported the use of aluminum alkoxides as stereoselective catalysts to form isotactic stereoblock poly(lactic acid) (PLA) and syndiotactic PLA, from *rac*-lactide (LA) and *meso*-LA respectively, with enhanced melting temperatures (T_m) compared to the atactic and enantiomerically pure polymers. Moreover, chiral metal complexes, organic catalysts such as thioureas,[24, 25] chiral BINOL-derived phosphoric acids,[26] phosphazenes,[27] and N-heterocyclic carbenes[28] have also been explored for enantioselective ring-opening polymerisation (ROP) of *rac*-LA.

Sustainable polyesters are particularly attractive in both plastic and biomedical applications because of their good biocompatible and biodegradable properties.[29, 30] Among them, poly-ε-caprolactones (PCLs) have demonstrated to be excellent candidates for the design of novel biomaterials and potential drug delivery systems,[31-34] owing to their robust mechanical properties and semicrystalline nature. However, the lack of pendant groups in the polymer backbone limits their mechanical performance and prevents further functionalization. Clamor *et al*. reported the synthesis of ε-alkyl-substituted PCLs with alkyl chain lengths varying from C_6 to C_{16} and the ability to tune the crystallinity and lipophilicity of the polymer by increasing

alkyl chain length.[35] Despite the extensive studies on the asymmetric polymerization of lactide, the synthesis and polymerisation of stereoregular substituted PCLs remain underdeveloped with very few examples in the literature, and the majority of research has been limited to methyl-substituted caprolactones (4-MeCL). Approaches to synthesise stereopure monomers usually involve complex synthetic procedures, as well as the use of harsh and toxic conditions, and a very small scale is required to obtain optically pure molecules, which precludes further polymerisation (**Figure 2.1A**). Buchwald and coworkers[36] described the synthesis of several enantioenriched β-substituted lactones with enantiomeric excess (*ee*) up to 93%, in a two-step synthetic route involving the ring-closing metathesis of dienes using a ruthenium catalyst followed by the enantioselective 1,4-reduction of the cycloenones using a chiral Cu(I)/*p*-tolBINAP catalyst. In another study, Li *et al.*[37] reported the synthesis of (*S*)-6-methyl-ε-caprolactone (6-MeCL) from commercially available *Z*-2-heptene through a novel palladium-catalysed asymmetric deoxygenation, followed by hydrolysis and a Cu-catalysed oxidative cyclization to yield the desired molecule in moderate yields and 92% *ee*. Alternatively, enantioenriched substituted ε-caprolactones (ε-SCLs) can be obtained by the ring-expansion of their cyclohexanone precursor. In 2009, the Strukul group[38] pioneered the enantioselective Baeyer-Villiger oxidation of meso-cyclohexanones in aqueous media using a Pt(II) catalyst to yield enantioenriched (*S*) caprolactones with *ee* values varying from 34% to 92% depending on the pendant functional group. Following these studies, Feng and coworkers[39] developed a novel chiral *N,N*'-dioxide-Sc(III) for the kinetic resolution of 2-aryl-substituted cyclohexanones to achieve enantiopure α-aryl-substituted caprolactones with 94% *ee* and 51% yield.

Recent reports have been focused on the AKRP of racemic ε-SCLs using either enzymatic catalysts,[40, 41] organometallic catalysts,[42] or chiral phosphoric acids.[43] While biocatalysts have proven to be highly enantioselective during polymerization, the substituent scope is limited to

methyl-substituted monomers. To date, there are only two studies from Wang and coworkers exploring the AKRP of substituted caprolactones different to methyl-ε-CL.[44, 45] In these reports, chiral BINOL-derived phosphoric acids were used as catalysts for the stereoselective ROP of 6-aryl-ε-caprolactones giving selective factors (*s*-factor) as high as 7.3 at low monomer conversion (**Figure 2.1B**). Despite these significant advances, the lack of catalytic selectivity and monomer limitations highlight the need to develop novel strategies for the stereoselective polymerization of substituted ε-CLs.

Herein, we focus on the preparation of functional ε-allyl-ε-caprolactone (εACL), bearing allyl pendant groups that serve as a functional handle for post-polymerisation modifications. We studied the asymmetric polymerisation of *rac*-ε-allyl-ε-caprolactone (εACL) using chiral 2,4,6-triisopropylphenyl (TRIP) BINOL catalyst to yield stereoregular poly(allyl-ε-caprolactone)s (PACL) and explored the synergistic effect during polymerisation of stereoselective TRIP BINOL catalysts in combination with enantioenriched (*R*)- or (*S*)-allyl-ε-caprolactone (**Figure 2.1C**). The enantioenriched monomers were isolated in gram-scale and with high enantiomeric excess (*ee*) through the deracemization of their racemic precursor, 2-allylcyclohexanone, in the presence of an optically active host molecule, followed by ring expansion. Stereo-defined allyl-functional PCLs with several levels of stereo-regularity were obtained by ROP and the effect of stereochemistry on their thermal properties were investigated.

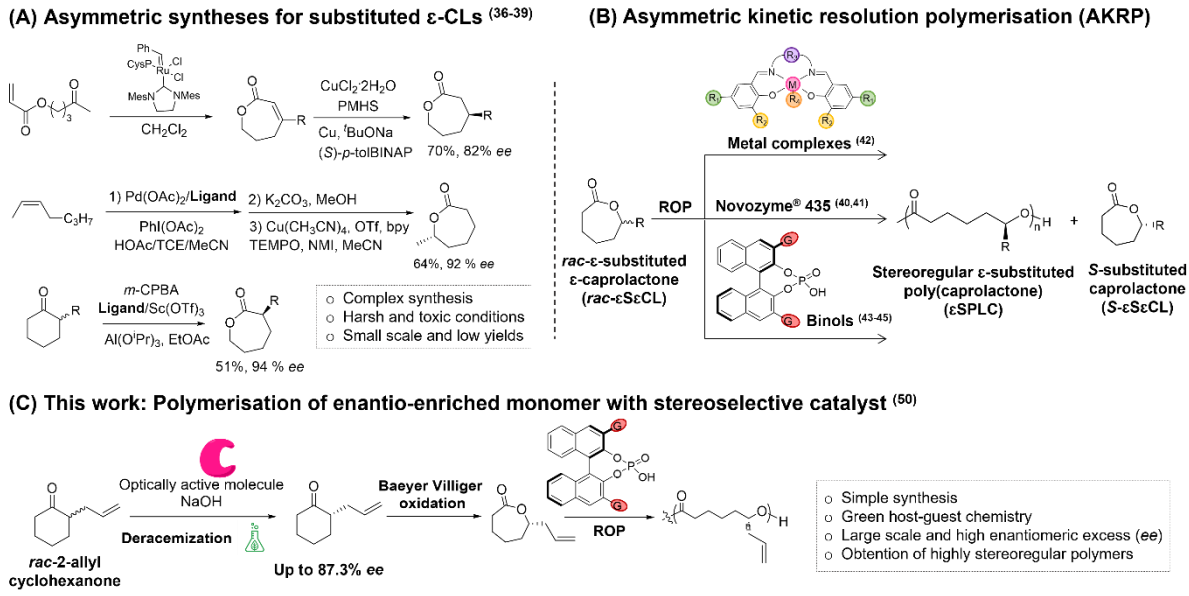
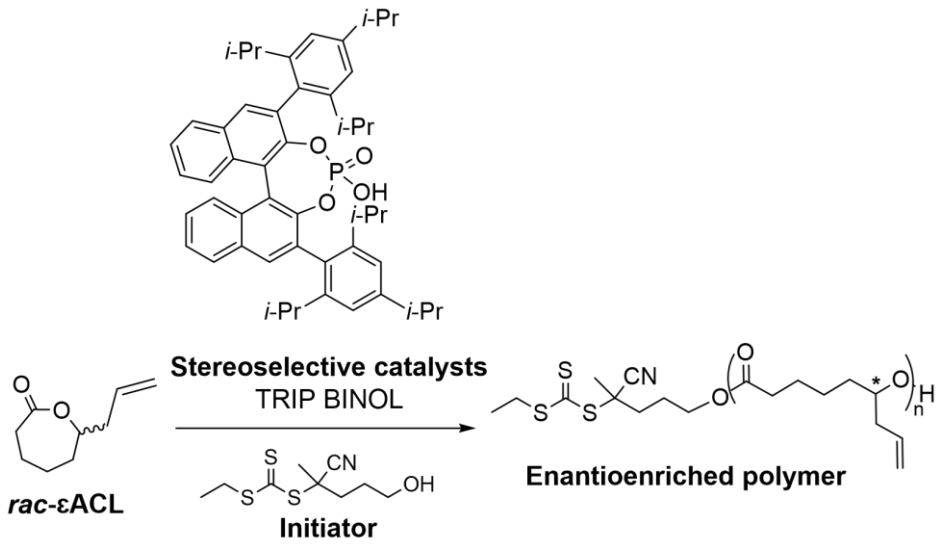


Figure 2.1. (A) Asymmetric syntheses of enantiopure substituted ε-caprolactones (ε-SCL). **(B)** Classical stereoselective ring-opening polymerizations (ROP) of ε-SCL. **(C)** This work: preparation of stereoregular allyl-substituted poly(caprolactones) combining a highly enantioenriched monomer with a stereoselective catalysts.

Results and discussion

To optimise the reaction conditions and investigate the enantiomeric selectivity of the catalysts, racemic ε-allyl-ε-caprolactone (*rac*-εACL) was prepared from 2-allylcyclohexanone through Bayer-Villiger oxidation and the subsequent ROP was carried out using 2-cyano-5-hydroxypentan-2-yl ethyl carbonotrithioate (CHPET) as initiator and catalysed by TRIP BINOL, a commercially available chiral phosphoric acid previously reported as the organocatalyst with the highest selectivity in the AKRP of substituted caprolactones (**Scheme 2.1** and **Table 2.1**).[43, 45]



Scheme 2.1. Stereo-selectivity studies of (*R*)- and (*S*)-TRIP BINOL catalysts.

The polymerisation of *rac*-εACL with (*R*)-TRIP BINOL was performed at both 25 °C and 40 °C. Order kinetic studies were assessed leaving the polymerisation to reach high monomer conversions (**Figure S2.9**) whereas asymmetric kinetic resolution studies were stopped prior reaching 50% monomer conversion in order to analyse the resultant enantiomeric ratio (*er*) and stereoselectivity of the catalyst. Size-exclusion chromatography (SEC) of allyl polymers showed monomodal distributions with low molar-mass dispersity ($Đ_M$), which suggested a controlled polymerisation (**Figures S2.10** and **S2.11**). A linear relationship between the molar mass of the polymers and the time, which reflects first-order kinetics, proved the livingness of the ROP and further supported a controlled polymerisation (**Figure 2.2A** and **Figure S2.12**). As expected, slower kinetic rates were observed at lower temperatures (Table 2.1, **entries 1** *vs*. **3**). However, in sharp contrast to previous studies,[25, 46-48] the enantiomeric excess (*ee*) of unreacted monomer was significantly higher at 40 °C than at room temperature (62.1% *vs.* 44.5% respectively), indicating that the chiral (*R*)-catalyst interacts with the monomer more efficiently at higher temperatures presenting a *s*-factor of 15.22 compared to 5.15 obtained at 25 °C (Table 2.1, **entries 4** and **2**). Following these studies, the catalytic activity and stereo-

selectivity between the (*R*)- and (*S*)-TRIP BINOL catalysts at 40 °C was investigated (**entries 5** and **6** in Table 2.1). As shown in **Figure 2.2A**, (*S*)-TRIP BINOL displayed considerably slower polymerisation rates compared to its (*R*)-enantiomer counterpart, requiring 854 h to achieve 79% of εACL conversion, as well as lower kinetic resolution with a moderate *s*-factor of 3.36 (**Figure 2.2B**). The thermal properties of the polymers were analysed by differential scanning calorimeter (DSC). Despite the promising results, all polymers obtained from the ROP of the racemic allyl monomer using either (*R*)- or (*S*)-TRIP BINOL were found amorphous, bearing very low glass transition temperatures ($T_g \leq -53.8$ °C, **Figure S2.15**). As an attempt to achieve stereo-defined polymers with a semicrystalline microstructure, *rac*-εACL was polymerised using a 1:1 mixture of (*R*)/(*S*)-TRIP BINOL (Table 2.1, **entry 7**). It was hypothesised that owing to the different polymerisation rates between the catalysts, the (*R*)-catalyst would have interacted first with the (*S*)-enantiomer of εACL, leaving the other enantiomer unreacted. The latter enantiomer could subsequently undergo polymerisation in the presence of the *S*-catalyst to yield a stereo-block poly(allyl-ε-caprolactone). However, the DSC traces of the resultant polymer did not present the characteristic melting (T_m) and crystallisation (T_c) peaks inherent to semicrystalline polymers, which suggested low stereocontrol during polymerisation (see infra).

Table 2.1. Screening of ε-ACL polymerisations conditions catalysed by TRIP-BINOL.[(a)]

Entry	Catalyst	$[ACL]_0:[CTA]_0:[Catalyst]_0$	T (°C)	Monomer conv. (%) [b]	Time (h)	$Đ_M$ [c]	ee_{ACL} (%) [d]	*s*-factor [e]
1	(*R*)	50:1:1	25	88.2	1246	1.17	-	-
2	(*R*)	100:1:1	25	45.0	380	1.08	44.5	5.15
3	(*R*)	50:1:1	40	92.7	404	1.07	-	-
4	(*R*)	100:1:1	40	44.3	136	1.08	62.1	15.22
5	(*S*)	100:1:1	40	45.0	193	1.09	34.4	3.36
6	(*S*)	50:1:1	40	79.1	854	1.08	-	-
7	(*R*)/(*S*)	70:1:(0.5/0.5)	40	83.7	208	1.08	-	-

[a] All polymerisations were performed in a nitrogen-filled glovebox using benzene-d_6 as a solvent with $[ACL]_0$= 1 M. [b] Calculated by ^{1}H NMR spectrometry. [c] Measured by SEC ($CHCl_3$ with 0.5% Et_3N, PMMA standards). [d] Determined by chiral GC-MS. [e] Selectivity factor (s) = ln[(1 − c)(1 − *ee*ACL)]/ln[(1 − c)(1 + *ee*ACL)], where ACL is the monomer recovered after polymerisation.

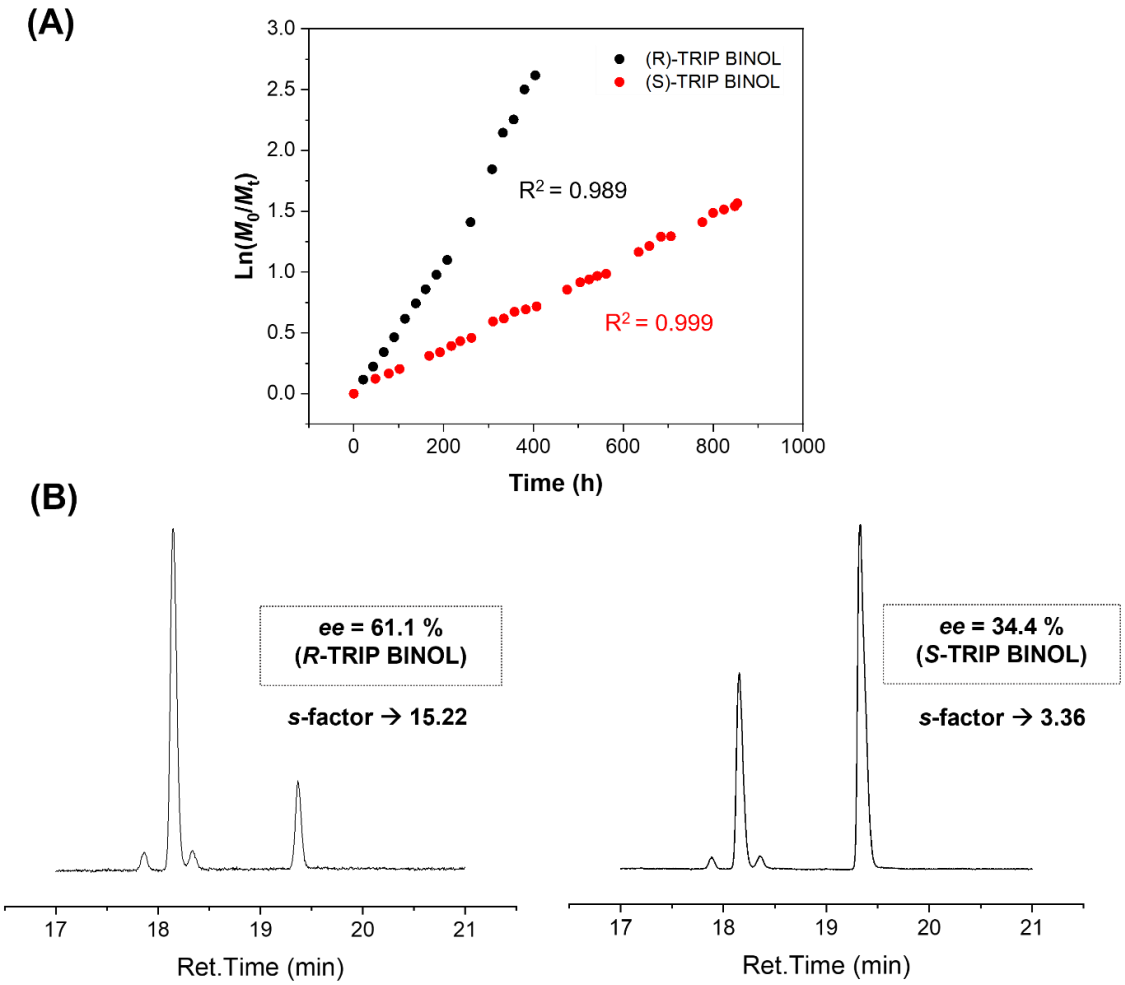


Figure 2.2. (A) Kinetic plots for the polymerisation of *rac*-εACL catalysed by (*R*)- and (*S*)-TRIP BINOL at 40 °C. **(B)** GC-MS chromatograms of *rac*-εACL (left), residual ACL after polymerisation with (*R*)-TRIP BINOL (middle) and residual εACL after polymerisation with (*S*)-TRIP BINOL (right).

To exploit the activity of the TRIP-BINOL catalyst and promote the preparation of stereoregular substituted polymers, the synergistic effect of using stereoselective catalysts with enantiopure monomers was then explored. Highly enantioenriched (*S*)- and (*R*)-ε-allyl-ε-caprolactones (87.3% and 80.3% *ee* respectively) were synthesised through the ring expansion of their chiral cyclohexanone precursor. (*S*)- and (*R*)-2-allylcyclohexanones (ACH) were prepared in large scale by deracemization of a racemic mixture in the presence of α,α,α',α'-tetraaryl-1,3-dioxolane-4,5-dimethanols (TADDOLs) as optically active molecules, following a procedure reported by Kaku *et al.*[49, 50] This methodology relies on the formation of molecular complexes

through non-covalent interactions between the chiral host molecule and one enantiomer of the substituted cyclohexanone to give enantioenriched (*S*)- and (*R*)-ACH (> 80% *ee*) that can be converted to enantioenriched εACL as previously reported (**Figure 2.3A**). The structure of the allyl-functional monomer was confirmed by ^{1}H NMR analysis, with the appearance of a new characteristic peak corresponding to O-COC*H* (δ = 4.28 ppm, **Figure 2.3B**). Chiral gas chromatography coupled with mass spectrometry (GC-MS) analysis showed no significant change in the enantiomeric excess between the chiral cyclohexanone and the enantioenriched allyl monomer, indicating that the chiral carbon is not affected by the Baeyer-Villiger oxidation (**Figures 2.3C, S2.21** and **S2.22**).

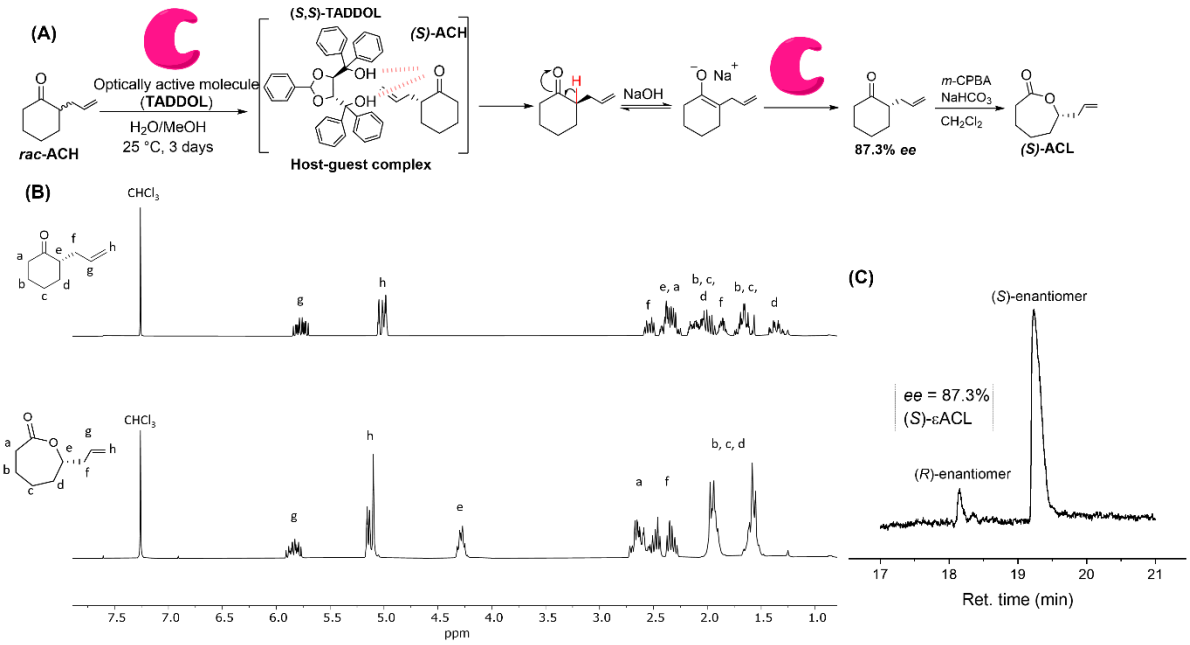


Figure 2.3. (A) Synthesis of enantioenriched (*S*)-allylcaprolactone ((*S*)-εACL) through deracemization of racemic 2-allylcyclohexanone (*rac*-ACH) *via* host-guest chemistry using a TADDOL as the chiral host molecule, followed by Bayer-Villiger oxidation. **(B)** Stacked ^{1}H NMR spectra ($CDCl_3$, 300 MHz) of (*S*)-εACH (top) and (*S*)-εACL (bottom). **(C)** GC-MS chromatogram of enantioenriched (*S*)-εACL.

A series of poly(allyl-ε-caprolactone)s (PACL) bearing different levels of stereoregularity were synthesised *via* ROP using (*R*)- or (*S*)-εACL with different enantiopurities (**Table 2.2**). Initially, to

assess whether the enantiopurity retained in the monomer could produce stereo-defined polymers with retained crystallinity, enantioenriched (*R*)-εACL (with an initial *ee* value of 79.0%) was polymerized using diphenyl phosphate (DPP) as a catalyst (Table 2.2, **entry 8**) with a targeted degree of polymerization (DP) of 50 (**Figure S2.23**). The kinetic trends of the DPP-catalysed polymerisation agreed with those obtained using TRIP BINOL as a catalyst (**Figure 2.4A**). Moreover, SEC analyses confirmed the synthesis of enantioenriched PACL with low molar-mass dispersity and a predictable molecular weight ($Đ_M$ = 1.08 and M_n = 10.5 kDa, **Figure S2.24**). However, thermal analyses of the resultant polymer showed a glass transition at −54.5 °C and no melting or crystallization transition, which indicated that the polymer remained amorphous despite the initial stereopurity of the monomer (see infra). Consequently, the stereoselective ROP of enantiopure εACLs was investigated to pursue enhanced stereoregularity. Chiral phosphoric acids (*i.e*. TRIP BINOL) are bifunctional catalysts bearing a Brønsted acidic site (−O**H**), which interacts with the carbonyl oxygen of the monomer, and a Lewis basic site (P=**O**), which interacts with the initiating alcohol. The chiral scaffold is created by the bifunctional bulky groups, which are responsible for the steric and electronic properties of the catalyst (**Figure 2.4B**).[51] To confirm the enantiomer selectivity of chiral TRIP BINOL catalysts, enantioenriched (*R*)-εACL (75.6 % *ee*) was polymerised with (*R*)-TRIP BINOL using the same conditions previously described but with a targeted DP of 100 (Table 2.2, **entry 9**). As observed in **Figure 2.4C**, the final *ee* value of the unreacted monomer was higher than the initial value, (87.4% *vs.* 75.6%), which indicated that the (*R*)-catalyst binds preferably the (*S*)-enantiomer of the monomer. Similarly, the AKRP of enantioenriched (*R*)- and (*S*)-allyl monomer (*ee* values of 80.3% and 87.3% respectively) using (*S*)- and (*R*)-TRIP BINOL were studied (Table 2.2, **entries 10** and **11**). Polymerisations were quenched at 45.0% and 42.0% of (*R*)- and (*S*)-monomer conversion respectively, to achieve high enantiomeric ratios

and a DP close to 50. The successful polymerisation was confirmed *via* ^{1}H NMR spectroscopy, which showed a shift in the resonance of O=COC*H* from δ = 4.28 ppm to δ = 4.9 ppm (**Figures S2.25** and **S2.26**). Moreover, a decrease in the final *ee* values of unreacted monomers for both polymerisations was observed by GC-MS, suggesting that the chiral catalyst interacted preferentially with the major enantiomer (**Figure 2.4D**). Unlike poly(lactic acid), whose stereosequence can be calculated upon analysis of the (*S*,*S*)-lactide and (*R*,*R*)-lactide tetrad intensities, the level of stereoregularity in poly(allyl-ε-caprolactone) cannot be determined using ^{1}H NMR spectroscopy techniques. Therefore, the preparation of stereoregular polymers was hypothesised as a consequence of the enantiomeric excess retained in the monomer.

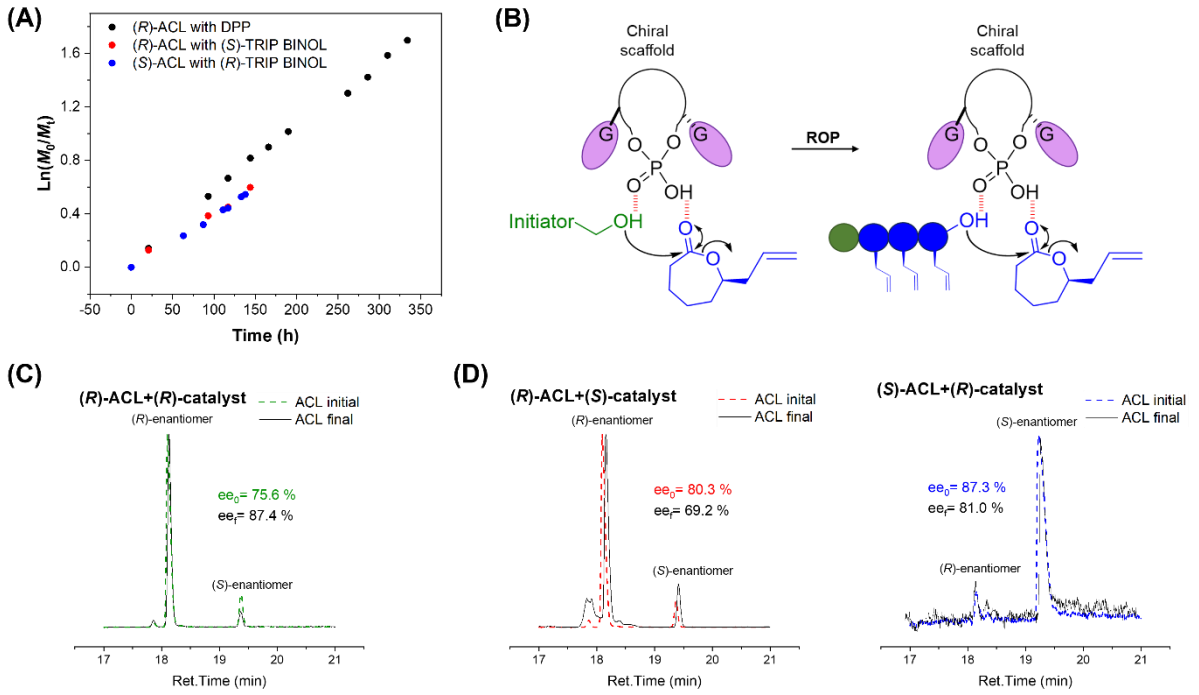
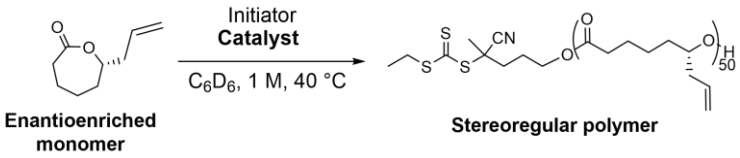


Figure 2.4. (A) Kinetic plots for the polymerisation of *rac*-ACL catalysed by DPP and enantioenriched εACL catalysed by (*R*)- and (*S*)-TRIP BINOL. Polymerisations were quenched before 50% conversion. **(B)** Model of AKRP of enantioenriched εACL with TRIP BINOL catalyst. **(C)** GC-MS chromatogram of unreacted monomer from (*R*)-TRIP BINOL-catalysed polymerization with enantioenriched (*R*)-ACL. **(D)** GC-MS chromatograms of unreacted monomer from (*R*)-TRIP BINOL-catalysed ROP with enantioenriched (*S*)-ACL (left) and (*S*)-TRIP BINOL-catalysed ROP with enantioenriched (*R*)-ACL (right).

These results prompt us to investigate how the monomer conversion affects the selectivity of the catalyst. It was expected that at lower monomer conversions, higher interaction between the chiral catalyst and the more reactive enantiomer of the monomer would occur since the monomer enantiomeric excess starts at a maximum value and decreases over the polymerisation time.[52] To examine if stereoregular polymers with retained crystallinity could be obtained by enhancing the catalytic selectivity, a series of polymerisations of (*S*)-εACL in combination with (*R*)-TRIP BINOL as a catalyst, with [monomer]:[catalyst]:[initiator]= 200:1:1, were performed and stopped at low monomer conversions, 35.5% and 23.2%, to yield highly enantioenriched PACLs (Table 2.2, **entries 12** and **13** respectively).

Table 2.2. Studies of the polymerization of enantioenriched (*S*)- or (*R*)-εACL with stereoselective catalysts.[(a)]



Entry	εACL	$ee_{initial}$ (%) [d]	Catalyst	$[ACL]_0$:$[CTA]_0$:$[Catalyst]_0$ [a]	Monomer conv. (%) [b]	Time (h)	$Đ_M$ [c]	T_g (°C) [e]
8	(*R*)	79.0	DPP	50:1:1	81.7	334	1.08	− 54.5
9	(*R*)	75.6	(*R*)-TRIP BINOL	100:1:1	46.1	222	1.08	− 57.0
10	(*R*)	80.3	(*S*)-TRIP BINOL	100:1:1	45.0	144	1.12	− 55.3
11	(*S*)	87.3	(*R*)-TRIP BINOL	100:1:1	42.0	138	1.15	− 58.0
12	(*S*)	87.3	(*R*)-TRIP BINOL	200:1:1	35.5	432	1.08	− 56.6
13	(*S*)	87.3	(*R*)-TRIP BINOL	200:1:1	23.2	290	1.12	− 68.0

[a] All polymerisations were performed in a nitrogen-filled glovebox using benzene-d_6 as a solvent with $[ACL]_0$= 1M. [b] Calculated by ^{1}H NMR spectrometry. [c] Measured by SEC ($CHCl_3$ with 0.5% Et_3N, PMMA standards). [d] Enantiomeric excess (*ee*) of unreacted monomer was measured by chiral GC-MS. [e] Measured by DSC in the second cycle −100 °C to 100 °C, 10 °C min^{-1}.

The asymmetric ROP of enantioenriched monomers produced polymers with predictable molecular weights (M_n) and narrow distributions ($Đ_M < 1.2$, **Figures 2.5A**, **S2.27** and **S2.28**). The thermal properties of the resultant stereoregular polymers were studied by differential scanning calorimetry (DSC). However, despite the combination of enantioenriched monomers with stereopure selective catalysts, no significant change in the thermal behaviour of polymers **10** and **11** compared to the amorphous polymers prepared from the racemic monomer was observed, exhibiting only low glass transition temperature (T_g) values for both polymers (**Figure 2.5B**). In addition, no enhanced thermal properties or semicrystalline profile was neither observed for polymers **12** and **13**, which were precipitated at low monomer conversions to increase the stereopurity of the system (**Figure S2.29**). These results suggested that small stereo-defects present in the polymer, resulting from monomer stereo-impurities, disrupted the packing of the polymer chains during the crystallisation process, leading to materials with poor thermal properties. While it remains uncertain whether stereopure PACL is semicrystalline, it was believed that the monomer level of enantiopurity played an essential role in providing stereoregular polymers with semicrystalline properties.

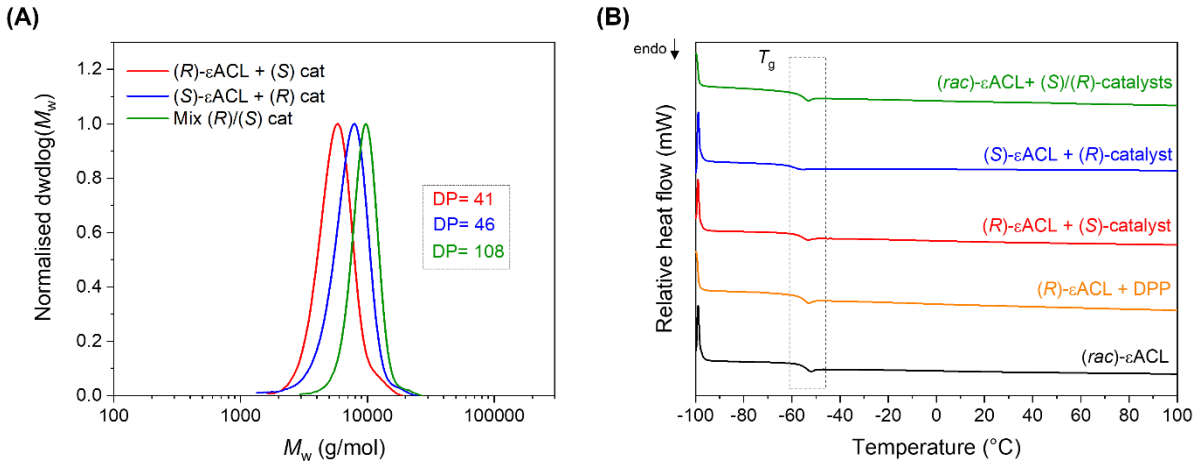


Figure 2.5. (A) SEC chromatograms of enantioenriched (*R*)- and (*S*)- polymers (**10** and **11**) and "stereoblock" PACL (**7**) ($CHCl_3$, with 0.5% Et_3N, PMMA standard). **(B)** DSC thermograms of *rac*-PACL, enantioenriched (*R*)-PACL catalysed by DPP (**8**), enantioenriched (*R*)-PACL catalysed by

(S)-TRIP BINOL (**10**), enantioenriched (*R*)-PACL catalysed by (*S*)-TRIP BINOL (**11**) and of *rac*-PACL catalysed by (*R*)- and (*S*)-TRIP BINOL (**7**) (−100 to 100 °C, 10 °C min^{-1}) showing the second heating cycle.

Conclusions

In summary, we have investigated the use of chiral TRIP BINOL as the catalyst for the AKRP of allyl-ε-caprolactone (εACL), demonstrating that the catalytic selectivity is enhanced at 40 °C, providing *s* values of up to 15.22 (*R*-catalyst) and 3.36 (*S*-catalyst). To exploit the catalyst selectivity, enantioenriched εACLs (87.3% *ee*) were achieved in gram scale *via* deracemization of the racemic cyclohexanone precursor, followed by Bayer-Villiger oxidation. Asymmetric ROP of enantioenriched monomers with chiral TRIP BINOL catalyst yielded a series of poly(allyl-ε-caprolactones) with a range levels of stereoregularity. These polymers exhibited low dispersities ($Đ_M$ = 1.0–1.2) and predictable molecular weights, indicating a controlled polymerization. To investigate the effect of controlling the substituent stereochemistry, the thermal properties of the resultant polymers were investigated by DSC. However, no semicrystalline microstructure or significant changes in the glass transition temperature were found in highly stereoregular poly(ε-allyl-ε-caprolactone)s compared to their racemic counterpart. In conclusion, stereo-defined allyl-functional PCL was achieved through ROP but the remaining stereo-defects within the polymer chain disrupt the crystallisation yielding amorphous polymers with a glass transition below room temperature. Despite the major advantages made in the area, relating stereochemistry to polymer properties has yet to be fully explored.

References

1. O. Wachsen, K. Platkowski and K. H. Reichert, *Polym. Degrad. Stab.*, 1997, **57**, 87-94.
2. K. Chen, K. Harris and S. Vyazovkin, *Macromol. Chem. Phys.*, 2007, **208**, 2525-2532.
3. M. B. Harney, Y. Zhang and L. R. Sita, *Angew. Chem. Int. Ed.*, 2006, **45**, 2400-2404.
4. Z.-Q. Wan, J. M. Longo, L.-X. Liang, H.-Y. Chen, G.-J. Hou, S. Yang, W.-P. Zhang, G. W. Coates and X.-B. Lu, *J. Am. Chem. Soc*, 2019, **141**, 14780-14787.
5. C. Zheng, Z. An, Y. Nakai, T. Tsuboi, Y. Wang, H. Shi, R. Chen, H. Li, Y. Ji, J. Li and W. Huang, *J. Mater. Chem. C*, 2014, **2**, 7336-7347.
6. C. He, J. Xian, H. Fu, F. Cheng, X. Han, X. Pan, Y. Tang and J. Wu, *J. Am. Chem. Soc*, 2023, **145**, 9786-9799.
7. S. Sarkar, A. Sarkar and S. J. George, *Angew. Chem. Int. Ed.*, 2020, **59**, 19841-19845.
8. X. Xie, Z. Huo, E. Jang and R. Tong, *Commun. Chem.*, 2023, **6**.
9. X. Tang, A. H. Westlie, E. M. Watson and E. Y.-X. Chen, *Science*, 2019, **366**, 754-758.
10. X. Chen, L. Caporaso, L. Cavallo and E. Y. X. Chen, *J. Am. Chem. Soc*, 2012, **134**, 7278-7281.
11. A. Sanchez-Sanchez, I. Rivilla, M. Agirre, A. Basterretxea, A. Etxeberria, A. Veloso, H. Sardon, D. Mecerreyes and F. P. Cossío, *J. Am. Chem. Soc*, 2017, **139**, 4805-4814.
12. H. Li, J. Ollivier, S. M. Guillaume and J. F. Carpentier, *Angew. Chem. Int. Ed.*, 2022, **61**.
13. M. J. Stanford and A. P. Dove, *Chem. Soc. Rev.*, 2010, **39**, 486-494.
14. M. I. Childers, A. K. Vitek, L. S. Morris, P. C. B. Widger, S. M. Ahmed, P. M. Zimmerman and G. W. Coates, *J. Am. Chem. Soc*, 2017, **139**, 11048-11054.
15. J. Li, B.-H. Ren, Z.-Q. Wan, S.-Y. Chen, Y. Liu, W.-M. Ren and X.-B. Lu, *J. Am. Chem. Soc*, 2019, **141**, 8937-8942.
16. T. Imai, K. Hayakawa, T. Satoh, H. Kaga and T. Kakuchi, *J. Polym. Sci., Part A: Polym. Chem.*, 2002, **40**, 3443-3448.
17. G. W. Coates, *Chem. Rev.*, 2000, **100**, 1223-1252.
18. C. R. Baar, C. J. Levy, E. Y. J. Min, L. M. Henling, M. W. Day and J. E. Bercaw, *J. Am. Chem. Soc*, 2004, **126**, 8216-8231.
19. T. G. Fox, B. S. Garrett, W. E. Goode, S. Gratch, J. F. Kincaid, A. Spell and J. D. Stroupe, *J. Am. Chem. Soc*, 1958, **80**, 1768-1769.
20. M. Tsuji, T. Aoki, R. Sakai, T. Satoh, H. Kaga and T. Kakuchi, *J. Polym. Sci., Part A: Polym. Chem.*, 2004, **42**, 4563-4569.
21. T. M. Ovitt and G. W. Coates, *J. Am. Chem. Soc*, 1999, **121**, 4072-4073.
22. T. M. Ovitt and G. W. Coates, *J. Polym. Sci., Part A: Polym. Chem.*, 2000, **38**, 4686-4692.
23. T. M. Ovitt and G. W. Coates, *J. Am. Chem. Soc*, 2002, **124**, 1316-1326.
24. J.-B. Zhu and E. Y. X. Chen, *J. Am. Chem. Soc*, 2015, **137**, 12506-12509.
25. C. Lv, L. Zhou, R. Yuan, Q. Mahmood, G. Xu and Q. Wang, *New J Chem*, 2020, **44**, 1648-1655.
26. K. Makiguchi, T. Yamanaka, T. Kakuchi, M. Terada and T. Satoh, *Chem. Commun.*, 2014, **50**, 2883-2885.

27. S. Liu, H. Li, N. Zhao and Z. Li, *ACS Macro Lett.*, 2018, **7**, 624-628.
28. A. P. Dove, H. Li, R. C. Pratt, B. G. G. Lohmeijer, D. A. Culkin, R. M. Waymouth and J. L. Hedrick, *Chem. Commun.*, 2006, DOI: 10.1039/b601393g, 2881.
29. L. S. Nair and C. T. Laurencin, *Prog. Polym. Sci.*, 2007, **32**, 762-798.
30. E. Malikmammadov, T. E. Tanir, A. Kiziltay, V. Hasirci and N. Hasirci, *J. Biomater. Sci. Polym. Ed.*, 2018, **29**, 863:893.
31. P. B. Sathish, R. Narmadha and R. Selvakumar, *Mater. Lett.*, 2021, **285**, 129038.
32. J. H. Park, H. J. Park, S. J. Tucker, S. K. Rutledge, L. Wang, M. E. Davis and S. J. Hollister, *Adv. Funct. Mater.*, 2023, **33**, 2215220.
33. M. C. Arno, M. Inam, Z. Coe, G. Cambridge, L. J. Macdougall, R. Keogh, A. P. Dove and R. K. O'Reilly, *J. Am. Chem. Soc*, 2017, **139**, 16980-16985.
34. T. Xia, Z. Tong, Y. Xie, M. C. Arno, S. Lei, L. Xiao, J. Y. Rho, C. T. J. Ferguson, I. Manners, A. P. Dove and R. K. O'Reilly, *J. Am. Chem. Soc*, 2023, DOI: 10.1021/jacs.3c08770.
35. C. Clamor, B. N. Cattoz, P. M. Wright, R. K. O'Reilly and A. P. Dove, *Polym. Chem.*, 2021, **12**, 1983-1990.
36. G. Hughes, M. Kimura and S. L. Buchwald, *J. Am. Chem. Soc*, 2003, **125**, 11253-11258.
37. X. Li, T. Yang, J. Li, X. Li, P. Chen, Z. Lin and G. Liu, *Nat Chem*, 2023, **15**, 862-871.
38. A. Cavarzan, G. Bianchini, P. Sgarbossa, L. Lefort, S. Gladiali, A. Scarso and G. Strukul, *Chem. Eur. J.*, 2009, **15**, 7930-7939.
39. L. Zhou, X. Liu, J. Ji, Y. Zhang, X. Hu, L. Lin and X. Feng, *J. Am. Chem. Soc*, 2012, **134**, 17023-17026.
40. J. W. Peeters, O. van Leeuwen, A. R. A. Palmans and E. W. Meijer, *Macromol.*, 2005, **38**, 5587-5592.
41. B. A. C. van As, J. van Buijtenen, A. Heise, Q. B. Broxterman, G. K. M. Verzijl, A. R. A. Palmans and E. W. Meijer, *J. Am. Chem. Soc*, 2005, **127**, 9964-9965.
42. M. R. T. Breteler, Z. Zhong, P. J. Dijkstra, A. R. A. Palmans, J. Peeters and J. Feijen, *J. Polym. Sci., Part A: Polym. Chem.*, 2007, **45**, 429-436.
43. C. Lv, G. Xu, R. Yang, L. Zhou and Q. Wang, *Polym. Chem.*, 2021, **12**, 4856-4863.
44. C. Lv, G. Xu, R. Yang, L. Zhou and Q. Wang, *Polym. Chem.*, 2020, **11**, 4203-4207.
45. C. Lv, R. Yang, G. Xu, L. Zhou and Q. Wang, *Eur. Polym. J.*, 2020, **133**, 109792.
46. J.-B. Zhu and E. Y. X. Chen, *J. Am. Chem. Soc*, 2015, **137**, 12506-12509.
47. G. H. He, B. H. Ren, S. Y. Chen, Y. Liu and X. B. Lu, *Angew. Chem. Int. Ed.*, 2021, **60**, 5994-6002.
48. W. M. Ren, Y. Liu, G. P. Wu, J. Liu and X. B. Lu, *J. Polym. Sci., Part A: Polym. Chem.*, 2011, **49**, 4894-4901.
49. H. Kaku, A. Nakamaru, M. Inai, T. Nishii, M. Horikawa and T. Tsunoda, *Tetrahedron*, 2010, **66**, 9450-9455.
50. H. Kaku, M. Ito, M. Horikawa and T. Tsunoda, *Tetrahedron*, 2018, **74**, 124-129.
51. W. Liu and X. Yang, *Asian J. Org. Chem.*, 2021, **10**, 692-710.

2.2 Supporting information

2.2.1 Experimental details

Materials

All solvents and chemicals were purchased from Sigma-Aldrich, Fisher Scientific, Alfa Aesar, or VWR International and used without further purification unless otherwise stated. 2-allylcyclohexanone was distilled before use. Deuterated benzene was ordered from Apollo Scientific, degassed by repeated freeze-pump-thawing and then dried under reflux over sodium and benzophenone before storing under an inert atmosphere of N_2. Amberlyst A21 free base was washed repeatedly with methanol and dried under reduced pressure prior to use. The monomer ε-allyl-ε-caprolactone was dried over calcium hydride for three days and distilled under reduced pressure before their storage under inert atmosphere of N_2 in a glove box. The initiator, 2-cyano-5-hydroxypentan-2-yl ethyl carbonotrithioate, was dried for five days over phosphorus pentoxide under vacuum before its introduction in a glove box.

Instrumentation

2.2.1.1 Nuclear magnetic resonance (NMR) spectroscopy

Proton (^{1}H) and carbon (^{13}C) resonance spectra were recorded on a Bruker 300 MHz or 400 MHz spectrometers at 298 K. Chemical shifts were reported as δ in parts per million (ppm) and referenced to the residual solvent signals ($CDCl_3$, ^{1}H: δ = 7.26 ppm, ^{13}C: δ = 77.16 ppm). The multiplicities were reported as s = singlet, d = doublet, dd = doublet of doublet, dddd = doublet of doublet of doublet of doublets, ddt = double of doublet of triplet, dddt = doublet of doublet of doublet of tripets t = triplet, q = quadruplet, p = pentaplet and m = multiplet. The coupling constant *J* was recorded in Hertz [Hz]. The obtained data were processed and analysed using MestReNova 12.0.3 software.

2.2.1.2 High-Resolution Mass Spectrometry (HRMS)

HRMS spectra were recorded by the MS Analytical Facility Service at the University of Birmingham on a Waters Xevo G2-XS Quadrupole Time-of-Flight mass spectrometer.

2.2.1.3 Flash Chromatography

Flash chromatography was performed on a Teledyne ISCO CombiFlash Rf+ Lumen equipped with two UV detectors (254 nm and 280 nm) and an internal evaporative light scattering detector (ELSD). Samples were purified with RediSep RF normal phase columns (from 4 g to 120 g flash columns).

2.2.1.4 Gas Chromatography-Mass Spectroscopy (GC-MS)

GCMS was performed on a Shimadzu GCMS QP2010 SE system with a CP-Chirasil-Dex CB 25 × 0.25 column. The temperature programming for the separation of 2-allylcyclohexanone was set to 90 °C for 13 min, ramped to 190 °C at 2 °C·min^{-1}; and for the separation of allyl-ε-caprolactone was set to 100 °C for 2 min, ramped to 150 °C at 2 °C·min^{-1} and held for 5 min and ramped to 180 °C at 10 °C·min^{-1} and held for other 5 min. The injection temperature was 170 °C and 225 °C respectively, with 1.0 µL injection volume. The helium carrier gas flow rate was set at 1 mL·min^{-1}. MS detection was used selective ion scanning m/z 30-500 amu.

2.2.1.5 Size exclusion chromatography (SEC)

GPC analyses were performed on an Agilent 1260 Infinity II Multi-Detector GPC/SEC System fitted with RI and ultraviolet (UV, λ = 309 nm), and viscosimeter detectors. The instrument is equipped with an Agilent guard column PLGel 3 µm (50 × 7.5 mm) and two Agilent mixed-C columns PLGel 5 µm (300 × 7.5 mm) using $CHCl_3$ (buffered 0.5% EtN_3) as the mobile phase (eluent). Number average molecular weights (M_n), weight average molecular weights (M_w) and dispersities ($Đ_M = M_w/M_n$) were determined using Agilent GPC/SEC software (vA.02.01) against

a 15-point calibration curve (M_p = 162 – 3,187,000 g mol^{-1}) based on poly(styrene) standards or a 12-point calibration curve (M_p = 550 – 2,210,000 g mol^{-1}) based on poly(methyl methacrylate) standards. Molecular weights (M_n), weight average molecular weights (M_w) are given in (g mol^{-1}).

2.2.1.6 Glove box

Air-free work was conducted in the nitrogen atmosphere of an Mbraun MB Unilab Pro SP or Mbraun MB-01 equipped with solvent filter.

2.2.1.7 Differential scanning calorimetry (DSC)

Determination of the DSC curves were carried out using a STARe system DSC3 with auto-sampler (Mettler Toledo). The samples (1 – 10 mg of polymer) were placed into aluminium pans measuring 5 mm in diameter and 0.4 – 0.6 mm in thickness. Thermograms obtained with a heating rate of 10 °C min^{-1} were recorded from −100 to 100 °C with a 10 °C min^{-1} heating and cooling rate over two cycles.

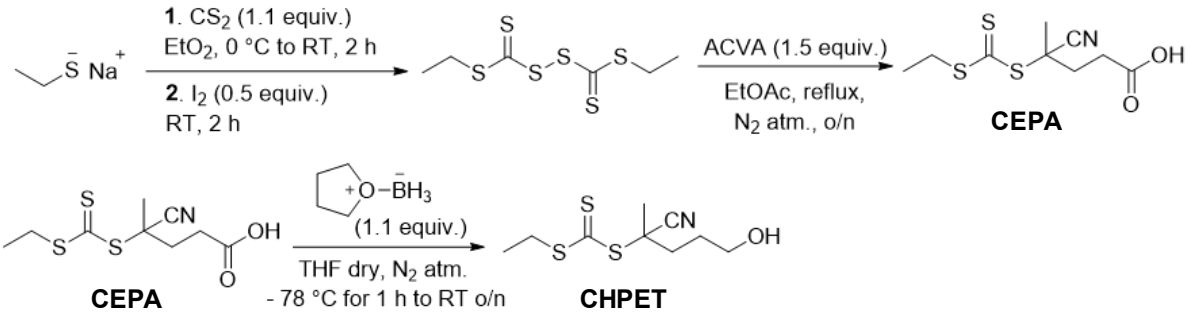
2.2.1.8 Polarimeter

Optical rotations [α] were measured on a polarimeter PolAAr 3001 operating at the sodium D line using a 2.5 cm micro-cell at 20 °C.

Experimental procedures

2.2.1.9 Synthesis of initiator

The synthesis of the initiator was adapted from literature.[1] It was performed by a three-step synthesis as indicated in the following scheme:



2.2.1.9.1 Synthesis of 4-cyano-4-(((ethylthio)carbonothioyl)thio)pentanoic acid (CEPA)

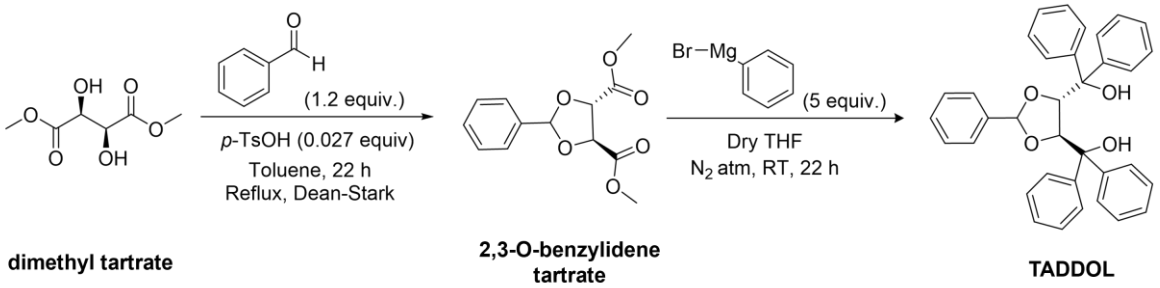
To an oven-dried round bottom flask, sodium ethanethiolate (10 g, 0.119 mol) was added followed by the addition of dry diethyl ether (500 mL) and the resulting solution was cooled to 0 °C. Carbon disulfide (7.74 mL, 0.131 mol) was subsequently added dropwise over 10 min, producing a thick yellow precipitate of sodium *S*-ethyl trithiocarbonate. After 2 h of stirring at room temperature, solid iodine (15.1 g, 0.0594 mol) was added, and the resultant reaction mixture was stirred for a further 2 h at room temperature. The reaction mixture was then washed with sodium thiosulfate solution (1 M, 3 × 100 mL), deionized water (3 × 100 mL) and finally with brine (3 × 100 mL). The organic layer was dried over $MgSO_4$, filtered, and evaporated to dryness leaving a residue of bis-(ethylsulfanylthiocarbonyl) disulfide (16.2 g, quantitative). A solution of 4,4'-azobis(4-cyanovaleric acid) (ACVA) (24.8 g, 0.885 mol) and bis-(ethylsulfanylthiocarbonyl) disulfide (16.2 g, 0.59 mol) in ethyl acetate (500 mL) was heated overnight at reflux under N_2 atmosphere. After removal of the volatile solvents *in vacuo*, purification was carried out using silica gel column chromatography (gradient elution – hexane:dichloromethane 1:1 to 1:5) affording 4-cyano-4-(((ethylthio) carbonothioyl)thio)pentanoic acid (CEPA) as an orange solid (27.4 g, 0.108 mol, 88%) with spectroscopic data in accordance with the literature[1]. **^{1}H NMR** (300 MHz, $CDCl_3$): δ/ppm= 3.35 (q, *J* = 7.4 Hz, 2H, -SC*H*$_2$CH$_3$), 2.69 (dd, *J* = 8.6, 6.6 Hz, 2H, -C(CN)(CH$_3$)CH$_2$C*H*$_2$), 2.64 – 2.29 (m, 2H, -C(CN)(CH$_3$)C*H*$_2$CH$_2$), 1.88 (s, 3H, -C(CN)(C*H*$_3$), 1.36 (t, *J* = 7.4 Hz, 3H, -SCH$_2$C*H*$_3$).

2.2.1.9.2 Synthesis of 2-cyano-5-hydroxypentan-2-yl ethyl carbonotrithioate (CHPET)

To a 500 mL flame-dried round bottom flask, 4-cyano-(((ethylthio)carbonothioyl)thio)pentanoic acid (CEPA) (2 g, 0.0076 mol) was added followed by the addition of dry tetrahydrofuran (50 mL) with the resulting solution cooled to −78 °C. Borane tetrahydrofuran complex solution (1 M, 7.97 mL, 0.0079 mol) was subsequently added dropwise over 30 min. The reaction mixture was left to stir for 1 h, after which the cooling bath was removed, and the reaction was stirred overnight at ambient temperature under N_2 atmosphere. After 18 h of stirring, methanol (100 mL) was added in five portions and stirred for 10 min after each addition or until no further bubbling was observed. After removal of the volatile solvents *in vacuo*, the organic residue was dissolved in diethyl ether (30 mL) and washed with saturated $NaHCO_3$ solution (3 × 30 mL) and then with brine (30 mL). Further extraction using diethyl ether from the collected aqueous layers was carried out. The combined organic layers were then dried over $MgSO_4$, filtered, and evaporated to dryness. Purification was carried out *via* silica gel column chromatography using petroleum ether:Ethyl acetate (1:1) as solvent eluent to afford 2-cyano-5-hydroxypentan-2-yl ethyl carbonotrithioate (CHPET) as an orange red oil (0.796 g, 42%) with spectroscopic data in accordance with the literature[1]. **^{1}H NMR** (400 MHz, $CDCl_3$): δ/ppm= 3.72 (t, J = 6.1, Hz, 2H, -CH_2OH), 3.35 (q, J = 7.4 Hz, 2H, -SCH_2CH$_3$), 2.34 – 2.02 (m, 2H, -C(CN)(CH$_3$)CH_2CH$_2$), 1.90 (s, 3H, -C(CN)(CH_3)CH$_2$CH$_2$), 1.88 – 1.81 (m, 2H, -C(CN)(CH$_3$)CH$_2$CH_2), 1.36 (t, J = 7.4 Hz, 3H, -SCH$_2$CH_3). **^{13}C NMR** (101 MHz, $CDCl_3$) δ/ppm= 217.40 (*C*=S), 119.57 (C(*C*N)(CH$_3$)CH$_2$CH$_2$), 61.79 (*C*H$_2$OH), 46.99 (*C*(CN)(CH$_3$)CH$_2$CH$_2$), 35.76 (C(CN)(CH$_3$)*C*H$_2$CH$_2$), 31.31 (S*C*H$_2$CH$_3$), 27.91 (C(CN)(CH$_3$)CH$_2$*C*H$_2$), 24.93 (C(CN)(*C*H$_3$)CH$_2$CH$_2$), 12.80 (SCH$_2$*C*H$_3$).

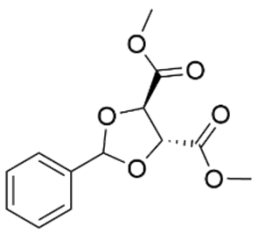
2.2.1.10 Synthesis of TADDOL host molecule

The synthesis of the host molecule for further deracemization of substituted cyclohexanones was performed by a two-step synthesis as indicated in the following scheme:



To a solution of dimethyl tartrate in toluene, benzaldehyde and *p*-TsOH were added. The solution was allowed to reflux with a dean-stark apparatus overnight. The reaction was quenched by the addition of triethylamine (Et_3N) and purified *via* silica gel chromatography. To a solution of 2,3-O-benzylidene tartrate in dry THF under N_2 atmosphere, a solution of phenylmagnesium bromide was added dropwise at 0 °C. After addition, the ice bath was removed, and the reaction was allowed to warm to room temperature and left stirring overnight. The reaction was quenched by the addition of a saturated aqueous solution of NH_4Cl. The product was extracted with ethyl acetate; the combined organic layers were dried over Mg_2SO_4 and concentrated *in vacuo*. Purification was carried out using gel silica chromatography.

2.2.1.10.1 Synthesis of 2,3-O-Benzylidene-D-tartrate

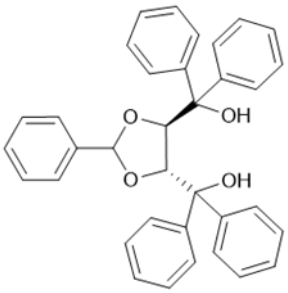


The procedure was adapted from literature.[2]

A mixture of dimethyl *D*-tartrate (5 g, 1 equiv.), benzaldehyde (2.84 mL, 1 equiv.), and *p*-toluenesulfonic acid monohydrate (0.15 g, 0.027 mmol) in toluene (60 mL) was heated under reflux, using a dean-stark device for the removal of water,

overnight reaction. After the addition of triethylamine (0.1 mL) to the cooled reaction mixture, the resultant crude was purified *via* silica column chromatography using hexane/ethyl acetate (8:2) as the eluent to afford the product (5.05 g, 68%) as white crystals. The same procedure was followed for the synthesis of 2,3-O-benzylidene-*L*-tartrate using dimethyl *L*-tartrate as the starting material. **^{1}H NMR** (300 MHz, $CDCl_3$): δ/ppm= 7.60 − 7.52 (m, 2H aromatic), 7.47 − 7.38 (m, 3H aromatic), 6.14 (s, 1H acetal, -*CCHOO*-), 4.99 (d, J= 4.0Hz, 1H), 4.87 (d, J= 4.0Hz, 1H), 3.88 (s, 3H, -COOC*H*$_3$), 3.83 (s, 3H, -COOC*H*$_3$). **^{13}C NMR** (101 MHz, $CDCl_3$): δ/ppm= 170.45 (*C*=O), 169.82 (*C*=O), 135.66 (1C aromatic), 130.41 (1C aromatic), 128.79 (2C aromatic), 127.59 (2C aromatic), 107.12 (*C*OO acetal), 77.83 (*C(*C=O), 77.57 (*C(*C=O), 53.25 (O*C*H$_3$), 53,24 (O*C*H$_3$). **HRMS (ESI-TOF)** *m/z*: $[M+H]^+$ Calc. for $C_{13}H_{14}O_6$ 267.0790; Found 267.0869.

2.2.1.10.2 Synthesis of (4R ,5R)-Pentaphenyl-1,3-dioxolane-4,5-dimethanol (TADDOL)



The procedure was adapted from literature.[3]

2,3-O-benzylidene-*L*-tartrate (1.565 g, 5.8 mmol, 1.0 equiv.) was diluted in dry THF (50 mL) and phenylmagnesium bromide (1.0 M in Et_2O, 29.4 mL, 29.4 mmol, 5.0 equiv.) was added at 0 °C. The reaction mixture was then stirred at 20 °C for 20 h and quenched with 60 mL of a saturated aqueous solution of NH_4Cl. The aqueous layer was extracted with ethyl acetate (50 mL x 3) and the combined organic layers were washed with water and brine, dried over $MgSO_4$ and concentrated under reduced pressure. The obtained crude mixture was purified *via* silica column chromatography using hexane/ethyl acetate (85:15) as eluent followed by recrystallization in a mixture of toluene and hexane to afford (*R,R*)-TADDOL as a white powder (3.03 g, 98%). Same procedure was followed for the synthesis of (4*S*,5*S*)-Pentaphenyl-1,3-dioxolane-4,5-dimethanol starting from 2,3-O-benzylidene-*L*-tartrate. **^{1}H NMR** (400 MHz,

$CDCl_3$): δ/ppm= 7.55 – 7.17 (m, 25H aromatic), 5.33 (d, *J* = 5.0 Hz, 1H), 5.17 (s, 1H acetal, -*CCHOO*-), 5.14 (d, *J* = 4.9 Hz, 1H), 3.27 (s, 1H, -O*H*), 2.05 (s, 1H, - O*H*). **^{13}C NMR** (101 MHz, $CDCl_3$): δ/ppm= 146.26, 144.43, 144.35, 143.11, 137.10, 129.50, 128,37, 128.30, 128.01, 127.85, 127.50, 127.36, 127.19, 127.02, 126.91 (15C aromatic), 105.07 (acetal, -*CCHOO*-), 81.67 (-*C*HC(Ph)(Ph)OH), 80.9 (-*CHC*(Ph)(Ph)OH), 78.72 (-CH*C*(Ph)(Ph)OH), 78.62 (-CH*C*(Ph)(Ph)OH). **HRIMS (ESI-TOF)** *m/z*: $[M + Na]^+$ Calc. for $C_{35}H_{30}O_4Na$ 537.2039; Found 537.2042. $[\boldsymbol{\alpha}]_{\boldsymbol{D}}^{\boldsymbol{20}\,^{\circ}\boldsymbol{C}}$ = (*R*,*R*-TADDOL) −24.1 (*c* 0.01 in $CHCl_3$); (*S*,*S*-TADDOL) +22.8 (*c* 0.01 in $CHCl_3$).

2.2.1.11 Deracemization of 2-allylcyclohexanone

The procedure was adapted from literature.[4]

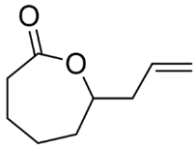
Distilled water (47.6 mL) and 1 M sodium hydroxide aqueous solution (34.2 mL, 4 equiv.) were added to a suspension of 2-allylcyclohexanone (1.2 mL, 1 equiv.) and chiral pentaphenyl-1,3-dioxolane-4,5-dimethanol, TADDOL, (4.2 g, 1 equiv.) in methanol (34.2 mL) to have a final water/methanol ratio of 7:3. The suspension was stirred vigorously at ambient temperature for 2 days. The mixture was filtered using a sintered funnel and the residue was washed with distilled H_2O (10 mL x 1) and with H_2O/MeOH (7:3) (10 mL x 2). The resulting solid phase was suspended again into a fresh mixture of H_2O/MeOH (7:3) at ambient temperature for 1 day. After filtration as previously stated, the solids were washed with H_2O/MeOH (7:3) (10 mL x 3) and dried under vacuum for one day. Isolation of the cyclohexanone was performed *via* silica column flash chromatography (hexane/ethyl acetate) to yield enantioenriched (*R*)- or (*S*)-2-allylcyclohexanone (ACH) (1.1 g, 95%) as a colourless oil. (*S*,*S*)-TADDOL interacts preferentially with (*R*)-2-allylcyclohexanone and (*R*,*R*)-TADDOL interacts with the (*S*)-enantiomer of 2-allylcyclohexanone. **^{1}H NMR** (300 MHz, $CDCl_3$): δ/ppm= 5.76 (dddd, *J* = 16.8, 10.1, 7.8, 6.3 Hz, 1H, C*H*=CH_2), 5.09 – 4.92 (m, 2H, CH=CH_2), 2.53 (dddt, *J* = 14.5, 6.6, 5.4, 1.5 Hz, 1H), 2.45 – 2.23

(m, 3H), 2.19 – 1.92 (m, 3H), 1.92 – 1.78 (m, 1H), 1.75 – 1.56 (m, 2H), 1.44 – 1.26 (m, 1H). **^{13}C NMR** (101 MHz, $CDCl_3$): δ/ppm= 212.55 (*C*=O), 136.50 (*C*H=CH_2), 116.23 (CH=*C*H_2), 50.29 (-*C*H-CH_2-CH=CH_2), 42.07 (-CH-*C*H_2-CH=CH_2), 33.78 (-*C*H_2-C=O), 33.39, 27.96, 24.97. **Chiral GC-MS analysis** (Et_2O, 90 °C – 130 °C – 190 °C, see instrumentation section for column and method details).

(R)-2-allylcyclohexanone: Retention time (t_R)= 15.392 (*R*), 15.969 (*S*), *er* ratio= 89.4:10.6.

(S)-2-allylcyclohexanone: Retention time (t_R)= 15.474 (*R*), 15.831 (*S*), *er* ratio= 9.5:90.4 $[\alpha]_D^{20\,°C}$ = −3.7 (*c* 0.01 in MeOH) {Lit.[4] (*ent*) +8.7 (*c* 1.08 in MeOH)}.

2.2.1.12 Synthesis of ε-allyl-ε-caprolactone (εACL) – Bayer-Villeger oxidation



The procedure was adapted from literature.[5]

To a solution of 2-allylcyclohexanone (8 g, 57.88 mmol) in CH_2Cl_2 (276 mL), $NaHCO_3$ (7.30 g, 86.82 mmol) was added followed by the addition of *m*-CPBA (12 g, 69.46 mmol) portion-wise at 0 °C, over 50 min. The resulting mixture was allowed to warm to room temperature and stirred for 48 h. After this time, $Na_2S_2O_3$ pentahydrate (7.20 g, 28.94 mmol) was added as a powder and was left stirring for 30 min. The reaction was filtered over celite and the plug was washed with excess of DCM (3 x 150 mL) to extract all the product. The crude mixture was concentrated *in vacuo* and purified by flash silica gel column chromatography using hexane/ethyl acetate (gradient elution, 4:1 to 1:1) to yield the desired product (5.5 g, 61.7%) as a colourless/light yellow oil. **^{1}H-NMR** (400 MHz, $CDCl_3$): *δ*/ppm= 5.91 – 5.68 (m, 1H, C*H*=CH_2), 5.21 – 4.95 (m, 2H, CH=C*H*$_2$), 4.26 (qd, *J* = 6.3, 2.2 Hz, 1H, -OC*H*), 2.70 – 2.51 (m, 2H, C*H*$_2$CH=CH_2), 2.49 – 2.21 (m, 2H, C*H*$_2$C=O), 2.03 – 1.74 (m, 3H), 1.71 – 1.35 (m, 3H). **^{13}C-NMR** (101 MHz, $CDCl_3$): *δ*/ppm= 175.51 (C=O), 133.51 (*C*H=CH_2), 118.24 (CH=*C*H_2), 79.90 (-OCH),

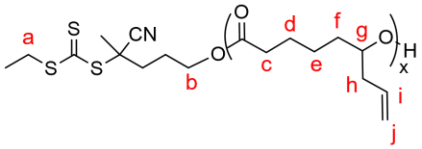
40.64 ($CH_2CH=CH_2$), 34.95 ($CH_2C=O$), 33.88 (CH_2CHCO-), 28.26 ($CH_2CH_2CH_2$), 23.01 ($CH_2CH_2C=O$).

Chiral GC-MS analysis (100 °C – 150 °C – 180 °C, see instrumentation section for column and method details).

(R)-εACL: Retention time (t_R)= 18.095 (*R*), 19.368 (*S*), *er* ratio= 90.2:9.8; $[\alpha]_D^{20\,°C}$ = −37.0 (*c* 0.01 in MeOH).

(S)- εACL: Retention time (t_R)= 18.154 (*R*), 19.236 (*S*), *er* ratio= 6.7:93.6; $[\alpha]_D^{20\,°C}$ = +36.5 (*c* 0.01 in MeOH).

2.2.1.13 Synthesis of $PACL_x$- General procedure for the ring opening polymerisation (ROP) of ε-allyl- ε-caprolactones (εACLs)



The procedure was adapted from literature.[6]

Using standard glovebox techniques, a solution of DPP, (*R*)-TRIP BINOL or (*S*)-TRIP BINOL (0.006 mmol, 1 equiv.) was added to a solution of ε-allyl-ε-caprolactone (0.0925 g, 0.6 mmol, 100 equiv.) and 2-cyano-5-hydroxypentan-2-yl ethyl carbonotrithioate (CHPET) (0.006 mmol, 1 equiv.) in dry deuterated benzene (0.6 mL). The NMR young tube was then removed from the glove box and placed in an oil bath at 40 °C or left inside the glovebox at 25 °C. After achieving the desired monomer conversion, the reaction was quenched outside the glovebox, by the addition of Amberlyst A21. After the removal of Amberlyst through filtration, the solution was precipitated two times into cold *n*-hexanes and dried under vacuum to afford the polymers as a yellow oil. **^{1}H NMR** (300 MHz, $CDCl_3$): δ/ppm= 5.72 (ddt, *J* = 16.5, 10.5, 7.1 Hz, 1H, H^i), 5.12 – 5.00 (m, 2H, H^j), 4.90 (p, *J* = 6.2 Hz, 1H, H^g), 4.11 (t, *J* = 6.1 Hz, 2H, H^b), 3.35 (d, *J* = 7.4 Hz, 2H, H^a), 2.39 – 2.18 (m, 4H, H^c and H^h), 1.66 – 1.48 (m, 4H, H^d and H^f), 1.45 – 1.20 (m, 2H, H^e). **^{13}C NMR** (126 MHz, $CDCl_3$)

δ/ppm= 173.25 (O(*C*=O)), 133.80 (C^i), 117.87 (C^j), 73.39 (C^g), 38.74 (C^h), 35.14 (C^e), 32.81 (C^c), 24.65 (C^d and C^f). **SEC:** M_n = 14.4 kDa, $Đ_M$ = 1.1

The % polymer conversion (% conv.) was calculated using the following equation, where [M] and [P] correspond to the proton integrations of the monomer peak (δ = 4.28 ppm) and polymer peak, respectively. In this case, since the polymer peaks overlapped with the monomer peaks, we selected the terminal alkene protons (δ = 5.15 – 4.80 ppm) to calculate ([M] + [P]).

$$\%\ conv. = 1\ - \left(\frac{[M]}{[M]+[P]}\right) \times 100$$

Equation 2.1. % Polymer conversion.

The kinetic resolution or selectivity factor (*s*) was calculated using the following equation, where: *conv.* correspond to the polymer conversion (Equation 1), and *ee* correspond to the enantiomeric excess of the residual monomer left in solution after quenching the polymerisation, which was determined by chiral GC-MS. Both, conv. and *ee* are given as between 0 and 1.

$$s = k(fast)/k(slow) = \frac{ln[(1-conv.) \times (1-ee)}{ln[(1-conv.) \times (1+ee)}$$

Equation 2.2 Kinetic resolution or selectivity factor (*s*).

2.3 Supplementary figures

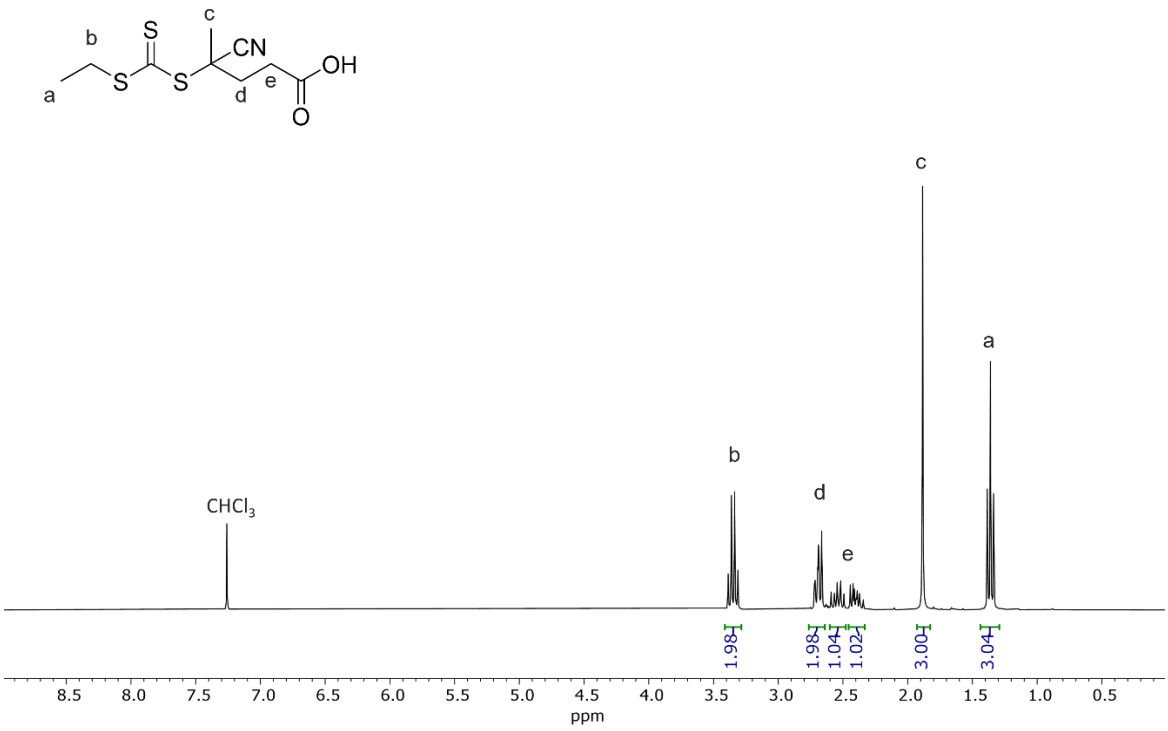


Figure S2.1. ^{1}H NMR spectrum of CEPA 300 MHz, 298 K, $CDCl_3$.

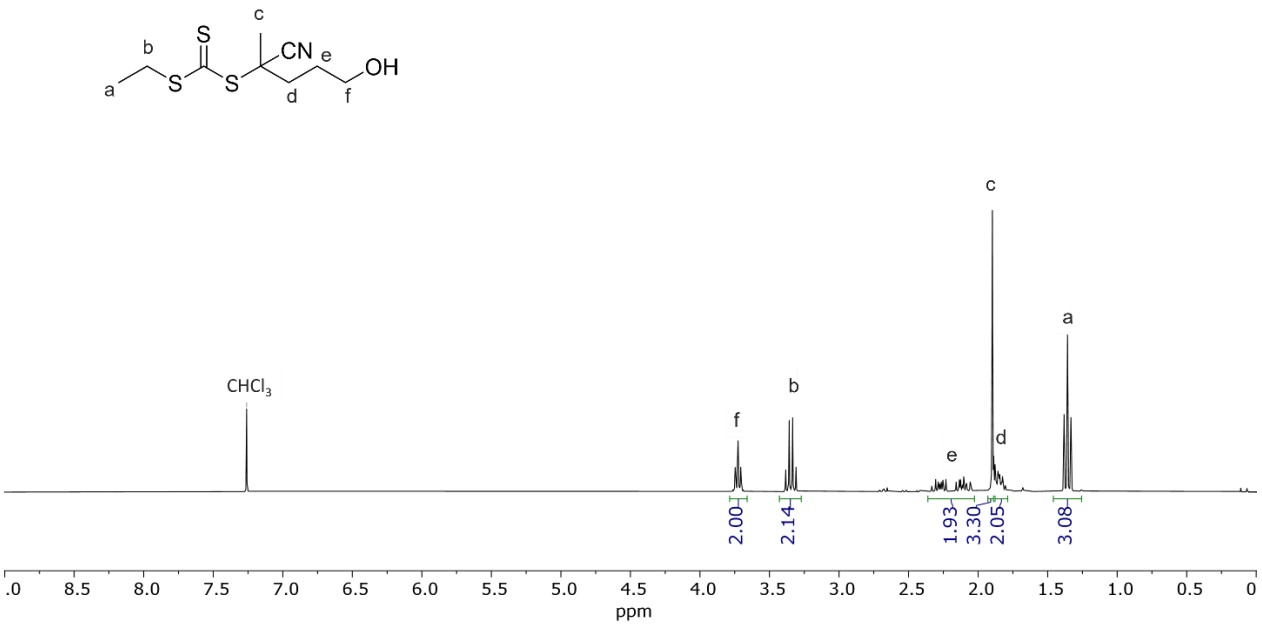


Figure S2.2. ^{1}H NMR spectrum of CHPET 300 MHz, 298 K, $CDCl_3$.

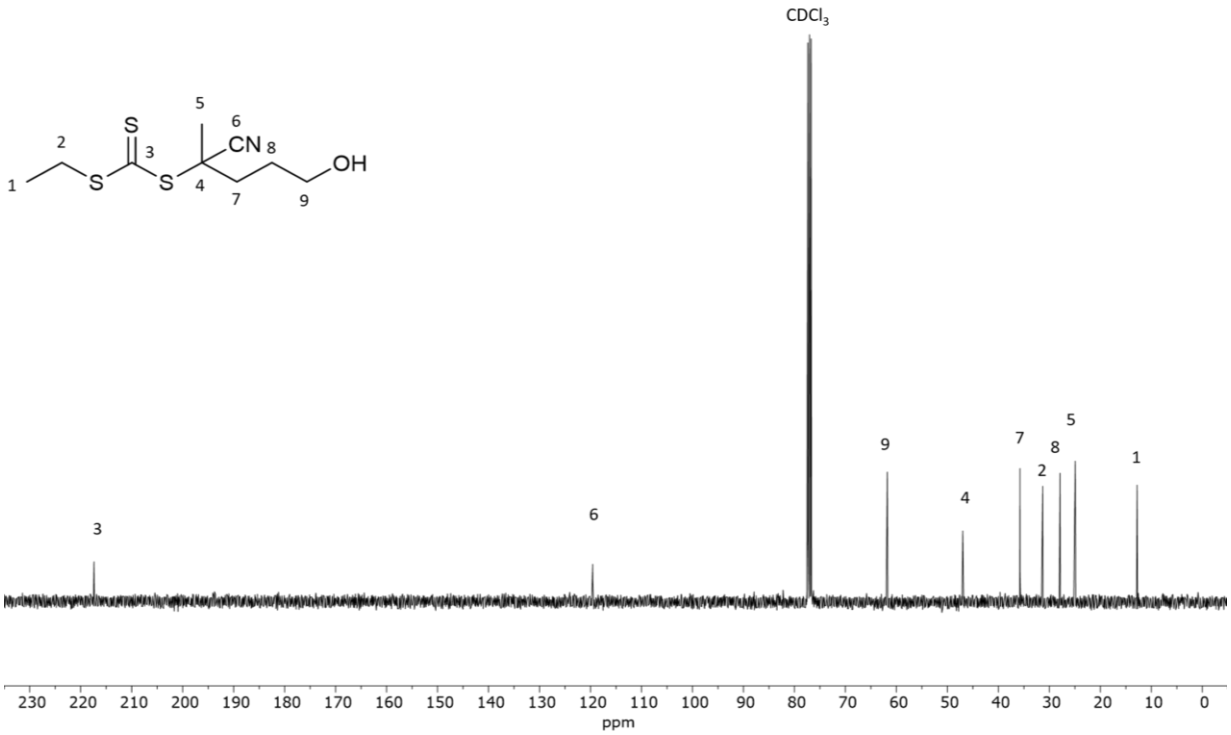


Figure S2.3. ^{13}C NMR spectrum of CHPET, 101 MHz, 298 K, $CDCl_3$.

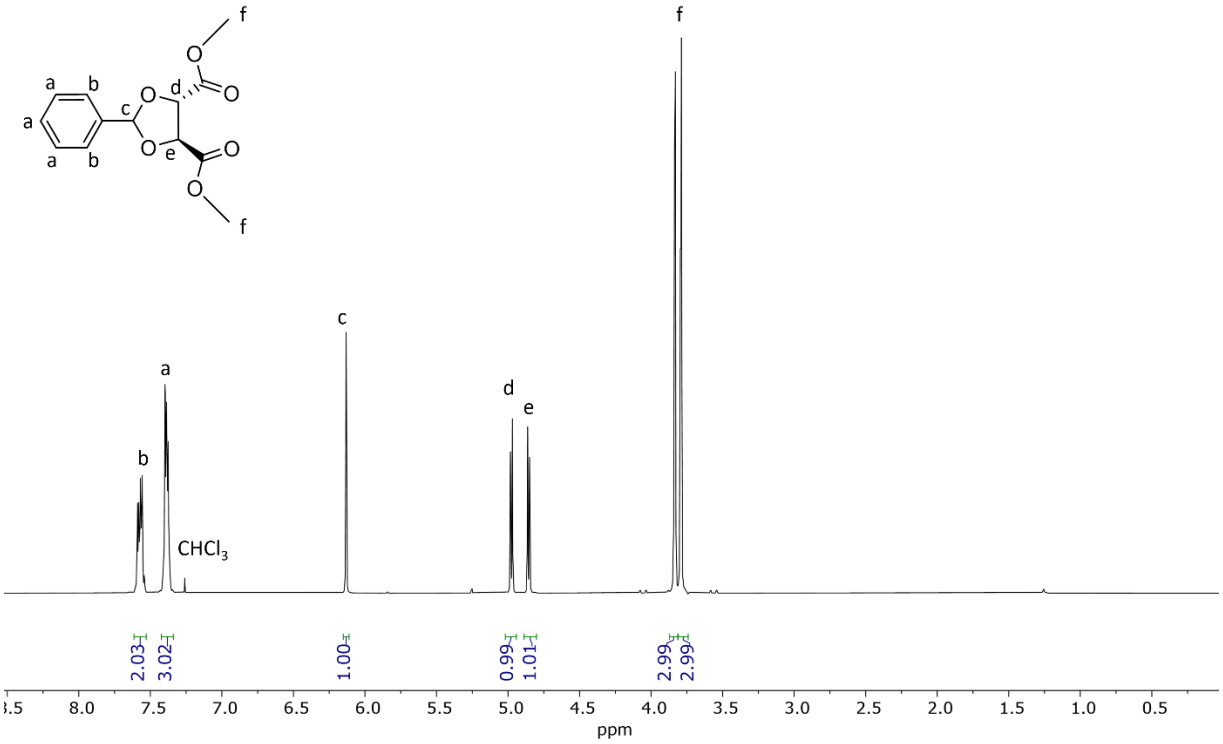


Figure S2.4. ^{1}H NMR spectrum of 2,3-O-benzylidene L-tartrate, $CDCl_3$, 298 K, 300 Hz.

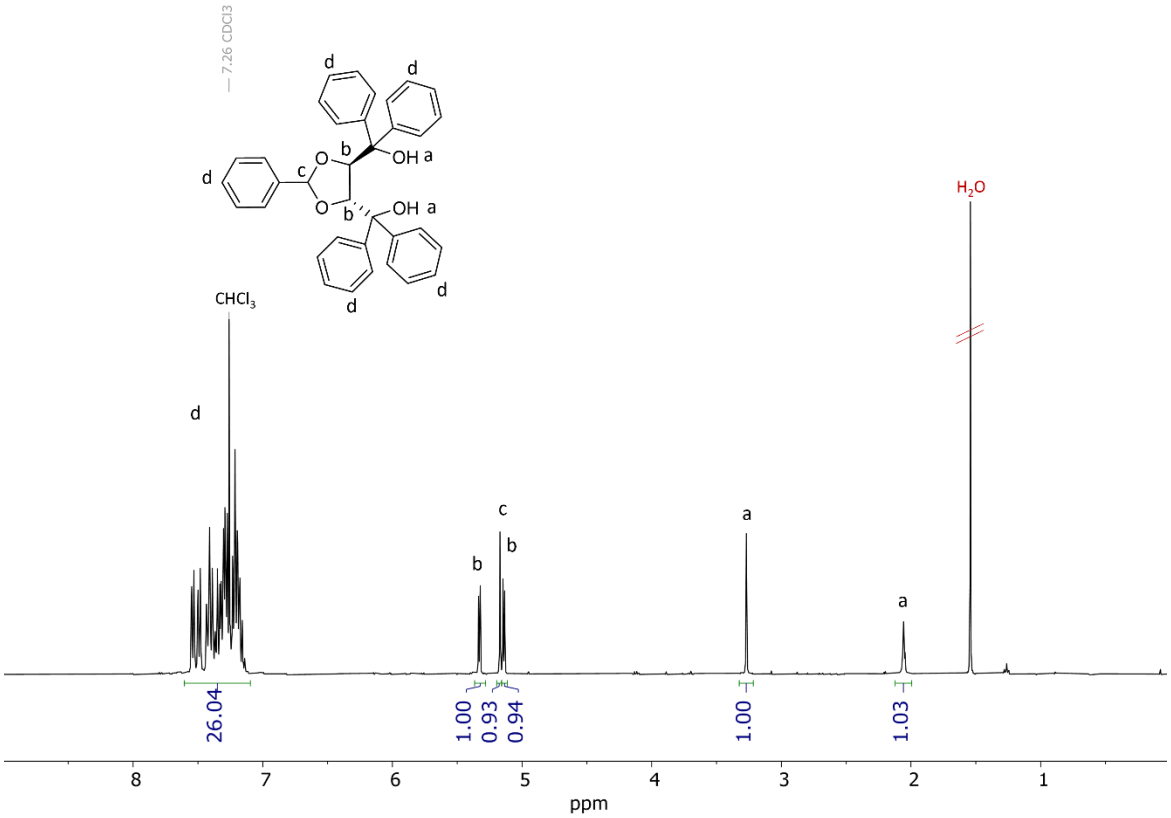


Figure S2.5. ^{1}H NMR spectrum of (4*R* ,5*R*)-Pentaphenyl-1,3-dioxolane-4,5-dimethanol (TADDOL), 101 MHz, 298 K, $CDCl_3$.

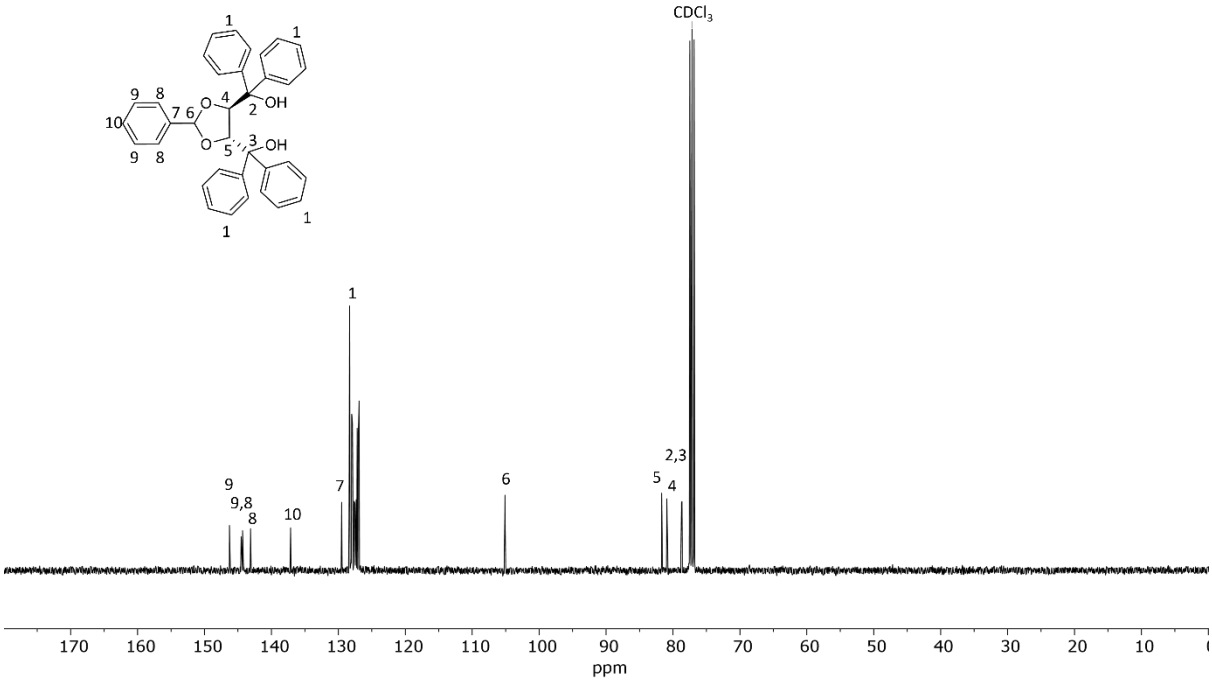


Figure S2.6. ^{13}C NMR spectrum of (4*R* ,5*R*)-Pentaphenyl-1,3-dioxolane-4,5-dimethanol (TADDOL), 101 MHz, 298 K, $CDCl_3$.

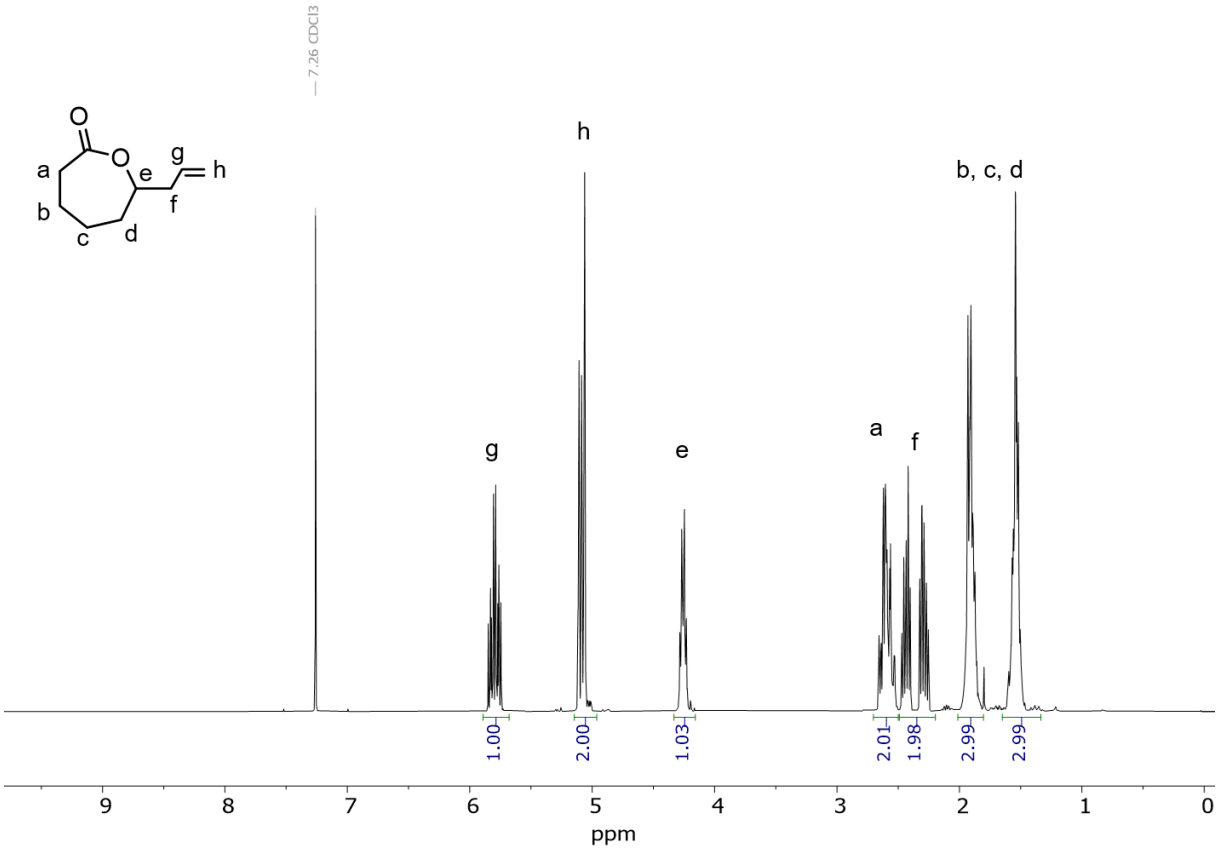


Figure S2.7. ^{1}H NMR spectrum of ε-allyl-ε-caprolactone (εACL), 400 MHz, 298 K, $CDCl_3$.

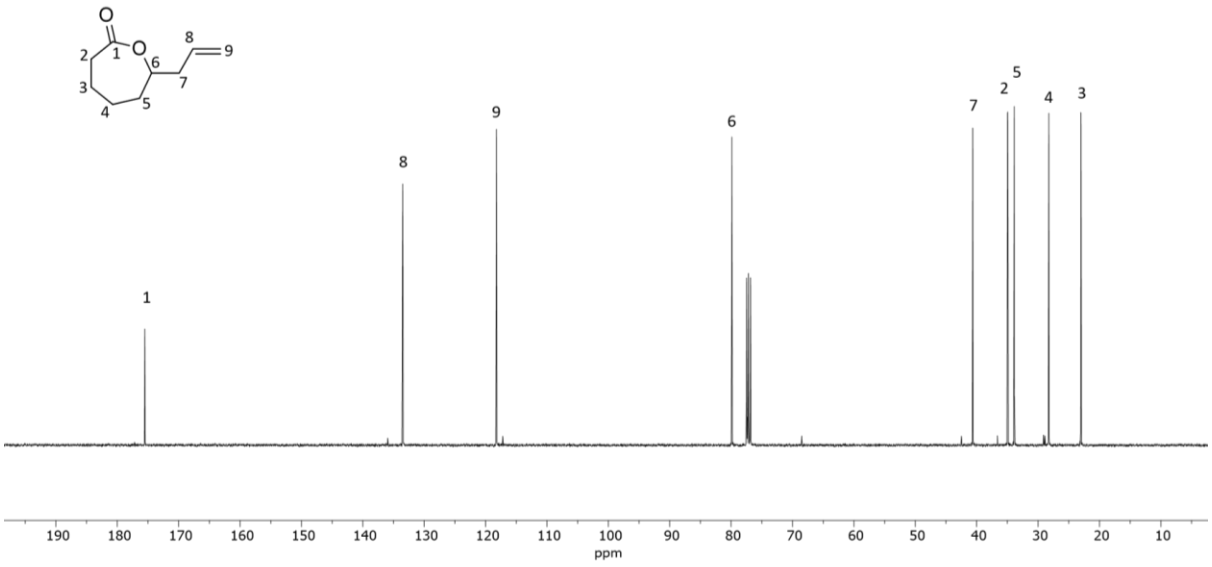


Figure S2.8. ^{13}C NMR spectrum of ε-allyl-ε-caprolactone (εACL), 101 MHz, 298 K, $CDCl_3$.

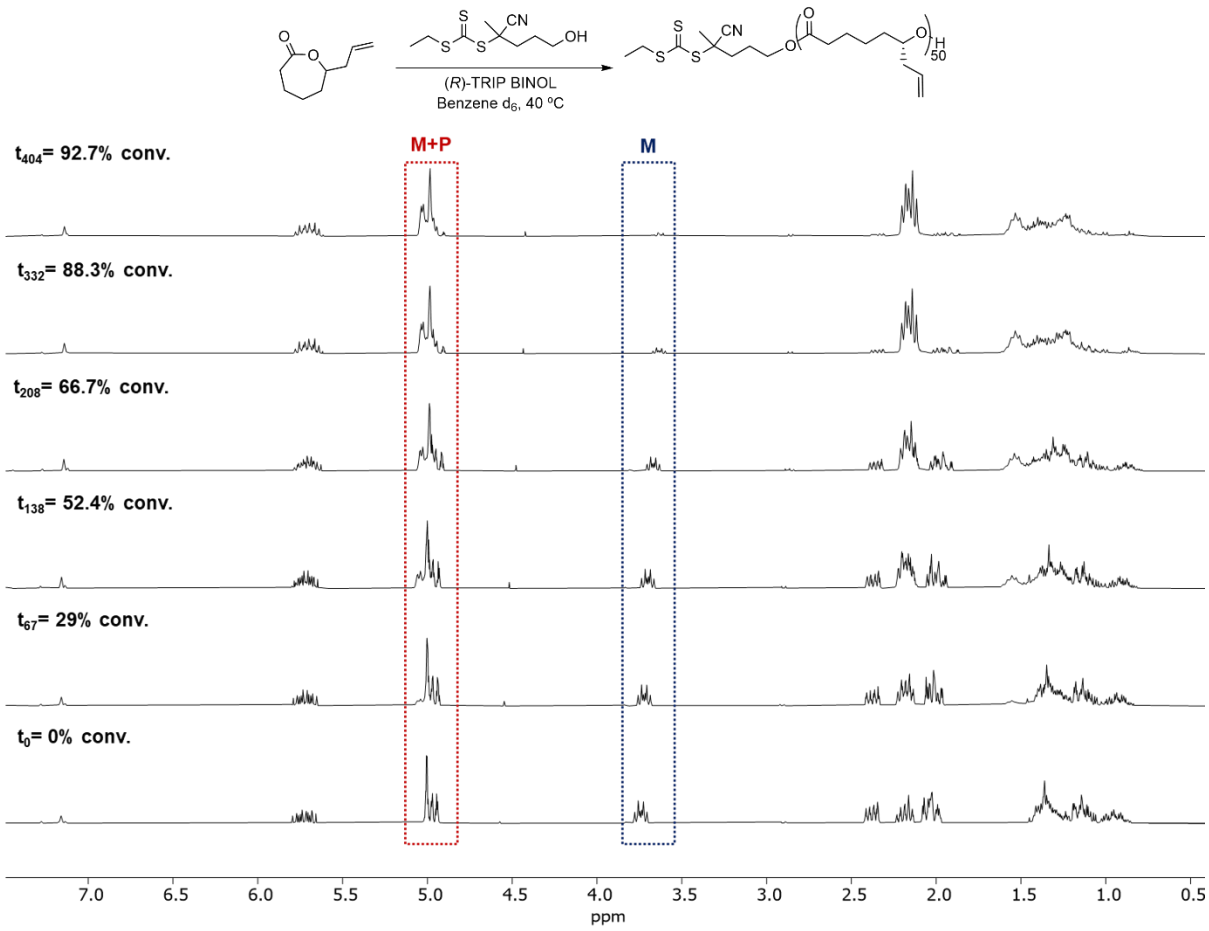


Figure S2.9. Example of kinetic studies for the ROP of εACL. Stacked ^{1}H NMR spectra at different times of polymerisation, C_6D_6, 298 K, 300Hz.

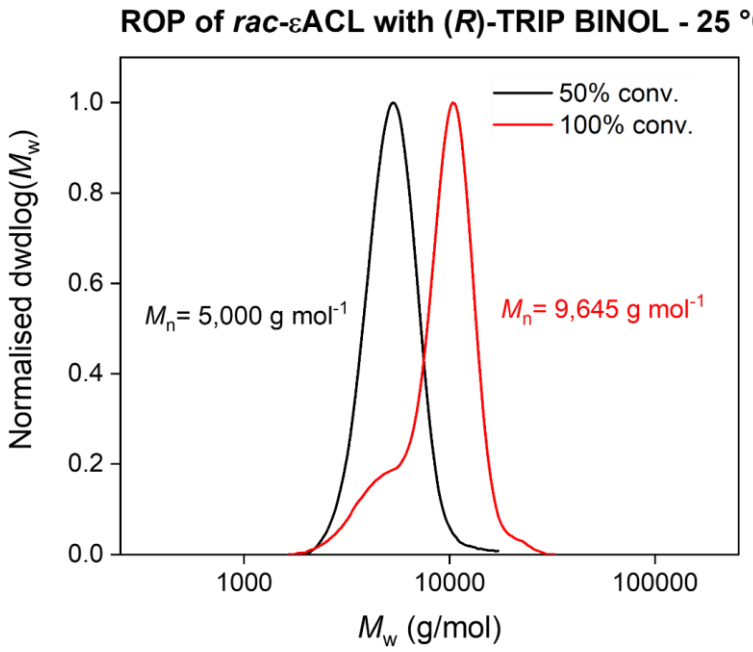


Figure S2.10. SEC chromatograms ($CHCl_3$, with 0.5% Et_3N, PMMA standard) for the polymerisation of *rac*-εACL catalysed by (*R*)-TRIP BINOL at 25 °C quenched at 50% monomer conversion and 100% monomer conversion (**entries 1 and 2, table 1**).

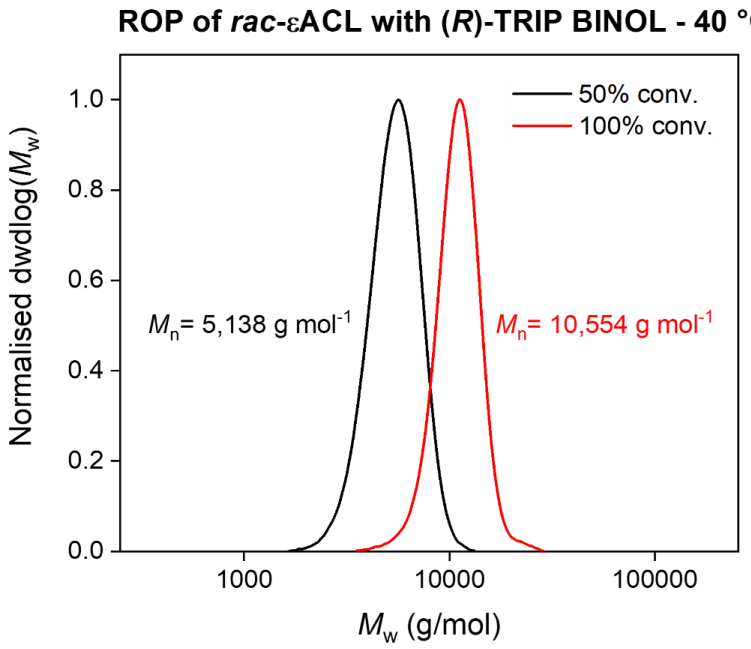


Figure S2.11. SEC chromatograms ($CHCl_3$, with 0.5% Et_3N, PMMA standard) for the polymerisation of *rac*-εACL catalysed by (*R*)-TRIP BINOL at 40 °C, quenched at 50% monomer conversion and 100% monomer conversion (**entries 3 and 4, table 1**).

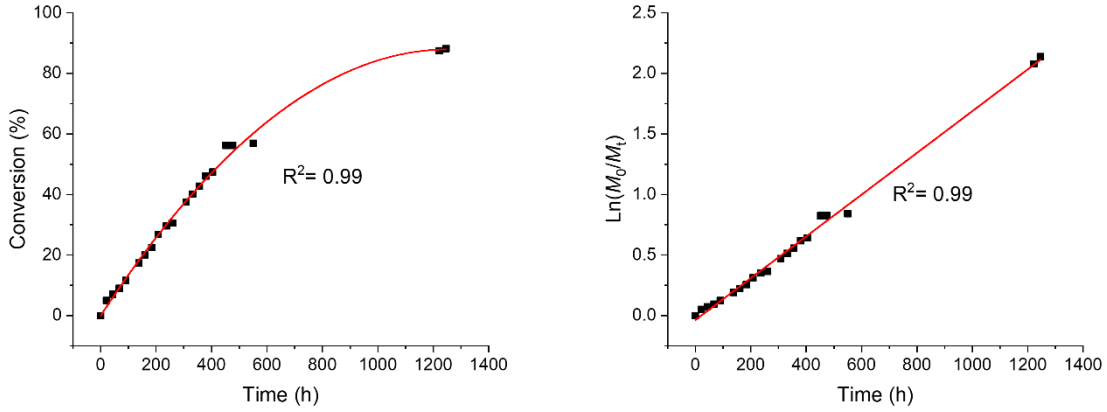
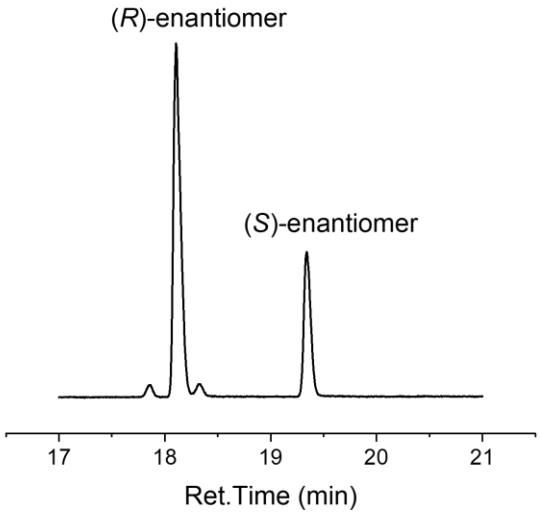


Figure S2.12. Kinetic plots for the polymerisation of rac-εACL catalysed by (*R*)-TRIP BINOL at 25 °C (**entry 2 table 1**).



***ee* = 44.5% (*R*)-enantiomer**

***s*-factor=** 5.15

Peak	R. Time	Area %
(R-isomer)	18.107	72.23
(S-isomer)	19.341	27.77

Figure S2.13. GC-MS chromatograms and *s*-factor of residual εACL resulting from the polymerisation of *rac*-εACL catalysed by (*R*)-TRIP BINOL at 25 °C (**entry 1, table 1**).

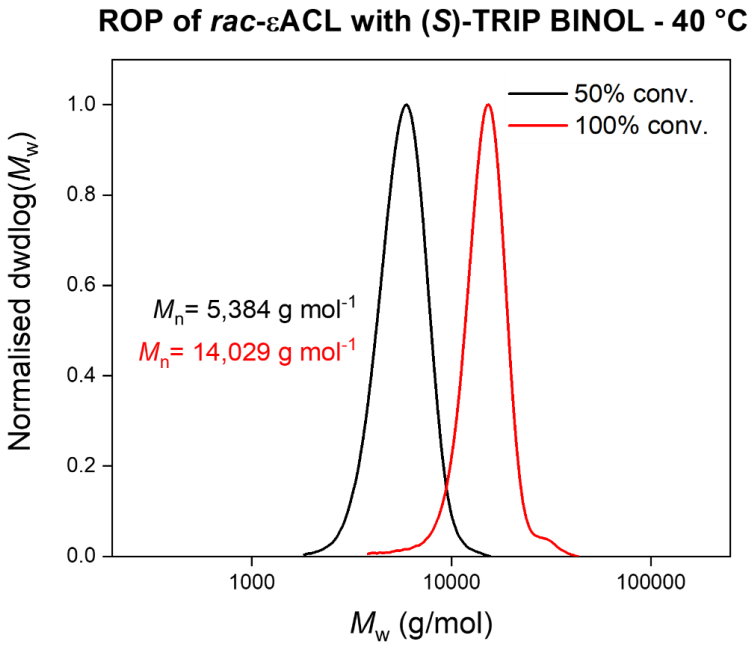


Figure S2.14. SEC chromatograms ($CHCl_3$, with 0.5% Et_3N, PMMA standard) for the polymerisation of *rac*-εACL catalysed by (*S*)-TRIP BINOL at 40 °C, quenched at 50% monomer conversion and 100% monomer conversion (**entries 5 and 6, table 1**).

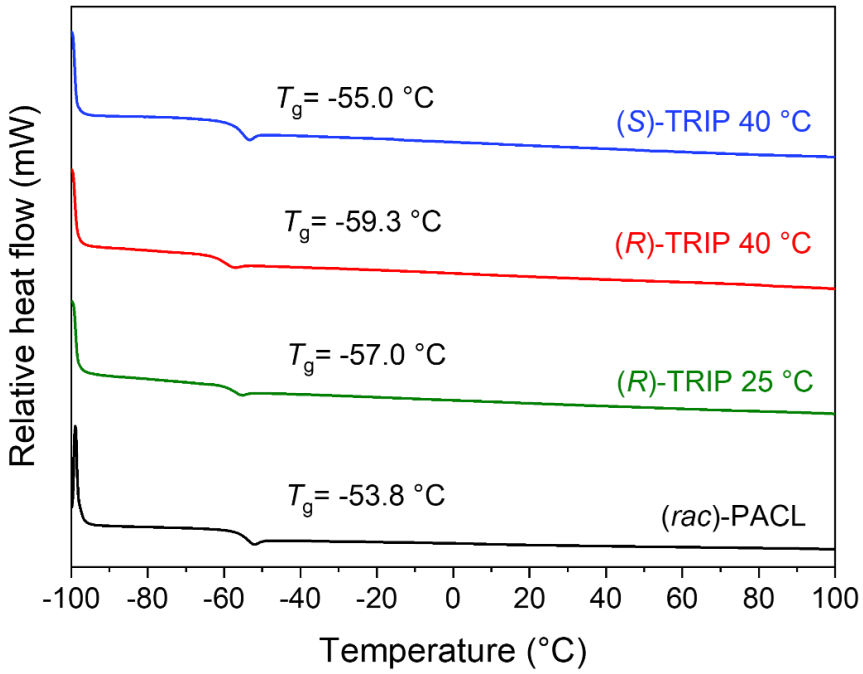


Figure S2.15. DSC thermograms for the polymerisations of *rac*-εACL (**Table 1**), showing the second heating cycle (−100 to 100 °C, 10 °C min^{-1}).

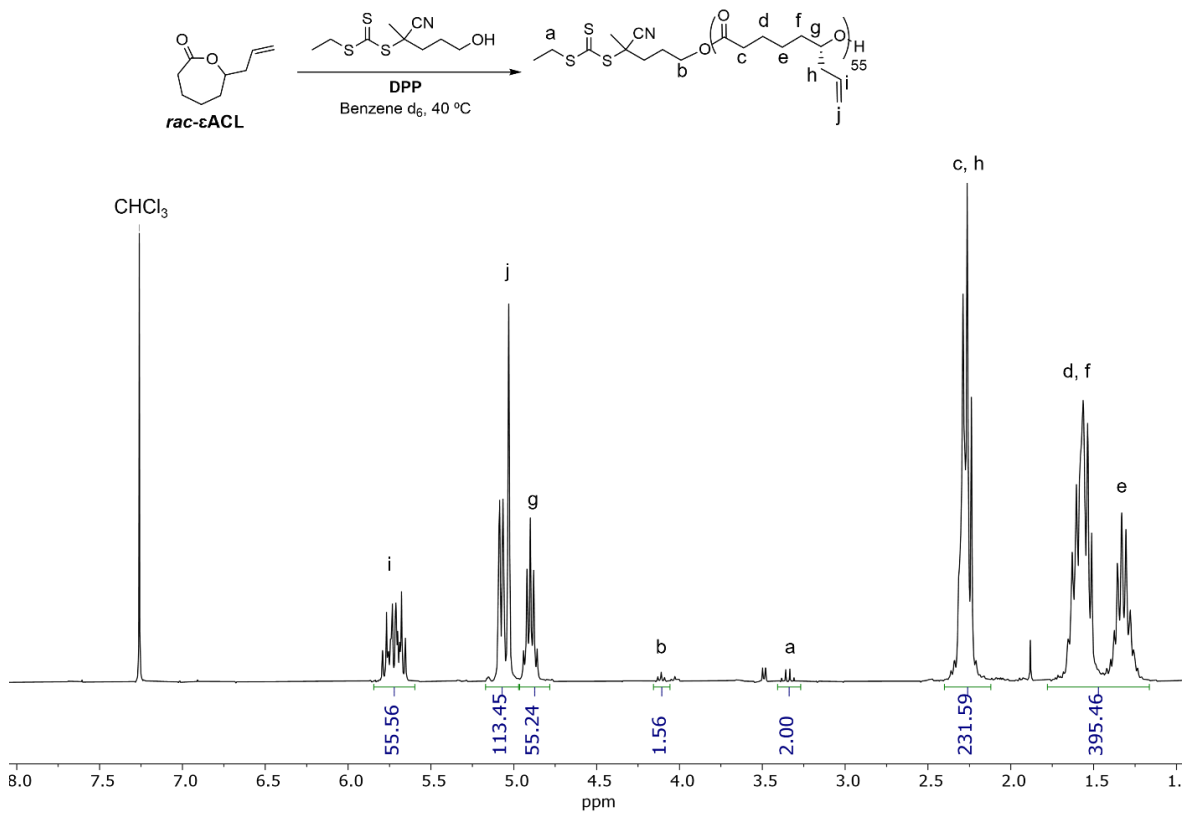


Figure S2.16. ^{1}H NMR spectrum of racemic poly(allyl-ε-caprolactone) (*rac*-PACL), $CDCl_3$, 298 K, 300Hz.

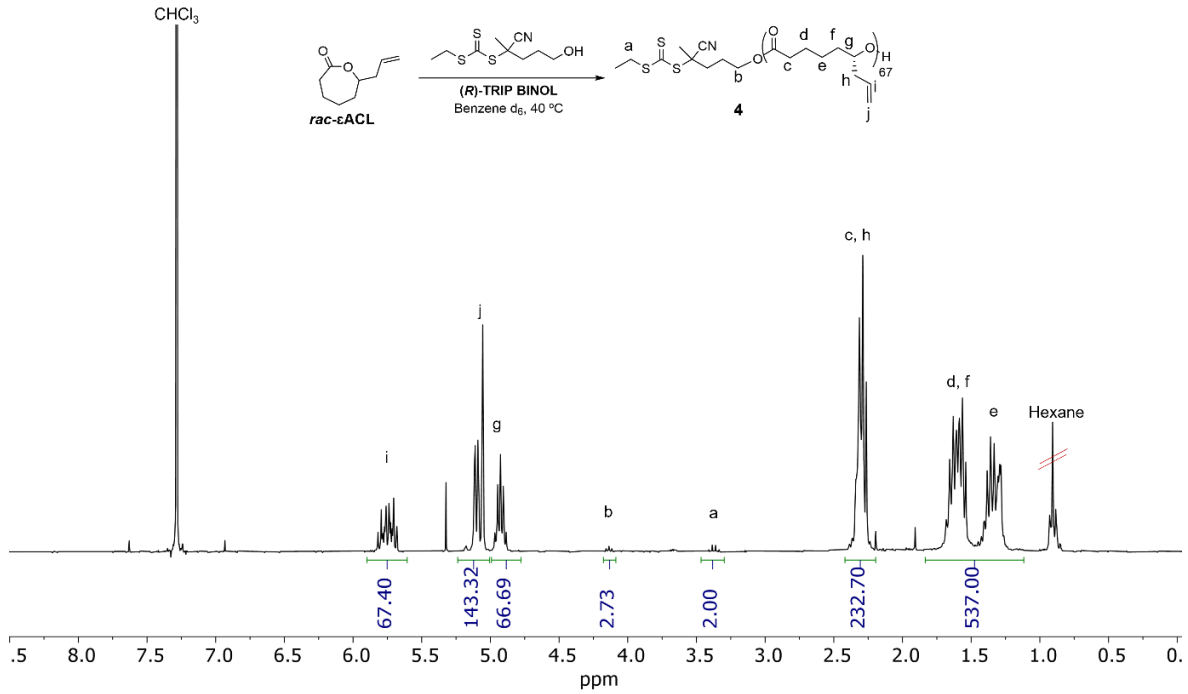


Figure S2.17. ^{1}H NMR spectrum of (*S*)-enantioenriched poly(allyl-ε-caprolactone) (PACL) obtained from the polymerisation of *rac*-εACL with (*R*)-TRIP BINOL (**entry 4 in Table 1**), $CDCl_3$, 298 K, 300Hz.

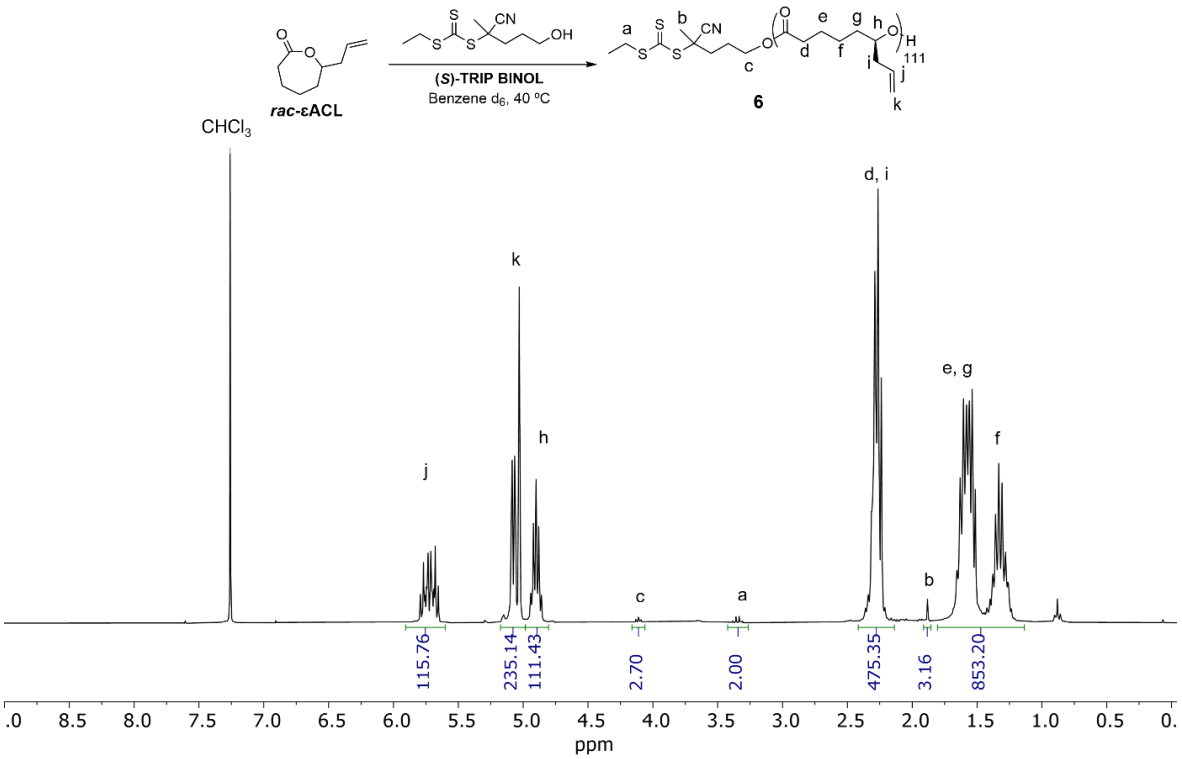


Figure S2.18. ^{1}H NMR spectrum of (*R*)-enantioenriched poly(allyl-ε-caprolactone) (PACL) obtained from the polymerisation of *rac*-εACL with (*S*)-TRIP BINOL (**entry 6 in Table 1**), $CDCl_3$, 298 K, 300Hz.

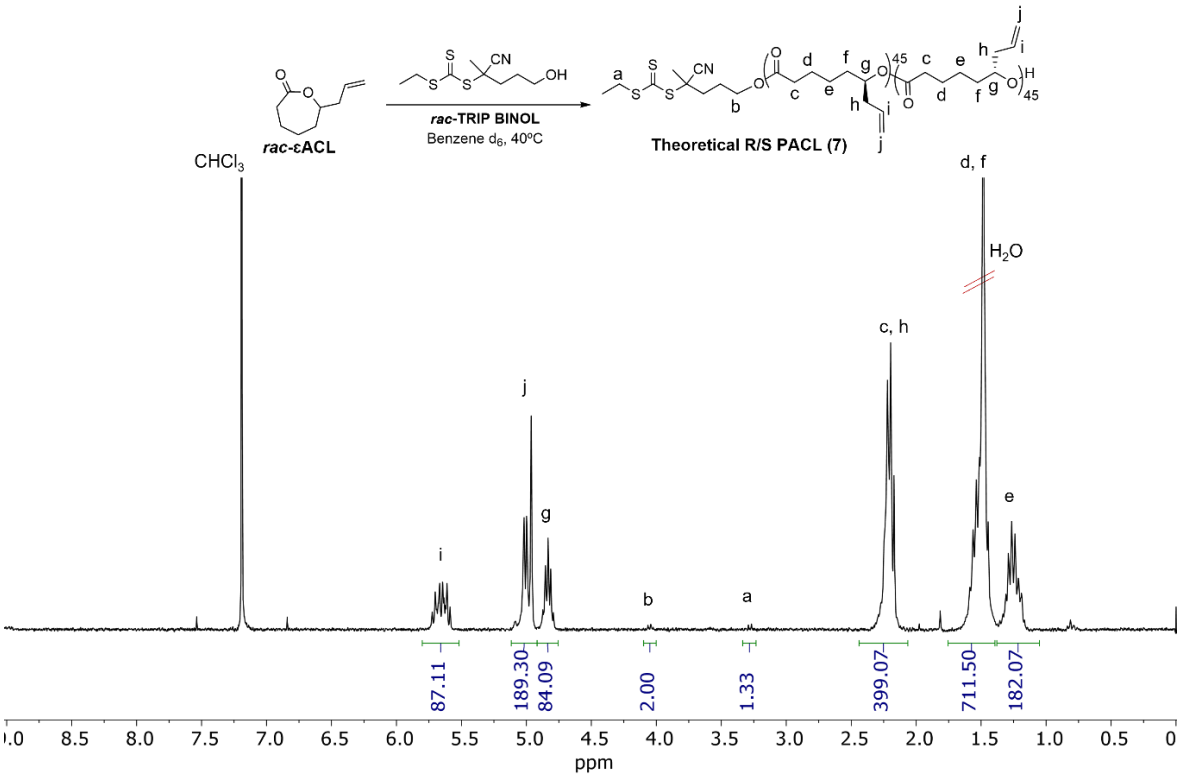


Figure S2.19. ^{1}H NMR spectrum of theoretical (*R*/*S*) poly(allyl-ε-caprolactone) stereoblock obtained from the polymerisation of *rac*-εACL with (*R*)+(*S*)-TRIP BINOL (1:1) (**entry 7 in Table 1**), $CDCl_3$, 298 K, 300 Hz.

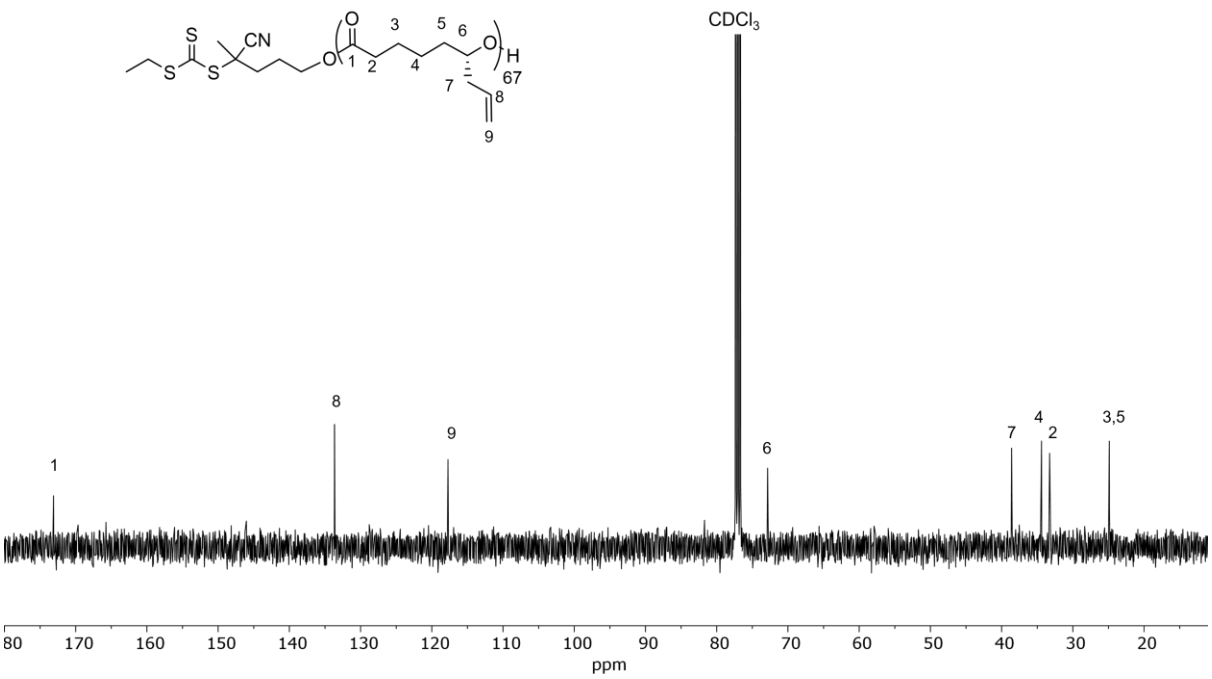
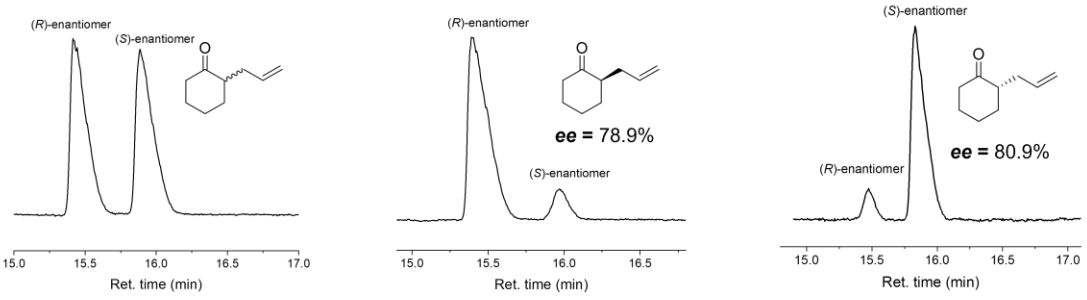


Figure S2.20. ^{13}C NMR spectrum of poly(allyl-ε-caprolactone) (PACL), 101 MHz, 298 K, $CDCl_3$.

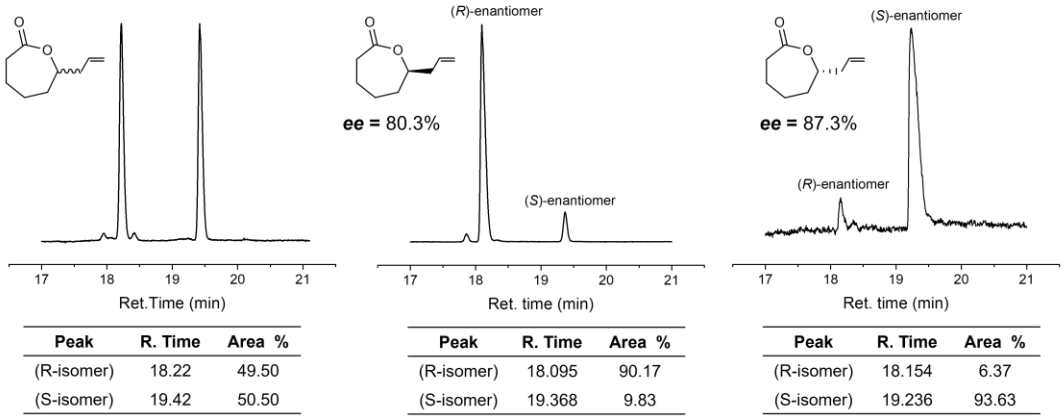


Peak	R. Time	Area %
(R-isomer)	15.417	50.20
(S-isomer)	15.886	49.80

Peak	R. Time	Area %
(R-isomer)	15.392	89.41
(S-isomer)	15.969	10.59

Peak	R. Time	Area %
(R-isomer)	15.474	9.56
(S-isomer)	15.831	90.44

Figure S2.21. GC-MS chromatogram of racemic 2-allylcyclohexanone (*rac*-ACH) (left), enantioenriched (*R*)-ACH (middle) and enantioenriched (*S*)-ACH (right).



Peak	R. Time	Area %
(R-isomer)	18.22	49.50
(S-isomer)	19.42	50.50

Peak	R. Time	Area %
(R-isomer)	18.095	90.17
(S-isomer)	19.368	9.83

Peak	R. Time	Area %
(R-isomer)	18.154	6.37
(S-isomer)	19.236	93.63

Figure S2.22. GC-MS chromatograms of *rac*-εACL (left), enantioenriched (*R*)-εACL (middle) and enantioenriched (*S*)-εACL (right).

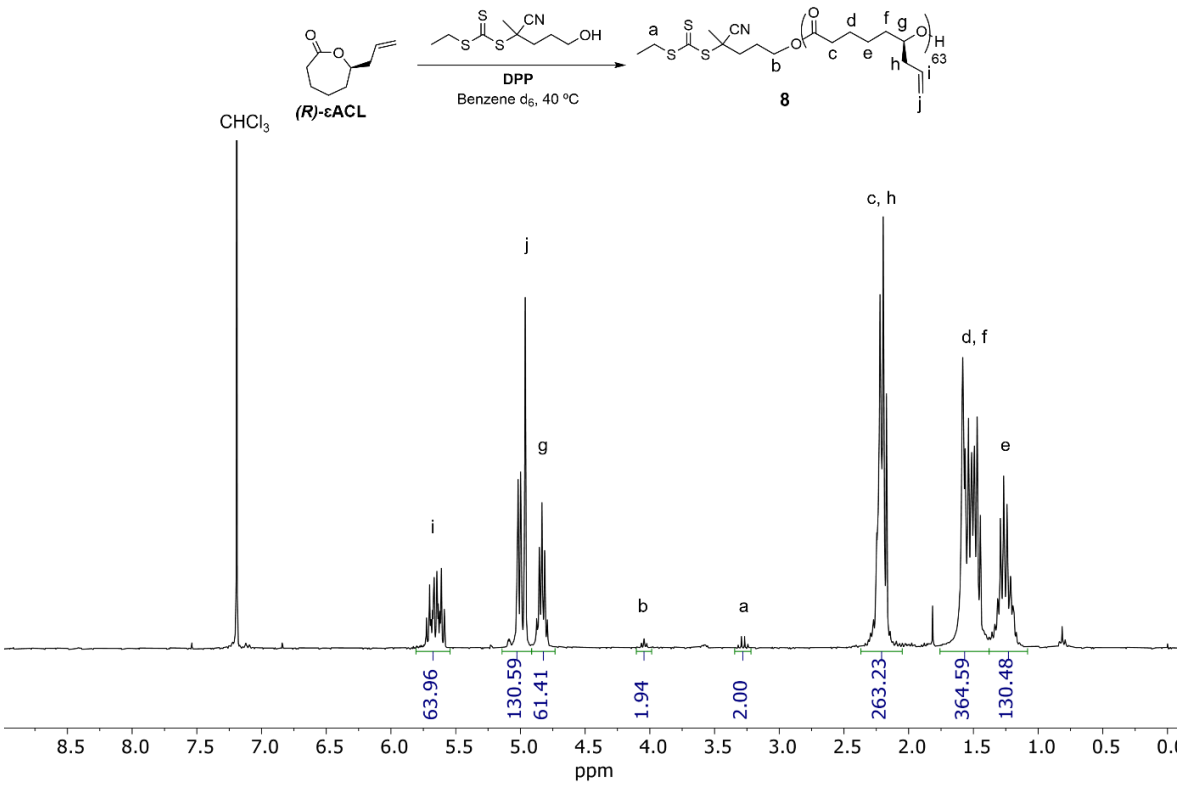


Figure S2.23. ^{1}H NMR spectrum of (*R*)-enantioenriched poly(allyl-ε-caprolactone) (PACL) obtained from the polymerisation of (*R*)-εACL (79.0% *ee*) with DPP (**entry 8 in Table 2**), $CDCl_3$, 298 K, 300 Hz.

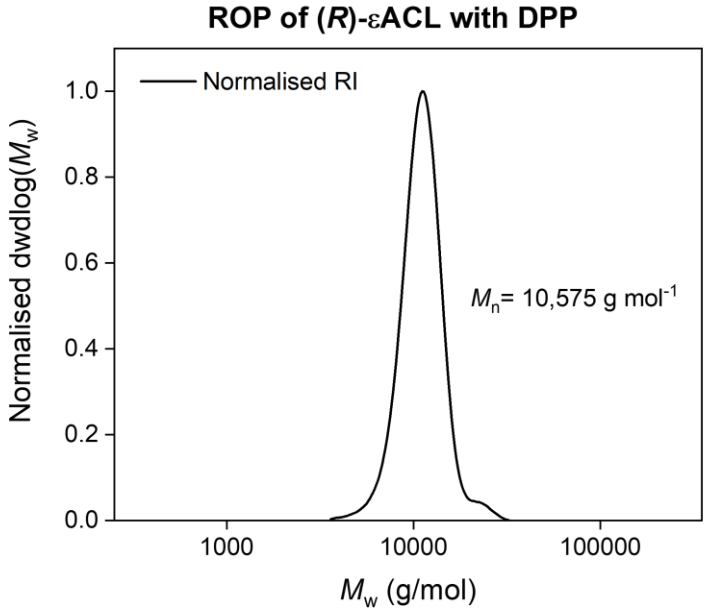


Figure S2.24. SEC chromatogram ($CHCl_3$, with 0.5% Et_3N, PMMA standard) for the polymerisation of (*R*)-εACL catalysed by DPP at 40 °C, polymerization quenched at 90% monomer conversion (**entry 8 in Table 2**).

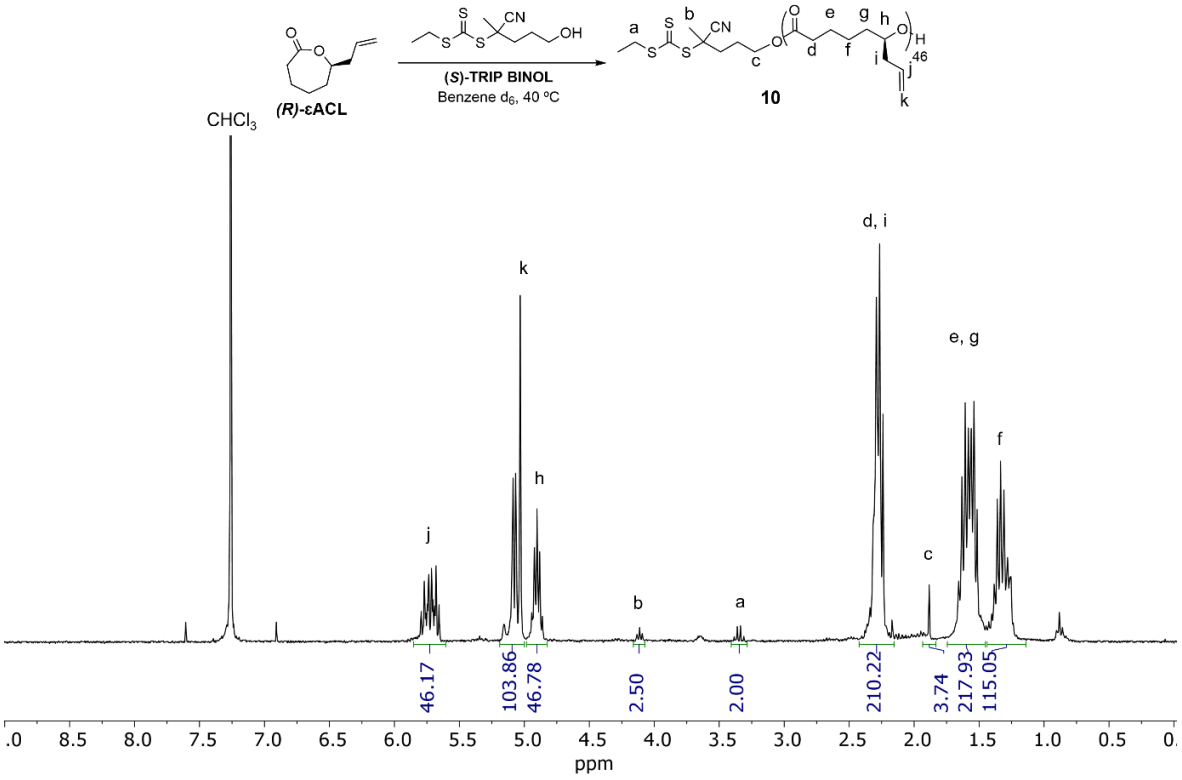


Figure S2.25. ^1H NMR spectrum of (*R*)-enantioenriched poly(allyl-ε-caprolactone) (PACL) obtained from the polymerisation of (*R*)-εACL (80.3% *ee*) with (*S*)-TRIP BINOL (**entry 10 in Table 2**), $CDCl_3$, 298 K, 300 Hz.

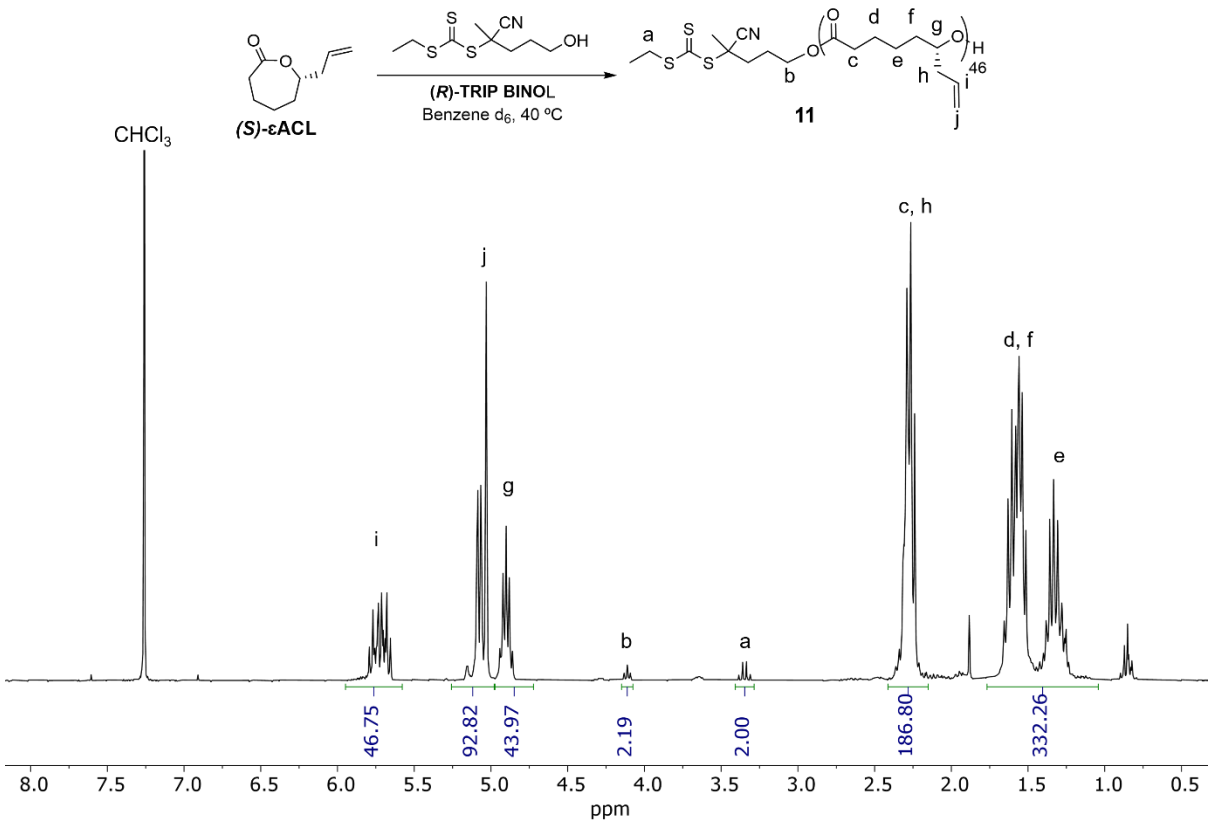


Figure S2.26. ^{1}H NMR spectrum of (*S*)-enantioenriched poly(allyl-ε-caprolactone) (PACL) obtained from the polymerisation of (*S*)-εACL (87.3% *ee*) with (*R*)-TRIP BINOL (**entry 11 in Table 2**), $CDCl_3$, 298 K, 300 Hz.

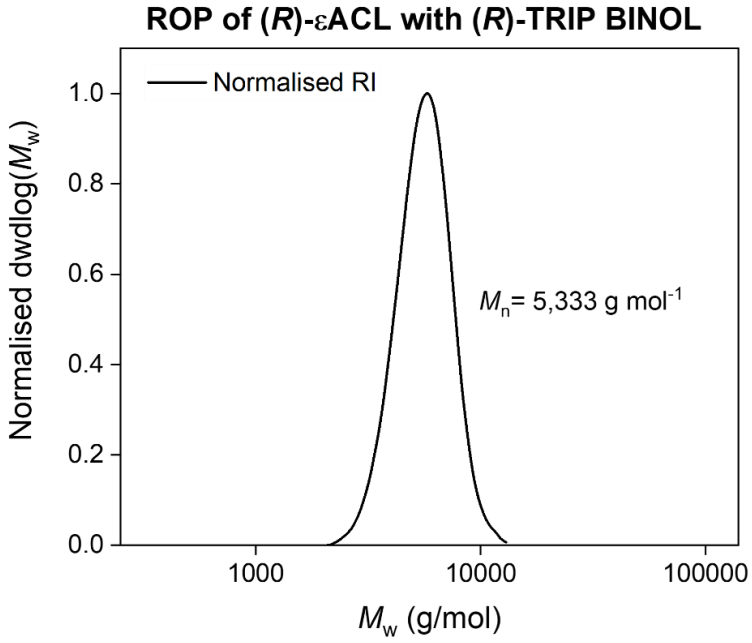


Figure S2.27. SEC chromatogram ($CHCl_3$, with 0.5% Et_3N, PMMA standard) for the polymerisation of (*R*)-εACL catalysed by (*R*)-TRIP BINOL at 40 °C, polymerization quenched at 50% monomer conversion (**entry 9, table 2**).

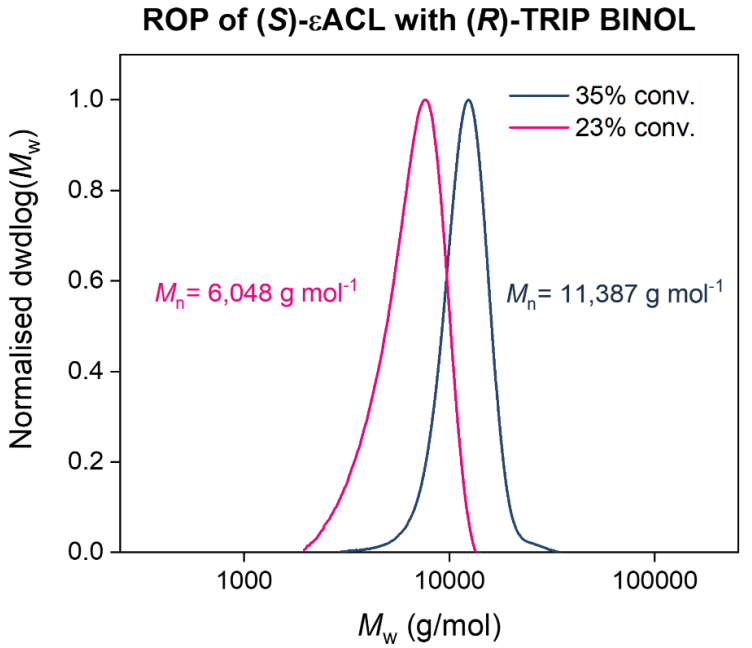


Figure S2.28. SEC chromatograms ($CHCl_3$, with 0.5% Et_3N, PMMA standard) for the polymerisation of (*S*)-εACL catalysed by (*R*)-TRIP BINOL at 40 °C, polymerization quenched at 35% and 23% monomer conversion (**entry 12 and 13, table 2**).

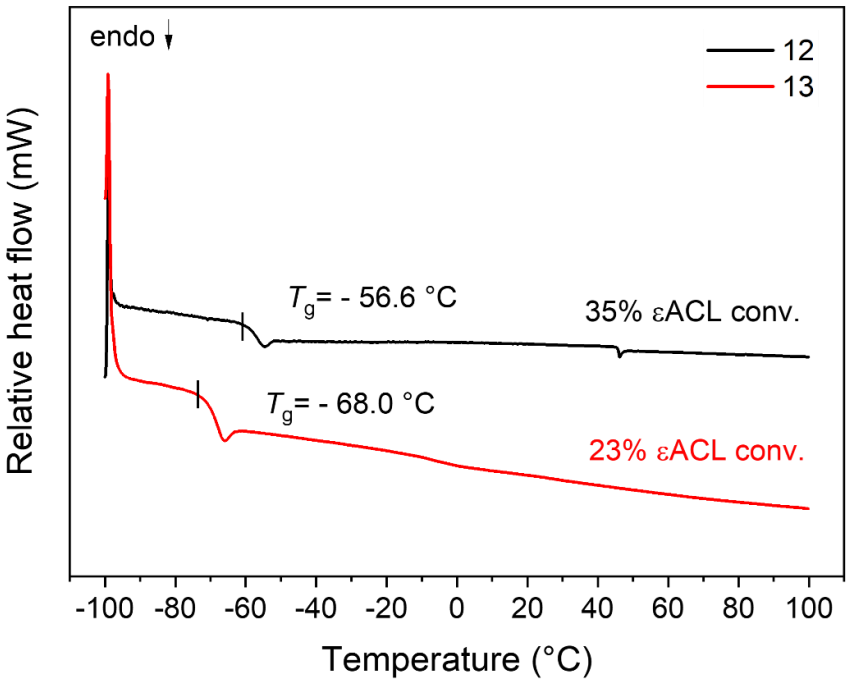


Figure S2.29. DSC thermograms for the polymerisations of (*S*)-εACL (*ee* = 87.3%) with (*R*)-TRIP BINOL after quenching the polymerization at 35% and 23% monomer conversion (**entries 12 and 13, Table 2**) showing the second heating cycle (−100 to 100 °C, 10 °C min^{-1}).

2.4 References

1. M. C. Arno, M. Inam, Z. Coe, G. Cambridge, L. J. Macdougall, R. Keogh, A. P. Dove and R. K. O'Reilly, *J. Am. Chem. Soc*, 2017, **139**, 16980-16985.
2. M. Ohno, K. Fujita, H. Nakai, S. Kobayashi, K. Inoue and S. Nojima, *Chem. Pharm. Bull.*, 1985, **33**, 572-582.
3. V. Pirenne, I. Traboulsi, L. Rouvière, J. Lusseau, S. Massip, D. M. Bassani, F. Robert and Y. Landais, *Org. Lett.*, 2020, **22**, 575-579.
4. H. Kaku, A. Nakamaru, M. Inai, T. Nishii, M. Horikawa and T. Tsunoda, *Tetrahedron*, 2010, **66**, 9450-9455.
5. G. Wang, Y. Shi, Z. Fu, W. Yang, Q. Huang and Y. Zhang, *Polymer*, 2005, **46**, 10601-10606.
6. C. Clamor, B. N. Cattoz, P. M. Wright, R. K. O'Reilly and A. P. Dove, *Polym. Chem.*, 2021, **12**, 1983-1990.

Chapter 3.

Synthesis of semicrystalline allyl-functionalised poly(ε-caprolactone) copolymers *via* ring-opening copolymerisation

3 Synthesis of semicrystalline allyl-functionalised poly(ε-caprolactone) copolymers *via* ring-opening polymerisation

3.1 Introduction

The use of polyesters in materials science has attracted great interest over the past decades owing to their robust mechanical properties, controlled biodegradation, and notable biocompatibility.[1-4] Among the most studied polyesters, poly(ε-caprolactone) (PCL) has been widely used in the biomedical field because of its compatibility with other polymers and its semicrystalline nature, enabling applications in areas such as surgical sutures, tissue engineering scaffolds and drug delivery systems.[5-7] The ring-opening polymerisation (ROP) of ε-caprolactone (εCL) has been previously investigated using metallic catalysts,[8-12] organocatalysts,[13-15] and biocatalysts[16, 17] to achieve polymers with controlled molecular weights and narrow molar-mass dispersities ($Đ_M$). However, the lack of functional side groups within the polymer backbone hinders the chemical modification of PCL after polymerisation. In this case, properties such as crystallinity, degradability, shape memory, and adherence cannot meet specific requirements for the use of these materials in advanced biological applications. [18-22]

To address the challenge associated with PCL modification, strategies such as the polymerisation of substituted ε-caprolactones (SεCLs),[23, 24] and the copolymerisation of CL with other functional monomers have been disclosed in the literature.[25-27] SεCLs can be synthesised through the ring expansion of their corresponding cyclohexanone precursors *via* Baeyer-Villiger oxidation.[28, 29] Even though the homopolymerisation of functional SεCLs can provide materials bearing reactive handles for post-polymerisation modifications, the presence of substituents and stereocenters tend to disrupt the crystallisation of the polymer

chains rendering materials with lower thermo-mechanical properties.[30] By contrast, the synthesis of copolymers from εCL and functional monomers enables the preparation of PCL-based materials with diverse structural characteristics, adaptable properties and a broad range of functionalities.[31, 32] Research into the ring-opening copolymerisation (ROCOP) of εCL with other monomers has been conducted in order to achieve random,[33, 34] block,[35-37] graft,[38-40] and alternating[41, 42] PCL-based copolymers. In their majority, functional monomers containing a reactive group that allow for a secondary polymerisation method are employed, such as atom-transfer radical polymerisation (ATRP), reversible addition-fragmentation chain-transfer polymerisation (RAFT) and Cu(0)-mediated controlled radical polymerisation (CRP).[43-46] For example, Yang and coworkers reported the synthesis of brush copolymers of monomethyl poly(ethylene glycol)-*block*-[(poly-ε-caprolactone)-*graft*-poly[(2-phenyl borate esters-1,3-dioxane-5-methyl)methyl acrylate] (MPEG-*b*-P(CL-*g*-PPBDMMA)) by combining ROP and ATRP polymerisation techniques to create glucose responsive insulin delivery systems.[47] MPEG-*b*-poly(α-bromo-ε-caprolactone) (MPEG-*b*-P(α-BrCL)) block copolymers were initially prepared *via* ROP of α-bromo-ε-caprolactone (α-BrCL) using MPEG as initiator. The obtained copolymer was then used as a macroinitiator for the ATRP polymerisation of the methyl acrylate monomer, thanks to the presence of the halogen group in the PCL backbone, to yield structurally well-defined brush copolymers.

Post-polymerisation modifications represent an attractive strategy to design polymers with numerous functionalities that are usually incompatible with the ring-opening polymerisation conditions.[48-50] In particular, thiol-based chemistry have become popular in the field to attach a wide range of molecules and macromolecules to the polymer backbone through the reaction of terminal thiols with alkenes (thiol-ene),[51-54] alkynes (thiol-yne),[55, 56] and some terminal halogens (thio-bromo and thio-fluoro).[57, 58] For example, Becker and coworkers reported the

fabrication of allyl- and DIBO-functionalised PCL-based nanofibers containing different allyl group gradients, and explored their dual surface modification with bioactive peptides and fluorescent molecules *via* both strain-promoted alkyne-azide cycloaddition (SPAAC) and radical thiol-ene addition.[59]

In this chapter, we report the design of a core-forming block copolymer *via* ring-opening polymerisation (ROP) of ε-caprolactone (εCL) and ε-allyl-ε-caprolactone (εACL) to produce a semicrystalline, biodegradable, and biocompatible copolymer with side-chains amenable of post-polymerisation functionalisation. Kinetic studies of the respective homopolymers and copolymers were performed to predict the sequencing of the copolymer and establish the limit of functionality that can be grafted into the polymer backbone while retaining the semicrystalline nature of PCL.

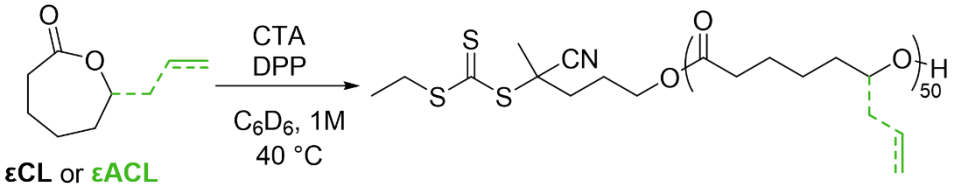
3.2 Results and discussion

In chapter 2 it was shown that highly stereoregular poly(ε-allyl-ε-caprolactone) (PACL) did not present a semicrystalline microstructure. To overcome this limitation and design functional poly(ε-caprolactone)s with retained crystallinity, copolymerisation reactions of ε-caprolactone (εCL) with ε-substituted ε-caprolactones (εSCLs) were investigated. ε-Allyl-ε-caprolactone (εACL) was chosen as the substituted monomer in reason of the simplicity of its synthesis, low cost and the presence of the reactive allyl group, which allows post-polymerisation modification reactions, such as thiol-ene addition.

3.2.1 Ring-opening polymerisation of ε-caprolactone and ε-allyl-ε-caprolactone

Initially, the homopolymerisation of ε-caprolactone (εCL) and ε-allyl-ε-caprolactone (εACL) was investigated to access the reaction kinetics of each monomer separately. The ROP of both

monomers were conducted in deuterated benzene (C_6D_6) at 40 °C using diphenyl phosphate (DPP, 10 mmol%) as the catalyst and 2-cyano-5-hydroxypentan-2-yl ethyl carbonotrithioate (CHPET), a chain transfer agent (CTA), as the initiator with [monomer] = 1 M and $[monomer]_0:[CTA]_0 = 50$ (**Scheme 3.1**).



Scheme 3.1. ROP of ε-caprolactone (εCL) or ε-allyl-ε-caprolactone (εACL). Reaction conditions: [monomer] = 1 M and $[monomer]_0:[CTA]_0 = 50$.

The polymerisations were monitored by ^{1}H NMR spectroscopy using the disappearance of the diagnostic O=COCH monomer resonance (δ = 3.61 ppm and 3.75 ppm for εCL and εACL respectively) and appearance of O=COCH polymer resonance (δ_{PCL} = 3.93 ppm and δ_{PACL} = 5.1 − 4.9 ppm) (**Figures S3.1 – S3.6**). First order kinetics were observed for both polymerisations, as suggested by the linear consumption of the monomers over time (**Figure 3.1**). To avoid transesterification side reactions, the polymerisations were stopped near 90% monomer conversion, with εCL and εACL reaching 88.6% and 87.0% conversion after 5 h and 246 h, respectively. Size exclusion chromatography (SEC) analyses of the homopolymers showed a monomodal distribution with low molar-mass dispersity ($Đ_{PCL}$ = 1.08 and $Đ_{PACL}$ = 1.11, **Figure S3.7**), further supporting a controlled polymerisation. Similarly, Hardouin *et al.*[60] reported lower reactivity of δ-hexalactone (5-methyl-δ-valerolactone) compared to its non-substituted counterpart, δ-valerolactone, when they were polymerised under the same ROP conditions. It is most likely that the different polymerisation rates between the monomers

occurred as a result of the greater steric hindrance near the ring-opening centre in the substituted monomer.

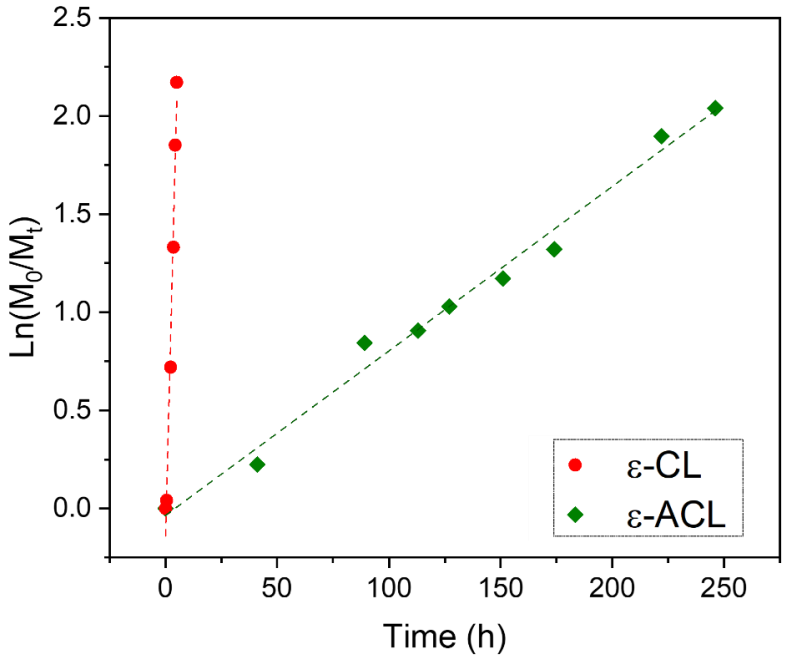
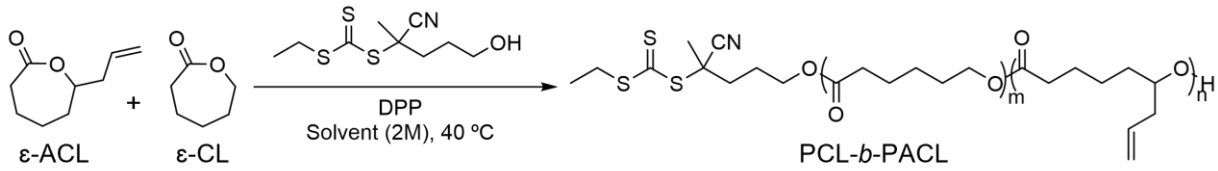


Figure 3.1. First order kinetic plot for the ROP of εCL and *rac*-εACL at 40 °C using DPP (10 mmol%), $[monomer]_0:[CTA]_0 = 50$ in C_6D_6.

3.2.2 Ring-opening copolymerisation (ROCOP) of ε-caprolactone and ε-allyl-ε-caprolactone

Following the investigation of the reactivity of both monomers separately, ring-opening copolymerisation reactions (ROCOP) of εACL and εCL were performed using CHPET as initiator and DPP (10 mmol%) as the catalyst with [monomers] = 2 M (**Scheme 3.2**). Copolymers with various monomer compositions were achieved by adjusting the [εCL]:[εACL] molar ratio while keeping the [CHPET]:[DPP] molar ratio constant at 1:1. The allyl-functional monomer was obtained from its racemic precursor, 2-allylcyclohexanone, *via* Baeyer-Villiger oxidation as detailed in Chapter 2.



Scheme 3.2. Ring-opening copolymerisation (ROCOP) of ε-caprolactone (εCL) and ε-allyl-ε-caprolactone (εACL). Deuterated benzene (C_6D_6) or toluene were used as solvents.

To investigate the effect of the pendent allyl groups on polymer crystallinity and polymerisation rates, a series of PCL-*co*-PACL copolymers containing different ratios of εACL were synthesised (**Table 3.1** and **Figures S3.9 – S3.11**). For this, copolymerisations were performed in 500 µL of deuterated benzene (C_6D_6) under the same conditions previously described but varying the εACL concentration from 6 to 40 wt.% in the formulations. Initially, the total degree of polymerisation (DP) was varied from 55 to 100, with the DP of εCL being kept constant at 50. To avoid transesterification reactions, all copolymerisations were stopped at 95% conversion of εCL, the most reactive monomer, and precipitated in cold *n*-hexanes to yield the desirable functional PCL copolymers. However, the obtained DPs and εCL: εACL ratios deviated from the original target, and this is strongly related to the slower reactivity of εACL in the ROP conditions as observed in the homo-polymerisation studies. For example, the copolymer PCL_{48}-*co*-$PACL_{24}$ (**CP6** in Table 3.1) resulted from the ROCOP with a targeted εCL:εACL molar ratio of 50:40 (**Figure 3.2**).

Table 3.1. ROCOP of εACL and εCL.[a]

Entry	Targeted PCL:PACL ratio	ACL units wt. % [b]	Reaction time (h)	εCL conversion [b] (%)	PCL:PACL ratio [b]	M_n (kDa) [c]	$Đ_M$ [c]
CP1	50:5	6	21	96.9	56:4	12.2	1.45
CP2	50:10	11	40	99.0	54:7	16.6	1.27
CP3	50:20	20	45	94.7	60:15	17.1	1.18
CP4	50:25	26	50	93.3	55:20	17.1	1.14
CP5	50:35	30	70	93.7	46:20	14.6	1.15
CP6	50:40	33	94	95.5	48:24	16.3	1.10
CP7	50:45	36	120	94.5	62:36	16.6	1.20
CP8	50:50	40	116	94.6	65:42	21.3	1.09

[a] Polymerisations were carried out in a glovebox using benzene-d_6 as a solvent with $[εCL]_0$:$[CHPET]_0$ = 50 and [monomers] = 2 M, using CHPET as initiator and DPP as catalyst (10 mol%). [b] Calculated by ^{1}H NMR spectroscopy. [c] Measured by SEC ($CHCl_3$ with 0.5% Et_3N, PMMA standards).

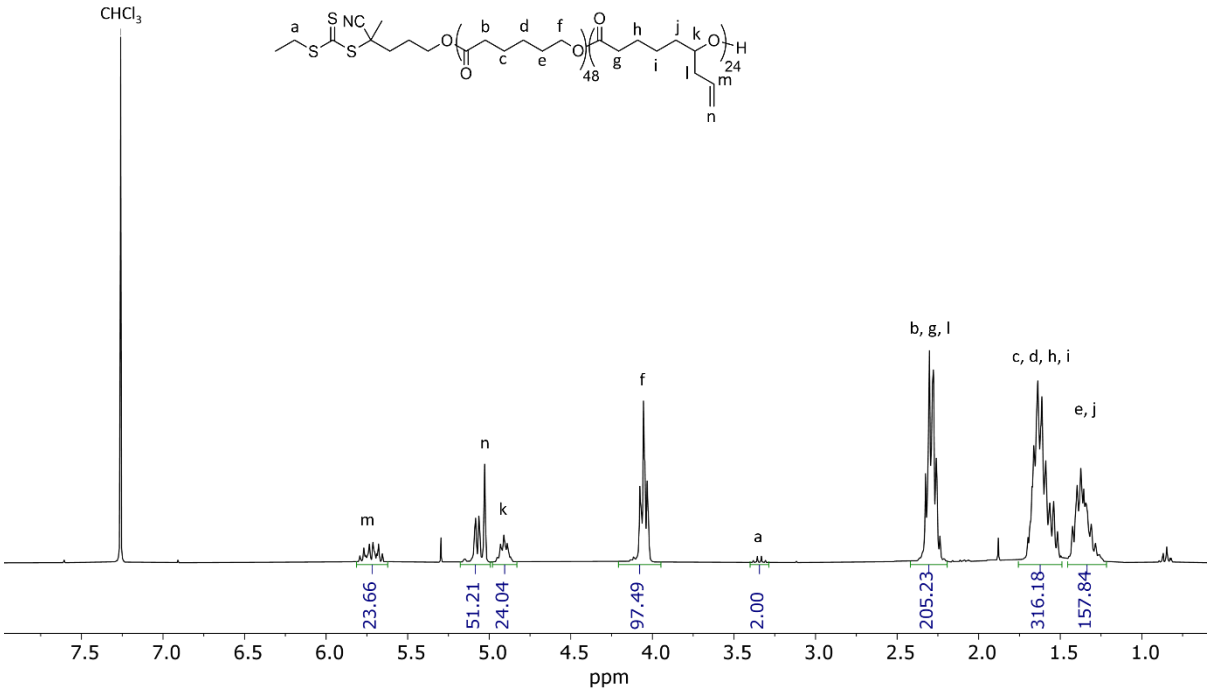


Figure 3.2. ^{1}H NMR spectrum (300 MHz, 298 K, $CDCl_3$) of PCL_{48}-*co*-$PACL_{24}$ copolymer (**CP6** in Table 3.1) with an initial PCL:PACL target = 50:40.

Just as with the homo-polymerisation studies, ^{1}H NMR spectroscopy was used to monitor the progress of the ROCOP by controlling the disappearance of the monomer resonances (δ = 3.64 ppm and δ = 3.82 ppm for C*H*$_2$OC=O and C*H*OC=O in εCL and εACL, respectively) and the appearance of new polymer resonances at δ = 3.93 ppm, corresponding to C*H*$_2$OC=O of PCL, and δ = 5.73 ppm, corresponding to C*H*CH$_2$ (allyl bond) of PACL (**Figure S3.8**). In agreement with previous studies, the polymerisation of εCL proceeded significatively faster than that of εACL. For a 50:50 feed ratio of monomers (entry CP8 in Table 3.1), 34.4% and 6.6% conversion of εCL and εACL was achieved after 29.5 h. As the concentration of εCL decreases throughout the time, the polymerisation rate of εACL increases while the polymerisation of εCL continue in a slightly reduced rate (**Figure 3.3**). These results suggest the formation of gradient copolymers, in which the average composition of the copolymer varies along the polymer chain, rather than copolymers with a random distribution of the monomeric units throughout the chain.[61] Considering the reactivity of εCL is notably higher than that of εACL, it was hypothesised that our copolymers would exhibit an initial PCL block followed by the gradual incorporation of allyl units. In addition, SEC analyses showed unimodal weight distributions for all copolymers, suggesting the presence of a single polymer form (**Figure S3.14**). A decrease in polymer dispersity ($Đ_M$), from 1.45 to 1.09, was observed when raising the concentration of εACL from 6 to 40 wt.% (Table 3.1). This could be related to the increase of side reactions at lower concentrations of the allyl monomer, with transesterification reactions of PCL chains taking place.[62] To further confirm the synthesis of copolymers, diffusion-ordered NMR spectroscopy (DOSY NMR) was used to investigate the diffusion rate of the copolymers. The spectra only exhibited a single diffusion coefficient for the copolymer signals, suggesting that PCL and PACL blocks are connected and not two separate homopolymers (**Figure 3.4**).

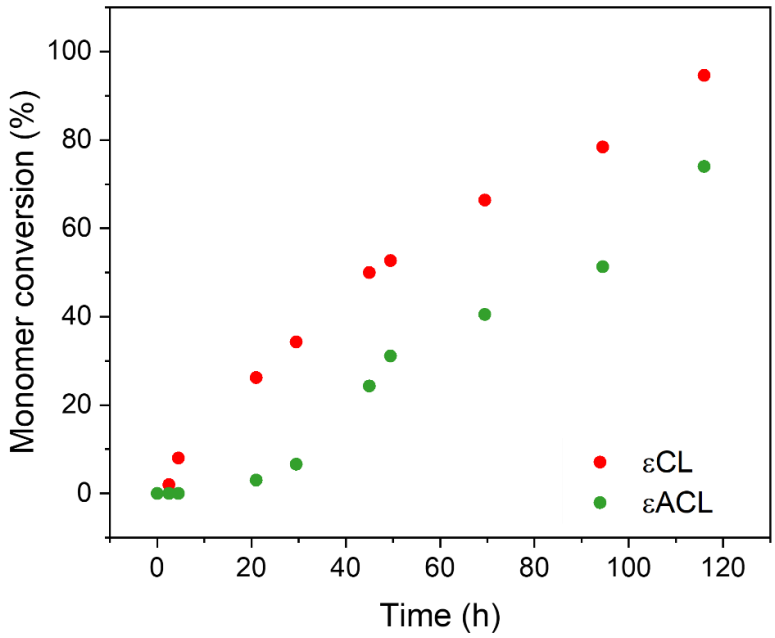


Figure 3.3. Kinetic plot of monomer conversion against time for the copolymerisation of εCL and εACL (**CP8** in Table 3.1). Conditions: overall monomer concentration ([M]) = 2 M in C_6D_6, [CL]:[ACL]:[CTA] = 50:50:1 using 2-cyano-5-hydroxypentan-2-yl ethyl carbonotrithioate (CHPET) as initiator, 10 mol% of DPP.

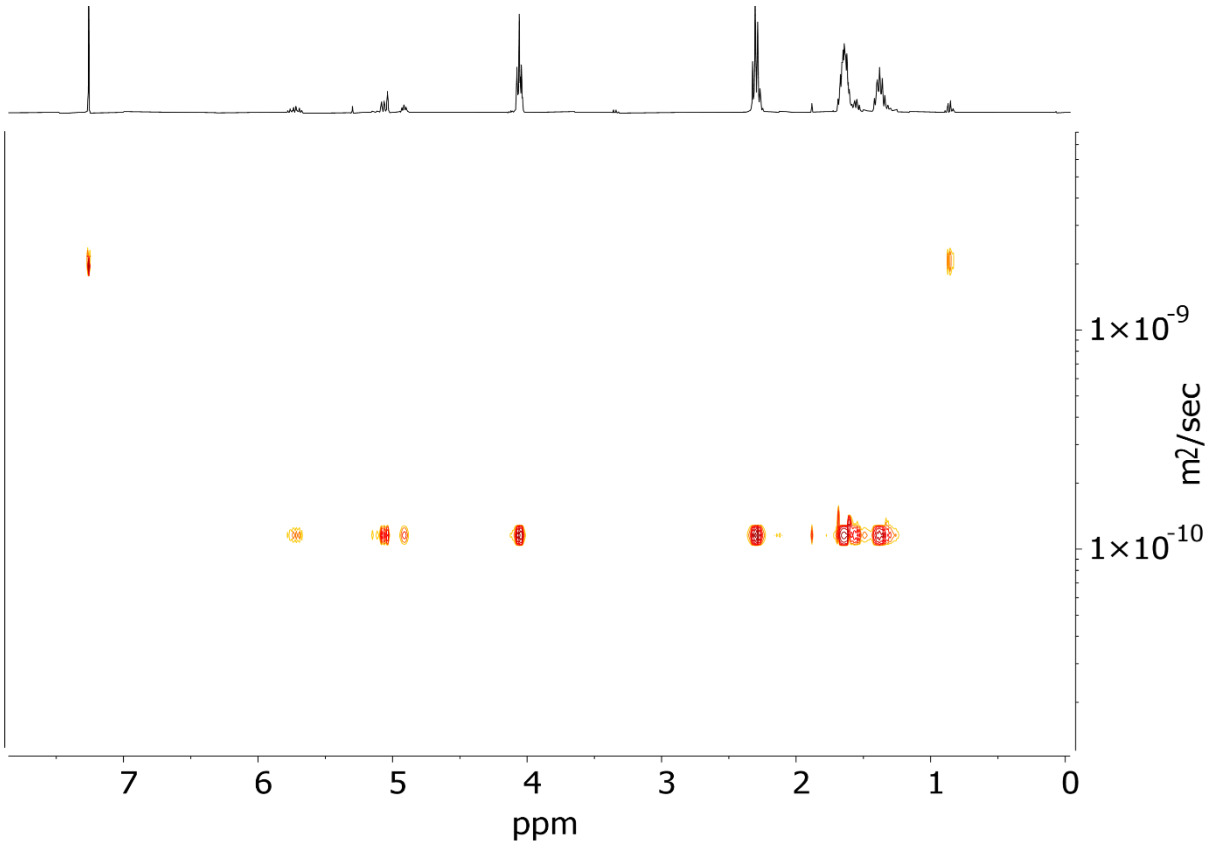


Figure *3.4.* DOSY ^{1}H NMR spectra (400 MHz, 298 K, $CDCl_3$) of PCL-*co*-PACL copolymer targeted at 50:50 (**CP8** in Table 3.1).

To elucidate the copolymer composition distribution, the monomer sequencing was investigated by quantitative ^{13}C NMR spectroscopy. For this, PCL_{54}-*co*-$PACL_7$ (**CP2**) and PCL_{108}-*co*-$PACL_{79}$ (**CP8**) copolymers were selected due to their different εACL molar ratios. Spectroscopy analyses showed two prominent carbonyl diad resonances at δ =173.6 ppm and δ =173.2 ppm corresponding to εCL*- εCL and εACL*- εACL, where * represents the observed carbonyl, in combination with other smaller diad resonances corresponding to monomer cross propagation (**Figure 3.5, S3.12 and S3.13**). This suggested the formation of statistical copolymers of different composition, in which the structure is determined by the statistical nature of the reactivity ratios, with predominant block-like distribution.

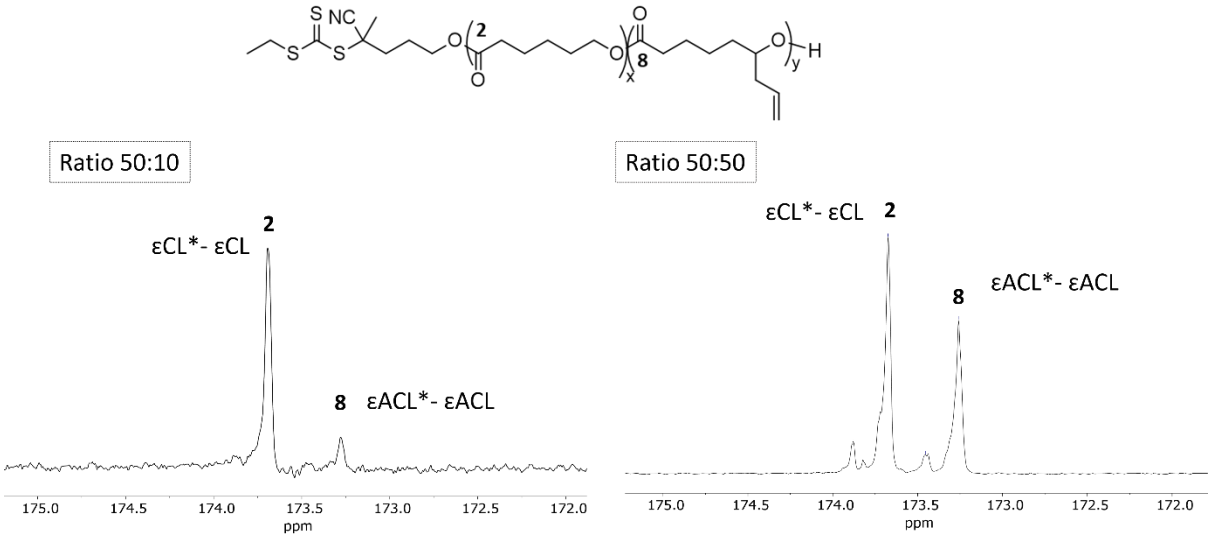


Figure 3.5. Quantitative ^{13}C NMR spectrum (500 MHz, 298 K, $CDCl_3$) corresponding to the carbonyl region of PCL-*co*-PACL copolymers targeted at 50:10 (left, **CP2** in Table 3.1) and 50:50 (right, **CP8** in Table 3.1).

3.2.3 Thermal properties of PCL-*co*-PACL copolymers

Following the synthesis of functional PCL-based copolymers, the effect of εACL concentration on their physical-chemical properties was investigated. It is well known that PCL is a semicrystalline polymer with low melting temperatures (T_m) ranging from 59 to 64 °C, and a low glass transition temperature (T_g) of approximately −60 °C.[63] On the other hand, poly(ε-ally-ε-caprolactone) (PACL) is an amorphous polymer that presents low T_g values (T < −53.8 °C), as reported in Chapter 2. Therefore, we envisaged that copolymers obtained from the ring opening copolymerisation (ROCOP) of εCL and εACL would present a wide range of transition temperatures, which could be adjusted by varying [εCL]:[εACL] ratio. The thermal properties of copolymers of different [εCL]:[εACL] composition were assessed by differential scanning calorimetry (DSC) (**Table 3.2** and **Figure 3.6**). As expected, amorphous and semicrystalline PCL-based copolymers were accessed, and this behaviour could be associated with the ratio of εACL within the polymer chain. While copolymers containing up to 26 wt.% of εACL (**CP1 to CP4,** Table 3.2) presented melting (T_m) and crystallisation (T_c) temperatures, only amorphous copolymers were obtained at higher concentrations of εACL (**CP6 to CP8,** Table 3.2). T_m and T_c decreased from 46.6 °C to 17.5 °C, and from 18 °C to −22.5 °C when the concentration of allyl units increased from 6 to 26 wt.%, respectively. At 30 wt.% εACL incorporation (**CP5** in Table 3.2) only the presence of T_g and a very small T_m could be appreciated in the DSC traces. This could be attributed to the disruption in the crystallinity of the copolymers at higher amounts of alkyl side chains. These analyses proved that through copolymerisation, semicrystalline allyl-functionalised polymers can be achieved, overcoming the major limitation encountered in substituted PCLs for their use in crystallisation-driven self-assembly.

Table 3.2. Thermal properties of PCL-*co*-PACL copolymers.

Entry	ACL units [a] (wt. %)	T_g [b] (°C)	T_m [b] (°C)	T_c [b] (°C)
CP1	6	-	46.6	18.0
CP2	11	-	40.9	−2.0
CP3	20	−64.7	28.9	−28.7
CP4	26	−66.3	17.5	−22.5[c]
CP5	30	−63.9	6.28	-
CP6	33	−62.2	-	-
CP7	36	−64.1	-	-
CP8	40	−61.4	-	-

[a] Calculated based on the PCL:PACL ratio observed by ^{1}H NMR spectrometry. [b] Measured by DSC in the second cycle (−100 to 100 °C, 10 °C min^{-1}). [c] Measured by DSC in the second heating cycle (−100 to 100 °C, 10 °C min^{-1}).

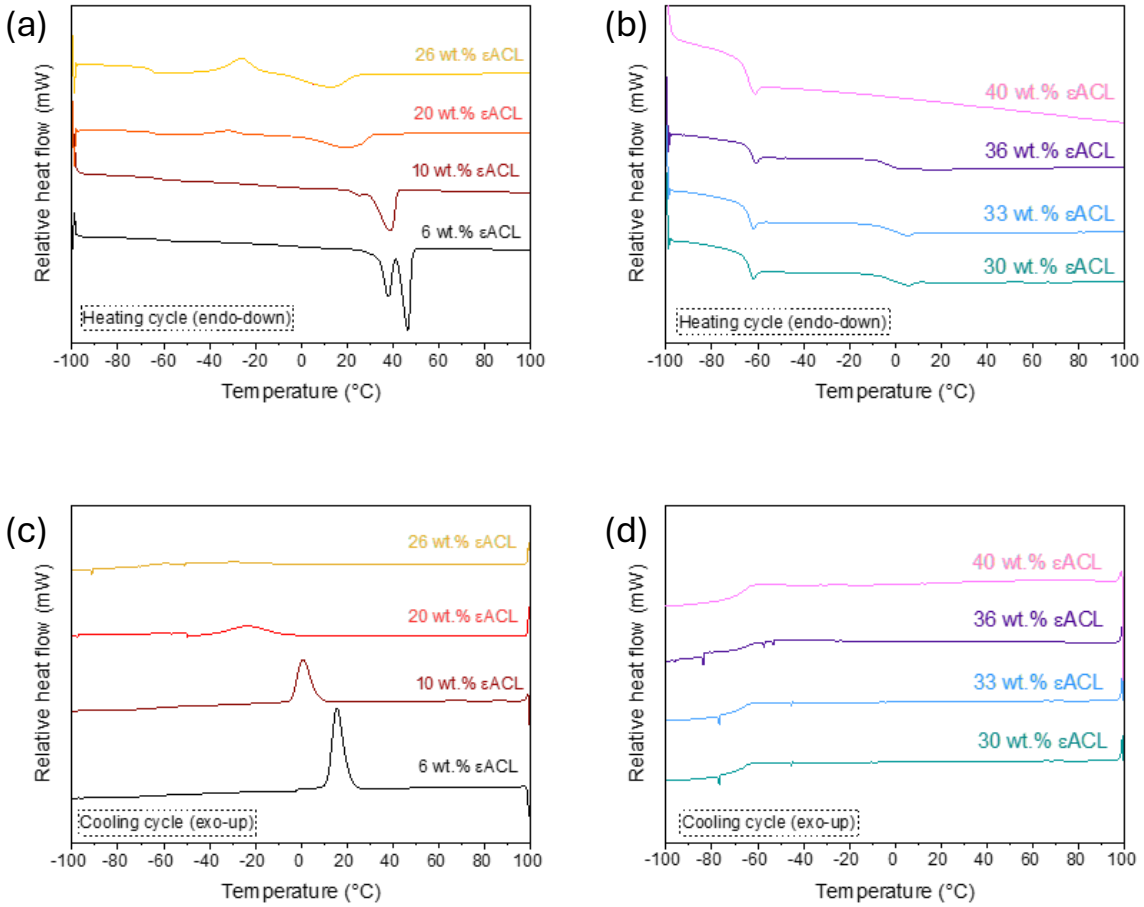


Figure 3.6. DSC thermograms of the PCL_x-*co*-$PACL_y$ copolymers (−100 to 100 °C, 10 °C min^{-1}) showing the second heating-cooling cycle. **(a)** and **(b)** correspond to the heating cycles (endothermic process). **(c)** and **(d)** correspond to the cooling cycles (exothermic process).

3.2.4 Scale-up ring-opening copolymerisation

After optimising the amount of εACL that could be copolymerised with εCL to obtain semicrystalline copolymers, a series of PCL_x-*co*-$PACL_y$ copolymers were synthesised in larger scale to be further used in post-polymerisation reactions. With the aim of mimicking the previous studies and maintain the crystalline behaviour of the final materials, copolymers of DP 50 were targeted and the concentration of εACL was varied between 5% and 26 wt.%, which showed to be the maximum limit of incorporation of allyl units before disrupting the polymer crystallinity (**Table 3.3**). All the other reaction conditions were kept unaltered, except for the solvent that was replaced by toluene.

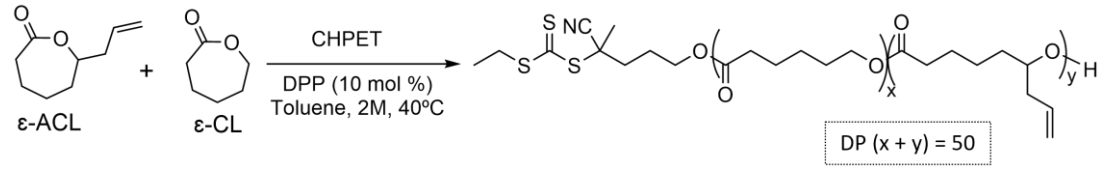


Table 3.3. Scaling-up of the copolymerisation of εACL and εCL.[a]

Entry	Targeted PCL:PACL ratio	Volume (mL) [b]	PCL:PACL ratio [c]	ACL units wt. % [d]	$M_{n,SEC}$ [e] (kDa)	$Đ_M$ [e]	T_m [f] (°C)	T_c [f] (°C)
CP9	45:5	**2.5**	47:3	6	11.6	1.28	42.8	16.8
CP10	40:10	2.5	44:8	15	11.9	1.21	36.4	−19.9
CP11	35:15	2.5	31:7	18	8.77	1.21	15.1	−30.6[g]
CP12	45:5	6	53:3	5	12.0	1.23	46.6	18.0
CP13	40:10	6	42:9	17	11.4	1.14	29.6	−15.9
CP14	45:5	10	56:5	8	10.6	1.41	45.8	13.2
CP15	40:10	10	43:8	15	6.23	1.58	31.9	−18.1
CP16	35:15	10	36:10	22	6.56	1.46	18.2	−19.7[g]

[a] Polymerisations were carried out in the glove box using toluene as a solvent with $[Monomers]_0:[Initiator]_0 = 50$ and [monomers] = 2 M, using CHPET as initiator and DPP as catalyst (10 mol%). [b] Total volume of toluene. [c] Calculated by ^{1}H NMR spectrometry. [d] Calculated based on the real PCL:PACL ratio. [e] Measured by SEC ($CHCl_3$ with 0.5% Et_3N, PMMA standards). [f] Measured by DSC in the second cycle (−100 to 100 °C, 10 °C min^{-1}). [g] Measured by DSC in the first heating cycle (−100 to 100 °C, 10 °C min^{-1}).

Initially, the scale was increased to 2.5 mL of solvent (5 mmol *vs.* 1 mmol of monomers) (**CP9 to CP11**). The successful syntheses of semicrystalline PCL-*co*-PACL block-like copolymers with increasing allyl content was confirmed by ^{1}H NMR spectroscopy, SEC, and DSC analyses (**Figure 3.7** and **Figure 3.8**). In agreement with the small-scale reactions performed previously (500 µL scale), the polymerisation of the allyl monomer took longer than caprolactone, and this caused deviations from the initially targeted DPs. Similarly to previous studies, higher $Đ_M$ was found for copolymers containing lower εACL content as a consequence of the differences

in the polymerisation rates of each monomer, which increases the chances of transesterification side reactions of PCL chains.

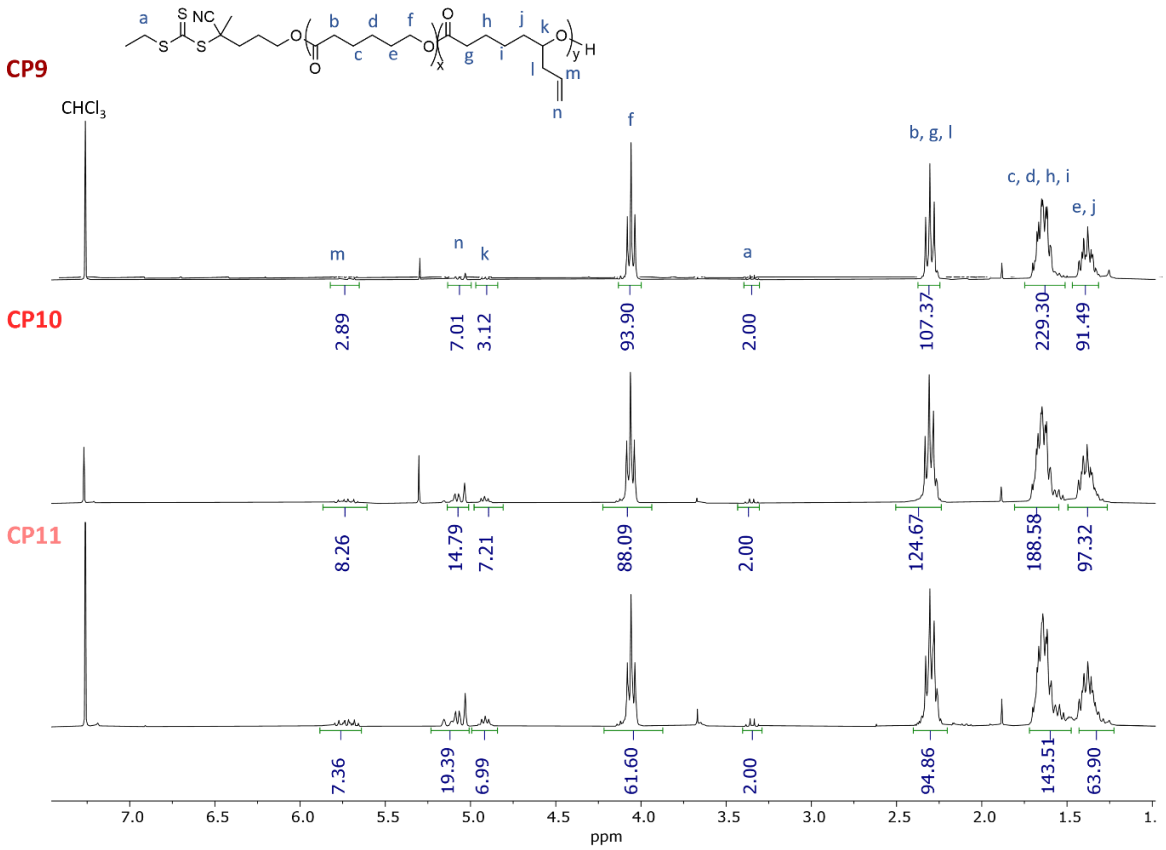


Figure 3.7. Stacked ^{1}H NMR spectra ($CDCl_3$, 300 MHz) of copolymers with 6 wt.%, 15 wt.% and 18 wt.% of εACL incorporation (entry **CP9, CP10** and **CP11** in Table 3.3).

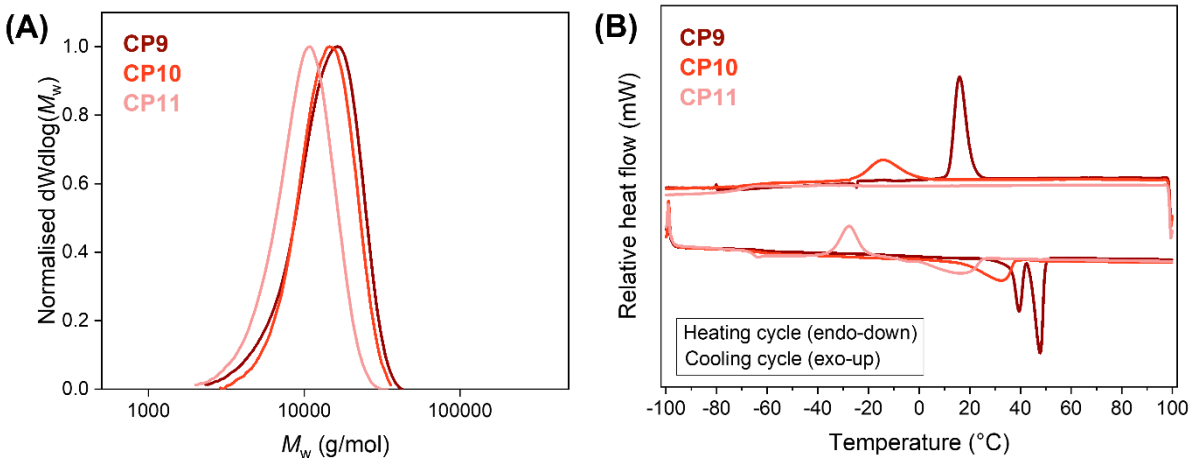


Figure 3.8. (A) SEC chromatograms of the PCL-*co*-PACL copolymers ($CHCl_3$, with 0.5% Et_3N, PMMA standard); **(B)** DSC thermograms of the respective copolymers (−100 to 100 °C, 10 °C min^{-1}) showing the second heating-cooling cycle (endo-down and exo-up).

To reduce batch-to-batch variations in future steps, ROCOP reactions were further scaled up to a final volume of 6 mL and 10 mL. While narrow dispersities ($Đ_M$) and predictable molecular weights (M_n) were achieved from copolymers synthesised at 6 mL scale (**CP12** an **CP13**), high polymer dispersity ($Đ_M$ > 1.4) was found when the reaction volume was increased to 10 mL (**CP14 to CP16**). This is possibly as consequence of inefficient stirring throughout the reaction caused by the volume increase and glassware incompatibilities. DSC analyses of all PCL-*co*-PACL copolymers obtained at larger scale showed the characteristic peaks corresponding to a semicrystalline polymer (**Figure S3.15**). However, the T_c of copolymers containing more ACL units (**CP11** and **CP16**) was only observed in the second heating cycle, indicating lower degree of crystallinity and slower crystallisation (**Figure S3.16**).

The self-assembly of copolymers *via* crystallisation-driven self-assembly (CDSA) requires high semicrystalline amphiphilic block copolymers with narrow dispersity to form structures with adjustable shape. For this reason, copolymers containing εACL units < 20% and a reaction volume of 6 mL were selected for further experiments.

3.3 Conclusions

To achieve semicrystalline functional PCL-based polymers, the copolymerisation of ε-caprolactone (εCL) and ε-allyl-ε-caprolactone (εACL) *via* ring-opening polymerisation was studied using DPP as a catalyst and a chain-transfer agent as an initiator. Initial studies for the homopolymerisations of εCL and εACL showed the excellent control and living nature of these polymerisations, in which the non-substituted lactone exhibited significantly faster polymerisation rates than its allyl-functional counterpart. The incorporation of allyl groups in the polymer backbone and the monomer sequencing of PCL copolymers was demonstrated through DOSY, ^{1}H and ^{13}C NMR spectroscopy. SEC analyses confirmed the synthesis of copolymers with monomodal distributions and narrow dispersities, supporting the synthesis of PCL-*co*-PACL gradient copolymers rather than two individual homopolymers. The thermal properties of the obtained copolymers were analysed by DSC, where a decrease in the polymer crystallinity was observed by increasing the allyl monomer concentration in the formulation. Indeed, concentrations higher than 26 wt.% of ACL only resulted in amorphous polymers with low glass transition temperatures. The ring opening copolymerisation was also investigated in different batches and scales to check the variability in the system, and results showed the potential to scale up the reactions from 1 mmol to 20 mmol of monomer addition.

3.4 Experimental

3.4.1 Materials

All solvents and chemicals were purchased from Sigma-Aldrich, Fisher Scientific, Alfa Aesar, or VWR International and used without further purification unless otherwise stated. Dry toluene was used from a solvent tower delivery system in the glovebox. Deuterated benzene was ordered from Apollo Scientific, degassed by repeated freeze-pump-thawing and then dried under reflux over sodium and benzophenone before storing under an inert atmosphere of N_2. Amberlyst A21 free base was washed repeatedly with methanol and dried under reduced pressure prior to use. The monomers ε-caprolactone and ε-allyl- ε-caprolactone were dried over calcium hydride for three days and distilled under reduced pressure before their storage under inert atmosphere of N_2 in a glove box. The chain transfer agent 2-cyano-5-hydroxypentan-2-yl ethyl carbonotrithioate (CHPET) was dried for five days over phosphorus pentoxide under vacuum before its introduction in a glove box.

3.4.2 Characterisation techniques

3.4.2.1 Glove box

Air-free work was conducted in the nitrogen atmosphere of an Mbraun MB Unilab Pro SP or Mbraun MB-01 equipped with solvent filter.

3.4.2.2 Nuclear magnetic resonance (NMR) spectroscopy

Diffusion-ordered spectroscopy (DOSY), proton (^{1}H) and carbon (^{13}C) resonance spectra were recorded on a Bruker 101 MHz, 300 MHZ, or 500 MHz spectrometers at 298 K. Chemical shifts were reported as δ in parts per million (ppm) and referenced to the residual solvent signals ($CDCl_3$, ^{1}H: δ = 7.26 ppm, ^{13}C: δ = 77.16 ppm). The multiplicities were reported as s = singlet,

d = doublet, dd = doublet in doublet, ddt = double of doublet of triplet, t = triplet, tdd = triplets of doublet of doublets, q = quadruplet, p = pentaplet and m = multiplet. The coupling constant *J* was recorded in Hertz (Hz). The obtained data were processed and analysed using MestReNova 12.0.3 software.

3.4.2.3 Size exclusion chromatography (SEC)

SEC analyses were performed on an Agilent 1260 Infinity II Multi-Detector GPC/SEC System fitted with RI and ultraviolet (UV, λ = 309 nm), and viscosimeter detectors. The instrument is equipped with an Agilent guard column PLGel 3 µm (50 × 7.5 mm) and two Agilent mixed-C columns PLGel 5 µm (300 × 7.5 mm) using $CHCl_3$ (buffered 0.5% Et_3N) as the mobile phase (eluent). Number average molecular weights (M_n), weight average molecular weights (M_w) and dispersities ($Đ_M = M_w/M_n$) were determined using Agilent GPC/SEC software (vA.02.01) against a 15-point calibration curve (M_p = 162 – 3,187,000 g mol^{-1}) based on poly(styrene) standards or a 12-point calibration curve (M_p = 550 – 2,210,000 g mol^{-1}) based on poly(methyl methacrylate) standards. Molecular weights (M_n), weight average molecular weights (M_w) are given in (g mol^{-1}).

3.4.2.4 Differential scanning calorimeter (DSC)

Determination of the DSC curves were carried out using a STARe system DSC3 with auto-sampler (Mettler Toledo). The samples (1 – 10 mg of polymer) were placed into aluminium pans measuring 5 mm in diameter and 0.4 – 0.6 mm in thickness. Thermograms obtained with a heating rate of 10 °C min^{-1} were recorded from −100 to 100 °C with a 10 °C min^{-1} heating and cooling rate over two cycles.

3.4.3 Experimental procedures

3.4.3.1 Synthesis of 2-cyano-5-hydroxypentan-2-yl ethyl carbonotrithioate (CHPET)

Refer to Chapter 2, Section 2.2.1.9 for the synthetic protocols and characterisation.

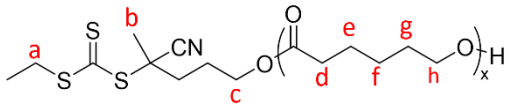
3.4.3.2 Synthesis of ε-allyl-ε-caprolactone (εACL)

Refer to Chapter 2, Section 2.2.1.12 for the synthetic protocols and characterisation.

3.4.3.3 Synthesis of poly(ε-caprolactone) (PCL) and poly(ε-allyl-ε-caprolactone (PACL) homopolymers – General procedure for the ring-opening polymerisation (ROP)

Using standard glovebox techniques, a solution of DPP (0.006 mmol, 1 equiv.) was added to a solution of the monomer (ε-caprolactone or ε-allyl-ε-caprolactone) (0.6 mmol, 100 equiv.) and 2-cyano-5-hydroxypentan-2-yl ethyl carbonotrithioate (CHPET) (0.006 mmol, 1 equiv.) in dry deuterated benzene (0.6 mL). The mixtures were placed into a J Young NMR tube, removed from the glove box and placed in an oil bath at 40 °C. After reaching the desired monomer conversion, the reaction was quenched outside the glovebox with the addition of Amberlyst A21. After the removal of Amberlyst through filtration, the solution was precipitated two times into cold *n*-hexanes and dried under vacuum to afford the polymers as a yellow solid (PCL) and a yellow oil (PACL).

- ***Poly(ε-caprolactone) (PCL)***



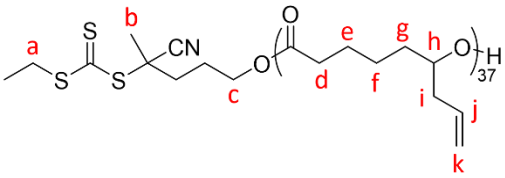
Procedure adapted from literature.[64]

^{1}H NMR (300 MHz, $CDCl_3$, 298 K): δ/ppm= 4.06 (t, J = 6.7 Hz, 97H, H^h), 3.64 (t, J = 6.5 Hz, 2H, H^c), 3.35 (d, J = 7.4 Hz, 2H, H^a), 2.30 (t, J = 7.5 Hz, 99H, H^d), 1.88 (s, 3H, H^c), 1.78 – 1.53 (m, 216H, H^e and H^g), 1.49 – 1.26 (m, 104H, H^f).

^{13}C NMR (126 MHz, $CDCl_3$, 298 K) δ/ppm= (101 MHz, $CDCl_3$, 298 K) δ/ppm= 173.66 (O(*C*=O)), 64.26 (C^h), 62.70 (C^c), 35.82 (*C*(CN)(CH_3)CH_2CH_2), 34.34 (C^d), 32.42 (C(CN)(CH_3)*C*H_2CH_2), 31.43 (C^a), 28.45 (C^g), 25.64 (C^e), 25.41 (C(CN)(CH_3)CH_2*C*H_2), 24.96 (C^b), 24.79 (C^f), 12.88 (SCH_2*C*H_3).

SEC ($CHCl_3$): M_n = 13.3 kDa, $Đ_M$ = 1.08

- ***Poly(ε-allyl-ε-caprolactone) (PACL)***



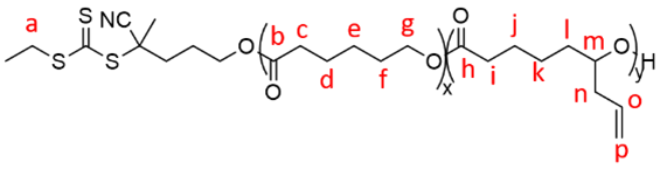
Procedure adapted from literature.[23]

^{1}H NMR (300 MHz, $CDCl_3$, 298 K): δ/ppm= 5.72 (ddt, J = 16.5, 10.5, 7.1 Hz, 38H, H^j), 5.12 – 5.00 (m, 78H, H^k), 4.90 (p, J = 6.2 Hz, 36H, H^h), 4.11 (t, J = 6.1 Hz, 2H, H^c), 3.35 (d, J = 7.4 Hz, 2H, H^a), 2.39 – 2.18 (m, 152H, H^d and H^i), 1.88 (s, 3H, H^b), 1.57 (tdd, J = 15.4, 10.8, 7.0 Hz, 163H, H^e and H^g), 1.44 – 1.16 (m, 101H, H^f).

^{13}C NMR (126 MHz, $CDCl_3$, 298 K) δ/ppm= 173.25 (O(*C*=O)), 133.80 (C^i), 117.87 (C^j), 73.39 (C^g), 38.74 (C^h), 35.14 (C^e), 32.81 (C^c), 24.65 (C^d and C^f).

SEC ($CHCl_3$): M_n = 9.5 kDa, $Đ_M$ = 1.11

3.4.3.4 Synthesis of PCL-*co*-PACL copolymers – General procedure for the ring-opening copolymerisation (ROCOP) of ε-caprolactone (εCL) and ε-allyl-ε-caprolactone (εACL).



Procedure adapted from literature.[59] Using standard glovebox techniques, a solution of DPP (0.1 mmol, 1 equiv.) and 2-cyano-5-hydroxypentan-2-yl ethyl carbonotrithioate (CHPET) (0.1 mmol, 1 equiv.) in dry benzene (0.6 mL) or dry toluene (2.5 – 10 mL) was added to a solution of ε-caprolactone (4.5 mmol/45 equiv. for 10 wt.% of εACL,4 mmol/40 equiv. for 20 wt.% of εACL , and 3.5 mmol/35 equiv. for 30 wt.% εACL) and ε-allyl-ε-caprolactone (0.5 mmol/5 equiv., 1 mmol/10 equiv.,and 1.5 mmol/15 equiv. for 10%, 20% and 30 wt.% of εACL, respectively) in dry benzene or dry toluene. The J Young NMR tubes or the ampoules were then removed from the glove box and placed in an oil bath at 40 °C. After stirring for a certain time (depending on the amount of εACL), the reaction was quenched by the addition of Amberlyst A21. After removal of Amberlyst by filtration, the solution was precipitated three times into cold *n*-hexane and dried under vacuum to afford the polymers as a yellow solid.

^{1}H NMR (300 MHz, $CDCl_3$): δ/ppm= 5.73 (ddt, J = 17.4, 10.4, 7.1 Hz, 1H, H^{o}), 5.13 – 4.99 (m, 2H, H^{p}), 4.91 (p, J = 6.2 Hz, 1H, H^{m}), 4.06 (t, J = 6.7 Hz, 2H, H^{g}), 3.35 (q, J = 7.4 Hz, 2H, H^{a}), 2.30 (t, J = 7.5 Hz, 6H, $H^{c, i, n}$), 1.74 – 1.51 (m, 8H, $H^{d, e, j, k}$), 1.46 – 1.31 (m, 4H, $H^{f, l}$).

^{13}C NMR (126 MHz, $CDCl_3$) δ/ppm= 173.69 (C^{b}, εCL*- εCL), 173.28 (C^{h}, εACL*- εACL), 133.80 (C^{o}), 117.86 (C^{p}), 72.99 (C^{m}), 64.29 (C^{g}), 38.76 (C^{n}), 34.53(C^{l}), 34.26 (C^{c}), 33.39 (C^{i}), 28.50 (C^{f}), 25.67 (C^{e}), 25.04 (C^{j}), 24.89 (C^{k}), 24.72 (C^{d}).

SEC ($CHCl_3$):

Copolymer	M_n (kDa)	$Đ_M$	Copolymer	M_n (kDa)	$Đ_M$
PCL_{56}-*co*-$PACL_4$	12.2	1.45	**PCL_{44}-*co*-$PACL_8$**	11.6	1.28
PCL_{54}-*co*-$PACL_7$	16.6	1.27	**PCL_{31}-*co*-$PACL_7$**	11.9	1.21
PCL_{60}-*co*-$PACL_{15}$	17.1	1.18	**PCL_{56}-*co*-$PACL_4$**	8.7	1.21
PCL_{35}-*co*-$PACL_{20}$	17.1	1.14	**PCL_{53}-*co*-$PACL_3$**	12.0	1.23
PCL_{46}-*co*-$PACL_{20}$	14.6	1.15	**PCL_{42}-*co*-$PACL_9$**	11.4	1.14
PCL_{48}-*co*-$PACL_{24}$	16.3	1.10	**PCL_{56}-*co*-$PACL_5$**	10.6	1.41
PCL_{62}-*co*-$PACL_{36}$	16.6	1.20	**PCL_{43}-*co*-$PACL_8$**	6.2	1.58
PCL_{47}-*co*-$PACL_3$	21.3	1.09	**PCL_{36}-*co*-$PACL_{10}$**	6.6	1.46

Polymer conversion (% conv.) was calculated using the following equation, where [M] and [P] correspond to the proton integrations of the monomer peak and polymer peak, respectively.

$$\%\ conv. = 1\ -\ \left(\frac{[M]}{[M]+[P]}\right) \times 100$$

Equation 3.1. % Polymer conversion.

To analyse the conversion of εCL, [M] correspond to the integration of the diagnostic O=COCH monomer resonance at δ_{CL} = 3.61 ppm and [P] correspond to the integration of the diagnostic O=COCH polymer resonance at δ_{PCL} = 3.93 ppm. Whereas, to analyse the conversion of εACL, [M] correspond to the integration of the diagnostic O=COCH monomer resonance at δ_{ACL} = 3.75 ppm and [M+P] correspond to the integration of the CHCH_2 terminal alkene resonance from both monomer and polymer at δ_{PACL} = 5.1 – 4.9 ppm.

3.5 References

1. A. Saumer and S. Mecking, *ACS Sustain. Chem. Eng.*, 2023, **11**, 12414-12422.
2. Z. Zhou, A. M. Lapointe, T. D. Shaffer and G. W. Coates, *Nat Chem*, 2023, **15**, 856-861.
3. L. Cederholm, J. Wohlert, P. Olsén, M. Hakkarainen and K. Odelius, *Angew. Chem. Int. Ed.*, 2022, **61**.
4. Y. He, J.-C. Eloi, R. L. Harniman, R. M. Richardson, G. R. Whittell, R. T. Mathers, A. P. Dove, R. K. O'Reilly and I. Manners, *J. Am. Chem. Soc*, 2019, **141**, 19088-19098.
5. T. K. Dash and V. B. Konkimalla, *Mol. Pharm.*, 2012, **9**, 2365-2379.
6. O. Gil-Castell, I. Ontoria-Oviedo, J. D. Badia, E. Amaro-Prellezo, P. Sepúlveda and A. Ribes-Greus, *React Funct Polym*, 2022, **170**, 105064.
7. J. H. Park, H. J. Park, S. J. Tucker, S. K. Rutledge, L. Wang, M. E. Davis and S. J. Hollister, *Adv. Funct. Mater.*, 2023, **33**, 2215220.
8. E. Martin, P. Dubois and R. Jérôme, *Macromol.*, 2003, **36**, 7094-7099.
9. Z. Florjańczyk, A. Plichta and M. Sobczak, *Polymer*, 2006, **47**, 1081-1090.
10. A. J. Chmura, M. G. Davidson, M. D. Jones, M. D. Lunn and M. F. Mahon, *Dalton Trans.*, 2006, DOI: 10.1039/b513345a, 887-889.
11. H.-J. Fang, P.-S. Lai, J.-Y. Chen, S. C. N. Hsu, W.-D. Peng, S.-W. Ou, Y.-C. Lai, Y.-J. Chen, H. Chung, Y. Chen, T.-C. Huang, B.-S. Wu and H.-Y. Chen, *J. Polym. Sci., Part A: Polym. Chem.*, 2012, **50**, 2697-2704.
12. L. Liao, L. Liu, C. Zhang and S. Gong, *Macromol. Rapid Commun.*, 2006, **27**, 2060-2064.
13. A. P. Dove, *ACS Macro Lett.*, 2012, **1**, 1409-1412.
14. C. Chen, R. Xu and B. Li, *Sci. China Chem.*, 2012, **55**, 1257-1262.
15. D. C. Batiste, M. S. Meyersohn, A. Watts and M. A. Hillmyer, *Macromol.*, 2020, **53**, 1795-1808.
16. A. Kumar and R. A. Gross, *Biomacromolecules*, 2000, **1**, 133-138.
17. Y. Hu, Y. Zhang, W. Xu, J. Xu, X. Lin and Q. Wu, *ACS Macro Lett.*, 2019, **8**, 1432-1436.
18. J. A. Wilson, S. A. Hopkins, P. M. Wright and A. P. Dove, *Macromol.*, 2015, **48**, 950-958.
19. N. Inverardi, M. Toselli, G. Scalet, M. Messori, F. Auricchio and S. Pandini, *Macromol.*, 2022, **55**, 8533-8547.
20. Q. Liu, S. Yuan, Y. Guo, A. Narayanan, C. Peng, S. Wang, T. Miyoshi and A. Joy, *Polym. Chem.*, 2019, **10**, 2579-2588.
21. B. D. Ulery, L. S. Nair and C. T. Laurencin, *J. Polym. Sci., Part B: Polym. Phys.*, 2011, **49**, 832-864.
22. T. C. Boire, M. K. Gupta, A. L. Zachman, S. H. Lee, D. A. Balikov, K. Kim, L. M. Bellan and H.-J. Sung, *Acta Biomater.*, 2015, **24**, 53-63.
23. C. Clamor, B. N. Cattoz, P. M. Wright, R. K. O'Reilly and A. P. Dove, *Polym. Chem.*, 2021, **12**, 1983-1990.
24. C. Lv, R. Yang, G. Xu, L. Zhou and Q. Wang, *Eur. Polym. J.*, 2020, **133**, 109792.

25. G. Ramos-Durán, A. D. C. González-Zarate, F. J. Enríquez-Medrano, M. Salinas-Hernández, M. A. De Jesús-Téllez, R. Díaz De León and H. R. López-González, *RSC Adv.*, 2022, **12**, 18154-18163.
26. W. Chen, H. Yang, R. Wang, R. Cheng, F. Meng, W. Wei and Z. Zhong, *Macromol.*, 2010, **43**, 201-207.
27. A. Galperin, T. J. Long, S. Garty and B. D. Ratner, *J. Biomed. Mater. Res. A*, 2013, **101A**, 775-786.
28. A. V. Bay, E. J. Farnam and K. A. Scheidt, *J. Am. Chem. Soc*, 2022, DOI: 10.1021/jacs.1c13105.
29. G. J. ten Brink, I. W. C. E. Arends and R. A. Sheldon, *Chem. Rev.*, 2004, **104**, 4105-4124.
30. D. Mecerreyes, R. D. Miller, J. L. Hedrick, C. Detrembleur and R. Jerome, *J. Polym. Sci., Part A: Polym. Chem.*, 2000, **38**, 870-875.
31. C. Feng, Y. Li, D. Yang, J. Hu, X. Zhang and X. Huang, *Chem. Soc. Rev.*, 2011, **40**, 1282-1295.
32. H. Jiang and F.-J. Xu, *Chem Soc Rev*, 2013, **42**, 3394.
33. N. Nomura, A. Akita, R. Ishii and M. Mizuno, *J. Am. Chem. Soc*, 2010, **132**, 1750-1751.
34. T. Fuoco and A. Finne-Wistrand, *Biomacromolecules*, 2019, **20**, 3171-3180.
35. H. Wang, C. V. Synatschke, A. Raup, V. Jérôme, R. Freitag and S. Agarwal, *Polym. Chem.*, 2014, **5**, 2453.
36. M. A. Childs, D. D. Matlock, J. R. Dorgan and T. R. Ohno, *Biomacromolecules*, 2001, **2**, 526-537.
37. T. Rosen, I. Goldberg, W. Navarra, V. Venditto and M. Kol, *Angew. Chem. Int. Ed.*, 2018, **57**, 7191-7195.
38. D.-K. Kweon, D.-S. Cha, H.-J. Park and S.-T. Lim, *J. Appl. Polym. Sci.*, 2000, **78**, 986-993.
39. M. Labet and W. Thielemans, *Polym. Chem.*, 2012, **3**, 679.
40. W. Chen, Y. Zou, F. Meng, R. Cheng, C. Deng, J. Feijen and Z. Zhong, *Biomacromolecules*, 2014, **15**, 900-907.
41. J. Fernández, A. Etxeberria and J.-R. Sarasua, *Eur. Polym. J.*, 2015, **71**, 585-595.
42. S. C. Lee, S. W. Kang, C. Kim, I. C. Kwon and S. Y. Jeong, *Polymer*, 2000, **41**, 7091-7097.
43. F. J. Xu, Z. H. Wang and W. T. Yang, *Biomater.*, 2010, **31**, 3139-3147.
44. S. Lenoir, R. Riva, X. Lou, C. Detrembleur, R. Jérôme and P. Lecomte, *Macromol.*, 2004, **37**, 4055-4061.
45. P. Bexis, A. W. Thomas, C. A. Bell and A. P. Dove, *Polym. Chem.*, 2016, **7**, 7126-7134.
46. J. Winninger, D. M. Iurea, L. I. Atanase, S. Salhi, C. Delaite and G. Riess, *Eur. Polym. J.*, 2019, **119**, 74-82.
47. X. Zhang, L. Zhao, J. Yang and J. Yang, *RSC Adv.*, 2016, **6**, 21486-21496.
48. R. M. Arnold, D. L. Patton, V. V. Popik and J. Locklin, *Acc. Chem. Res.*, 2014, **47**, 2999-3008.
49. R. M. Arnold, N. E. Huddleston and J. Locklin, *J. Mater. Chem.*, 2012, **22**, 19357.
50. B. Pektas, G. Sagdic, O. Daglar, S. Luleburgaz, U. S. Gunay, G. Hizal, U. Tunca and H. Durmaz, *Polymer*, 2022, **253**, 124989.

51. A. K. Williams, J. Tropp, E. R. Crater, N. Eedugurala and J. D. Azoulay, *ACS Appl. Polym. Mater.*, 2019, **1**, 309-314.
52. L. M. Campos, K. L. Killops, R. Sakai, J. M. J. Paulusse, D. Damiron, E. Drockenmuller, B. W. Messmore and C. J. Hawker, *Macromol.*, 2008, **41**, 7063-7070.
53. N. Francini, L. Purdie, C. Alexander, G. Mantovani and S. G. Spain, *Macromol.*, 2015, **48**, 2857-2863.
54. T. T. Truong, S. H. Thai, H. T. Nguyen, V.-D. Vuong and L.-T. T. Nguyen, *J. Polym. Sci., Part A: Polym. Chem.*, 2017, **55**, 928-939.
55. J. C. Worch, C. J. Stubbs, M. J. Price and A. P. Dove, *Chem. Rev.*, 2021, **121**, 6744-6776.
56. D. Funes-Hernando, P. Hermosilla, E. Vispe, A. Di Giuseppe, R. Castarlenas, L. A. Oro and J. J. Pérez-Torrente, *Polym. Chem.*, 2018, **9**, 1298-1302.
57. S. Agar, E. Baysak, G. Hizal, U. Tunca and H. Durmaz, *J. Polym. Sci., Part A: Polym. Chem.*, 2018, **56**, 1181-1198.
58. Y. Dai, Z. Hu, X. Wang, X. Liu, Y. Li, Y. Shi and Y. Chen, *Polym. Chem.*, 2021, **12**, 2592-2597.
59. E. A. Silantyeva, R. K. Willits and M. L. Becker, *Biomacromolecules*, 2019, **20**, 4494-4501.
60. V. Hardouin Duparc, R. M. Shakaroun, M. Slawinski, J.-F. Carpentier and S. M. Guillaume, *Eur. Polym. J.*, 2020, **134**, 109858.
61. M. M. Alam, K. S. Jack, D. J. T. Hill, A. K. Whittaker and H. Peng, *Eur. Polym. J.*, 2019, **116**, 394-414.
62. J. A. Wilson, S. A. Hopkins, P. M. Wright and A. P. Dove, *ACS Macro Lett.*, 2016, **5**, 346-350.
63. R. Dwivedi, S. Kumar, R. Pandey, A. Mahajan, D. Nandana, D. S. Katti and D. Mehrotra, *J Oral Biol Craniofac Res*, 2020, **10**, 381-388.
64. M. C. Arno, M. Inam, Z. Coe, G. Cambridge, L. J. Macdougall, R. Keogh, A. P. Dove and R. K. O'Reilly, *J. Am. Chem. Soc*, 2017, **139**, 16980-16985.

3.6 Appendix (supporting figures)

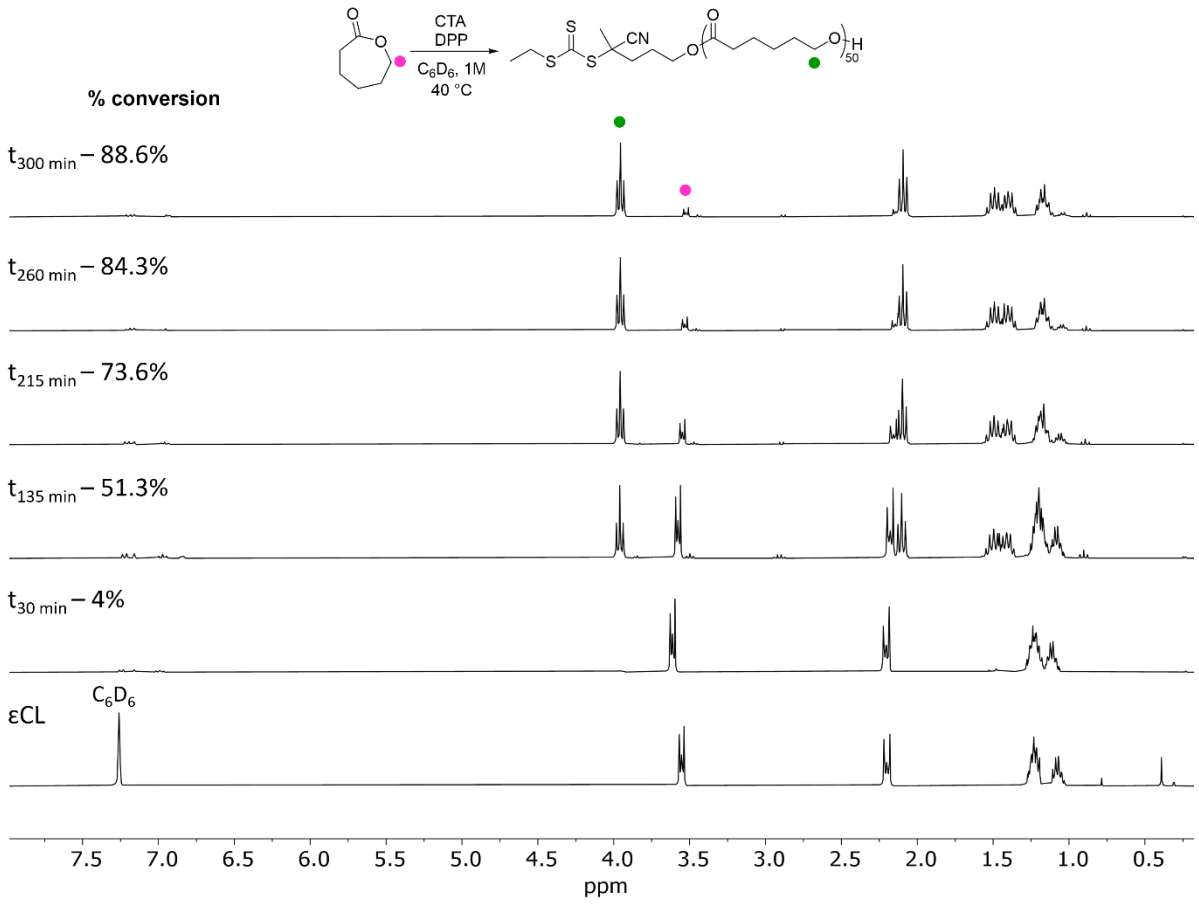


Figure S3.1. Kinetic studies for the polymerisation of ε-caprolactone (εCL) catalysed by DPP at 40 °C. Stacked ^{1}H NMR spectra (300 MHz, 298 K, C_6D_6) of εCL homopolymerisation at different reaction times with pink and green circle representing monomer and polymer peaks, respectively.

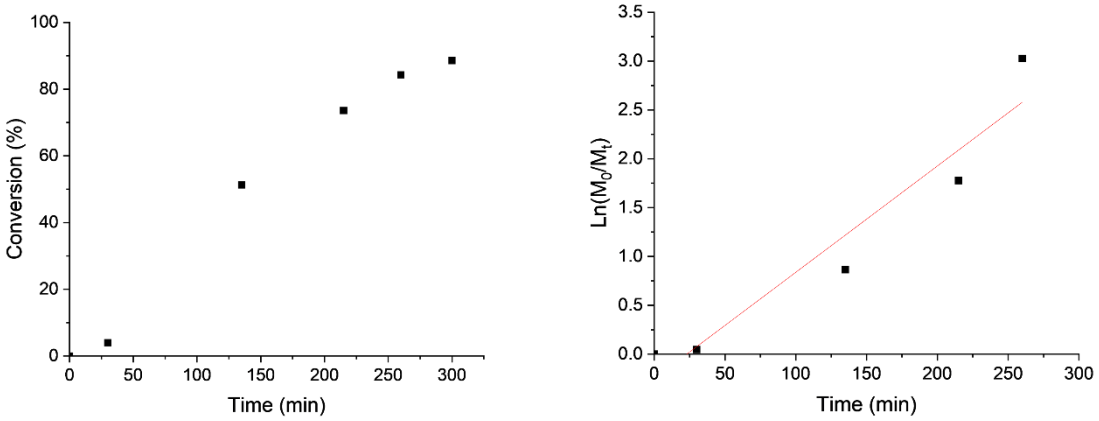


Figure S3.2. Kinetic plots for the homopolymerisation of εCL. Polymer conversion over time (left) and monomer consumption (right).

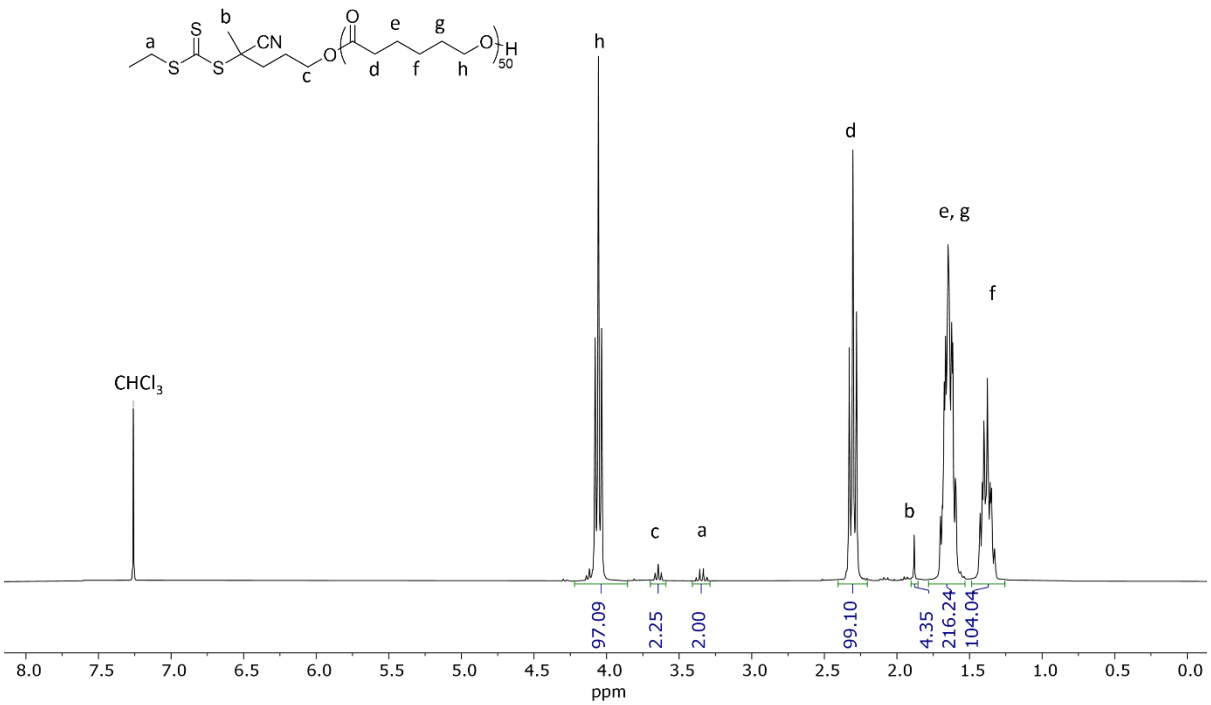


Figure S3.3. ^{1}H NMR spectrum (300 MHz, 298 K, $CDCl_3$) of poly(ε-caprolactone) (PCL).

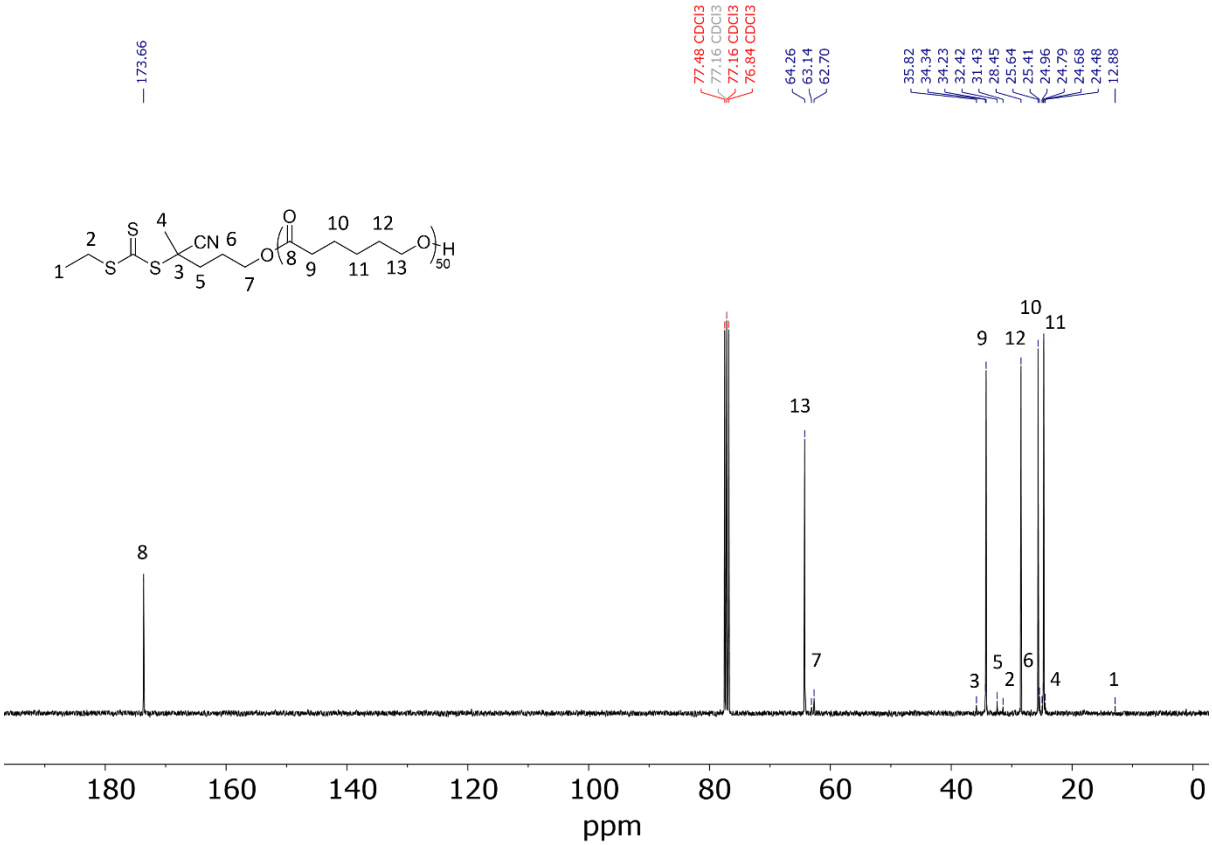


Figure S 3.4. ^{13}C NMR (101 MHz, 298 K, $CDCl_3$) spectrum of poly(ε-caprolactone) (PCL).

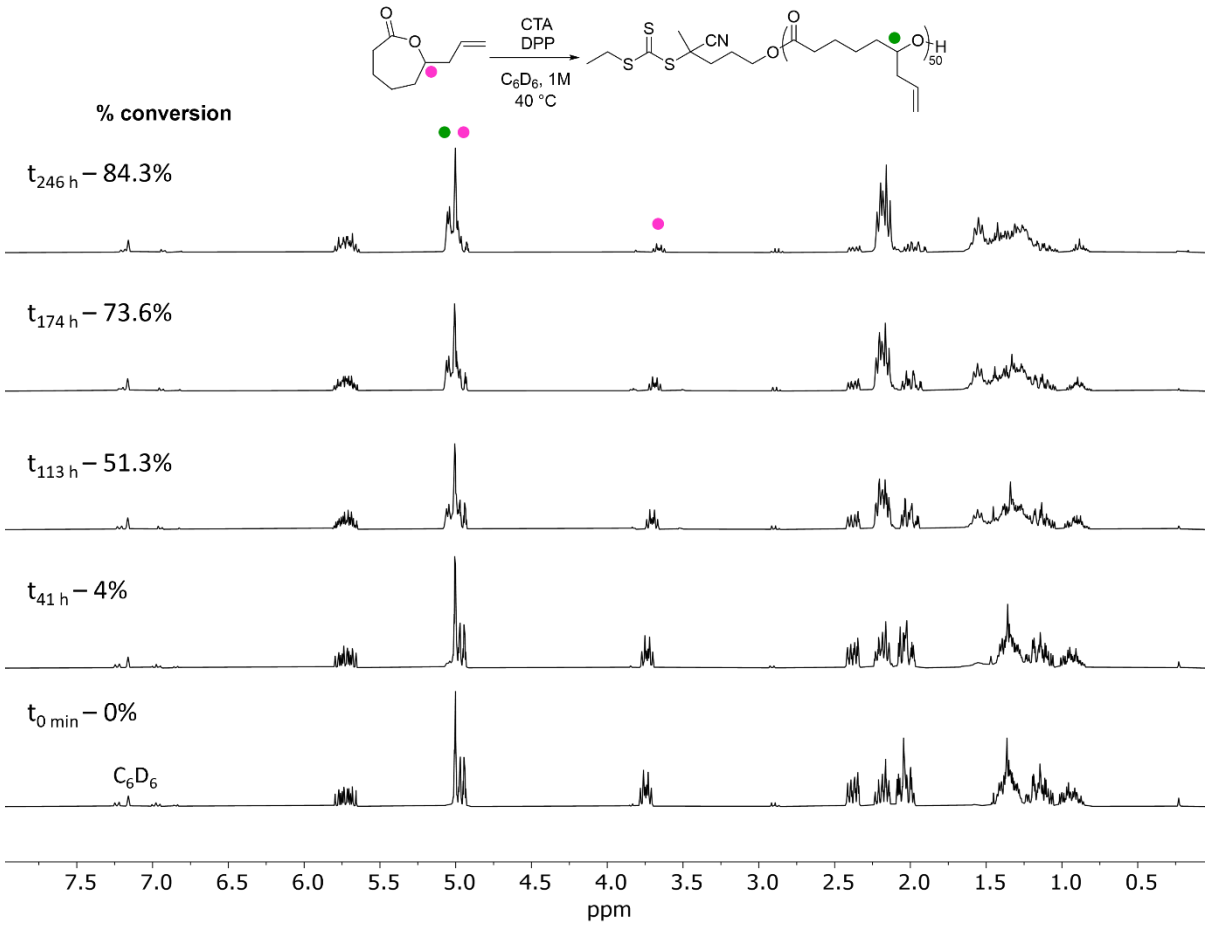


Figure S3.5. Kinetic studies for the polymerisation of εACL catalysed by DPP at 40 °C. Stacked ^{1}H NMR spectra (300 MHz, 298 K, C_6D_6) of εACL homo-polymerisation at different reaction times with pink and green circle representing monomer and polymer peaks, respectively.

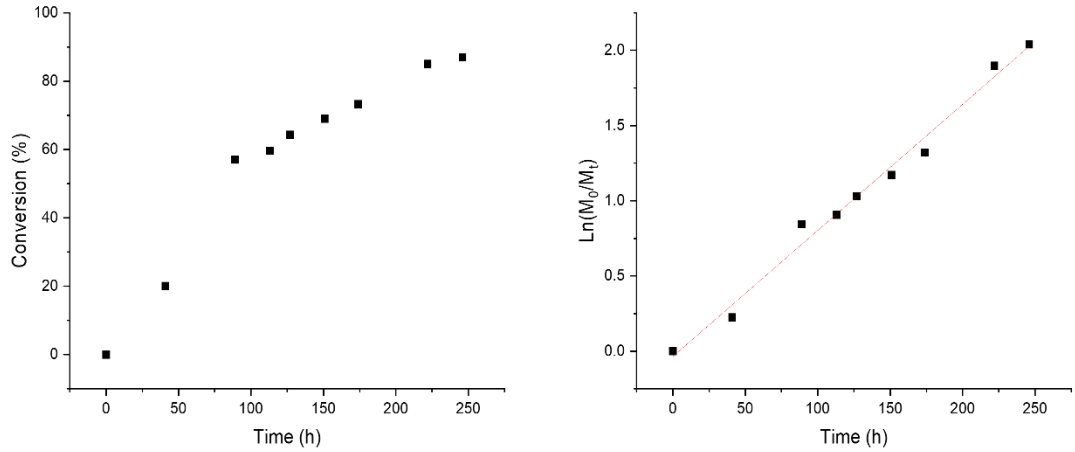


Figure S3.6. Kinetic plots for the homo-polymerisation of εACL. Polymer conversion over time (left) and monomer consumption (right).

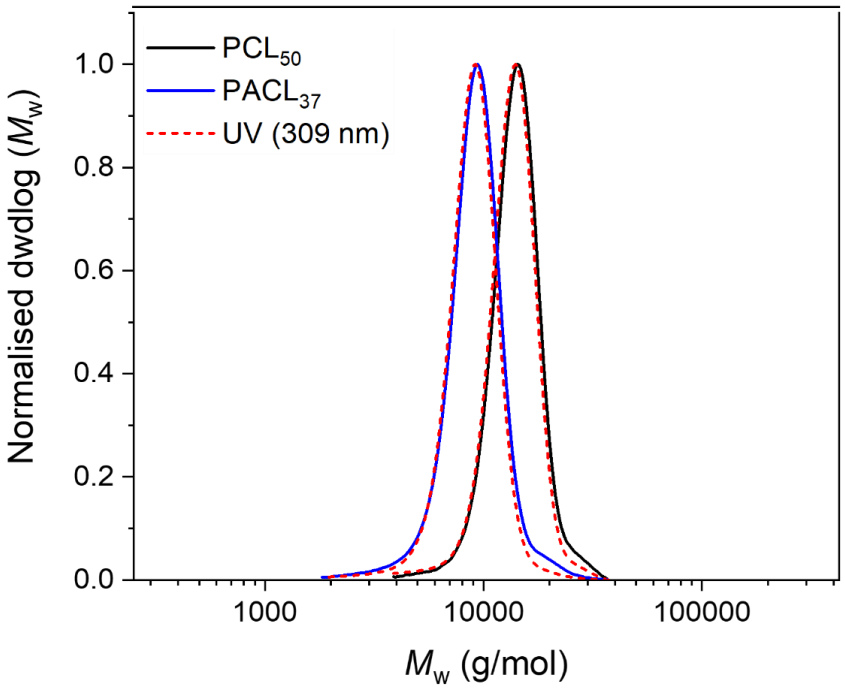


Figure S3.7. SEC chromatograms of PCL and PACL resulting from the ROP of εCL and εACL ($CHCl_3$, with 0.5% Et_3N, PMMA standard).

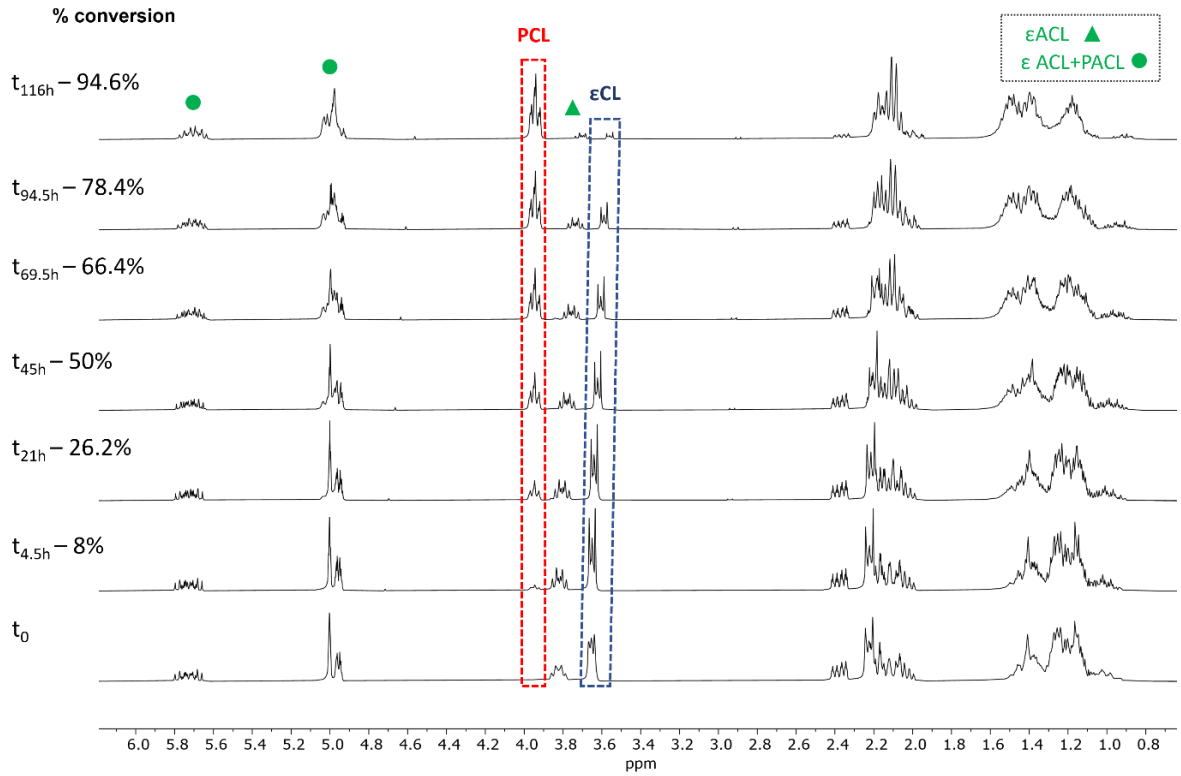


Figure S3.8. Stacked ^1H NMR spectra (300 MHz, 298 K, C_6D_6) of the ring-opening copolymerisation of εCL and εACL at 1:1 ratio (**CP8** in Table 3.1) at different reaction times. % conversion correspond to the conversion of εCL. Blue box: $CH_2OC{=}O$ monomer resonance. Red box: CH_2OH polymer resonance.

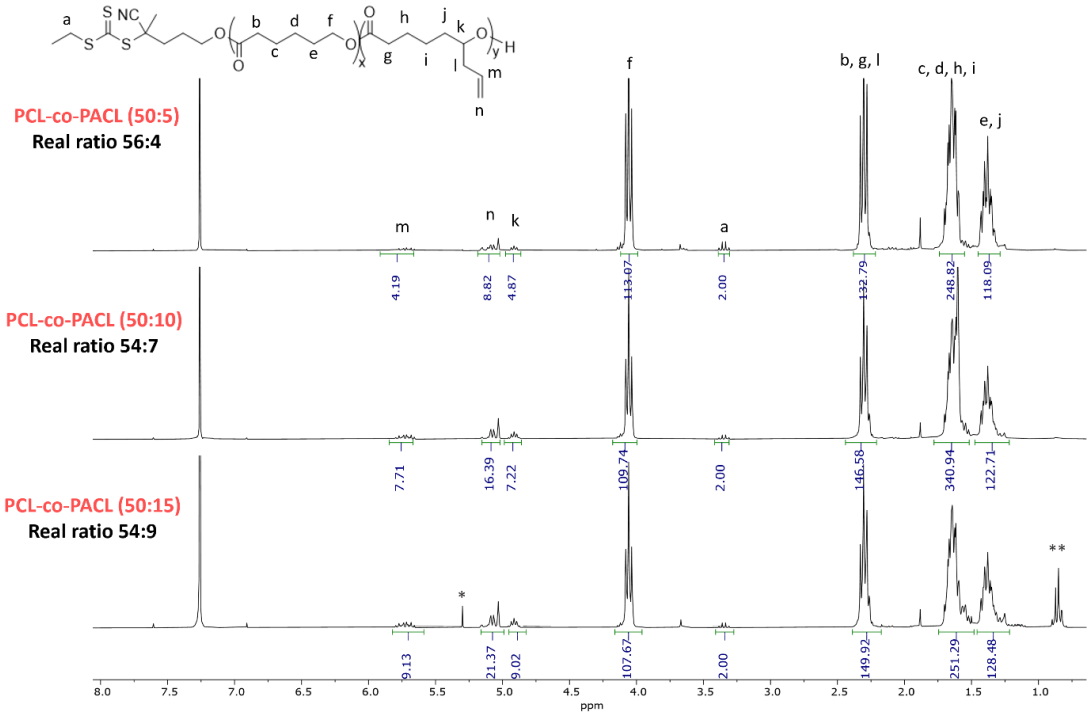


Figure S3.9. Stacked ^{1}H NMR spectra (300 MHz, 298 K, $CDCl_3$) of copolymers PCL_{56}-*co*-$PACL_4$, PCL_{54}-*co*-$PACL_7$ and, PCL_{54}-*co*-$PACL_9$ (targeted at 50:5, 50:10 and 50:15 respectively). * Peak corresponding to residual DCM. ** Peak corresponding to residual n-hexane.

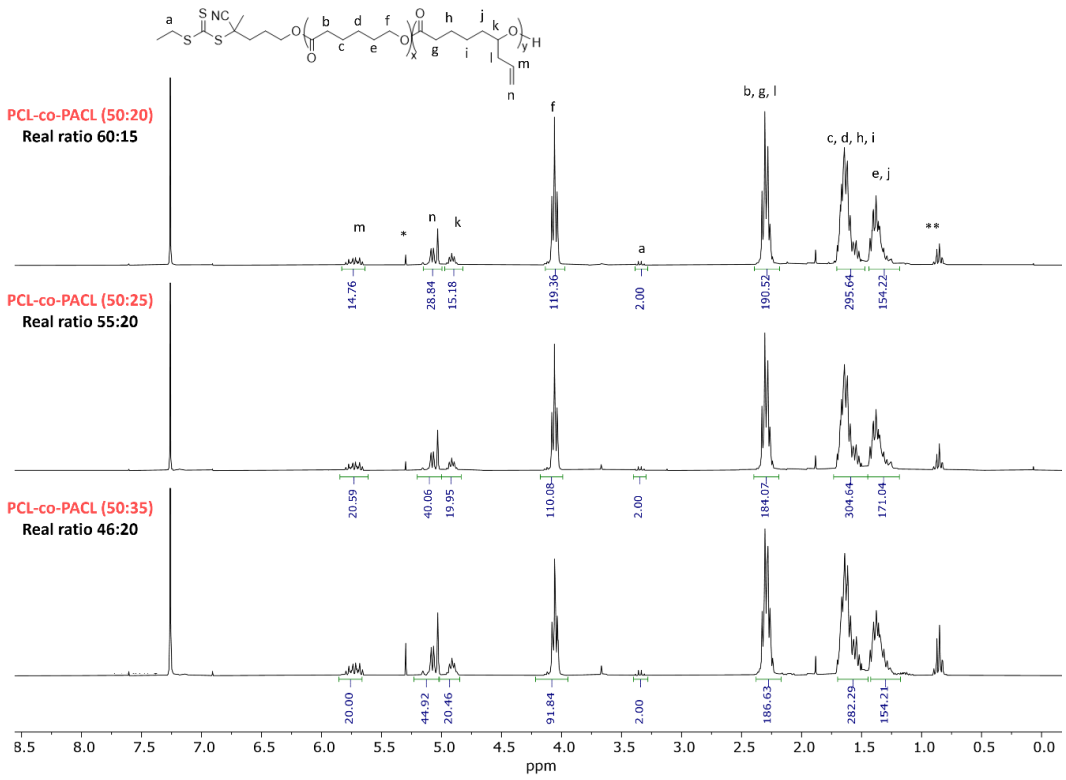


Figure S3.10. Stacked ^{1}H NMR spectra (300 MHz, 298 K, $CDCl_3$) of copolymers PCL_{60}-*co*-$PACL_{15}$, PCL_{55}-*co*-$PACL_{20}$ and, PCL_{46}-*co*-$PACL_{20}$ (targeted at 50:20, 50:25 and 50:35 respectively). * Peak corresponding to residual DCM. ** Peak corresponding to residual n-hexane.

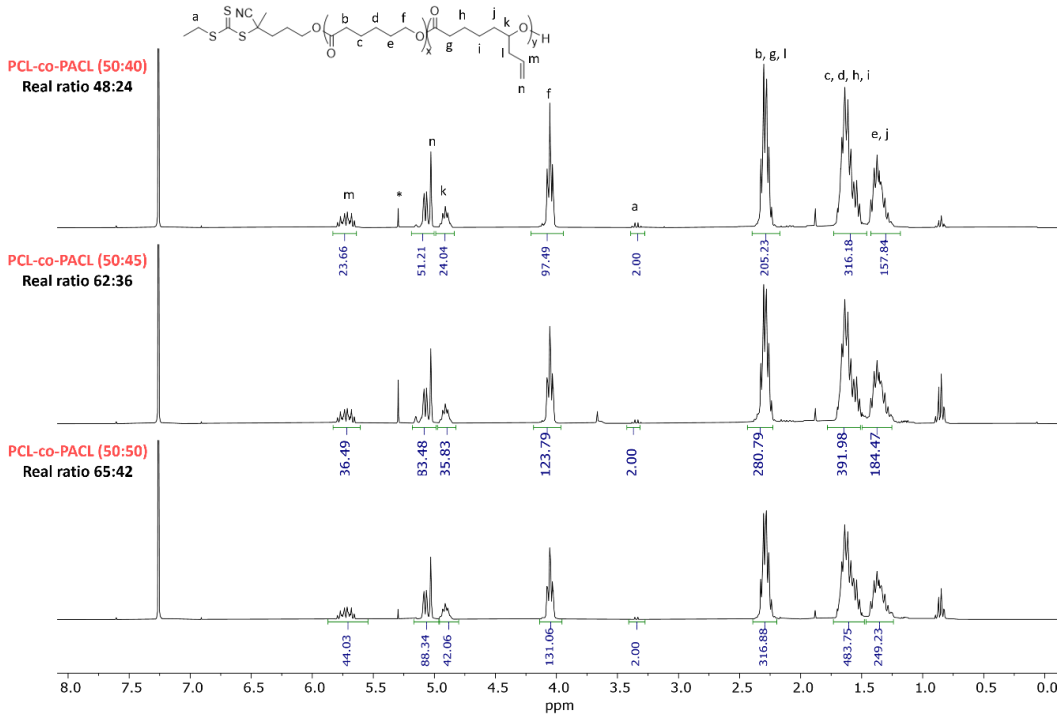


Figure S3.11. Stacked ^{1}H NMR spectra (300 MHz, 298 K, $CDCl_3$) of copolymers PCL_{48}-*co*-$PACL_{24}$, PCL_{62}-*co*-$PACL_{36}$ and, PCL_{65}-*co*-$PACL_{42}$ (targeted at 50:40, 50:45 and 50:50 respectively). * Peak corresponding to residual DCM. ** Peak corresponding to residual n-hexane.

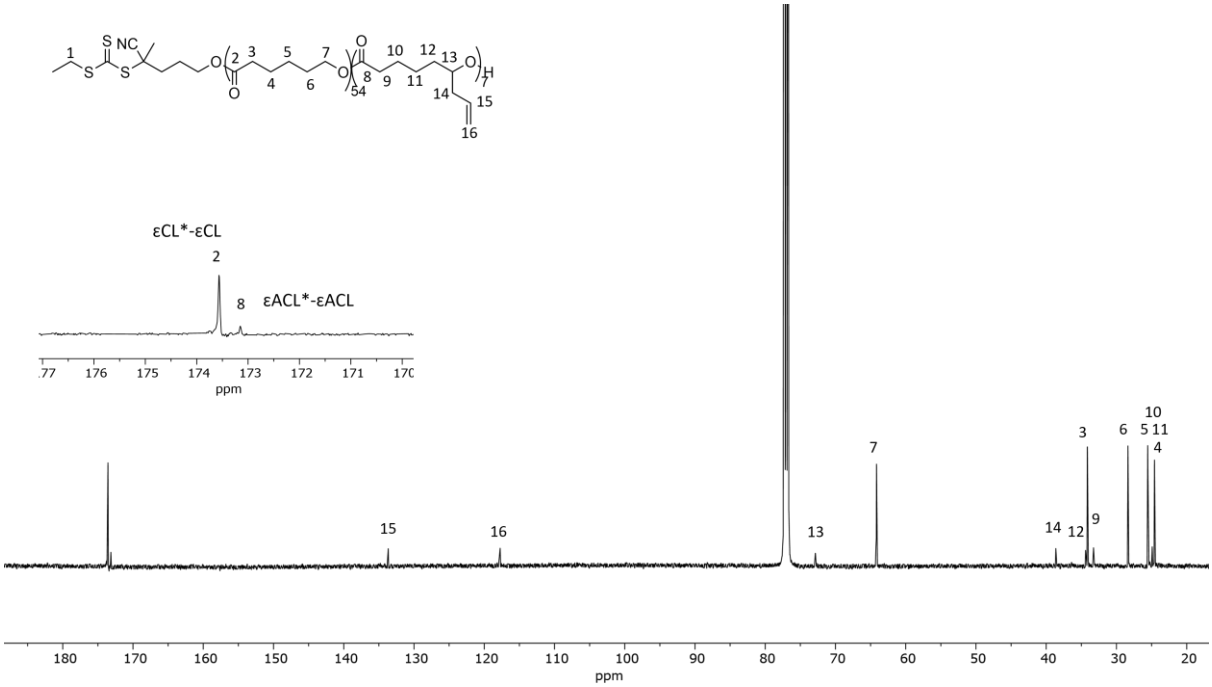


Figure S3.12. Quantitative ^{13}C NMR spectrum (500 MHz, 298 K, $CDCl_3$) of PCL_{54}-*co*-$PACL_{7}$. Zoom showing the carbonyl region.

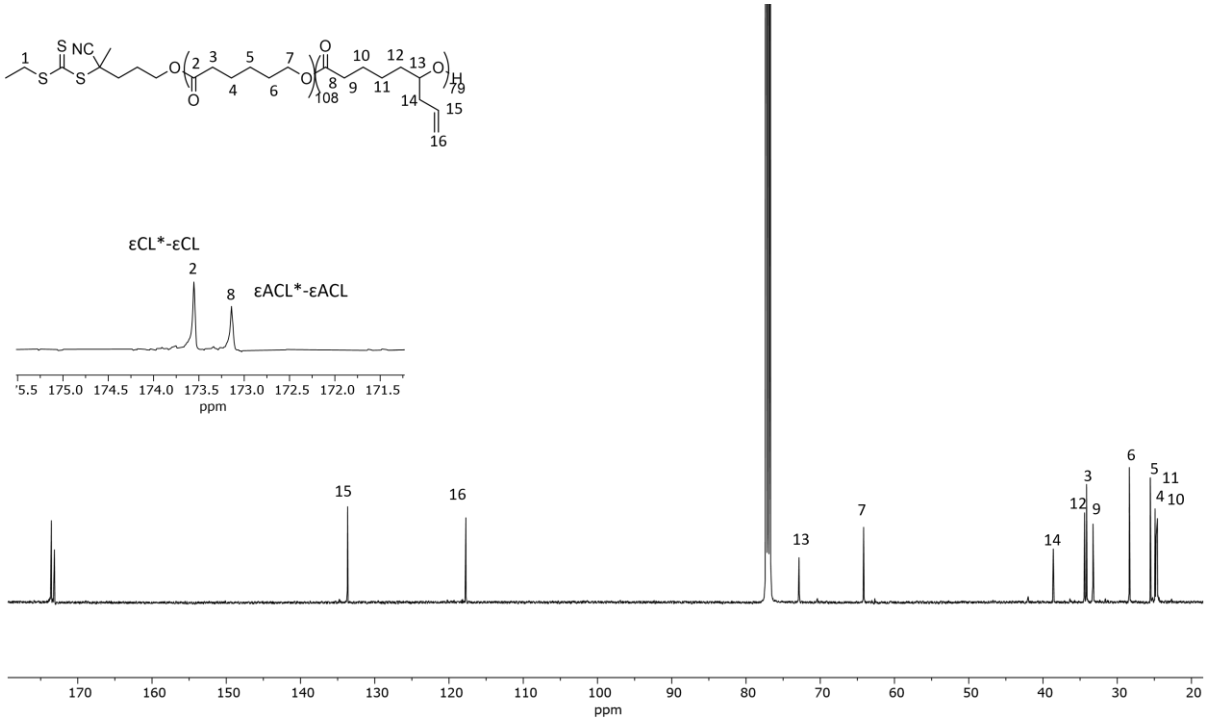


Figure S3.13. Quantitative ^{13}C NMR spectrum (500 MHz, 298 K, $CDCl_3$) of PCL_{108}-*co*-$PACL_{79}$. Zoom showing the carbonyl region.

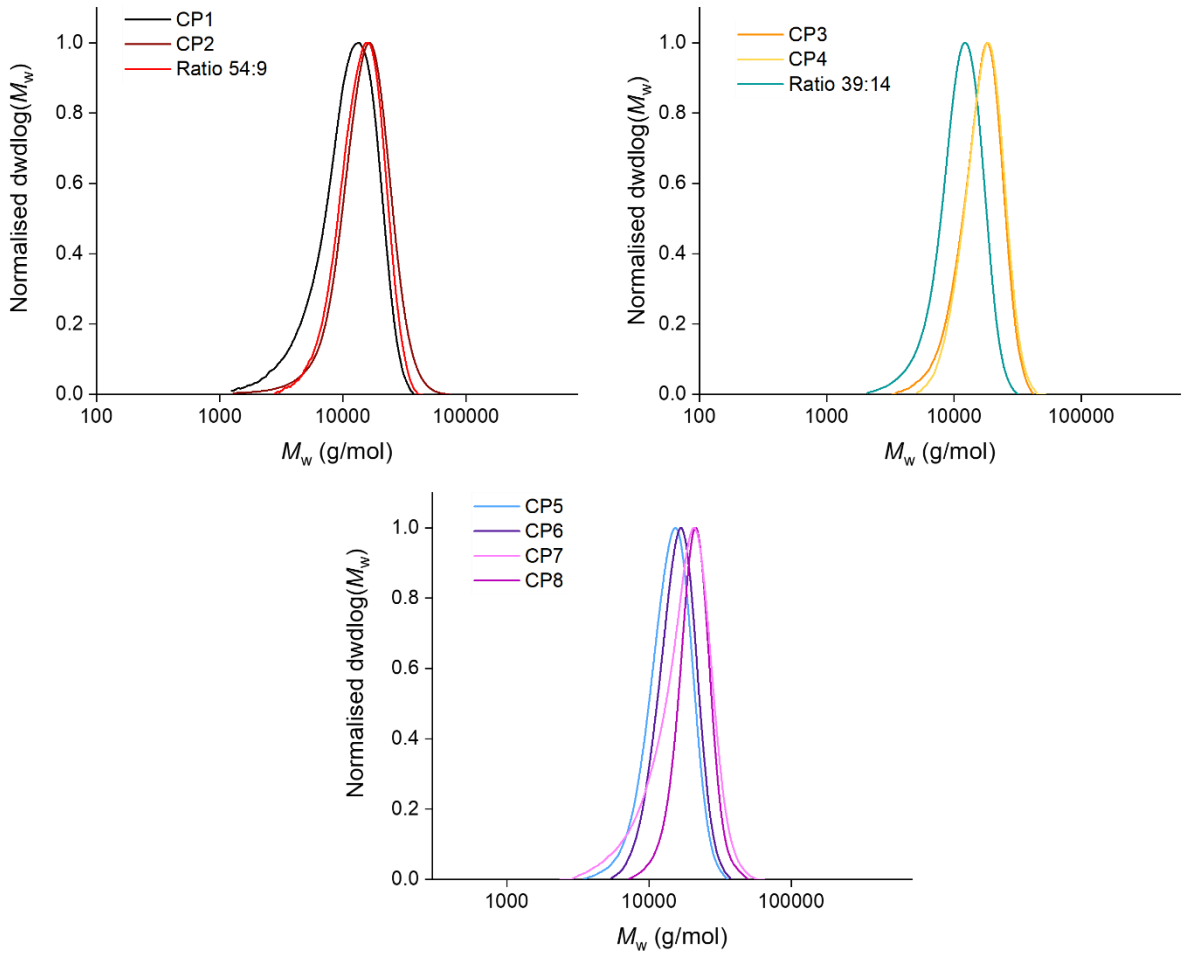


Figure S3.14. SEC chromatograms of the respective PCL_x-*co*-$PACL_y$ copolymers in Table 3.1 ($CHCl_3$, with 0.5% Et_3N, PMMA standard).

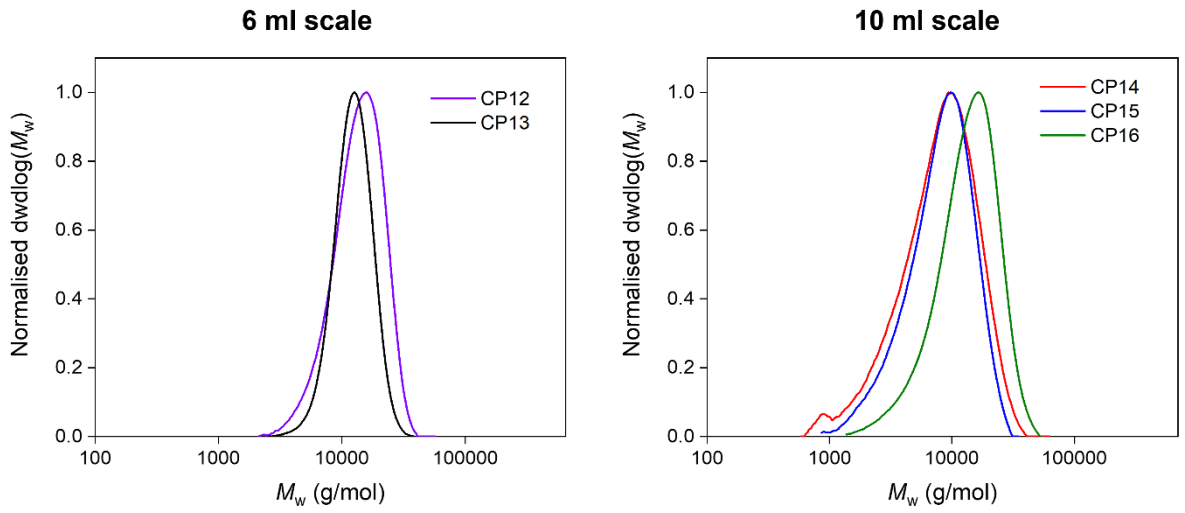


Figure S3.15. SEC chromatograms of PCL_x-*co*-$PACL_y$ copolymers synthesised in larger scales presented in Table 3.3 ($CHCl_3$, with 0.5% Et_3N, PMMA standard).

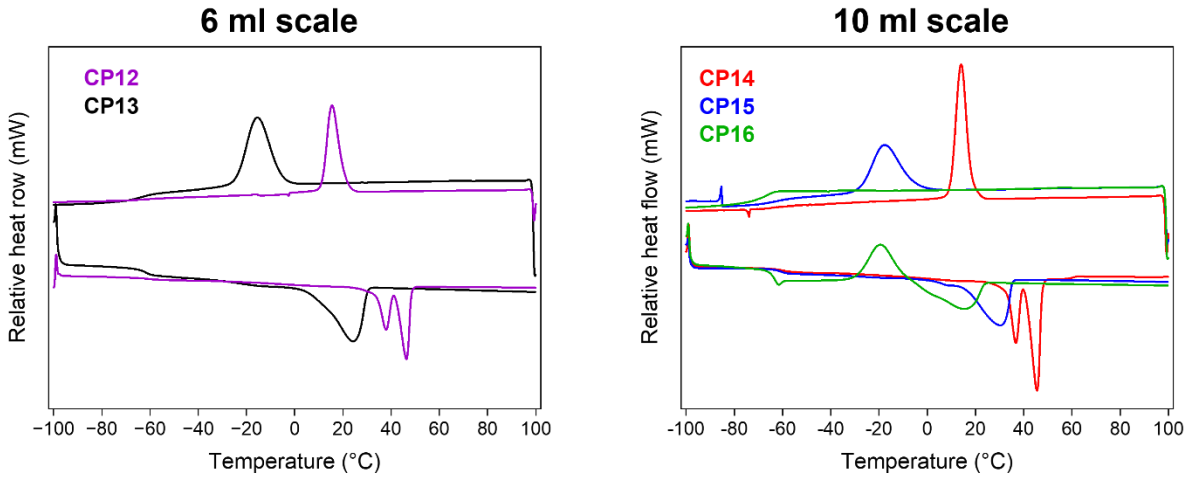


Figure S3.16. SEC thermograms (−100 to 100 °C, 10 °C min^{-1}) of PCL_x-*co*-$PACL_y$ copolymers synthesised in larger scales presented in Table 3.3 showing the second heating-cooling cycle (endo-down and exo-up).

Chapter 4.

Crystallisation-Driven Self-Assembly (CDSA) of semicrystalline functional PCL amphiphilic block copolymers.

4 Crystallisation-driven self-assembly of semicrystalline functional PCL amphiphilic block copolymers

4.1 Introduction

The use of amphiphilic block copolymers (BCPs) to create nano-objects and nanostructures has attracted increasing attention in various fields,[1-9] owing to their easy post-polymerisation modification, which allows the incorporation of a wide range of functionalities, and their ability to form self-assemblies with a rich variety of architectures without altering the polymer chemistry.[10-14] In 2000, Winnik and Manners introduced the concept of crystallisation-driven self-assembly (CDSA),[15, 16] where the crystallisation of the core-forming block triggers the formation of core-shell structures with low interfacial curvature structures such as 1D cylindrical micelles and 2D diamond-shaped platelets.[17-19]

During CDSA, the resultant morphology can be influenced by a range of parameters, including the chemistry of the semicrystalline block,[20, 21] the corona-core block ratios,[22] the temperature,[23] and the solvent conditions.[24] For example, Inam e*t al.* studied the shape selectivity of poly(*L*-lactide) (PLLA) BCPs by varying block ratios and temperature. They observed a clear transition from 2D platelet micelles obtained from the assembly of PLLA-based amphiphiles with larger corona-core ratios (20:1) to elongated cylindrical micelles through decreasing the corona block length (3:1).[25] Prior to this, Eisenberg and coworkers[26] reported a transformation in the morphology of poly(ε-caprolactone) (PCL) -based assemblies in aqueous solution from spheres, to rods, to wider 2D lamellae structures upon increasing the concentration of PCL homopolymer post-assembly. Moreover, the formation of more complex structures such as patchy block comicelles,[27] branched micelles,[28] and windmill micelles[29] using poly(ferrocenyldimethylsilane) (PFDMS) has been reported by Winnik and

Manners, which demonstrates the great potential of CDSA as a methodology to create precisely defined nanostructures with a broad range of morphologies.

Despite the noteworthy advances made through CDSA, the fabrication of monodisperse, biocompatible, and biodegradable nanostructures in biologically relevant solvents that include functionalisation in the corona or core blocks remains a significant challenge, and only a few promising examples have been reported.[30-32] Previous studies have proven that performing CDSA directly in water is challenging,[33, 34] consequently, the self-assembly of water dispersible semicrystalline BCPs is usually carried out in organic solvents followed by dialysis of the particle solution against water.[35] The Dove and O'Reilly research groups have pioneered the research of CDSA in aqueous media.[36] For example, the synthesis and self-assembly of poly(*L*-lactide)-*b*-poly(acrylic acid) (PLLA-*b*-PAA) and poly(*L*-lactide)-*b*-poly(dimethyl aminoethyl acrylate) (PLLA-*b*-PDMAEA) BCPs was achieved directly in water to obtain cylindrical micelles, whose length could be kinetically controlled by reheating the solution post-assembly while tuning the temperature and time of heating. In addition, Arno *et al.* demonstrated that the addition of a glassy, hydrophobic block between the core and corona of a poly(ε-caprolactone)-*b*-poly(*N*,*N*-dimethylacrylamide) (PCL-*b*-PDMA) copolymer allowed the transference of the assemblies into water without particle fracture, as well as the self-nucleation of the triblock copolymers in water, followed by sonication and epitaxial growth that resulted in monodisperse cylindrical micelles with high biocompatibility. Taking advantage of the unprecedented control achieved, a hydrogel material for cell culture was obtained through the sequential addition of unimer into water for the first time.[37]

Moreover, the conjugation of small molecules or fluorescent dyes into amphiphilic BCPs is of great interest for the application of these nanoparticles in the biomedical field.[38] However, the

introduction of functionalities into semicrystalline polymers tends to yield amorphous polymers, which are unable to undergo CDSA.[39] In the majority of cases, the modification occurs in the corona block restricting the use of these structures as drug delivery systems. To the best of our knowledge, there has been only one reported example for the self-assembly of block copolymers containing crystalline side chains within the core-forming block,[40] in which 2D hexagonal platelets were achieved from poly(behenyl acrylate)-*b*-poly(*N*,*N*-dimethylacrylamide) copolymers bearing long crystalline pendant aliphatic chains. However, there have been no prior reports of self-assembly of semicrystalline amphiphilic core-functionalised copolymers, and only one similar strategy was reported by the Dove and O'Reilly research groups where the introduction of a third, amorphous, functional block into PLLA diblock-based copolymers enabled the introduction of small thiol molecules at the core-shell interface before and after their self-assembly into cylindrical micelles through photo-induced thiol-ene click reactions.[41]

Herein, we have designed a series of amphiphilic functional PCL block copolymers by the incorporation of a biocompatible PDMA block to our previous synthesised PCL-*co*-PACL copolymers through reversible addition-fragmentation chain transfer (RAFT) polymerisation, followed by the conjugation of benzyl mercaptan in the core-forming block *via* photoinitiated thiol-ene addition. In addition, we present a comprehensive CDSA study of conjugated and non-conjugated PCL-based block copolymers with varying corona:core ratios and diverse allyl wt.% incorporation. Parameters such as temperature, solvent type and degree of functionalisation were investigated and their effect on the resultant nanoparticle's morphology was highlighted.

4.2 Results and discussion

4.2.1 Synthesis of PDMA-*b*-PCL block copolymers as "control"

A series of PDMA$_x$-*b*-PCL$_{49}$ block copolymers with corona-to-core ratios ranging from 2:1 to 9.6:1 were initially prepared by ROP of ε-caprolactone (εCL) using a dual-head chain-transfer agent (CTA), followed by reversible addition-fragmentation chain transfer (RAFT) polymerisation with dimethyl acrylamide (DMA). The ROP of the lactone was performed at room temperature in a nitrogen-filled glovebox, using diphenyl phosphate (DPP) and anhydrous toluene as catalyst and solvent respectively, with a [εCL]:[CTA]:[DPP] molar ratio of 60:1:1. After 6 h, polymer was precipitated in cold *n*-hexanes to yield semicrystalline PCL$_{49}$ as a yellow solid. Chain extension of the PCL-macroinitiator with a DMA hydrophilic block was carried out at 70 °C under inert conditions using 2,2-azobis(2-methylpropionitrile) (AIBN) as a radical initiator (10 mol%) and 1,4-dioxane (25 wt.%) as solvent. Monomer incorporation varied depending on the targeted corona-to-core (m_{PDMA}/m_{PCL}) ratio ranging from 150 to 600 equivalents (equiv.). After two hours, the polymerisation was quenched by submerging the reaction vessel in an ice bath and precipitated in cold diethyl ether to obtain the desirable PDMA-*b*-PCL$_{49}$ amphiphilic BCPs with m_{PDMA}/m_{PCL} ratios varying from 2:1 to 9:6 (**Figure S4.1 – S4.5**). A summary of the synthesised polymers that has been used as a control for the self-assembly can be found in **Table 4.1**.

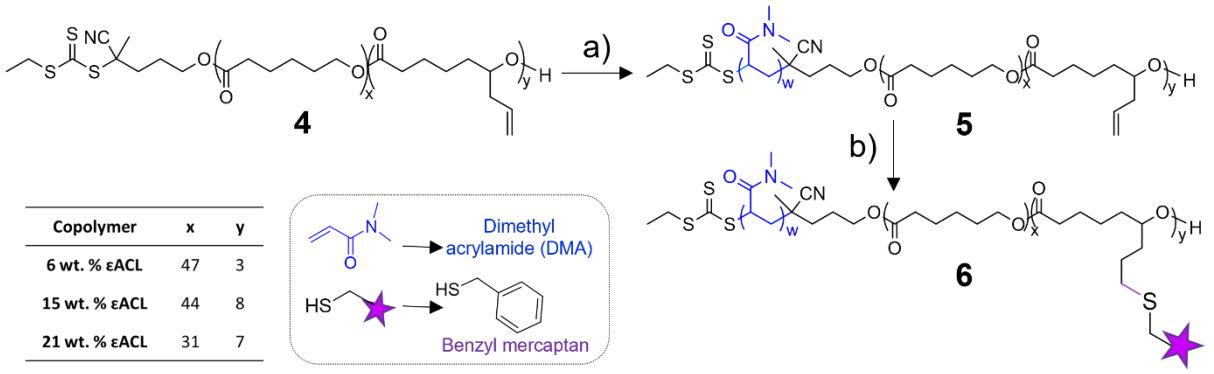
Table 4.1. Synthesis of $PDMA_x$-*b*-PCL_{49} block copolymer with different core and corona lengths.

Polymer	PDMA:PCL ratio[a]	$Đ_M$[b]	$M_{n,SEC}$[b] (kDa)	T_m[c] (°C)	T_c[c] (°C)
PCL_{49}	-	1.07	12.4	53.3	32.4
$PDMA_{96}$-*b*-PCL_{49}	2:1	1.40	17.4	38.6	18.8
$PDMA_{163}$-*b*-PCL_{49}	3:1	1.34	22.4	38.8	18.1
$PDMA_{204}$-*b*-PCL_{49}	4.2:1	1.34	26.6	38.7	17.5
$PDMA_{309}$-*b*-PCL_{49}	6.3:1	1.30	34.4	37.4	15.0
$PDMA_{474}$-*b*-PCL_{49}	9.6:1	1.38	39.7	38.5	14.5

[a] Ratio between the PDMA block (corona) and the PCL block (core) obtained from ^{1}H NMR spectroscopy. [b] Measured by SEC ($CHCl_3$ with 0.5% Et_3N, PMMA standard). [c] Measured by nano DSC, triblock copolymers in ethanol (100 to 0 °C, 1 °C min^{-1}).

4.2.2 Synthesis of PDMA-*b*-PCL-*co*-PACL copolymers and functionalisation

To form functional amphiphilic block copolymers with a semicrystalline core-forming block, the semicrystalline PCL-*co*-PACL copolymers previously synthesised in Chapter 3 (**4** in Scheme 4.1) – with targeted % of allyl-monomer incorporation varying from 5 to 26% – were chain-extended with DMA to obtain amphiphilic copolymers (**5** in Scheme 4.1), thanks to the presence of the dual-head initiator used for the copolymerisation of εCL and εACL, which also allows RAFT polymerisation. Finally, photoinitiated thiol-ene click addition of benzyl mercaptan to the allyl groups was performed to yield thiol-conjugated block copolymers (**6** in Scheme 4.1).



Copolymer	x	y
6 wt. % εACL	47	3
15 wt. % εACL	44	8
21 wt. % εACL	31	7

Scheme 4.1. General procedure for the synthesis of functional amphiphilic BCPs with x and y corresponding to εCL and εACL units. (a) DMA monomer, AIBN (10 mmol%), 1,4-dioxane, 70 °C; (b) benzyl mercaptan (thiol:ene ratio = 10:1), Irgacure 819 (10 mmol% based on thiol), chloroform, 25 °C, 3 h.

4.2.2.1 Synthesis of semicrystalline amphiphilic block copolymers *via* RAFT polymerisation.

Initially, to achieve amphiphilic block copolymers with a 3:1 ratio of PDMA to (PCL-*co*-PACL) units, a degree of polymerisation (DP) of 200 units of DMA was targeted. The reaction was stopped after 2 hours and precipitated in cold diethyl ether to yield a yellow solid, and a block copolymer containing 208 units of PDMA, $PDMA_{208}$-*b*-PCL_{44}-*co*-$PACL_{7}$, was confirmed by ^{1}H NMR analysis (**Figure 4.1**). However, unlike previous studies where RAFT polymerisation of acrylamides led to the formation of well-defined amphiphilic block copolymers,[24, 42, 43] SEC analysis of the respective copolymer showed a bimodal distribution, which indicates the presence of two different polymer species (**Figure 4.2**).

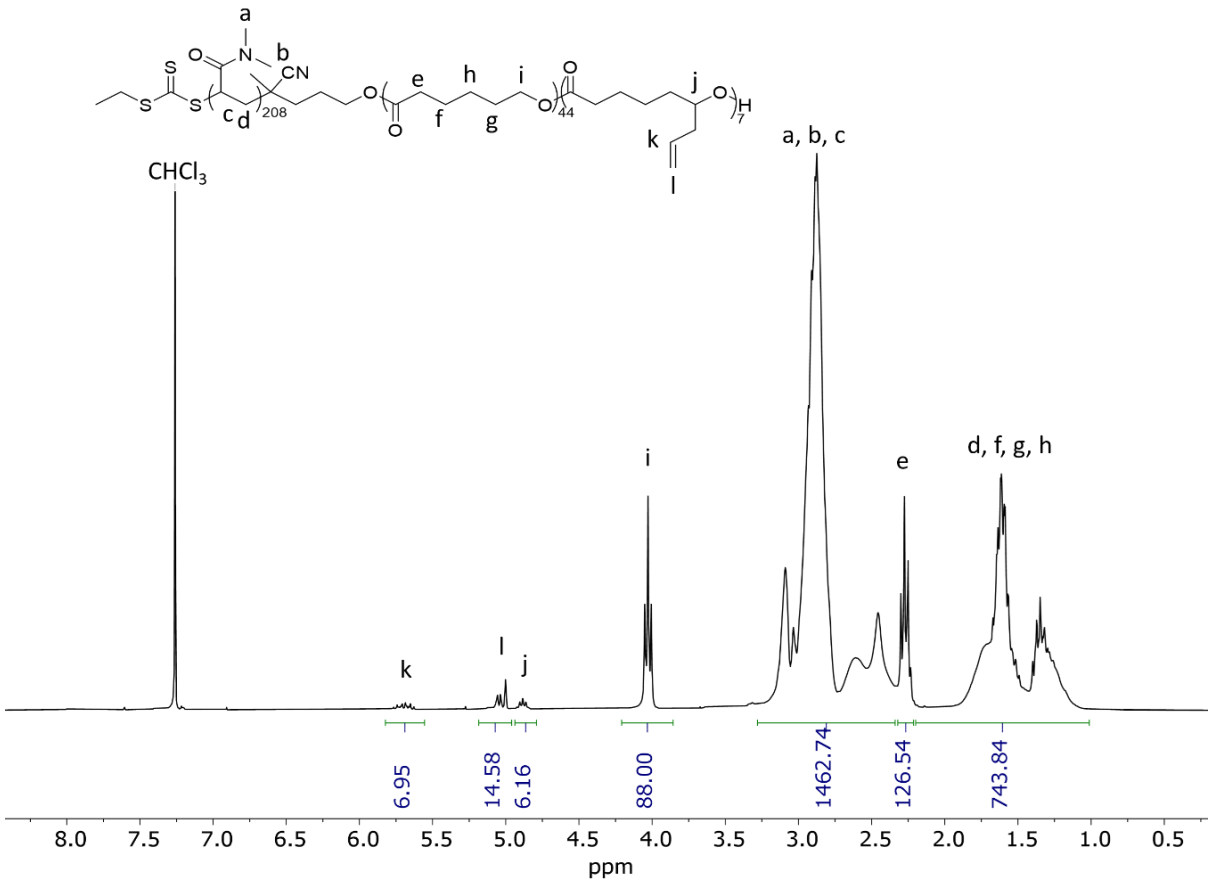


Figure 4.1. ^{1}H NMR spectrum ($CDCl_3$, 300 MHz) of $PDMA_{208}$-*b*-PCL_{44}-*co*-$PACL_7$ block copolymer.

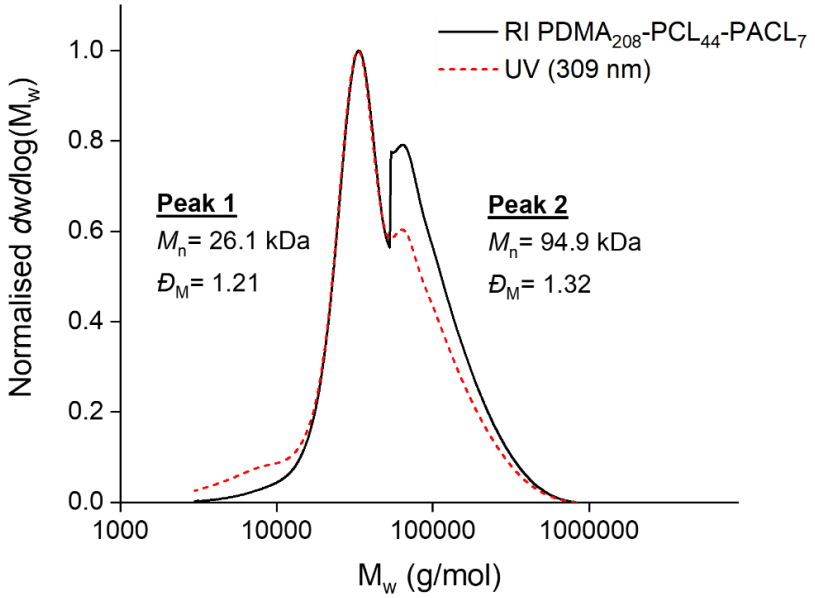


Figure 4.2. SEC chromatogram of $PDMA_{208}$-*b*-PCL_{44}-*co*-$PACL_7$ block copolymer ($CHCl_3$, with 0.5% Et_3N, PMMA standard).

It was hypothesised that the allyl-pendant group from PACL, which is susceptible to RAFT polymerisation and/or crosslinking, reacted with the free radicals at low concentrations of the more reactive vinyl monomer.[44] To investigate this phenomenon, the RAFT polymerisation of DMA using a poly(ε-allyl-ε-caprolactone) macroinitiator (CTA-PACL) was explored using the same reaction conditions previously reported (Figure **4.3A**). After 2 hours of reaction, the reaction mixture yielded a very viscous material that couldn't be dissolved. This gelation process is believed to happen as a result of crosslinking side reactions between the allyl pendant groups present in the polymer backbone, further confirming our initial theory (Figure **4.3B** and **4.3C**). To avoid this uncontrolled polymerisation, the reactions were carried out using an excess of DMA in the formulation and were stopped at around 40% of monomer conversion.

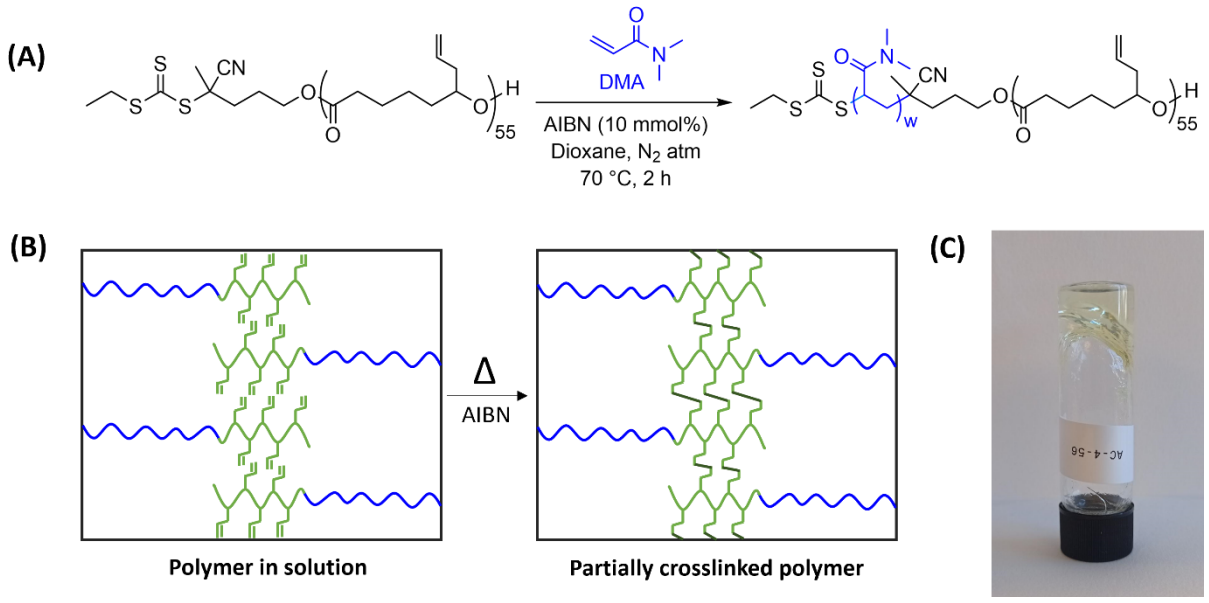


Figure 4.3. (A) Scheme for the RAFT polymerisation scheme of DMA with poly(ε-allyl-ε-caprolactone) macroinitiator (CTA-PACL). **(B)** Schematic illustration of hypothesised crosslinking side reaction. **(C)** PDMA-*b*-PACL$_{55}$ gel.

With the aim to design copolymers with different lengths of core and corona blocks, a series of $PDMA_w$-*b*-PCL_x-*co*-$PACL_y$ block copolymers with PDMA:PCL-based block ratios varying from 2:1 to 10:1 were synthesised (**Table 4.2**). The obtention of the desired functional block copolymers was confirmed by ^{1}H NMR spectroscopy (**Figures S4.6 – S4.16**) and SEC analyses, which showed monomodal narrow distributions ($Đ_M$ < 1.3) and predictable molecular weights (M_n) for all polymers (**Figure 4.4**).

Table 4.2. Block copolymers of $PDMA_w$-*b*-PCL_x-*co*-$PACL_y$ with different core and corona lengths.[a]

Entry	Block copolymer	Corona:core ratio[b]	$M_{n,}$[c] (kDa)	$Đ_M$[c]	DMA units (wt.%)
T1	$PDMA_{94}$-*b*-PCL_{44}-*co*-$PACL_3$	2:1	19.5	1.21	27.0
T2	$PDMA_{130}$-*b*-PCL_{43}-*co*-$PACL_7$	2.6:1	12.2	1.30	27.2
T3	$PDMA_{165}$-*b*-PCL_{48}-*co*-$PACL_3$	3.2:1	20.2	1.27	29.4
T4	$PDMA_{175}$-*b*-PCL_{47}-*co*-$PACL_3$	3.5:1	20.5	1.20	22.2
T5	$PDMA_{295}$-*b*-PCL_{56}-*co*-$PACL_4$	5:1	28.1	1.26	31.0
T6	$PDMA_{237}$-*b*-PCL_{36}-*co*-$PACL_3$	6:1	18.5	1.22	41.2
T7	$PDMA_{362}$-*b*-PCL_{46}-*co*-$PACL_8$	6.7:1	36.6	1.22	35.6
T8	$PDMA_{350}$-*b*-PCL_{41}-*co*-$PACL_6$	7.5:1	40.8	1.28	25.0
T9	$PDMA_{328}$-*b*-PCL_{31}-*co*-$PACL_7$	8.7:1	20.0	1.20	34.5
T10	$PDMA_{456}$-*b*-PCL_{43}-*co*-$PACL_7$	9.1:1	32.0	1.25	47.8
T11	$PDMA_{412}$-*b*-PCL_{36}-*co*-$PACL_4$	10.3:1	40.2	1.23	42.9

[a] All polymerisations were carried out in 1,4-dioxane at 70 °C and quenched after 35 min. [b] Ratio between the PDMA block (corona) and the PCL-based BCP (core) obtained from ^{1}H NMR spectroscopy. [c] Measured by SEC ($CHCl_3$ with 0.5% Et_3N, PMMA standard).

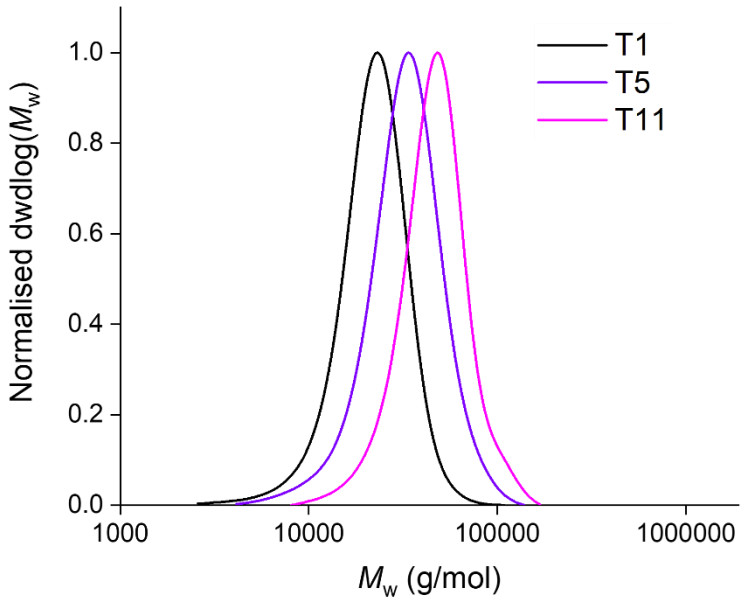
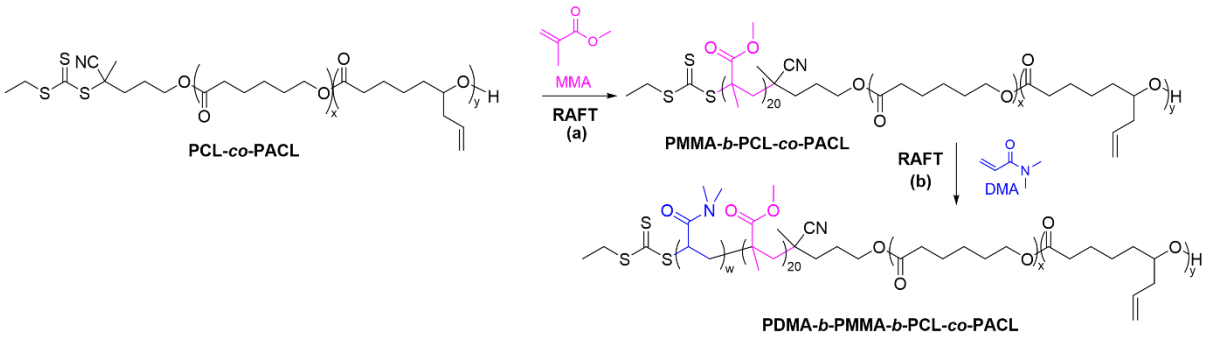


Figure 4.4. SEC chromatograms of $PDMA_w$-*b*-PCL_x-*co*-$PACL_y$ copolymers T1, T5 and T11 in Table 4.2 ($CHCl_3$, with 0.5% Et_3N, PMMA standard).

In addition, since previous research in CDSA reported increasing micelle stability in aqueous solution with polymers bearing a short hydrophobic block,[37] a series of amphiphilic block copolymers bearing a middle block of poly(methyl methacrylate) (PMMA) were prepared *via* RAFT polymerisation as illustrated in **Scheme 4.2** and **Table S4.1**. It was believed that short blocks of poly(methyl methacrylate) (PMMA), which has a higher glass transition temperature (T_g) than PCL, could decrease the tension between polymer chains (caused by the higher affinity of PDMA to water than ethanol), thereby preventing the collapse of the PCL block.



Scheme 4.2. Synthesis of PDMA-*b*-PMMA-*b*-PCL-*co*-PACL amphiphilic block copolymers *via* RAFT polymerisation of methyl methacrylate (MMA) and dimethyl acrylamide (DMA). (a) MMA (100 equiv.), AINB (20 mmol %), dioxane (30 wt.%), 70 °C, N_2 atmosphere. (b) DMA (600 equiv.), AINB (10 mmol %), dioxane (30 wt.%), 70 °C, N_2 atmosphere.

The successful chain extension of PCL-*co*-PACL block-like copolymers by RAFT polymerisation with methyl methacrylate (MMA) was demonstrated by ^{1}H NMR spectroscopy, with the appearance of new characteristic PMMA peaks corresponding to O-CH_3 at δ = 3.59 ppm, C(CH$_3$)CH_2 at δ = 1.95 – 1.80 ppm, and C(CH_3)CH$_2$ at δ = 1.01 – 0.83 ppm (pink boxes in **Figure 4.5**). Subsequent chain extension of these PMMA-*b*-PCL-*co*-PACL block polymers with DMA, as previously described, allowed the obtention of amphiphilic PDMA-*b*-PMMA-*b*-PCL-*co*-PACL block copolymers (**Figures S4.17 – S4.21**) with narrow dispersities ($Đ_M$ < 1.2) and predictable molecular weights (**Figure 4.6**).

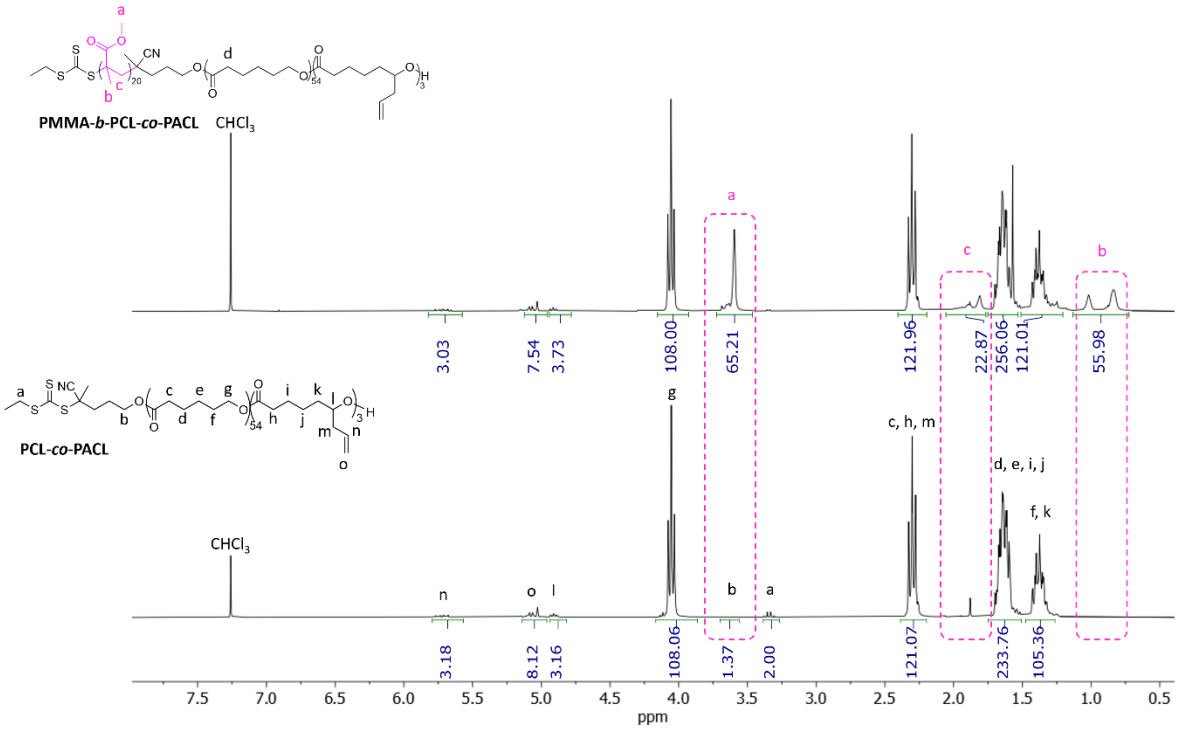


Figure 4.5. Stacked ^{1}H NMR spectra ($CDCl_3$, 300 MHz) of PCL_{54}-*co*-$PACL_3$ copolymer (bottom) and $PMMA_{20}$-*b*-PCL_{54}-*co*-$PACL_3$ block copolymers (top).

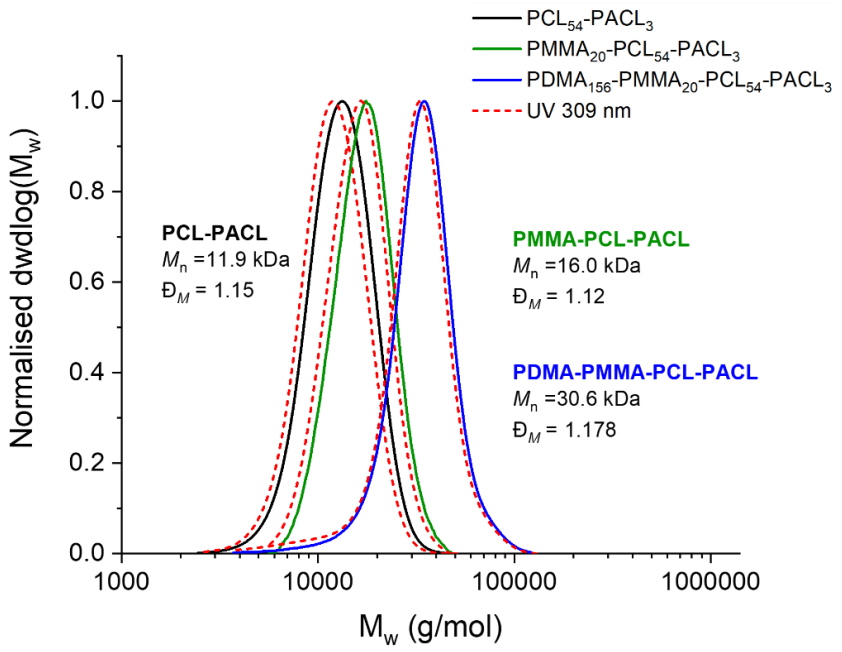


Figure 4.6. SEC chromatograms of PCL_{54}-*co*-$PACL_3$, $PMMA_{20}$-*b*-PCL_{44}-*co*-$PACL_3$ and $PDMA_{156}$-*b*-$PMMA_{20}$-*b*-PCL_{44}-*co*-$PACL_3$ block copolymers ($CHCl_3$, with 0.5% Et_3N, PMMA standard).

4.2.2.2 Functionalisation *via* thiol-ene click addition with benzyl mercaptan

The post-polymerisation modification of selected copolymers (**Table S4.2**) was carried out *via* photoinitiated thiol-ene reaction on the pendant allyl-functionality. For this, benzyl mercaptan and phenylbis(2,4,6-trimethylbenzoyl)phosphine oxide, Irgacure 819, were used as thiol and photoinitiator, respectively. After irradiation with UV light (λ = 405 nm) for 3 h, the modified copolymer was precipitated in cold diethyl ether to give a white solid. ^{1}H NMR spectroscopy was used to monitor the thiol-ene addition reaction, in which it was possible to observe the disappearance of the characteristic ally peaks at δ = 5.70 ppm and 5.02 – 5.10 ppm, corresponding to C*H*=CH_2 and CH=CH_2 respectively, and the appearance of aromatic protons and the S-CH_2 moiety from the benzyl mercaptan at δ = 7.28 – 7.56 ppm and δ = 3.67 ppm, respectively. The absence of allyl peaks in the purified polymer indicated successful attachment of benzyl mercaptan (**Figure 4.7** and **Figure S4.22**). SEC analysis of the modified polymer showed a small increase in the M_n and dispersity in comparison to the native polymer, supporting the attachment of the benzyl group to the polymer (**Figure 4.8**).

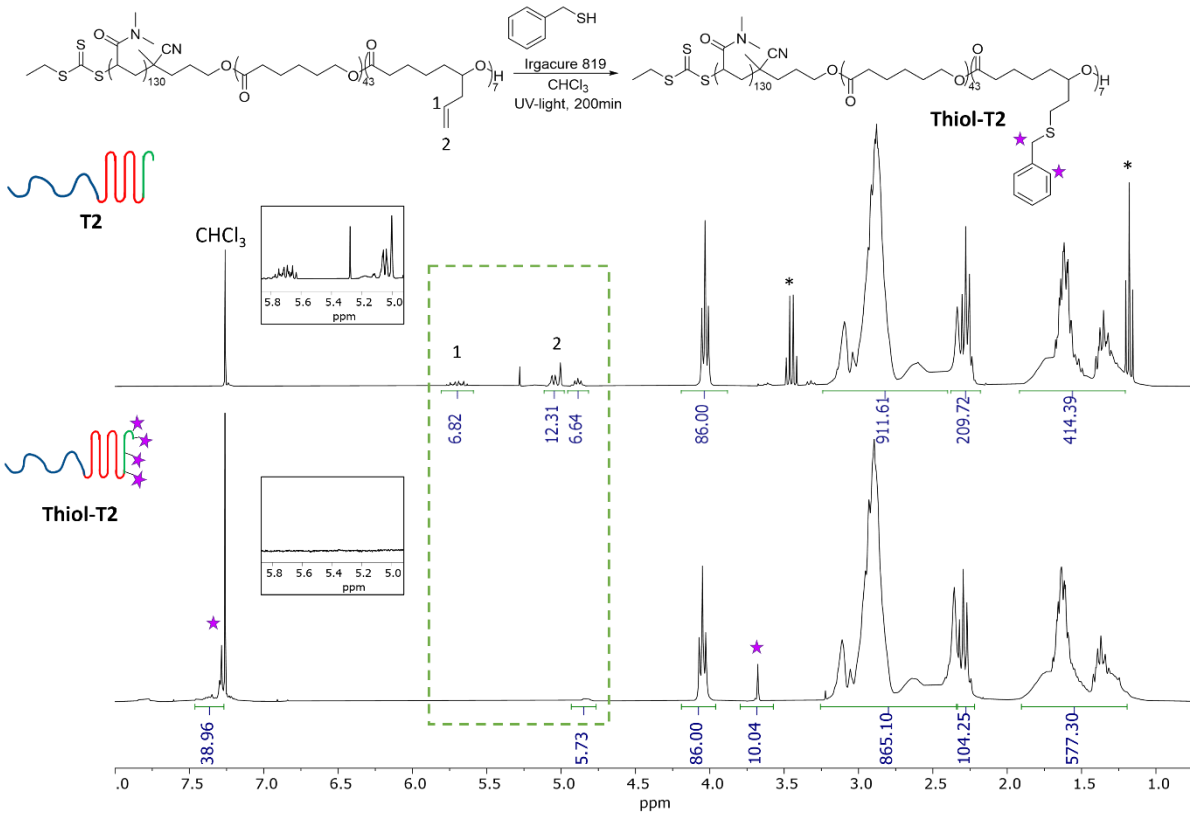


Figure 4.7. Stacked ^{1}H NMR spectra ($CDCl_3$, 300 MHz) of $PDMA_{130}$-*b*-PCL_{43}-*co*-$PACL_7$ copolymer (**T2** in Table 4.2, top) and benzyl functionalised $PDMA_{130}$-*b*-PCL_{43}-*co*-$PACL_7$ block copolymers (**Thiol-T2** in Table S4.2, bottom). Zoom showing the allyl protons. *Correspond to diethyl ether peaks.

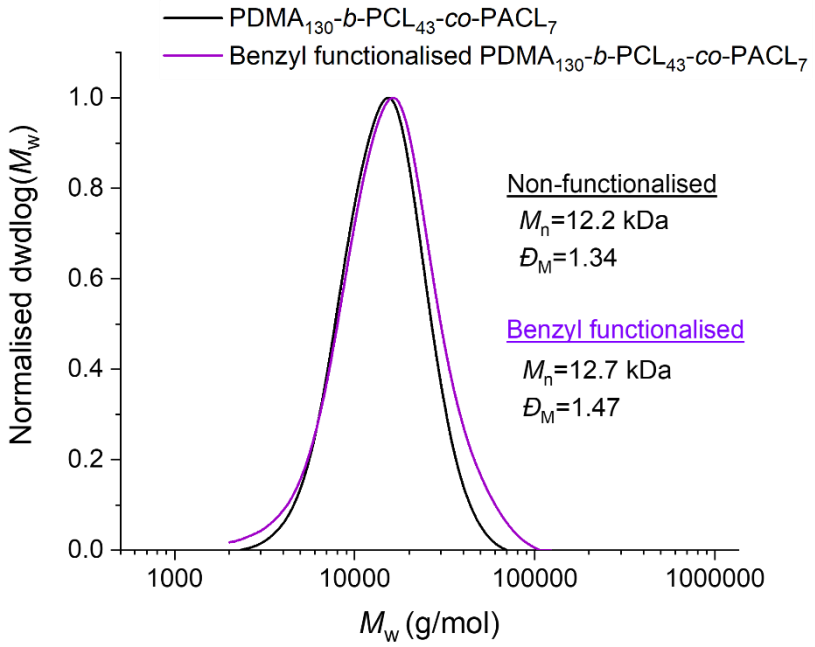


Figure 4.8. SEC chromatograms of $PDMA_{130}$-*b*-PCL_{43}-*co*-$PACL_7$ (**T2**, black line) and benzyl functionalised $PDMA_{130}$-*b*-PCL_{43}-*co*-$PACL_7$ block copolymers (**Thiol-T2**, purple line) ($CHCl_3$, with 0.5% Et_3N, PMMA standard).

4.2.3 Crystallisation-driven self-assembly of PCL-based block copolymers.

In seeking to design non-spherical nanostructures with controlled morphology and tuneable dimensions, these amphiphilic copolymers underwent thermally induced crystallisation-driven self-assembly (CDSA). Based on previous reports,[37] ethanol (EtOH) was initially chosen as the solvent for the polymer assembly at a concentration of 5 mg mL^{-1}. It is well established in the literature that the morphology of PLLA-containing nanoparticles, formed *via* CDSA, can be tuned from diamond-shaped platelets to cylindrical micelles by altering the length of the hydrophobic and hydrophilic blocks, core and corona blocks respectively.[25, 45] Inspired by these reports, the corona-to-core ratio of PDMA-*b*-PCL-based BCPs was varied to understand its effect on nanoparticle structure.

4.2.3.1 Investigating the influence of the corona:core ratio of block copolymers during self-assembly.

Initially, previously synthesised PDMA$_{\mathbf{x}}$-*b*-PCL$_{49}$ block copolymers with corona-to-core ratios ranging from 2:1 to 9.6:1 were self-assembled in ethanol (5 mg mL^{-1}) by heating up the polymer suspension at 70 °C for 3 h to ensure complete dissolution, followed by slowly cooling to room temperature. After 1 week of aging at room temperature, the solution appeared highly cloudy and the Tyndall phenomenon was observed for all PDMA$_{\mathbf{x}}$-*b*-PCL$_{49}$ copolymer solutions, which indicated the presence of self-assembled structures. The morphology of the assemblies was investigated by transmission electron microscopy (TEM), where a clear transition from 1D cylindrical micelles to 2D platelet-like micelles was observed with increasing corona-to-core ratios (**Figure 4.9**). As expected, copolymers with lower corona-to-core ratios (2:1 and 3:1) are less soluble in ethanol, consequently, the BCPs exhibited faster crystallisation kinetics, which led to a rapid self-nucleation of the semicrystalline PCL block followed by growth of a single crystal face, resulting in more kinetically stable 1D assemblies (cylindrical micelles). Differently, copolymers with higher ratios (6.3:1 and 9.6:1) are more soluble in the solvent, therefore presenting slower crystallisation rates of the core-forming block. As a result, all crystal faces are able to grow evenly leading to thermodynamic 2D lamellae assemblies (platelet-like micelles).

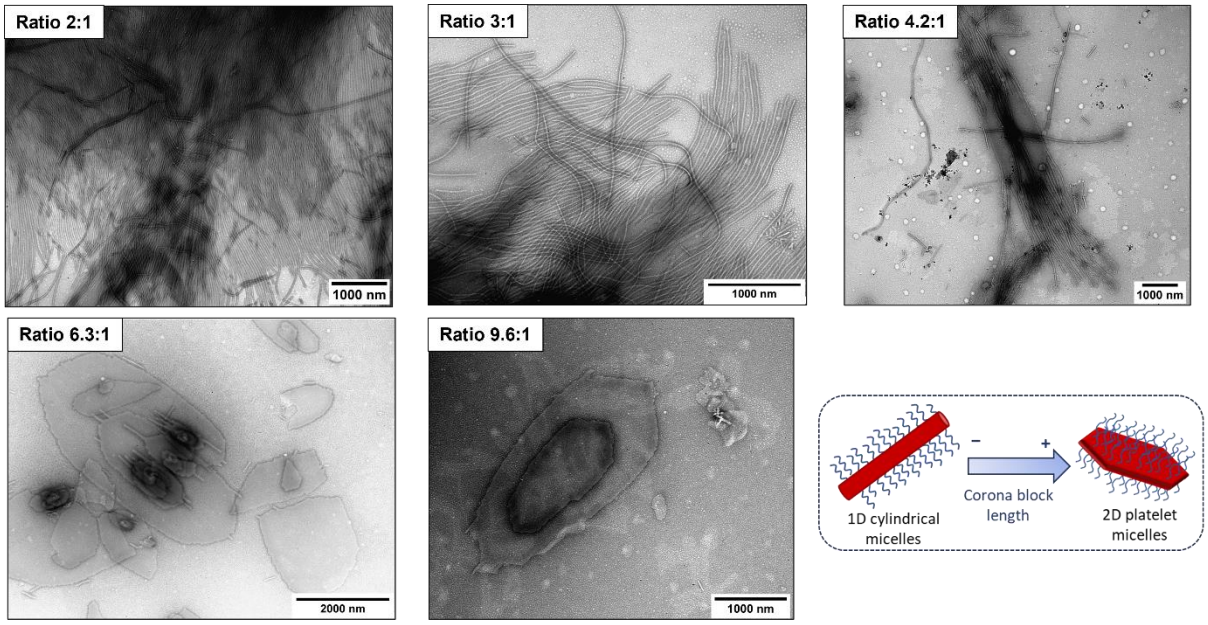


Figure 4.9. Self-assembly of $PDMA_x$-*b*-PCL_{49} block copolymers with different corona lengths. TEM micrographs of $PDMA_{96}$-*b*-PCL_{49} (ratio 2:1), $PDMA_{163}$-*b*-PCL_{49} (ratio 3:1), $PDMA_{204}$-*b*-PCL_{49} (ratio 4.2:1), $PDMA_{309}$-*b*-PCL_{49} (ratio 6.3:1), $PDMA_{474}$-*b*-PCL_{49} (ratio 9.6:1) after one week of aging. Samples were negatively stained using uranyl acetate (0.5 wt.%).

4.2.3.1.1 Crystallisation-driven self-assembly of $PDMA_w$-*b*-PCL_x-*co*-$PACL_y$ series.

After studying how the architecture of PDMA-*b*-PCL particles changed while varying the corona-to-core ratio, the self-assembly of allyl functional-PCL amphiphilic block copolymers with varying ratios from 2:1 to 10:1 was explored. The self-assembly of $PDMA_w$-*b*-PCL_x-*co*-$PACL_y$ block copolymers (**Table 4.3** and **Figure 4.10**) was performed following the same conditions as for PDMA-*b*-PCL copolymers. Similar trends to the previous studies were observed for allyl-containing copolymers with low allyl-monomer incorporation and short corona-to-core ratios (**T1**). However, changes in morphology were found and significantly longer aging times were needed when increasing both the poly(allyl-caprolactone) block length (**T2** and **T7**) and/or the corona block length (**T10** and **T11**). These differences during the self-assembly process could result from the lower crystallinity degree of PCL-*co*-PACL copolymers compared to PCL homopolymer, in combination with the slower crystallisation

effect caused by the increase of the hydrophilic block. Nano-DSC analyses of the resultant particles showed an obvious decrease in crystallinity while increasing the allyl content and the hydrophilic ratio (**Figure S4.23**), confirming our hypothesis. While it was possible to identify the melting temperature (T_m) of functional block copolymers with hydrophilic ratios up to 85.9% (**T6**), very weak or no T_m peak could be noticed for copolymers with higher hydrophilic and allyl-monomer content (**T7 to T11**). For these reasons, very few and small rod-shaped micelles were obtained from the assembly of $PDMA_{328}$-*b*-PCL_{31}-*co*-$PACL_7$ copolymers, which possess high allyl incorporation and large coronal block (**T9**).

Table 4.3. Crystallisation-driven self-assembly of triblock copolymers of $PDMA_w$-*b*-PCL_x-*co*-$PACL_y$ with different core and corona lengths.

Entry	Block copolymer	Hydrophilic block (%)	Allyl units (wt. %)	Aging time[a]	Morphology[b]
T1	$PDMA_{94}$-*b*-PCL_{44}-*co*-$PACL_3$	66.7	6.4	1 wk	Cylinders
T2	$PDMA_{130}$-*b*-PCL_{43}-*co*-$PACL_7$	72.2	14.0	11 wk	Wide-core cylinders
T4	$PDMA_{175}$-*b*-PCL_{47}-*co*-$PACL_3$	77.8	6.0	9 wk	Cylinders
T5	$PDMA_{295}$-*b*-PCL_{56}-*co*-$PACL_4$	83.1	6.7	2 wk	Cylinders
T6	$PDMA_{237}$-*b*-PCL_{36}-*co*-$PACL_3$	85.9	7.7	12 wk	Cylinders
T7	$PDMA_{362}$-*b*-PCL_{46}-*co*-$PACL_8$	87.0	15.4	16 wk	Wide-core cylinders
T8	$PDMA_{350}$-*b*-PCL_{41}-*co*-$PACL_6$	88.1	12.7	20 wk	Cylinders
T9	$PDMA_{328}$-*b*-PCL_{31}-*co*-$PACL_7$	89.6	18.4	10 wk	Rods
T10	$PDMA_{456}$-*b*-PCL_{43}-*co*-$PACL_7$	90.1	14.0	18 wk	Scarf micelles
T11	$PDMA_{412}$-*b*-PCL_{36}-*co*-$PACL_4$	91.2	10.0	18 wk	Scarf micelles

[a] Time between self-assembly and TEM imaging (weeks). [b] Observed by TEM. Samples were negatively stained using uranyl acetate (0.5 wt.%).

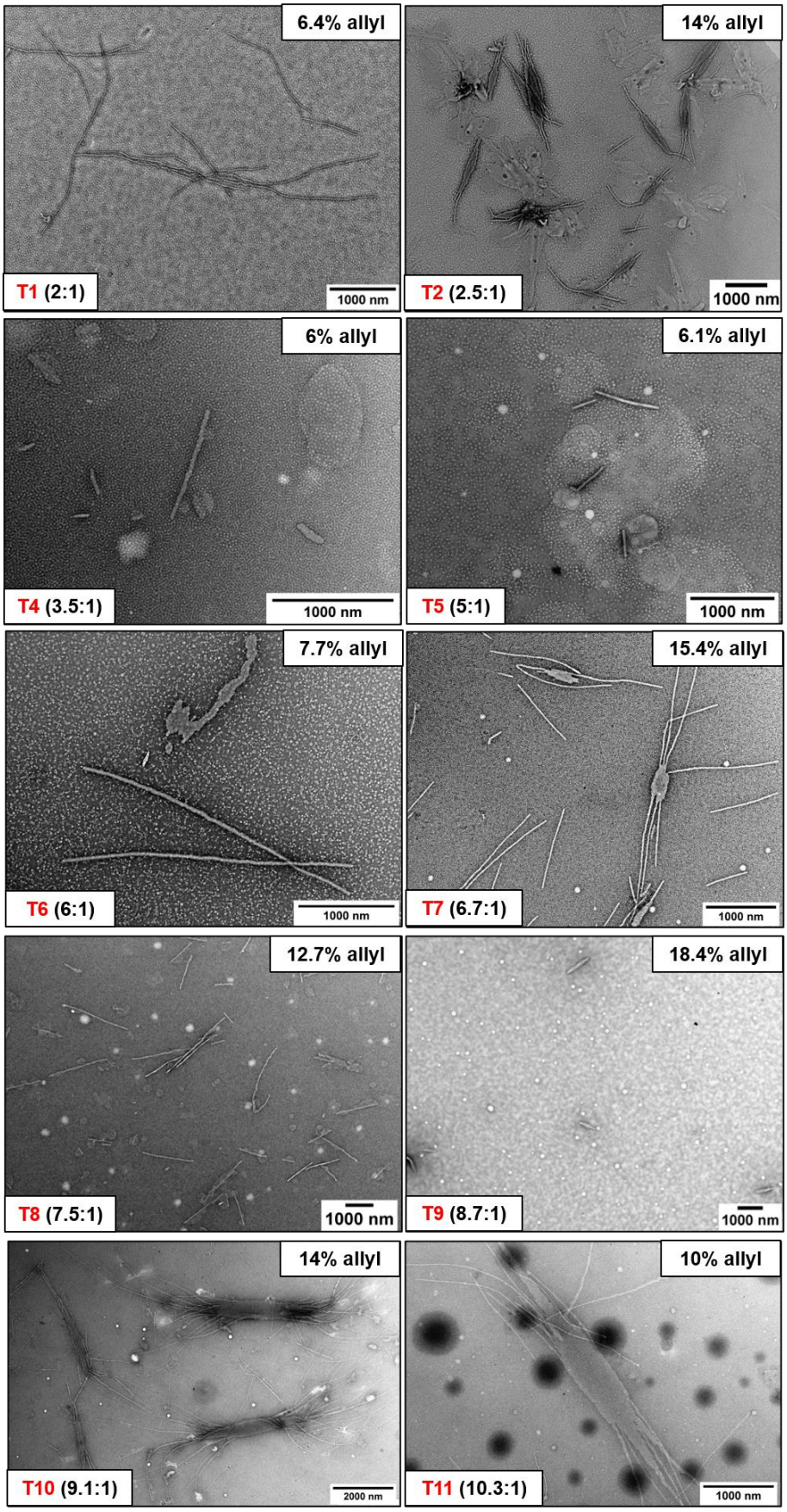


Figure 4.10. Self-assembly of $PDMA_w$-*b*-PCL_x-*co*-$PACL_y$ block copolymers with different corona lengths (Table 4.2). Samples were negatively stained using uranyl acetate (0.5 wt.%).

- *Effect of allyl monomer incorporation on the assembly morphology*

It was observed that the incorporation of allyl pendant groups in the polymer backbone affected the crystallisation of the semicrystalline block causing changes in the morphology of the assemblies obtained. These differences became more pronounced in polymers with high allyl incorporation (allyl wt.% > 10%), since the crystallisation rate of the core-forming block significantly decreases, resulting in structures that lack of clear definition with mixed crystallisation phases. For example, we previously reported how $PDMA_{474}$-*b*-PCL_{49} block copolymers with long corona blocks (corona-to-core ratio of 9.6:1) assembled into hexagonal lamellae structures as a consequence of the increase of the polymer solubility, which slows down the crystallisation of PCL block. As a result, more thermodynamically stable 2D platelet-like micelles are obtained instead of kinetically favoured cylindrical micelles. Therefore, the obtention of pure 2D structures would be expected from the assembly of allyl-functional block copolymers as the crystallisation process is slightly hindered by the amorphous PACL block, leading to longer crystallisation times. However, the assembly of $PDMA_{456}$-*b*-PCL_{43}-*co*-$PACL_7$ block copolymers, with a very similar corona-to-core ratio (9.1:1) to their non-allyl functionalised counterparts, resulted in the formation of scarf-like structures appearing as large platelet micelles ending in cylindrical micelles (**Figure 4.11**). It is theorized that there is a significant reduction in polymer crystallization rates, caused by the introduction of allyl pendant groups, in combination with the high solubility of the BCP in ethanol. This combination of factors significantly led to hybrid micelles containing cylindrical micelles within platelet micelles.[46]

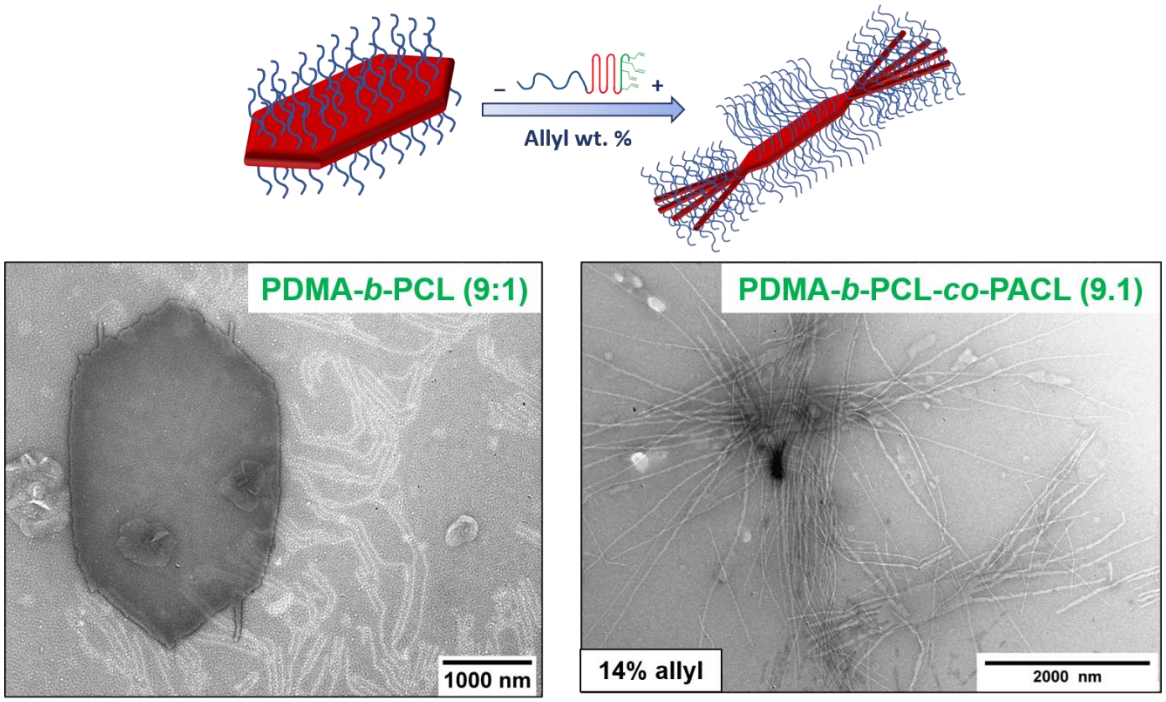


Figure 4.11. TEM images for the self-assembly of $PDMA_{474}$-*b*-PCL_{49} (left) and $PDMA_{456}$-*b*-PCL_{43}-*co*-$PACL_{7}$ (T10, right). Samples were imaged after 1 and 18 weeks respectively. Samples were negatively stained using uranyl acetate (0.5 wt.%), and white marks in TEM images correspond to grid artefacts.

Similar findings were made when comparing PDMA-*b*-PCL-*co*-PACL functional block copolymers with low and high allyl wt.% incorporations while maintaining the corona block length. Since the PCL_x-*co*-$PACL_y$ copolymers were formed by chain growth polymerisation, the sequence of the copolymer is not absolute but a distribution of products. Gody *et al*. studied the probability of monomer placement in chain growth polymerisation and showed how copolymers containing short blocks are more prone to exhibit higher defective chains than copolymers with longer blocks.[47] This suggests that in copolymers with low allyl incorporation there will be chains that contain allyl groups, as well as chains with no allyl units. Consequently, block copolymers with corona-to-core ratios up to 6:1 bearing a low degree of allyl-functionality (< 10% incorporation) were able to undergo fast crystallisation yielding polydisperse cylindrical micelles (Figure **4.12A** and **4.12B**). In contrast, the shape of $PDMA_{130}$-

b-PCL_{43}-*b*-$PACL_7$ and $PDMA_{362}$-*b*-PCL_{46}-*co*-$PACL_8$ micelles, with allyl-monomer inclusions of 14.0% and 15.4% respectively, were not well-defined resulting in cylindrical micelles with a wide core for copolymers with low corona-to-core ratios (Figure **4.12C**) and branched structures with 2D irregular lamellae centres and long cylindrical protrusions (Figure **4.12D**).

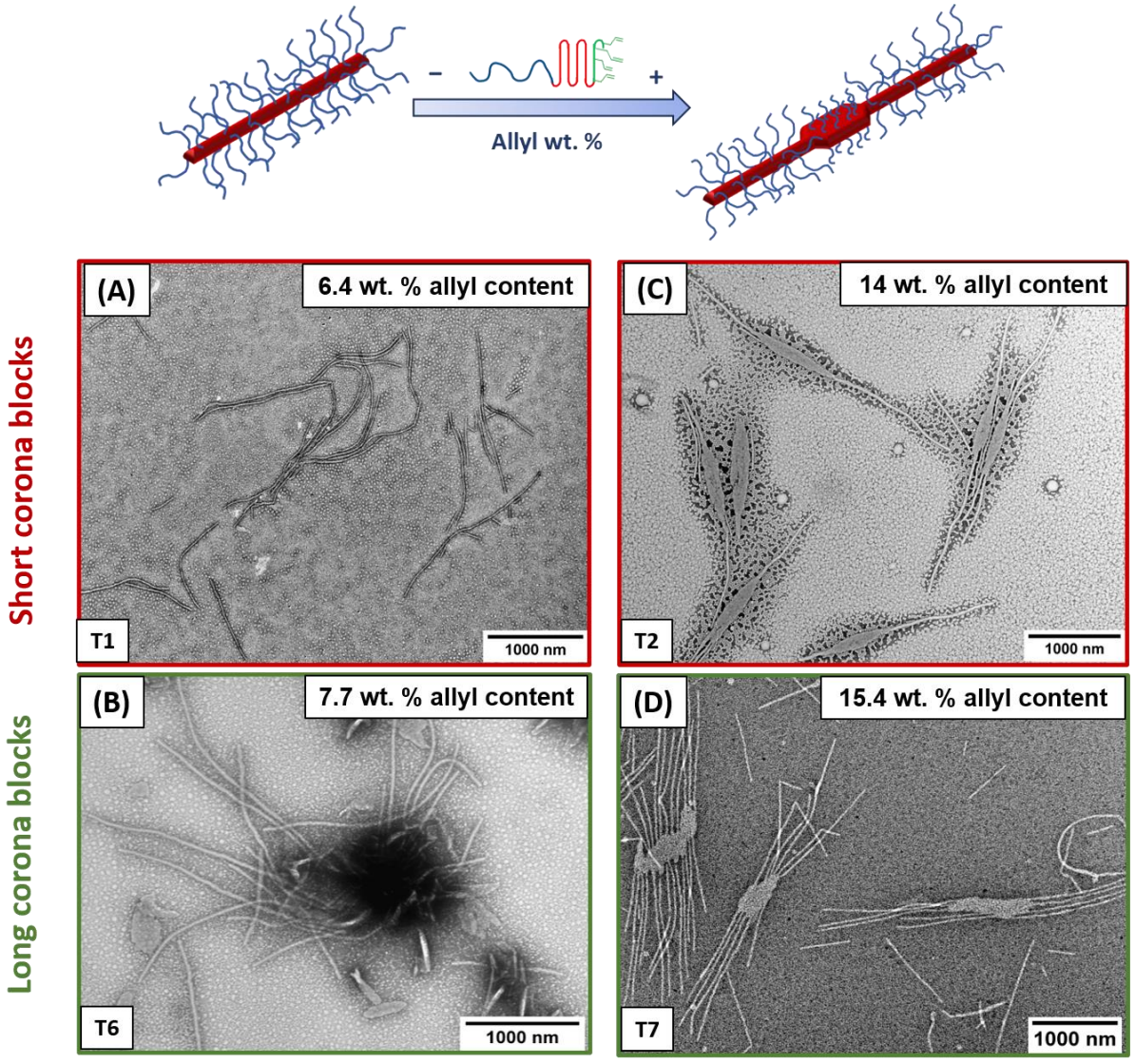


Figure 4.12. Changes in the morphology of $PDMA_w$-*b*-PCL_x-*co*-$PACL_y$ assemblies with increased allyl content (wt.%) maintaining similar corona block length. **A)** Self-assembly of $PDMA_{94}$-*b*-PCL_{44}-*co*-$PACL_3$ (**T1**) and $PDMA_{130}$-*b*-PCL_{43}-*co*-$PACL_7$ (**T2**) block copolymers (red boxes). **B)** Self-assembly of $PDMA_{237}$-*b*-PCL_{36}-*co*-$PACL_3$ (**T6**) and $PDMA_{362}$-*b*-PCL_{46}-*co*-$PACL_8$ (**T7**) block copolymers (green boxes). Samples were negatively stained using uranyl acetate (0.5 wt.%).

To analyse how the corona block length affected the self-assembly of $PDMA_w$-*b*-PCL_x-*co*-$PACL_y$ functional block copolymers, PCL_{43}-*co*-$PACL_7$, containing 14 wt. % of allyl monomer incorporation was chosen as core-forming block and chain extended with DMA to obtain amphiphilic PDMA-*b*-PCL_{43}-*co*-$PACL_7$ with corona-to-core ratios 2:1 and 9:1 (**T2** and **T10**). In agreement with our previous observations, the self-assembly of these BCPs in EtOH after applying a similar heating-cooling-aging process resulted in the formation of mixed morphologies. Whilst block copolymers with 2:1 corona-to-core ratio led to the development of ill-defined cylinders, the self-assembly of block copolymers with PDMA:(PCL-PACL) ratio = 9:1 yielded branched micelles, presented as platelets-like structures ending in cylinders (**Figure 4.13**).

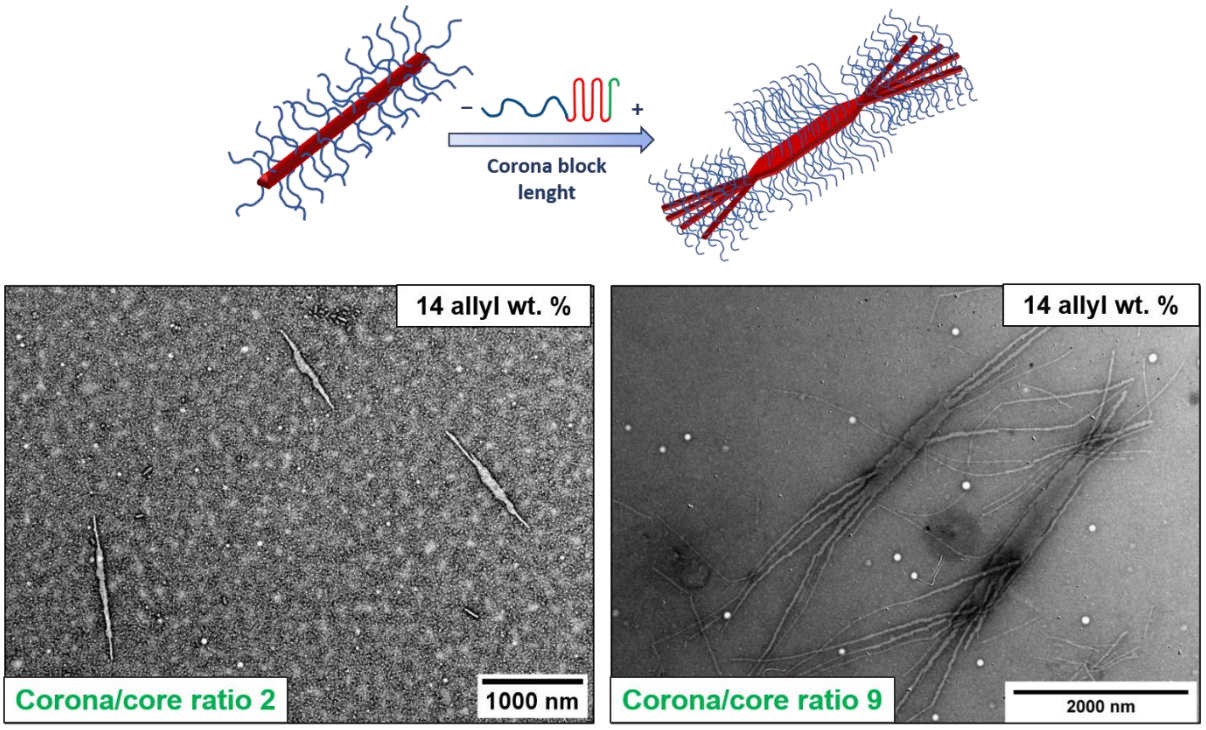


Figure 4.13. Changes in the morphology of $PDMA_w$-*b*-PCL_x-*co*-$PACL_y$ assemblies with increased corona block length maintaining the same allyl content (wt. %). Self-assembly of $PDMA_{130}$-*b*-PCL_{43}-*co*-$PACL_7$ block copolymers (**T2**, left) and $PDMA_{456}$-*b*-PCL_{43}-*co*-$PACL_7$ (**T10**, right). Samples were aged for 11 weeks and 18 weeks respectively. Samples were negatively stained using uranyl acetate (0.5 wt.%).

These studies demonstrated that $PDMA_w$-*b*-PCL_x-*co*-$PACL_y$ polymers with less than 10% degree of functionalisation and low corona-to-core ratios assembled in more uniform structures.

- *Effect of the PMMA block during self-assembly.*

Previous reports showed higher aqueous stability of particles when a small hydrophobic block was introduced between the corona and PCL-core blocks. However, no observations were made regarding the effect of the PMMA block on the self-assembly morphology, since amphiphilic PDMA-*b*-PCL copolymers follow a rapid crystallisation yielding well-defined cylindrical micelles in short aging times.[37]

As previously mentioned, the hydrophilic/hydrophobic content is a key parameter during the self-assembly of $PDMA_w$-*b*-PCL_x-*co*-$PACL_y$ block copolymers, as it regulates the solubility degree of the polymer, which has a direct effect on the crystallisation kinetics. PMMA, being an amorphous hydrophobic polymer, will not contribute to the crystallinity of the core-forming block. However, it will make the polymer less soluble, increasing the solvophobic content of the polymer. Consequently, the crystallisation rate will be enhanced and therefore should drive the formation of kinetically favoured assemblies (cylindrical micelles) rather than 2D structures or mixed morphologies. To prove this, a series of $PDMA_w$-*b*-$PMMA_n$-*b*-PCL_x-*co*-$PACL_y$ with corona-to-core ratios varying from 1:1 to 9:1 and a fixed PMMA block length (DP = 20) were synthesised (**Table 4.4** and **Table S4.1**). Self-assembly of these copolymers in ethanol following the same heating-cooling conditions previously employed resulted in the formation of cylindrical micelles for all block copolymers, even those with long corona block lengths (**M5** in Table 4.4), which confirmed our theory (**Figure 4.14**). In agreement with our previous observations, the self-assembly of copolymers bearing allyl % incorporations higher than 10% (**M3** and **M4** in Table 4.4) resulted in shorter and less defined cylinders.

Table 4.4. CDSA of block copolymers of $PDMA_w$-*b*-$PMMA_n$-*b*-PCL_x-*co*-$PACL_y$ with different core and corona lengths.

Entry	Diblock copolymer	Corona:core ratio[a]	Hydrophilic block (%)	Allyl units (wt. % core)	Aging time[b]
M1	$PDMA_{57}$-*b*-$PMMA_{20}$-*b*-PCL_{38}-*co*-$PACL_4$	1:1	47.9	6.4	2 wk
M2	$PDMA_{156}$-*b*-$PMMA_{20}$-*b*-PCL_{54}-*co*-$PACL_3$	2:1	66.9	3.9	1.5 wk
M3	$PDMA_{233}$-*b*-$PMMA_{19}$-*b*-PCL_{43}-*co*-$PACL_7$	3.4:1	77.1	10.1	13 wk
M4	$PDMA_{330}$-*b*-$PMMA_{18}$-*b*-PCL_{46}-*co*-$PACL_8$	6.4:1	82.0	11.1	14 wk
M5	$PDMA_{348}$-*b*-$PMMA_{20}$-*b*-PCL_{36}-*co*-$PACL_4$	9.2:1	85.3	6.7	16 wk

[a] Ratio between the PDMA block (corona) and the PMMA-*b*-PCL-*co*-PACL BCP (core) obtained from ^{1}H NMR spectroscopy. [b] Time (weeks) between self-assembly and TEM imaging.

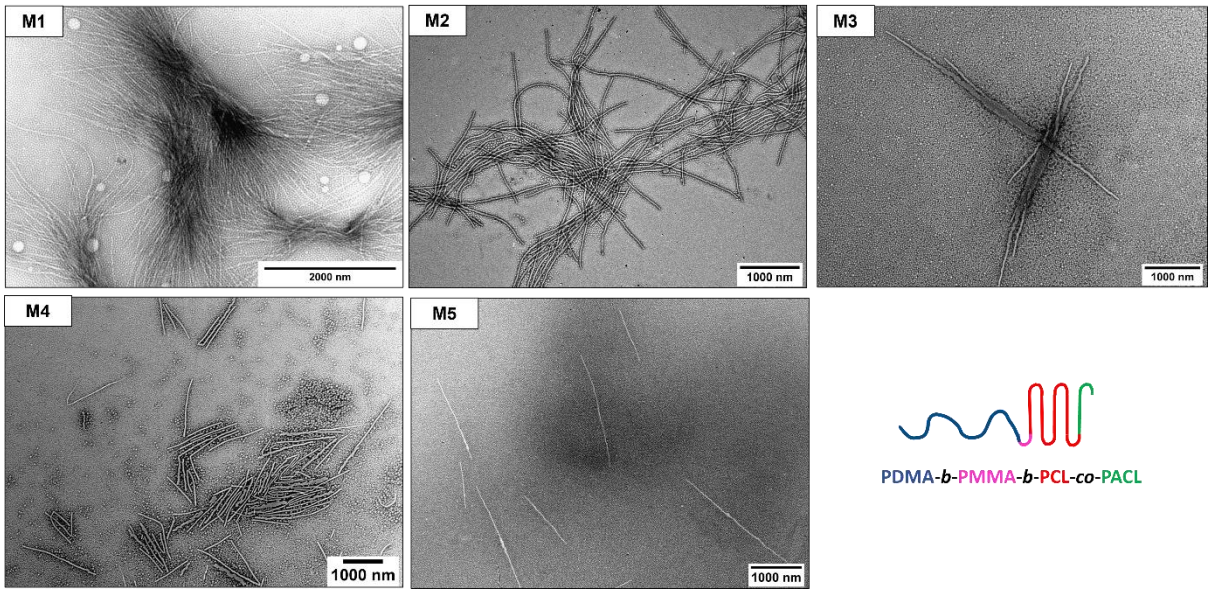


Figure 4.14. Self-assembly of $PDMA_w$-*b*-$PMMA_n$-*b*-PCL_x-*co*-$PACL_y$ block copolymers with different corona lengths (Table 4.4). Samples were negatively stained using uranyl acetate (0.5 wt.%).

The growth of $PDMA_w$-*b*-$PMMA_n$-*b*-PCL_x-*co*-$PACL_y$ cylindrical micelles was further explored. Assembled morphologies of $PDMA_{57}$-*b*-$PMMA_{20}$-*b*-PCL_{38}-*co*-$PACL_4$ (**M1**) were captured by TEM at various aging times (1 week, 4 weeks and 11 weeks) and an analysis of the morphological changes over time were made (**Figure 4.15**). After 1 week of aging at room temperature cylindrical micelles of short lengths and spherical micelles were observed. After 4 weeks, significant growth in micelle length was highlighted. However, the micelle growth became evident after 11 weeks of aging, where several micron well-defined cylinders were found by TEM imaging.

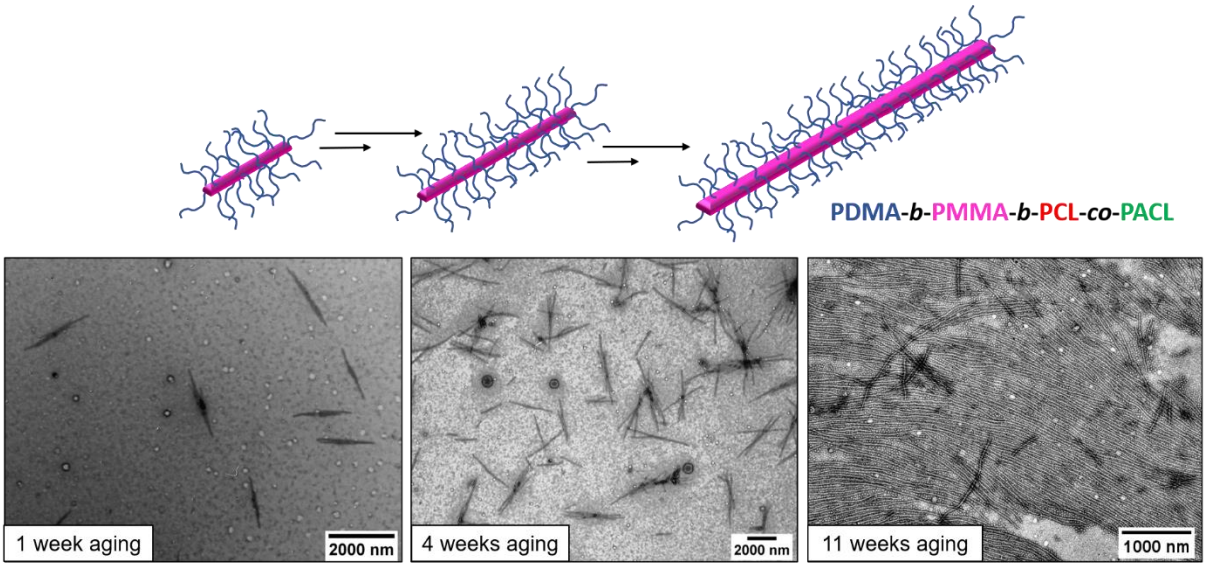


Figure 4.15. Growth over time of cylindrical micelles from $PDMA_{57}$-*b*-$PMMA_{20}$-*b*-PCL_{38}-*co*-$PACL_4$ (**M1**). Samples were negatively stained using uranyl acetate (0.5 wt.%).

4.2.3.1.2 Crystallisation-driven self-assembly of benzyl functionalised block copolymers.

Following the self-assembly studies of PCL-based block copolymers bearing allyl pendant groups, the CDSA process of these block copolymers after the conjugation of benzyl mercaptan *via* thiol-ene addition was explored. Self-assembly of benzyl-functionalised polymers was carried out in ethanol, following the same heating-cooling conditions previously as for PDMA-

b-PCL and PDMA-*b*-PCL-*co*-PACL polymers, to yield polydisperse structures with diverse morphologies depending on the polymer composition and the degree of conjugation (**Figure 4.16** and **Table S4.3**).

Initial studies showed the attachment of benzyl mercaptan units to the core-forming block triggered a general transition from non-defined 1D morphologies to well-defined 2D lamellae structures. All benzyl-functionalised polymers with short allyl blocks (Thiol-T1, -T4, -T5 and -T11 in Tables S4.2 and S4.3) resulted in non-defined cylindrical micelles with a wide inner core, in contrast to their allyl counterparts that assembled into defined cylinders (**Figures 4.17A** and **4.17B**). To our surprise, unlike non-modified polymers, where ill-defined or mixed structures were achieved from polymers bearing high allyl incorporation and/or high coronal block length, benzyl-conjugated PCL-based copolymers with high allyl content and large corona-to-core ratios (Thiol-T2, -T7 and -T10 in Table S4.2) formed well-defined 2D platelets in ethanol (**Figures 4.17C** and **4.17D**). The obtention of 2D morphologies with increasing benzyl incorporation, particularly in block copolymers with lower corona-to-core ratios was unexpected, considering the studies previously done with allyl-functionalised PCL copolymers and the nano DSC analyses, which showed a decrease in intensity of the melting temperature (T_m) peak for functionalised polymers, indicating lower crystallinity degree of benzyl-functionalised structures compared to their allyl counterparts (purple and black lines respectively, in **Figure 4.18** and **Figure S4.24**).

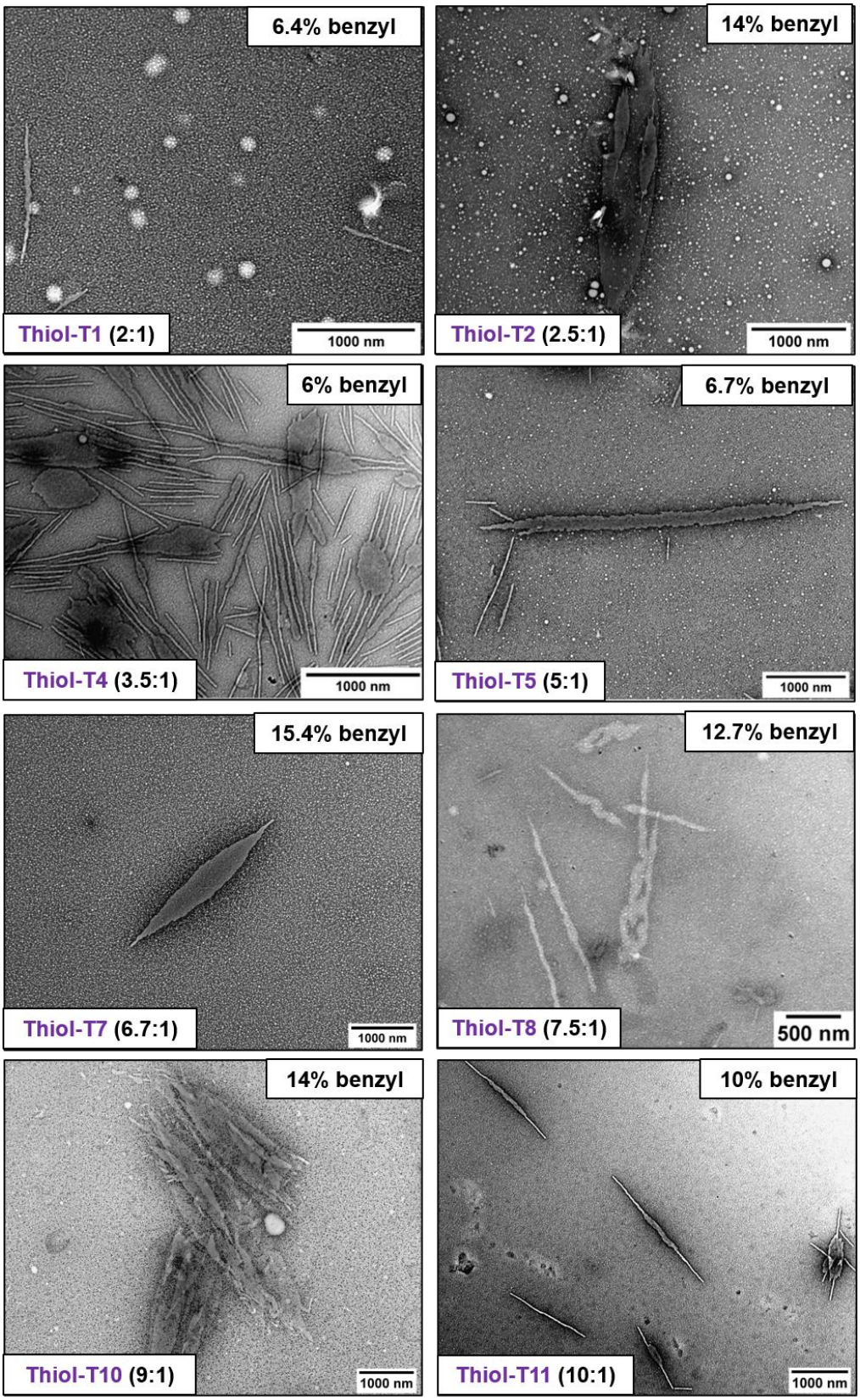


Figure 4.16. Self-assembly of benzyl functionalised $PDMA_w$-*b*-PCL_x-*co*-$PACL_y$ block copolymers with different corona lengths (Table S4.3). Samples were negatively stained using uranyl acetate (0.5 wt.%). White spots correspond to grid artefacts.

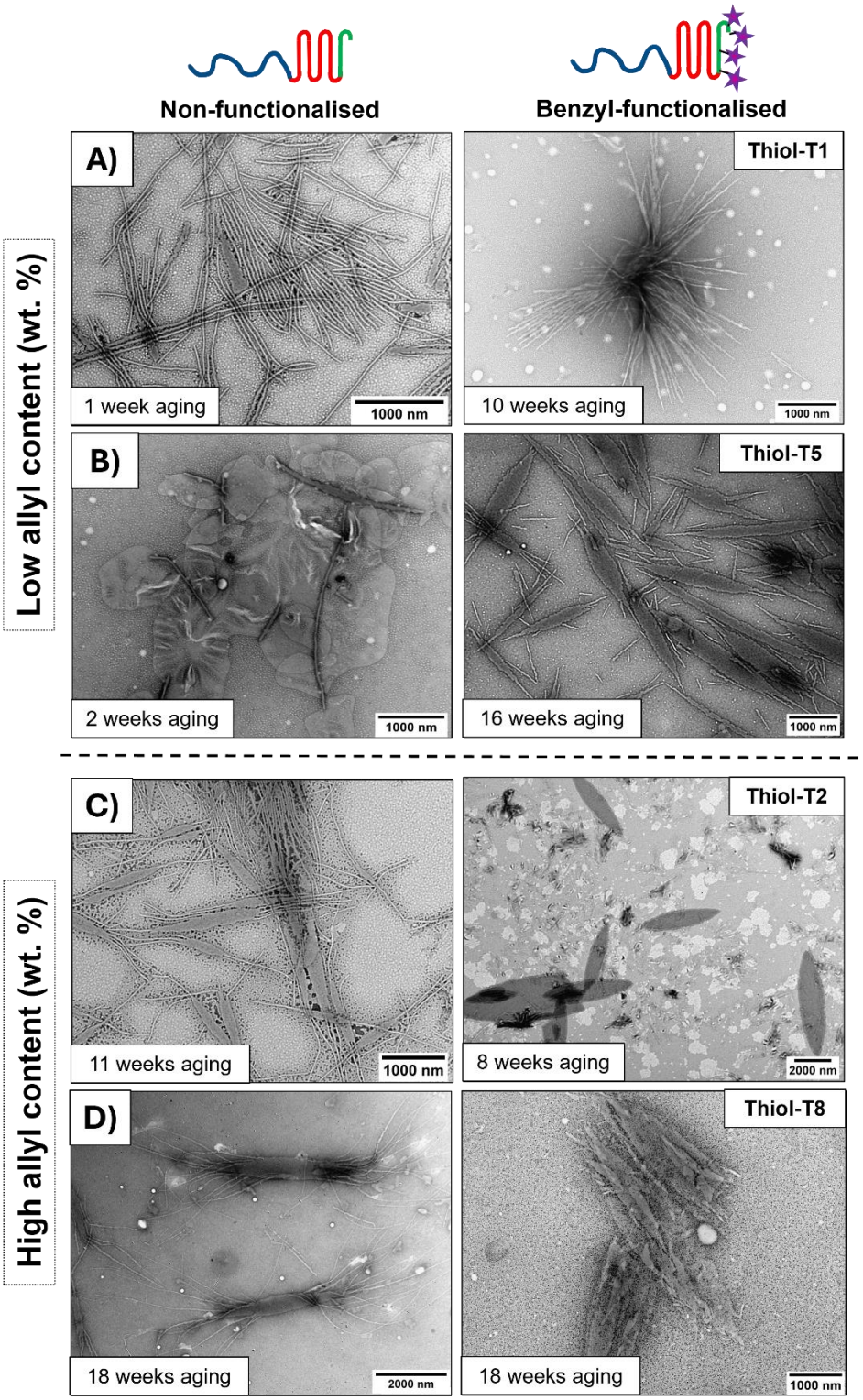


Figure 4.17. A) Self-assembly of T1 (left) and Thiol-T1 (right). **B)** Self-assembly of T5 (left) and Thiol-T5 (right). **C)** Self-assembly of T2 (left) and Thiol-T2 (right). **D)** Self-assembly of T10 (left) and Thiol-T10 (right). All samples were 100% functionalized. Samples were negatively stained using uranyl acetate (0.5 wt.%). White spots correspond to grid artefacts.

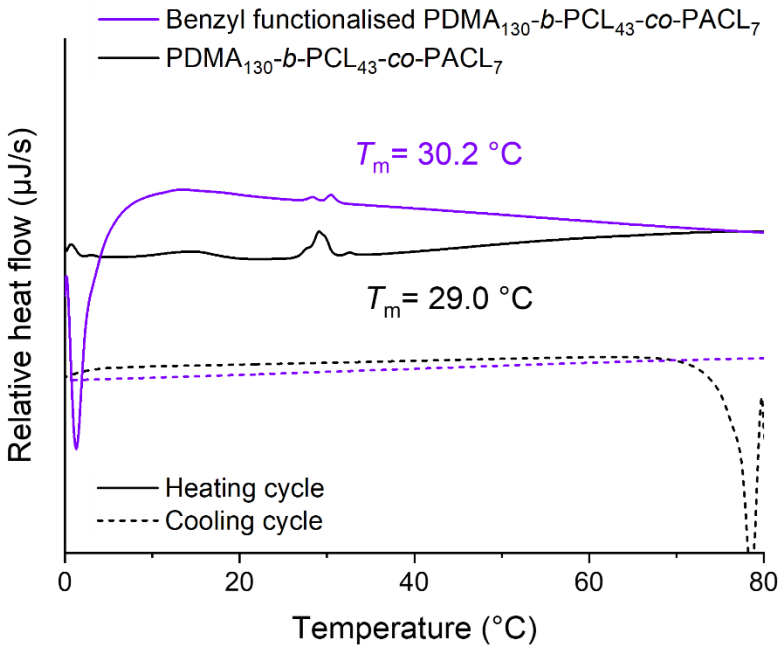


Figure 4.18. Nano DSC thermograms of $PDMA_{130}$-*b*-PCL_{43}-*co*-$PACL_7$ and benzyl conjugated $PDMA_{130}$-*b*-PCL_{43}-*co*-$PACL_7$ assemblies (**T2** and **Thiol-T2**, respectively) (100 to 0 °C, 1 °C min^{-1}) at a conc. = 5 mg mL^{-1}, showing the first heating-cooling cycle.

As an attempt to elucidate the mechanism of growth of 2D nanostructures from benzyl conjugated BCPs, we next studied how copolymers behave with different % benzyl conjugation. For this, $PDMA_{362}$-*b*-PCL_{46}-*co*-$PACL_8$ (**Thiol-T7**) and $PDMA_{412}$-*b*-PCL_{36}-*co*-$PACL_4$ (**Thiol-T11**) with 50% and 100% of benzyl attachment were prepared (**Figures S4.25** and **S4.26**). More kinetically favoured morphologies were observed from the assembly in ethanol of polymers with 50% benzyl conjugation, while small protuberances can be seen on micelles obtained from Thiol-T11, cylindrical micelles fused on 2D sheets were observed for Thiol-T7 with higher allyl content. However, well-defined 2D nanoplatelets and more crystalline non-defined structures were obtained for the self-assembly of 100% functionalised Thiol-T7 and Thiol-T11 respectively, which indicated that the benzyl group significantly affected the self-assembly. These results made us believe that the benzyl groups could be interacting through π-π interactions during the self-assembly process,[48] changing crystal packing and leading to

the formation of 2D platelets rather than branched structures containing mixed morphologies (**Figure 4.19**).

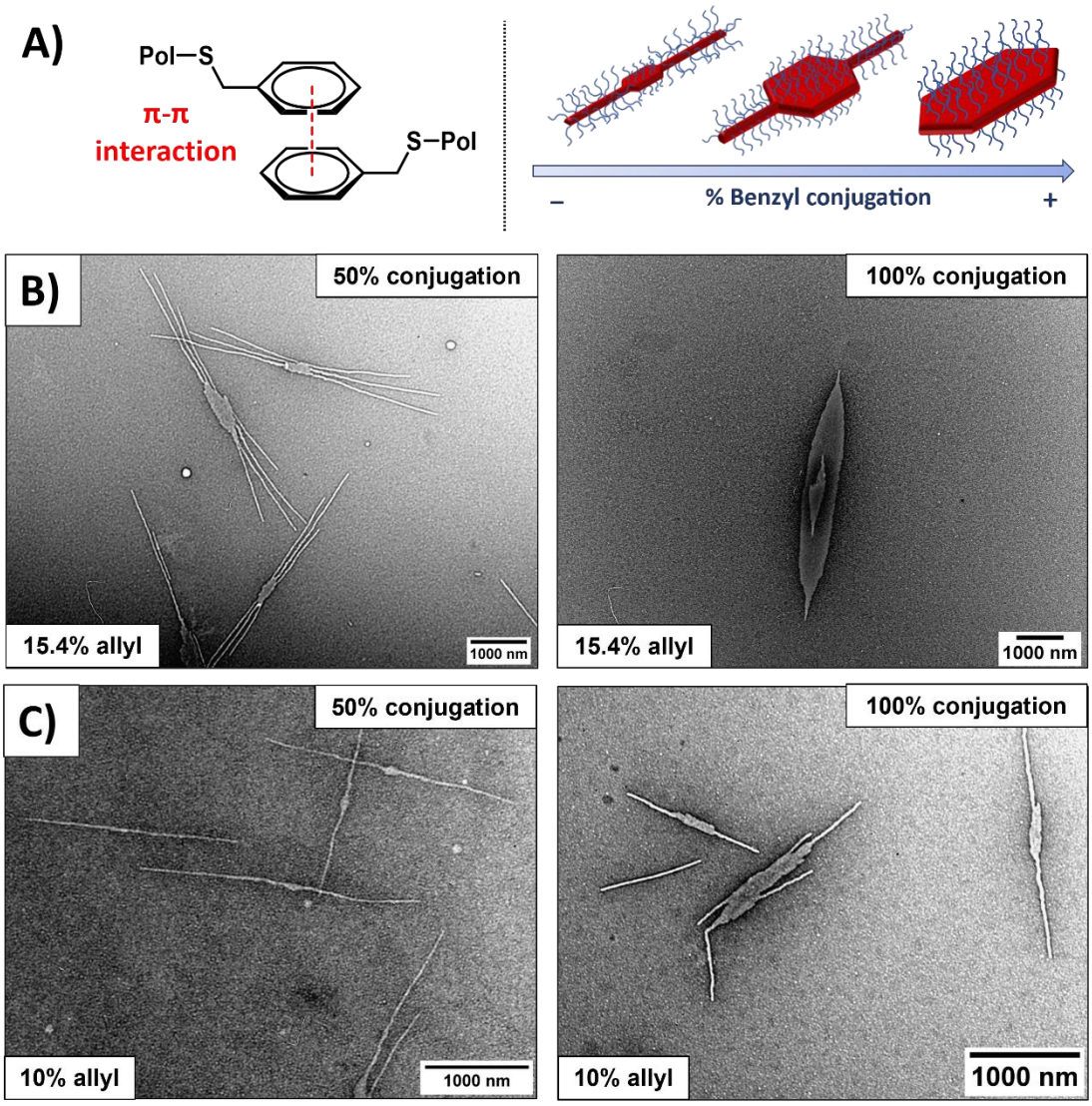


Figure 4.19. Changes in nanostructure morphology with the increase of benzyl conjugation (%). **A)** Schematic illustration of hypothesised benzyl groups effect during self-assembly. **B)** Self-assembly of benzyl functionalised $PDMA_{362}$-*b*-PCL_{46}-*co*-$PACL_8$ (**Thiol-T7**) with 50% conjugation (left) and 100% conjugation (right). **C)** Self-assembly of benzyl functionalised $PDMA_{412}$-*b*-PCL_{36}-*co*-$PACL_4$ (**Thiol-T11**) with 50% conjugation (left) and 100% conjugation (right). All samples were aged for 18 weeks before imaging. Samples were negatively stained using uranyl acetate (0.5 wt.%).

Finally, to evaluate if similar trends occurred with BCPs containing a short PMMA intermediate block, the assembly of benzyl conjugated PDMA$_w$-*b*-PMMA$_n$-*b*-PCL$_x$-*co*-PACL$_y$ block copolymers was explored (**Thiol-M1 to M4** in Table S4.2). TEM analyses showed a transition from defined several micron-long cylindrical micelles to platelet-like micelles was observed when using copolymers with increasing benzyl units and corona block lengths (**Figure 4.20**). Unlike their non-modified analogues, the incorporation of benzyl groups within the core-forming block led preferentially to the formation of 2D platelet-like morphologies compared to 1D polydisperse cylindrical structures. These observations were consistent with earlier findings; however, further investigation is required to elucidate the effects of benzyl ring moieties during CDSA of PCL-based copolymers.

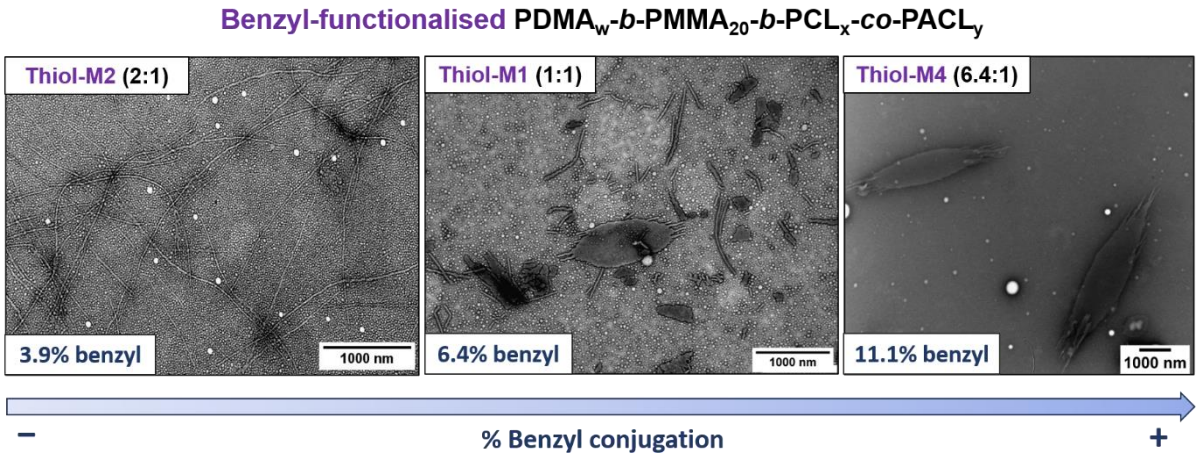


Figure 4.20. Self-assembly of benzyl functionalised PDMA$_{156}$-*b*-PMMA$_{20}$-*b*-PCL$_{54}$-*co*-PACL$_3$ (**Thiol-M2**), benzyl functionalised PDMA$_{57}$-*b*-PMMA$_{20}$-*b*-PCL$_{38}$-*co*-PACL$_4$ (**Thiol-M1**) and benzyl functionalised PDMA$_{330}$-*b*-PMMA$_{18}$-*b*-PCL$_{46}$-*co*-PACL$_8$ (**Thiol-M4**). Samples were aged for 2, 3 and 6 weeks before imaging respectively. Samples were negatively stained using uranyl acetate (0.5 wt.%). White spots correspond to grid artefacts.

4.2.4 Exploring the optimal conditions for CDSA of PCL-based copolymers.

In the preceding section, it was demonstrated how 1D and 2D structures could be achieved from the solution self-assembly of PDMA-*b*-PCL-based BCPs featuring diverse functionalities. It was found that the architecture of the resultant assemblies could be predicted considering the copolymer composition, allyl block content and degree of benzyl conjugation. However, a lack of consistency over the morphology obtained and considerable high aging times (t_{aging} > 2 weeks) were observed for all block copolymers with long corona block lengths and high allyl-functionality incorporation. The crystallisation of polymers can be influenced by several factors such as temperature,[49] solvents,[50] polymer composition,[51] and the presence of additives[52]. In this section, the self-assembly of PCL-based copolymers in various solvents, including ethanol (EtOH), methanol (MeOH) and isopropyl alcohol (IPA) under different aging temperatures was investigated.

4.2.4.1 Temperature of aging and cooling rates

Semicrystalline polymers are characterised for having a melting temperature (T_m) and a crystallisation temperature (T_c). These temperatures indicate when the crystalline chains of a polymer melt and re-crystallised, respectively. During CDSA, the amphiphilic block copolymers are first dissolved in a solvent by heating the polymer solution above the T_m, followed by cooling down below the T_c of the polymer. This allows the semicrystalline polymer chains to fold in an orderly manner, leading to the formation of primary crystalline nuclei and subsequent nanostructure growth. However, functional-PCL block copolymers possess low T_c and degree of crystallinity, resulting in slow crystallisation rates and long aging times at room temperature. Based on this, it was hypothesized that aging the polymeric solutions at low temperatures could promote higher degrees of supersaturation, which increases the

crystallisation rate and therefore, decreases the self-assembly aging time. Consequently, control over particle morphology could be potentially achieved as more kinetically favoured structures (1D cylinders over 2D platelets) could be obtained.

To confirm this theory, the assembly of $PDMA_w$-*b*-PCL_x copolymers with long corona-to-core ratios in ethanol was first investigated, as initial self-assembly studies yielded structures with mixed morphologies. For this, a suspension of $PDMA_{204}$-*b*-PCL_{49}, $PDMA_{309}$-*b*-PCL_{49} and $PDMA_{474}$-*b*-PCL_{49} with corona-to-core ratios 4.2:1, 6.3:1 and 9.6:1 respectively, in EtOH was heated at 70 °C for 3 h. After this time, the dissolved polymer solutions were left to age in a fridge at 4 °C. After one week of aging, the presence of large micelles for the three polymers was observed by TEM analyses (**Figure 4.21**). As expected, self-assembly at low temperature of $PDMA_{204}$-*b*-PCL_{49} resulted in the formation of long well-defined micelles with cylindrical morphology, whereas at room temperature scarf-like micelles were obtained. Moreover, $PDMA_{309}$-*b*-PCL_{49} and $PDMA_{474}$-*b*-PCL_{49} block copolymers, which assembled into 2D platelet-like and hexagonal platelet micelles at room temperature, formed hybrid structures composed of long cylindrical micelles fused into smaller platelet micelles when aged at 4 °C.

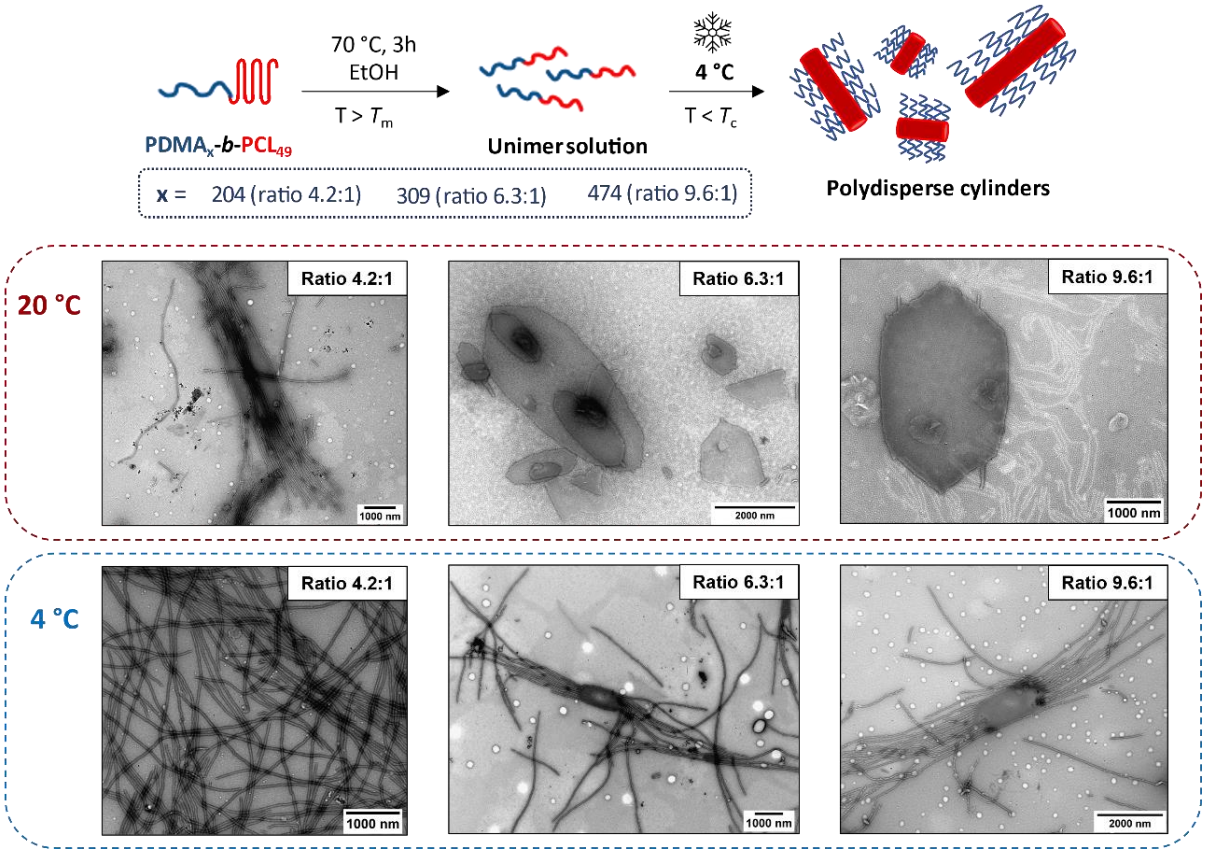


Figure 4.21. Self-assembly of PDMA$_x$-*b*-PCL$_{49}$ block copolymers with corona:core ratios of 4.2:1, 6.3:1 and 9.6:1 after one week of aging at room temperature (20 °C) (up) and in the fridge (4 °C) (down). Samples were negatively stained using uranyl acetate (0.5 wt.%).

The effect of the temperature during self-assembly was then explored in allyl-functional PCL copolymers bearing long corona-to-core ratios (**T10** and **T11)**. Similarly, 1D cylindrical micelles were achieved in both cases after 2 weeks of aging at 4 °C, compared to scarf-like morphology obtained after 18 weeks while aging at 20 °C (**Figure 4.22**). Furthermore, comparable trends were observed for the rest of PDMA$_w$-*b*-PCL$_x$-*co*-PACL$_y$ and PDMA$_w$-*b*-PMMA$_n$-*b*-PCL$_x$-*co*-PACL$_y$ block copolymers (**Figures S4.27** and **S4.28**). These results suggested that cooling the assemblies promotes shorter aging times and underscores the potential impact of the temperature on the morphology.

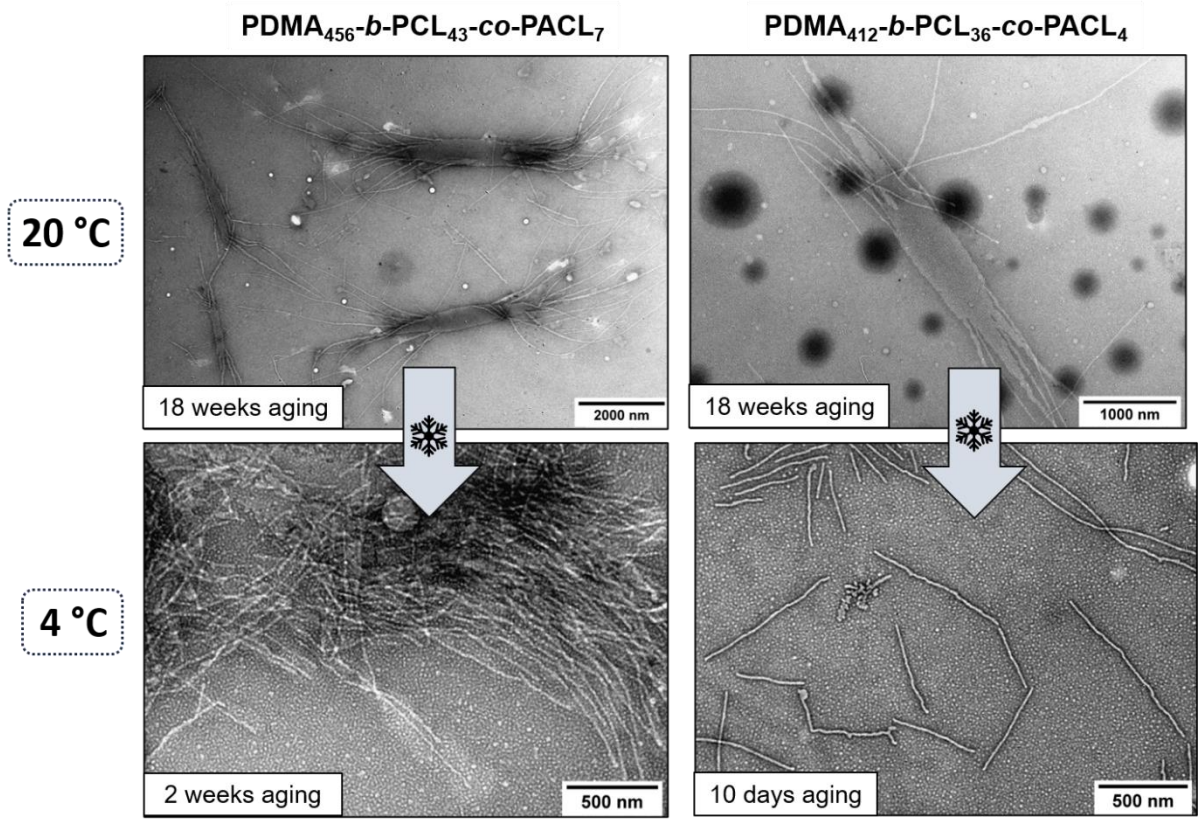


Figure 4.22. TEM micrographs of $PDMA_{456}$-*b*-PCL_{43}-*co*-$PACL_7$ (**T10**, left) and $PDMA_{412}$-*b*-PCL_{36}-*co*-$PACL_4$ (**T11**, right) at room temperature (20 °C) (up) and in the fridge (4 °C) (down). Samples were negatively stained using uranyl acetate (0.5 wt.%).

After the promising results obtained with PDMA-*b*-PCL and PDMA-*b*-PCL-*co*-PACL copolymers, the effect of aging temperature on the self-assembly of benzyl functionalized block copolymers was explored. In this case, we focused on functional amphiphilic block copolymers with low benzyl % incorporation, since ill-defined micelles were obtained during their assembly at room temperature (20 °C). Therefore, benzyl conjugated $PDMA_{122}$-*b*-PCL_{53}-*co*-$PACL_3$ (**Thiol T1**), $PDMA_{237}$-*b*-PCL_{36}-*co*-$PACL_3$ (**Thiol T6**) and $PDMA_{412}$-*b*-PCL_{36}-*co*-$PACL_4$ (**Thiol T11**) were self-assembled in ethanol at 4 °C. Significantly longer and higher number of semicrystalline nanostructures were formed after 3 weeks and 14 weeks of aging at low temperatures from **Thiol T1** and **Thiol T6** polymers respectively (**Figure 4.23A-D**). The obvious increase in crystallisation rates caused by the decrease in temperature can be observed in the self-

assembly of **Thiol T11**, where structures with mixed morphologies were only noticed after 18 weeks of aging at room temperature, while some crystalline ill-defined cylindrical micelles were obtained after 1 week aging at 4 °C (**Figure 4.23E-F**). Interestingly, the self-assembly of benzyl functionalised polymers usually resulted in less defined 1D cylindrical micelles compared to their non-functionalised counterparts. This could happen because of the presence of a higher number of crystal defects caused by the increase in the crystallisation rate.

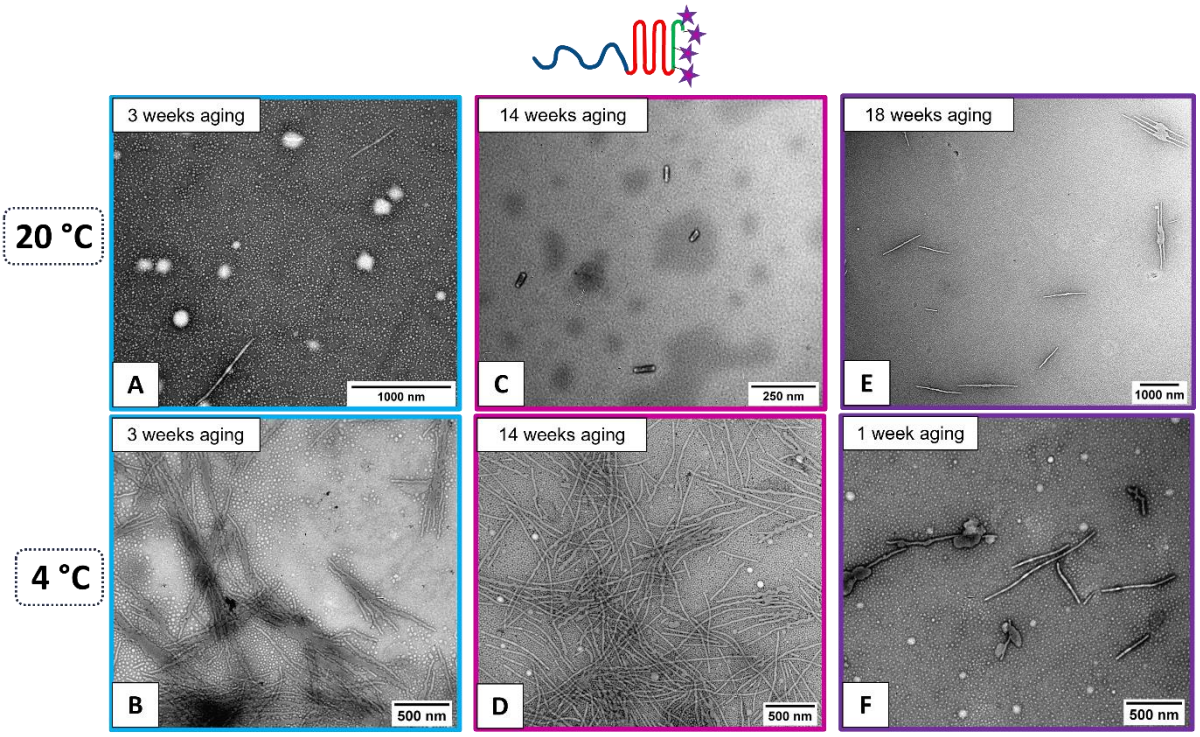


Figure 4.23. A-B) TEM micrographs of **Thiol-T1** aged at 20 °C and 4 °C respectively (light blue box). **C-D)** TEM micrographs of **Thiol-T6** aged at 20 °C and 4 °C respectively (pink box). **E-F)** TEM micrographs of **Thiol-T11** aged at 20 °C and 4 °C respectively (purple box). Samples were negatively stained using uranyl acetate (0.5 wt.%) and analysed at a conc. = 5 mg mL^{-1}.

To gain further insights into these self-assembly observations, **T1** and **M4** whose assembly at ambient temperature resulted in the formation of cylindrical structures, were assembled at 4 °C. In agreement with previous observations, while changes in morphology were not observed, crystalline cylindrical structures were formed faster (**Figure 4.24**). These experiments suggested that low aging temperatures favour the crystallisation of the semicrystalline PCL-based block during assembly, leading to the obtention of preferentially 1D kinetically stable morphologies in higher quantities and significatively shorter times compared to the assemblies obtained at room temperature.

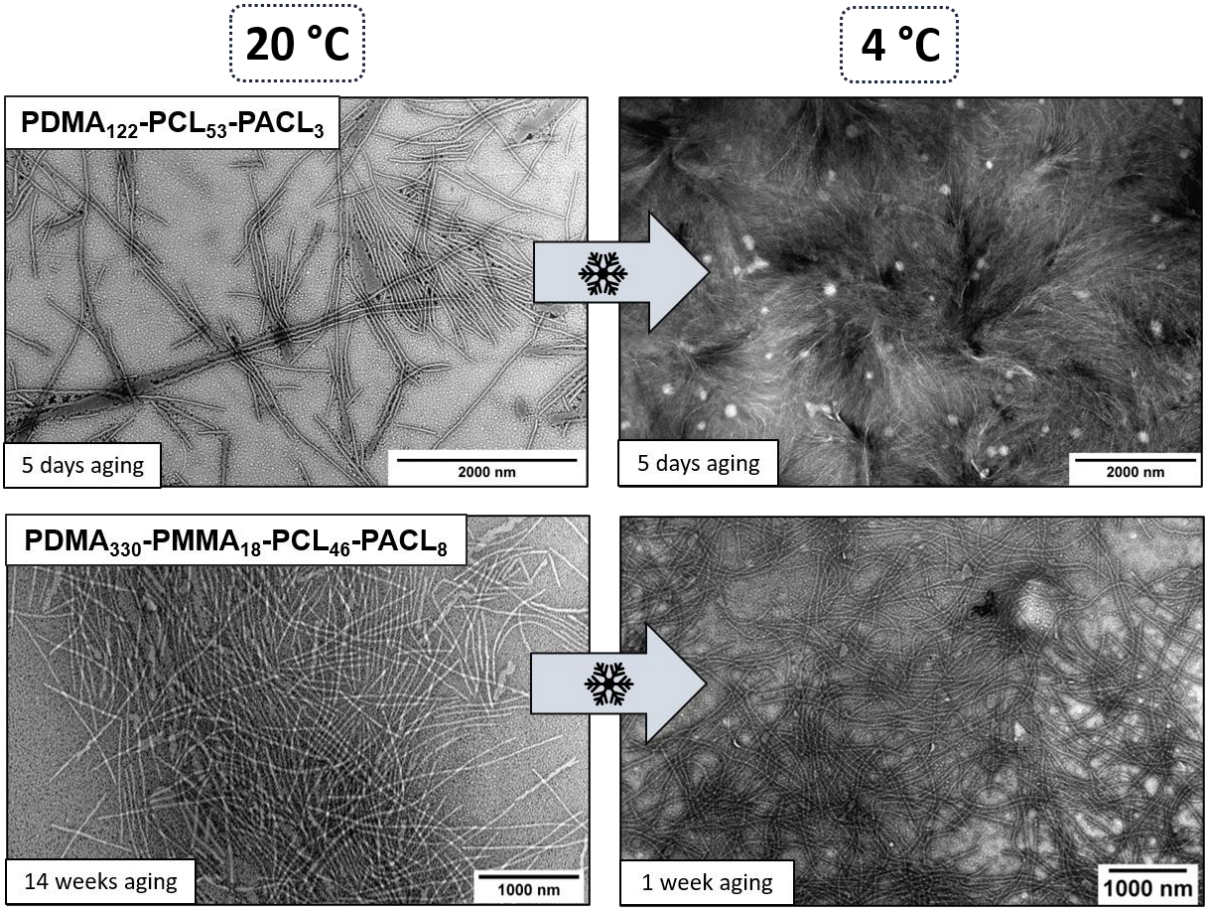


Figure 4.24. Effect of aging temperature on the quantitative appearance. TEM micrographs of $PDMA_{122}$-*b*-PCL_{53}-*co*-$PACL_3$ (**T1**, up) and $PDMA_{330}$-*b*-$PMMA_{18}$-*b*-PCL_{46}-*co*-$PACL_8$ (**M4**, down) at room temperature (20 °C) (left) and in the fridge (4 °C) (right). Samples were negatively stained using uranyl acetate (0.5 wt.%) and analysed at a conc. = 5 mg mL^{-1}.

In previous reports,[53] Manners and Winnik explored the influence of cooling rate on the micelle morphology for PFS-based block copolymers (PFS = poly(ferrocenyldimethylsilane)). They showed faster cooling rates led to more branched structures, whereas elongated fibre-like micelles were obtained by slow cooling. Inspired by these studies, to obtain a broader perspective on the role of temperature and cooling rate in CDSA, $PDMA_{89}$-*b*-PCL_{39}-*co*-$PACL_3$ was assembled in ethanol at 20 °C and 4 °C employing two different cooling rates and the thermodynamic parameters of the assemblies were assessed *via* nano-DSC. All four self-assembly experiments were performed following the same heating conditions as previously reported. After heating for 3 h, two vial solutions were immediately removed from the oil bath and were stored in the fridge and at room temperature respectively (fast cooling down rate). On the contrary, the other two self-assembly vials were left inside the oil bath (T_0 = 70° C) to cool down to room temperature in a slow fashion, afterwards, one sample was stored in the fridge (4 °C) whereas the other one was left at room temperature (slow cooling down rate). Nano DSC analysis after 2 weeks of aging showed slight differences in crystallinity between the samples. Similar melting and crystallisation temperatures were present in the first heating-cooling cycle for all samples, T_m = 24.1–24.5 °C and T_c = 8.5–8.9 °C. Moreover, slight increases in the enthalpy and entropy of melting ($\Delta H_{melting}$ = 218.4 and 229.8 KJ mol^{-1} and $\Delta S_{melting}$ = 0.721 and 0.77 KJ mol K^{-1} at 20 and 4 °C respectively) of polymeric assemblies were observed in samples subjected to low temperatures (**Figure S4.29**). This indicated that greater amounts of unimer crystallised during the self-assembly at 4 °C rather than at ambient temperature. Even though the different cooling rates showed no significant thermodynamic differences, they appeared to play a key role in the resultant crystal definition. Samples cooled down in a slow fashion resulted in more defined cylinders than those cooled down radically, which appeared as short ill-shaped cylinders (**Figure 4.25**). These results demonstrated that

the temperature of aging and the cooling rates crucially affect the self-assembly process. Low temperatures and fast cooling lead to more crystalline but less defined structures, whereas longer cylindrical micelles with higher definition were obtained after slow cooling and aging at room temperature.

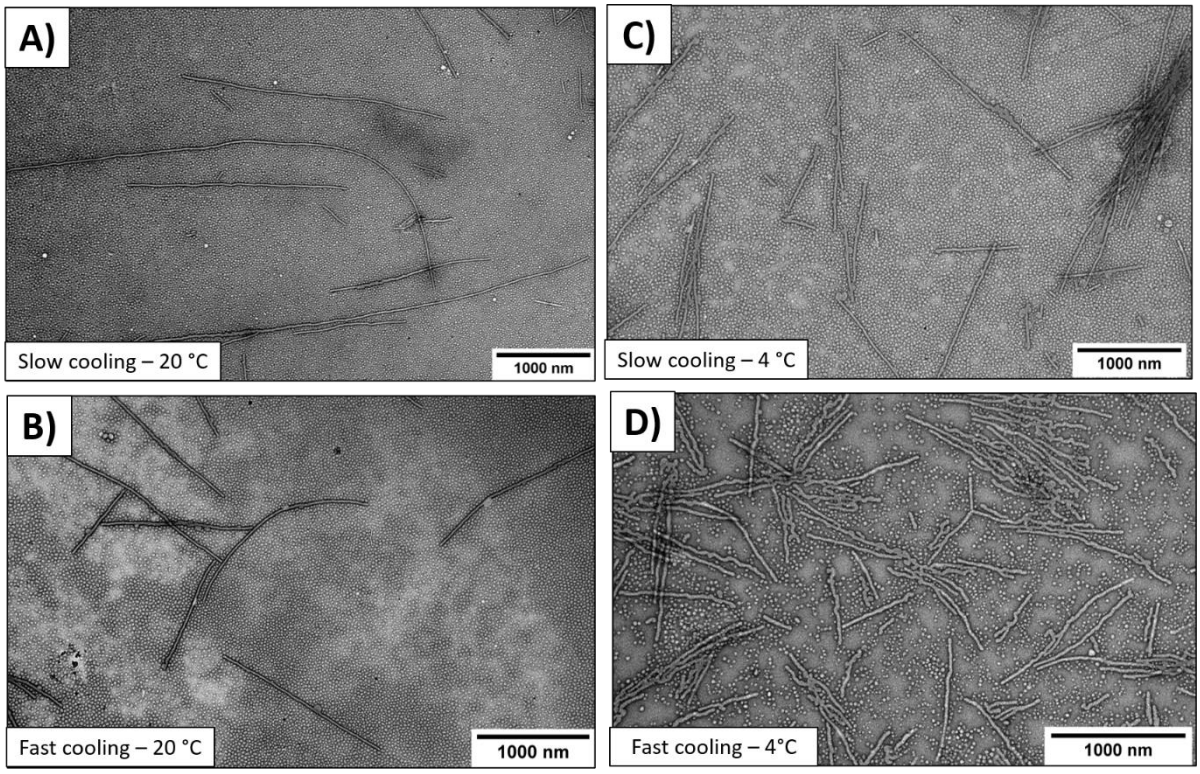


Figure 4.25. TEM micrographs of $PDMA_{89}$-*b*-PCL_{39}-*co*-$PACL_3$ cylindrical micelles. **A)** slow cool down to T < T_c and aged at room temperature (20 °C). **B)** fast cool down to T < T_c and aged at room temperature (20 °C). **C)** slow cool down to T < T_c and aged in the fridge (4 °C). **D)** fast cool down to T < T_c and aged in the fridge (4 °C) (right). Samples were aged for 2 weeks and negatively stained using uranyl acetate (0.5 wt.%).

4.2.4.2 Solvent effects

To evaluate how changes in the solubility affect the morphology of PDMA-*b*-PCL-*co*-PACL and benzyl functionalized PDMA-*b*-PCL-*co*-PACL assemblies, methanol (MeOH) and isopropyl alcohol (IPA) were chosen as alternative solvents for the CDSA of selected functional PCL-based copolymers. Owing to different solvent properties, self-assembly experiments conducted in MeOH were heated up to 60 °C, while 75 °C was applied for those in IPA. After heating to respective temperatures for 3 h, samples were aged at both room temperature (20 °C) and fridge (4 °C) for 1 to 3 weeks before their analysis *via* TEM.

The self-assembly in MeOH and IPA of $PDMA_{295}$-*b*-PCL_{56}-*co*-$PACL_4$ (**T5**), $PDMA_{237}$-*b*-PCL_{36}-*co*-$PACL_3$ (**T6**) and $PDMA_{362}$-*b*-PCL_{46}-*co*-$PACL_8$ (**T7**) bearing moderate corona-to-core ratios and $PDMA_{456}$-*b*-PCL_{43}-*co*-$PACL_7$ (**T10**) and $PDMA_{412}$-*b*-PCL_{36}-*co*-$PACL_4$ (**T11**) with higher corona-to-core ratios was investigated. Previous experiments in EtOH showed that **T5** and **T6** appeared as short cylindrical micelles when aged at room temperature, whereas scarf-like micelles were observed after aging at cold temperatures (**Figure S4.27**). Whilst **T7** resulted in branched structures consisting of multiple cylinder micelles attached to a common core at both aging temperatures. On the other hand, **T10** and **T11** bearing long coronal blocks self-assembled similarly yielding scarf-like structures and cylindrical micelles at room temperature and in the fridge respectively.

It was hypothesized that the self-assembly of these copolymers in MeOH could alter the resultant particle architecture as methanol is slightly more polar and hydrophilic than ethanol. Consequently, the PDMA corona block would be more soluble, delaying the crystallization of the functional PCL-forming block. As expected, 2D platelet-like morphologies were obtained from the self-assemblies of **T5** and **T6** at both aging temperatures (blue and pink box

respectively, in **Figure 4.26**), more defined structures were observed for those samples aging at 20 °C rather than at 4 °C, as slow crystallization usually leads to the presence of fewer crystal defects. In contrast, no visible crystalline structures were observed TEM analysis of **T7** (red box in **Figure 4.26**) after 2 weeks of aging at 20 °C, indicating a slower crystallization rate than their counterparts. This could be expected as the allyl wt. % incorporation is significantly higher in **T7** compared to **T5** and **T6**, which also affected the assembly morphology leading to long fiber-like micelles at 4 °C. In addition, the assembly of long corona block BCPs **T10** and **T11** resulted in 1D cylindrical structures at both 20 °C and 4 °C after two weeks of aging (green and purple boxes respectively, in **Figure 4.26**).

In a similar manner, a change in the morphology from previous studies in EtOH was observed during the self-assembly of these block copolymers in IPA. As opposed to MeOH, IPA is slightly more hydrophobic than ethanol, which would affect the solubility of the corona and core-forming blocks. For the CDSA in IPA at 20 °C, TEM analyses showed 2D platelets, short cylindrical micelles, and trapped spherical micelles for **T5**, **T6** and **T7** respectively, whilst at 4 °C elongated platelets with cylindrical protrusions were observed after 1 and 3 weeks for **T5** and **T6** respectively, and polydisperse cylindrical micelles resulted from **T7** after 2 weeks of aging. In the case of **T10**, crystalline assemblies with cylindrical morphology were only observed after two weeks at 4 °C. These results differ from MeOH owing to the higher hydrophobicity of IPA. Consequently, the BCPs become less soluble, leading to faster crystallisation, and rendering less thermodynamically stable structures (**Figure 4.27**).

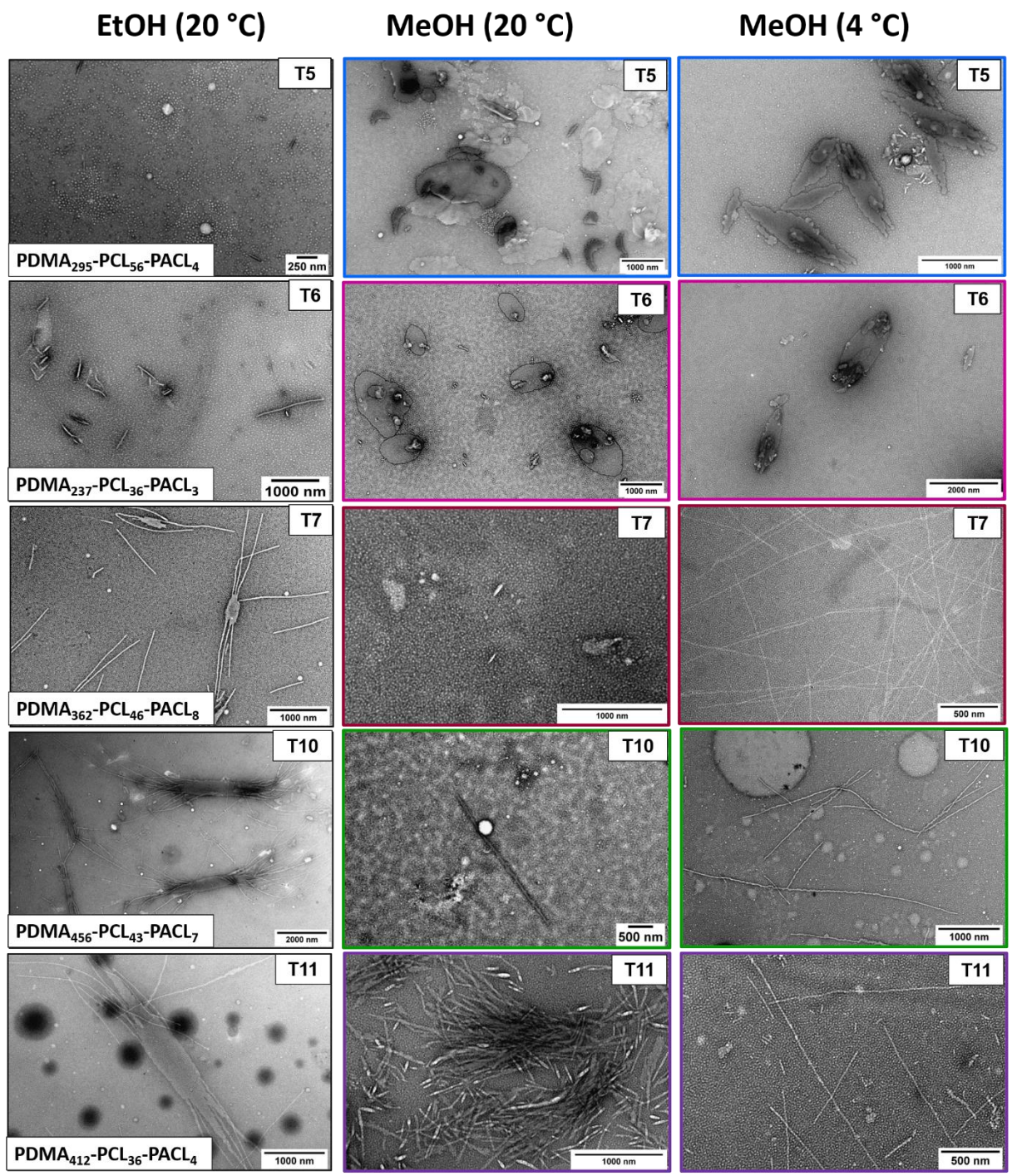


Figure 4.26. TEM micrographs of self-assembly in **MeOH** of T5 (blue box), T6 (pink box) T7 (red box), T10 (green box) and T11 (purple box) aged for 1, 3 and 2 weeks respectively, at 20 °C and 4 °C. Samples were negatively stained using uranyl acetate (0.5 wt.%) and analysed at conc. = 5 mg mL^{-1}.

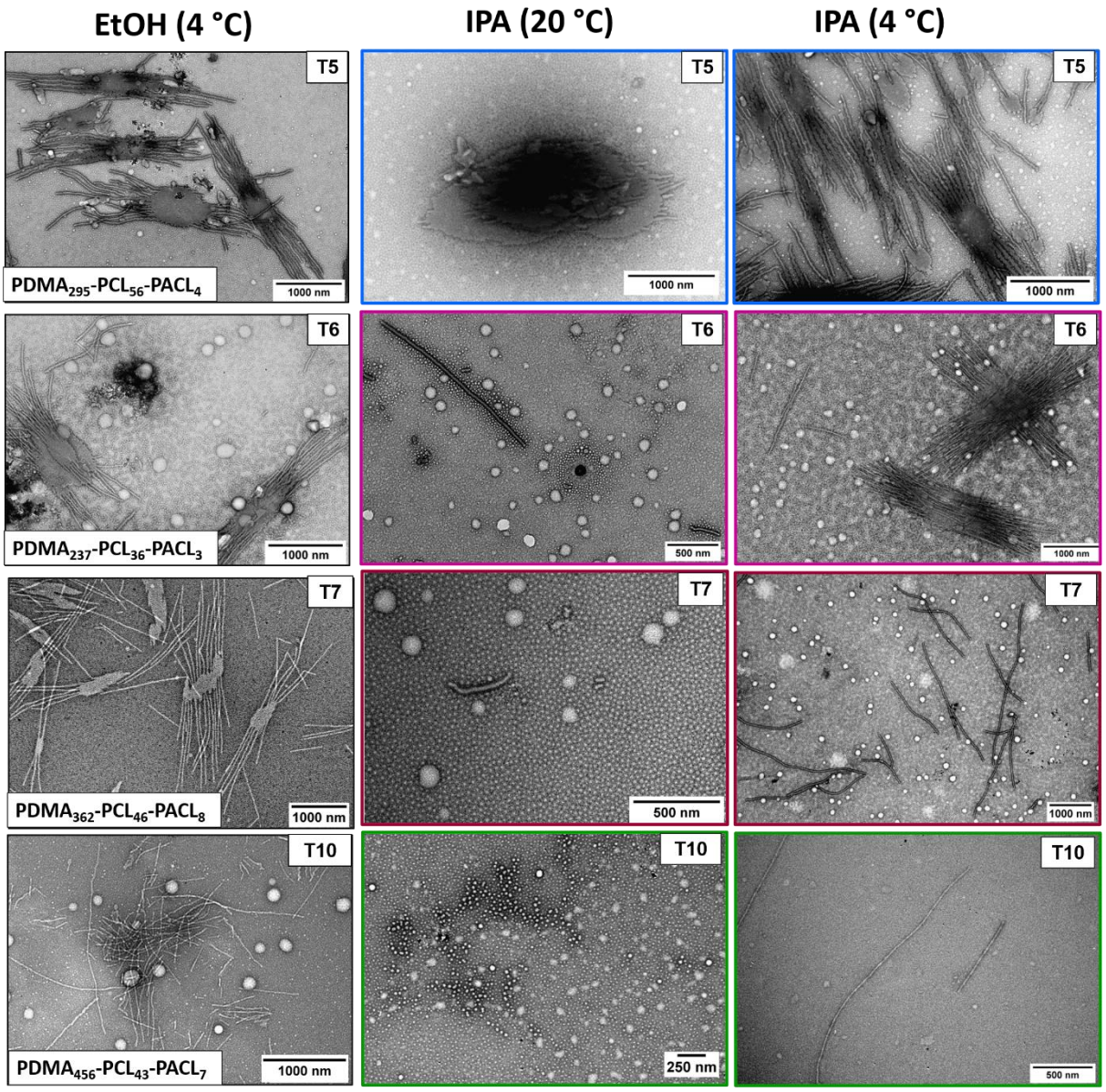


Figure 4.27. TEM micrographs of self-assembly in **IPA** of T5 (blue box), T6 (pink box) T7 (red box), T10 (green box) aged for 1, 3 and 2 weeks respectively, at 20 °C and 4 °C. Samples were negatively stained with uranyl acetate (0.5 wt.%) and analysed at conc. = 5 mg mL^{-1}. White spots correspond to grid artefacts.

Finally, the self-assembly in MeOH and IPA of PCL-based block copolymers with different coronal block lengths and benzyl groups attached to the core-forming block was investigated. For these experiments, benzyl-functionalised $PDMA_{237}$-*b*-PCL_{36}-*co*-$PACL_3$ (**Thiol-T6**, pink box) and $PDMA_{412}$-*b*-PCL_{36}-*co*-$PACL_4$ (**Thiol-T11**, purple box) were assembled in MeOH and IPA, as

indicated in previous sections, and the morphology of the resultant nanostructures was analysed by TEM after 3 weeks of aging at 20 °C and 4 °C. At 20 °C only trapped spherical micelles were observed, which was expected owing to the lower degree of crystallinity present in benzyl functionalised polymers, except for **Thiol-T11** that rendered ill-shaped platelets in MeOH. However, at 4 °C TEM analyses of **Thiol-T6** and **Thiol-T11** self-assemblies showed the presence of 2D lamellae structures in MeOH and cylindrical micelles in IPA (**Figure 4.28**). The observed variations in shape between MeOH and IPA may stem from their differing polarities, influencing the strength of repulsion forces within the core-forming block and impacting chain folding. Consequently, the chains of semicrystalline block containing benzyl rings capable of π-π bonding interactions will be more compact in highly polar solvents (MeOH) due to increased solvent-PCL interactions, resulting in 2D morphologies compared to less polar solvents (IPA), which favours 1D assemblies.

The results observed for the self-assembly in MeOH and IPA of PDMA-*b*-PCL-*co*-PACL copolymers and benzyl-functionalised copolymers with different corona-to-core blocks and allyl wt.% incorporations show the complexity of the crystallisation-driven self-assembly process and the great potential of this strategy to design structures with anisotropic morphologies.

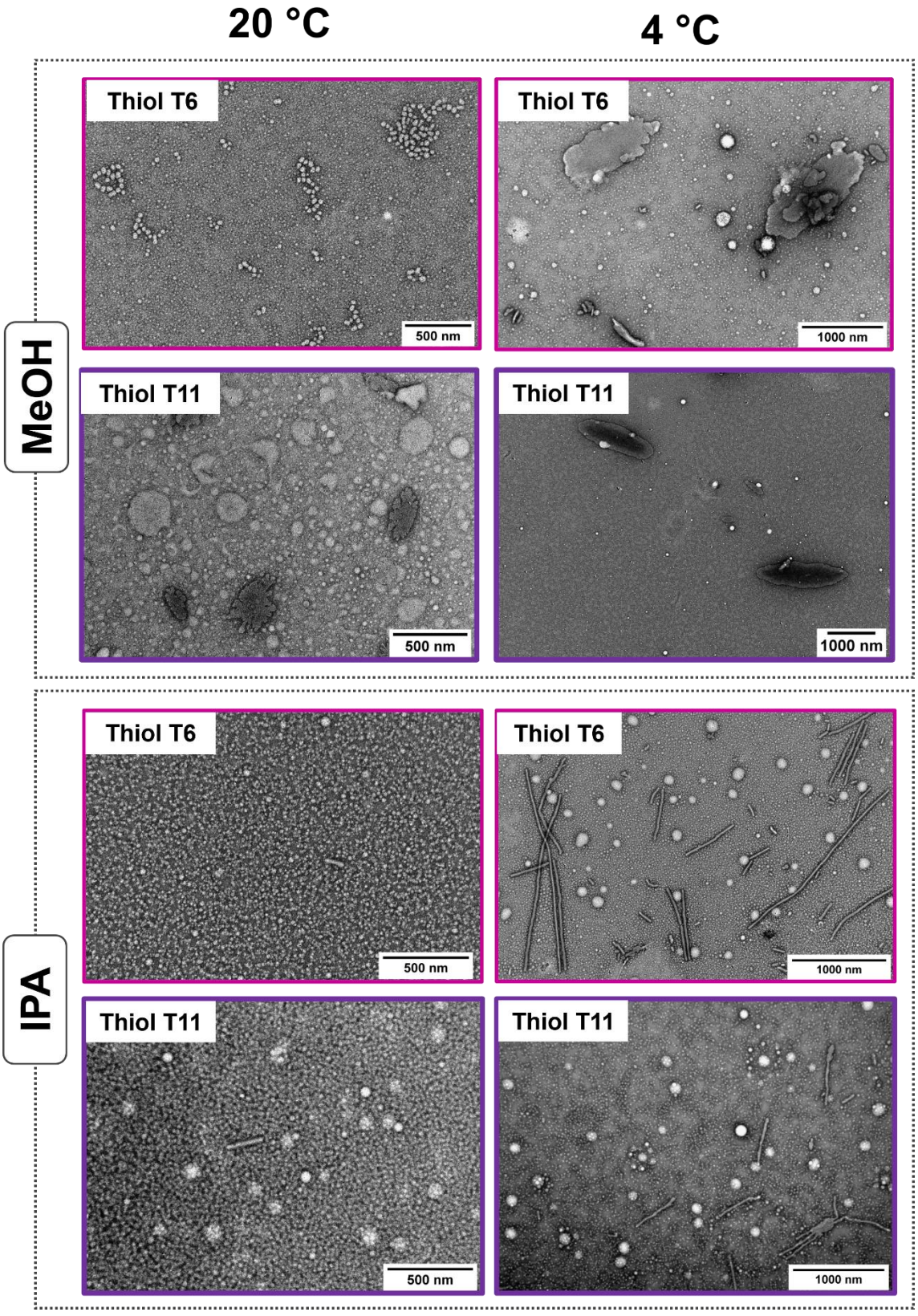


Figure 4.28. TEM micrographs of **Thiol-T6** and **Thiol-T11** in MeOH and IPA after 3 weeks aging at 20 °C and 4 °C respectively. Samples were negatively stained using uranyl acetate (0.5 wt.%) and analysed at conc. = 5 mg mL^{-1}. White spots correspond to grid artefacts.

4.3 Conclusions

In this work, the synthesis of semicrystalline amphiphilic PCL-based block copolymers (BCPs) with various corona-to-core ratios and the presence of allyl functionalities in the core-forming block was conducted through a combination of ROP and RAFT polymerisation. Furthermore, it was demonstrated that small molecules could be covalently attached to the allyl-functionalities *via* photo-induced thiol-ene chemistry while retaining the semicrystalline nature of the PCL copolymer. These functional BCPs were assembled in ethanol, methanol, and isopropanol through thermally initiated CDSA to yield a range of 1D and 2D nanostructures. Parameters such as polymer composition, solubility, aging temperature, and cooling rates were found to be key factors in the crystallisation of these copolymers in solution. Morphological changes were observed in all solvents when altering the hydrophilic/hydrophobic polymer content, as well as the allyl or benzyl functionality incorporation in the core-forming block. Copolymers with higher hydrophobic ratios led to 1D cylindrical structures, whereas 2D lamellae structures were obtained with polymers with long corona blocks. In addition, a transition from 1D to 2D structures can be observed when increasing the allyl wt.% incorporation and benzyl functionalisation. Moreover, faster crystallisation rates and more semicrystalline structures were observed during self-assembly at low temperatures and slow cooling rates, leading to the formation of more kinetically stable structures. This study opens a new pathway to create well-defined 1D and 2D functional nanostructures *via* CDSA that can be further investigated and translated into biomedical delivery devices.

4.4 Experimental section

4.4.1 Materials

All solvents and chemicals were purchased from Sigma-Aldrich, Fisher Scientific, Alfa Aesar, or VWR International and used without further purification unless otherwise stated. 2,2'-Azobis(isobutyronitrile) (AIBN) was recrystallised from methanol and was stored at 4 °C. The monomers dimethyl acrylamide (DMA) and methyl methacrylate (MMA) were filtered through a plug of basic alumina before their use. RAFT polymerisation solutions were degassed by bubbling N_2 gas into the reaction vessel for the polymerisation of DMA and through freeze-pump-thaw for the polymerisation of MMA, before heating up. All solvents used in CDSA were filtered prior to use through a 0.45 µm syringe filter.

4.4.2 Characterisation techniques

4.4.2.1 Nuclear magnetic resonance (NMR) spectroscopy

Diffusion-ordered spectroscopy (DOSY), proton (^{1}H), and carbon (^{13}C) resonance spectra were recorded on a Bruker 101 MHz, 300 MHZ, or 500 MHz spectrometers at 298 K. Chemical shifts were reported as δ in parts per million (ppm) and referenced to the residual solvent signals ($CDCl_3$, ^{1}H: δ = 7.26 ppm, ^{13}C: δ = 77.16 ppm). The multiplicities were reported as s = singlet, d = doublet, dd = doublet in doublet, ddt = double of doublet of triplet, t = triplet, tdd = triplets of doublet of doublets, q = quadruplet, p = pentaplet, pd = pentaplet of doublets and m = multiplet. The coupling constant (J) was recorded in Hertz [Hz]. The obtained data were processed and analysed using MestReNova 12.0.3 software.

4.4.2.2 Size exclusion chromatography (SEC)

SEC analyses were performed on an Agilent 1260 Infinity II Multi-Detector GPC/SEC System fitted with RI and ultraviolet (UV, λ = 309 nm), and viscosimeter detectors. The instrument is equipped with an Agilent guard column PLGel 3 µm (50 × 7.5 mm) and two Agilent mixed-C columns PLGel 5 µm (300 × 7.5 mm) using $CHCl_3$ (buffered 0.5% Et_3N) as the mobile phase (eluent). Number average molecular weights (M_n), weight average molecular weights (M_w) and dispersities ($Đ_M = M_w/M_n$) were determined using Agilent GPC/SEC software (vA.02.01) against a 15-point calibration curve (M_p = 162 – 3,187,000 g mol^{-1}) based on poly(styrene) standards or a 12-point calibration curve (M_p = 550 – 2,210,000 g mol^{-1}) based on poly(methyl methacrylate) standards. Molecular weights (M_n), weight average molecular weights (M_w) are given in (g mol^{-1}).

4.4.2.3 Differential scanning calorimeter (DSC)

Determination of the DSC curves was carried out using a STARe system DSC3 with an auto-sampler (Mettler Toledo). The samples (1 – 10 mg of polymer) were placed into aluminium pans measuring 5 mm in diameter and 0.4 – 0.6 mm in thickness. Thermograms obtained with a heating rate of 10 °C min^{-1} were recorded from −100 to 100 °C with a 10 °C min^{-1} heating and cooling rate over two cycles.

4.4.2.4 Nano differential scanning calorimetry (nano-DSC)

Nano differential scanning calorimetry (Nano-DSC) was performed on a TA Nano DSC. 800 µL of the nanoparticle solutions were introduced in the instrument and run from 0 °C to 100 °C at a heating or cooling ramp of 1 °C min^{-1} in triplicate under a constant atmosphere pressure. T_c and T_m were obtained using the first run and were taken as the midpoint of the inflection tangent.

4.4.2.5 Transmission electron microscopy (TEM)

Transmission electron microscopy (TEM) was performed using a JEOL 1400 microscope operating at an acceleration voltage of 80 kV. TEM samples were prepared by depositing 8 µL of sample solution (5 mg mL^{-1}) on a formvar/carbon (300 mesh copper) film TEM grid and left air drying. Afterwards, 8 µL of uranyl acetate solution (UA, 1% in water) was then dropped on the grid and left for 60 seconds before blotting. The sample was kept in a desiccator overnight before characterisation.

4.4.3 Experimental procedures

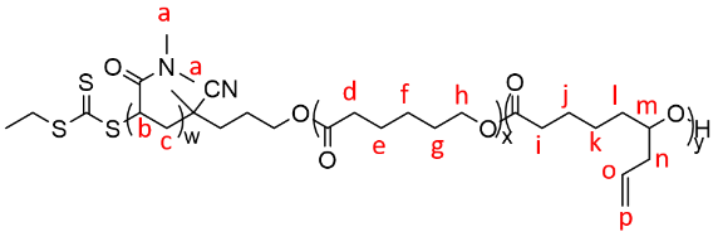
4.4.3.1 Synthesis of PCL-*co*-PACL copolymers – General procedure for the ring opening copolymerisation (ROCOP) of ε-caprolactone (εCL) and ε-allyl-ε-caprolactone (εACL).

Refer to Chapter 3, Section 3.4.3.4 for the synthetic protocols and characterisation.

4.4.3.2 General procedure for RAFT polymerisation

The procedure for the chain extension with DMA and MMA was adapted from the literature.[37] PCL_x-*co*-$PACL_y$ copolymers (1 equiv.) and DMA (300 equiv. – 600 equiv.) or MMA (100 equiv.) were dissolved in 1,4-dioxane (5.5 mL) and sonicated in a vial. After complete dissolution, a solution of AIBN (0.1 equiv. for DMA polymerisation and 0.2 equiv. for MMA polymerisation) in 1,4-dioxane was added to the mixture and transferred to a vial or an ampoule. The reaction solution was then degassed and heated for 45 min (DMA) and 2 h (MMA) at 70 °C. The reaction was quenched by the immersion of the reaction vessel in ice and the polymer was precipitated in ice-cold diethyl ether three times before being dried under vacuum to yield the amphiphilic block copolymer as a light-yellow solid.

- ***PDMA$_w$-b-PCL$_x$-co-PACL$_y$ block copolymers***

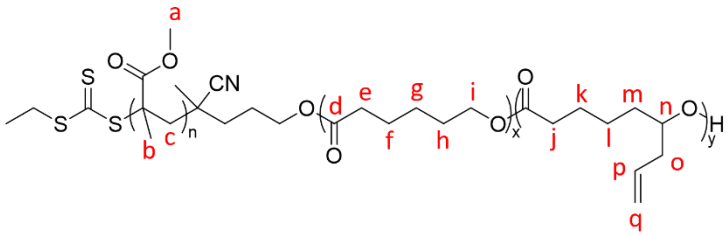


^{1}H NMR (300 MHz, $CDCl_3$, 298 K): δ/ppm= 5.70 (ddt, J = 17.3, 10.4, 7.1 Hz, 6H, H^o), 5.18 – 4.96 (m, 12H, H^p), 4.88 (p, J = 6.2 Hz, 6H, H^m), 4.03 (t, J = 6.7 Hz, 86H, H^h), 3.28 – 2.34 (m, 911H, $H^{a, b}$), 2.32 – 2.21 (m, 109H, $H^{d, i, n}$), 2.20 – 1.01 (m, 415H, $H^{c, e, f, g, j, k, l}$).

^{13}C NMR (101 MHz, $CDCl_3$, 298 K) δ/ppm= 175.09 ((*C*=O)N(CH_3)(CH_3)), 173.95 (O(*C*=O)), 134.04 (C^o), 118.11 (C^p), 73.24 (C^m), 64.54 (C^h), 39.01 (C^n), 37.51 (C^a), 36.20 (C^b), 36.06 (C^c), 34.78 (C^l), 34.51 (C^d), 33.64 (C^i), 28.74 (C^g), 25.92 (C^f), 25.28(C^k), 25.14 (C^j), 24.97 (C^e).

SEC: M_n = 12.2 kDa, $Đ_M$ = 1.30

- ***PMMA$_n$-b-PCL$_x$-co-PACL$_y$ block copolymers***

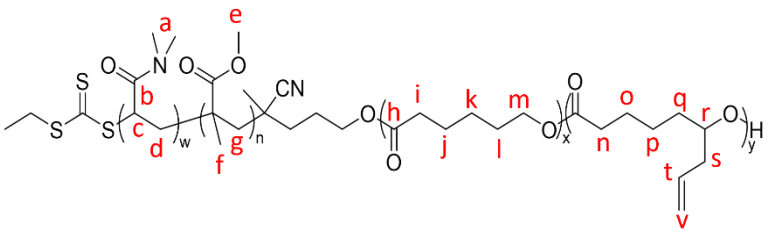


^{1}H NMR (300 MHz, $CDCl_3$, 298 K): δ/ppm= 5.84 – 4.64 (m, 4H, H^p), 5.17 – 4.99 (m, 8H, H^q), 4.91 (t, J = 6.2 Hz, 4H, H^n), 4.06 (t, J = 6.7 Hz, 75H, H^i), 3.74 – 3.47 (m, 65H, H^a), 2.40 – 2.18 (m, 88H, $H^{e, j, o}$), 2.04 – 1.75 (m, 26H, H^c), 1.73 – 1.51 (m, 253H, $H^{f, g, k, l}$), 1.49 – 1.18 (m, 84H, $H^{h, m}$), 0.93 (d, J = 54.1 Hz, 56H, H^b).

^{13}C NMR (101 MHz, $CDCl_3$, 298 K) δ/ppm= 173.66 (C^d), 133.77 (C^p), 117.82 (C^q), 72.96 (C^n), 64.26 (C^i), 51.93 (C^a), 45.00 (C^c), 44.64 (C^b), 38.73 (C^o), 34.50 (C^j), 34.23 (C^e), 33.36 (C^m), 32.43 (C^l), 28.46 (C^h), 25.64 (C^g), 25.00 (C^k), 24.69 (C^f).

SEC: M_n = 13.1 kDa, $Đ_M$ = 1.24

- ***PDMA$_w$-b-PMMA$_n$-b-PCL$_x$-co-PACL$_y$ block copolymers***



^{1}H NMR (300 MHz, $CDCl_3$, 298 K): δ/ppm= 5.93 – 5.62 (m, 3H, H^t), 5.15 – 5.02 (m, 7H, H^v), 4.98 – 4.86 (m, 3H, H^r), 4.07 (t, J = 6.7 Hz, 75H, H^m), 3.61 (s, 68H, H^e), 3.30 – 2.37 (m, 401H, $H^{a,\ c}$), 2.37 – 2.23 (m, 96H, $H^{i,\ n,\ s}$), 1.87 – 1.15 (m, 379H, $H^{d,\ g,\ j,\ k,\ l,\ o,\ p,\ q}$), 0.95 (d, J = 53.6 Hz, 58H, H^f).

^{13}C NMR (101 MHz, $CDCl_3$, 298 K) δ/ppm= 174.73 (C^b), 173.56 (C^h), 133.67 (C^t), 117.69 (C^v), 72.68 (C^r), 64.15 (C^m), 51.81 (C^e), 38.61 (C^f), 37.12 (C^a), 36.27 (C^c), 35.83 (C^d), 34.40 (C^n), 34.11 (C^i), 28.34 (C^l), 25.52 (C^k), 24.88 (C^o), 24.73 (C^p), 24.66 (C^q), 24.56 (C^j).

SEC: M_n = 26.0 kDa, $Đ_M$ = 1.20

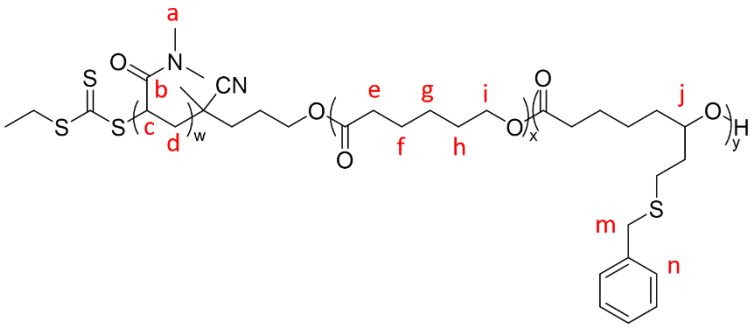
4.4.3.3 General procedure for radical thiol-ene click addition.

The procedure was adapted from the literature.[54]

PDMA$_w$-*b*-PCL$_x$-*co*-PACL$_y$ triblock copolymer (0.2 g, 4.6 x 10^{-3} mmol. 1 equiv.) was dissolved in chloroform (1.5 mL) and thiol (0.23 mmol, 10 equiv. per olefin) was added, followed by Irgacure 819 (9.6 mg, 0.023 mmol, 1 equiv. per olefin). The solution was irradiated with a UV lamp (315–400 nm) at room temperature for 180 min, precipitated three times into ice-cold diethyl ether

and dried under vacuum to obtain the thiol-functionalised PCL-based copolymer as a white solid.

- ***Benzyl functionalised PDMA$_w$-b-PCL$_x$-co-PACL$_y$ block copolymers***

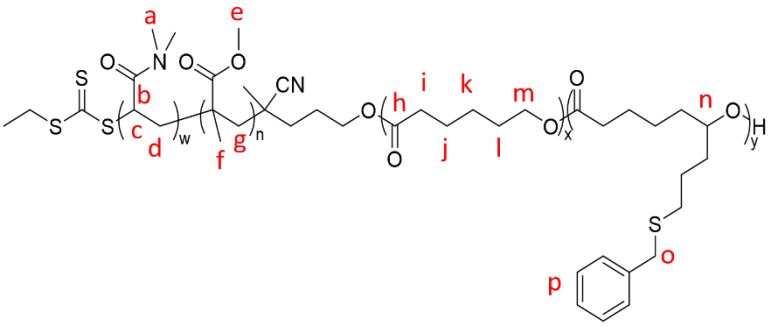


^{1}H NMR (300 MHz, $CDCl_3$, 298 K): δ/ppm= 7.64 – 7.27 (m, 39H, H^n), 4.83 (s, 6H, H^j), 4.05 (t, J = 6.7 Hz, 86H, H^e), 3.68 (s, 1H, H^m), 3.22 – 2.45 (m, 865H, $H^{a,\,c}$), 2.28 (q, J = 7.8 Hz, 104H, H^i), 1.74 – 1.45 (m, 433H, $H^{d,\,f,\,g}$), 1.45 – 1.29 (m, 144H, H^h).

^{13}C NMR (101 MHz, $CDCl_3$, 298 K) δ/ppm= 174.78 (C^b), 173.58 (O(*C*=O)), 129.48 ($C^{aromatics}$), 128.73 ($C^{aromatics}$), 128.45 ($C^{aromatics}$), 64.15 (C^i), 37.49 (C^a), 3713 (C^c), 36.05 (C^e), 28.33 (C^h), 25.51 (C^g), 24.56 (C^f).

SEC: M_n = 12.2 kDa, $Đ_M$ = 1.34

- ***Benzyl functionalised PDMA$_w$-b-PMMA$_n$-b-PCL$_x$-co-PACL$_y$ block copolymers***



^{1}H NMR (300 MHz, $CDCl_3$, 298 K): δ/ppm= 7.23 (s, 7H, H^p), 4.77 (s, 2H, H^n), 3.99 (t, J = 6.7 Hz, 108H, H^m), 3.65 – 3.58 (m, 2H, H^o), 3.53 (s, 66H, H^e), 3.14 – 2.32 (m, 108H, $H^{a,\,b}$), 2.22 (q, J = 8.3,

7.9 Hz, 103H, H^{i}), 1.58 (pd, *J* = 7.0, 6.6, 2.7 Hz, 560H, $H^{d, g, j, k}$), 1.45 – 1.08 (m, 108H, H^{l}), 0.86 (d, *J* = 53.4 Hz, 51H, H^{f}).

^{13}C NMR (101 MHz, $CDCl_3$, 298 K) *δ*/ppm= 175.07 (C^{b}), 173.20 (C^{h}), 129.66 ($C^{aromatics}$), 128.48 ($C^{aromatics}$), 126.83 ($C^{aromatics}$), 63.49 (C^{m}), 50.68(C^{e}), 45.19 (C^{g}), 44.17 (C^{f}), 38.46 (C^{a}), 36.28 (C^{c}), 35.87 (C^{d}), 28.34 (C^{i}), 25.55 (C^{l}), 25.52 (C^{k}), 24.57 (C^{j}).

SEC: M_n = 23.1 kDa, $Đ_M$ = 1.37

4.4.3.4 General procedure for crystallization-driven self-assembly of PDMA-*b*-PCL-containing block copolymers.

$PDMA_w$-*b*-($PMMA_n$)-*b*-PCL_x-*co*-$PACL_y$ and thiol-conjugated $PDMA_w$-*b*-($PMMA_n$)-*b*-PCL_x-*co*-$PACL_y$ block copolymers (25 mg) were suspended in 5 mL of the solvent of choice (5.0 mg mL^{-1}) in a vial. The samples were heated without stirring for 3 h at 70 °C for experiments conducted in ethanol, 65 °C for experiments conducted in methanol, and 75 °C for experiments conducted in isopropanol, before cooling to room temperature. Afterwards, the samples were left aging at room temperature (20 °C) or inside a fridge with a controlled temperature set at 4 °C for 2 to 18 weeks before being imaged by TEM.

4.5 References

1. M. Chen, N. Gong, W. Sun, J. Han, Y. Liu, S. Zhang, A. Zheng, H. J. Butt, X. J. Liang and S. Wu, *Small*, 2022, **18**, 2201672.
2. A. Nag, K. Banerjee, R. Barman, J. Kar, D. P. Sarkar, S. S. Jana and S. Ghosh, *J. Am. Chem. Soc*, 2023, **145**, 579-584.
3. M. Zhang, X. Xiao, L. Liu, S. Liu, H. Liu, T. Fan, B. Zhang, S. Wageh, A. Al-Ghamdi, M. Wang, J. Wang, C. Du, N. Jiang, H. Zhang and Q. Peng, *Adv Nanobiomed Res*, 2022, **2**, 2200014.
4. S.-H. Hwang, S.-Y. Kang, S. Yang, J. Lee and T.-L. Choi, *J. Am. Chem. Soc*, 2022, **144**, 5921-5929.
5. X. Li, P. J. Wolanin, L. R. MacFarlane, R. L. Harniman, J. Qian, O. E. C. Gould, T. G. Dane, J. Rudin, M. J. Cryan, T. Schmaltz, H. Frauenrath, M. A. Winnik, C. F. J. Faul and I. Manners, *Nat. Commun.*, 2017, **8**, 15909.
6. C. Clamor, S. D. Dale, J. Beament, E. Mould, R. K. O'Reilly and A. P. Dove, *Macromol.*, 2023, **56**, 9821-9828.
7. A. Rajak and A. Das, *Angew. Chem. Int. Ed.*, 2022, **61**.
8. X. Solimando, P. Champagne and M. F. Cunningham, *Macromolecular Reaction Engineering*, 2020, **14**, 2000029.
9. J. Tian, Y. Zhang, L. Du, Y. He, X.-H. Jin, S. Pearce, J.-C. Eloi, R. L. Harniman, D. Alibhai, R. Ye, D. L. Phillips and I. Manners, *Nat Chem*, 2020, **12**, 1150-1156.
10. S. Lei, J. Tian, Y. Kang, Y. Zhang and I. Manners, *J. Am. Chem. Soc*, 2022, **144**, 17630-17641.
11. A. E. Masucci, M. Ghasemi, C. W. Pester and E. D. Gomez, *Mater. Adv.*, 2023, **4**, 2586-2594.
12. X. Bai, Q. Sun, H. Cui, L. P. B. Guerzoni, S. Wuttke, F. Kiessling, L. De Laporte, T. Lammers and Y. Shi, *Adv. Mater.*, 2022, **34**, 2109701.
13. H. Yu, L. Wang, S. Liu, B. Zhao, K. Xiao, B. Yang, H. Duan, H. Zhao and J. Deng, *Carbohydrate Polymers*, 2022, **296**, 119944.
14. I. R. Dorsman, M. J. Derry, V. J. Cunningham, S. L. Brown, C. N. Williams and S. P. Armes, *Polym. Chem.*, 2021, **12**, 1224-1235.
15. J. A. Massey, K. Temple, L. Cao, Y. Rharbi, J. Raez, M. A. Winnik and I. Manners, *J. Am. Chem. Soc*, 2000, **122**, 11577-11584.
16. J. Raez, I. Manners and M. A. Winnik, *J. Am. Chem. Soc*, 2002, **124**, 10381-10395.
17. J. B. Gilroy, T. Gadt, G. R. Whittell, L. Chabanne, J. M. Mitchels, R. M. Richardson, M. A. Winnik and I. Manners, *Nat Chem*, 2010, **2**, 566-570.
18. J. C. Foster, S. Varlas, B. Couturaud, Z. Coe and R. K. O'Reilly, *J. Am. Chem. Soc*, 2019, **141**, 2742-2753.
19. U. Tritschler, S. Pearce, J. Gwyther, G. R. Whittell and I. Manners, *Macromol.*, 2017, **50**, 3439-3463.

20. Y. He, J.-C. Eloi, R. L. Harniman, R. M. Richardson, G. R. Whittell, R. T. Mathers, A. P. Dove, R. K. O'Reilly and I. Manners, *J. Am. Chem. Soc*, 2019, **141**, 19088-19098.
21. G. Rizis, T. G. M. Van De Ven and A. Eisenberg, *ACS Nano*, 2015, **9**, 3627-3640.
22. T. Gädt, N. S. Ieong, G. Cambridge, M. A. Winnik and I. Manners, *Nat. Mater.*, 2009, **8**, 144-150.
23. Z. Wang, M. Lin, C. Bonduelle, R. Li, Z. Shi, C. Zhu, S. Lecommandoux, Z. Li and J. Sun, *Biomacromolecules*, 2020, **21**, 3411-3419.
24. W. Yu, J. C. Foster, A. P. Dove and R. K. O'Reilly, *Macromol.*, 2020, **53**, 1514-1521.
25. M. Inam, G. Cambridge, A. Pitto-Barry, Z. P. L. Laker, N. R. Wilson, R. T. Mathers, A. P. Dove and R. K. O'Reilly, *Chem. Sci.*, 2017, **8**, 4223-4230.
26. G. Rizis, T. G. M. Van De Ven and A. Eisenberg, *Angew. Chem.*, 2014, **126**, 9146-9149.
27. S. Song, X. Liu, E. Nikbin, J. Y. Howe, Q. Yu, I. Manners and M. A. Winnik, *J. Am. Chem. Soc*, 2021.
28. L. Jia, A. Petretic, G. Molev, G. Guerin, I. Manners and M. A. Winnik, *ACS Nano*, 2015, **9**, 10673-10685.
29. X. Li, Y. Gao, C. E. Boott, M. A. Winnik and I. Manners, *Nat. Commun.*, 2015, **6**, 8127.
30. J. R. Finnegan, E. H. Pilkington, K. Alt, M. A. Rahim, S. J. Kent, T. P. Davis and K. Kempe, *Chem. Sci.*, 2021, **12**, 7350-7360.
31. J. Schöbel, M. Karg, D. Rosenbach, G. Krauss, A. Greiner and H. Schmalz, *Macromol.*, 2016, **49**, 2761-2771.
32. S. Ganda, C. K. Wong and M. H. Stenzel, *Macromol.*, 2021, **54**, 6662-6669.
33. Y. Cha, C. Jarrett-Wilkins, M. A. Rahman, T. Zhu, Y. Sha, I. Manners and C. Tang, *ACS Macro Lett.*, 2019, **8**, 835-840.
34. A. Nazemi, C. E. Boott, D. J. Lunn, J. Gwyther, D. W. Hayward, R. M. Richardson, M. A. Winnik and I. Manners, *J. Am. Chem. Soc*, 2016, **138**, 4484-4493.
35. Z. Tong, Y. Su, Y. Jiang, Y. Xie, S. Chen and R. K. O'Reilly, *Macromol.*, 2021, **54**, 2844-2851.
36. N. Petzetakis, A. P. Dove and R. K. O'Reilly, *Chem. Sci.*, 2011, **2**, 955-960.
37. M. C. Arno, M. Inam, Z. Coe, G. Cambridge, L. J. Macdougall, R. Keogh, A. P. Dove and R. K. O'Reilly, *J. Am. Chem. Soc*, 2017, **139**, 16980-16985.
38. Y. Su, Y. Jiang, L. Liu, Y. Xie, S. Chen, Y. Wang, R. K. O'Reilly and Z. Tong, *Macromol.*, 2022.
39. D. Mecerreyes, R. D. Miller, J. L. Hedrick, C. Detrembleur and R. Jerome, *J. Polym. Sci., Part A: Polym. Chem.*, 2000, **38**, 870-875.
40. F. Teng, B. Xiang, L. Liu, S. Varlas and Z. Tong, *J. Am. Chem. Soc*, 2023, **145**, 28049-28060.
41. L. Sun, A. Pitto-Barry, A. W. Thomas, M. Inam, K. Doncom, A. P. Dove and R. K. O'Reilly, *Polym. Chem.*, 2016, **7**, 2337-2341.
42. J. Wang, W. Zhu, B. Peng and Y. Chen, *Polymer*, 2013, **54**, 6760-6767.
43. S. Shin, F. Menk, Y. Kim, J. Lim, K. Char, R. Zentel and T.-L. Choi, *J. Am. Chem. Soc*, 2018, **140**, 6088-6094.
44. J. Lyu, Y. Li, Z. Li, P. Polanowski, J. K. Jeszka, K. Matyjaszewski and W. Wang, *Angew. Chem. Int. Ed.*, 2023, **62**.

45. W. Yu, M. Inam, J. R. Jones, A. P. Dove and R. K. O'Reilly, *Polym. Chem.*, 2017, **8**, 5504-5512.
46. S. Agbolaghi, S. Abbaspoor and F. Abbasi, *Prog. Polym. Sci*, 2018, **81**, 22-79.
47. G. Gody, P. B. Zetterlund, S. Perrier and S. Harrisson, *Nat. Commun.*, 2016, **7**, 10514.
48. J. Nie, X. Huang, G. Lu, M. A. Winnik and C. Feng, *Polym. Chem.*, 2023, **14**, 137-151.
49. X. Zhai, W. Wang, G. Zhang and B. He, *Macromol.*, 2006, **39**, 324-329.
50. S. Song, M. Puzhitsky, S. Ye, M. Abtahi, C. K. Rastogi, E. Lu, G. Hicks, I. Manners and M. A. Winnik, *Macromol.*, 2020, **53**, 6576-6588.
51. J. Wang, J. Si, J. Zhu, Y. Nie, Y. Lu and Y. Chen, *Polymer*, 2023, **284**, 126292.
52. Z. Tong, R. Zhang, P. Ma, H. Xu, H. Chen, Y. Li, W. Yu, W. Zhuo and G. Jiang, *Langmuir*, 2017, **33**, 176-183.
53. S. Song, J. Jiang, E. Nikbin, J. Y. Howe, I. Manners and M. A. Winnik, *Chem. Sci.*, 2022, **13**, 396-409.
54. C. Clamor, B. N. Cattoz, P. M. Wright, R. K. O'Reilly and A. P. Dove, *Polym. Chem.*, 2021, **12**, 1983-1990.

4.6 Supporting figures

4.6.1 $PDMA_w$-*b*-PCL_x copolymers

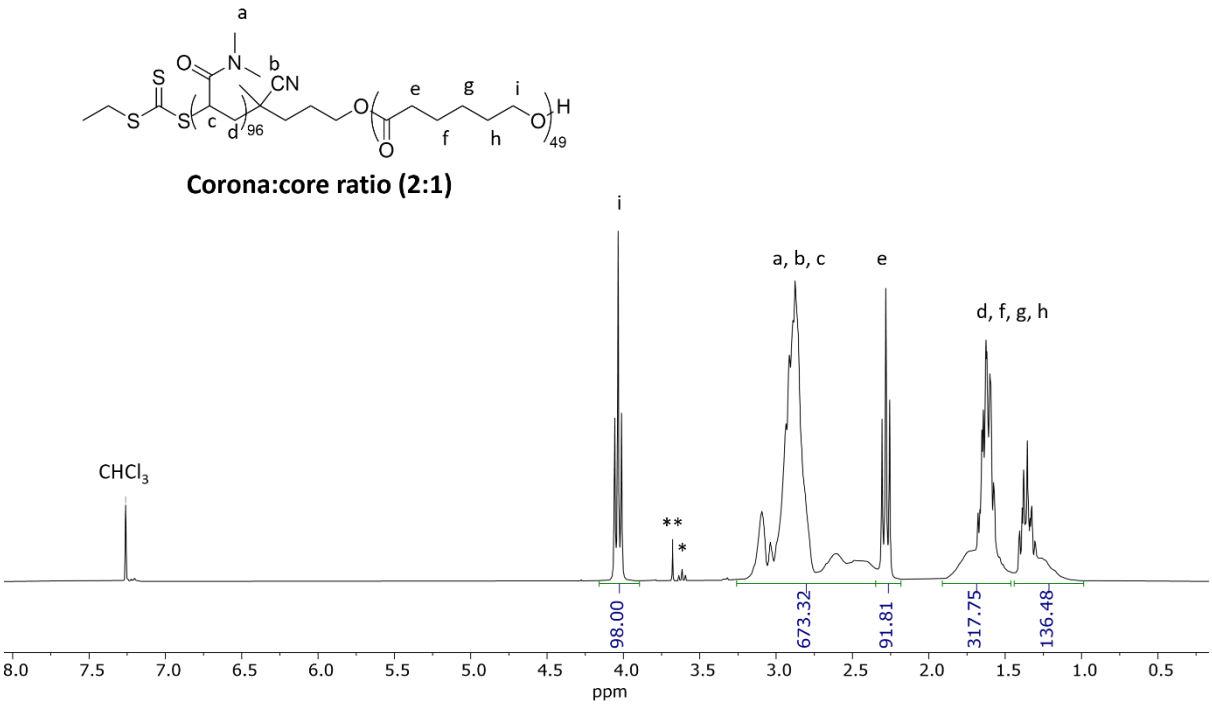


Figure S4.1. ^{1}H NMR spectrum ($CDCl_3$, 300 MHz, 298 K) of $PDMA_{96}$-*b*-PCL_{49} (entry 1 in Table 4.2). * Correspond to diethyl ether peaks and **correspond to dioxane peak.

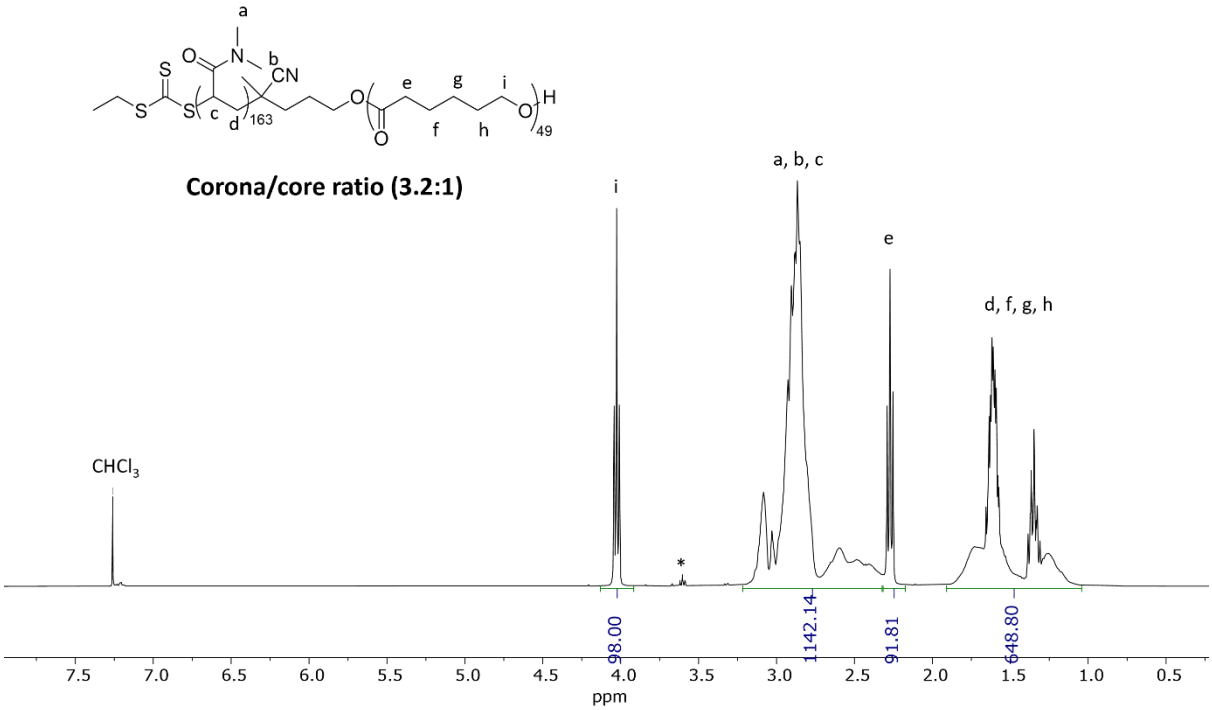


Figure S4.2. ^{1}H NMR spectrum ($CDCl_3$, 300 MHz, 298 K) of $PDMA_{163}$-*b*-PCL_{49} (entry 2 in table 4.2). * Correspond to diethyl ether peaks.

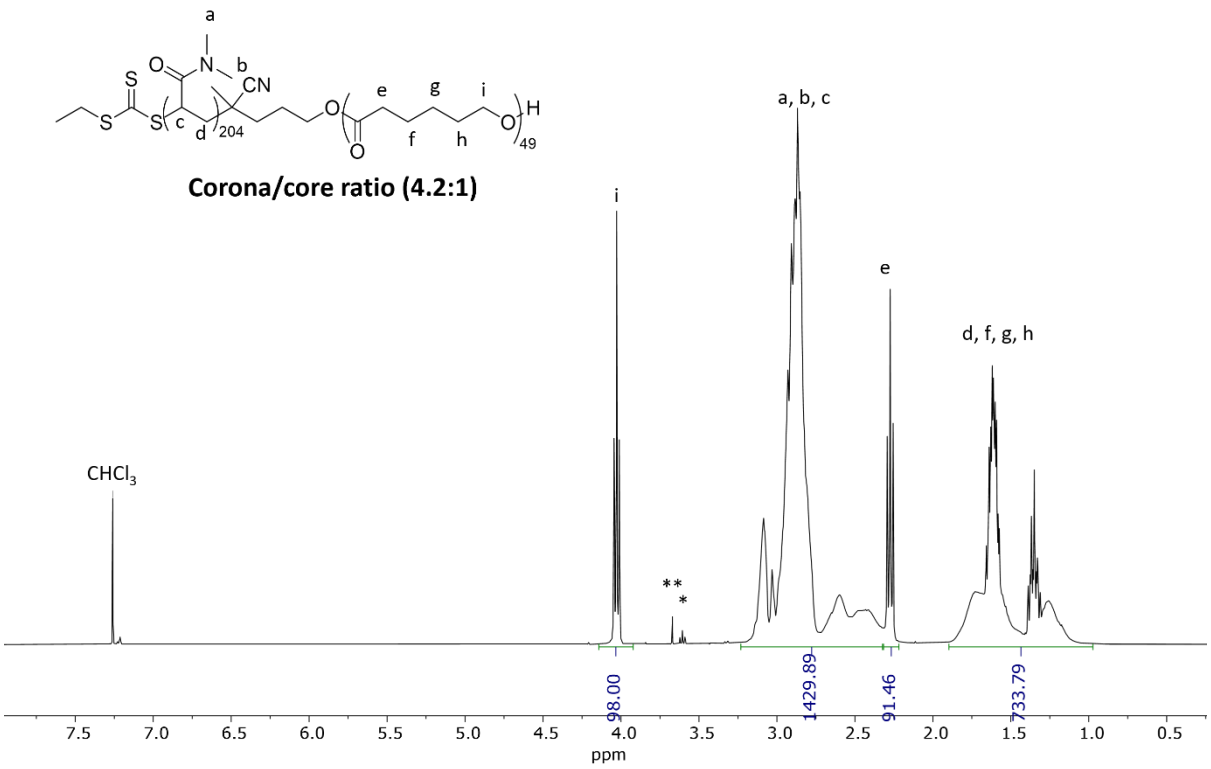


Figure S4.3. ^{1}H NMR spectrum ($CDCl_3$, 300 MHz, 298 K) of $PDMA_{204}$-*b*-PCL_{49} (entry 3 in table 4.2). * Correspond to diethyl ether peaks and **correspond to dioxane peak.

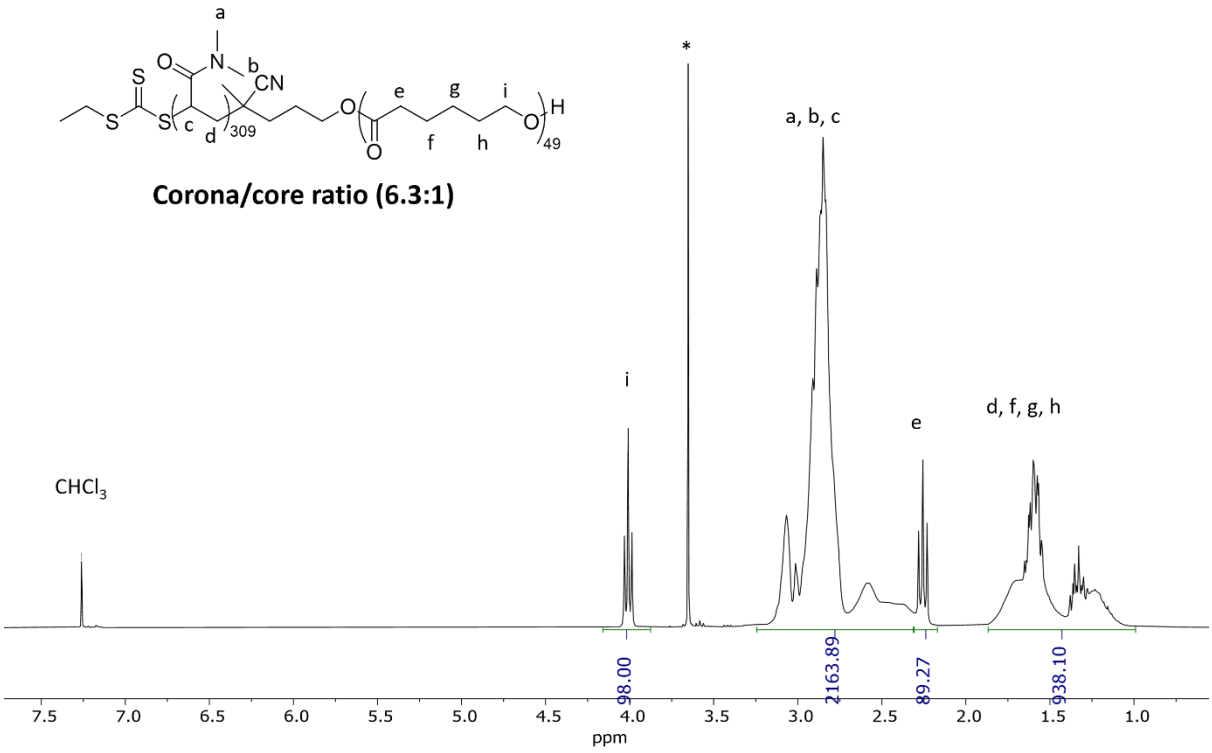


Figure S4.4. ^{1}H NMR spectrum ($CDCl_3$, 300 MHz, 298 K) of $PDMA_{309}$-*b*-PCL_{49} (entry 4 in table 4.2). * Correspond to dioxane peak.

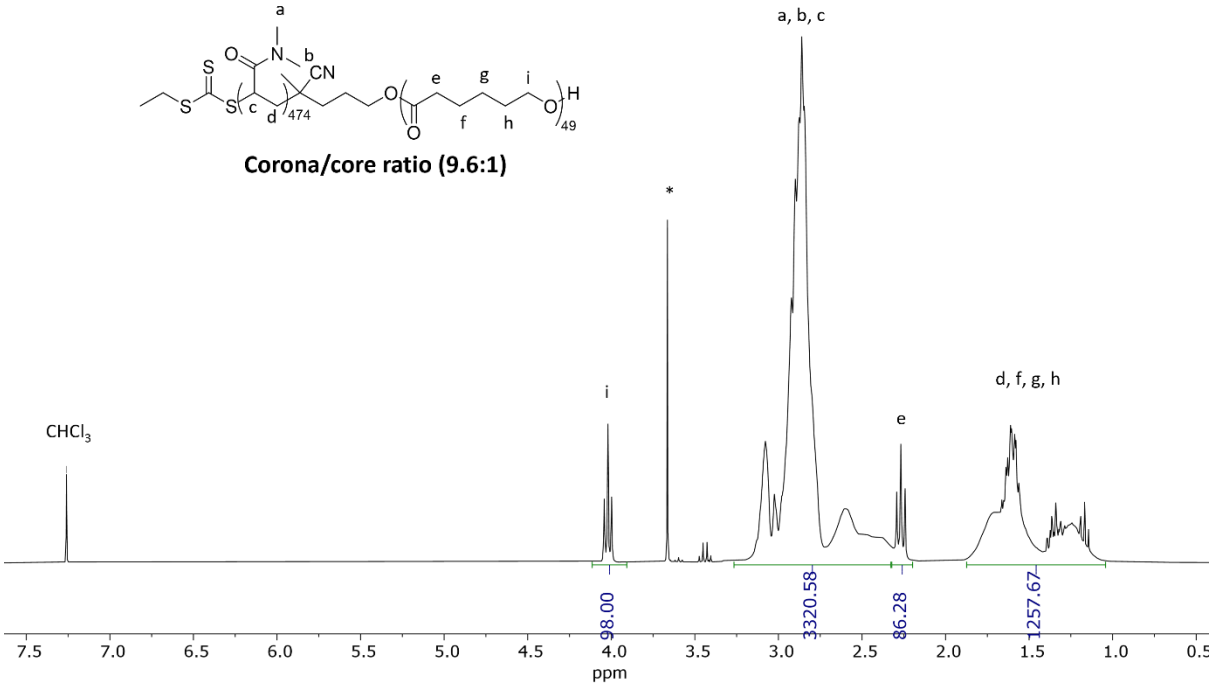


Figure S4.5. ^{1}H NMR spectrum ($CDCl_3$, 300 MHz, 298 K) of $PDMA_{474}$-*b*-PCL_{49} (entry 5 in table 4.2). * Correspond to dioxane peaks.

4.6.2 Amphiphilic functional block copolymers

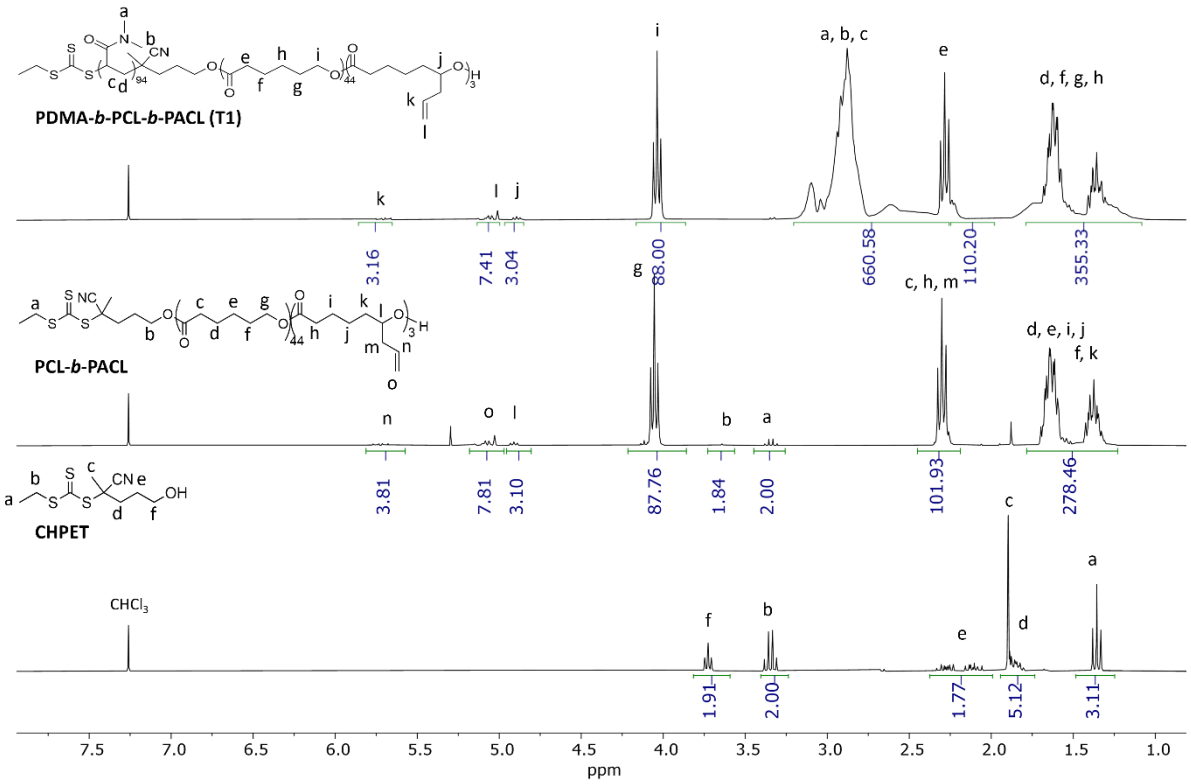


Figure S4.6. Stacked ^{1}H-NMR spectra ($CDCl_3$, 300 MHz, 298 K) of CHPET-CTA (down), PCL_{44}-*co*-$PACL_3$ copolymer (middle) and $PDMA_{94}$-*b*-PCL_{44}-*co*-$PACL_3$ (T1 in table 4.2) block copolymers (top).

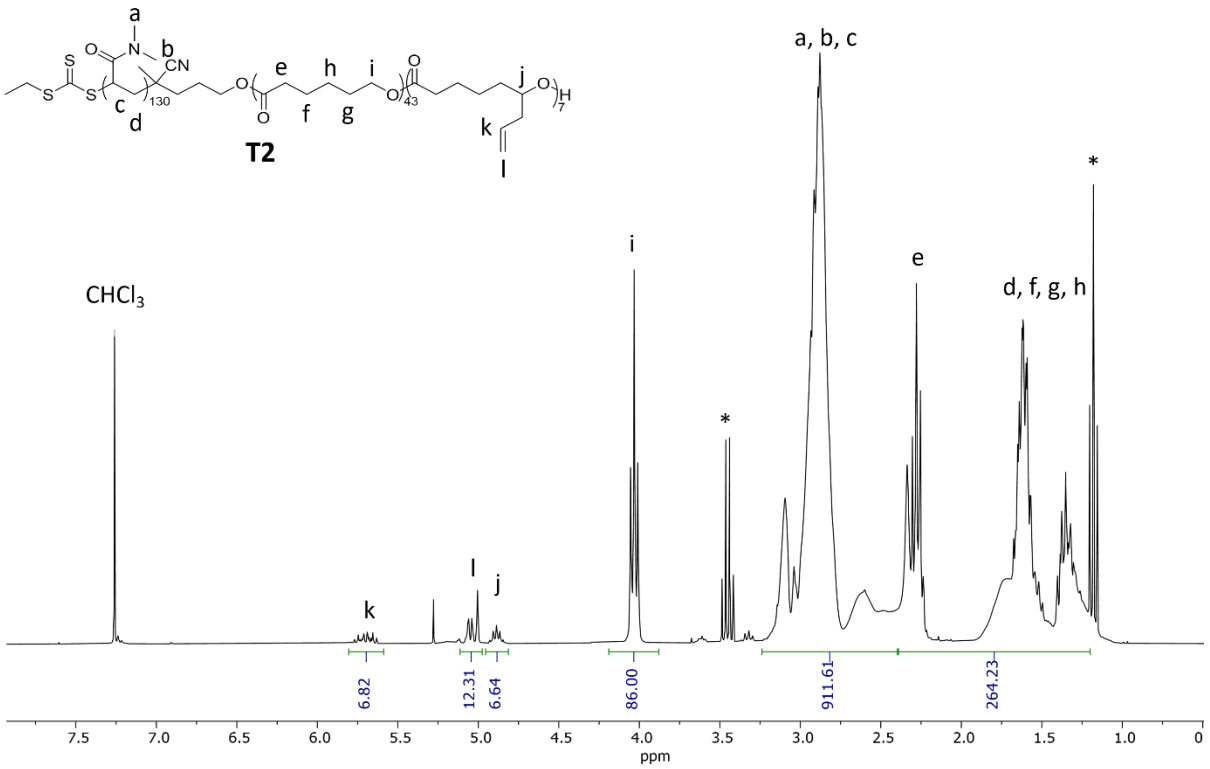


Figure S4.7. ^{1}H NMR spectrum ($CDCl_3$, 300 MHz, 298 K) of $PDMA_{130}$-*b*-PCL_{43}-*co*-$PACL_7$ (T2 in Table 4.2). *Correspond to diethyl ether peaks.

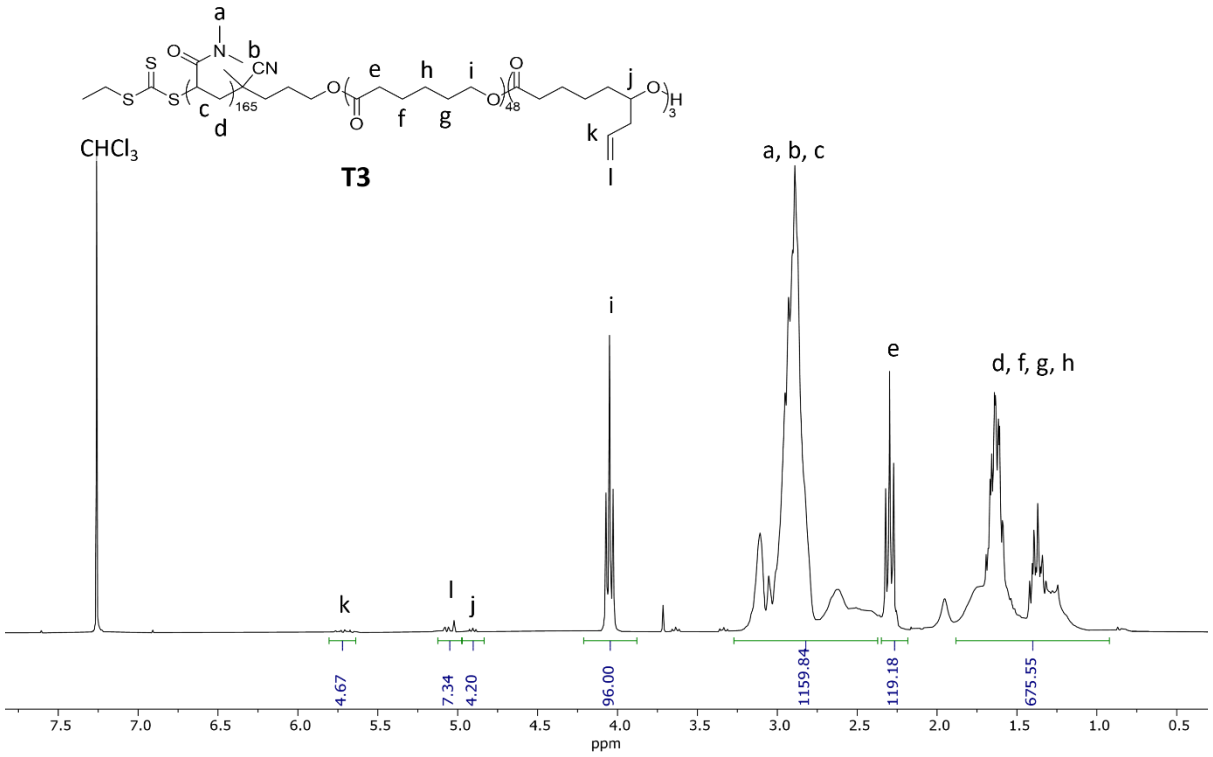


Figure S4.8. ^{1}H NMR spectrum ($CDCl_3$, 300 MHz, 298 K) of $PDMA_{165}$-*b*-PCL_{48}-*co*-$PACL_3$ (T3 in Table 4.2).

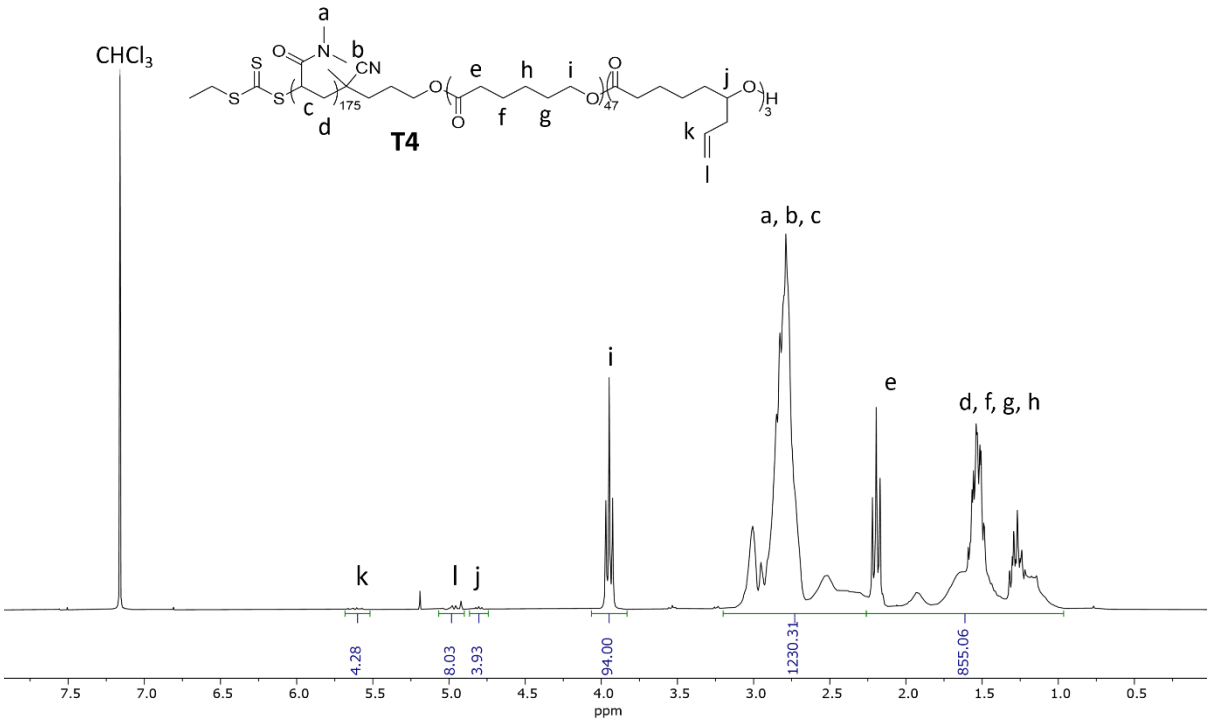


Figure S4.9. ^{1}H NMR spectrum ($CDCl_3$, 300 MHz, 298 K) of $PDMA_{175}$-*b*-PCL_{47}-*co*-$PACL_3$ (T4 in Table 4.2).

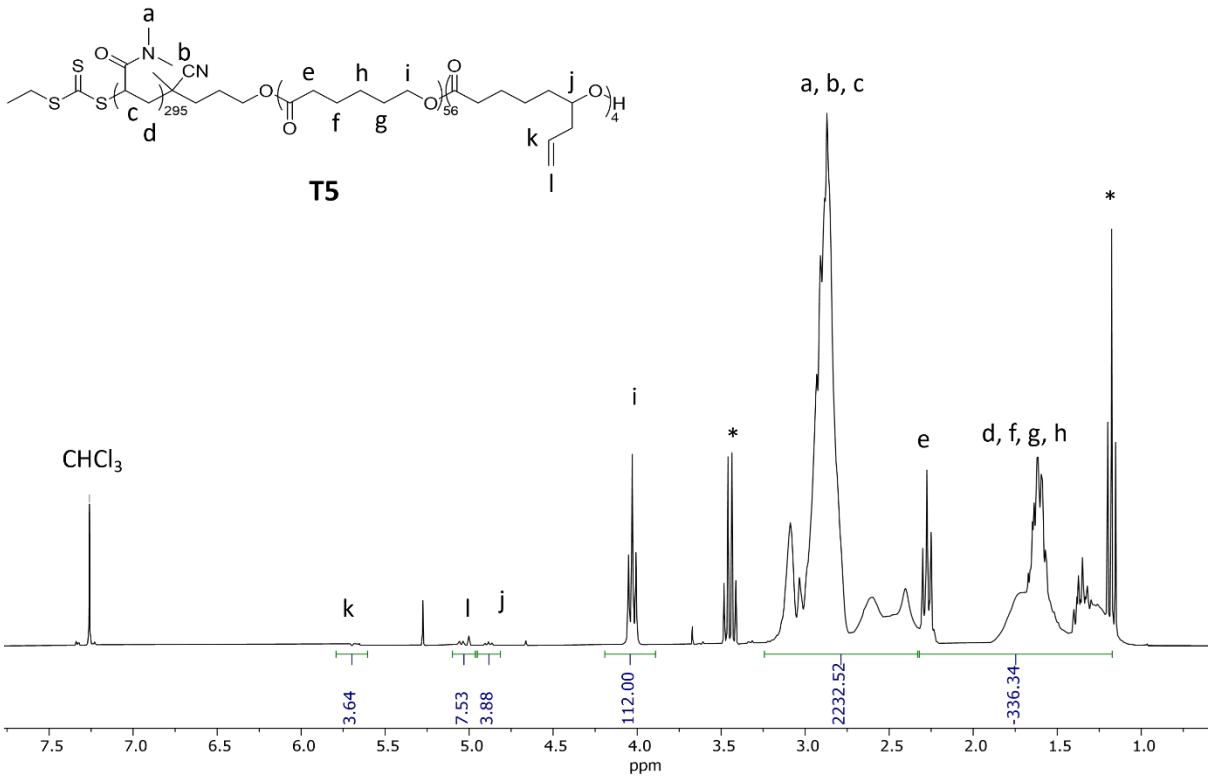


Figure S4.10. ^{1}H NMR spectrum ($CDCl_3$, 300 MHz, 298 K) of $PDMA_{295}$-*b*-PCL_{58}-*co*-$PACL_4$ (T5 in Table 4.2). *Correspond to diethyl ether peaks.

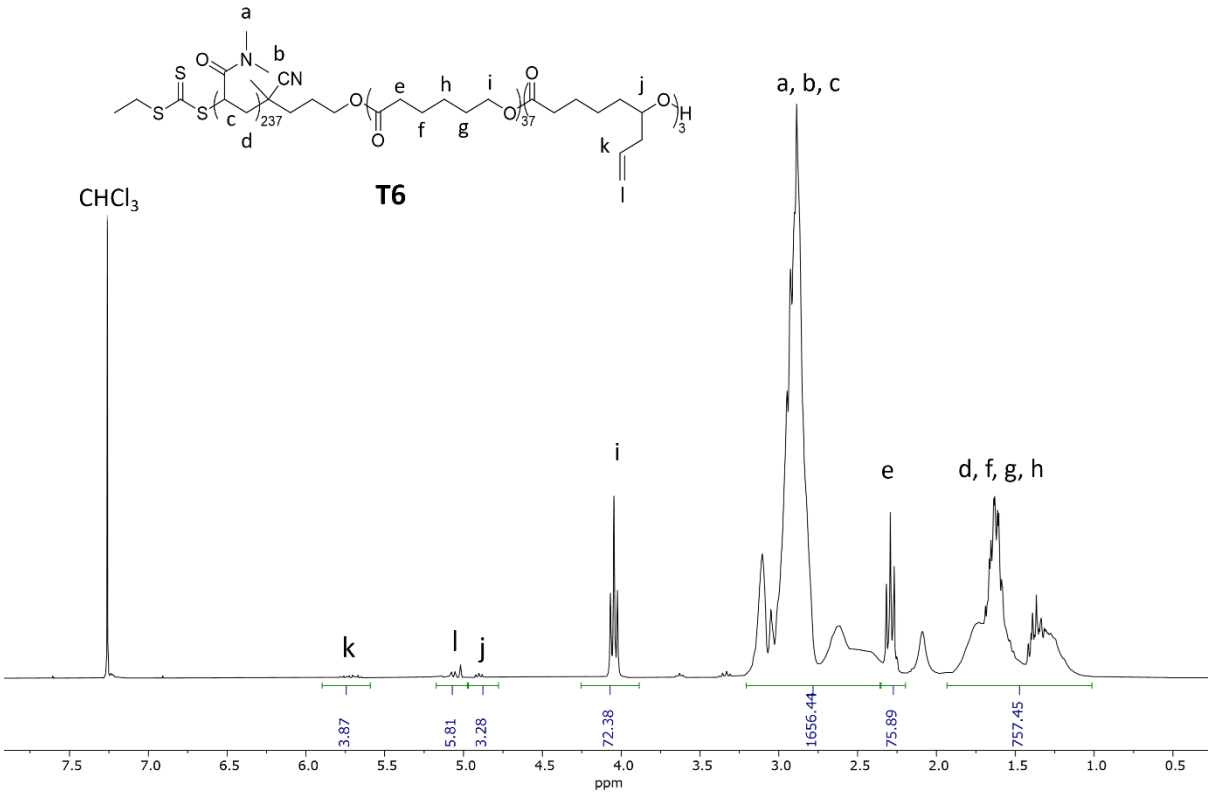


Figure S4.11. ^{1}H NMR spectrum ($CDCl_3$, 300 MHz, 298 K) of $PDMA_{237}$-*b*-PCL_{37}-*co*-$PACL_3$ (T6 in Table 4.2).

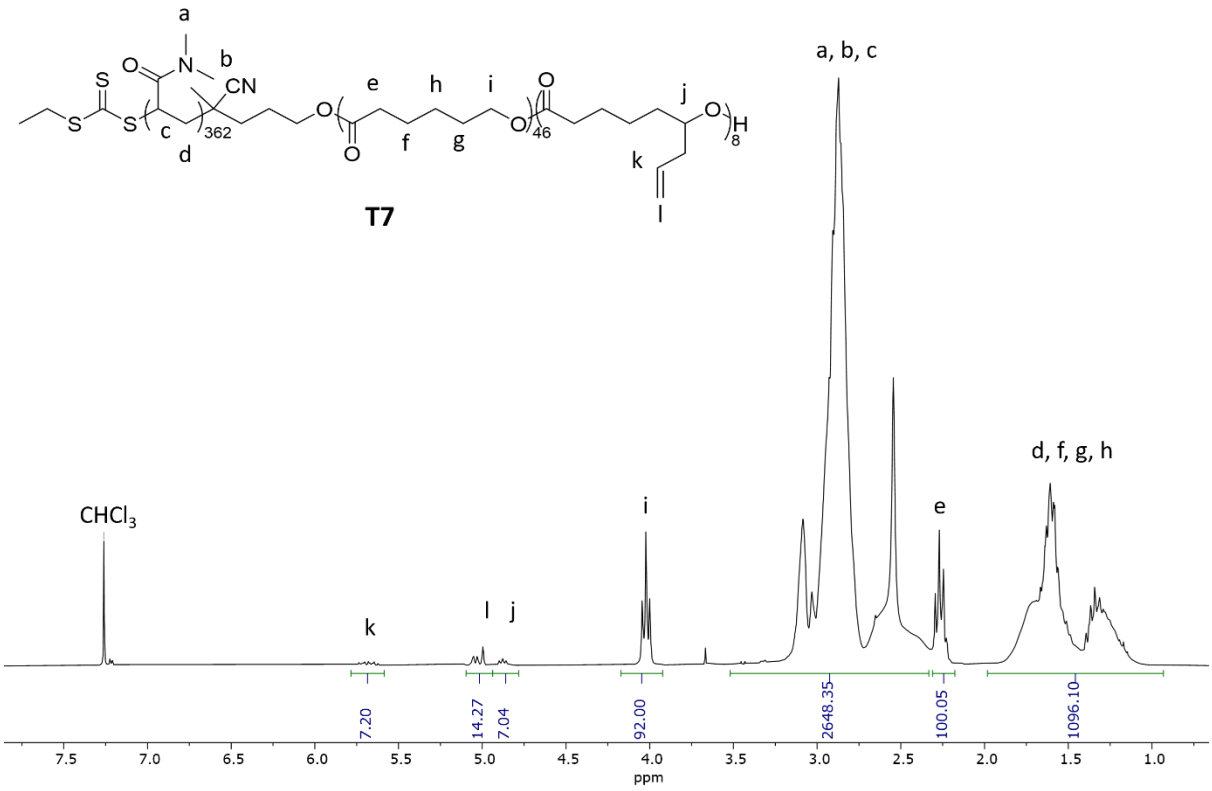


Figure S4.12. ^{1}H NMR spectrum ($CDCl_3$, 300 MHz, 298 K) of $PDMA_{362}$-*b*-PCL_{48}-*co*-$PACL_8$ (T7 in Table 4.2).

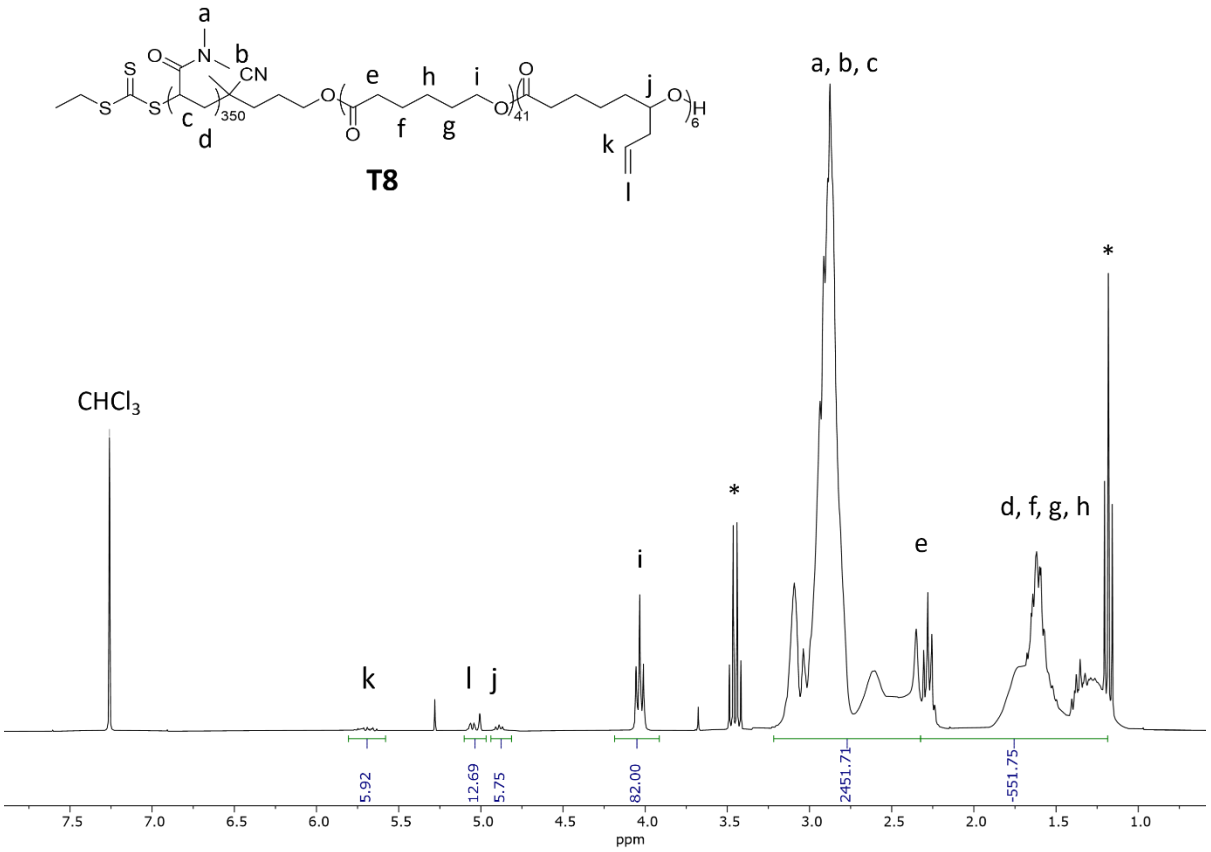


Figure S4.13. ^{1}H NMR spectrum ($CDCl_3$, 300 MHz, 298 K) of $PDMA_{350}$-*b*-PCL_{41}-*co*-$PACL_6$ (T8 in Table 4.2). *Correspond to diethyl ether peaks.

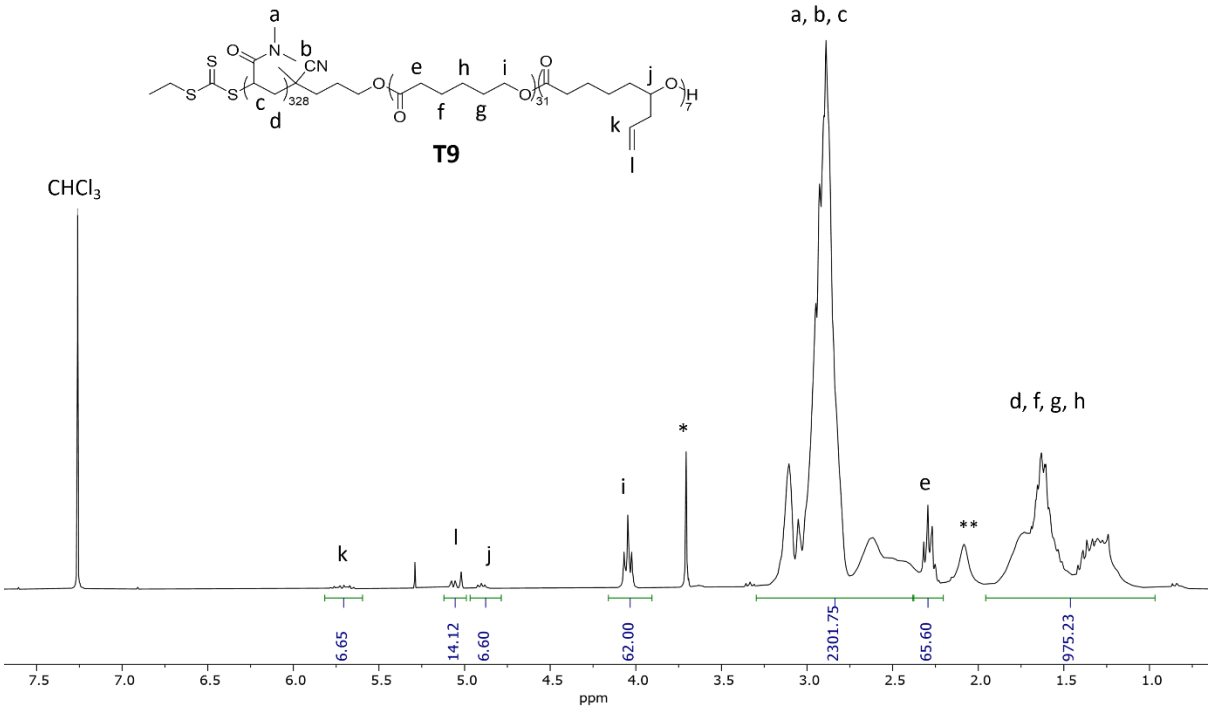


Figure S4.14. ^{1}H NMR spectrum ($CDCl_3$, 300 MHz, 298 K) of $PDMA_{328}$-*b*-PCL_{31}-*co*-$PACL_7$ (T9 in Table 4.2). *Correspond to dioxane peak. **Correspond to acetone peak.

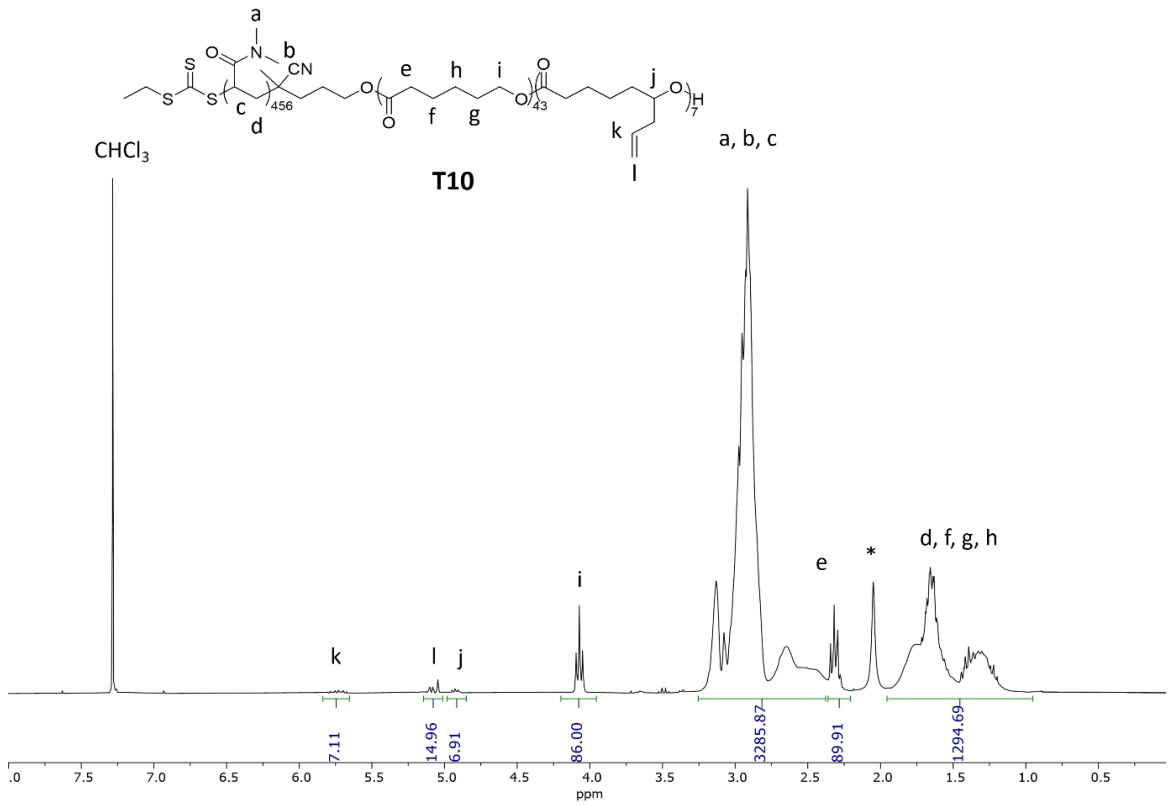


Figure S4.15. ^{1}H NMR spectrum ($CDCl_3$, 300 MHz, 298 K) of $PDMA_{456}$-*b*-PCL_{43}-*co*-$PACL_7$ (T10 in Table 4.2). *Correspond to acetone peak.

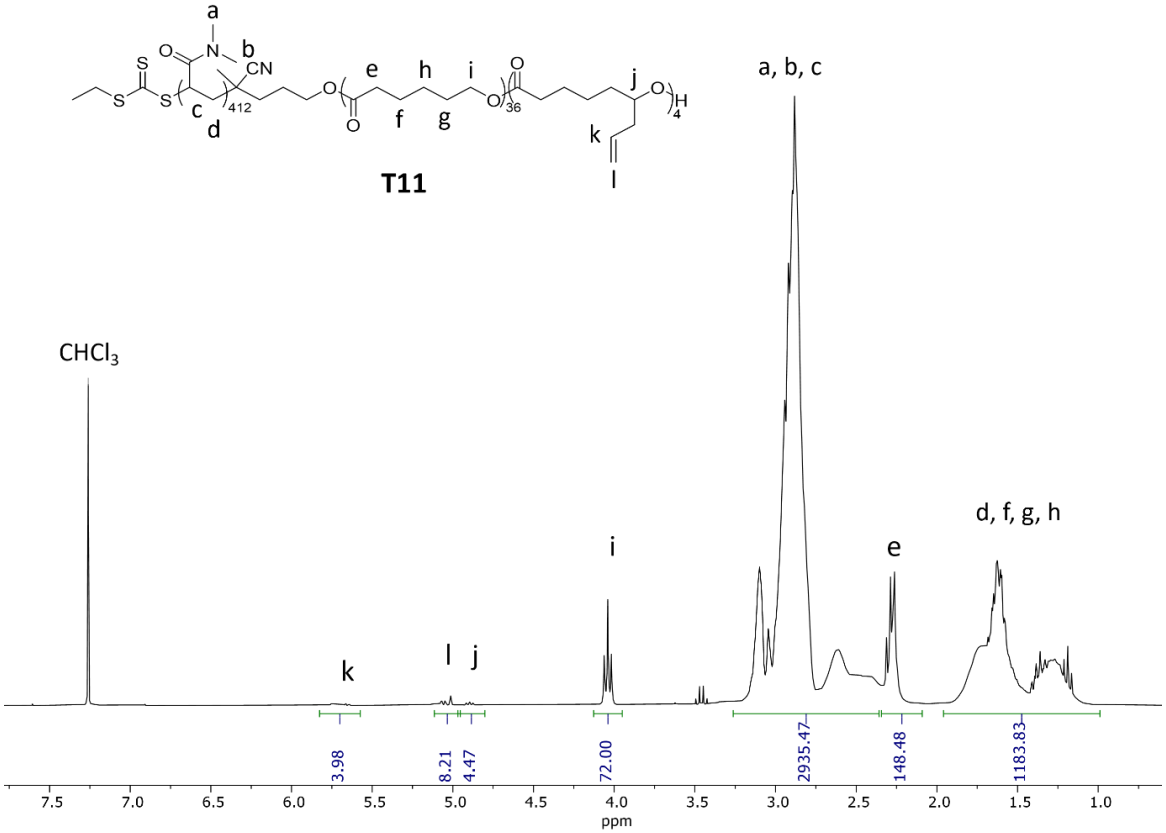


Figure S4.16. ^{1}H NMR spectrum ($CDCl_3$, 300 MHz, 298 K) of $PDMA_{412}$-*b*-PCL_{36}-*co*-$PACL_4$ (T11 in Table 4.2).

Table S4.1. Synthesis of $PDMA_w$-*b*-PMMA-*b*-PCL_x-*co*-$PACL_y$ block copolymers with different core and corona lengths.[a]

Entry	Block copolymer	Corona:core ratio[b]	$M_{n,}$[c] (kDa)	$Đ_M$[c]	DMA units (wt.%)	T_m[d] (°C)
M1	$PDMA_{57}$-*b*-$PMMA_{20}$-*b*-PCL_{38}-*co*-$PACL_4$	1:1	26.0	1.20	28.9	33.8
M2	$PDMA_{156}$-*b*-$PMMA_{20}$-*b*-PCL_{54}-*co*-$PACL_3$	2:1	30.5	1.18	30.0	34.8
M3	$PDMA_{233}$-*b*-$PMMA_{19}$-*b*-PCL_{43}-*co*-$PACL_7$	3.4:1	29.5	1.31	22.9	29.4
M4	$PDMA_{330}$-*b*-$PMMA_{18}$-*b*-PCL_{46}-co-$PACL_8$	6.4:1	43.8	1.18	30.0	25.9
M5	$PDMA_{348}$-*b*-$PMMA_{20}$-*b*-PCL_{36}-*co*-$PACL_4$	9.2:1	50.8	1.17	30.0	*

[a] All polymerisations were carried out in 1,4-dioxane at 70 °C and quenched after 35 min. [b] Ratio between the PDMA block (corona) and the PMMA-*b*-PCL-based BCP (core) obtained from ^{1}H NMR spectroscopy. [c] Measured by SEC ($CHCl_3$ with 0.5% Et_3N, PMMA standard). [d] Measured by nano DSC, triblock copolymers in ethanol (100 to 0 °C, 1 °C min^{-1}).

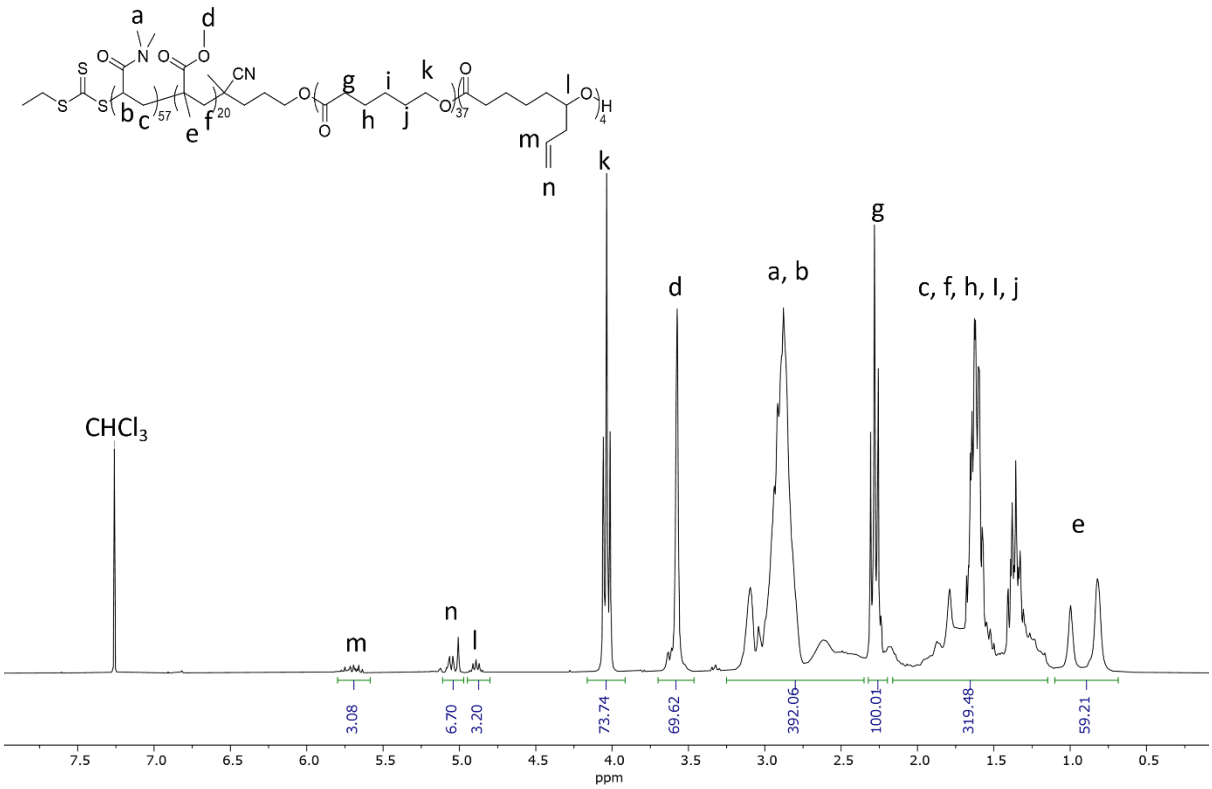


Figure S4.17. ^{1}H NMR spectrum ($CDCl_3$, 300 MHz, 298 K) of $PDMA_{57}$-*b*-$PMMA_{20}$-*b*-PCL_{37}-*co*-$PACL_4$ (**M1** in Table S4.1).

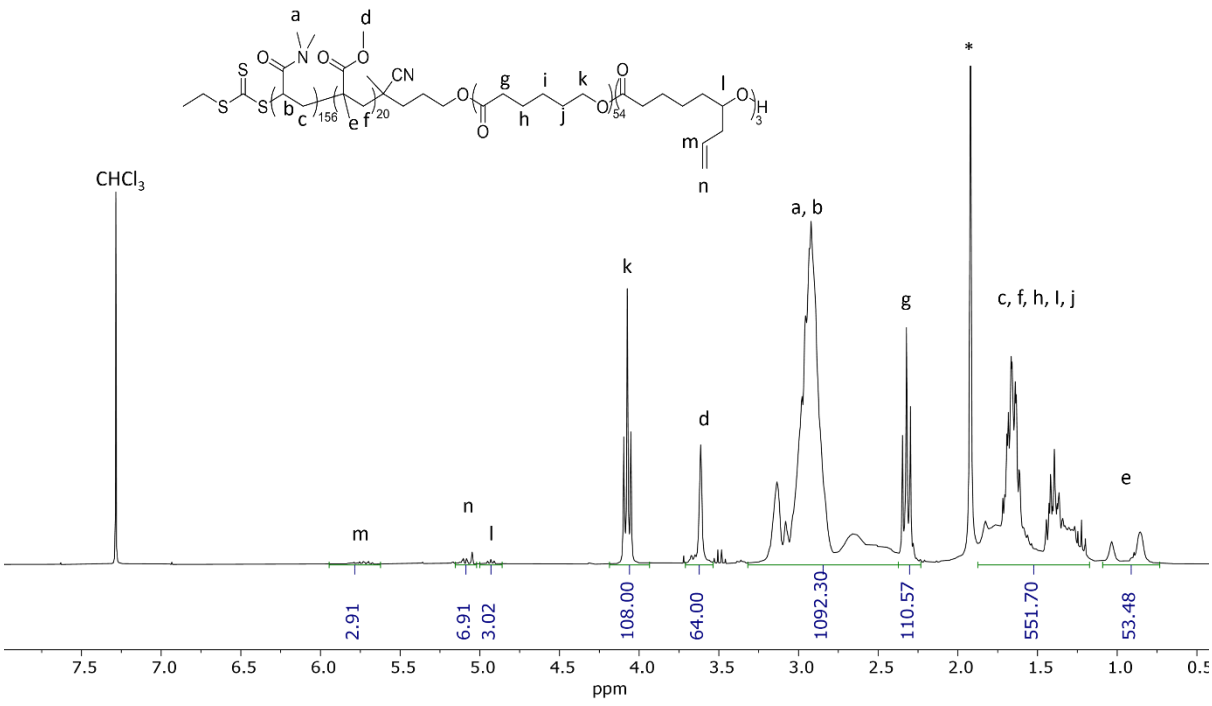


Figure S4.18. ^{1}H NMR spectrum ($CDCl_3$, 300 MHz, 298 K) of $PDMA_{156}$-*b*-$PMMA_{20}$-*b*-CL_{54}-*co*-$PACL_3$ copolymer (**M2** in table S4.1). *Corresponds to acetone peak.

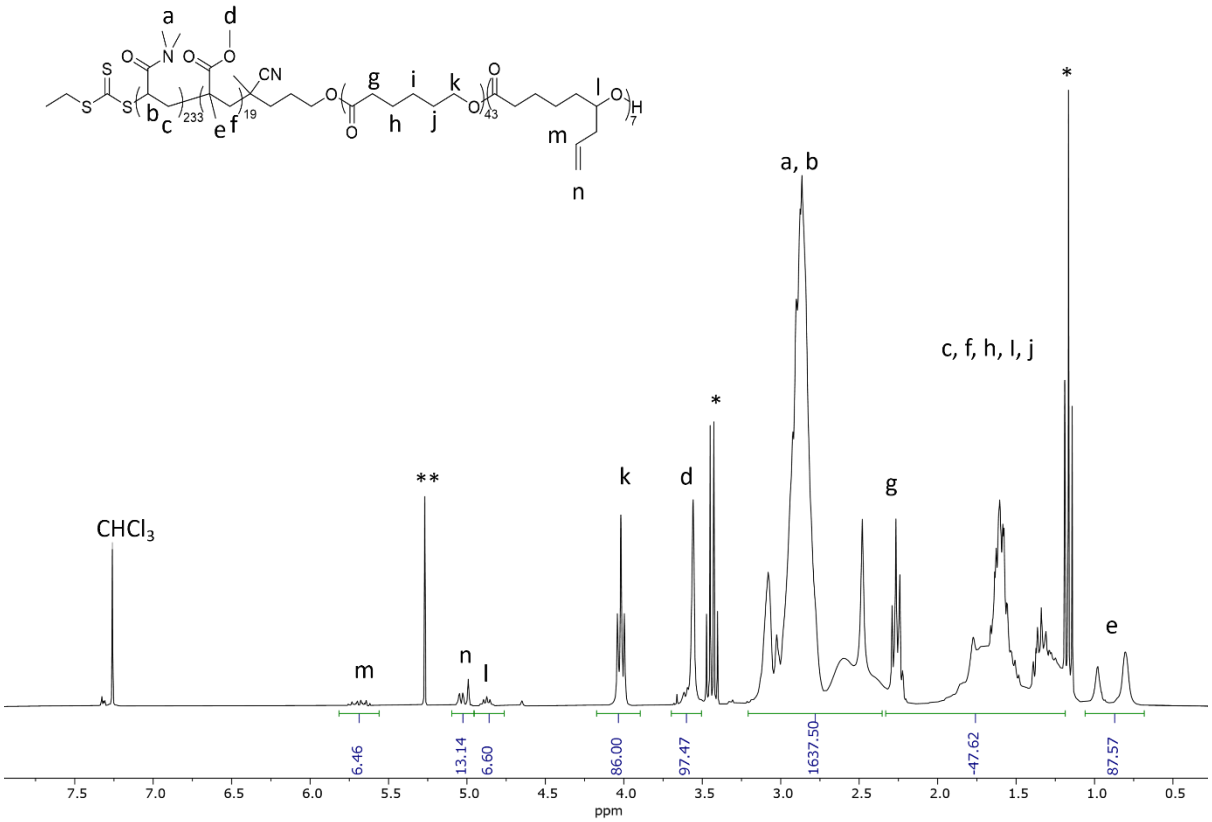


Figure S4.19. ^{1}H NMR spectrum ($CDCl_3$, 300 MHz, 298 K) of $PDMA_{233}$-*b*-$PMMA_{19}$-*b*-PCL_{43}-*co*-$PACL_7$ (**M3** in Table S4.1). *Correspond to diethyl ether peak and ** correspond to dichloromethane peak.

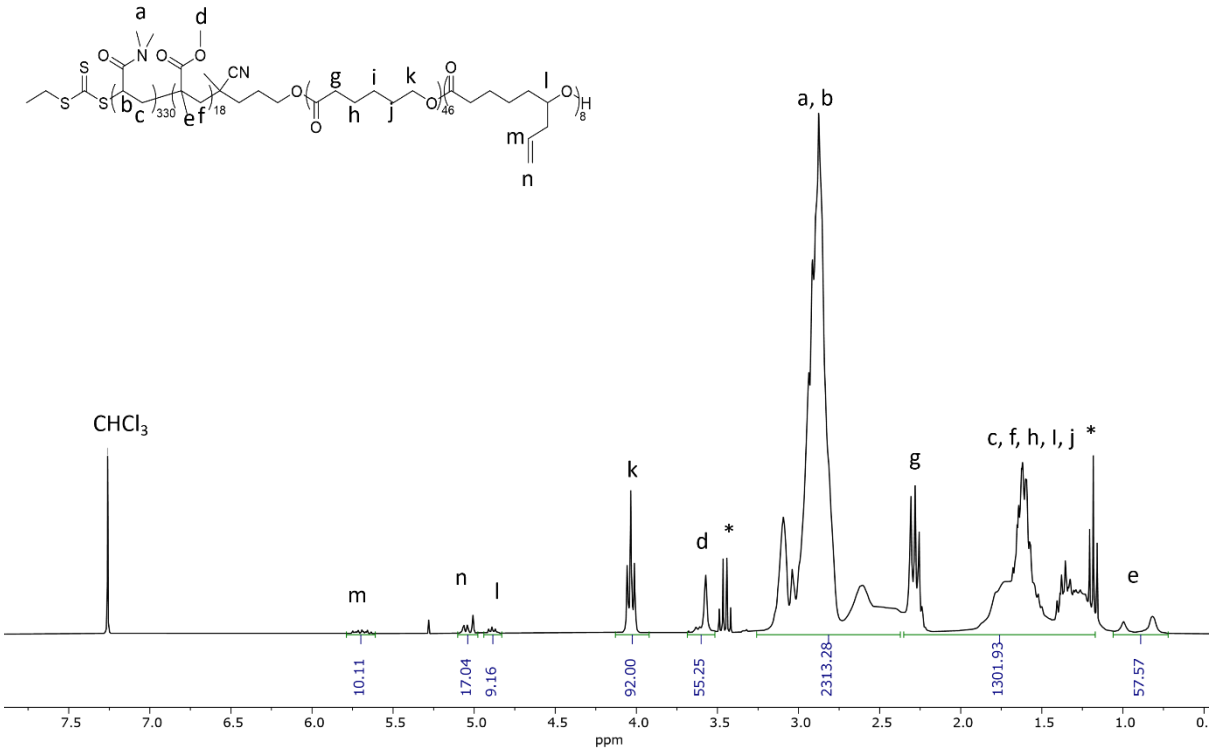


Figure S4.20. ^{1}H NMR spectrum ($CDCl_3$, 300 MHz, 298 K) of $PDMA_{330}$-*b*-$PMMA_{18}$-*b*-PCL_{46}-*co*-$PACL_8$ (**M4** in Table S4.1). *Correspond to diethyl ether peak.

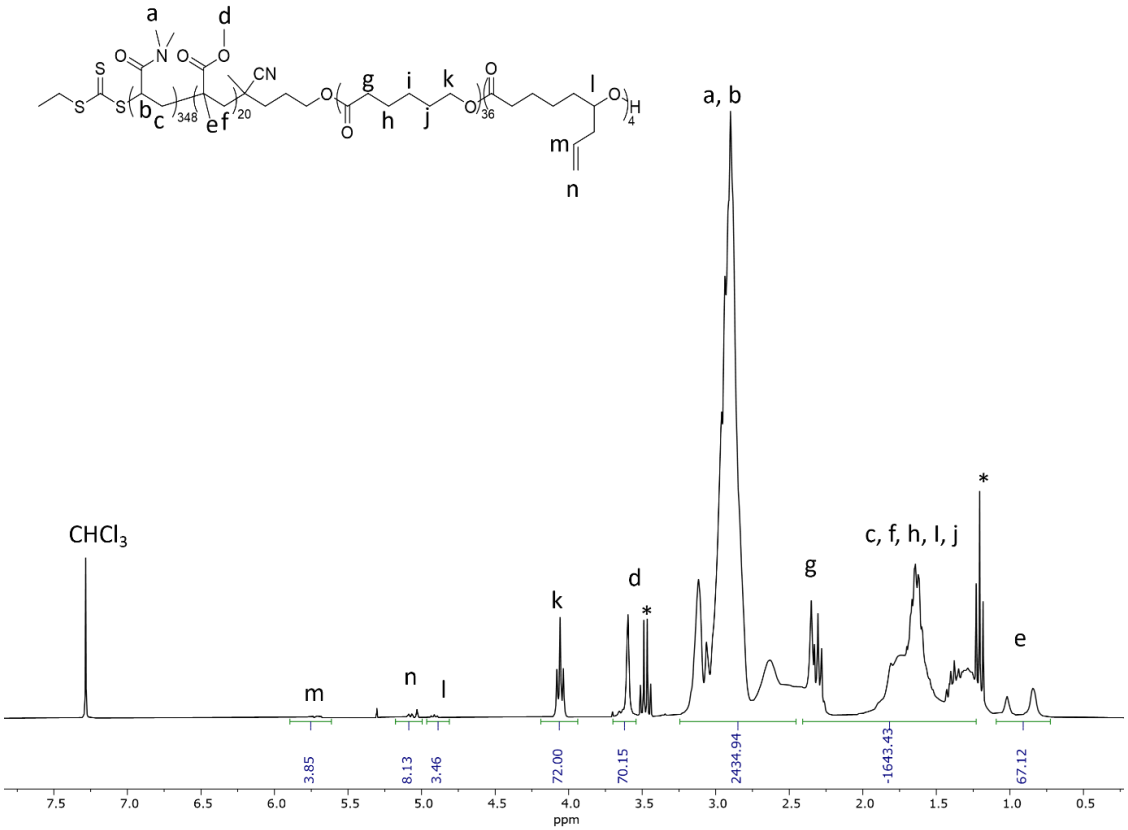


Figure S4.21. ^{1}H NMR spectrum ($CDCl_3$, 300 MHz, 298 K) of $PDMA_{348}$-*b*-$PMMA_{20}$-*b*-PCL_{36}-*co*-$PACL_4$ (**M5** in Table S4.1). *Correspond to diethyl ether peak.

Table S4.2. Summary of thiol-ene addition reactions with 2-mercapto benzyl.[a]

Entry	Block copolymer	Corona:core ratio[b]	$M_{n,}$[c] (kDa)	$Đ_M$[c]
Thiol-T1	$PDMA_{94}$-*b*-PCL_{44}-*co*-$PACL_3$	2:1	19.5	1.21
Thiol-T2	$PDMA_{130}$-*b*-PCL_{43}-*co*-$PACL_7$	2.6:1	12.2	1.34
Thiol-T3	$PDMA_{165}$-*b*-PCL_{48}-*co*-$PACL_3$	3.2:1	20.2	1.27
Thiol-T4	$PDMA_{175}$-*b*-PCL_{47}-*co*-$PACL_3$	3.5:1	20.5	1.20
Thiol-T5	$PDMA_{295}$-*b*-PCL_{56}-*co*-$PACL_4$	5:1	28.1	1.26
Thiol-T6	$PDMA_{237}$-*b*-PCL_{36}-*co*-$PACL_3$	6:1	18.5	1.22
Thiol-T7	$PDMA_{362}$-*b*-PCL_{46}-*co*-$PACL_8$	6.7:1	36.6	1.22
Thiol-T8	$PDMA_{350}$-*b*-PCL_{41}-*co*-$PACL_6$	7.5:1	40.8	1.28
Thiol-T9	$PDMA_{328}$-*b*-PCL_{31}-*co*-$PACL_7$	8.7:1	20.0	1.20
Thiol-T10	$PDMA_{456}$-*b*-PCL_{43}-*co*-$PACL_7$	9.1:1	32.0	1.25
Thiol-T11	$PDMA_{412}$-*b*-PCL_{36}-*co*-$PACL_4$	10.3:1	40.2	1.23
Thiol-M1	$PDMA_{57}$-*b*-$PMMA_{20}$-*b*-PCL_{37}-*co*-$PACL_4$	1:1	23.1	1.37
Thiol-M2	$PDMA_{156}$-*b*-$PMMA_{20}$-*b*-PCL_{54}-*co*-$PACL_3$	2:1	29.0	1.26
Thiol-M4	$PDMA_{330}$-*b*-$PMMA_{18}$-*b*-PCL_{46}-*co*-$PACL_8$	6.4	42.1	1.60

[a] All thiol-ene additions were carried out in a UV light chamber (λ = 350-400 nm) and quenched after 3 h of exposure. [b] Ratio between the PDMA block (corona) and the functional-PCL copolymer (core) obtained from ^{1}H NMR spectroscopy. [c] Measured by SEC ($CHCl_3$ with 0.5% Et_3N, PMMA standard).

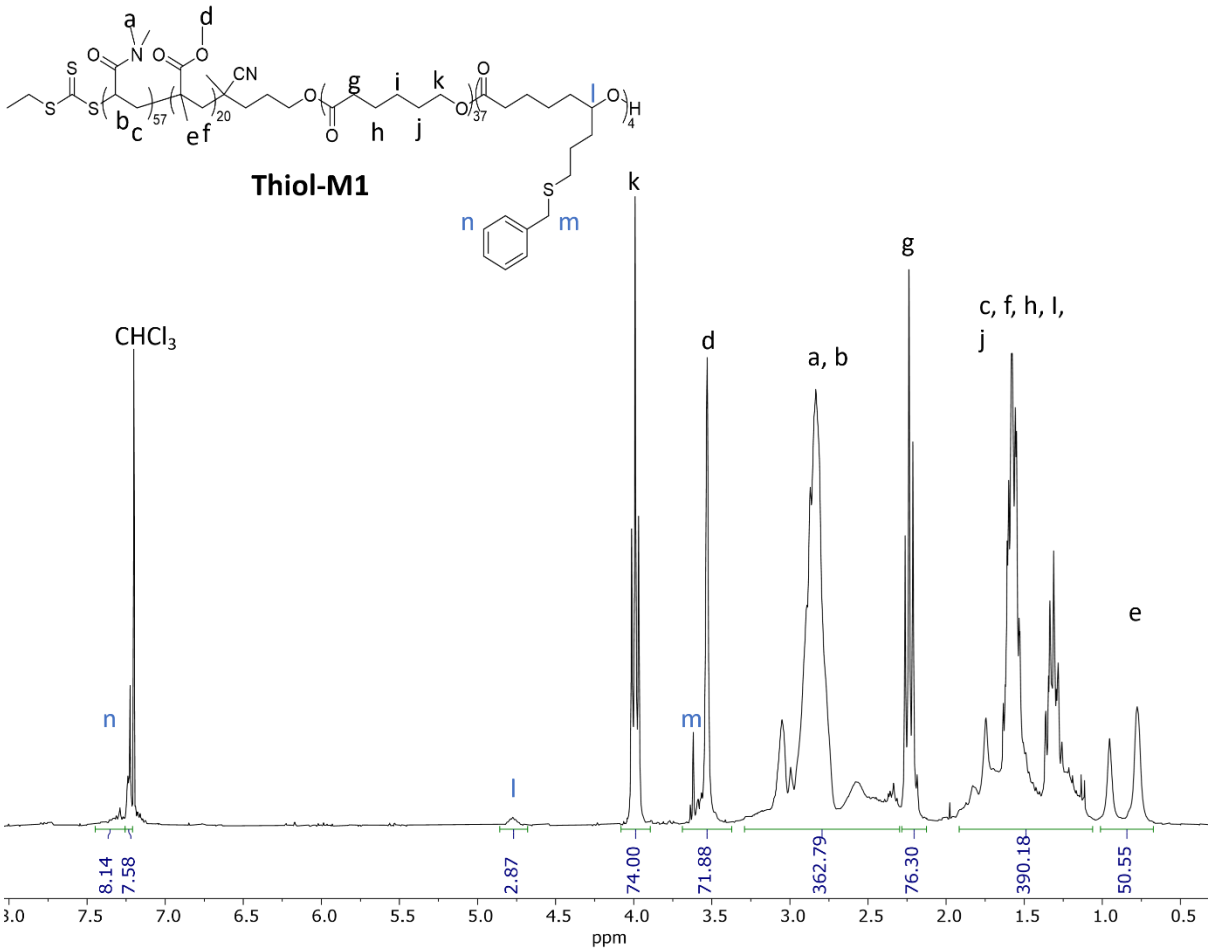


Figure S4.22. ^{1}H NMR spectrum ($CDCl_3$, 300 MHz, 298 K) of benzyl functionalised $PDMA_{57}$-*b*-$PMMA_{20}$-*b*-PCL_{37}-*co*-$PACL_4$ (Thiol-M1 in Table S4.2).

4.6.3 Crystallisation-driven self-assembly

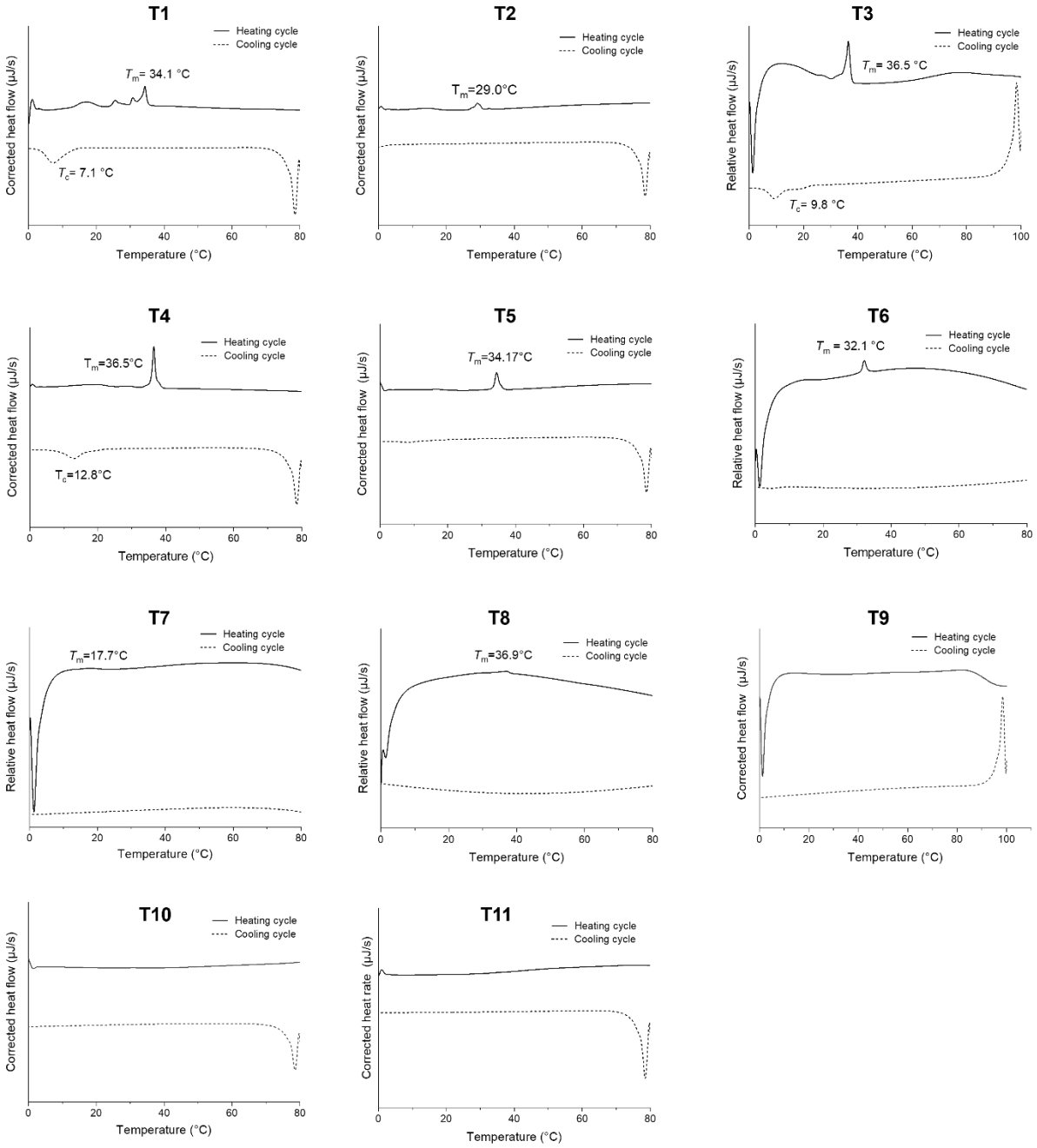


Figure S4.23. Nano DSC thermograms of $PDMA_w$-*b*-PCL_x-*co*-$PACL_y$ assemblies (100 to 0 °C, 1 °C min^{-1}) showing the first cooling-heating cycle (exo-down, endo-up).

Table S4.3. Summary of CDSA of benzyl-functionalised block copolymers.[a]

Entry	Diblock copolymer	Self-assembly morphology [b]	Aging time [c]
Thiol-T1	$PDMA_{122}$-*b*-PCL_{53}-*co*-$PACL_3$	Wide-core cylinders	10 weeks
Thiol-T2	$PDMA_{130}$-*b*-PCL_{43}-*co*-$PACL_7$	Platelets	8 weeks
Thiol-T4[d]	$PDMA_{175}$-*b*-PCL_{47}-*co*-$PACL_3$	Wide-core cylinders	20 weeks
Thiol-T5	$PDMA_{295}$-*b*-PCL_{56}-*co*-$PACL_4$	Wide-core cylinders	16 weeks
Thiol-T7	$PDMA_{362}$-*b*-PCL_{46}-*co*-$PACL_8$	Platelets	18 weeks
Thiol-T8	$PDMA_{350}$-*b*-PCL_{41}-*co*-$PACL_6$	Wide-core cylinders	18 weeks
Thiol-T10	$PDMA_{456}$-*b*-PCL_{43}-*co*-$PACL_7$	Platelets	18 weeks
Thiol-T11	$PDMA_{412}$-*b*-PCL_{36}-*co*-$PACL_4$	Wide-core cylinders	18 weeks
Thiol-M1	$PDMA_{57}$-*b*-$PMMA_{20}$-*b*-PCL_{38}-*co*-$PACL_4$	Mixed morphologies	3 weeks
Thiol-M2	$PDMA_{156}$-*b*-$PMMA_{20}$-*b*-PCL_{54} *co*-$PACL_3$	Cylinders	2 weeks
Thiol-M4	$PDMA_{330}$-*b*-$PMMA_{18}$-*b*-PCL_{46} *co*-$PACL_8$	Platelets	6 weeks

[a] Full benzyl mercaptan conjugation previously confirmed by ^{1}H NMR spectroscopy. [b] Observed by TEM. Samples negatively stained using uranyl acetate (0.5 wt %). [c] Time between self-assembly and TEM imaging. [d] % benzyl conjugation = 66.7%.

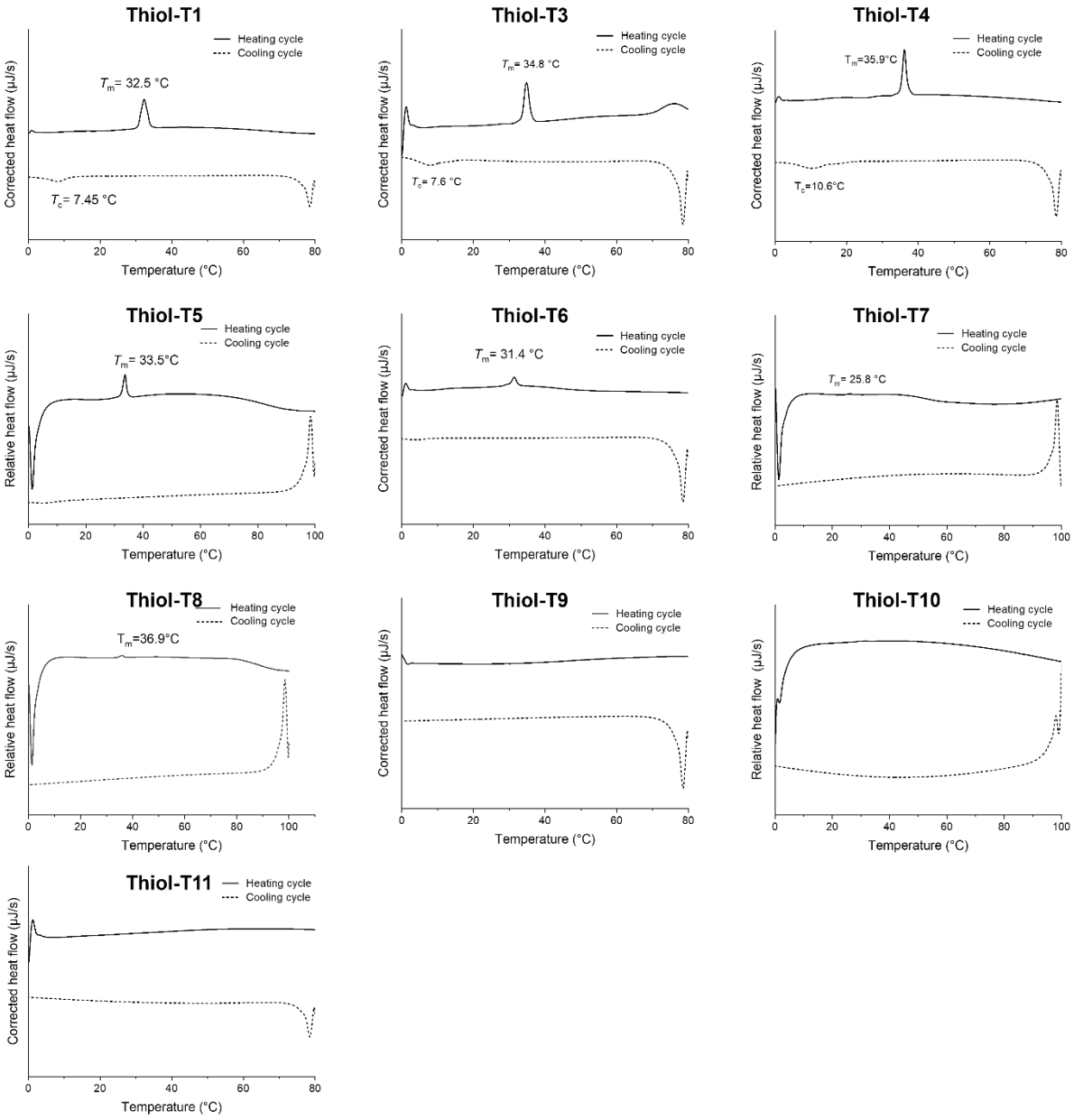


Figure S4.24. Nano DSC thermograms of benzyl functionalised $PDMA_w$-*b*-PCL_x-*co*-$PACL_y$ assemblies (100 to 0 °C, 1 °C min^{-1}) showing the first cooling-heating cycle (exo-down, endo-up).

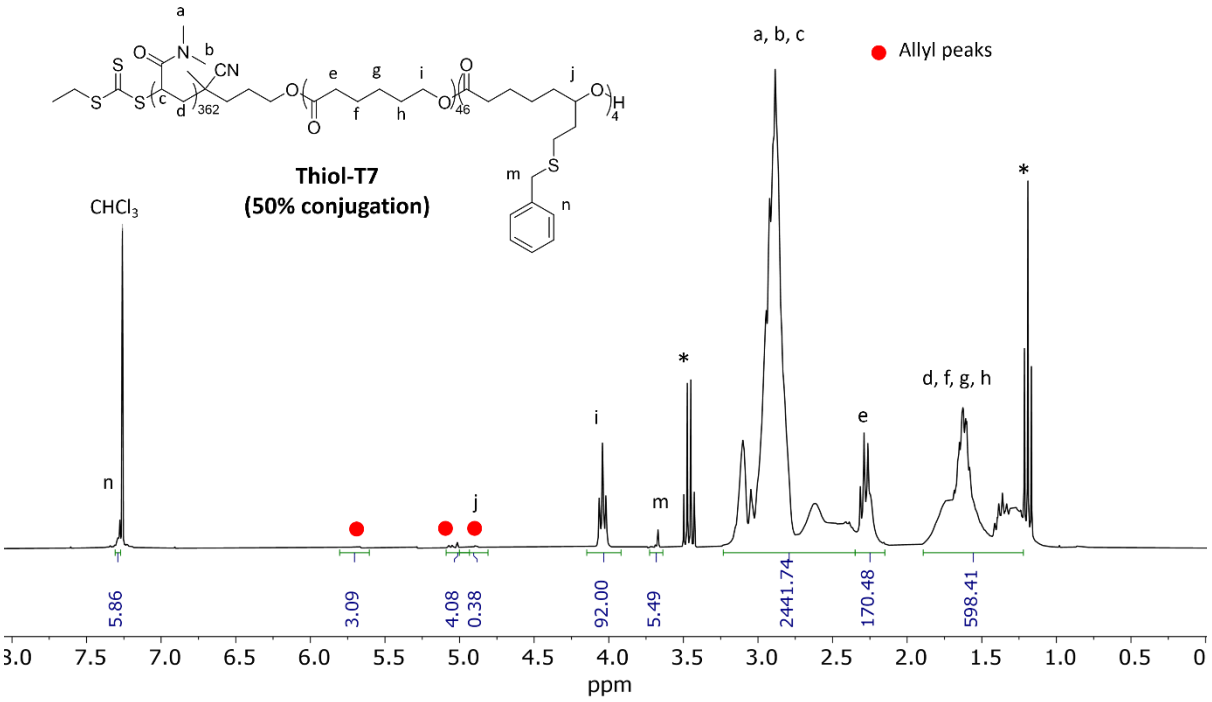


Figure S4.25. ^{1}H NMR spectrum ($CDCl_3$, 300 MHz, 298 K) of 50% benzyl functionalised $PDMA_{362}$-*b*-PCL_{46}-*co*-$PACL_8$ (Thiol-T7). *Corresponds to diethyl ether peak and red dots correspond to non-conjugated allyl pendant group protons.

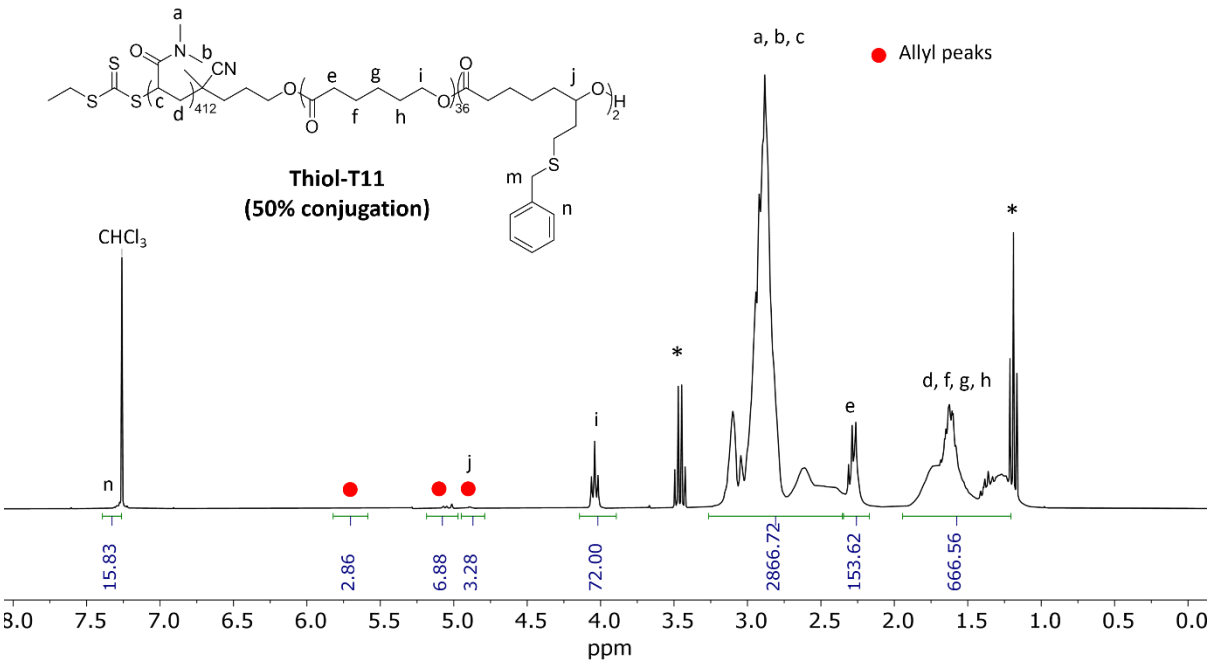


Figure S4.26. ^{1}H NMR spectrum ($CDCl_3$, 300 MHz, 298 K) of 50% benzyl functionalised $PDMA_{412}$-*b*-PCL_{36}-*co*-$PACL_4$ (Thiol-T11). *Corresponds to diethyl ether peak and red dots correspond to non-conjugated allyl pendant group protons.

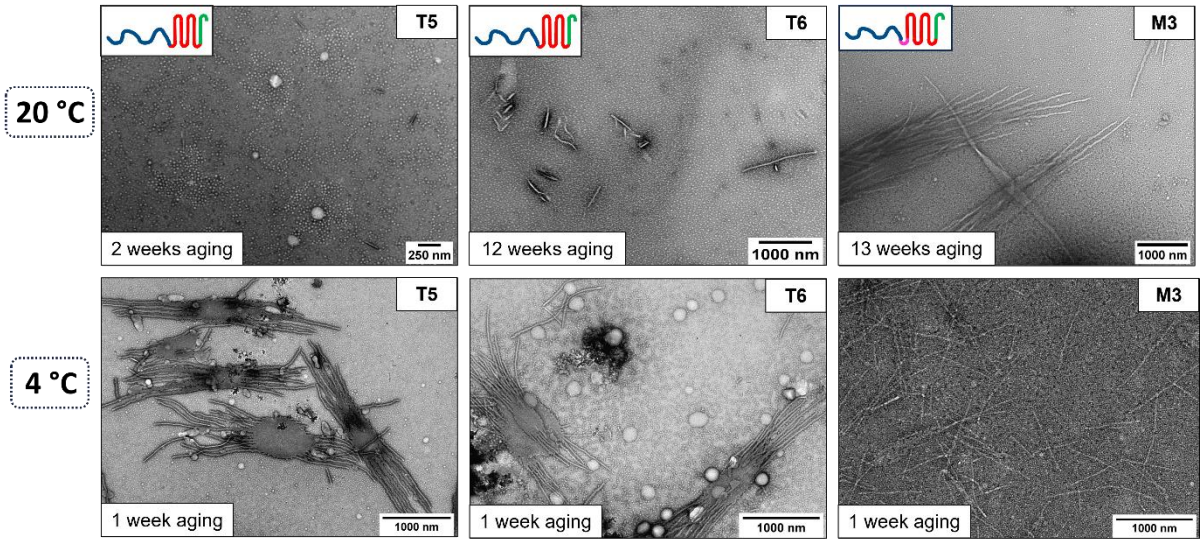


Figure S4.27. Effect of aging temperature on the self-assembly morphology. TEM micrographs of $PDMA_{295}$-*b*-PCL_{56}-*co*-$PACL_4$ (T5 in table 4.3) (left), $PDMA_{237}$-*b*-PCL_{36}-*co*-$PACL_3$ (T6 in table 4.3) (middle) and $PDMA_{233}$-*b*-$PMMA_{19}$-*b*-PCL_{43}-*co*-$PACL_7$ (M3 in table 4) (left) at room temperature (20 °C) (up) and in the fridge (4 °C) (down). Samples were negatively stained using uranyl acetate (0.5 wt. %).

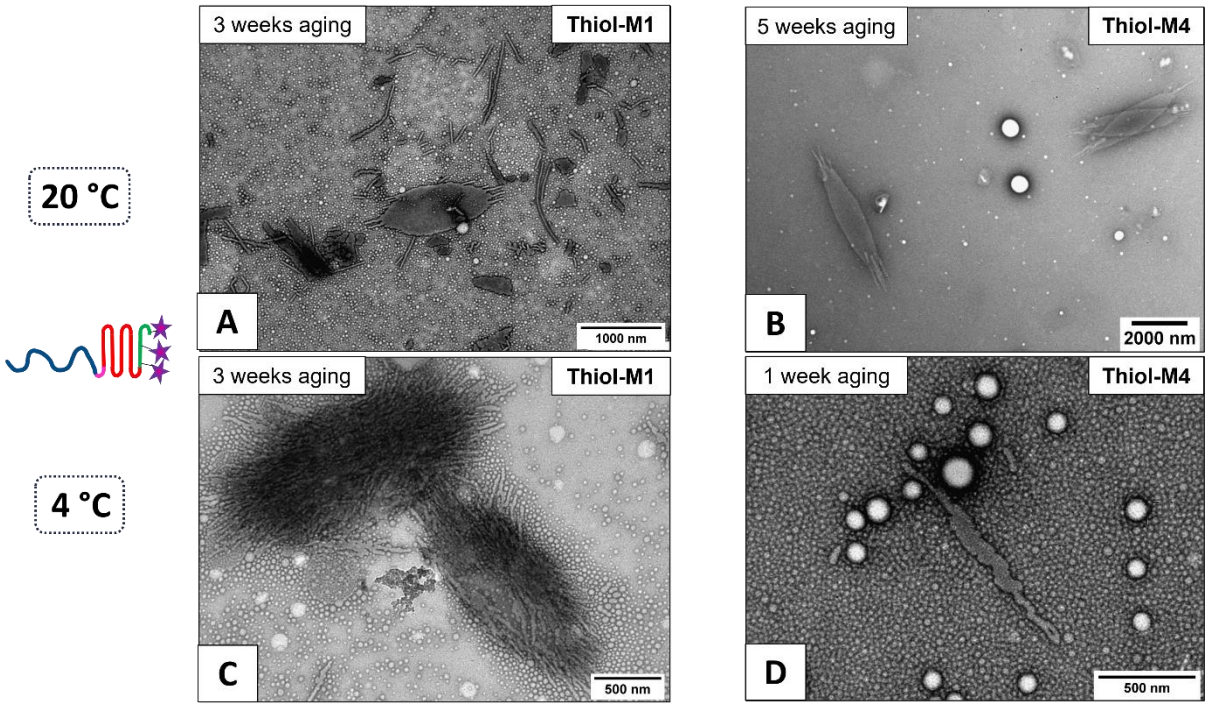


Figure S4.28. Effect of aging temperature on the self-assembly morphology. A) and C) TEM micrographs of benzyl functionalised $PDMA_{57}$-*b*-$PMMA_{20}$-*b*-PCL_{38}-*co*-$PACL_4$ (**Thiol-M1**) aged at 20 °C and 4 °C respectively. B) and D) TEM micrographs of benzyl functionalised $PDMA_{330}$-*b*-$PMMA_{18}$-*b*-PCL_{46}-*co*-$PACL_8$ (**Thiol-M4**) aged at 20 °C and 4 °C respectively. Samples were negatively stained using uranyl acetate (0.5 wt. %). White spots correspond to grid artifacts.

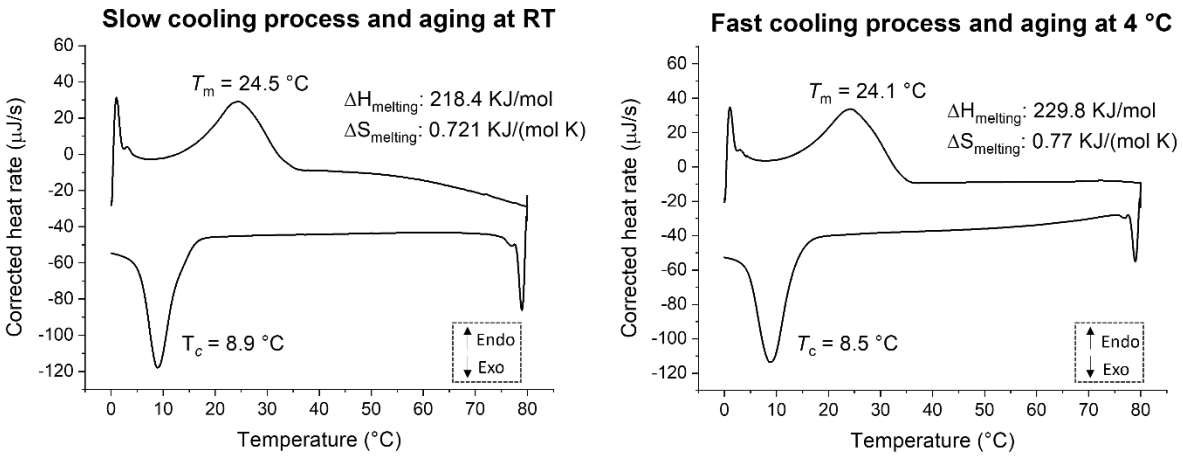


Figure S4.29. Nano DSC thermograms (100 to 0 °C, 1 °C min^{-1}) showing first cooling-heating cycle of $PDMA_{89}$-*b*-PCL_{39}-*co*-$PACL_3$ self-assemblies in ethanol (conc. = 5 mg mL^{-1}) after slow cooling and aging at 20 °C (left) and fast cooling and aging at 4 °C (right). Showing the melting enthalpy ($\Delta H_{melting}$) and entropy ($\Delta S_{melting}$) of the processes in the mentioned conditions.

Chapter 5.

Understanding the living CDSA and biological performance of $PDMA_w$-*b*-($PMMA_{20}$)-*b*-PCL_x-*co*-$PACL_y$ copolymers.

5 Understanding the living CDSA and biological performance of $PDMA_w$-*b*-($PMMA_{20}$)-*b*-PCL_x-*co*-$PACL_y$ copolymers.

5.1 Introduction

Developing functional nanoparticles for bioimaging and therapeutic applications is critical to enhance drug bioavailability and mitigate the side effects of traditional therapies.[1-4] Over the past decades, biocompatible and biodegradable polymeric materials as nanomedicines have received significant interest. For most, their ability to enhance drug delivery and cell targeting, allied with their superior mechanical and physical properties, are crucial challenges facing current drug therapies.[5-8] However, traditional self-assembly strategies often generate polydisperse spherical micelles with dimensions difficult to control,[9-12] disregarding the great influence of particle morphology and dimensions on their biological interactions.[13-16] For example, Discher and coworkers[17] demonstrated that polymeric filament micelles have higher circulation half-life and drug delivery efficacy than their spherical counterparts. Additionally, Huang *et al.* demonstrated that longer rod-shaped nanoparticles presented faster internalisation rates than short rod-shaped and spherical nanoparticles. This study showed that higher anisotropy, which leads to a larger contact area between the nanocarrier and the cell membrane, improved cellular uptake.[18]

Crystallisation-driven self-assembly (CDSA) is a novel and versatile strategy that uses amphiphilic semi-crystalline block copolymers (BCPs) to create a notable range of well-defined anisotropic particles. Examples include diamond-shaped platelets, cylindrical particles and even more complex structures with controlled dimensions.[19-25] To enhance control and tuneability of these self-assemblies, Manners and Winnik introduced the concept of “living” CDSA, a seeded-growth strategy for controlled BCP crystallisation in solution. In CDSA, the

growth of the micelles is governed by the amount of unimer added to a crystalline seed solution.[26, 27] This methodology has proven to be compatible with a variety of semi-crystalline core-forming blocks, including poly(ferrocenylsilane) (PFS), poly(lactic acid) PLA, and poly(caprolactone) PCL.[28-34] The broad scope of core-blocks also allows for a range of applications [35, 36] which include nanomedicine,[37-39] responsive sensors,[40, 41] catalysis[42, 43] and optoelectronics.[44, 45]

Despite the noteworthy advances made through CDSA, the fabrication of monodisperse, biocompatible, and biodegradable functionalised nanostructures in biologically relevant remains a significant challenge, and only a few promising examples have been reported.[46-50] Kempe and coworkers recently reported the preparation of stealthy uniform nanorods with varying lengths from poly(2-methyl-2-oxazoline)-*b*-poly(2-2isopropyl-2-oxazoline) (PMeOX-*b*-PiPrOx) *via* seeded CDSA.[51] In this work, well-defined nanostructures underwent surface modification with a nanobody (7D12) and a cell internalization sensor (sCy5-TCO), which led to biocompatible rod-shaped particles with antigen-binding properties and unprecedented length-dependent cellular internalisation. However, in most cases the modification occurs in the corona block in order to not disrupt the densely packed crystalline core segments. Ultimately, this restricts the use of these structures as drug delivery systems, considering only hydrophilic drugs can be attached to the corona. To the best of our knowledge, there have been no prior reports of CDSA with BCPs bearing direct functionalisation on the core block.

In this chapter, the preparation of uniform and well-defined 1D and 2D nanoparticles bearing BODIPY molecules attached to the semicrystalline core-block *via* living CDSA and the effect of the nanoparticle's dimensions over the biological response were explored. To do this, a functional semicrystalline core-forming block was designed *via* ring-opening copolymerisation

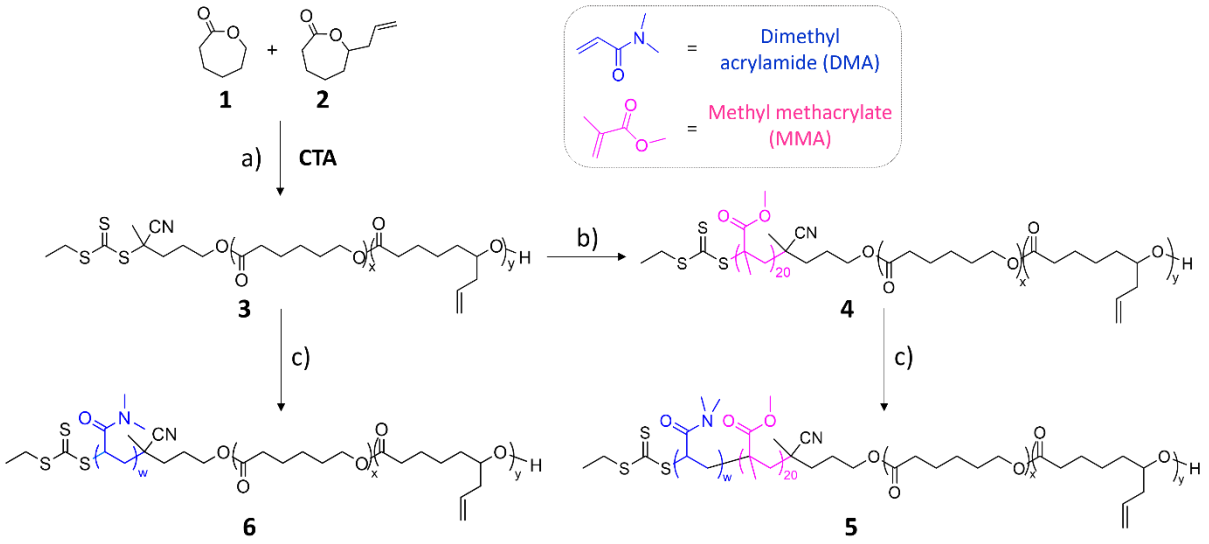
of ε-caprolactone (εCL) and ε-allyl-ε-caprolactone (εACL). Amphiphilic BCPs were prepared by polymerising a short glassy poly(methyl methacrylate) (PMMA) block and a biocompatible hydrophilic poly(*N*,*N*-dimethyl acrylamide) (PDMA) block from this hydrophobic semicrystalline polymer *via* reversible addition/fragmentation chain transfer (RAFT) polymerisation to yield amphiphilic BCPs. In addition, a BODIPY thiol dye was attached to the allyl-pendant group present in the core-forming block (PCL-*co*-PACL) *via* thiol-ene addition, while retaining the semicrystalline nature of PCL. Using CDSA, these BCPs were self-assembled into anisotropic nanostructures, which can be transferred into water. Uniform cylindrical and platelet-like micelles with diverse size were obtained *via* living CDSA, in which the nanoparticle's dimensions can be controlled through the amount of unimer added to solution. Finally, anisotropic core-functionalised nanoparticles demonstrated good cytocompatibility and efficient cell internalisation during preliminary cell studies, showing their great potential as delivery systems.

5.2 Results and discussion

5.2.1 Synthesis of amphiphilic, semicrystalline, functional BCPs

Following our previous studies on polymer design and self-assembly described in Chapter 4, semicrystalline PCL copolymers bearing allyl functional groups (**3**, Scheme 5.1) were synthesised *via* ring-opening polymerisation (ROP) of εCL (**1**, Scheme 5.1) and εACL (**2**, Scheme 5.1) in the presence of diphenyl phosphate (DPP) catalyst. In this polymerisation 2-cyano-5-hydroxypentan-2-yl ethyl carbonotrithioate (CHPET), a hydroxy-terminated dual-head chain transfer agent (CTA) was chosen to allow the ROP and subsequent RAFT polymerisation. To minimise the comonomer effecting the copolymer crystallisation during the self-assembly process, low allyl monomer incorporation (5.2 to 7.3 wt. % of εACL) for all polymerisations was

targeted (**P1-P3**, **Table 5.1**). The successful preparation of poly(ε-caprolactone)-*co*-poly(allyl-ε-caprolactone) (PCL-*co*-PACL) copolymers was confirmed by ^{1}H NMR spectroscopy (**Figure 5.1**). In addition, size-exclusion chromatography (SEC) analyses showed monomodal distributions, with predictable molecular weights and narrow dispersities, further supporting a controlled polymerisation.



Scheme 5.1. Synthesis of amphiphilic PCL-based block copolymers by ring-opening copolymerisation of ε-caprolactone (1) and ε-allyl-ε-caprolactone (2) using a chain-transfer agent as initiator, followed by RAFT polymerisation of PMMA or/and PDMA. (a) DPP (10 mol%), toluene with $[monomers]_0$:$[initiator]_0$ = 50 and [monomers] = 2 M, 40 °C, N_2 filled glovebox, 7 h. (b) MMA (100 equiv.), AIBN (20 mmol %), dioxane (30 wt. %), 70 °C, N_2 atmosphere, 2.5 h. (c) DMA (600 equiv.), AINB (10 mmol %), dioxane (30 wt. %), 70 °C, N_2 atmosphere, 50 min.

Amphiphilic block copolymers **5** and **6** were then prepared by RAFT polymerisation of methyl methacrylate (MMA) and/or dimethyl acrylamide (DMA) respectively (**entries P4-P7, Table 5.1**). It was hypothesised that the allyl-pendant group present in the PACL chain, which is susceptible to RAFT polymerisation, reacted with the free radicals in the reaction at low concentrations of the vinyl monomer.[52] To avoid polymerising the less-active allyl-group, which would lead to polymers with bimodal distributions with high molar-mass dispersity, an excess

of acrylate and acrylamide monomers was used and monomer conversions were kept below 70%. ^{1}H NMR spectroscopy and SEC analyses showed block copolymers **4**, **5** and **6** obtained predictable molecular weights (M_n) and narrow dispersities ($Đ_M$ = 1.12 – 1.25, **Figure 5.1** and **Figure S5.8**).

Table 5.1. Synthesis of amphiphilic PCL-based copolymers.

Entry	Block copolymer	ACL units (wt. % core)[a]	Corona:Core ratio[b]	$Đ_M$[c]	$M_{n,SEC}$[c] (kDa)	T_m (°C)	T_c (°C)
P1	PCL_{39}-*co*-$PACL_3$	7.3	Core block	1.25	11.1	46.7[d]	13.7[d]
P2	PCL_{44}-*co*-$PACL_3$	6.4	Core block	1.21	11.0	48.5[d]	15.8[d]
P3	PCL_{54}-*co*-$PACL_3$	5.2	Core block	1.15	11.9	45.8[d]	13.2[d]
P4	$PMMA_{20}$-*b*-PCL_{54}-*co*-$PACL_3$	5.2	Core block	1.12	16.0	*	*
P5	$PDMA_{89}$-*b*-PCL_{39}-*co*-$PACL_3$	7.3	2:1	1.18	21.6	24.5[e]	8.9[e]
P6	$PDMA_{94}$-*b*-PCL_{44}-*co*-$PACL_3$	6.4	2:1	1.21	19.5	34.1[e]	7.1[e]
P7	$PDMA_{156}$-*b*-$PMMA_{20}$-*b*-PCL_{54}-*co*-$PACL_3$	5.2	2:1	1.17	30.5	34.8[e]	–

[a] Calculated based on the PCL:PACL ratio. [b] Ratio between the PDMA block (corona) and the PCL-based BCP (core) obtained from ^{1}H NMR spectrometry. [c] Measured by GPC ($CHCl_3$ with 0.5% Et_3N, PMMA standards). [e] Measured by DSC in the second cycle (−100 to 100 °C, 10 °C min^{-1}). [d] Measured by DSC in the second heating cycle (−100 to 100 °C, 10 °C min^{-1}). [e] Measured by nano DSC, triblock copolymers in ethanol (100 to 0 °C, 1 °C min^{-1}). *Not measured.

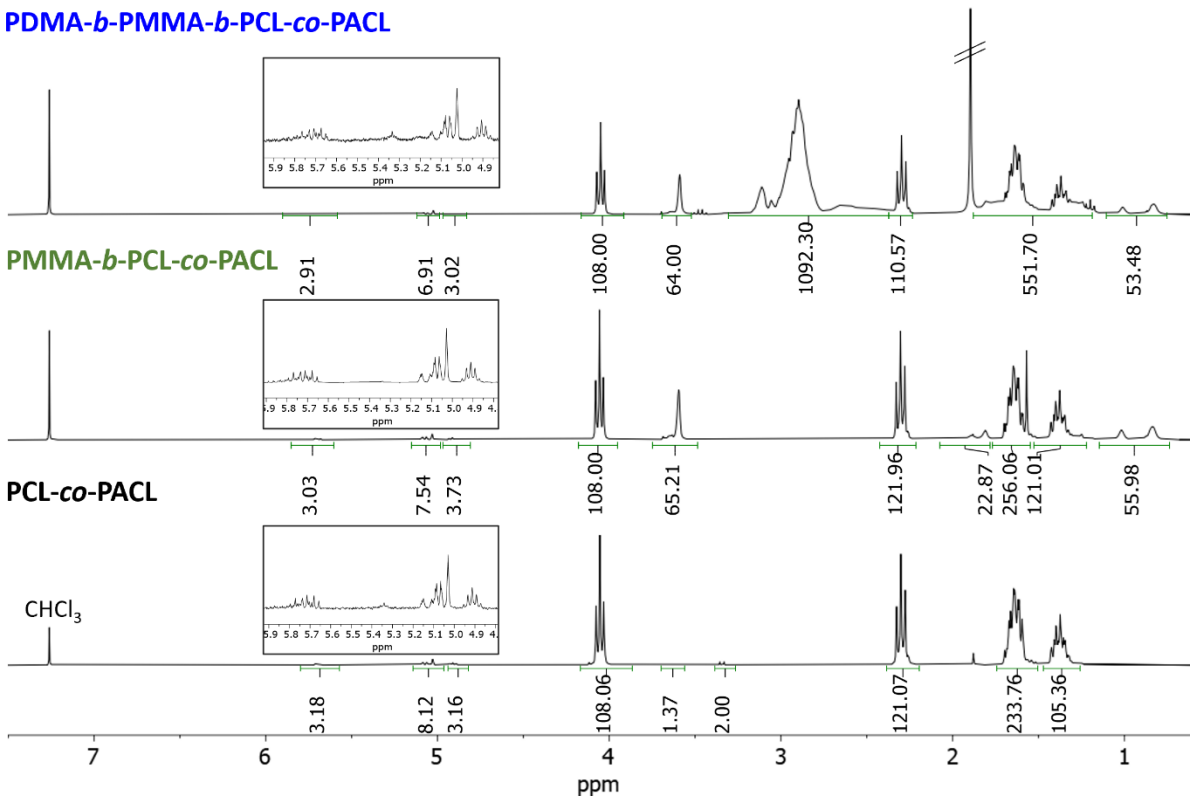
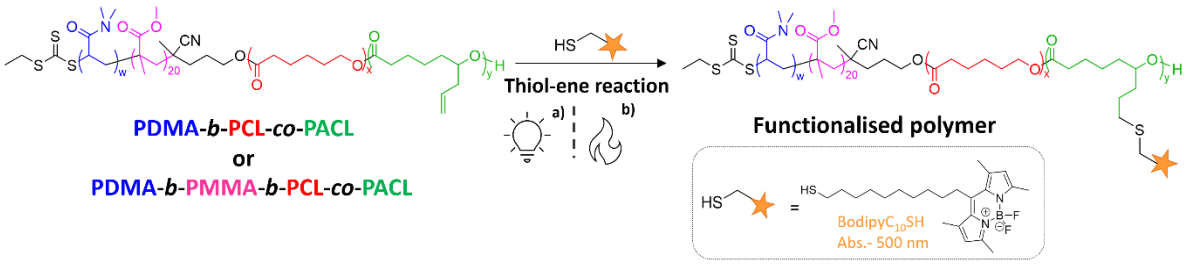


Figure 5.1. Stacked ^{1}H NMR spectra ($CDCl_3$, 300 MHz, 298 K) of PCL_{54}-*co*-$PACL_3$, $PMMA_{20}$-*b*-PCL_{54}-*co*-$PACL_3$, and $PDMA_{156}$-*b*-$PMMA_{20}$-*b*-PCL_{54}-*co*-$PACL_3$ block copolymers (P3, P4, and P7 in Table 5.1 respectively).

5.2.1.1 Functionalisation with $BODIPYC_{10}SH$ *via* thiol-ene addition

Post-polymerisation functionalisation of amphiphilic PCL-based block copolymers was achieved *via* thiol-ene click addition on the pendant allyl group using a thiol-modified BODIPY dye, which can be visualised after cell internalisation (**Scheme 5.2** and **Table 5.2**).



Scheme 5.2. General scheme for the thiol-ene addition of $BODIPYC_{10}SH$ (2 equiv./allyl unit) to amphiphilic PCL-based block copolymers. (a) DMPA or Irgacure 819 (10 mmol % of thiol), chloroform (b) AINB (10 mmol % of thiol), toluene (10-15 wt. %), 80 °C, N_2 atmosphere, 24 h.

In 2015, Kaga *et al*.[53] reported the synthesis of BODIPY-functionalised hydrogels from triblock dendron-polyester conjugates containing alkene end-groups *via* subsequent photochemical radical thiol-ene reactions using 2,2-dimethoxy-2-phenylacetophenone (DMPA) as photo-initiator. Inspired by this work, the photoinitiated thiol-ene addition of BODIPY-C_{10}-SH to $PDMA_{89}$-*b*-PCL_{39}-*co*-$PACL_3$ copolymers (P5) was performed in chloroform using DMPA as source of radicals (**entry 1**, Table 5.2). After 20 min of UV irradiation (λ = 320 – 500 nm), a slight change in the colour of the reaction mixture colour could be observed. However, ^{1}H NMR spectroscopy analysis of the polymer after precipitation in cold diethyl ether did not show a decrease in the characteristic allyl proton peaks at δ = 5.70 ppm and δ = 5.02 – 5.10 ppm, corresponding to C*H*=CH_2 and CH=CH_2 respectively. This indicated that no thiol conjugation had occurred (**Figure S5.9**). It is well-known that chloroform can act as a radical scavenger,[54-56] therefore to ensure the solvent was not negatively affecting the radical addition, thiol-ene addition was repeated using tetrahydrofuran (THF) as a solvent but leaving the rest of the conditions unchanged (**entry 2**, Table 5.2). In a similar manner, no dye conjugation was observed by ^{1}H NMR spectroscopy after 30 minutes of UV irradiation (**Figure S5.10**). Subsequently, the conditions previously used for the conjugation of benzyl mercaptan to the polymer were explored. For this, an excess of BODIPY dye (2 equiv./alkene) and Irgacure 819 (10 mmol % of thiol) were used as thiol and photo-initiator respectively. After irradiation with UV light (λ = 405 nm) for 3 h, the polymer was precipitated in cold diethyl ether to give a dark red polymer. In sharp contrast to our previous thiol-ene studies performed in Chapter 4 with benzyl mercaptan, the disappearance of alkene protons could not be observed by ^{1}H NMR analyses (**Figures S5.11** and **S5.12**). It was hypothesised that the lack of reactivity during the BODIPY conjugation could be as a result of disulphide bond formation. To avoid the formation

of disulfide bonds and enhance the yields of the thiol-ene click reaction, tris(2-carboxyethyl)phosphine (TCEP) was added to the reaction vessel. However, no change in the ^{1}H NMR spectrum was observed in this case, indicating that the BODIPY dye couldn't be attached to the allyl-functional PCL (**entries 3** and **4**, Table 5.2).

Table 5.2. Summary of thiol-ene click additions of BODIPY-C_{10}-SH (screening reactions).

Entry	Conditions	Initiator[a] (equiv./thiol)	Absorbance[b] (nm)	Solvent	T (°C)	Time (min)
1	UV 320-500 nm	DMPA (0.1)	310-390	$CHCl_3$	20	20
2	UV 320-500 nm	DMPA (0.1)	310-390	THF	20	30
3	UV 405 nm	Irgacure 819 (0.1)	360-450	$CHCl_3$	20	180
4	UV 405 nm + TCEP	Irgacure 819 (0.1)	360-450	$CHCl_3$	20	180
5	Temperature	AIBN (0.1)	-	Toluene	80	25 h
6	Temperature	AIBN (0.24)	-	Toluene	80	44 h

[a] Equivalents of initiator proportional to equivalents of thiol molecule. [b] Absorbance of initiator.

The lack of BODIPY thiol conjugation and the evident colour alteration after irradiation under UV light indicated signs of BODIPY degradation under UV light. To confirm our theory, the photoinitiated thiol-ene addition of the thiol-dye to allyl(ε-caprolactone) (εACL) using Irgacure 819 (20 mmol%) as photoinitiator was monitored by ^{1}H NMR spectroscopy. After irradiation for 4.5 h with UV light (λ = 405 nm) no thiol conjugation was observed by ^{1}H NMR spectroscopy. Moreover, the appearance of new proton peaks and darkening in the colour of the reaction mixture suggested that photobleaching processes were taking place (**Figure 5.2**). For this reason, thermo-initiated thiol-ene addition using 2,2'-azobis(2-methylpropionitrile) (AIBN) and heat to generate radicals was explored (**entries 5** and **6,** Table 5.2).

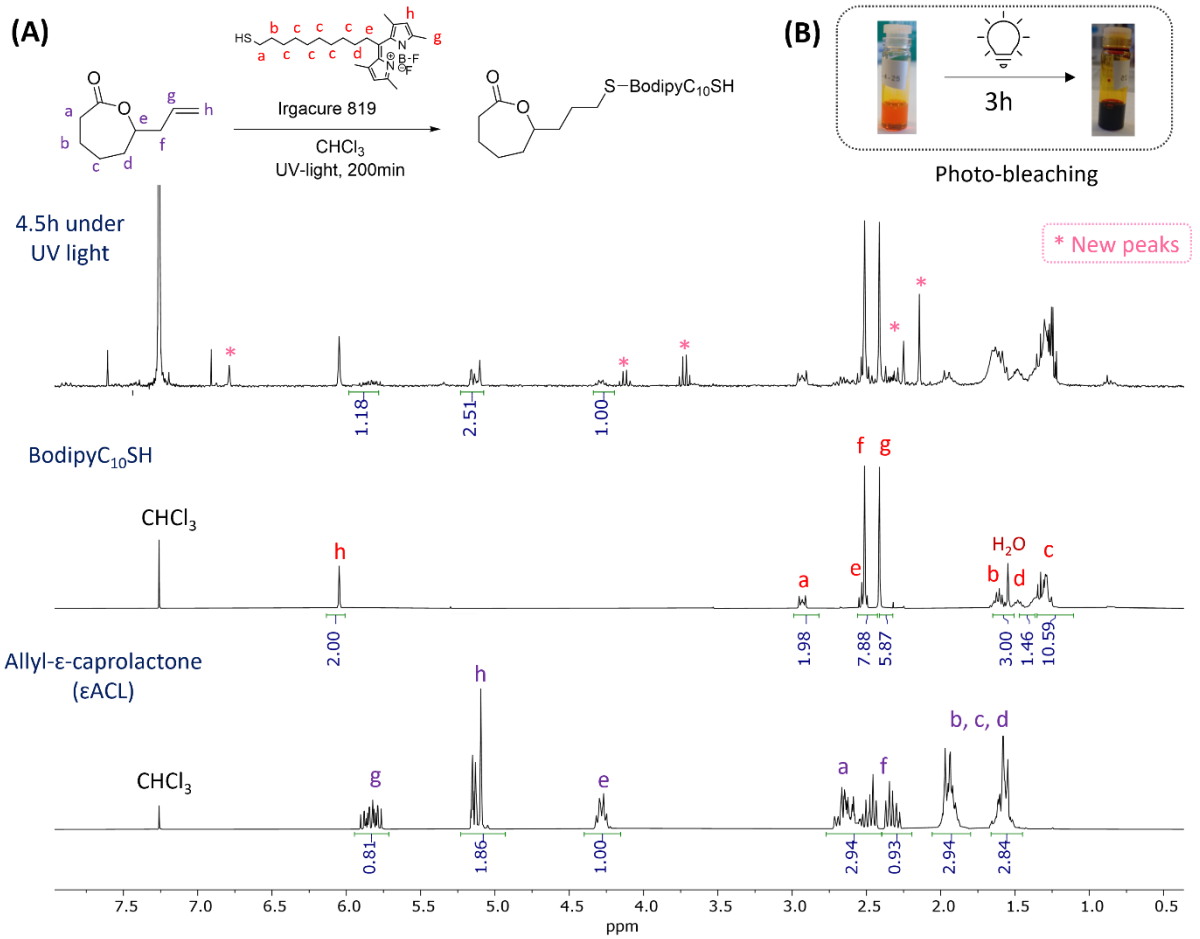


Figure 5.2. Photo-initiated thiol-ene addition of BODIPYC$_{10}$SH to εACL using irgacure 819 (20 mmol%) as photo-intiator. [Monomer]:[thiol] ratio 1:1, 56 wt. %, UV source of 405 nm**. (A)** Stacked ^{1}H NMR spectra ($CDCl_3$, 300 MHz, 298 K) of allyl monomer (bottom), bodipyC$_{10}$SH (middle) and reaction mixture after 4.5 h of UV radiation (top). * Correspond to BODIPY-C$_{10}$-SH degradation peaks. **(B)** Image of reaction mixture before (left) and after UV radiation (right) indicating photo-bleaching of BODIPY dye.

To ensure the integrity of the thiol after UV-light exposure, the thermo-initiated thiol-ene addition of BODIPY-C$_{10}$-SH to εACL was primarily conducted using a thiol-to-alkene ratio of 1:1. As observed in **Figure 5.3**, ^{1}H NMR spectroscopy analyses showed a slight decrease in the number of allyl group protons (CH=CH_2) at δ = 5.02 – 5.10 ppm, indicating that some thiol was attached to the allyl-monomer. Successful dye conjugation to the monomer was further confirmed by thin-layer chromatography (TLC), where a new spot with similar retention factor

to εACL, which is not visible under UV-light, appeared under UV-light. Moreover, no additional peaks corresponding to dye degradation were present after 2.5 days, confirming the stability of the dye in these conditions.

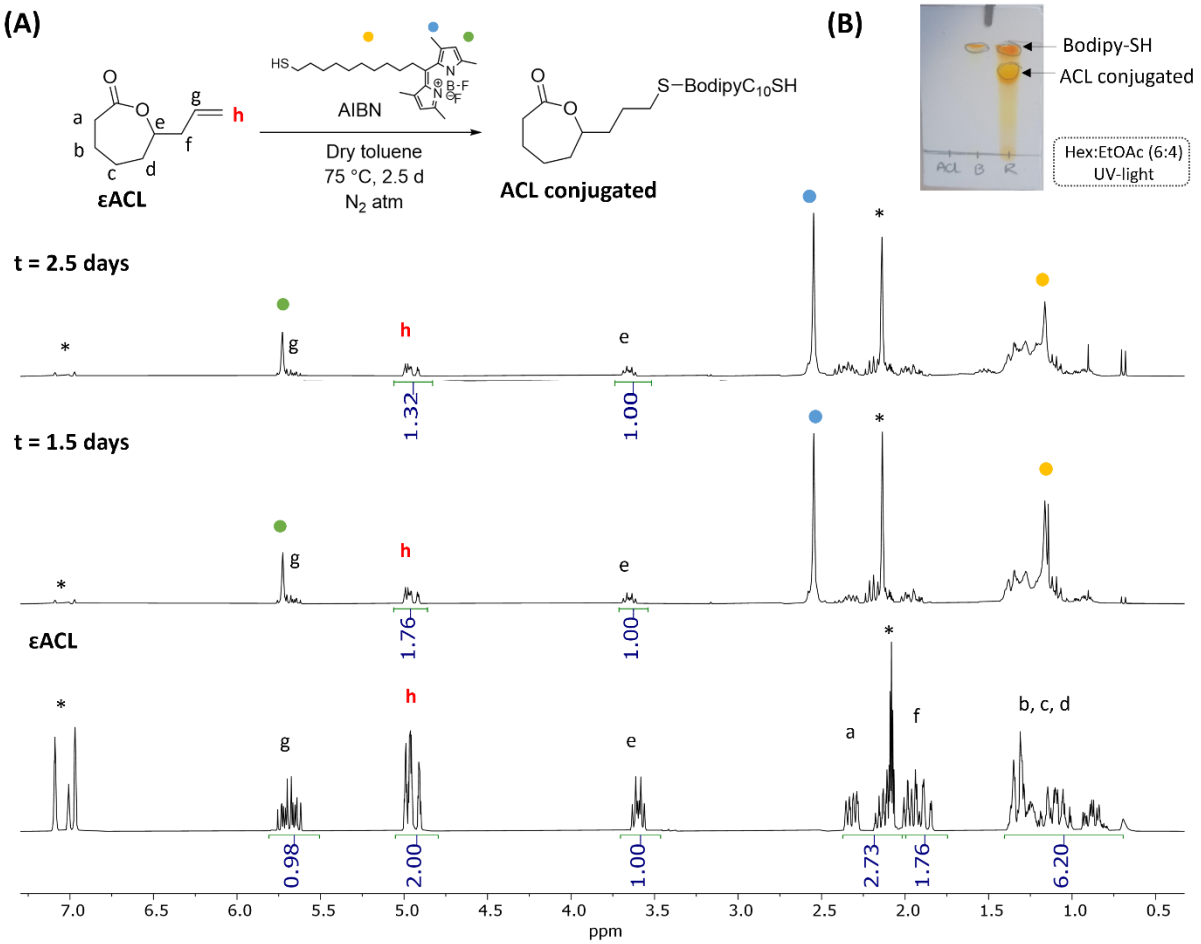


Figure 5.3. (A) Stacked ^{1}H NMR spectra (d_8-toluene (*), 300 MHz, 298 K) of the reaction crude for the thermo-initiated thiol-ene addition of $BODIPYC_{10}SH$ to allyl(ε-caprolactone) after 1.5 days and 2.5 days. **(B)** Thin layer chromatography of monomer (left spot), $BODIPYC_{10}SH$ (middle spot) and reaction crude after 2.5 days (right spot) under UV-light.

After optimising the thiol-ene conditions, post-polymerisation functionalisation reactions of $PDMA_{89}$-*b*-PCL_{39}-*co*-$PACL_3$ and $PDMA_{156}$-*b*-$PMMA_{20}$-*b*-PCL_{54}-*co*-$PACL_3$ block copolymers (**P5** and **P7**) were conducted in toluene (10-15 wt. %) at 80 °C, using BODIPY-C_{10}-SH and AIBN as the thiol and initiator respectively. After 24 h, the reaction mixtures were precipitated in cold

diethyl ether to isolate the BODIPY-conjugated polymers, as an orange solid. Quantitative analysis of the thiol-ene reactions by ^{1}H NMR spectroscopy showed low dye conjugation into the block copolymer (< 33% functionalisation) (**Figures 5.4**). The low functionalisation efficiency could explained by insufficient thiol.[57-59] Successful dye conjugation was further confirmed by SEC analyses, where conjugated polymers exhibited characteristic UV absorptions at λ = 309 and 500 nm, corresponding to the trithiocarbonate group present in the CTA and the $BODIPYC_{10}SH$ dye respectively, in contrast to the free block copolymers that presented a single UV absorption at λ = 309 nm (**Figure 5.5**).

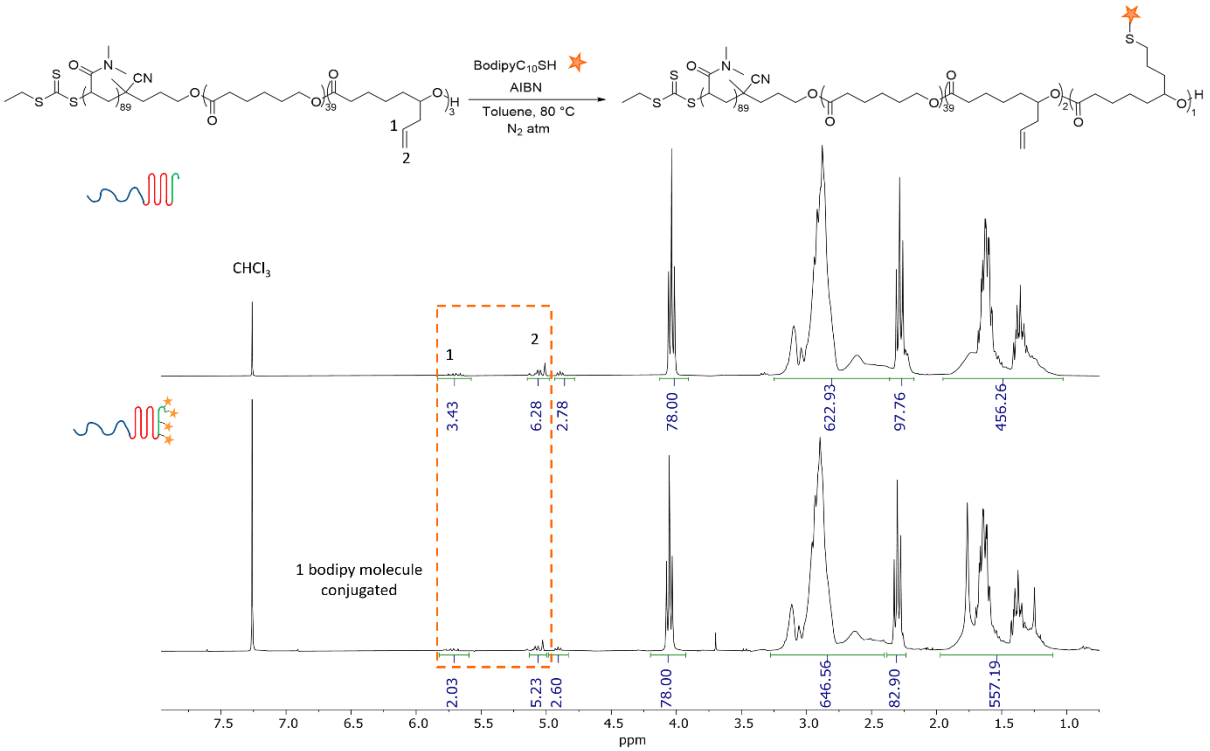


Figure 5.4. Stacked ^{1}H NMR spectra ($CDCl_3$, 300 MHz) of $PDMA_{89}$-*b*-PCL_{39}-*co*-$PACL_3$ (P5, top) and BODIPY-conjugated $PDMA_{89}$-*b*-PCL_{43}-*co*-$PACL_3$ block copolymer (bottom).

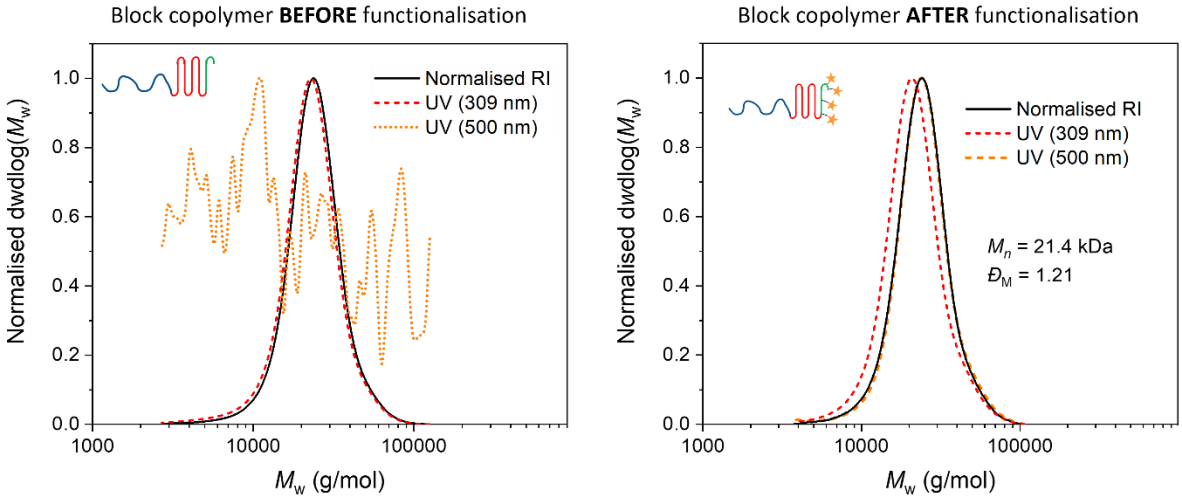


Figure 5.5. SEC chromatograms of PDMA$_{89}$-*b*-PCL$_{39}$-*co*-PACL$_3$ (**P5**) before and after functionalisation with BODIPYC$_{10}$SH *via* thermo-initiated thiol-ene addition (CHCl$_3$, with 0.5% Et$_3$N, PMMA standard, UV sensors λ = 309 nm and 500 nm).

5.2.2 Crystallisation-driven self-assembly

Polydisperse cylindrical micelles from non-conjugated and BODIPY-functionalised block copolymers with similar block lengths and short corona:core ratios (2:1 and 1:1) were prepared *via* CDSA in ethanol (5 mg mL^{-1}), a good solvent for the PDMA corona block, as it was found in previous CDSA studies reported in Chapter 4. As expected, transmission electron microscopy (TEM) analysis of the non-functionalised assembly solutions (**entries P5-P7** in Table 5.1) demonstrated that low % incorporation of εACL does not affect the core-block crystallisation process, yielding well-defined several micron-long cylinders with a functionalised core (**Figure 5.6** and **Figure S5.13**).

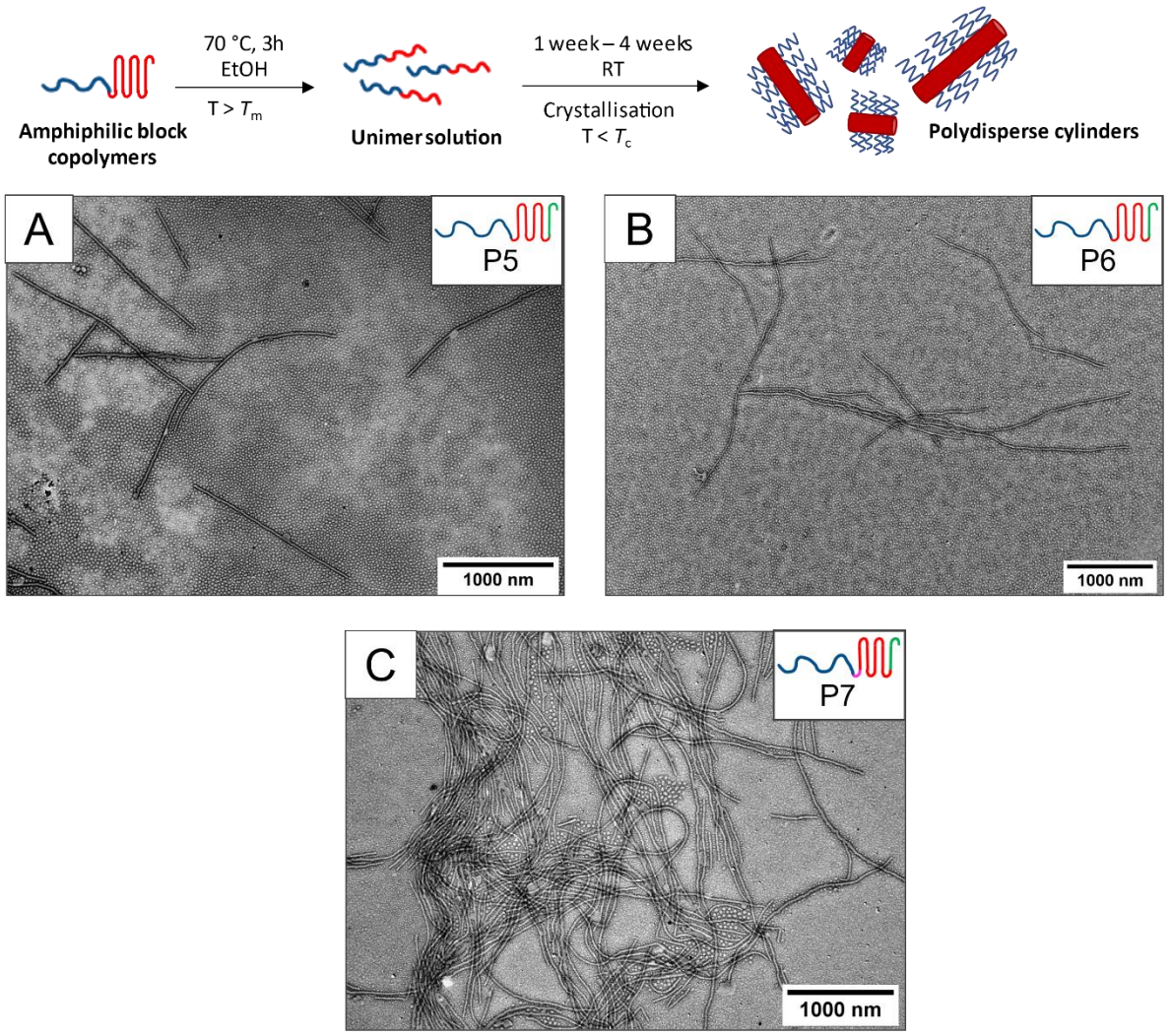


Figure 5.6. General procedure for the crystallization-driven self-assembly (CDSA) of amphiphilic block copolymers with a semicrystalline core block. **A)** TEM micrograph of $PDMA_{89}$-*b*-PCL_{39}-*co*-$PACL_3$ (P5) assemblies. **B)** TEM micrograph of $PDMA_{94}$-*b*-PCL_{44}-*co*-$PACL_3$ (P6) assemblies. **C)** TEM micrograph of $PDMA_{156}$-*b*-$PMMA_{20}$-*b*-PCL_{54}-*co*-$PACL_3$ (P7) assemblies. Samples were negatively stained using uranyl acetate (0.5 wt %).

TEM analyses of the self-assembly of BCPs with a BODIPY dye attached to the core-forming block also showed the formation of well-defined polydisperse particles with cylindrical morphology. This demonstrated retention of crystallinity in the PCL-based block after post-polymerisation modification with BODIPY-C_{10}-SH dye (**Figures 5.7** and **S5.14**). Crystallinity was further confirmed by nano-DSC analysis of the fluorescent particles, where a sharp melting

peak can be observed in the thermograms. In agreement with our previous observations in Chapter 4, in which crystallinity was inversely proportional to thiol attachment, BODIPY-functionalised particles presented a slightly lower melting temperature (T_m) than their non-conjugated counterparts, 31.9 °C *vs*. 34.8 °C respectively, (**Figure 5.8**).

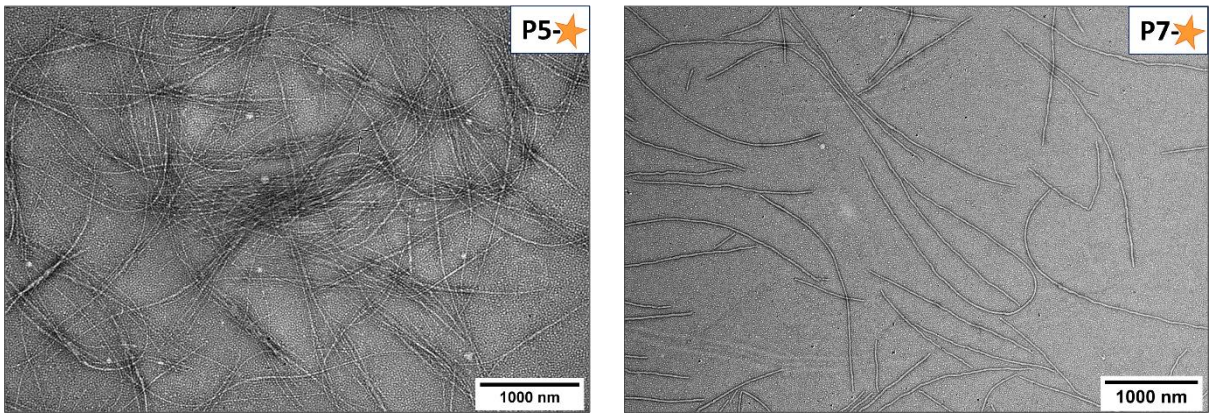


Figure 5.7. TEM micrographs of the self-assembly of BODIPY conjugated $PDMA_{89}$-*b*-PCL_{39}-*co*-$PACL_3$ (**P5**) and $PDMA_{156}$-*b*-$PMMA_{20}$-*b*-PCL_{54}-*co*-$PACL_3$ (**P7**) assemblies. Samples were negatively stained using uranyl acetate (0.5 wt %).

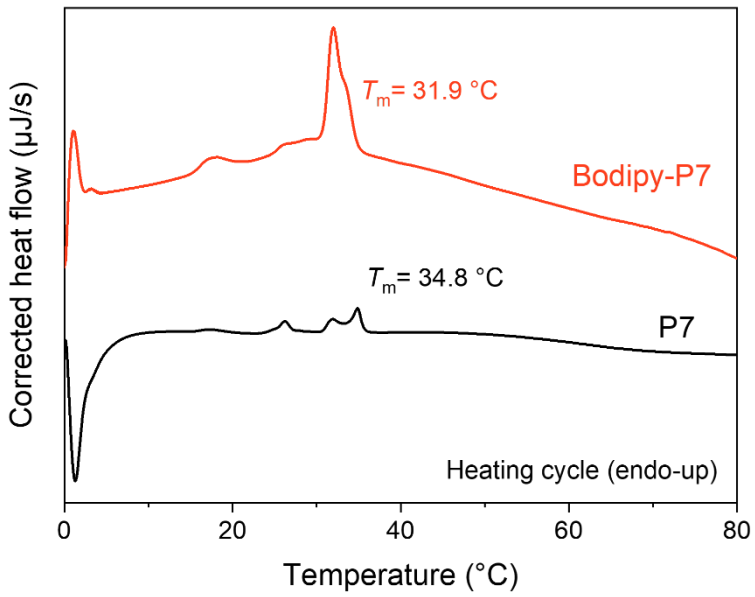


Figure 5.8. Nano DSC thermograms (100 to 0 °C, 1 °C min^{-1}) showing first cooling-heating cycle of $PDMA_{156}$-*b*-$PMMA_{20}$-*b*-PCL_{54}-*co*-$PACL_3$ (P7) and BODIPY conjugated $PDMA_{156}$-*b*-$PMMA_{20}$-*b*-PCL_{54}-*co*-$PACL_3$ (Bodipy-P7).

5.2.2.1 Aqueous stability of CDSA cylindrical particles

To examine the stability of CDSA nanoparticles under conditions akin to those found in the body, cylinders bearing a short PMMA block were transferred into water and compared to those without the glassy polymer (*i.e*. without the PMMA block) after dialysis. In agreement with previous literature,[50] TEM analyses showed higher aqueous stability for cylindrical micelles containing the PMMA block, whose morphology showed no significant difference upon solvent change. Conversely, $PDMA_w$-*b*-PCL_x-*co*-$PACL_y$ structures, without the PMMA stabilising block, generated shorter and damaged cylindrical micelles when transferred into water (**Figure 5.9** and **Figures S5.15 and 16**). This is believed to happen because of increased hydration of the PDMA in water than ethanol, which leads to swelling of the hydrophilic coronal block. This causes higher strain between the corona and core blocks, resulting in water reaching the PCL core and the disassembly or break of nanostructures.

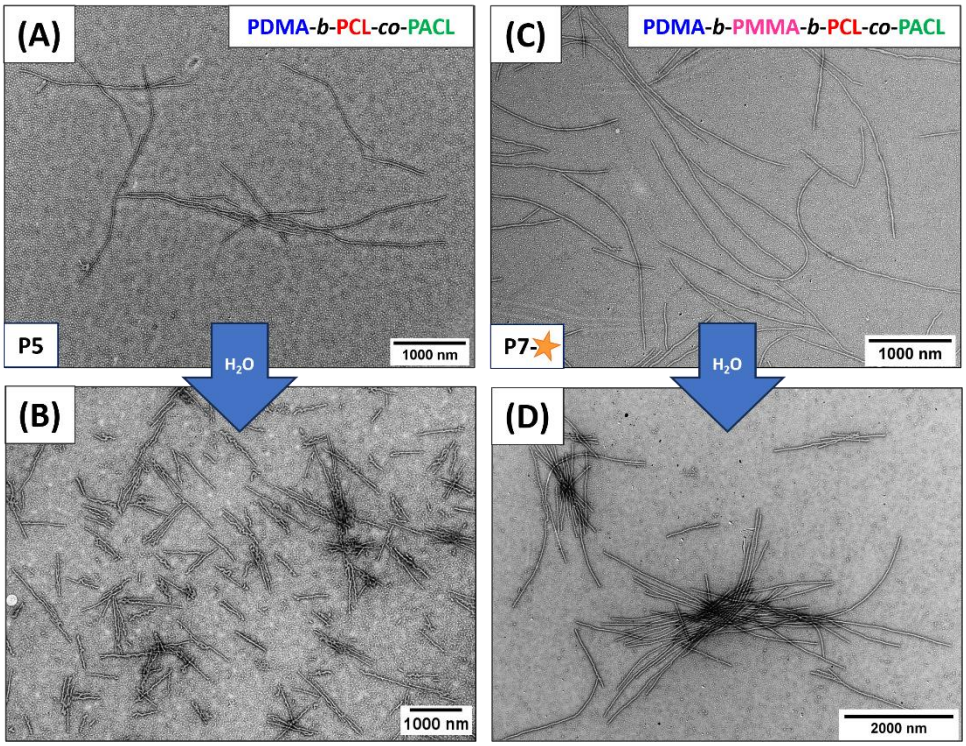
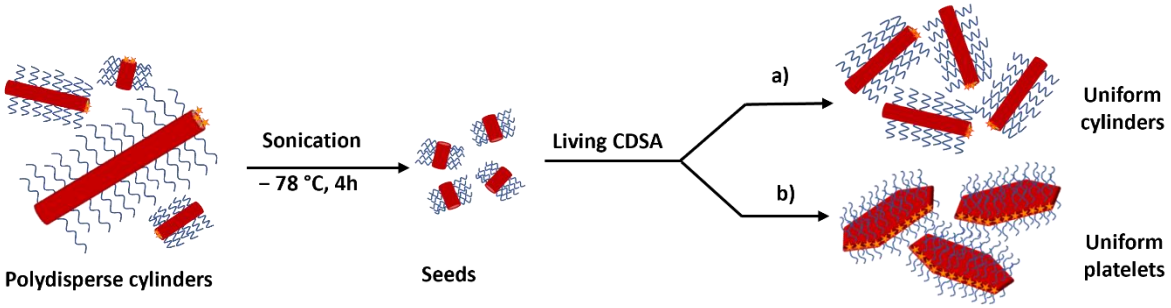


Figure 5.9. (A-B) TEM micrographs of $PDMA_{89}$-*b*-PCL_{39}-*co*-$PACL_3$ in ethanol and water, respectively**. (C-D)** TEM micrographs of BODIPY conjugated $PDMA_{156}$-*b*-$PMMA_{20}$-*b*-PCL_{54}-*co*-$PACL_3$.

5.2.3 Living CDSA of functional PCL-containing copolymers

Amphiphilic functional PCL block copolymers underwent epitaxial growth in ethanol *via* seeded CDSA resulting in uniform anisotropic structures. 1D cylindrical micelles and 2D platelet-like micelles with low size dispersity and tuneable dimensions were obtained based on the amount of unimer added to seeds and the conditions used for growth (**Scheme 5.3**).



Scheme 5.3. General procedure for the seeded growth living CDSA. **a)** 1D epitaxial growth – seed solution at 2.5 mg mL^{-1}, addition of triblock copolymer solubilised in THF, aging at room temperature. **b)** 2D epitaxial growth – seed solution at 0.01-0.1 mg mL^{-1}, addition solution of homopolymer (PCL) + triblock copolymer (1:1) solubilised in $CHCl_3$, 30 °C, aging at room temperature.

To synthesise 1D and 2D anisotropic structures, crystalline seed micelles were first prepared by sonicating cylindrical micelles (5 mg mL^{-1}) at −78 °C, using a dry ice/acetone bath. For this, $PDMA_w$-*b*-PCL_x copolymers with corona-to-core ratios of 2:1 and 3:1, synthesised in Chapter 3, as well as the BCPs $PDMA_{94}$-*b*-PCL_{44}-*co*-$PACL_3$ and $PDMA_{156}$-*b*-$PMMA_{20}$-*b*-PCL_{54}-*co*-$PACL_3$ (**P6** and **P7** respectively) were selected. After sonicating for 4 h, the fragmentation of initial polydisperse cylinders resulted in the formation of short cylindrical micelles with lengths (L_n) of 30.6, 35.5, 32.0 and 25.5 nm, respectively, and low length dispersities (L_w/L_n < 1.04, where L_n = number-average length and L_w = weight-average length) (**Figure 5.10** and **S5.17**).

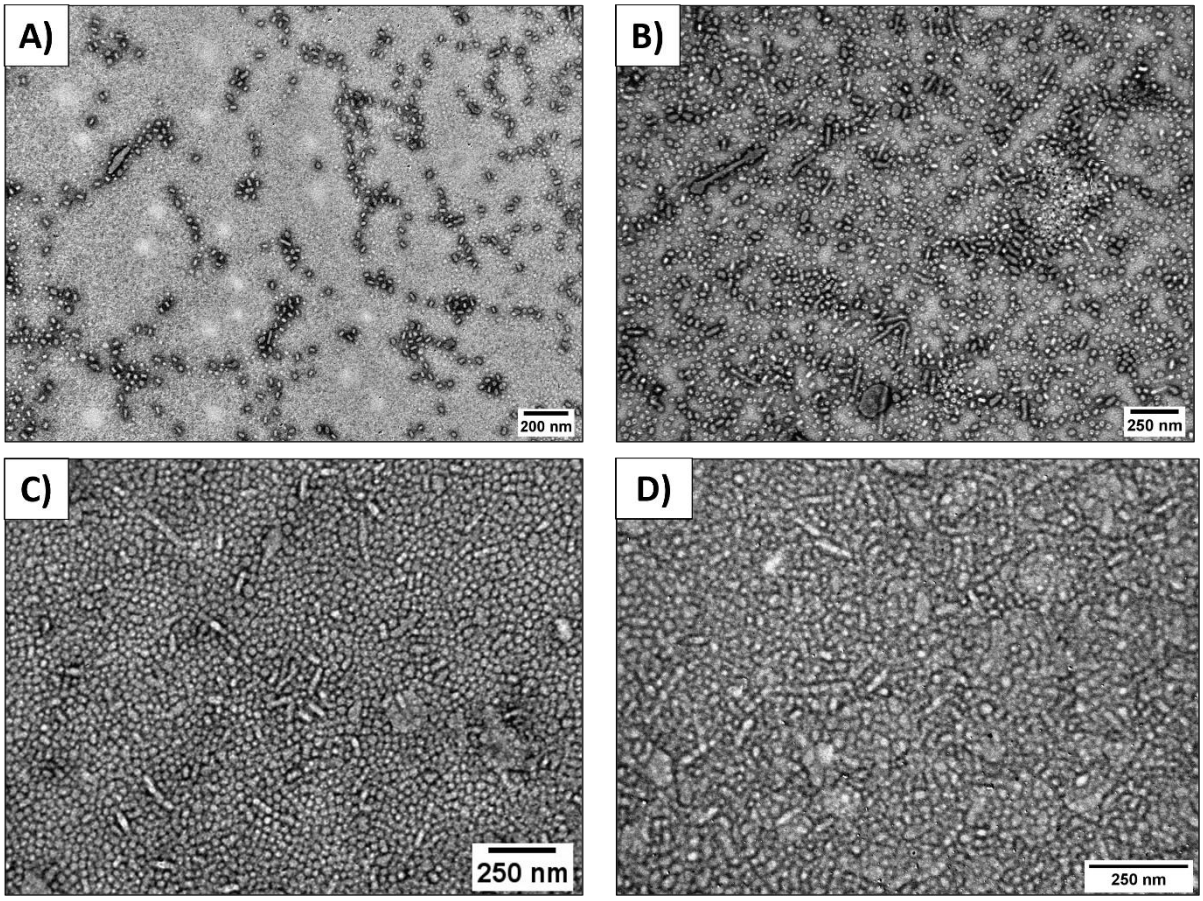


Figure 5.10. TEM micrographs of polymer seeds after sonication for 4 h. **A)** $PDMA_{117}$-*b*-PCL_{48} seed solution. **B)** $PDMA_{154}$-*b*-PCL_{48} seed solution. **C)** of $PDMA_{94}$-*b*-PCL_{44}-*co*-$PACL_3$ seed solution. **D)** of $PDMA_{112}$-*b*-PCL_{53}-*co*-$PACL_3$ seed solution. Samples were negatively stained using uranyl acetate (0.5 wt %).

5.2.3.1 Epitaxial growth of 1D cylindrical micelles

Initially, the living CDSA in ethanol of $PDMA_{117}$-*b*-PCL_{48} and $PDMA_{122}$-*b*-PCL_{53}-*co*-$PACL_3$ block copolymers to afford uniform cylinders with short unimer/seed ratios (m_{unimer}/m_{seed} = 2 and 4) were investigated. For this, solutions of the block copolymers at distinct concentrations in tetrahydrofuran (THF), equivalent to different targeted values of m_{unimer}/m_{seed}, were added to a solution of crystalline seed micelles (conc. = 2.5 mg mL^{-1}). While uniform cylindrical micelles with predictable average lengths were achieved from $PDMA_{117}$-*b*-PCL_{48} BCPs, the living growth of allyl-functionalised polymers with both $PDMA_{154}$-*b*-PCL_{48} and $PDMA_{122}$-*b*-PCL_{53}-*co*-$PACL_3$

seeds resulted in the formation of bulky cylinders with lower uniformity (**Figure 5.11**). This was ascribed to the slower crystallisation rates of the allyl-functional semicrystalline block compared to PCL, which could cause unspecific unimer self-nucleation and uncontrolled micelle growth. Therefore, it was envisioned that the subsequent addition of small aliquots of unimer solution to the seeds, in a typical epitaxial growth fashion, could decrease the number of self-nucleation events and provide higher control over the particle's morphology.

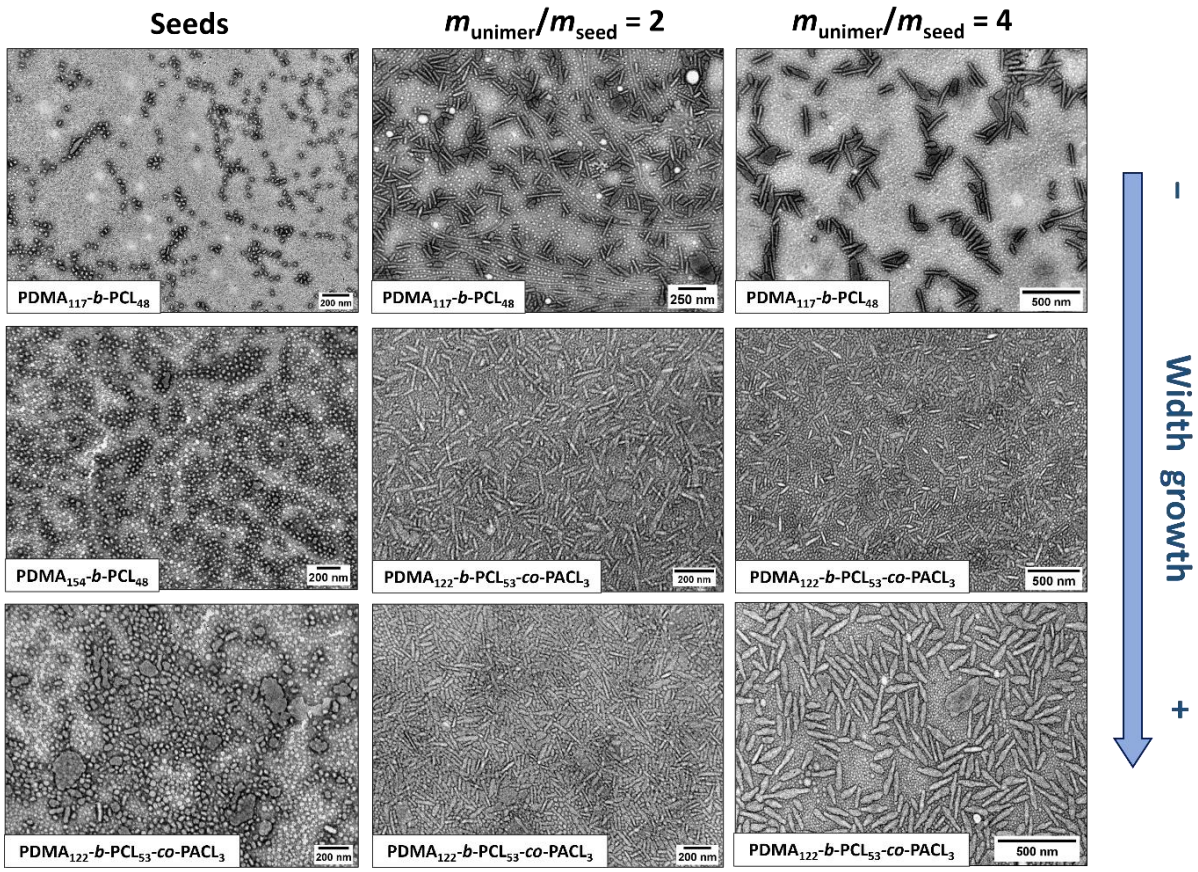


Figure 5.11. 1D living CDSA of $PDMA_{117}$-*b*-PCL_{48} and $PDMA_{122}$-*b*-PCL_{53}-*co*-$PACL_3$ block copolymers using both BCPs seed solutions with targeted unimer/seed ratios 2 and 4. Samples were negatively stained using uranyl acetate (0.5 wt %).

The epitaxial growth of $PDMA_{94}$-*b*-PCL_{44}-*co*-$PACL_3$ by subsequent addition of unimer solution (25 µL, at a concentration corresponding to m_{unimer}/m_{seed} = 2) to a solution of $PDMA_{154}$-*b*-PCL_{48} polymeric seeds was then explored. To avoid oversaturating the CDSA solution, a variable number of aliquots of 25 µL were added 2 h apart from each other depending on the targeted unimer to seed ratio. The assembly process was monitored by TEM. Using this method, we observed uniform fiber-like micelles of $PDMA_{94}$-*b*-PCL_{44}-*co*-$PACL_3$ with low length dispersity (L_w/L_n < 1.06) and lengths (L_n) varying from 98 to 822 nm (**Figure 5.12** and **Figure S5.18**). Moreover, dynamic light scattering (DLS) analyses further confirmed the formation of cylinders with increasing lengths, indicating a controlled linear epitaxial growth for all cases (**Figure 5.13**). However, unlike previous reports in which the dimensions of the micelles obtained were proportional to the amount of unimer added to the seed solution,[26, 30, 50] the resultant micelle length obtained in our case was significantly higher than the theoretical targeted length corresponding to the unimer to seed ratios (green and pink boxes respectively in Table 5.3). It was hypothesised that the small amount of cosolvent added (THF) could redissolve some semicrystalline structures, which then grew on the remaining cylinders, resulting in longer cylindrical micelles (**Table 5.3**).

Table 5.3. Length dispersity of $PDMA_{94}$-*b*-PCL_{44}-*co*-$PACL_3$ cylindrical micelles.

m_{unimer}/m_{seed}	Target (nm)	L_n (nm)	L_w (nm)	L_w/L_n
2	91.8	85.4	87.8	1.03
4	153.0	256.6	271.2	1.05
6	214.2	544.9	565.6	1.04
8	275.4	742.6	754.2	1.02

Micelle lengths (L_n) were analysed by hand using ImageJ software after counting ≥ 100 particles.

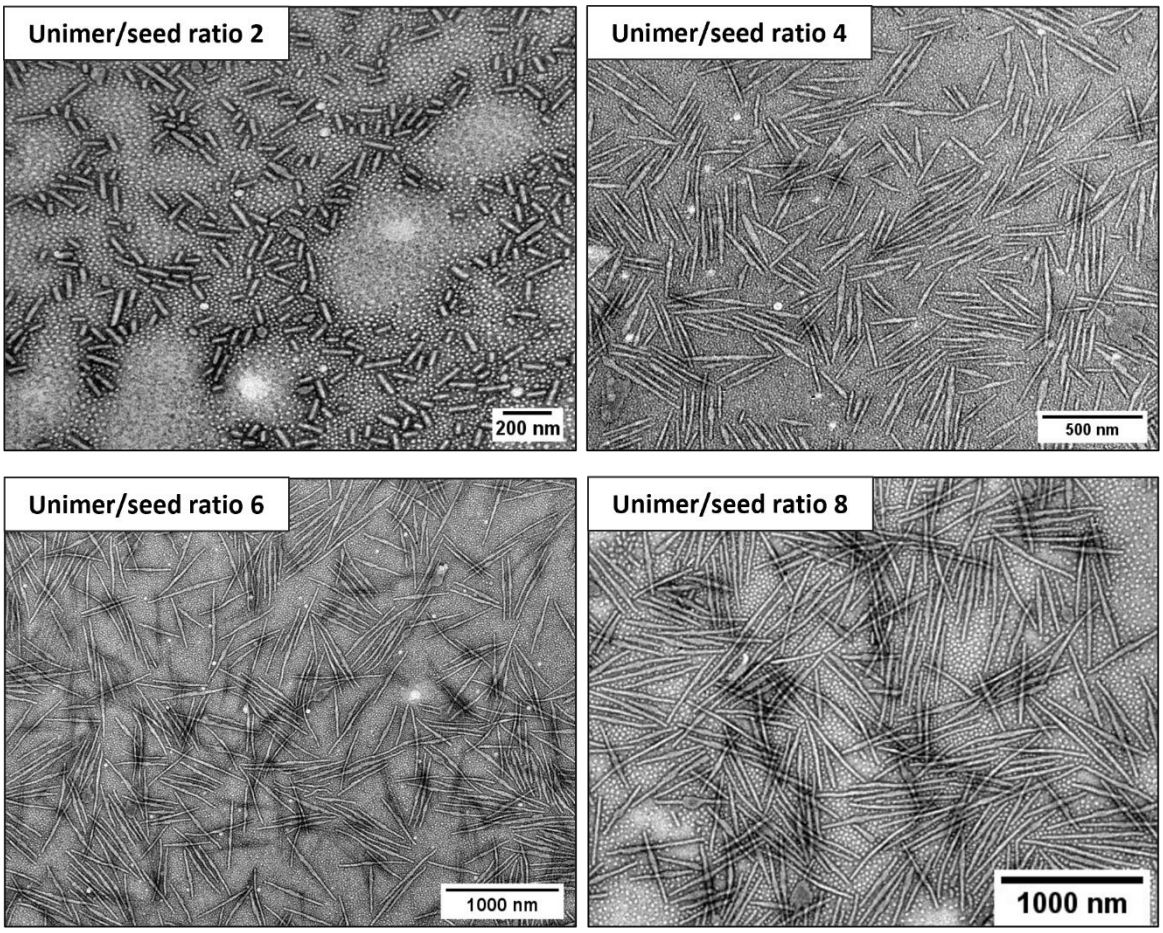


Figure 5.12. TEM micrographs for the 1D epitaxial growth of $PDMA_{94}$-*b*-PCL_{44}-*co*-$PACL_3$ (P6) self-assembled in ethanol using $PDMA_{154}$-*b*-PCL_{48} seeds with m_{unimer}/m_{seeds} ratios 2, 4, 6, and 8. Samples were negatively stained using uranyl acetate (0.5 wt %).

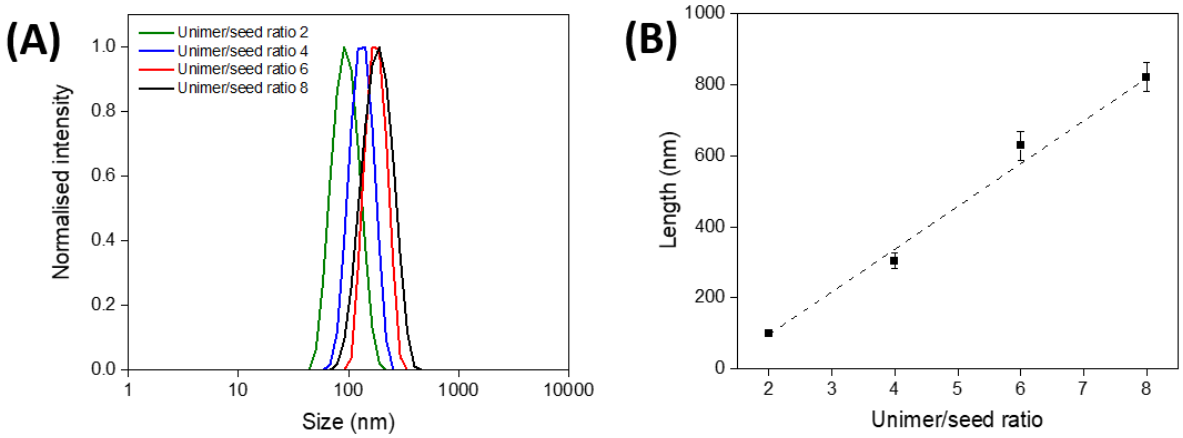
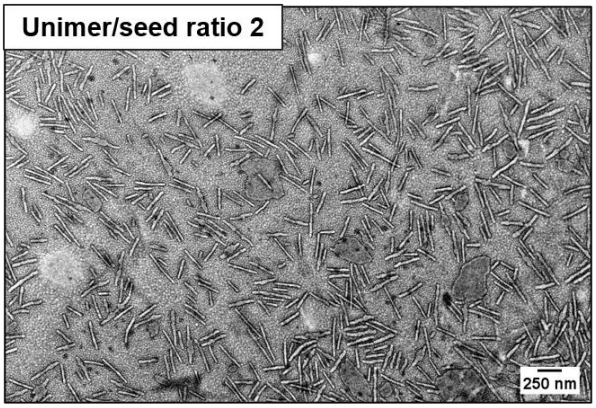
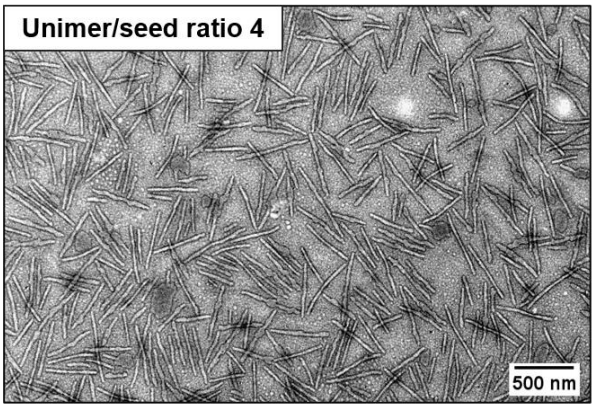
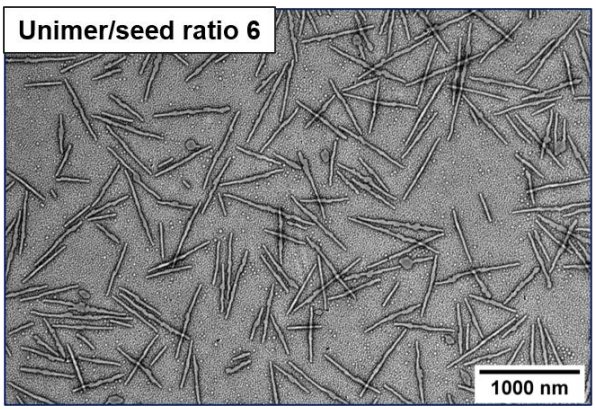


Figure 5.13. A) Size distribution averaged by intensity over the same time. Measured by dynamic light scattering (DLS). Each sample was repeated three times. **B)** Number length average (L_n) *vs*. unimer/seed ratio for the 1D epitaxial growth of $PDMA_{94}$-*b*-PCL_{44}-*co*-$PACL_3$ (P6), calculated from particle analysis-based TEM images.

Following the successful formation of size-controlled cylindrical micelles of allyl-functionalised PCL polymers, cylindrical micelles with tuneable lengths from 243 to 633 nm ($L_w/L_n < 1.1$) containing a $BODIPYC_{10}SH$ dye in the inner core were prepared through multiple additions (25 µL each) of BODIPY-functionalised $PDMA_{156}$-*b*-$PMMA_{20}$-*b*-PCL_{54}-*co*-$PACL_3$ solution (100 mg mL^{-1}), proving for the first time the living CDSA of block copolymers with a molecule attached to the semicrystalline core (**Figure 5.14** and **Figure S5.19 and S5.20**). In addition, well-defined non-fluorescent cylindrical micelles with similar low-length dispersities ($L_w/L_n < 1.1$) were formed using $PDMA_{94}$-*b*-PCL_{44}-*co*-$PACL_3$ seeds (**Figures S5.21-S5.23**).







Epitaxial growth of BODIPY-conjugated block copolymers

Unimer/seed ratio	L_n (nm)	L_w (nm)	L_w/L_n
2	243.2	257.6	1.06
4	416.9	440.3	1.06
6	633.4	692.2	1.09

Figure 5.14. TEM micrographs for the 1D epitaxial growth of BODIPY-conjugated $PDMA_{156}$-*b*-$PMMA_{20}$-*b*-PCL_{54}-*co*-$PACL_3$ (BODIPY-P7) using $PDMA_{154}$-*b*-PCL_{48} seeds with m_{unimer}/m_{seed} ratios varying from 2, 4, and 6. Samples were negatively stained using uranyl acetate (0.5 wt %). Table with micelle length summary.

5.2.3.2 Seeded growth of 2D platelet-like micelles

After determining that 1D structures could be obtained *via* seeded living CDSA, our attention turned towards the formation of 2D platelets with a functional core. To prepare 2D platelets micelles, a solution of crystalline $PDMA_{154}$-*b*-PCL_{48} seeds at 0.01 mg mL^{-1} was prepared by sonication of long cylindrical micelles. The addition of unimers (homopolymer/PCL-based block copolymer, in a 1:1 molar ratio) in chloroform, with different concentrations corresponding to different targeted m_{unimer}/m_{seed}, to these preformed seeds, previously heated for 5 minutes at 30 °C, led to uniform 2D platelet-like structures with controlled dimensions (**Table 5.4**, **Figures S5.24** and **S5.25**). To prove the livingness of the assembly process, 2D platelets of BODIPY-P7 with different unimer/seed ratios (5, 10, 20, 30 and 45) were assessed (**Figure 5.15A-E**). TEM analyses showed a linear relationship between the mean area (A_n) and the unimer to seed mass ratio, which demonstrated the 2D epitaxial growth of platelets occurred in a controlled manner (**Figure 5.16**). Moreover, confocal microscopy confirmed the ubiquity of the fluorescent dye within the particle, proving the obtention of well-defined core-functionalised 2D structures (**Figure 5.15F-J**).

Table 5.4. Dimensions of BODIPY-conjugated $PDMA_{156}$-*b*-$PMMA_{20}$-*b*-PCL_{54}-*co*-$PACL_3$ platelets.

Unimer/seed ratio	Average length (L_n) (nm)	Average width (W_n) (nm)	Average area (A_n) (nm^2)
5	328	135	42750
10	424	177	63639
20	678	265	157848
30	957	353	279476
45	1071	362	396782

Length (L_n), width (W_n), and area (A_n) of platelets were analysed by hand using ImageJ software after counting ≥ 100 particles.

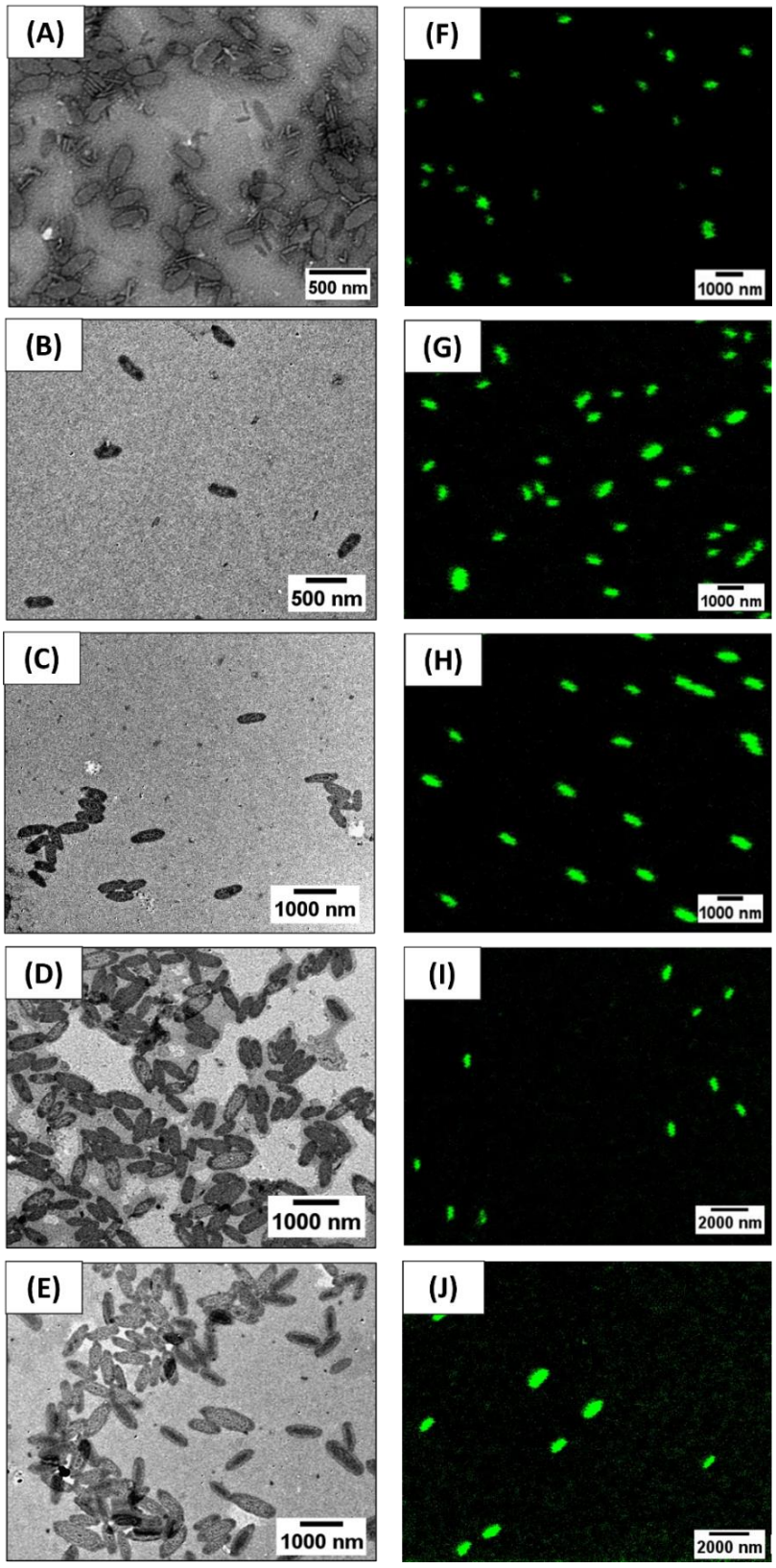


Figure 5.15. 2D epitaxial growth of BODIPY conjugated $PDMA_{156}$-*b*-$PMMA_{20}$-*b*-PCL_{54}-*co*-$PACL_3$ (BODIPY-P7) self-assembled in ethanol at 0.01 mg ml^{-1} with m_{PCL48}/m_{unimer} = 1. **A)-E)** TEM micrographs showing platelet growth with m_{unimer}/m_{seeds} ratios of 5, 10, 20, 30 and 45 respectively. Samples were negatively stained using uranyl acetate (0.5 wt %). **F)-J)** Confocal

images of corresponding BODIPY-conjugated platelets, showing the fluorescence field. (confocal images collected by Mr. Tianlai Xia).

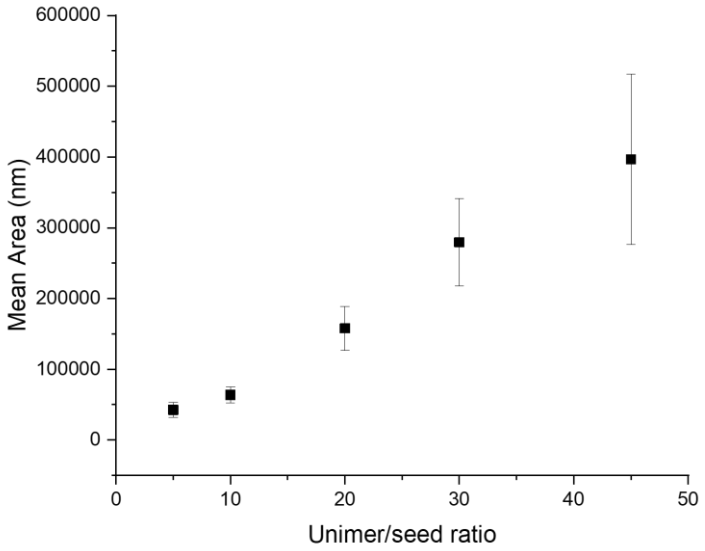


Figure 5.16. Number area average (A_n) *vs*. unimer/seed ratio, calculated from particle analysis-based TEM images, for the 2D epitaxial growth of BODIPY-P7 using $PDMA_{154}$-*b*-PCL_{48} seeds.

5.2.3.2.1 Aqueous stability of 2D platelet micelles

Previous studies for cylindrical micelles showed the incorporation of a PMMA intermediate block was necessary to maintain the particle stability in water. In this section, we also wanted to explore the aqueous stability of the 2D platelet structures. Initially, 2D structures with and without the short PMMA intermediate block were dialysed in water for 3 days and left at room temperature for a month. After this time, the aqueous solutions were concentrated by evaporation and characterised. TEM analyses showed the retention of morphology and no particle fragmentation for both platelet types, highlighting their stability in the aqueous environment (**Figure 5.17**). These findings were in sharp contrast to our previous observations with 1D cylindrical micelles. It was hypothesised that in 2D structures, the semicrystalline

chains within the core block were more compact compared to those found in cylinders. This tighter packing might provide greater resistance to the additional strain caused by the interaction between the corona block and the solvent.

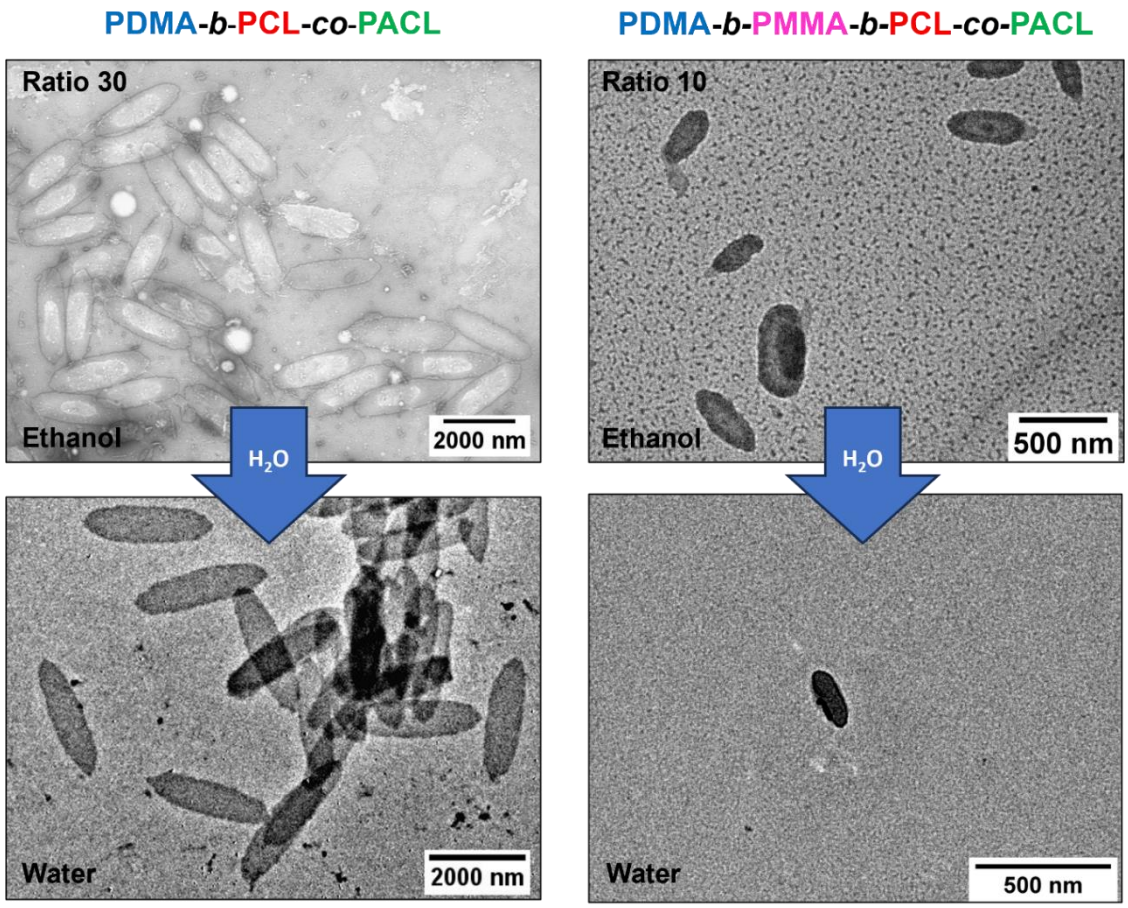


Figure 5.17. TEM micrographs of 2D platelets of $PDMA_{94}$-*b*-PCL_{44}-*co*-$PACL_3$ (**P6**) and $PDMA_{156}$-*b*-$PMMA_{20}$-*b*-PCL_{54}-*co*-$PACL_3$ (**P7**) with m_{PCL48}/m_{unimer} = 1 and m_{unimer}/m_{seeds} ratios corresponding to 30 and 10 respectively, before dialysis to water and after aging for 1 month in water. Samples were negatively stained using uranyl acetate (0.5 wt.%).

Following these studies, the stability of platelets containing BODIPY molecules in the core with a range of m_{unimer}/m_{seed} ratios (10, 20 and 30) was investigated. TEM analysis of the different platelets in aqueous solution was performed after 1 month since their transfer to water (**Figure 5.18**). In contrast to their allyl counterparts, BODIPY conjugated particles presented lower stability in water, which allowed the disassembly of 2D platelets into 1D cylindrical

micelles to be observed. Moreover, the particle disassembly rate was found to be highly influenced by the particle size. While the start of the morphology transition was observed at the edges of platelets with higher unimer/seed ratios (m_{unimer}/m_{seed} = 20 and 30), complete disassembly to cylindrical micelles was observed in smaller platelets. It was hypothesised that the steric hindrance caused by the BODIPY in the core-forming block slightly disrupts the packing of the semicrystalline chains, resulting in less tight packing and therefore lower chain strain resistance. Consequently, platelets with low m_{unimer}/m_{seed} ratios would disassembly faster into the initial unimers with preferential cylindrical morphology compared to larger platelets, which contain higher amounts of unimer.

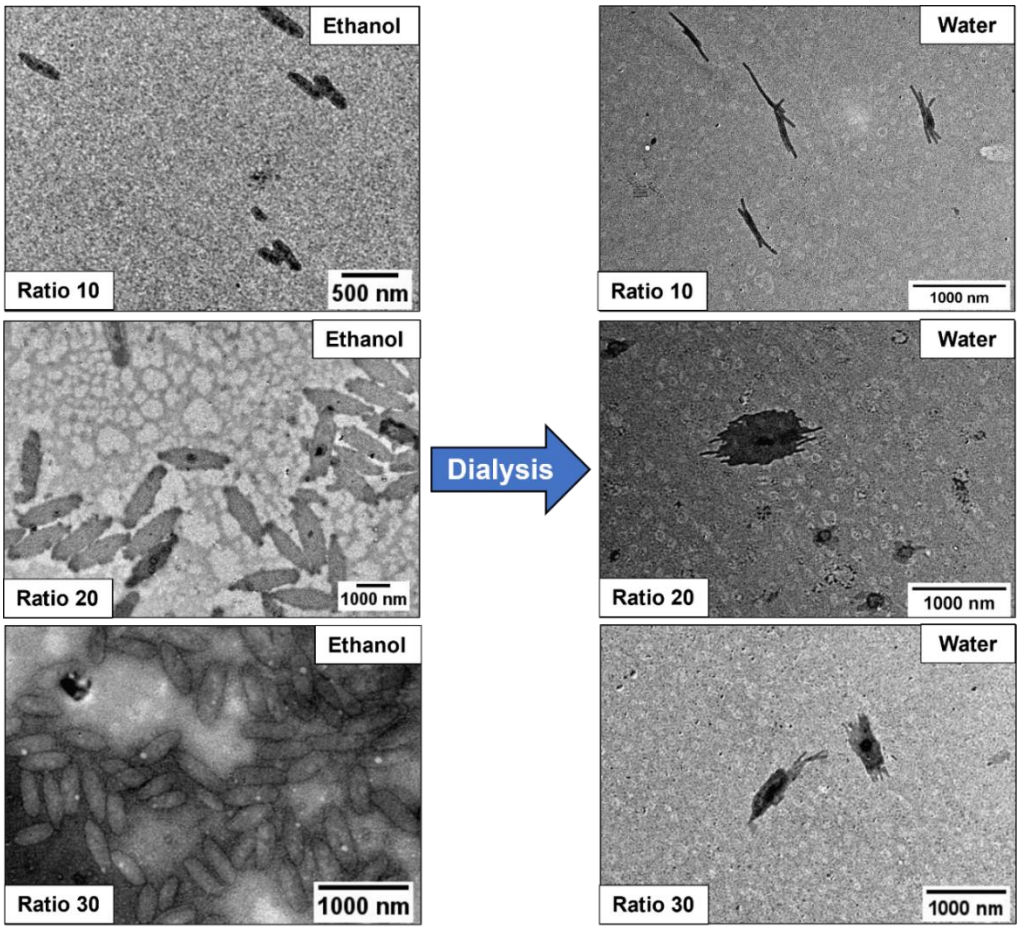


Figure 5.18. TEM micrographs of 2D platelets of BODIPY functionalized $PDMA_{156}$-*b*-$PMMA_{20}$-*b*-PCL_{54}-*co*-$PACL_3$ with m_{PCL48}/m_{unimer} = 1 and m_{unimer}/m_{seeds} ratios corresponding to 10, 20 and 30 before dialysis to water and after 1 month into water. Samples were negatively stained using uranyl acetate (0.5 wt %).

5.2.3.2.2 Multilayered platelets

To further explore the applicability of this strategy to achieve particles with higher complexity and chemical diversity, double-layered platelets were prepared following a reported procedure.[60] Block copolymers of $PDMA_{127}$-*b*-PCL_{48}, $PDMA_{122}$-*b*-PCL_{53}-*co*-$PACL_3$ and BODIPY-conjugated $PDMA_{156}$-*b*-$PMMA_{20}$-*b*-PCL_{54}-*co*-$PACL_3$ were used in combination to form double-layered platelets with distinct core-block chemistries. Multilayered platelets were achieved by successive addition of unimers ($m_{homopolymer}/m_{block\ copolymer}$ = 1) to a preformed seed solution (**Figure 5.19A**). Initially, simple $PDMA_w$-*b*-PCL_x copolymers were chosen for the first layer in the platelet, as it has been previously reported to be stable enough to undergo a second epitaxial growth.[61] Subsequently, addition of blended unimers (PCL and PDMA-*b*-PCL-*co*-PACL or BODIPY-PDMA-*b*-PMMA-*b*-PCL-*co*-PACL block copolymers) to previously formed platelets led to the formation of platelets with two separated regions (**Table S5.1** and, **Figure S5.26**). Furthermore, well-defined double-layered platelets using allyl-incorporated PCL copolymers in the first layer, in combination with BODIPY-conjugated polymers, were prepared (**Figure 5.19B**). The assembly of multilayer platelets with different core chemistries was further confirmed by confocal microscopy. As expected, the resulting double layered platelet showed a fluorescence hexagonal shape with a hollow non fluorescent centre associated with the non-dye containing region of the particle. (**Figures 5.19C** and **S5.27**). These results highlight the great potential of our system to design multi-component particles with different core-functionalized regions that could be used in the biomedical field for improved theragnostic applications.

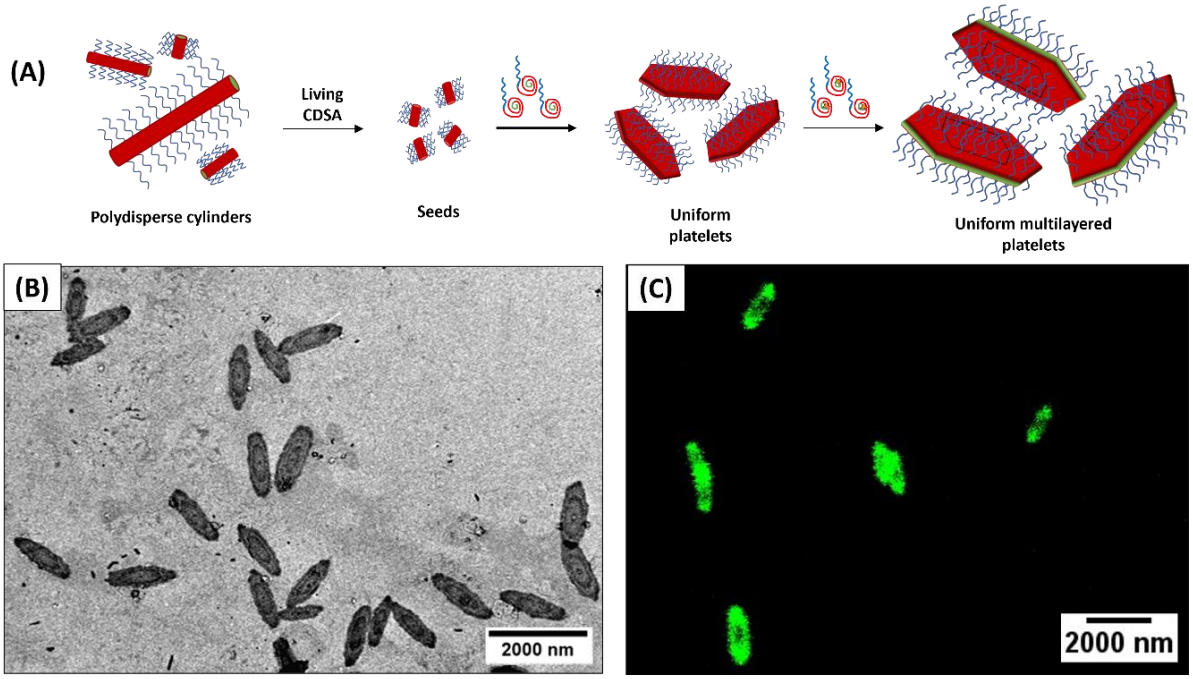


Figure 5.19. 2D epitaxial growth of multilayered platelets of bodipy-conjugated $PDMA_{156}$-*b*-$PMMA_{20}$-*b*-PCL_{54}-*co*-$PACL_3$ (BODIPY-P7) self-assembled in ethanol at 0.1 mg ml^{-1}. **A)** Schematic illustration for the 2D epitaxial growth of multilayered platelets **B)** TEM micrographs of bilayered platelets. Samples were negatively stained using uranyl acetate (0.5 wt %). **C)** Confocal images of correspondent multilayered platelets, showing the fluorescence field (confocal images collected by Mr. Tianlai Xia).

5.2.4 Biological essays

After confirming the stability of living CDSA structures in biologically relevant solvents and inspired by recent reports from Stenzel and coworkers, in which poly(*L*-lactic acid)-based 2D platelets microparticles (with average lengths of 1 µm and 2 µm) exhibited higher margination rates in blood than 2 µm spherical particles,[62] the biocompatibility of functional 2D platelet micelles was assessed.

5.2.4.1 Preparation of 2D platelet micelles for cell studies

Well-defined allyl functionalised and BODIPY conjugated 2D platelet micelles were prepared in ethanol at large scale using a seed solution of $PDMA_{154}$-*b*-PCL_{48}. Whilst m_{PCL48}/m_{unimer} was

kept constant at 1, the m_{unimer}/m_{seed} ratios were varied at 5 and 10. This was achieved through the addition of 583 µL of a 60 mg mL^{-1} solution of PCL_{48} and triblock copolymer in chloroform to 35 mL of a 0.1 or 0.2 mg mL^{-1} seed solution at 30 °C to achieve a m_{unimer}/m_{seed} ratio = 10 and 5 respectively. To ensure homogenous growth, the solution was stirred vigorously for 2 minutes. The solutions were then aged for 2 days and analysed by TEM. To prevent fluctuations in solvent polarity, which could result in changes on the targeted particle size, PCL/unimer stock solutions were created to incorporate less than 2% v/v of cosolvent into the seeds. TEM analyses of the resultant particles showed the formation of platelets with low size dispersity and predictable length and width. Platelets targeted for m_{unimer}/m_{seed} ratio 5 presented an average length (L_n) and average width (W_n) of 350 nm and 148 nm respectively, whereas those with a targeted ratio of 10 exhibited larger dimensions, with L_n and W_n = 393 nm and 174 nm respectively (**Figures 5.20**, **S5.28** and **S5.29**).

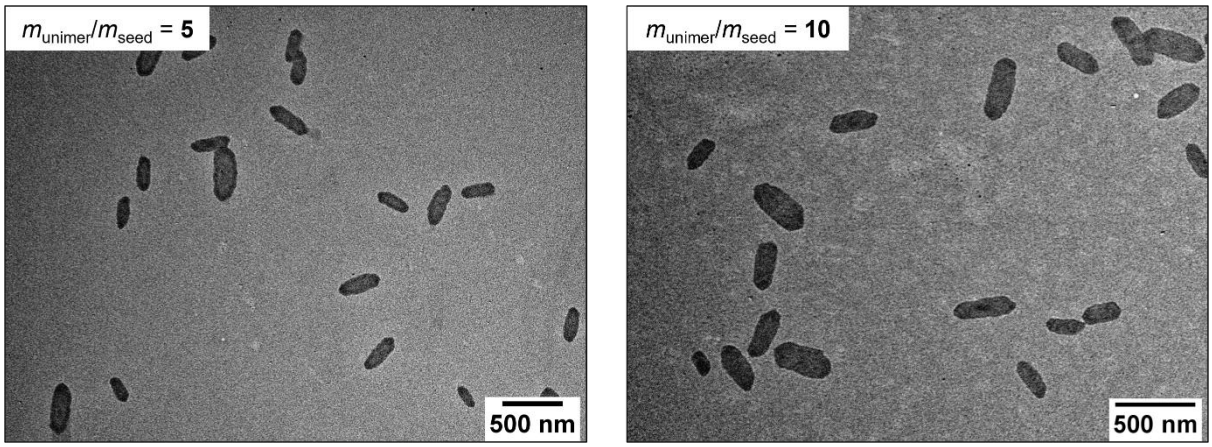


Figure 5.20. TEM micrographs of 2D living growth solutions of $PDMA_{94}$-*b*-PCL_{44}-*co*-$PACL_3$ unimer co-crystallized with PCL_{48} homopolymer onto seeds of $PDMA_{154}$-*b*-PCL_{48} where m_{PCL48}/m_{unimer} = 1, with m_{unimer}/m_{seeds} ratios 5 and 10.

5.2.4.2 Biological studies

The cell viability of the polymer and 2D nanoparticles synthesised in this chapter was assessed using a mouse embryonic fibroblast cell line, NIH 3T3, in cell-culture Dulbecco's Modified Eagle's medium (DMEM) with the addition of 10% fetal bovine serum (FBS), 1% *L*-glutamine (GlutaMAX) and 1% penicillin/streptomycin.

5.2.4.2.1 Cytocompatibility of PDMA-*b*-PCL-*co*-PACL block copolymer

Cell viability studies were performed in 12-well plates after seeding 25,000 cells/well. After 24 h of incubation at 37 °C and 5% CO_2 with saturating humidity, the fibroblasts had adhered to the bottom of the well. Next, 1 mL of the polymer solution ($PDMA_{94}$-*b*-PCL_{44}-*co*-$PACL_3$) suspended in cell media at various concentrations (0 to 2 mg mL^{-1}) was added to the cells. To avoid chemical cross-contamination, the polymer was dialysed into water followed by freeze-drying before its use. The cytotoxicity of the polymer was then measured after 24 and 72 h through the addition of 500 µL of PrestoBlue solution, after removing the polymer solution and washing cells thoroughly with phosphate-buffered saline (PBS) solution. This phenoxazine dye (*i.e*. PrestoBlue) gets modified by the reducing environment of living cells, which triggers a change in colour from blue to fluorescent pink, allowing the quantification of viable cells. After 1 to 4 h of incubation with the PrestoBlue solution, changes in absorbance in different wells were analysed in triplicate using a microplate reader. Cell viability was found to be 91% and 87% after 24 and 72 h, respectively, with the highest concentration of polymer we tested (2 mg mL^{-1}). This suggests our functional PCL system is highly biocompatible with live cells, and therefore, could potentially be used for biological applications, such as drug delivery (**Figure 5.21**).

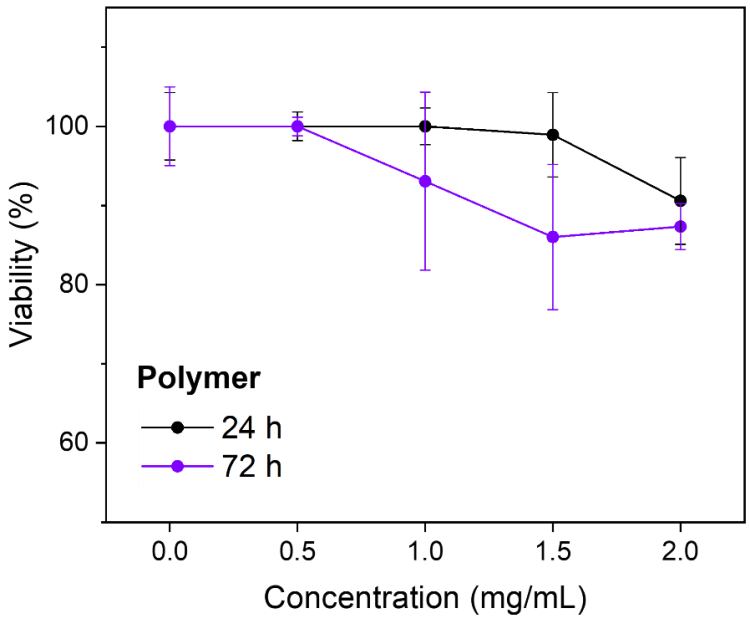


Figure 5.21. Cell viability at 24 and 72 h of NIH 3T3 cell using concentrations of $PDMA_{94}$-*b*-PCL_{44}-*co*-$PACL_3$ from 0 to 2 mg mL^{-1}.

5.2.4.2.2 Cytocompatibility of PDMA-*b*-PCL-*co*-PACL 2D platelets

After the promising results obtained for the polymer, the cytocompatibility of $PDMA_{94}$-*b*-PCL_{44}-*co*-$PACL_3$ 2D platelets with m_{unimer}/m_{seed} ratios = 5 and 10 was investigated. These platelets were transferred to cell media by drying the ethanol with pressurised air for 24 h and resuspended in 7 mL of DMEM medium to achieve stock solutions of platelets with ratios 5 and 10 with a final concentration of 6.1 and 5.5 mg mL^{-1} respectively. From these stock solutions, nanoparticle solutions with concentrations ranging from 0.5 to 2 mg mL^{-1} were prepared and added to seeded 12-well plates. Cells were seeded following the procedure previously reported for the polymer cytocompatibility studies. After 24 and 72 h in contact with the particles, the cell viability was measured through adding PrestoBlue solution. However, a sharp decrease in cell viability was observed for both types of platelets, even at the lowest concentrations (0.5 mg mL, 30% viability after 24 h) (**Figure 5.22**).

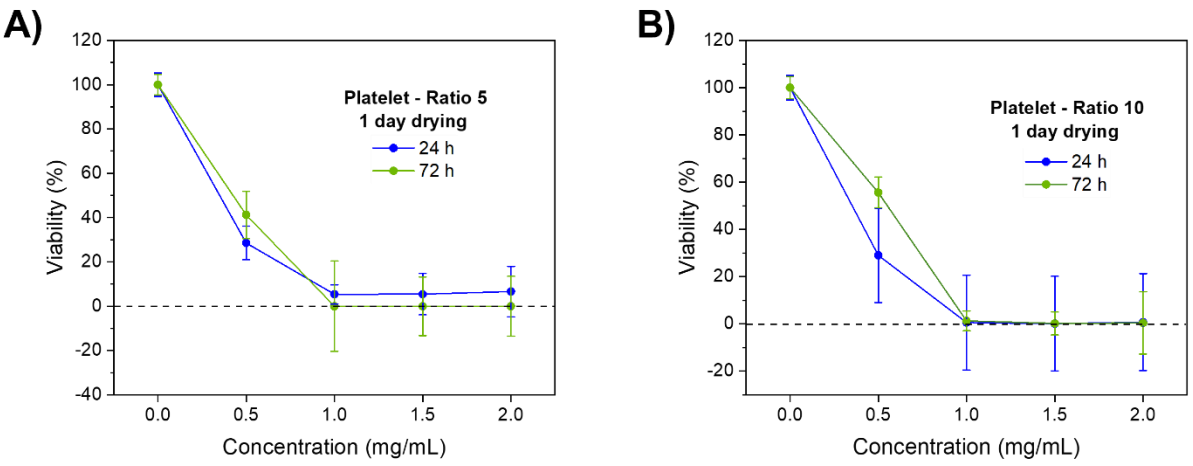


Figure 5.22. Cell viability percentages at 24 and 72 h of NIH 3T3 using platelet particles with **(A)** m_{unimer}/m_{seeds} ratio 5 and **(B)** ratio 10 at concentrations ranging from 0 to 2 mg mL^{-1} after 24 h drying.

It was hypothesised that the low cell viability observed could result from some remaining ethanol present in the solution. Any excess ethanol could, independent of the platelets, also effect the cell metabolism or even cell death. For this reason, experiments were repeated after drying the nanoparticle solution for 5 days instead of 24 h, following the same procedure previously described. Analysis of PrestoBlue solutions showed a slightly enhanced viability after 24 and 27 h for both particle solutions. However, the viability values are still very far from those obtained with the polymer solution. Remarkably, platelets with unimer/seed ratio 10 exhibited considerably higher viability values than particles with a targeted ratio of 5 after both 24 and 72 h (**Figure 5.23 A-B**). To explore this further, lower nanoparticle concentrations of small platelets (m_{unimer}/m_{seed} ratio of 5) were investigated. As expected, higher cell viabilities were observed when the platelet concentration was decreased. After 24 h and 72 h, the percentage of viable cells ranged from 91% to 21% and 63% to 7%, with nanoparticle concentrations between 0.1 to 0.4 mg mL^{-1}, respectively (**Figure 5.23C**). These results indicated that: 1) the small amount of residual ethanol was not the cause of the poor cell

viability observed. 2) Platelets with m_{unimer}/m_{seed} ratio = 5 are more cytotoxic than those with a ratio 10. This could result from larger particle agglomerations formed upon resuspension in cell media, which could potentially damage cells. This hypothesis was further investigated by assessing the cytocompatibility of cells added onto the nanoparticles. For this study, 500 µL of platelets with m_{unimer}/m_{seed} ratio = 10 at concentrations ranging from 1 to 4 mg mL^{-1} were first added into the 12-well plates. After a 24 h incubation to ensure the structures had been deposited in the bottom of the wells, 500 µL of NIH 3T3 cell stock solution was incorporated to achieve a total of 25,000 cell per well. Cell viability was analysed after 24 and 72 h by adding PrestoBlue reagent, revealing higher cytocompatibility across all concentrations than those found when 12-well plates were initially seeded with cells (**Figure 5.23D**). However, the viability values obtained appeared significantly lower compared to those obtained with the polymer solution (23.5% *vs*. 87.0% after 72 h at a conc. = 2 mg mL^{-1}). It is believed that the stability of polymeric particles in cell culture media differs from that in water, leading to platelet agglomeration and precipitation in the bottom of wells. As a result, the surface area available for cells to adhere would be decreased, hindering cell growth but not necessarily increasing cytotoxicity. To prove this hypothesis, future studies should include DLS or static light scattering (SLS) analyses in ethanol, water, and DMEM, which could give valuable information regarding changes in particle size and morphology in different solvent environments. Moreover, polymerase chain reaction (PCR) analyses could elucidate the exact number of cells and surviving cells before and after contact with the nanoparticle solution.

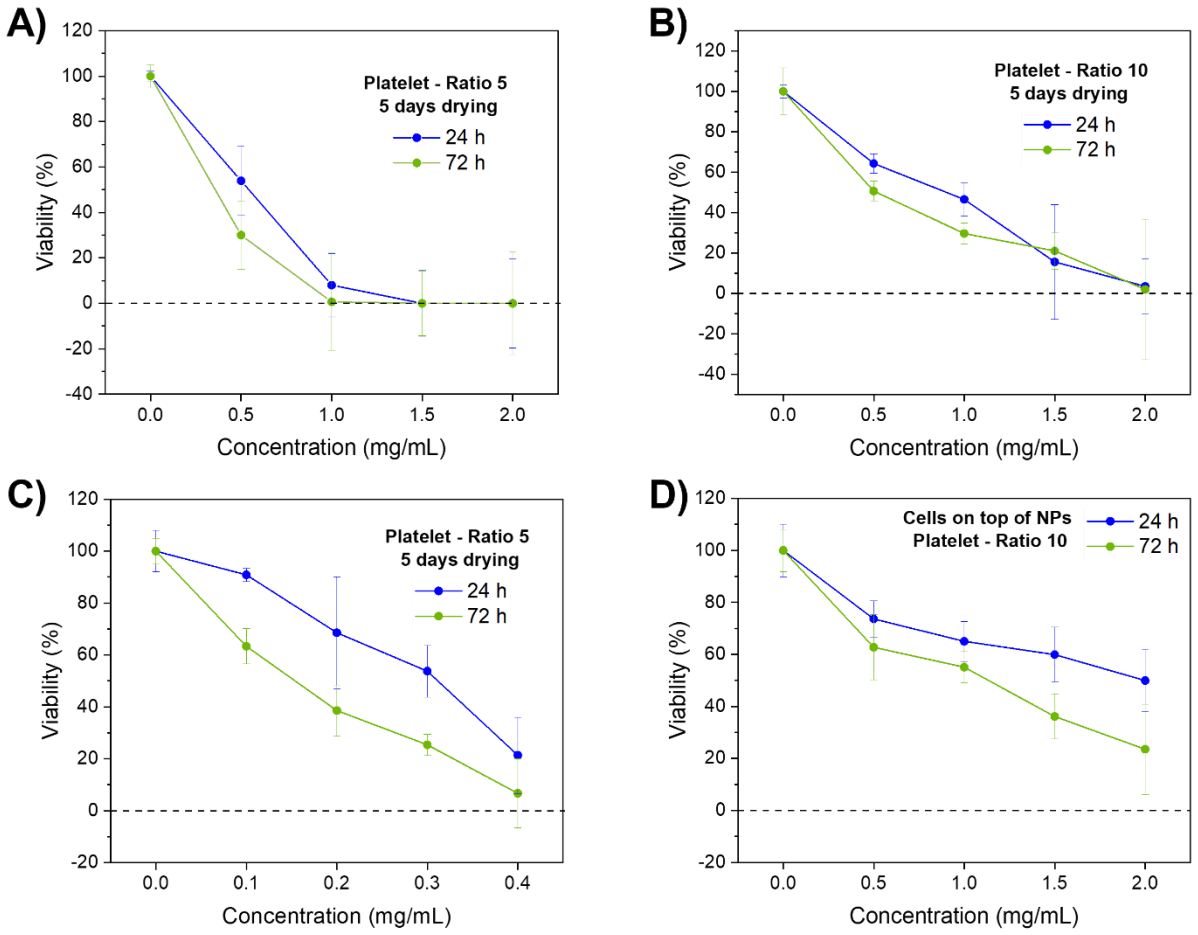


Figure 5.23. (A-B) Cell viability percentages at 24 and 72 h using platelet with m_{unimer}/m_{seeds} ratios 5 and 10 at concentrations ranging from 0 to 2 mg mL^{-1} after 5 days drying. **(C)** Cell viability percentages at 24 and 72 h using platelet with ratio 5 at concentrations ranging from 0 to 0.4 mg mL^{-1} after 5 days drying. **(D)** Cell viability percentages over 24 and 72 h after placing cells on top of platelet solutions from 0.5 to 2 mg mL^{-1}.

5.2.4.3 Cell internalisation studies

Preliminary internalisation studies were conducted to explore how anisotropic nanoparticles interact with cells. For this reason, we exposed the NIH 3T3 cell line to BODIPY-functionalised $PDMA_{156}$-*b*-$PMMA_{20}$-*b*-PCL_{54}-*co*-$PACL_3$ (BODIPY-P7) platelets with a m_{unimer}/m_{seeds} ratio of 10 (L_n = 594 nm and W_n = 244 nm) at a concentration of 1 mg mL^{-1} for 24 h in an incubator at 37 °C. Before testing, to ensure the removal of any free dye remaining in solution, the particles were dialysed in ethanol before drying *via* evaporation for one week. Confocal microscopy of

the treated cells showed the presence of particle agglomerates of multiple sizes, potentially due to the platelet drying process. Some particle internalisation was observed in the fluorescent field (λ = 503-512 nm) after applying a z-stack scan to obtain a three-dimensional visual (**Figure S5.30**). To enhance cell visualisation, both the control group (not exposed to platelets) and nanoparticle-treated group were washed with PBS, to remove the excess of nanoparticles that were not uptaken by the cell. Two drops of a nuclear stain (NucRed Live 647, 12.5X) was added to the cell media to determine the cell nucleus localisation (**Figure S5.31**). Confocal imaging after washing and staining cells allowed precise visualisation of nanoparticle uptake by NIH 3T3 cells (**Figures 5.24** and **S5.32**). While some non-internalised nanoparticles could be observed in the background, a significant concentration of nanoparticles was found distributed within the cytoplasm of the cells but not covering the nuclei. By contrast, the control or untreated group showed no fluorescence in the BODIPY emission region. These preliminary studies demonstrated that functional 2D nanoplatelets are efficiently taken up by NIH 3T3 cells after incubation for 24 h. However, further studies are needed to elucidate the impact of nanoparticle morphology during cell uptake as well as the cell internalisation pathway.

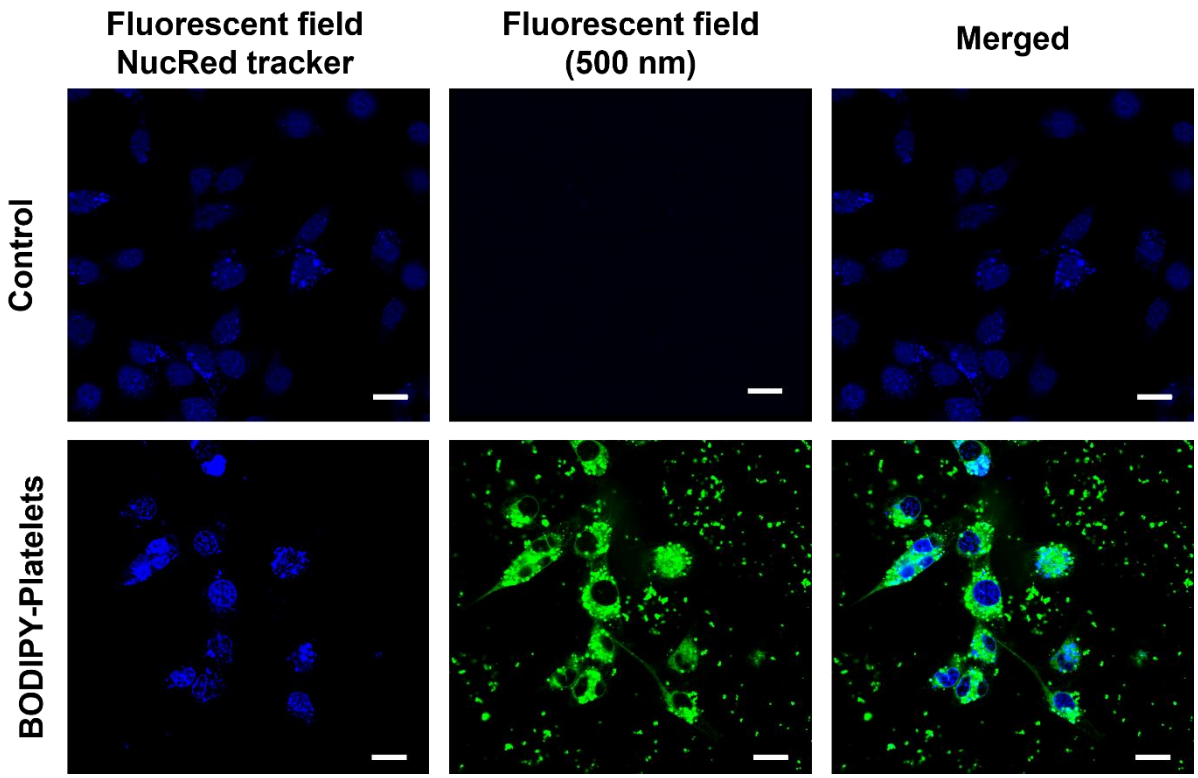


Figure 5.24. Confocal imaging of NIH 3T3 after 24 h of incubation with BODIPY-Platelets (1 mg mL^{-1}). Cells were washed with PBS and cell tracker (NucRed) was added before imaging. Showing fluorescent fields at λ = 647-665 nm (NucRed) and λ = 503-512 nm (BODIPY), and merged fields. Scale bar = 20 µm.

5.3 Conclusions

In summary, we have reported the preparation of well-defined PCL-based cylinders and platelets containing functionalities in the core-forming block, using living crystallization-driven self-assembly. For this, amphiphilic semicrystalline block copolymers with allyl functionalities were first synthesised. A fluorescent dye was then attached to the PCL-core *via* thiol-ene addition without disrupting the semicrystalline nature of PCL. Self-assembly of these functional polymers in ethanol resulted in fluorescent 1D and 2D nanoparticles with controlled dimensions and shape that can be transferred to aqueous solution. Uniform cylindrical micelles with varying lengths, as well as platelet-shaped micelles containing a thiol-BODIPY molecule inside, were obtained and characterized by TEM and confocal microscopy. Doubled-layered platelets with diverse core block chemistries were accessed by selective sequential addition of non-fluorescent and fluorescent-conjugated PCL-based copolymers together with PCL homopolymer. These platelet structures comprise two separate regions that respond differently to light stimuli. Moreover, cell viability studies showed excellent compatibility of the block copolymer and acceptable levels of toxicity at nanoparticle concentrations 0.1 – 2 mg mL^{-1}. Cell internalization studies demonstrated NIH 3T3 cells were able to efficiently internalise BODIPY-functionalised platelets, which were distributed in the cellular cytoplasm. These promising results open the possibility of attaching key biomolecules inside of non-spherical particles. This work highlights the incredible biological potential for stable non-spherical particles using CDSA.

5.4 Experimental section

5.4.1 Materials

All solvents and chemicals were purchased from Sigma-Aldrich, Fisher Scientific, Alfa Aesar, or VWR International and used without further purification unless otherwise stated. 2,2'-Azobis(isobutyronitrile) (AIBN) was recrystallised from methanol and was stored at 4 ℃. The monomers dimethyl acrylamide (DMA) and methyl methacrylate (MMA) were filtered through a plug of basic alumina before use. For DMA polymerisation, solutions were degassed by bubbling N_2 gas into the reaction vessel for 40 min. For MMA polymerisation, solutions were degassed via freeze pump thaw cycles. All solvents used in CDSA were filtered prior to use through a 0.45 μm syringe filter. Fetal Bovine Serum (FBS) was purchased from Merk Life Science. GlutaMAX, DMEM cell culture media and Dulbecco's Modified Phosphate buffer solution (DPBS) were purchased from Fisher Scientific. Penicillin/streptomycin solution was purchased from Corning. NIH 3T3 cells with a passage number of 4 were thawed from −80 °C freezer.

5.4.2 Characterisation techniques

5.4.2.1 Nuclear magnetic resonance (NMR) spectroscopy

Diffusion-ordered spectroscopy (DOSY) proton (^{1}H) and carbon (^{13}C) resonance spectra were recorded on a Bruker 101 MHz, 300 MHZ, or 500 MHz spectrometers at 298 K. Chemical shifts were reported as δ in parts per million (ppm) and referenced to the residual solvent signals ($CDCl_3$, ^{1}H: δ = 7.26 ppm, ^{13}C: δ = 77.16 ppm). The multiplicities were reported as s = singlet, d = doublet, dd = doublet in doublet, ddt = double of doublet of triplet, t = triplet, tdd = triplets

of doublet of doublets, q = quadruplet, p = pentaplet, pd = pentaplet of doublets and m = multiplet. The coupling constant (*J*) was recorded in Hertz [Hz]. The obtained data were processed and analysed using MestReNova 12.0.3 software.

5.4.2.2 Size exclusion chromatography (SEC)

SEC analyses were performed on an Agilent 1260 Infinity II Multi-Detector GPC/SEC System fitted with RI and ultraviolet (UV, λ = 309 and 500 nm), and viscosimeter detectors. The instrument is equipped with an Agilent guard column PLGel 3 µm (50 × 7.5 mm) and two Agilent mixed-C columns PLGel 5 µm (300 × 7.5 mm) using $CHCl_3$ (buffered 0.5% Et_3N) as the mobile phase (eluent). Number average molecular weights (M_n), weight average molecular weights (M_w) and dispersities ($Đ_M = M_w/M_n$) were determined using Agilent GPC/SEC software (vA.02.01) against a 15-point calibration curve (M_p = 162 – 3,187,000 g mol^{-1}) based on poly(styrene) standards or a 12-point calibration curve (M_p = 550 – 2,210,000 g mol^{-1}) based on poly(methyl methacrylate) standards. Molecular weights (M_n), weight average molecular weights (M_w) are given in (g mol^{-1}).

5.4.2.3 Differential scanning calorimeter (DSC)

Determination of the DSC curves was carried out using a STARe system DSC3 with an auto-sampler (Mettler Toledo). The samples (1 – 10 mg of polymer) were placed into aluminium pans measuring 5 mm in diameter and 0.4 – 0.6 mm in thickness. Thermograms obtained with a heating rate of 10 °C min^{-1} were recorded from −100 to 100 °C with a 10 °C min^{-1} heating and cooling rate over two cycles.

5.4.2.4 Nano differential scanning calorimetry (nano-DSC)

Nano differential scanning calorimetry (Nano-DSC) was performed on a TA Nano DSC. For analysis, 800 µL of the nanoparticle solutions were introduced in the instrument and run from 0 °C to 100 °C at a heating or cooling ramp of 1 °C min^{-1} in triplicate under a constant atmosphere pressure. T_c and T_m were obtained using the first run and were taken as the midpoint of the inflection tangent.

5.4.2.5 Dynamic light scattering (DLS)

Dynamic light scattering (DLS) analyses of cylindrical micelles were conducted using a Malvern Zetasizer Nano instrument equipped with a 4 mW He-Ne 633 nm laser module at 25 ℃, with data analysis using Malvern DTS 6.20 software. Measurements were carried out at a detection angle of 173° (back scattering). All determinations were made in triplicate, with 10 measurements recorded for each run.

5.4.2.6 Transmission electron microscopy (TEM)

Transmission electron microscopy (TEM) was performed using a JEOL 1400 microscope operating at an acceleration voltage of 80 kV. TEM samples were prepared by depositing 8 µL of sample solution (5 mg mL^{-1}) on a formvar/carbon (300 mesh copper) film TEM grid and left air drying. Afterwards, 8 µL of uranyl acetate solution (UA, 1% in water) was then dropped on the grid and left for 60 seconds before blotting. The sample was kept in a desiccator overnight before characterisation.

To analyse the particle length, width, and area, ≥ 100 particles were traced manually using the ImageJ software package (NIH, US). The number average micelle length (L_n) and weight average micelle length (L_w) were calculated using the following equations:

$$L_n = \frac{\sum_{i=1}^{n} N_i L_i}{\sum_{i=1}^{n} N_i}$$

$$L_w = \frac{\sum_{i=1}^{n} N_i L_i^2}{\sum_{i=1}^{n} N_i L_i}$$

where N_i is the number of micelles of length L_i, and n is the number of micelles examined in each sample. The distribution of micelle lengths is characterised by L_w/L_n.

The distribution of micelle width and area (W_w/W_n and A_w/A_n) were calculated similarly after measuring the widths and areas of a minimum of 100 nanoparticles.

5.4.2.7 Confocal Laser Scanning Microscopy (CLSM)

BODIPY-conjugated particles were imaged using Leica TCS SP8 STED 3X microsystem confocal fluorescence microscope. The fluorescence signal was detected by a Hybrid Detector (HyD, Standard mode, with an observation window of 503– 512 nm) after passing through an Acousto-Optical Beam Splitter (AOBS). Some images of platelet micelles were performed by Mr. Tianlai Xia.

5.4.3 Experimental procedures

5.4.3.1 Synthesis of PCL-*b*-PACL copolymers

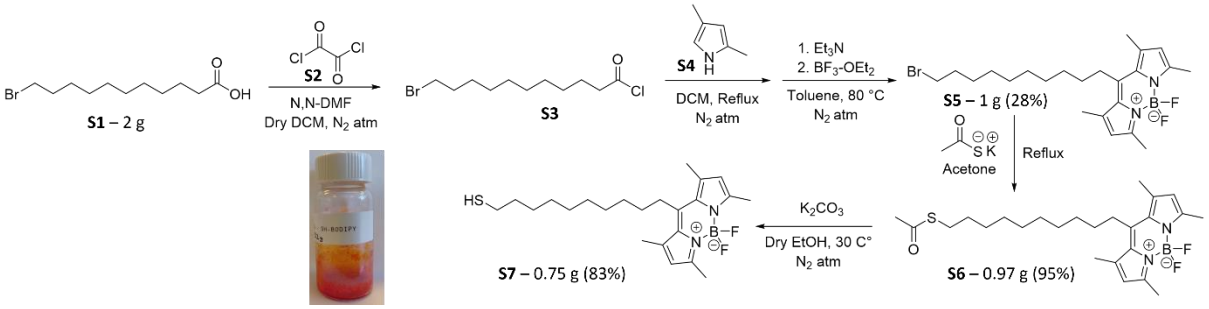
Refer to Chapter 3, Section 3.4.3.4 for the synthetic protocols and characterisation.

5.4.3.2 Synthesis of PDMA-*b*-PCL-*co*-PACL and PDMA-*b*-PMMA-*b*-PCL-*co*-PACL block copolymers.

Refer to Chapter 4, Section 4.4.3.2 for the synthetic protocols and characterisation.

5.4.3.3 Synthesis of 4,4-difluoro-1,3,5,7-tetramethyl-8-[(10-mercapto)]-4-bora-3a,4a-diaza-*s*-indacene (BODIPY-C_{10}-SH)

The synthesis of BODIPY-C_{10}-SH (**S7**) was adapted from literature.[63] It was performed as indicated in the following scheme:



In a dry two-necked round bottom flask, 2.0 grams of 11-bromoundecanoic acid **S1** (7.54 mmol, 1.0 equiv.) were combined with 2 drops of *N,N*-dimethylformamide in 40 mL of dichloromethane dried over 3 Å molecular sieves under N_2 inert atmosphere. Oxalyl chloride **S2** (1.0 g, 7.88 mmol, 1.05 equiv.) was dissolved in 5.0 mL of anhydrous dichloromethane and added dropwise. The reaction mixture was stirred for one hour, then the crude mixture was concentrated on the schlenk line, using a second trap to remove any unreacted oxalyl chloride, and dried on a vacuum overnight. The resulting acid chloride **S3** was dissolved in 50 mL of dichloromethane, followed by the addition of 2,4-dimethylpyrrole **S4** (0.772 mL, 7.50 mmol, 0.99 equiv.) in 5.0 mL of dichloromethane. The resulting reaction mixture was heated to reflux for 3 hours under a nitrogen atmosphere, during which time the mixture became dark red. After three hours, the reaction mixture was cooled to room temperature, and the solvent was removed from the rotary evaporator until approximately 5.0 mL of the dichloromethane solution remained. Then, 200 mL of *n*-hexanes were added to the flask, and the mixture was cooled overnight in the freezer at −20 °C. The hexanes were decanted from the insoluble oil

and precipitated. The resulting crude product was dissolved in 75 mL of toluene under inert conditions, followed by the addition of 1.0 mL of triethylamine (Et_3N, 7.17 mmol, 0.95 equiv.) and 1.0 mL of boron trifluoride etherate (BF_3-OEt_2, 8.10 mmol, 1.07 equiv.) while stirring. The reaction mixture was then heated to 80 °C for 30 minutes, during which time the colour of the mixture darkened and became fluorescent. The reaction mixture was cooled to room temperature, and the product was extracted 3 times with brine (50 mL each time). The organic layer was dried over magnesium sulphate, filtered, and concentrated. The crude product was purified by flash chromatography (1:1 dichloromethane: hexanes) to yield 4,4-difluoro-1,3,5,7-tetramethyl-8-[(10-bromodecyl)]-4-bora-3a,4a-diaza- *s*-indacene (**S5**) in 28% yield (1 g) with spectroscopic data in accordance with the literature. **^{1}H NMR** (300 MHz, $CDCl_3$): δ/ppm = 6.05 (s, 2H), 3.41 (t, *J* = 6.8 Hz, 2H), 3.01 – 2.84 (m, 2H), 2.51 (d, *J* = 1.3 Hz, 6H), 2.41 (s, 6H), 1.85 (dt, *J* = 14.4, 6.8 Hz, 2H), 1.70 – 1.56 (m, 2H), 1.52 – 1.23 (m, 10H).

The bromide **S5** (0.96 g, 2.07 mmol, 1.0 equiv.) and potassium thioacetate (0.27 g, 2.36 mmol, 1.1 equiv.) were dissolved in 50 mL of acetone. The reaction mixture was heated to reflux for two hours. After two hours, the reaction mixture was cooled to room temperature, acetone was removed in-vacuo, and the crude solid was redissolved in dichloromethane and washed with water. The organic extract was dried over magnesium sulphate, filtered, and concentrated to yield compound **S6** in 95% yield (0.97 g) with spectroscopic data in accordance with the literature. **^{1}H NMR** (400 MHz, $CDCl_3$): δ/ppm = 6.05 (s, 2H), 2.98 – 2.89 (m, 2H), 2.86 (t, *J* = 7.4 Hz, 2H), 2.51 (s, 6H), 2.41 (s, 6H), 2.32 (d, *J* = 1.6 Hz, 3H), 1.68 – 1.45 (m, 28H), 1.31 (d, *J* = 23.8 Hz, 11H).

The resultant thioacetate compound **S6** (0.9 grams, 1.94 mmol, 1.0 equiv.) was dissolved in 150 mL of anhydrous ethanol under N_2 inert atmosphere. Potassium carbonate (0.4 g, 2.91

mmol, 1.5 equiv.) was added, and the reaction mixture was warmed to 30 °C for 4 hours while stirring. After this time, 40 mL of aqueous saturated ammonium chloride were poured over the contents of the flask, at this point, the solution turned bright orange, and a bright orange precipitate was formed. The product was dried in the rotary evaporator, redissolved in 50 mL of dichloromethane, and washed several times with water until no green fluorescence appeared in the aqueous phase). The organic layer was dried over magnesium sulphate, filtered, and concentrated. The product was purified via flash chromatography (1:1 dichloromethane: hexanes) to yield 4,4-difluoro-1,3,5,7-tetramethyl-8-[(10-mercapto)]-4-bora-3a,4a-diaza-*s*-indacene (BODIPY-C_{10}-SH, **S7**) in 83% yield (0.75 g) as a bright orange solid. **^{1}H NMR** (400 MHz, $CDCl_3$): δ/ppm = 6.05 (s, 2H, C*H*=C(CH_3)N), 2.98 – 2.89 (m, 2H, CH_2SH), 2.60 – 2.47 (m, 8H, CH_2CH=C and CH=C(CH_3)N), 2.41 (s, 6H, CH=C(CH_3)N), 1.62 (ddt, *J* = 14.9, 11.9, 7.5 Hz, 2H, CH_2CH_2SH), 1.53 – 1.43 (m, 2H, CH_2CH_2CH=C), 1.41 – 1.17 (m, 11H, intermediate CH_2CH_2 chain). **^{13}C NMR** (101 MHz, $CDCl_3$) δ/ppm = 154.37, 148.08, 140.26, 131.10, 120.90, 34.13, 32.06, 30.99, 30.53, 29.62, 29.57, 29.18, 28.65, 28.47, 24.78, 16.53, 14.02. **HRMS (ESI-TOF)** *m*/*z*: $[M + Na]^+$ Calc. for BODIPYC_{10}SH 420.41; Found 420.2582.

5.4.3.4 Thermo-initiated thiol-ene addition

Amphiphilic block copolymers (0.45 g, 0.018 mmol, 1 equiv.) were dissolved in 4.0 mL of toluene. BODIPY-C_{10}-SH (0.095 mmol, 2 equiv. per olefin) and AIBN (0.1 mmol % of thiol) dissolved in 0.5 mL of toluene were added to the polymer solution. The solution mixture was purged with N_2 gas for 20 min before placing it into an oil bath at 80 °C. After 24 h, the solution was precipitated three times into ice-cold diethyl ether and dried under vacuum to obtain 0.43 g of BODIPY-functionalised PCL-based copolymer as an orange solid.

^{1}H and ^{13}C NMR: No visible changes from spectra obtained with non-conjugated block copolymers.

SEC: Absorbance signal at λ = 309 and 500 nm.

5.4.3.5 General procedure for crystallization-driven self-assembly of amphiphilic PCL-based block copolymers

All amphiphilic copolymers were assembled in ethanol using the following general protocol described in Chapter 4, Section 4.4.3.4. The assembly solutions were aged for 5 – 10 days at ambient temperature in a sealed vial.

5.4.3.6 Preparation of crystalline seed solution

The polydisperse cylindrical assemblies (5 mg mL^{-1}) were sonicated using a Bandelin Sonopuls sonication probe in a dry ice/acetone bath (−78 °C) for 40 min. The polymer solution was fractured for 120 cycles of 20 s sonication, each with an interval of 100 s to yield short crystalline cylinders (seeds).

5.4.3.7 Living CDSA: 1D Epitaxial growth

Various aliquots (25 µL) of a solution of BCP (unimer) in THF, at a concentration of 50 mg/500 µL, were added to 500 µL of crystalline seeds (2.5 mg mL^{-1}), depending on their targeted m_{unimer}/m_{seed} ratios as indicated in the Table below. Intervals of 2 h between additions were required to not oversaturate the solution. After addition of unimer solution, the assembly solutions were left to age at ambient temperature for 1 to 8 weeks.

Targeted m_{unimer}/m_{seed} ratio	**Polymer to add (mg)**	**Nº of aliquots (25 µL of a 50 mg/500 µL polymer solution**
2	2.5	1
4	5	2
6	7.5	3
8	10	4

5.4.3.8 Living CDSA: 2D Epitaxial growth

The protocols to form mono-layered and doubled-layered 2D platelets micelles were adapted from literature.[61]

A solution of PDMA-*b*-PCL-*co*-PACL or PDMA-*b*-PMMA-*b*-PCL-*co*-PACL and PCL (homopolymer) in chloroform, with a molar ratio = 1:1 and concentrations ranging from 10 mg mL^{-1} to 45 mg mL^{-1} (depending on the m_{unimer}/m_{seed} targeted) was added to a 1 mL dispersion of crystalline seeds (0.01 mg mL^{-1}) in a screw cap vial. After shaking the vials for 30 s, the solution was aged for 2 days at room temperature. The unimer/seed ratio was altered by adding different volumes of unimer solution (homopolymer + block copolymer) concentrations to the dispersion of seed. The number average length (L_n), width (W_n) and area (A_n) were measured from TEM images.

The methodology to form 2D platelets on a larger scale is the same but fixing the concentrations of PCL/BCPs to the new volume. The unimer solution was added to seed solution at 30 °C while stirring vigorously to achieve a homogeneous distribution of unimer to seeds.

5.4.3.8.1 Sequential growth of multilayered 2D platelets

A solution of PDMA-*b*-PCL-*co*-PACL or PDMA-*b*-PMMA-*b*-PCL-*co*-PACL and PCL in chloroform (10 mg mL^{-1} and a molar ratio = 1:1) was added to a dispersion of already prepared platelets, which act as crystalline seeds. Assemblies were aged for 2 days before TEM analysis.

5.4.3.9 Cell viability studies

For biocompatibility studies, NIH 3T3 cells were seeded on 12 well plates at 25,000 cells/well and left to adhere to the bottom of the wells for 24 h. Polymer and platelet concentrations from 0 to 2 mg mL^{-1} were then prepared in culture medium and cells were incubated with the polymer for 24 and 72 h. PrestoBlue metabolic assay was then used to assess cell viability. Fluorescence was measured using a Biotek plate reader, with Ex. = 530 nm and Em. = 590 nm. Experiments were done in triplicate. Cell viability is express as a percentage related to the control sample (0 mg/mL of polymer or nanoparticle).

5.5 References

1. G. Villaverde, A. Alfranca, Á. Gonzalez-Murillo, G. J. Melen, R. R. Castillo, M. Ramírez, A. Baeza and M. Vallet-Regí, *Angew. Chem. Int. Ed.*, 2019, **58**, 3067-3072.
2. B. R. Mandal A, Pal D, Mitra AK, in *Emerging Nanotechnologies for Diagnostics, Drug Delivery and Medical Devices*, Elsevier, Boston, 2017, ch. 4, pp. 59-83.
3. C. K. Wong, F. Chen, A. Walther and M. H. Stenzel, *Angew. Chem.*, 2019, **131**, 7413-7418.
4. N. L. Fletcher, K. Kempe and K. J. Thurecht, *Macromol. Rapid Commun.*, 2020, **41**, 2000319.
5. M. Caldorera-Moore, N. Guimard, L. Shi and K. Roy, *Expert Opin Drug Deliv*, 2010, **7**, 479-495.
6. L. Zhang, C. Chen, S. S. Tay, S. Wen, C. Cao, M. Biro, D. Jin and M. H. Stenzel, *ACS Appl Mater Interfaces*, 2021, **13**, 16142-16154.
7. S. De Luca, J. Treny, F. Chen, P. Seal, M. H. Stenzel and S. C. Smith, *Adv. Theory Simul.*, 2021, **4**, 2000247.
8. H. Lu, J. Su, R. Mamdooh, Y. Li and M. H. Stenzel, *Macromol. Biosci.*, 2020, **20**, 1900221.

9. F. Wang, J. Xiao, S. Chen, H. Sun, B. Yang, J. Jiang, X. Zhou and J. Du, *Adv. Mater.*, 2018, **30**, 1705674.
10. S.-Y. Huang and C.-C. Cheng, *Nanomater.*, 2020, **10**, 2006.
11. E. Locatelli and M. Comes Franchini, *J Nanopart Res*, 2012, **14**.
12. Z. Q. Jie Liu, Shenqi Wang, Lei Zhou, Shengmin Zhang, *Biomed. Mater.*, 2010, **5**.
13. K. C. Tjandra, C. R. Forest, C. K. Wong, S. Alcantara, H. G. Kelly, Y. Ju, M. H. Stenzel, J. A. McCarroll, M. Kavallaris, F. Caruso, S. J. Kent and P. Thordarson, *Adv. Healthc. Mater.*, 2020, **9**, 2000261.
14. Y. Y. Khine and M. H. Stenzel, *Mater. Horiz.*, 2020, **7**, 1727-1758.
15. A. C. Anselmo, C. L. Modery-Pawlowski, S. Menegatti, S. Kumar, D. R. Vogus, L. L. Tian, M. Chen, T. M. Squires, A. Sen Gupta and S. Mitragotri, *ACS Nano*, 2014, **8**, 11243-11253.
16. N. Doshi, B. Prabhakarpandian, A. Rea-Ramsey, K. Pant, S. Sundaram and S. Mitragotri, *J. Contr. Release*, 2010, **146**, 196-200.
17. Y. Geng, P. Dalhaimer, S. Cai, R. Tsai, M. Tewari, T. Minko and D. E. Discher, *Nat. Nanotechnol*, 2007, **2**, 249-255.
18. X. Huang, X. Teng, D. Chen, F. Tang and J. He, *Biomater.*, 2010, **31**, 438-448.
19. J. Massey, K. Nicole Power, I. Manners and M. A. Winnik, *J. Am. Chem. Soc*, 1998, **120**, 9533-9540.
20. J. C. Foster, S. Varlas, B. Couturaud, Z. Coe and R. K. O'Reilly, *J. Am. Chem. Soc*, 2019, **141**, 2742-2753.
21. U. Tritschler, S. Pearce, J. Gwyther, G. R. Whittell and I. Manners, *Macromol.*, 2017, **50**, 3439-3463.
22. S. Song, X. Liu, E. Nikbin, J. Y. Howe, Q. Yu, I. Manners and M. A. Winnik, *J. Am. Chem. Soc*, 2021.
23. L. Jia, A. Petretic, G. Molev, G. Guerin, I. Manners and M. A. Winnik, *ACS Nano*, 2015, **9**, 10673-10685.
24. X. Li, Y. Gao, C. E. Boott, M. A. Winnik and I. Manners, *Nat. Commun.*, 2015, **6**, 8127.
25. M. Inam, G. Cambridge, A. Pitto-Barry, Z. P. L. Laker, N. R. Wilson, R. T. Mathers, A. P. Dove and R. K. O'Reilly, *Chem. Sci.*, 2017, **8**, 4223-4230.
26. X. Wang, G. Guerin, H. Wang, Y. Wang, I. Manners and M. A. Winnik, *Science*, 2007, **317**, 644-647.
27. J. B. Gilroy, T. Gadt, G. R. Whittell, L. Chabanne, J. M. Mitchels, R. M. Richardson, M. A. Winnik and I. Manners, *Nat Chem*, 2010, **2**, 566-570.
28. T. Gädt, N. S. Ieong, G. Cambridge, M. A. Winnik and I. Manners, *Nat. Mater.*, 2009, **8**, 144-150.
29. Y. Cha, C. Jarrett-Wilkins, M. A. Rahman, T. Zhu, Y. Sha, I. Manners and C. Tang, *ACS Macro Lett.*, 2019, **8**, 835-840.

30. J. R. Finnegan, X. He, S. T. G. Street, J. D. Garcia-Hernandez, D. W. Hayward, R. L. Harniman, R. M. Richardson, G. R. Whittell and I. Manners, *J. Am. Chem. Soc*, 2018, **140**, 17127-17140.
31. N. Petzetakis, A. P. Dove and R. K. O'Reilly, *Chem. Sci.*, 2011, **2**, 955-960.
32. C. Wang, F. Huang, X. Huang, G. Lu and C. Feng, *Macromol. Rapid Commun.*, **n/a**, 2300482.
33. N. M. Warne, A. Elbourne, M. P. Tran, J. R. Finnegan, O. M. Feeney and K. Kempe, *Polym. Chem.*, 2023, DOI: 10.1039/d3py00399j.
34. J. Wang, W. Zhu, B. Peng and Y. Chen, *Polymer*, 2013, **54**, 6760-6767.
35. S. Ganda and M. H. Stenzel, *Prog. Polym. Sci*, 2020, **101**, 101195.
36. L. Macfarlane, C. Zhao, J. Cai, H. Qiu and I. Manners, *Chem. Sci.*, 2021, **12**, 4661-4682.
37. J. R. Finnegan, E. H. Pilkington, K. Alt, M. A. Rahim, S. J. Kent, T. P. Davis and K. Kempe, *Chem. Sci.*, 2021, **12**, 7350-7360.
38. Z. Li, Y. Zhang, L. Wu, W. Yu, T. R. Wilks, A. P. Dove, H.-M. Ding, R. K. O'Reilly, G. Chen and M. Jiang, *ACS Macro Lett.*, 2019, **8**, 596-602.
39. S. T. G. Street, Y. He, X.-H. Jin, L. Hodgson, P. Verkade and I. Manners, *Chem. Sci.*, 2020, **11**, 8394-8408.
40. S. Lei, J. Tian, Y. Kang, Y. Zhang and I. Manners, *J. Am. Chem. Soc*, 2022, **144**, 17630-17641.
41. Y. Gao, H. Qiu, H. Zhou, X. Li, R. Harniman, M. A. Winnik and I. Manners, *J. Am. Chem. Soc*, 2015, **137**, 2203-2206.
42. J. Schöbel, M. Burgard, C. Hils, R. Dersch, M. Dulle, K. Volk, M. Karg, A. Greiner and H. Schmalz, *Angew. Chem. Int. Ed.*, 2017, **56**, 405-408.
43. J. Tian, Y. Zhang, L. Du, Y. He, X.-H. Jin, S. Pearce, J.-C. Eloi, R. L. Harniman, D. Alibhai, R. Ye, D. L. Phillips and I. Manners, *Nat Chem*, 2020, **12**, 1150-1156.
44. S. Shin, F. Menk, Y. Kim, J. Lim, K. Char, R. Zentel and T.-L. Choi, *J. Am. Chem. Soc*, 2018, **140**, 6088-6094.
45. A. Rajak and A. Das, *Angew. Chem. Int. Ed.*, 2022, **61**.
46. J. Schöbel, M. Karg, D. Rosenbach, G. Krauss, A. Greiner and H. Schmalz, *Macromol.*, 2016, **49**, 2761-2771.
47. S. Ganda, C. K. Wong and M. H. Stenzel, *Macromol.*, 2021, **54**, 6662-6669.
48. A. Nazemi, C. E. Boott, D. J. Lunn, J. Gwyther, D. W. Hayward, R. M. Richardson, M. A. Winnik and I. Manners, *J. Am. Chem. Soc*, 2016, **138**, 4484-4493.
49. Z. Tong, Y. Su, Y. Jiang, Y. Xie, S. Chen and R. K. O'Reilly, *Macromol.*, 2021, **54**, 2844-2851.
50. M. C. Arno, M. Inam, Z. Coe, G. Cambridge, L. J. Macdougall, R. Keogh, A. P. Dove and R. K. O'Reilly, *J. Am. Chem. Soc*, 2017, **139**, 16980-16985.
51. J. R. Finnegan, L. I. FitzGerald, M. Z. Chen, N. M. Warne, D. Yuen, T. P. Davis, A. P. R. Johnston and K. Kempe, *Nano Lett.*, 2023, DOI: 10.1021/acs.nanolett.3c03342.

52. J. Lyu, Y. Li, Z. Li, P. Polanowski, J. K. Jeszka, K. Matyjaszewski and W. Wang, *Angew. Chem. Int. Ed.*, 2023, **62**.
53. S. Kaga, T. N. Gevrek, A. Sanyal and R. Sanyal, *J. Polym. Sci., Part A: Polym. Chem.*, 2016, **54**, 926-934.
54. J. N. Baxter and N. E. Bibler, *Chem. Phys.*, 1970, **53**, 3444-3450.
55. A. Karki, R. Baral, S. Karki, B. Neupane, P. Koirala, S. Baral and S. Panta, *CUPMAP*, 2021, DOI: 10.38093/cupmap.896273.
56. P. O. Staneke, G. Groothuis, S. Ingemann and N. M. M. Nibbering, *Int. J. Mass Spectrom.*, 1995, **142**, 83-93.
57. T. T. Truong, S. H. Thai, H. T. Nguyen, V.-D. Vuong and L.-T. T. Nguyen, *J. Polym. Sci., Part A: Polym. Chem.*, 2017, **55**, 928-939.
58. S. P. S. Koo, M. M. Stamenović, R. A. Prasath, A. J. Inglis, F. E. Du Prez, C. Barner-Kowollik, W. Van Camp and T. Junker, *J. Polym. Sci., Part A: Polym. Chem.*, 2010, **48**, 1699-1713.
59. P. Derboven, D. R. D'hooge, M. M. Stamenovic, P. Espeel, G. B. Marin, F. E. Du Prez and M.-F. Reyniers, *Macromol.*, 2013, **46**, 1732-1742.
60. Y. Su, Y. Jiang, L. Liu, Y. Xie, S. Chen, Y. Wang, R. K. O'Reilly and Z. Tong, *Macromol.*, 2022.
61. T. Xia, Z. Tong, Y. Xie, M. C. Arno, S. Lei, L. Xiao, J. Y. Rho, C. T. J. Ferguson, I. Manners, A. P. Dove and R. K. O'Reilly, *J. Am. Chem. Soc*, 2023, DOI: 10.1021/jacs.3c08770.
62. J. T. Lovegrove, R. Raveendran, P. Spicer, S. Förster, C. J. Garvey and M. H. Stenzel, *ACS Macro Lett.*, 2023, **12**, 344-349.
63. N. Serio, K. Miller and M. Levine, *Chem. Commun.*, 2013, **49**, 4821.

5.6 Supporting figures

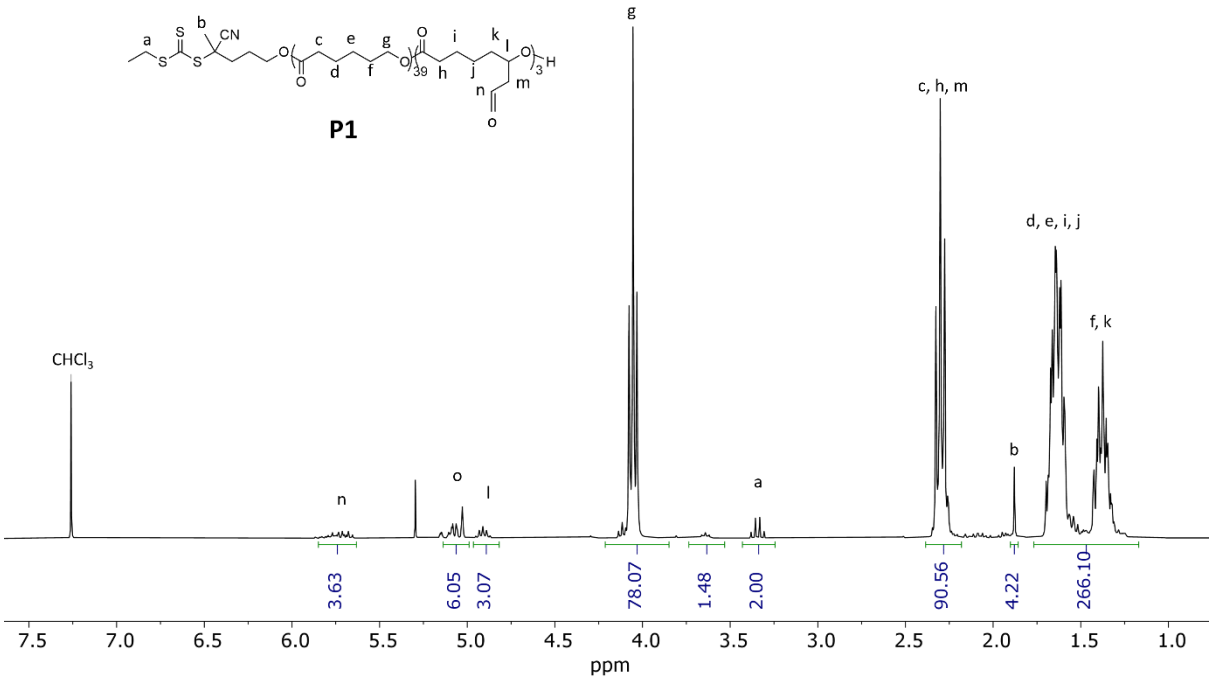


Figure S5.1. ^{1}H NMR spectrum of PCL_{39}-*co*-$PACL_3$ (P1), 300 MHz, 298 K, $CDCl_3$.

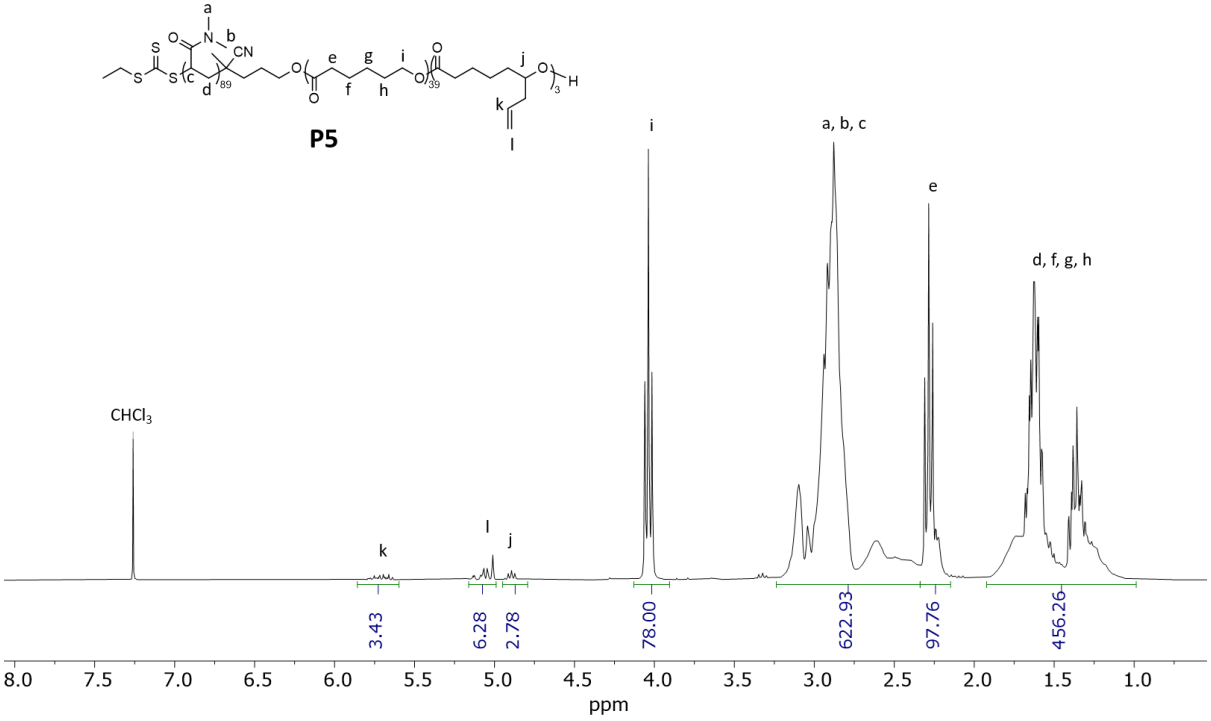


Figure S5.2. ^{1}H NMR spectrum of $PDMA_{89}$-*b*-PCL_{39}-*co*-$PACL_3$ (P5), 300 MHz, 298 K, $CDCl_3$.

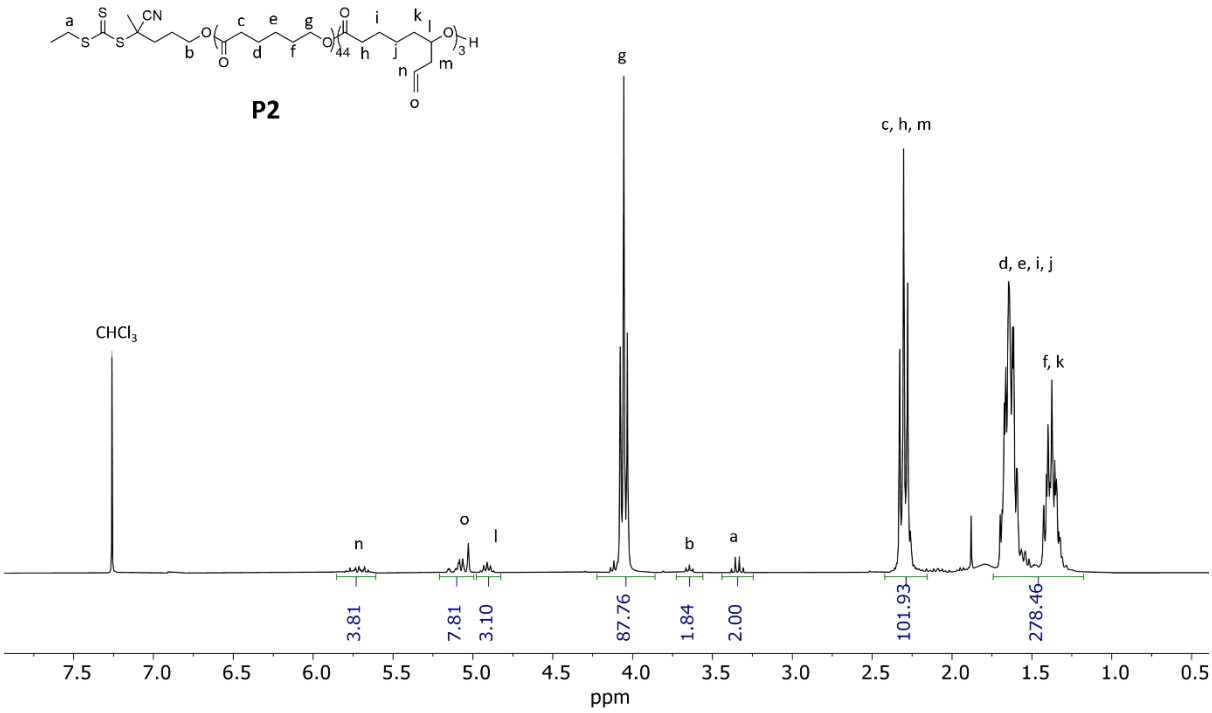


Figure S5.3. ^1H NMR spectrum PCL_{44}-*co*-$PACL_3$ (P2), 300 MHz, 298 K, $CDCl_3$.

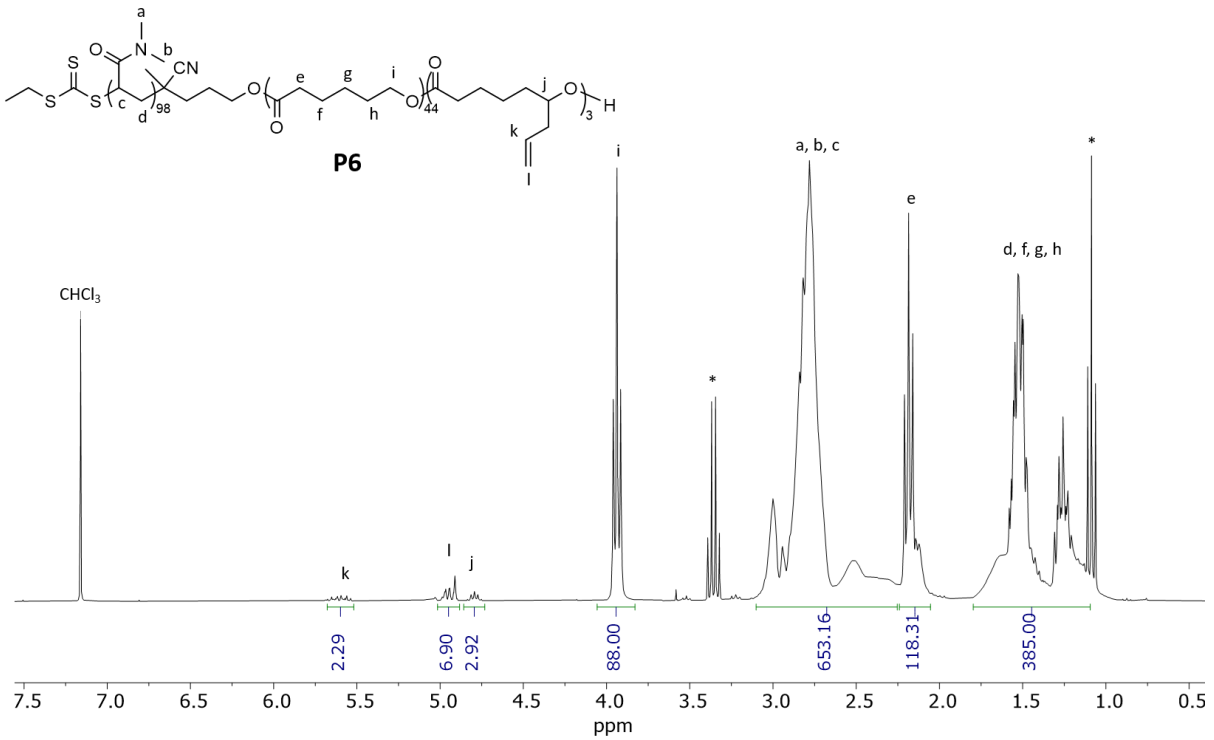


Figure S5.4. ^{1}H NMR spectrum of $PDMA_{94}$-*b*-PCL_{44}-*co*-$PACL_3$ (P6), 300 MHz, 298 K, $CDCl_3$. * Correspond to diethyl ether peaks.

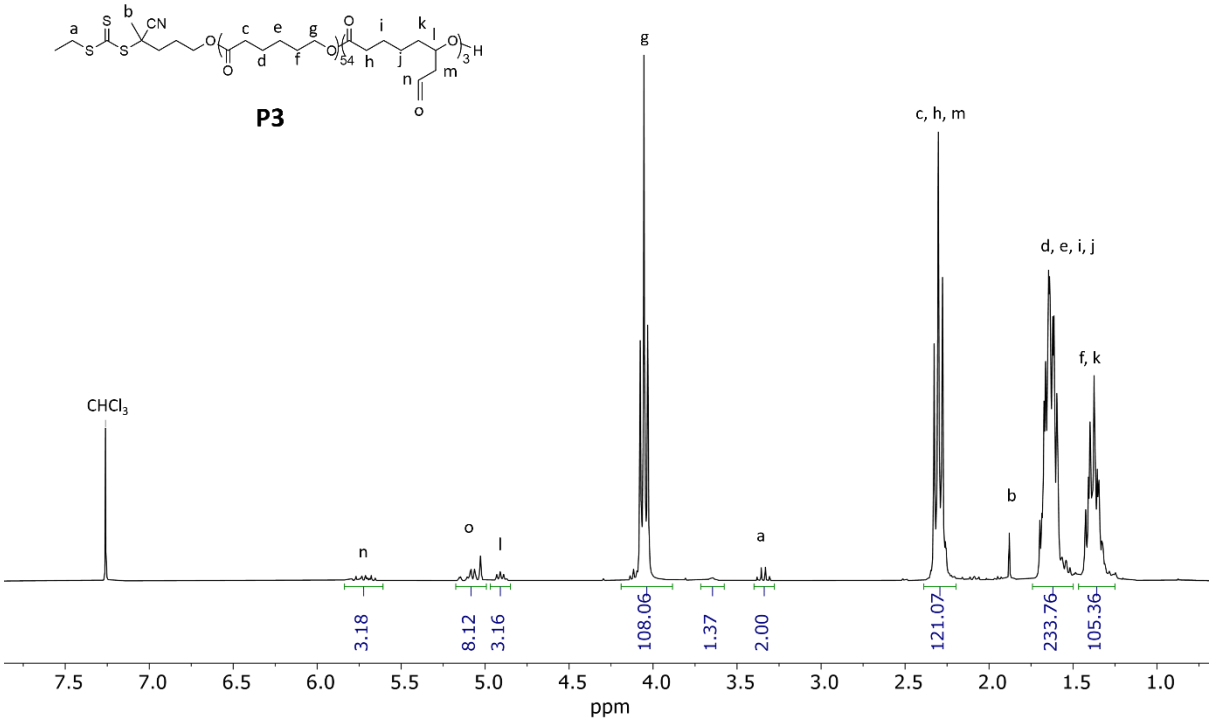


Figure S5.5. ^{1}H NMR spectrum PCL_{54}-*co*-$PACL_3$ (P3), 300 MHz, 298 K, $CDCl_3$.

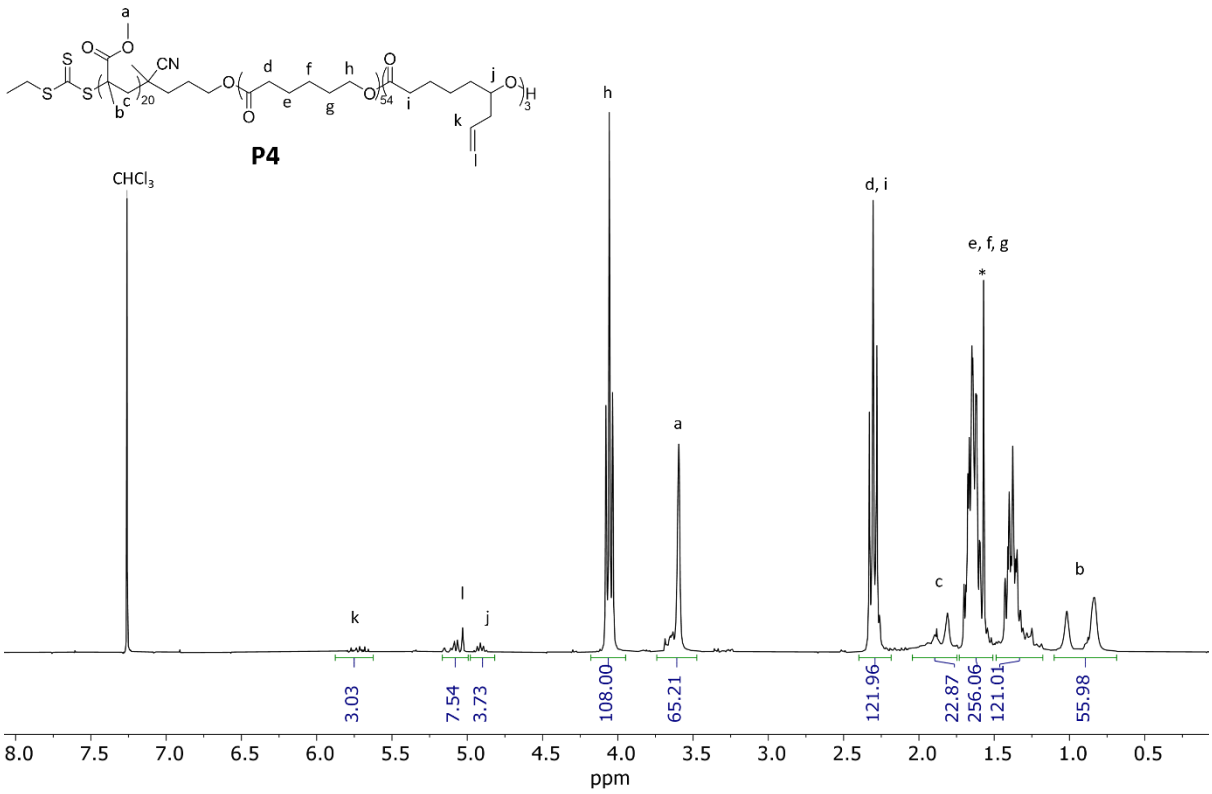


Figure S5.6. ^{1}H NMR spectrum of $PMMA_{20}$-*b*-PCL_{54}-*co*-$PACL_3$ (P4), 300 MHz, 298 K, $CDCl_3$. * Correspond to water peak.

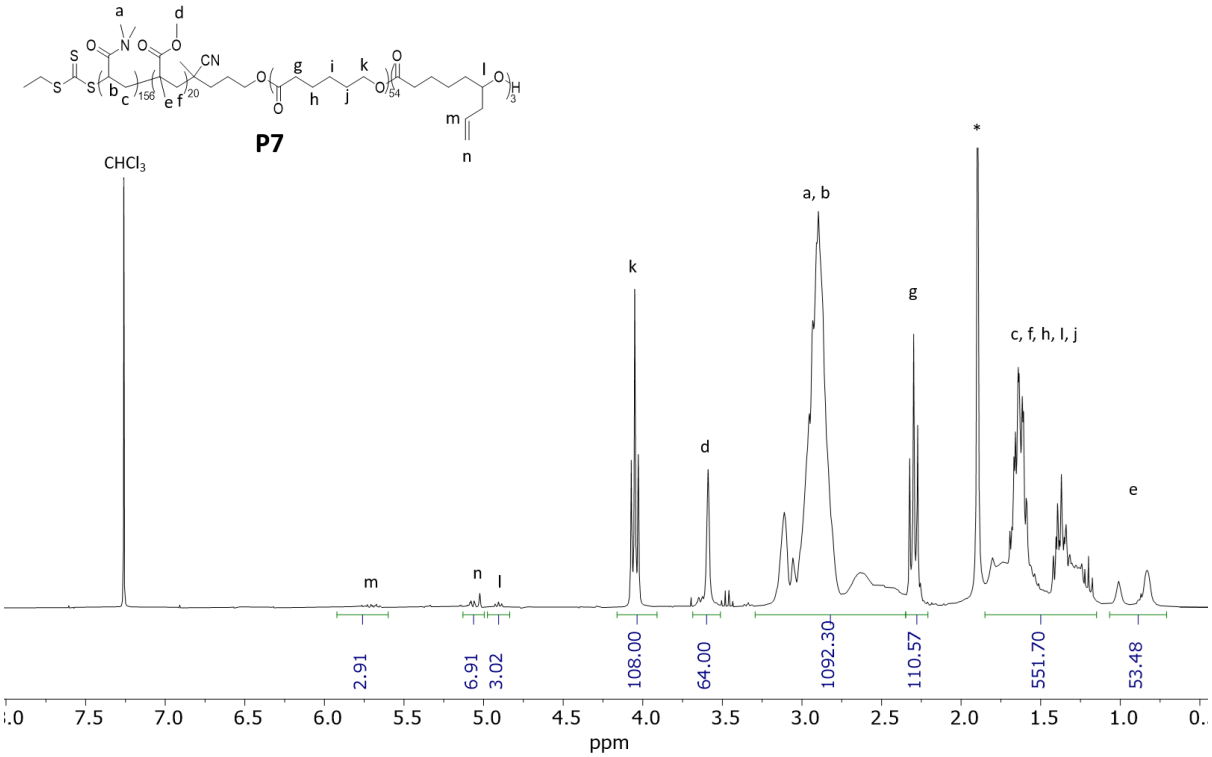


Figure S5.7. ^{1}H NMR spectrum of $PDMA_{156}$-*b*-$PMMA_{20}$-*b*-PCL_{54}-*co*-$PACL_3$ (P7), 300 MHz, 298 K, $CDCl_3$. * Correspond to acetone peak.

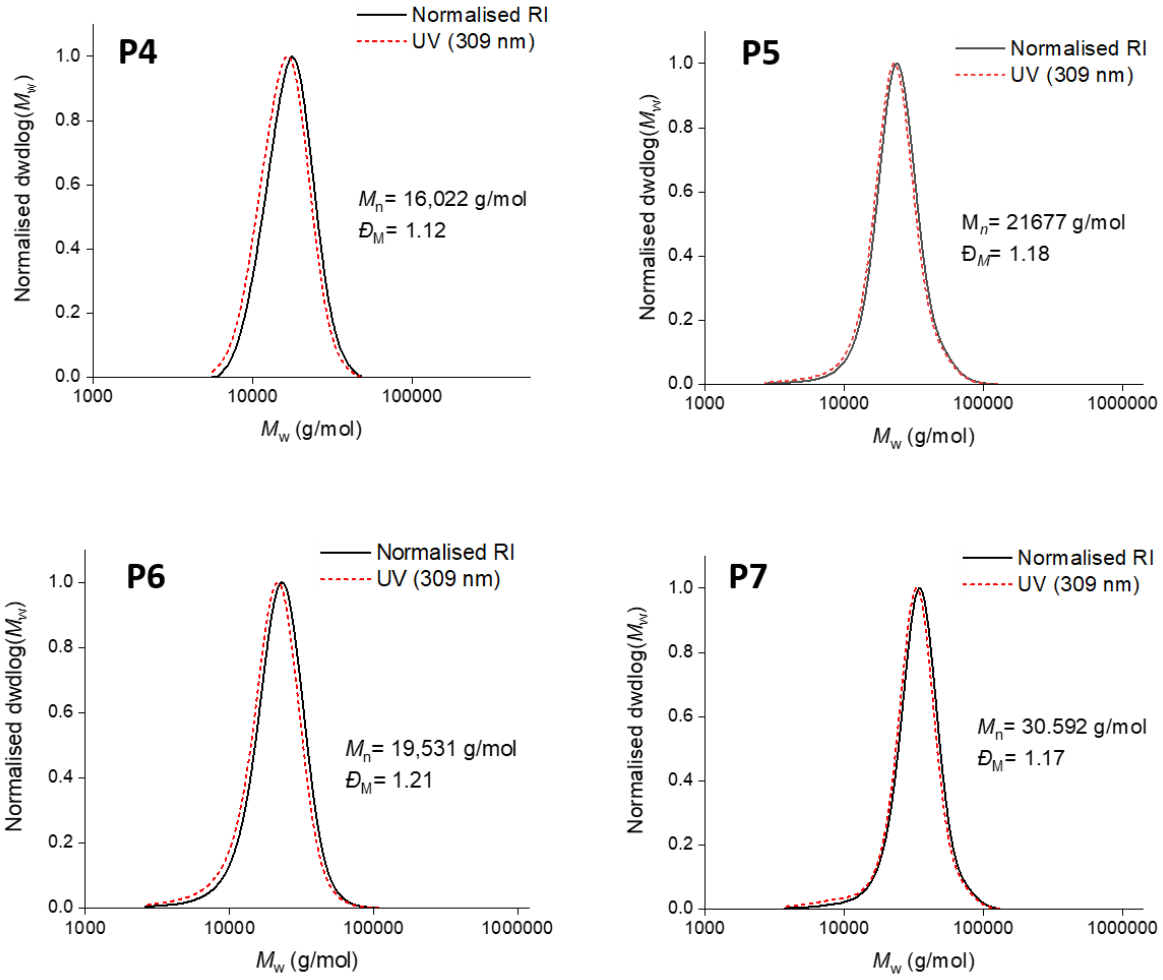


Figure S5.8. SEC chromatograms of block copolymers P4 to P7 in Table 5.2 ($CHCl_3$, with 0.5% Et_3N, PMMA standard).

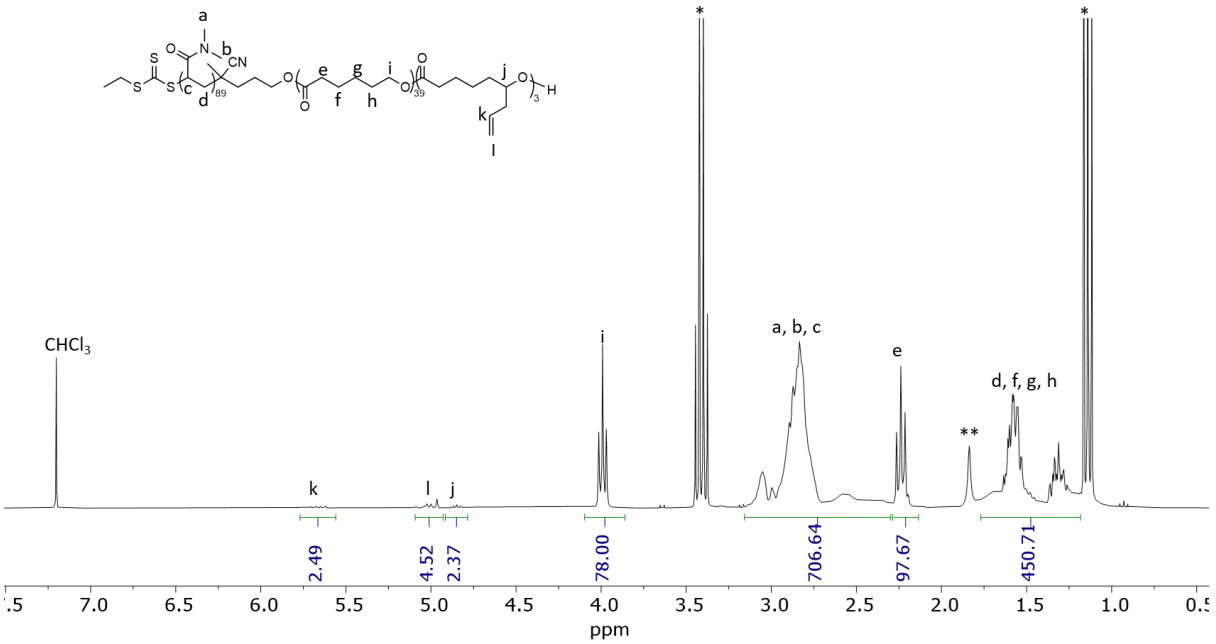


Figure S5.9. ^{1}H NMR spectrum (300 MHz, 298 K, $CDCl_3$) of $PDMA_{89}$-*b*-PCL_{39}-*co*-$PACL_3$ (P5) after photo-initiated thiol-ene addition in chloroform (DMPA, 320-500 nm, 20 min). * Correspond to diethyl ether peaks. ** Correspond to acetone peak.

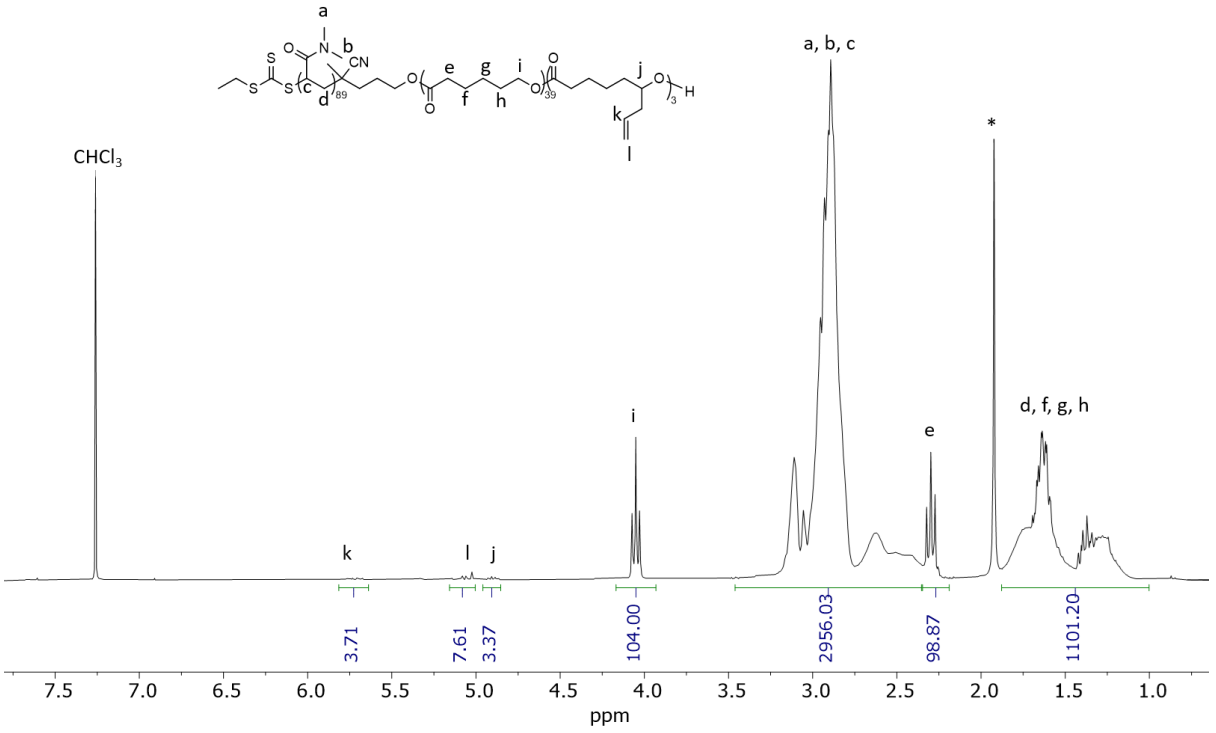


Figure S5.10. ^{1}H NMR spectrum (300 MHz, 298 K, $CDCl_3$) of $PDMA_{89}$-*b*-PCL_{39}-*co*-$PACL_3$ (P5) after photo-initiated thiol-ene addition in THF (DMPA, 320-500 nm, 30 min). * Correspond to diethyl ether peaks. ** Correspond to acetone peak.

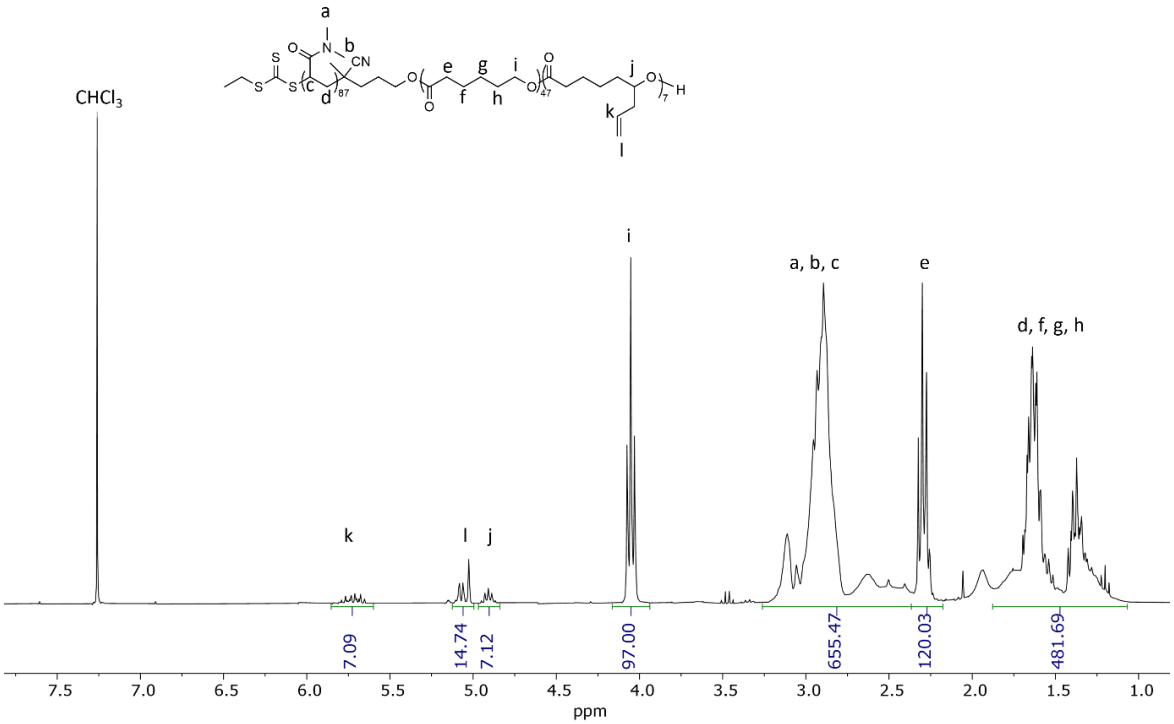


Figure S5.11. ^{1}H NMR spectrum (300 MHz, 298 K, $CDCl_3$) of $PDMA_{87}$-*b*-PCL_{47}-*co*-$PACL_7$ after photo-initiated thiol-ene addition in chloroform (Irgacure 918, 405 nm, 180 min).

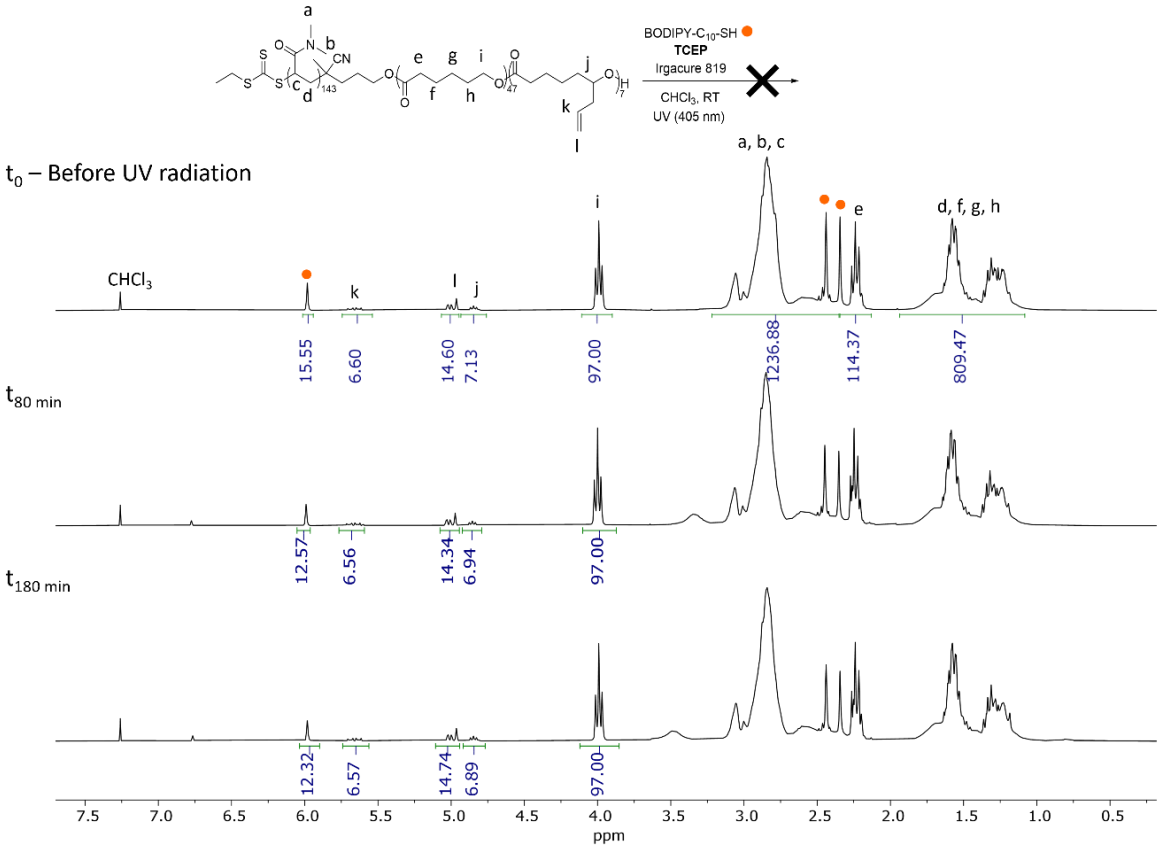


Figure S5.12. Stacked ^1H NMR spectra (300 MHz, 298 K, $CDCl_3$) of photo-initiated thiol-ene addition in chloroform (Irgacure 918, 405 nm) of $PDMA_{143}$-*b*-PCL_{47}-*co*-$PACL_7$ in the presence of TCEP.

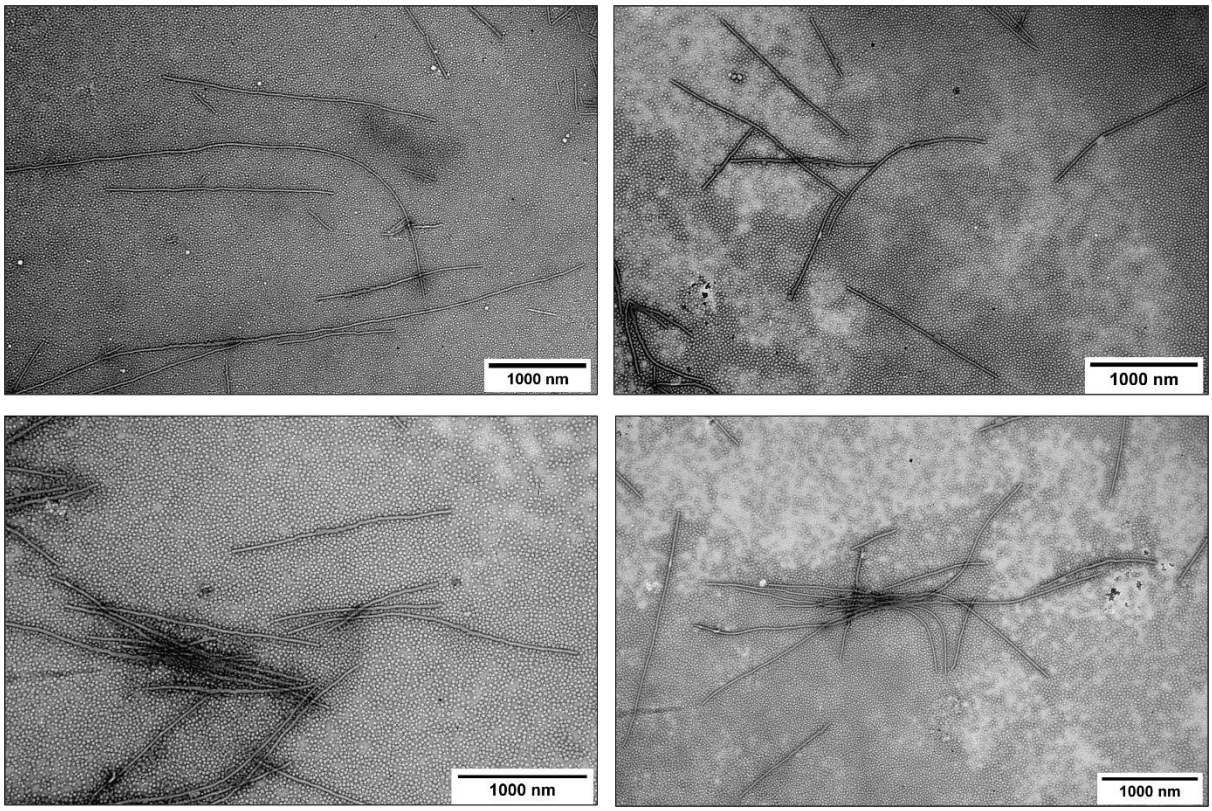


Figure S5.13. TEM images of cylindrical micelles obtained from the CDSA in ethanol of $PDMA_{89}$-*b*-PCL_{39}-*co*-$PACL_3$ block copolymer (P5) after 3 weeks of aging at room temperature. Samples were negatively stained using uranyl acetate (0.5 wt %).

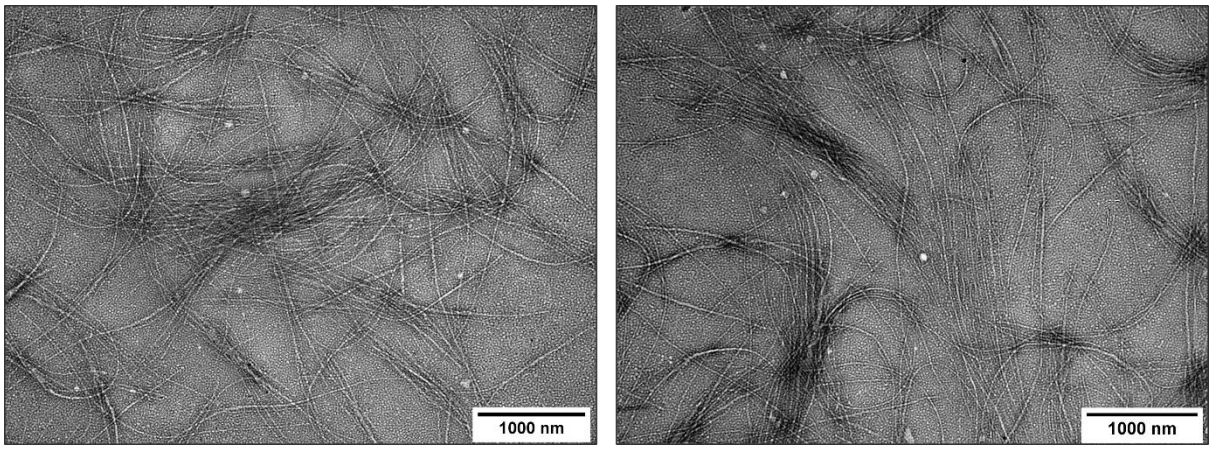


Figure S5.14. TEM images of cylindrical micelles obtained from the CDSA in ethanol of BODIPY-conjugated $PDMA_{89}$-*b*-PCL_{39}-*co*-$PACL_3$ block copolymer (BODIPY-P5) after 3 weeks of aging at room temperature. Samples were negatively stained using uranyl acetate (0.5 wt.%).

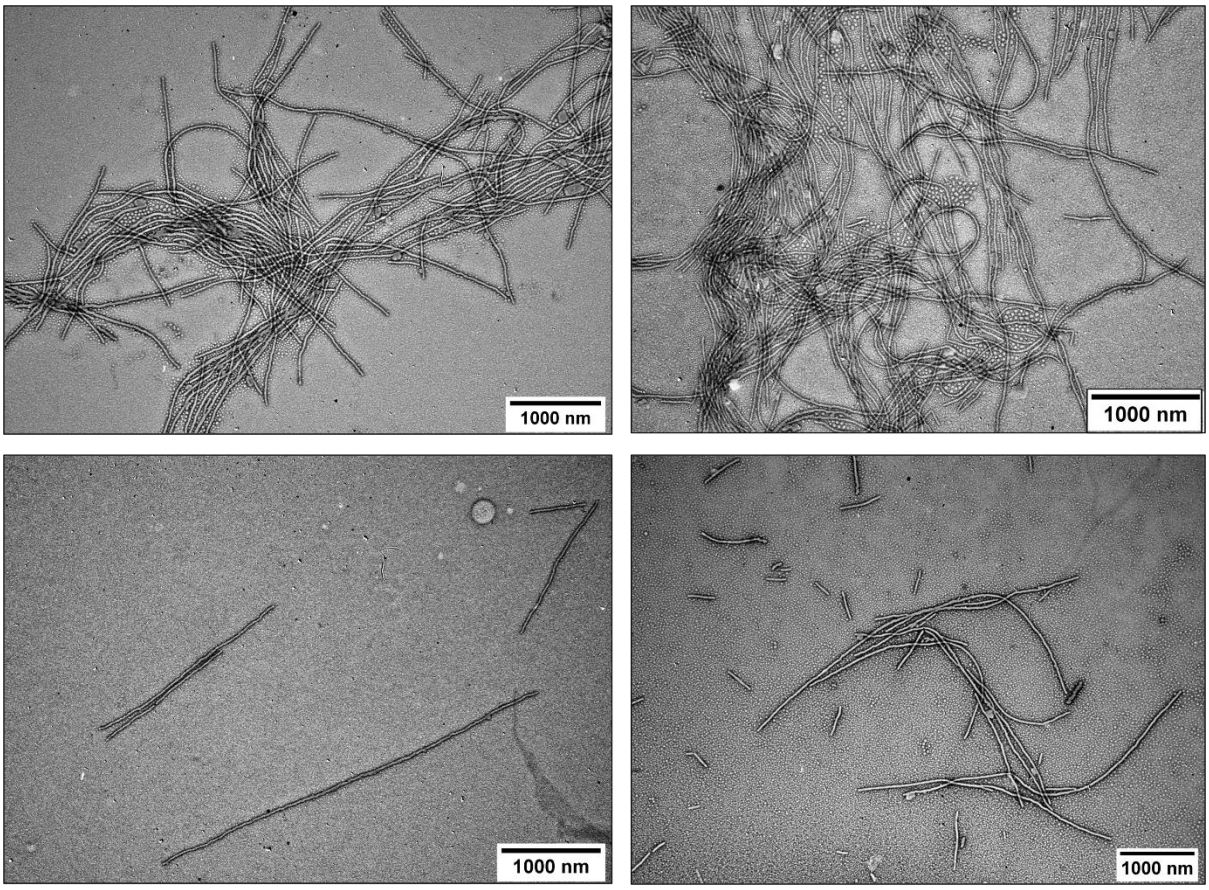


Figure S5.15. TEM micrographs of cylindrical micelles obtained from the CDSA in ethanol of $PDMA_{156}$-*b*-$PMMA_{20}$-*b*-PCL_{54}-*co*-$PACL_3$ block copolymer (P7) after 1 week of aging at room temperature. Samples were negatively stained using uranyl acetate (0.5 wt %).

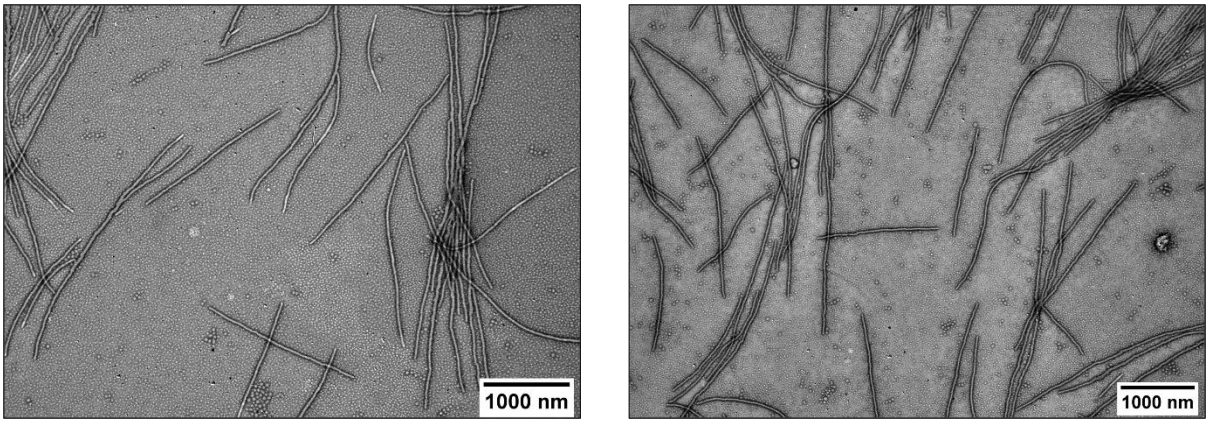


Figure S5.16. TEM micrographs of cylindrical micelles obtained from the CDSA of $PDMA_{156}$-*b*-$PMMA_{20}$-*b*-PCL_{54}-*co*-$PACL_3$ block copolymer (P7) after dialysis to water. Samples were negatively stained using uranyl acetate (0.5 wt %).

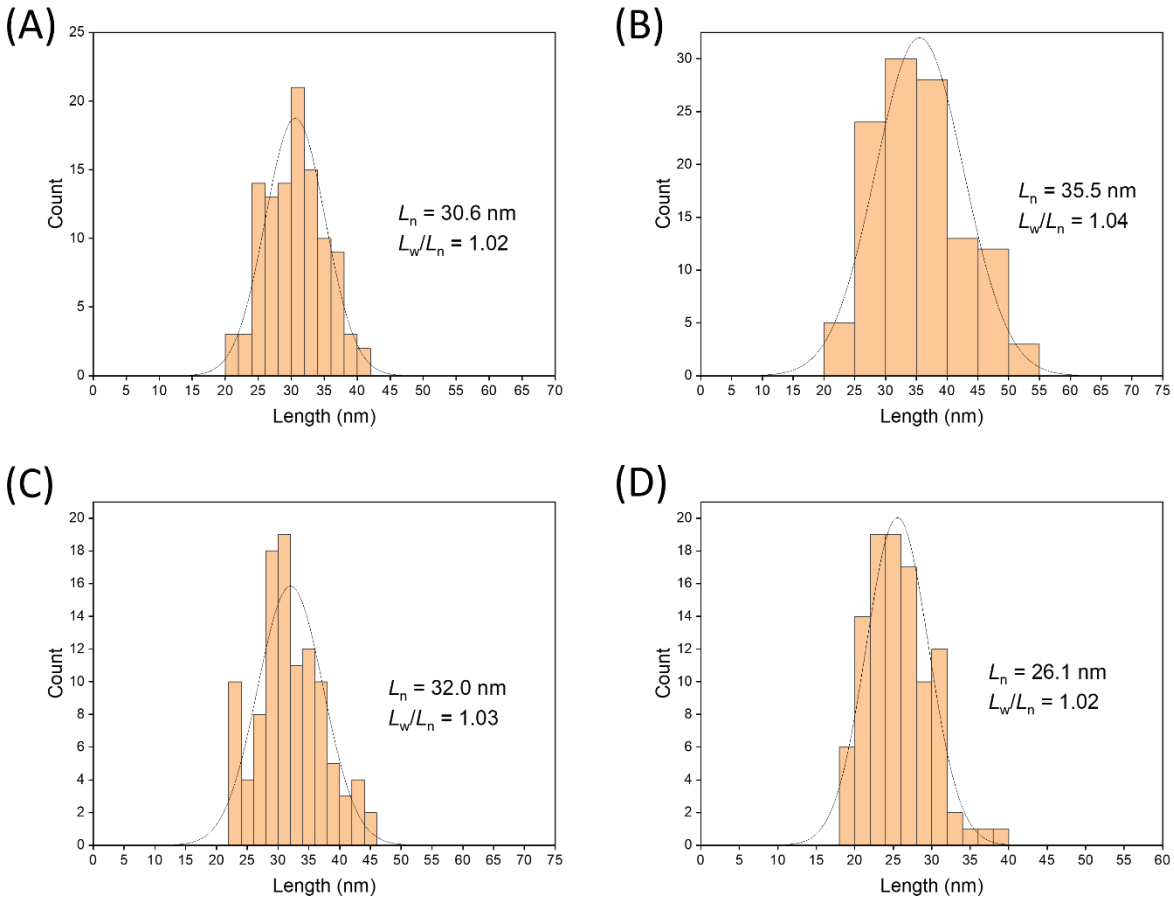


Figure S5.17. Number length average (L_n) plots, calculated from particle analysis-based TEM images, for the polymer seeds after sonication for 4 h (20 s – ON; 100 s – OFF). **A)** $PDMA_{117}$-*b*-PCL_{48} seed solution. **B)** $PDMA_{154}$-*b*-PCL_{48} seed solution. **C)** of $PDMA_{94}$-*b*-PCL_{44}-*co*-$PACL_3$ seed solution. **D)** of $PDMA_{112}$-*b*-PCL_{53}-*co*-$PACL_3$ seed solution.

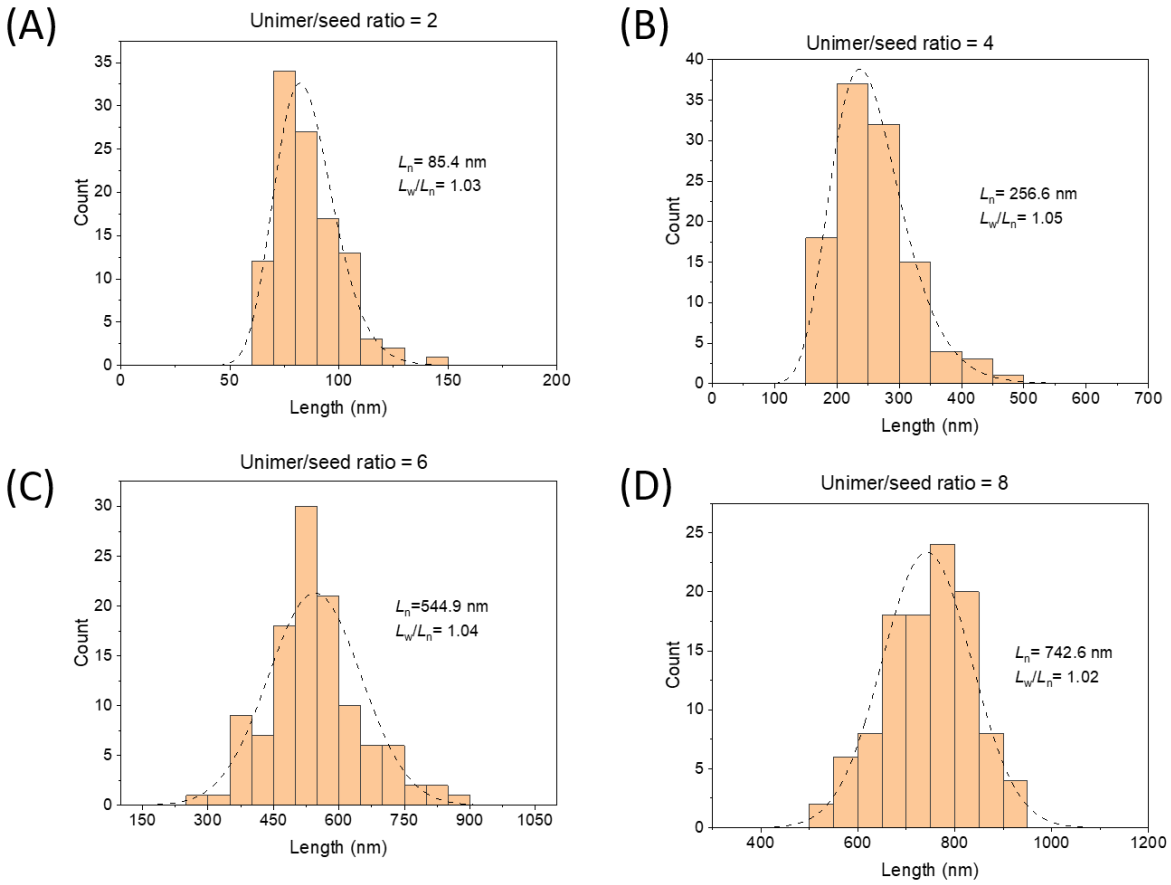


Figure S5.18. Number length average (L_n) plots, calculated from particle analysis-based TEM images, for the 1D epitaxial growth of PDMA$_{94}$-*b*-PCL$_{44}$-*co*-PACL$_3$ (P6) block copolymer **(A)** m_{unimer}/m_{seed} = 2; **(B)** m_{unimer}/m_{seed} = 4; **(C)** m_{unimer}/m_{seed} = 6; **(D)** m_{unimer}/m_{seed} = 8; using PDMA$_{154}$-b-PCL$_{48}$ seeds.

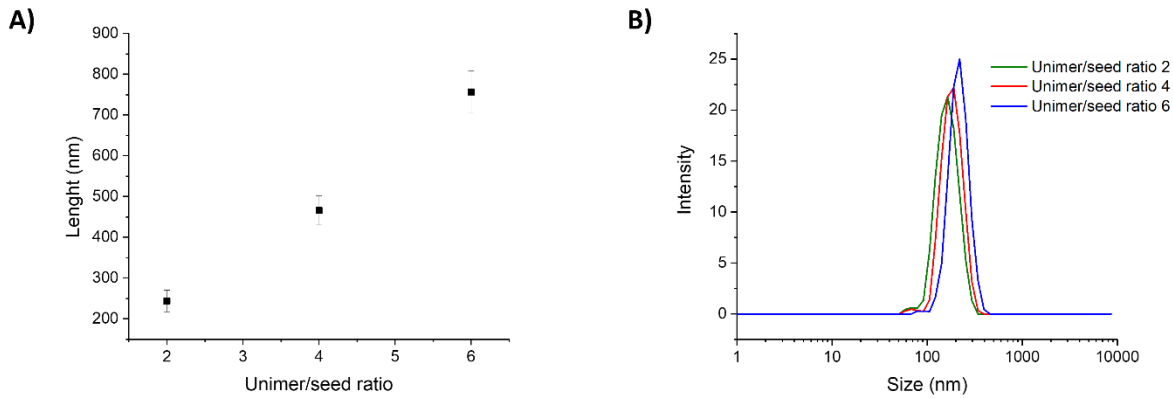


Figure S5.19. A) Number length average (L_n) vs unimer/seed ratio, calculated from particle analysis-based TEM images, for the 1D epitaxial growth of bodipy conjugated PDMA$_{156}$-*b*-PMMA$_{20}$-*b*-PCL$_{54}$-*co*-PACL$_3$ (Bodipy-P7) block copolymers using PDMA$_{154}$-*b*-PCL$_{48}$ seeds. **B)** Size distribution averaged by intensity over the same time. Measured by dynamic light scattering (DLS). Each sample was repeated three times.

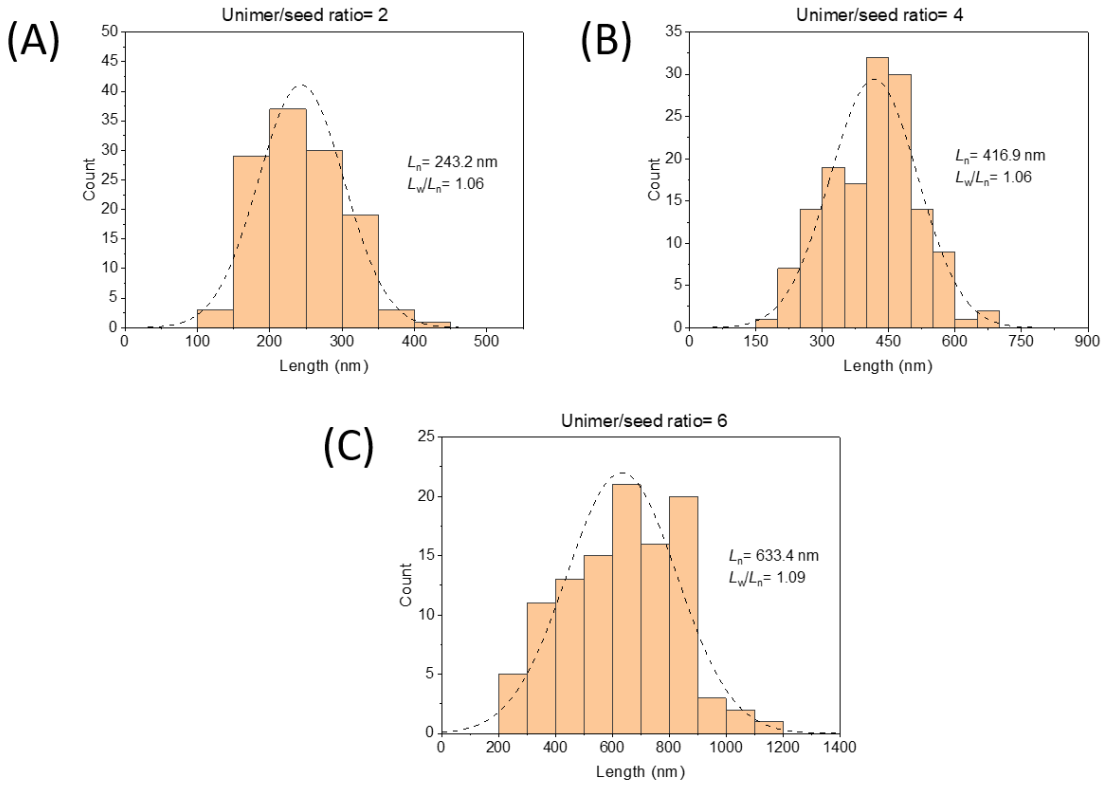


Figure S5.20. Number length average (L_n) plots, calculated from particle analysis-based TEM images, for the 1D epitaxial growth of BODIPY-P7 block copolymers **(A)** m_{unimer}/m_{seed} = 2; **(B)** m_{unimer}/m_{seed} = 4; **(C)** m_{unimer}/m_{seed} = 6; using $PDMA_{154}$-*b*-PCL_{48} seeds.

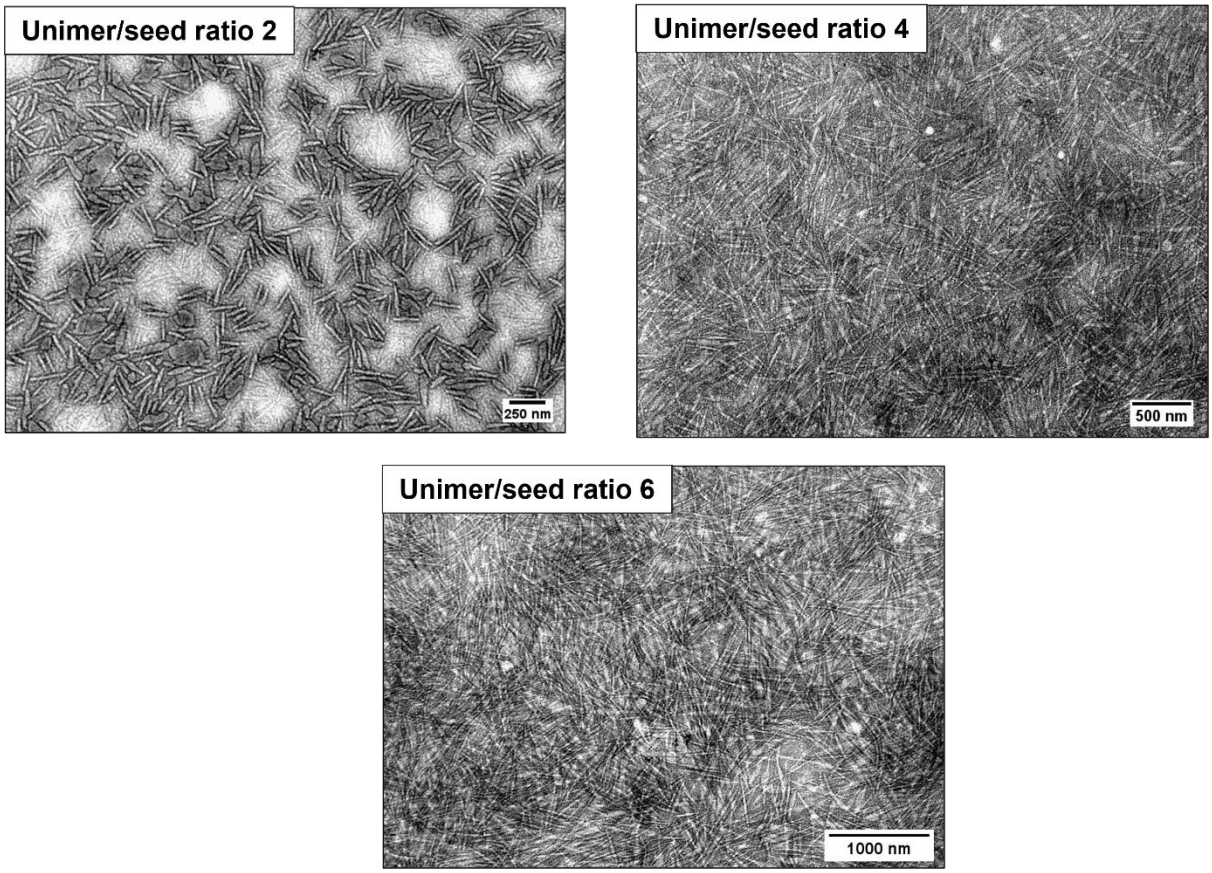
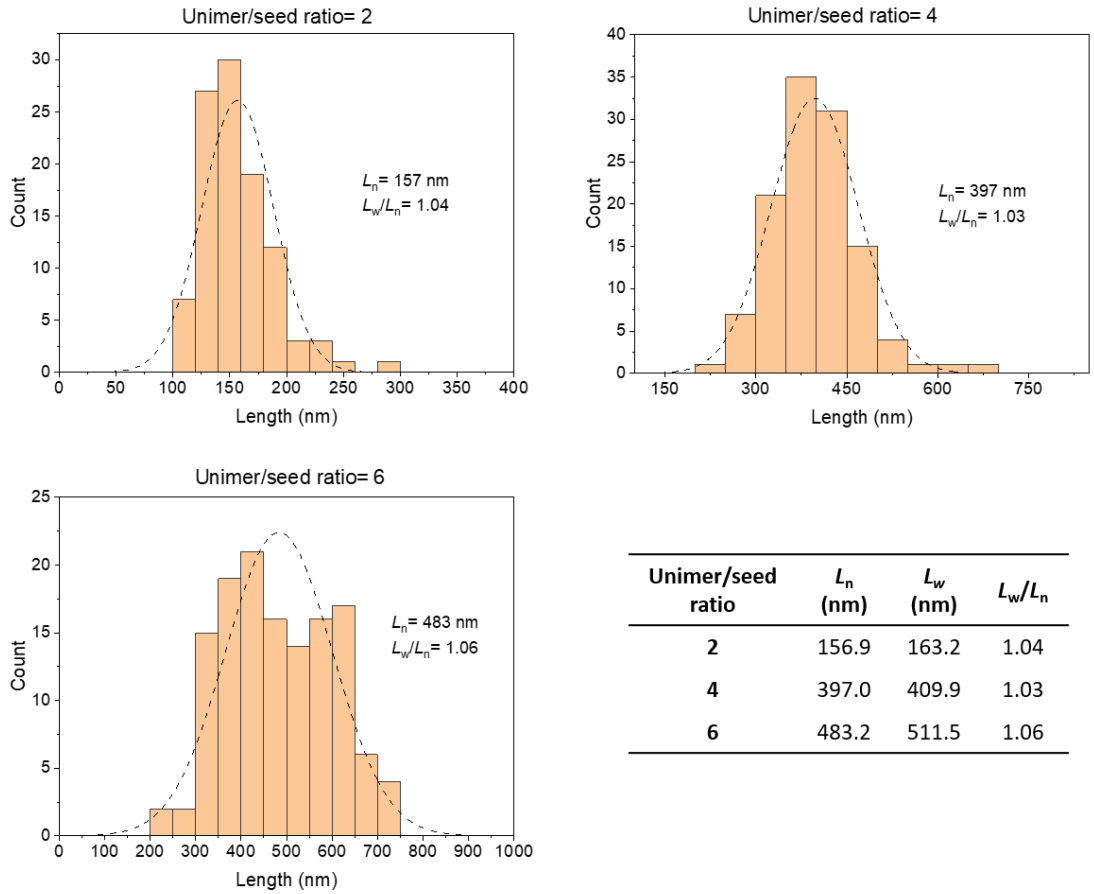


Figure S5.21. TEM micrographs for the 1D epitaxial growth $PDMA_{94}$-*b*-PCL_{44}-*co*-$PACL_3$ (P6) block copolymers using P6 crystalline seeds with unimer/seed ratios of 2, 4, and 6. Samples were negatively stained using uranyl acetate (0.5 wt %).



Unimer/seed ratio	L_n (nm)	L_w (nm)	L_w/L_n
2	156.9	163.2	1.04
4	397.0	409.9	1.03
6	483.2	511.5	1.06

Figure S5.22. Number length average (L_n) plots, calculated from particle analysis-based TEM images, for the 1D epitaxial growth PDMA$_{94}$-*b*-PCL$_{44}$-*co*-PACL$_3$ (P6) block copolymers using P6 crystalline seeds with unimer/seed ratios of 2, 4, and 6. Table summary with lengths.

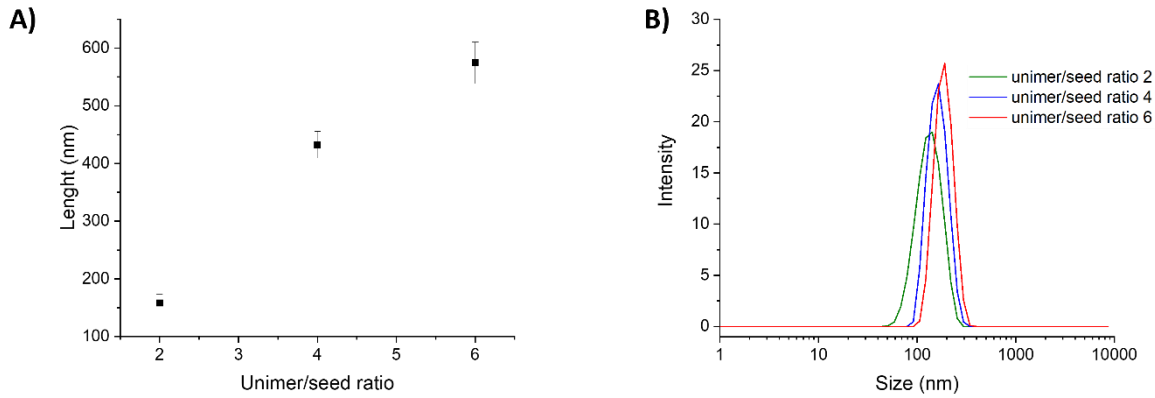


Figure S5.23. A) Number length average (L_n) *vs.* unimer/seed ratio, calculated from particle analysis-based TEM images, for the 1D epitaxial growth of PDMA$_{94}$-*b*-PCL$_{44}$-*co*-PACL$_3$ (P6) block copolymers using P6 crystalline seeds with unimer/seed ratios of 2, 4, and 6. **B)** Size distribution averaged by intensity over the same time. Measured by dynamic light scattering (DLS). Each sample was repeated three times.

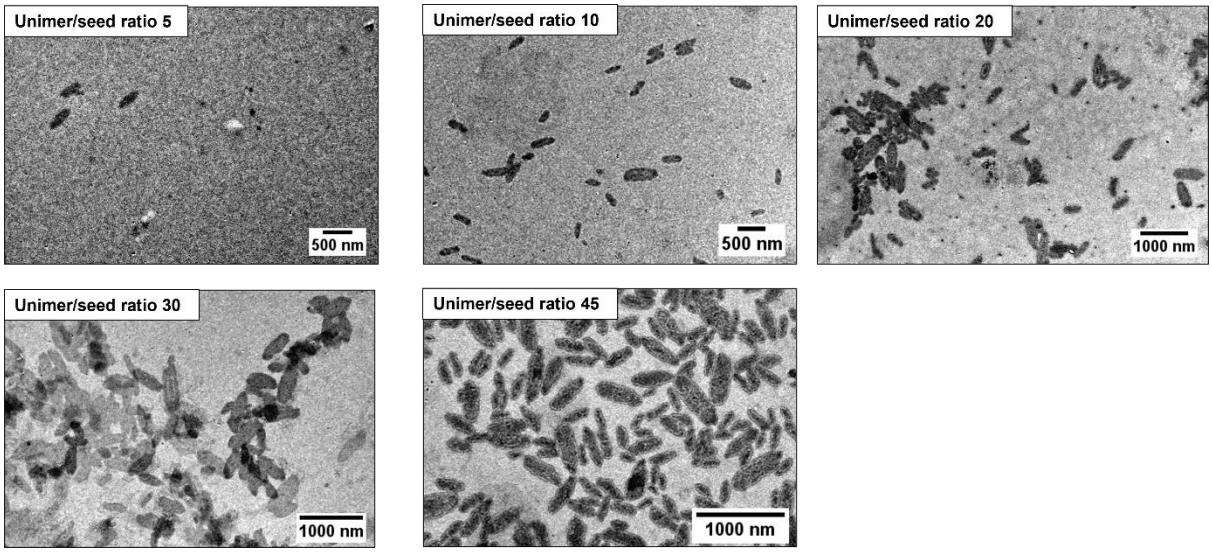
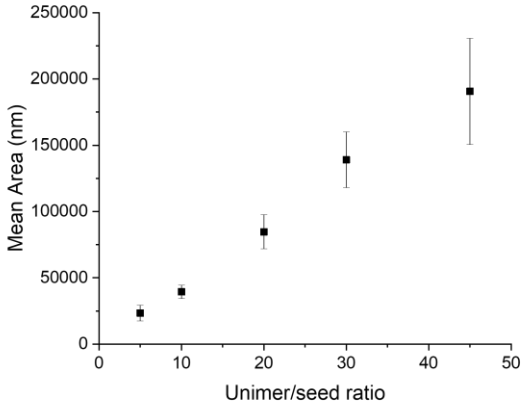


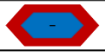
Figure S5.24. TEM micrographs for the 2D epitaxial growth of $PDMA_{94}$-*b*-PCL_{44}-*co*-$PACL_3$ (P6) block copolymers using $PDMA_{154}$-*b*-PCL_{48} seeds with different unimer/seed ratios. Samples were negatively stained using uranyl acetate (0.5 wt %).



Unimer/seed ratio	Average length (L_n) (nm)	Average width (nm)	Average area (A_n) (nm²)
5	280.5	122.2	23459.5
10	355.6	137.7	39494.3
20	474.5	186.4	84716.1
30	524.7	205.5	139028.2
45	588.0	219.8	190636.3

Figure S5.25. Number area average (A_n) *vs*. unimer/seed ratio, for the 2D epitaxial growth of $PDMA_{94}$-*b*-PCL_{44}-*co*-$PACL_3$ (P6) block copolymers using $PDMA_{154}$-*b*-PCL_{48} seeds, calculated from particle analysis-based TEM images. Table summary with particle dimensions.

Table S5.1. Summary for 2D uniform multilayered platelets.

Block copolymers		Average length (L_n) (nm)	Average width (W_n) (nm)	Average area (A_n) (nm²)
$PDMA_{127}$-*b*-PCL_{48} + $PDMA_{122}$-*b*-PCL_{53}-*co*-$PACL_3$		1949	574	966303
$PDMA_{127}$-*b*-PCL_{48} + bodipy conjugated $PDMA_{156}$-*b*-$PMMA_{20}$-*b*-PCL_{54}-*co*-$PACL_3$		2001	647	1314025

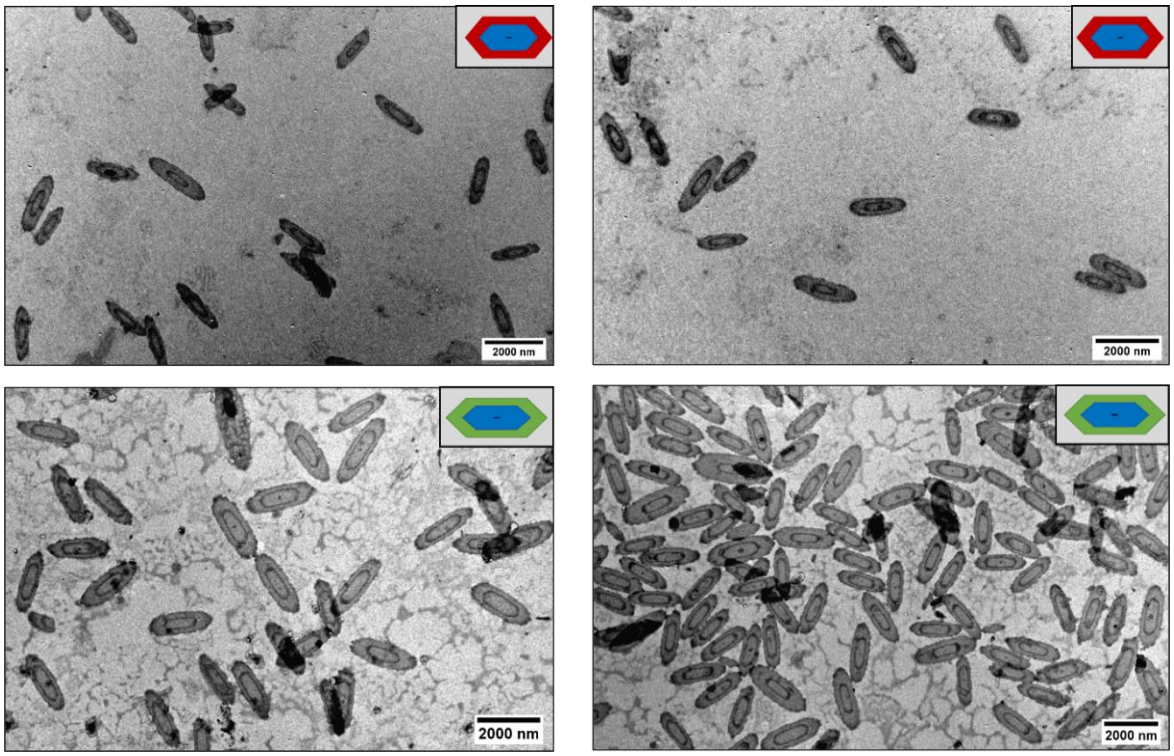


Figure S5.26. TEM micrographs of 2D multilayered platelets described in Table S5.1. Samples were negatively stained using uranyl acetate (0.5 wt %).

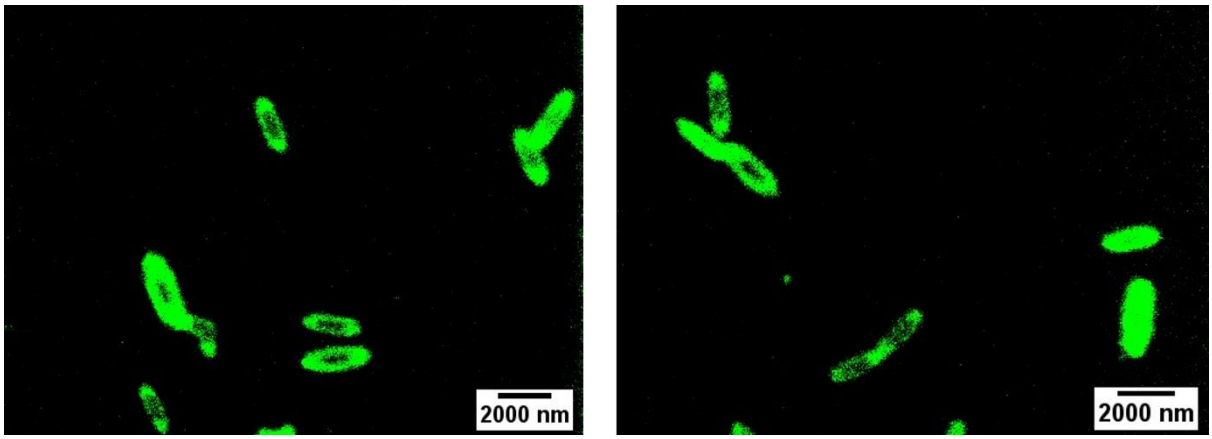


Figure S5.27. Confocal images of $PDMA_{127}$-*b*-PCL_{48} + BODIPY-conjugated conjugated $PDMA_{156}$-*b*-$PMMA_{20}$-*b*-PCL_{54}-*co*-$PACL_3$ multilayered platelets, sowing the fluorescence field. Image taken by Mr. Tianlai Xia.

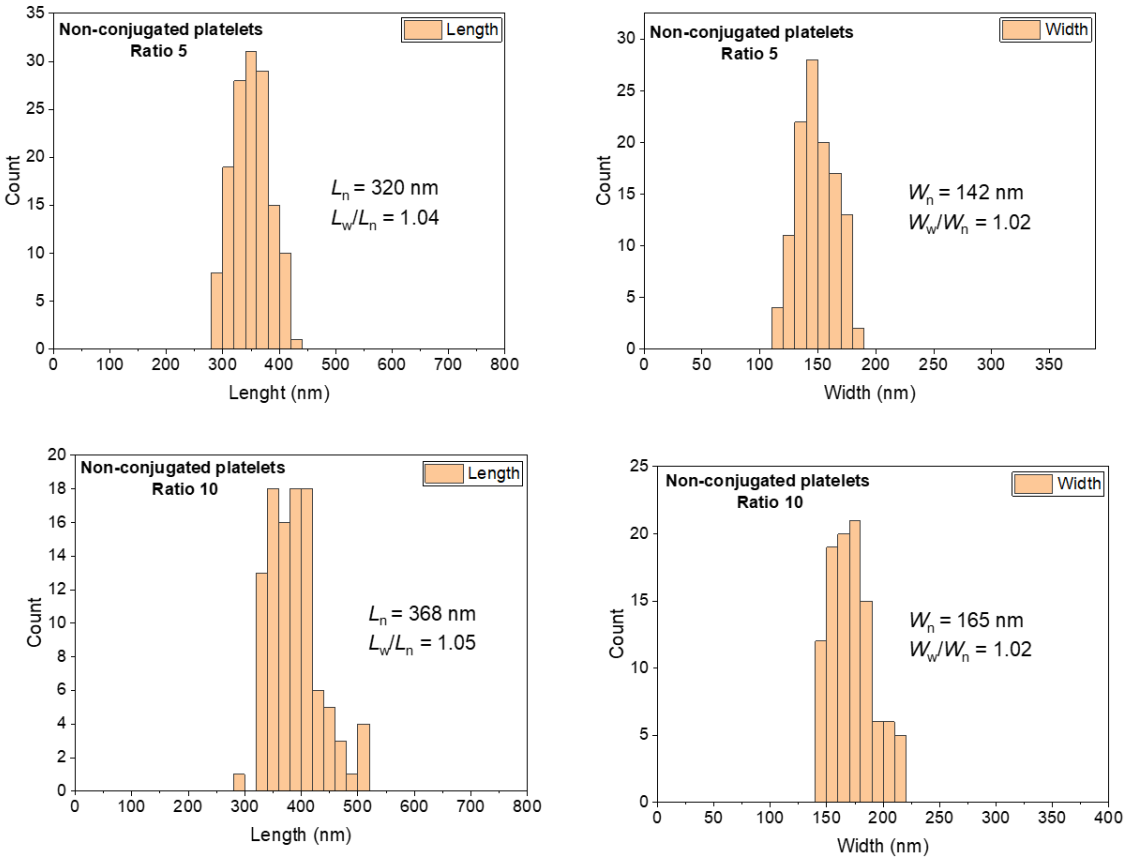


Figure S5.28. Number length average (L_n) and number witdh average (W_n) of 2D platelets used in biological studies of $PDMA_{94}$-*b*-PCL_{44}-*co*-$PACL_3$ unimer co-crystallized with PCL_{48} homopolymer onto seeds of $PDMA_{154}$-*b*-PCL_{48} with m_{unimer}/m_{seeds} ratios 5 and 10.

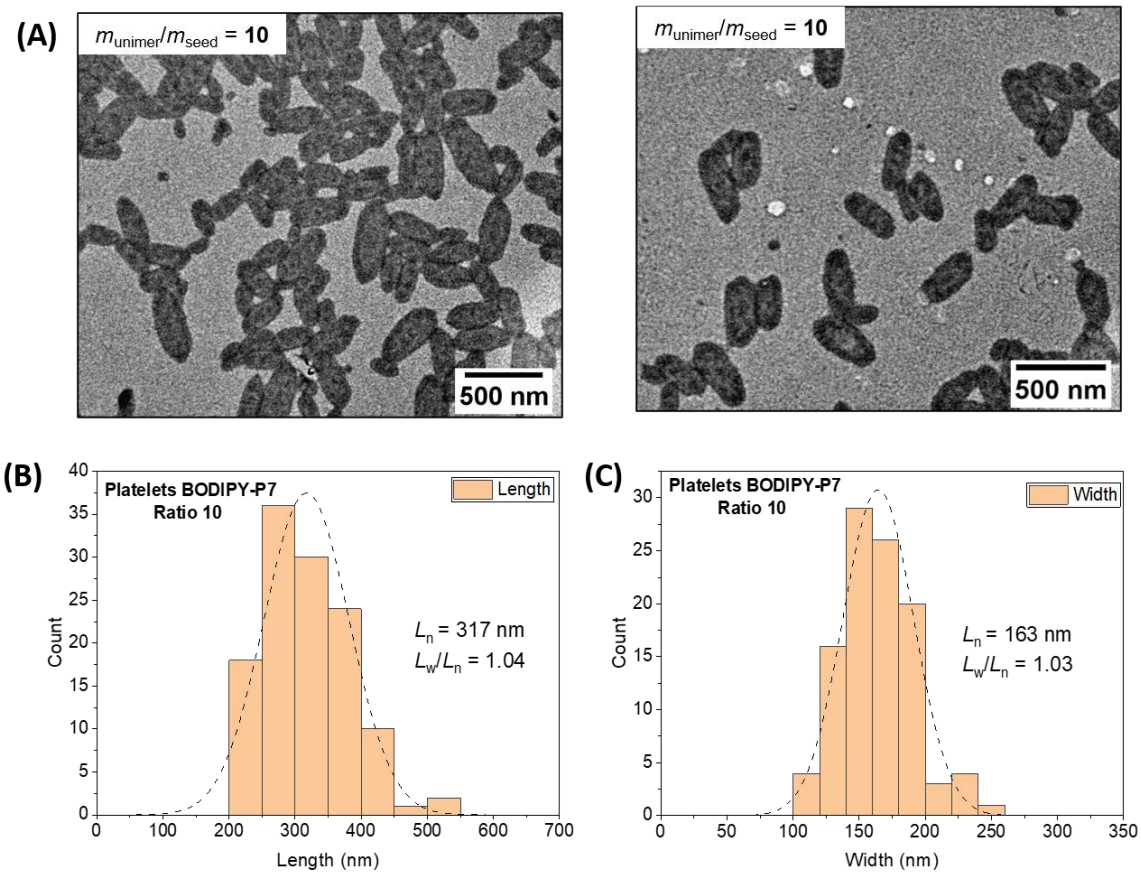


Figure S5.29. 2D platelets used in biological studies **A)** TEM micrographs of 2D living growth solutions of BODIPY-conjugated $PDMA_{156}$-*b*-$PMMA_{20}$-*b*-PCL_{54}-*co*-$PACL_3$ (BODIPY-P7) unimer co-crystallized with PCL_{48} homopolymer onto seeds of $PDMA_{154}$-*b*-PCL_{48} where m_{PCL48}/m_{unimer} = 1, with m_{unimer}/m_{seeds} ratio 10. **(B)** Number length average (L_n) and **(C)** Number witdh average (W_n) of respective particles.

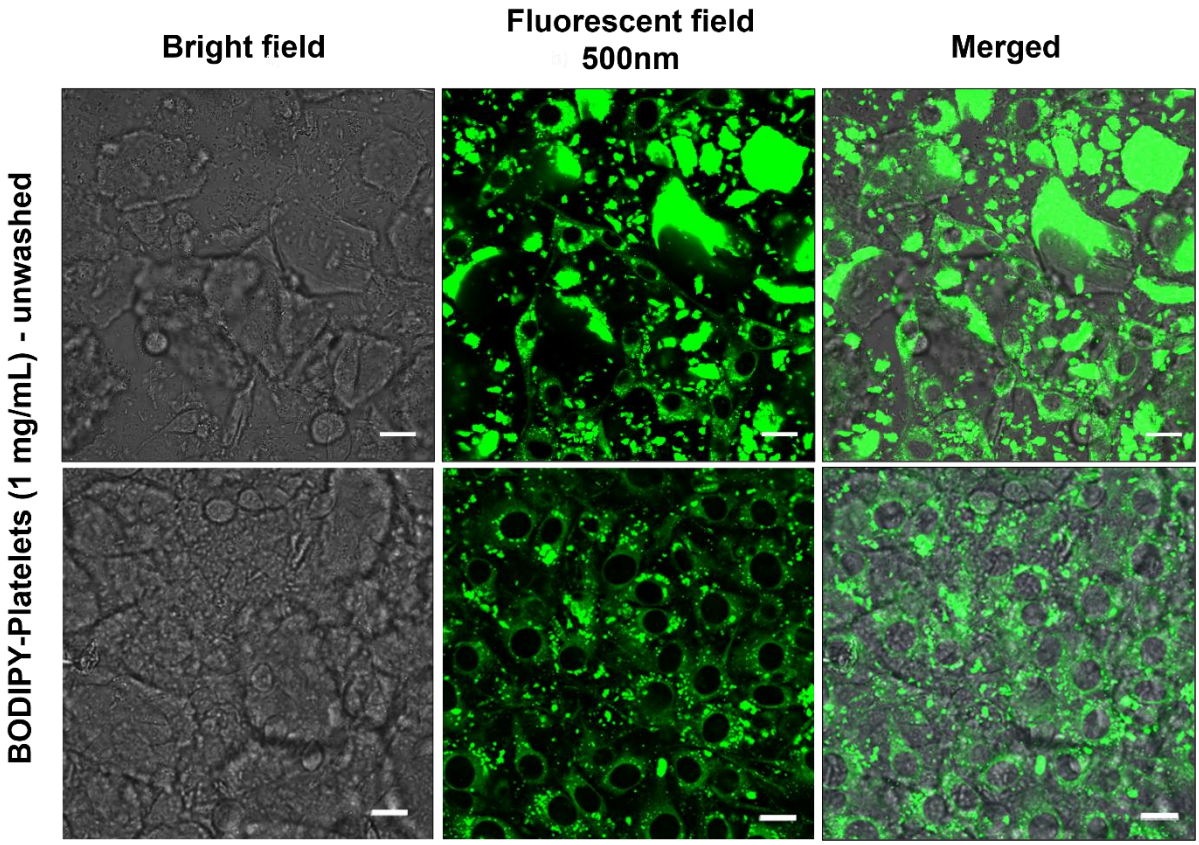


Figure S5.30. Confocal imaging NIH 3T3 + BODIPY-Platelets (1 mg mL^{-1}) before washing the excess of nanoparticle aggregates with PBS (*Z*-scan slides). Showing bright, fluorescent (λ = 503 -512 nm), and merged fields. Scale bar = 20 µm.

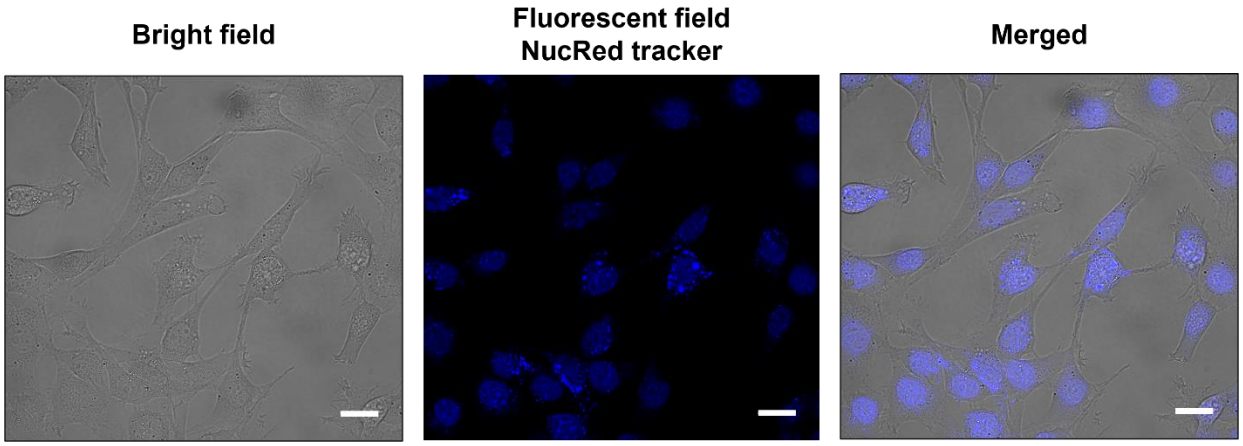


Figure S5.31. Confocal imaging of NIH 3T3 control group during internalisation studies after addition of NucRed Live 647, showing the bight, fluorescent (λ = 647 – 665 nm), and merged fields. Scale bar = 20 µm.

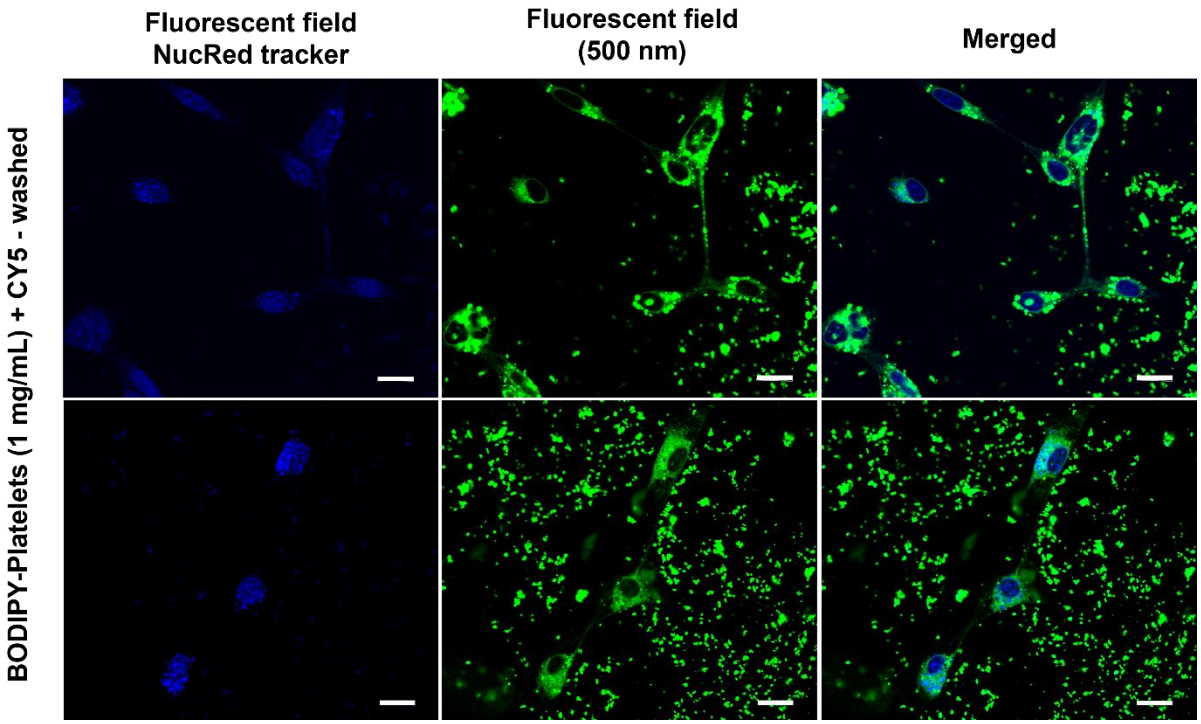


Figure S5.32. Confocal imaging NIH 3T3 + BODIPY-Platelets (1 mg mL^{-1}) after washing the with PBS and adding cell tracker (NucRed Live 647). Showing fluorescent fields at λ = 647 – 665 nm (NucRed) and λ = 503 – 512 nm (BODIPY), and merged fields. Scale bar = 20 µm.

Chapter 6.

Conclusions

6 Conclusions and future perspectives

In this thesis well-defined anisotropic micro and nanoparticles with small molecules covalently attached to their inner core were assessed by the combination of living ring-opening polymerisation (ROP), RAFT polymerisation, click chemistry and crystallisation-driven self-assembly (CDSA) techniques. In order to investigate the effect of polymer composition on crystallinity, materials were designed using two different strategies that were focused on the organocatalytic ROP of substituted ε-caprolactones. In Chapter 2, highly stereoregular poly(ε-allyl-ε-caprolactones) (PACLs) were prepared by polymerising enantioenriched ε-allyl-ε-caprolactone (εACL) using diphenyl phosphate and stereoselective TRIP BINOL as catalysts. Despite the use of monomers with high stereocontrol in their composition, only amorphous polymers with low T_g values (T_g = −54.5 to −68.0 °C) were obtained. Alternatively, a new approach based on copolymerisation strategies of ε-caprolactone (εCL) and εACL *via* ring-opening copolymerisation was presented in Chapter 3. PCL-based copolymers with allyl incorporations ranging from 6 to 40 wt.% presented predictable molecular weights and narrow dispersities (M_n = 11.6–21.3 kDa and $Đ_M$ = 1.45–1.08). Reaction kinetics and spectroscopy analysis revealed the formation of statistical PCL-*co*-PACL copolymers, in which the crystallinity of the copolymer was strongly related to the amount of allyl monomer incorporated. While copolymers with allyl incorporation up to 26 wt.% exhibited semicrystalline properties, higher functionalisation led to disruption of the crystallinity.

In Chapter 4, amphiphilic block copolymers containing a semicrystalline allyl-functional PCL-block were prepared *via* RAFT polymerisation. The addition of an excess of RAFT monomers was found to be crucial to achieve amphiphilic block polymers with controlled molecular weight and dispersity ($Đ_M \leq 1.3$). Following this, post-polymerisation modification was

performed for the addition of small thiols into the available allyl groups from PACL *via* thiol-ene click chemistry. Selected modified and non-modified copolymers were then assembled in different polar solvents *via* crystallisation-driven self-assembly (CDSA) to yield core-functionalised anisotropic micro- and nanostructures, whose final morphology could be predicted depending on the corona-core ratio and % of allyl-monomer incorporation. Moreover, parameters such as temperature, aging, percentage of thiol modification, and solvent conditions strongly affected the final morphology of the nanostructures. Finally, in Chapter 5, well-defined 1D cylindrical micelles and 2D single or double-layered platelets containing a small fluorescent BODIPY dye in the PCL core-forming block were accessed in various lengths by living CDSA. The nanostructures showed good stability in biologically relevant solvents as well as excellent biocompatibility in NIH 3T3 cells. Moreover, preliminary cell internalisation studies demonstrated that BODIPY-functionalised 2D single platelets were efficiently taken up to the cellular cytoplasm, proving the great potential of our system for drug delivery applications.

Overall, the preparation *via* crystallisation-driven self-assembly of biocompatible non-spherical nanoparticles with small molecules attached to the semicrystalline core-forming block was reported for the first time. In this work, copolymerisation studies demonstrated the formation of statistical PCL-*co*-PACL copolymers, in which the crystallinity was closely related to the allyl-monomer incorporation. However, the monomer sequencing, which has a great impact on the crystallisation process, was not fully investigated. Therefore, the calculation of monomer reactivity ratios could provide useful information to elucidate the structure of PCL-*co*-PACL copolymers and further insights into how the copolymer crystallises during self-assembly. Furthermore, initial cell studies with polymer solution and 2D nanoparticles demonstrated good biocompatibility and substantial nanoparticle internalisation.

Nevertheless, the significant difference in cell viability values between the polymer solution and 2D nanoparticles highlighted the need to further investigate the nanoparticles' stability in cell culture media. Additionally, the use of a quantitative methodology, which enables precise cell analysis, such as PCR techniques or flow cytometry, in combination with traditional viability essays would provide a valuable insight into the nanoparticles' cytotoxicity. On the other hand, further internalisation studies are required to determine the cell uptake pathway as well as the different biological responses for 1D and 2D micelles. Finally, exploring alternative click chemistry strategies to attach other small molecules or drugs into the nanoparticle core, as well as degradation studies and drug release kinetics would be of great importance to optimise the efficacy of the system for controlled release.

The true potential of this work lies in its versatility with respect to chemical handles that can be added within the polymer backbone without affecting its crystallisation. For example, the preparation of 2D multi-layered platelets or 1D patchy comicelles using block copolymers with various molecules attached to the core-block could lead to the design of multicompartmental delivery systems, in which each segment or layer of the nanoparticle has a different active principle. This would allow the development of tailored therapies with potential sustained or controlled drug release. Moreover, small molecules such as proteins, antibodies, or active metabolites can be added to the corona-block post-polymerisation, which could provide numerous recognition sites on the nanoparticle surface to promote active targeting of specific cell types. Therefore, the work presented in this thesis opens a new pathway to design functional 1D and 2D nanostructures that can be further investigated and translated into biomedical delivery systems.